C55.2:C61/2/991

# Proceedings of the Sixteenth Annual Climate Diagnostics Workshop

Dept. of Atmospheric Sciences
University of California, Los Angeles
Los Angeles, California
October 28-November 1, 1991

PENNSYLVANIA STATE
UNIVERSITY

APR 3 0 1992

DOCUMENTS COLLECTION
U.S. Depository Copy

**U.S. DEPARTMENT OF COMMERCE**
**National Oceanic and Atmospheric Administration**
National Weather Service
Climate Analysis Center / NMC

Publications listed below are available in both hard copy and microfiche form from the National Technical Information Service, U.S. Department of Commerce, Sills Building, 5285 Port Royal Road, Springfield, VA 22161. (Prices on request; order by accession number.)

If an author wishes to reference an article from any of the Proceedings, please include the appropriate number at the end of the reference. This allows various journals to accept these references more readily.

| PROCEEDINGS | ACCESSION NO. |
|---|---|
| First Climate Diagnostics Workshop | (PB264993) |
| Second Climate Diagnostics Workshop | (PB282151) |
| Third Climate Diagnostics Workshop | (PB298355) |
| Fourth Climate Diagnostics Workshop | (PB80-201130) |
| Fifth Climate Diagnostics Workshop | (PB81-222200) |
| Sixth Climate Diagnostics Workshop | (PB82-219486) |
| Seventh Climate Diagnostics Workshop | (PB83-208033) |
| Eighth Climate Diagnostics Workshop | (PB84-192418) |
| Ninth Climate Diagnostics Workshop | (PB85-183911) |
| Tenth Climate Diagnostics Workshop | * |
| Eleventh Climate Diagnostics Workshop | (PB87-175741) |
| Twelfth Climate Diagnostics Workshop | (PB88-191747) |
| Thirteenth Climate Diagnostics Workshop | (PB89-178115) |
| Fourteenth Climate Diagnostics Workshop | (PB90-198573) |
| Fifteenth Climate Diagnostics Workshop | (PB91-171082) |

* (The Proceedings of the Tenth Climate Diagnostics Workshop was combined with the First WMO Workshop on the Diagnosis and Prediction of Monthly and Seasonal Variations over the Globe. Reference is WMO/Long-Range Forecasting Research Report Series No. 6, Volumes I and II, WMO/TD-No. 87, January 1986.)

# Proceedings of the Sixteenth Annual Climate Diagnostics Workshop

Held at the

Dept. of Atmospheric Sciences
University of California, Los Angeles
Los Angeles, California

March 1992

**U.S. DEPARTMENT OF COMMERCE**
**Robert A. Mosbacher, Secretary**

**National Oceanic and Atmospheric Administration**
Dr. John A. Knauss, Under Secretary

National Weather Service
Dr. Elbert W. Friday, Jr., Assistant Administrator

## Sixteenth Annual
## Climate Diagnostics Workshop
## Los Angeles, CA
## October 28 - November 1, 1991

## PREFACE

The Sixteenth Annual Climate Diagnostics Workshop was hosted by the Department of Atmospheric Sciences at the University of California in Los Angeles. The Workshop was enhanced by the work of Dr. C. Roberto Mechoso and the UCLA organizing committee, who with the NMC/Climate Analysis Center jointly planned and organized the Workshop at the Lake Arrowhead Conference Center. The excellent facilities, arrangements, and hospitality provided by the UCLA staff made the Workshop a pleasant and intellectually stimulating experience for all.

I would also like to express my appreciation to the Session Chairpersons: Gene Rasmusson, Vern Kousky, C. Roberto Mechoso, David Neelin, Y. Chao, David Baumhefner, David Halpern, Chet Ropelewski, Michael Ghil, John Janowiak, Kingtse Mo, John Roads, Huug van den Dool, Bob Livezey, Ed O'Lenic, and Tony Barnston for their effective and enthusiastic management of the sessions.

The Proceedings of this Workshop is being dedicated to Dr. Jerry Namias, who has such a pervasive and long-term influence on climate prediction. These Proceedings provide a published record of the presentations made at the Workshop. Sessions were conducted on the following topics: ENSO, Low-Frequency Variability, Stratosphere, Ocean Circulation, Ocean-Atmosphere Interaction, Contemporary Climate Variations and Issues, Global Climate Change, Hydrology and Precipitation, ENSO and Seasonal Forecasts, and Climate Prediction.

At the Climate Analysis Center, Kingtse Mo served as Chairperson of the organizing committee; Peggy Davis and Elaine Michaelides provided secretarial services; and Luke Mannello served as editor and was responsible for the timely publication of these Proceedings.

Finally, I would like to sincerely thank all participants for their contributions to another successful Workshop.

David R. Rodenhuis, Director
Climate Analysis Center
February 1992

## Dedication to Jerry Namias

This Climate Diagnostic Workshop brought back memories of the Workshop 2 years ago, also held in Southern California. To be precise: at Scripps Institution for Oceanography in La Jolla, home of Jerry Namias since 1970. This came on the heels of a long and distinguished career with the U. S. Weather Bureau, as the Head of the Long-Range Forecast Section.

At the La Jolla Workshop Jerry, then 79 years old, was an active participant, outspoken and supportive in his frank assessment of the work presented. Many of his comments were intended to help a generation of new researchers along the way, boost their morale, and remind them of ideas that have been around for half a century or longer. Jerry's paper was about the reversal of flow patterns from fall to winter 1988/89 and how it affected the success of his winter forecast in that year. Obviously the state of the Pacific Ocean and air-sea interaction, which Namias pioneered, played an important role in his forecast. Surprisingly, though, his forecast also depended on a numerical model. This model, I would say a smart barotropic model, was based on Rossby's principles that Jerry had used most of his life, but in a descriptive manner only.

After that Workshop I had the pleasure of staying a few days at Scripps, in the company of this strong and vibrant man. Unfortunately, Jerry had a stroke shortly thereafter, and his recovery has been slow. His absence was noted by many at this year's Workshop at Lake Arrowhead. The presentations about ENSO and their impact on mid-latitudes would not have gone by without Jerry pointing out that we should not forget the interaction going the other way as well. Also, several of the Global Climate Change papers could have benefited from a question or two from Jerry about fact and fiction in what we, with our short memory, perceive as climate change. I also entertain the thought that Jerry would have given a paper about the winter forecast for 1990/91, and likely pointing out why CAC's winter forecast was unsuccessful.

Since Lake Arrowhead is only a 2 hour drive from San Diego, several of the Workshop participants went to see Jerry afterwards. This turned out to be a rewarding trip. It was easy to communicate with Jerry, even though we had to do most of the talking. His wife Edith was there to receive us and we ended up discussing meteorology from 1900 to 1991 as we have always done.

It is entirely appropriate, therefore, to dedicate these Proceedings to Dr. Jerome Namias, because he pioneered so many of these issues, and being in Southern California we could almost hear his comments. In fact we were telling each other what he would have said.

Huug van den Dool
Chief, Prediction Branch
NMC/Climate Analysis Center

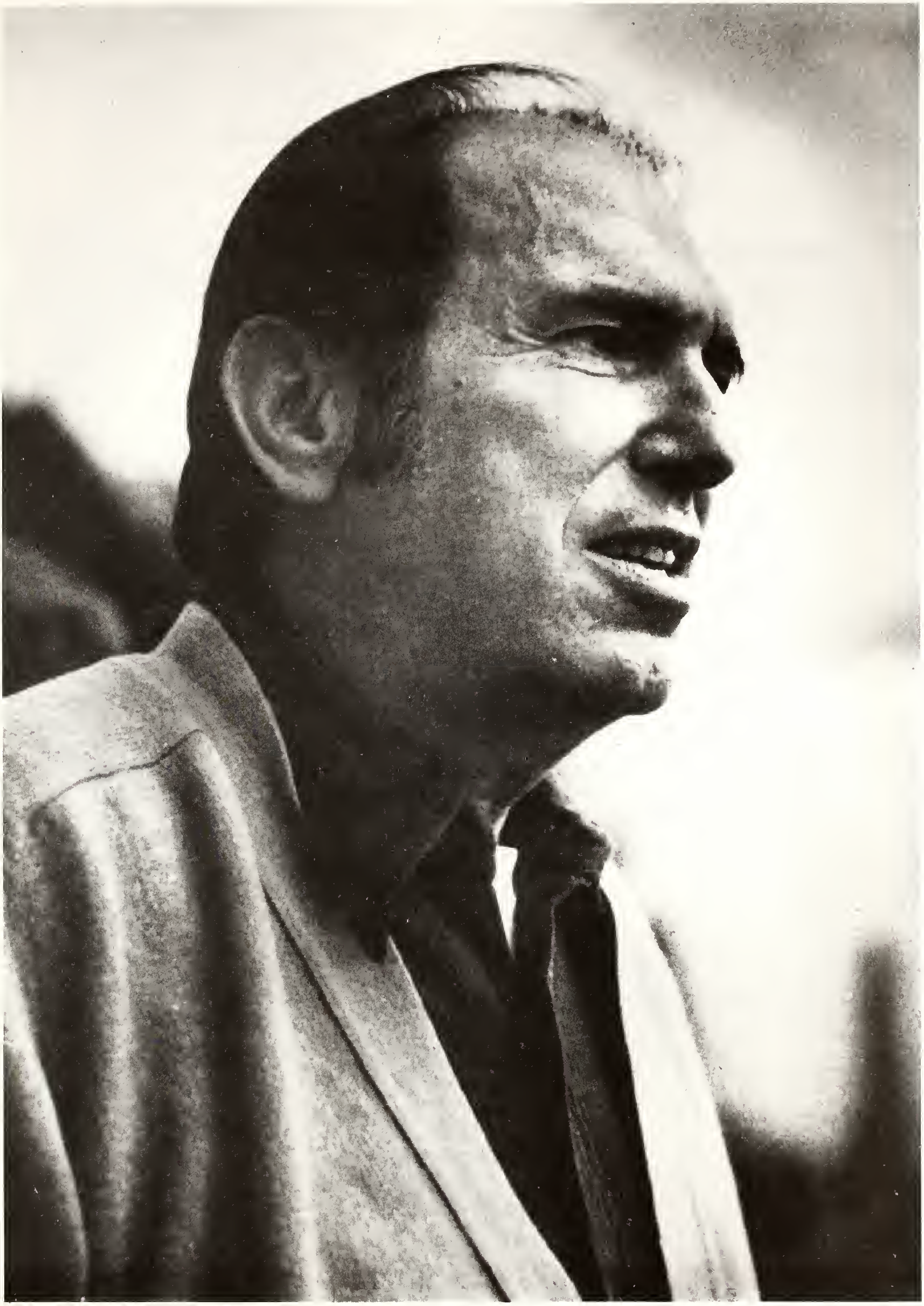

Digitized by the Internet Archive
in 2012 with funding from
LYRASIS Members and Sloan Foundation

http://archive.org/details/proceedingsofsix00clim

## Sixteenth Annual
## Climate Diagnostics Workshop
## Los Angeles, CA
## October 28 - November 1, 1991

### ATTENDEES

| | |
|---|---|
| Patricio Aceituno | University of Chile |
| Timothy P. Barnett | Scripps Institution of Oceanography |
| Tony Barnston | NOAA/NWS/CAC |
| David Baumhefner | NOAA/NCAR - Boulder, CO |
| Gerald D. Bell | NOAA/NWS/CAC |
| Richard Berk | UCLA |
| James S. Boyle | Lawrence Livermore National Laboratory |
| Michael Changery | National Climatic Data Center |
| Yi Chao | UCLA |
| Mutu Chelliah | NOAA/NWS/CAC |
| Shyh-Chin Chen | Scripps Institution of Oceanography |
| Wen-Yuan Chen | NOAA/NWS/CAC |
| Michael A. Chotkowski | UCLA |
| Kenneth Davidson | NCDC |
| Michael Dettinger | U. S. Geological Survey |
| Art Douglas | Creighton University |
| John Dracup | UCLA Dept. of Civil Engineering |
| Edward S. Epstein | NOAA/NWS/CAC |
| John D. Farrara | UCLA |
| Robert Fovell | UCLA |
| F. M. Fujioka | U.S. Forest Service/USDA |
| Michael Ghil | UCLA |
| Hans F. Graf | Humboldt Universitatzu, Berlin GDR |
| Nick Graham | Scripps Institution of Oceanography |
| William Gray | Colorado State University |
| Stanley L. Grotch | Lawrence Livermore National Laboratory |
| Patrick A. Harr | Naval Postgraduate School |
| Kaz Higuchi | Canadian Climate Centre |
| M. Hoerling | NOAA/CIRES |
| Jin Huang | NOAA/NWS/CAC |
| John Janowiak | NOAA/NWS/CAC |
| Fei-Fei Jin | UCLA |
| William H. Klein | University of Maryland |
| John L. Knox | Canadian Climate Centre |
| G. P. Konnen | Royal Netherlands Meteorologist Institute |
| Vernon Kousky | NOAA/NWS/CAC |
| George Kukla | Lamont Observatory |
| John R. Lanzante | Princeton University |
| Robert E. Livezey | NOAA/NMC/CAC |
| Chung-Chun Ma | UCLA |
| Diane Marsico | NOAA/NMC |
| Wilhel May | NCAR/CDG |
| John McAfee | NOAA/ERL |
| Morris H. McCutchan | USDA Forest Service |
| Carlos Mechoso | UCLA |
| Bernard N. Meisner | U.S. Forest Service/USDA |
| Arthur J. Miller | Scripps Institution of Oceanography |
| Kikuro Miyakoda | NOAA/GFDL |

| | |
|---|---|
| Kingtse C. Mo | NOAA/NWS/CAC |
| Allan Murphy | NOAA/NWS/CAC |
| J. Paul Mutschlecner | Los Alamos National Laboratory |
| David Neelin | UCLA |
| Sharon E. Nicholson | Florida State University |
| Ed O'Lenic | NOAA/NWS/CAC |
| Tomoaki Ose | UCLA |
| Jan Paegle | University of Utah |
| Julia Nogues-Paegle | University of Utah |
| Cecile Penland | University of Colorado at Boulder |
| Thomas Phillips | Lawrence Livermore National Laboratory |
| Walter G. Planet | NOAA/NESDIS |
| Charles Quon | UCLA |
| Eugene M. Rasmusson | CICS/University of Maryland |
| Robert W. Reeves | NOAA/CS |
| Michael B. Richman | The University of Oklahoma |
| John O. Roads | Scripps Institution of Oceanography |
| David R. Rodenhuis | NOAA/NWS/CAC |
| Chester F. Ropelewski | NOAA/NWS/CAC |
| Richard D. Rosen | Atmosphere and Environment Research, Inc. |
| David A. Salstein | Atmosphere and Environment Research, Inc. |
| Prashant Sardeshmukh | University of Colorado at Boulder |
| Neil Sargent | Canadian Climate Centre |
| Steven R. Silberberg | University of Wisconsin |
| Tom Smith | NOAA/NWS/CAC |
| B. J. Sohn | NASA/USRA |
| Xu Jin Song | Max-Planck Instit fur Meteorologie |
| Kenneth R. Sperber | Lawrence Livermore National Laboratory |
| Christopher M. Strong | UCLA |
| Hsin-Hsin Syu | UCLA |
| Kyozo Ueyoshi | Scripps Institution of Oceanography |
| Huug van den Dool | NOAA/NWS/CAC |
| Hans von Storch | Max-Planck Institute fur Meteorologie |
| Xueliang Wang | NOAA/NWS/CAC |
| S. L. Weber | Royal Netherland Meteorological Institute |
| Klaus W. Weickmann | NOAA/ERL |
| T.M.L. Wigley | Climatic Research Unit, UK |
| Christopher Williams | University of Colorado at Boulder |
| Chien-Hsiung Yang | Hanscom AFB, MA |
| Jia-Yuh Yu | UCLA |

# Sixteenth Annual
# Climate Diagnostics Workshop
# Los Angeles, California
# October 28 - November 1, 1991

## PROGRAM

### SESSION I - ENSO
Chair - David R. Rodenhuis

Page

Origins of the quasi-bienniel oscillation in the tropical Pacific . . . . . . . T. P. Barnett, N. Graham and M. Latif 1

A potential vorticity analysis of interannual atmospheric variability . . . . . . . . . . . . . . . . . . . M. P. Hoerling 5

TEDAZ: A new look at ENSO cycle teleconnections . . . . . . . . . . . . . . . . . . . . . . . . . E. M. Rasmusson and K. C. Mo 11

TEDAZ 2: A second look at tropical and extratropical circulation anomalies . . . . . . . K. C. Mo and V. E. Kousky 16

ENSO's precipitation signature in the U. S. Are wet days wetter or more frequent? . . . . . . . . . . . E. S. Epstein 22

Seasonality in ENSO scale variability . . . . M. Chelliah 29

### SESSION II - LOW FREQUENCY VARIABILITY
Chair - Eugene Rasmusson and Vernon Kousky

Resonant modulation of Nordeste precipitation by tropical Atlantic and Pacific sea-surface temperatures . . . . . . . . . . . . . . . . . . . . . . . K. R. Sperber and S. Hameed 35

An assessment of the interannual variability of the divergent circulation as determined from NMC and ECMWF analyses . . . . . . . . . . P. Sardeshmukh and B. Liebmann *

Westerly wind anomalies in the central Pacific and rainfall epilsodes in central Chile . . P. Aceituno and J. Rutllant 41

Angular momentum variability using climate data sets . . . . . . . . . . . . . . . . . . D. A. Salstein and R. D. Rosen 47

The atmospheric angular momentum budget during a Madden - Julian Oscillation . . . . K. Weickmann and P. Sardeshmukh 53

Atmospheric energy fluxes along the Pacific-North American arc . . . . . . . . . . . . . . . . N. E. Sargent and A. Shabbar 59

---

* Presentation was made; however, a paper was not submitted.

Page

Vertical motions over Christmas Island: Observations by the 50 MhZ profiler: . . J. R. McAfee, K. S. Gage and C. G. Reid 63

A first look at annual and interannual variability of tropospheric diurnal and semi-diurnal oscillations using the Christmas Island wind profiler . . . . . . . . . . . . . C. R. Williams, S. K. Avery, J. R. McAfee and K. S. Gage 69

Diagnosis of a blocking episode over the south-central South Pacific . . . . . . . . . . . . . . . . . . . . . . G. D. Bell 74

Establishment, maintenance and breakdown of a blocking regime . . . . . . . . . . . . . . . . . . . . . . W. Chen 80

Sensitivity of UCLA atmospheric general circulation model simulations to different global sea surface temperature distributions . . . . . T. Ose, C. R. Mechoso and D. Halpern 86

Modeling the seasonal dependence of the Northern Hemisphere 40-day oscillation . . C. M. Strong, F. F. Jin and M. Ghil 92

Intraseasonal oscillation and response to sea surface temperature anomalies in a linear tropical atmospheric model . . . . . . . . . . . . . . . . . J-Y. Yu and D. J. Neelin 98

**SESSION III - STRATOSPHERE**
Chair - C. Roberto Mechoso

Operational monitoring of the stratosphere . . W. G. Planet *

Upper level waves and ozone patterns during the 1986-1989 austral springs..J. Nogues-Paegle, K.C. Mo and K.P. Callahan 104

QBO modulation of tropical convection and ENSO variability . . . . . . . . . M. Gray, J. D. Sheaffer and J. A. Knaff 110

**SESSION IV - OCEAN CIRCULATIONS**
Chair - David Neelin and Y. Chao

Annual and interannual variability of the tropical Pacific during 1985-89 . . . . . . . . . . . . . . . . . . . . . . . . X. Wang, Z. Dai, J. Carton and E. M. Rasmusson 115

Diagnosing ocean energy transports from earth radiation budget measurements . . . . . . . . . . . . . . B. J. Sohn *

---

* Presentation was made; however, a paper was not submitted.

Page

Low frequency variability in blended SST and Ocean temperature analysis . . . . . . . . . . . . . . . . . . . . . . . . . . . . . . . T. Smith, M. Chelliah and C. F. Ropelewski 121

On sensible and latent heat fluxes at Ocean Weather Station P . . . . . . . . . . K. Higuchi, M. A. Jenkins, and W. Wong *

Uncertainties in SST analyses due to historical changes in data distribution . . . . . . . . . . . . . . . . . . . D. C. Marsico, R. W. Reynolds and C. F. Ropelewski 126

Comparison of vertical mixing schemes for ocean general circulation models . . . . . . . . . . . . . . . . . . . . C-C. Ma, Y. Chao, C. R. Mechoso, W. M. Weibel and D. Halpern 132

Different surface wind products in the tropical Pacific and their impacts on oceanic circulation . . . . . . . Y. Chao 138

## SESSION V - OCEAN-ATMOSPHERE INTERACTION

Chair - David P. Baumhefner and David Halpern

Coupled interaction in the equatorial eastern Pacific . . . . . . . . . . . . . . . . M. Ji, A. Kumar, and A. Leetmaa 144

The observed global low frequency variability in the atmosphere-ocean system from 1967 to 1986 . . . . . J-S. Xu 153

Large scale atmosphere-ocean heat exchange and the maintenance of extratropical kinetic energy . . . . . . . . . . . . . . . . . . . . . . . . . . . . . . . . . S. R. Silberberg A-1#

Simulations of the seasonal cycle with a coupled atmosphere-ocean GCM . . . . . . . . . . . . . . . . . . . . . C. R. Mechoso, C-C. Ma, J. D. Farrara and J. A. Spahr 157

Coupling an ocean wave model to an atmospheric general circulation model . . . . . . S. L. Weber and H. von Storch 163

Tropical ocean-atmosphere interaction in intermediate and hybrid coupled models . . . . . . . . . . . . . . . . . . . . . . . D. Neelin, F. F. Jin, H. M. Syu and W. Weibel *

Models of interannual tropical ocean-atmosphere interaction- A unified view . . . . . . . . . . F. F. Jin and D. Neelin *

---

* Presentation was made; however, a paper was not submitted.
# Paper arrived late; see Appendix.

## SESSION VI - SPECIAL SECTION ON CONTEMPORARY CLIMATE: VARIATIONS , PROBLEMS AND ISSUES

Chair - Chester F. Ropelewski

Page

Recent changes in atmospheric and oceanic anomaly patterns related to the Southern Oscillation . . . . . . V. E. Kousky 166

Temperature pattern variability on the USSR territory in 1931-1990...A. Belokrylova, O.N. Bulygina and V.N. Razuvayev 173

Temperature anomalies in cold periods on the USSR territory . . . . . . . O. Bulygina, N. Korshunova and V. Razuvayev 179

Africa rainfall 1981-1990 . . . . . . . . . S. E. Nicholson 185

Large scale climate and Kuwait oil fires: Model versus observations . . . . . . . . . . . . . . . . . . . H. F. Graf 192

Recent global temperature changes: Ozone and aerosol aerosol influences . . . . . . . . . . . . . . . . . . . . . . . T. M. L. Wigley, P. D. Jones, P. M. Kelly and M. Hulme 194

Public perception of global warming . . . . . . . . . . . . . . . . . . . . . . . . . . R. Berk, E. Hanley and P. Kwon *

## SESSION VII - GLOBAL CLIMATE CHANGE

Chair - Michael Ghil and John Janowiak

Greenhouse signal in the glacier recession on Mount Kenya . . . . . . . . . . . . . . . . . . . . . . S. Hastenrath 203

Climate data CD-ROMS developed at NCDC and their use in climate research . . . . . . . . . . . . . . . . M. Changery *

Interannaul and interdecadal variability of surface-air temperature in the United States . M.D. Dettinger and M. Ghil 209

Seasonal cycle of insolation and climate change . . . . . . . . . . . . . . . . . . . . . . . . . G. Kukla and T. Karl 215

Climatic zones of the United States deduced from temperature and precipitation data . . R. G. Fovell and M-Y. C. Fovell 223

A circulation-based consistency check for trends in surface temperature..E. A. O'Lenic, H. van den Dool and W. H. Klein 228

Interannual oscillations and sea level rise . . . . . . . . . . . . . . . . . . . . . . . . . . Y. Sezginer and M. Ghil 237

---

* Presentation was made; however, a paper was not submitted.

Page

Downscaling of global climate change estimates to regional scales an application to Iberian rainfall in winter time. . . . . . . . . H. von Storch, E. Zorita and Ulrich Cubasch *

A comparison of the stationary wave responses in several GFDL increased $CO_2$ GCM experiments . . . . . J. R. Lanzante 241

Interannual variability in a 10-yr run of the NMC model: Global and hemispheric mean surface temp, precip and precipitable water . . . . . . . . . . . H. M. van den Dool 247

Inter-decadal variability of U. S. Westcoast precipitation in a GCM . . . . . . . . . . . . . . . . . . . . S-C. Chen 256

## SESSION VIII - HYDROLOGY AND PRECIPITATION

Chair - Kingtse Mo and John Roads

A model of the gobal hydrologic cycle . . . . . . . . . . . J. Roads, S-C. Chen, J. Kao, D. Langley and G. Glatzmaier 262

Diurnal variations in tropial rainfall during 1986-90 . . . . . . . . . . . . . . . . . . . . . . . . J. E. Janowiak 268

Analysis of Sahel rainfall in the context of the global tropics . . . . . . . . . . . . . S. E. Nicholson and I. Palao 274

Surface temperature and precipitation patterns during the 1980's . . . . . . . . . . C. F. Ropelewski and M. S. Halpert 280

Cluster analysis of growing season precipitation in central and eastern North America . . . M. B. Richman and X-F. Gong 286

Relationships between the water vapor budget components over central North America in summer 1979 . . . . . . . . . . . . . . . . . A. Zangvil, D. H. Portis and P. J. Lamb 298

Examination of precipitation data at Ocean Weather Station P, before and after 1967 . . . . . . . . . . . . . . . W. Wong, J. L. Knox, M. A. Jenkins and K. Higuchi *

Comparison of climate data sets using spatial histograms. . . . . . . . . . . . . . . . . . . . . . . . . . . . S. L. Grotch 305

Moisture flux estimates in the vicinity of South America. . . . . . . . . . . . M. Wang, J. Paegle, and J. Nogues-Paegle 311

---

* Presentation was made, however; paper was not submitted.

## SESSION IX - ENSO AND SEASONAL FORECASTS
Chair - Huug van den Dool

Page

Experimental seasonal forecasts using an air-sea model . . . . . . . K. Miyakoda, A. Rosati, J. Sirutis and R. Gudgel *

A comparison of tropical ocean models: Hindcast skill scores and physical processes during El Niño events. . A. J. Miller T. P. Barnett, N. E. Graham, J. M. Oberhuber and M. Latif 317

Considerations of the predictability of ENSO with a low order coupled model-N. E. Graham, T. P. Barnett and M. Latif 323

Seasonal forecasts can be used in fire management planning M. McCutchan, B. N. Meisner, F. M. Fujioka and R. A. Chase 330

Forecast skill and low frequency variability in 90-day integrations of a GCM . . . . . . W. Chen and H. M. van den Dool 336

A study of seasonal climate prediction with a simple coupled ocean-atmosphere model. . . . . . . . . . . . T. J. Phillips 348

Prediction of Niño 3 sea-surface temperatures using linear inverse modeling . . . . . . . . C. Penland and T. Magorian 354

The potential for long-range streamflow forecasting based on ENSO . . . . . . . . . . J. A. Dracup and E. Kahya 359

## SESSION X - CLIMATE PREDICTION
Chair - Robert E. Livezey, Edward A. O'Lenic
and Tony Barnston

Regime transitions during the winter of 90-91: Their influence on numerical extended-range prediction . . . . . . . . . . . . . . . . . . . . . . . . . . . . . . D. P. Baumhefner 369

Examination of actual analysis differences for use in Monte Carlo forecasting . . . . . . . . . . . . . . . . . . . . . . . . . . S. J. Augustine, S. L. Mullen and D. P. Baumhefner 375

Potential for long-range prediction of monthly mean surface temperatures over Eurasia . . . . . W. May and R. A. Madden 379

Can precipitation be used as a predictor in long-range temperature forcasts? . . . J. Huang and H. M. van den Dool 384

On the quality of CAC'S probabilistic 30-day and 90-day forecasts . . . . . . . . . . . . . A. H. Murphy and J. Huang 390

---

* Presentation was made; however, paper was not submitted.

Page

A numerical simulation of the catalina eddy . . . . . . . . . . . . . . . . . . . . . . . K. Ueyoshi, J. Roads and J. Alpert 400

Preferred modes of season to season changes in 700 mb height anomalies . . . . . . . . A. Douglas and P. J. Englehart 406

Strong extended range seasonal predictive potential for Atlantic hurricane activity . . . . . . . . . . . . . . . . . . . W. M. Gray, C. W. Landsea, P. Mielke and K. J. Berry 412

Predictability of intense Atlantic hurricanes and western Sahel rainfall from West African rainfall . . . . . . . . . . . . . . . . . . . . . . . . . . . C. W. Landesa and W. M. Gray 417

Long-lead forecasts of time-mean U. S. surface temperature using canonical correlation analysis . . . . A. G. Barnston 423

Further studies of skill characteristics of U. S. long-range forecasts. Part I: Surface temperature and precipitation forecasts . . . . . . . R. E. Livezey and J. D. Hoopingarner 430

Further studies of skill characteristics of U. S. long-range forecasts. Part II: N. H. monthly mean 700 mb anomaly forecasts . . . . . J. D. Hoopingarner and R. E. Livezey 434

Verification of monthly mean outlooks for temperature, dew point and wind speed in the contiguous United States . . . . . . . . . . . . . . . . . . W. H. Klein and J. J. Charney 441

Verifying monthly fire weather forecasts: Presenting expected accuracy to users . . . . . . . . . B. N. Meisner 446

# Sixteenth Annual Climate Diagnostics Workshop

## Author Index

| Author | Page |
|---|---|
| Aceituno, P. | 41 |
| Alpert, J. | 400 |
| Augustine, S. J. | 375 |
| Avery, S. K. | 69 |
| Barnett, T. P. | 1, 317, 323 |
| Barnston, A. G. | 423 |
| Baumhefner, D. P. | 369, 375 |
| Bell, G. D. | 74 |
| Belokrylova, A. | 173 |
| Berry, K. J. | 412 |
| Bulygina, O. N. | 173, 179 |
| Callahan, K. P. | 104 |
| Carton, J. | 115 |
| Chao, Y. | 132, 138 |
| Charney, J. J. | 441 |
| Chase, R. A. | 330 |
| Chelliah, M. C. | 29, 121 |
| Chen, S-C. | 256, 262 |
| Chen, W. | 80, 336 |
| Dai, Z. | 115 |
| Dettinger, M. D. | 209 |
| Douglas, A. | 406 |
| Dracup, J. A. | 359 |
| Englehart, P. J. | 406 |
| Epstein, E. S. | 22 |
| Farrara, J. D. | 157 |
| Fovell, M-Y. | 223 |
| Fovell, R. G. | 223 |
| Fujioka, F. M. | 330 |
| Gage, K. S. | 63, 69 |
| Ghil, M. | 92, 209, 237 |
| Glatzmaier, G. | 262 |
| Gong, X-F. | 286 |
| Graf, H. F. | 192 |
| Graham, N. | 1, 317, 323 |
| Gray, W. M. | 110, 412, 417 |
| Grotch, S. L. | 305 |
| Halpern, D. | 86, 132 |
| Halpert, M. S. | 286 |
| Hameed, S. | 35 |
| Hastenrath, S. | 203 |
| Hoerling, M. P. | 5 |
| Hoopingarner, J. D. | 430, 434 |
| Huang, J. | 384, 390 |
| Hulme, M. | 194 |
| Janowiak, J. E. | 268 |
| Ji, M. | 144 |
| Jin, F. F. | 92 |
| Jones, P. D. | 194 |
| Kahya, E. | 359 |
| Kao, J. | 262 |
| Karl, T. | 215 |
| Kelly, P. M. | 194 |
| Klein, W. H. | 228, 441 |
| Knaff, J. A. | 110 |
| Korshunova, N. | 179 |
| Kousky, V. E. | 16, 166 |
| Kukla, G. | 215 |
| Kumar, A. | 144 |
| Lamb, P. J. | 298 |
| Landsea, C. W. | 412, 417 |
| Langley, D. | 262 |
| Lanzante, J. R. | 241 |
| Latif, M. | 1, 317, 323 |
| Leetmaa, A. | 144 |
| Livezey, R. E. | 430, 434 |
| Ma, C-C. | 132, 157 |
| Madden, R. A. | 379 |
| Magorian, T. | 354 |
| Marsico, D. | 126 |
| May, W. | 379 |
| McAfee, J. R. | 63, 69 |
| McCutchan, M. H. | 330 |
| Mechoso, C. R. | 86, 132, 157 |
| Meisner, B. N. | 330, 446 |
| Mielke, P | 412 |
| Miller, A. J. | 317 |
| Mo, K. C. | 11, 16, 104 |
| Mullen, S. L. | 375 |
| Murphy, A. H. | 390 |
| Neelin, D. | 98 |
| Nicholson, S. E. | 185, 274 |
| Nogues-Paegle, J. | 104, 311 |
| Oberhuber, J. M. | 317 |
| O'Lenic, E. A. | 228 |
| Ose, T. | 86 |
| Paegle, J. | 311 |
| Palao, I. | 274 |
| Penland, C. | 354 |
| Phillips, T. J. | 348 |
| Portis, D. H. | 298 |

| Author | Page |
|---|---|
| Rasmusson, E. M. | 11, 115 |
| Razuvayev, V. N. | 173, 179 |
| Reid, C. G. | 63 |
| Reynolds, R. W. | 126 |
| Richman, M. B. | 286 |
| Roads, J. O. | 262, 400 |
| Ropelewski, C. F. | 121, 126, 280 |
| Rosen, R. D. | 47 |
| Rutllant, J. | 41 |
| Salstein, D. A. | 47 |
| Sardeshmukh, P. | 53 |
| Sargent, N. | 59 |
| Sezginer, Y. | 237 |
| Shabbar, A. | 59 |
| Sheaffer, J. D. | 110 |
| Silberberg, S. R. | A-1 |
| Smith, T. | 121 |
| Spahr, J. A. | 157 |
| Sperber, K. R. | 35 |
| Strong, C. M. | 92 |
| Ueyoshi, K. | 400 |
| van den Dool, H. | 228, 247<br>336, 384 |
| von Storch, H. | 163 |
| Wang, M. | 311 |
| Wang, X. | 115 |
| Weber, S. L. | 163 |
| Weibel, W. M. | 132 |
| Weickmann, K. W. | 53 |
| Wigley, T. M. L. | 194 |
| Williams, C. R. | 69 |
| Xu, J-S. | 153 |
| Yu, J. Y. | 98 |
| Zangvil, A. | 298 |

# Origins of the Quasi-biennial Oscillation in the Tropical Pacific

*T. P. Barnett*[1], *N. Graham*[1], *and M. Latif*[2]

[1] Scripps Institution of Oceanography, La Jolla, CA 92093

[2] Max Planck Institute fur Meteorologie, Hamburg, Germany

A primitive equation ocean general circulation model (OGCM) of the tropical Pacific (Latif, 1987) is coupled to a statistical atmospheric model (SAM). The latter model uses observed sea surface temperature (SST) to specify the concurrent (FSU) wind stress. The OGCM is spunup with the observed SST being used in the SAM to produce reconstructed stress fields that force the OGCM. The coupled model is started from a January, 1973 initial condition.

The behavior of the hybrid coupled model (HCM) is characterized by NINO3 SST (Fig. 1). For the first 350 months of integration, the HCM shows irregular behavior with typical period 22 months. Then there is an abrupt shift to a biennial oscillation and that lasts until about month 1230 of the integration. At this point, there is again a sharp transition to a purely triennial oscillation, which persists to the limit of the integration (1800 months). Detailed analysis showed the shifts of time scales are associated with shifts of the mean background state of the model ocean.

Comparison of the spatial structures of the above signal show they reproduce many aspects of real observations: i) Sea level anomalies off the equator (latitude 5-8°) originating in mid-ocean and moving westward to Asia, ii) An equatorial mode of SST that closely couples to the atmosphere and moves eastward: essentially the air/sea interaction mode described in Barnett *et al.*, 1991. Interestingly, the spatial structure of the signals is more or less independent of the time scales they possess.

If the model is at all realistic, as the comparisons with observations suggest, then the QB variability, schematically drawn in Fig. 2, can be understood as follows: The slow eastward propagation of SST along the equator has a characteristic time scale of about 6-8 months. As it moves east the off-equatorial winds associated with it generate an off-equatorial Rossby wave that may take 6-8 months to reach the western boundary. The speed of this wave depends on the latitude at which it is generated and these critical latitudes change as expected in the model as the time scale of oscillation changes. The conversion of the Rossby wave into the wave guide and the associated SST anomaly give the air/sea mode discussed above but with opposite sign. The cycle is half over. Allowing an additional random variation in either the wind, SST, or heat content will give a "quasi" character to the oscillation (vs. the regular behavior seen here.)

The above set of physics represents a normal mode of the tropical Pacific ocean-atmosphere system. Like the atmospheric PNA pattern, it can presumably be triggered by a variety of processes (mid-latitude incursion, monsoon variations, etc.) But once triggered, it will more or less demonstrate a similarity behavior. The ideas expressed above are similar to those first proposed by Graham and White (1990) and include elements proposed by Schopf and Suarez (1988), Barnett *et al.*, 1991, and others.

## References

Barnett, T.P., E. Kirk, M. Latif, and E. Roeckner, 1991: On ENSO physics. *J. Clim.*, **4**, 487-515.

Graham, N., and W. White, 1990: On the role of the western boundary in the ENSO cycle: Experiments with Coupled Models. *J. Phys. Oceanog.*, in press.

Latif, M., 1987: Tropical Ocean Circulation Experiments. *J. Phys. Oceanography*, **17**, 246-263.

Schopf, P., and M. J. Suarez, 1988: Vacillations in a Coupled Ocean Atmosphere Model. *J. Atmos. Sci.*, **45**, 549-566.

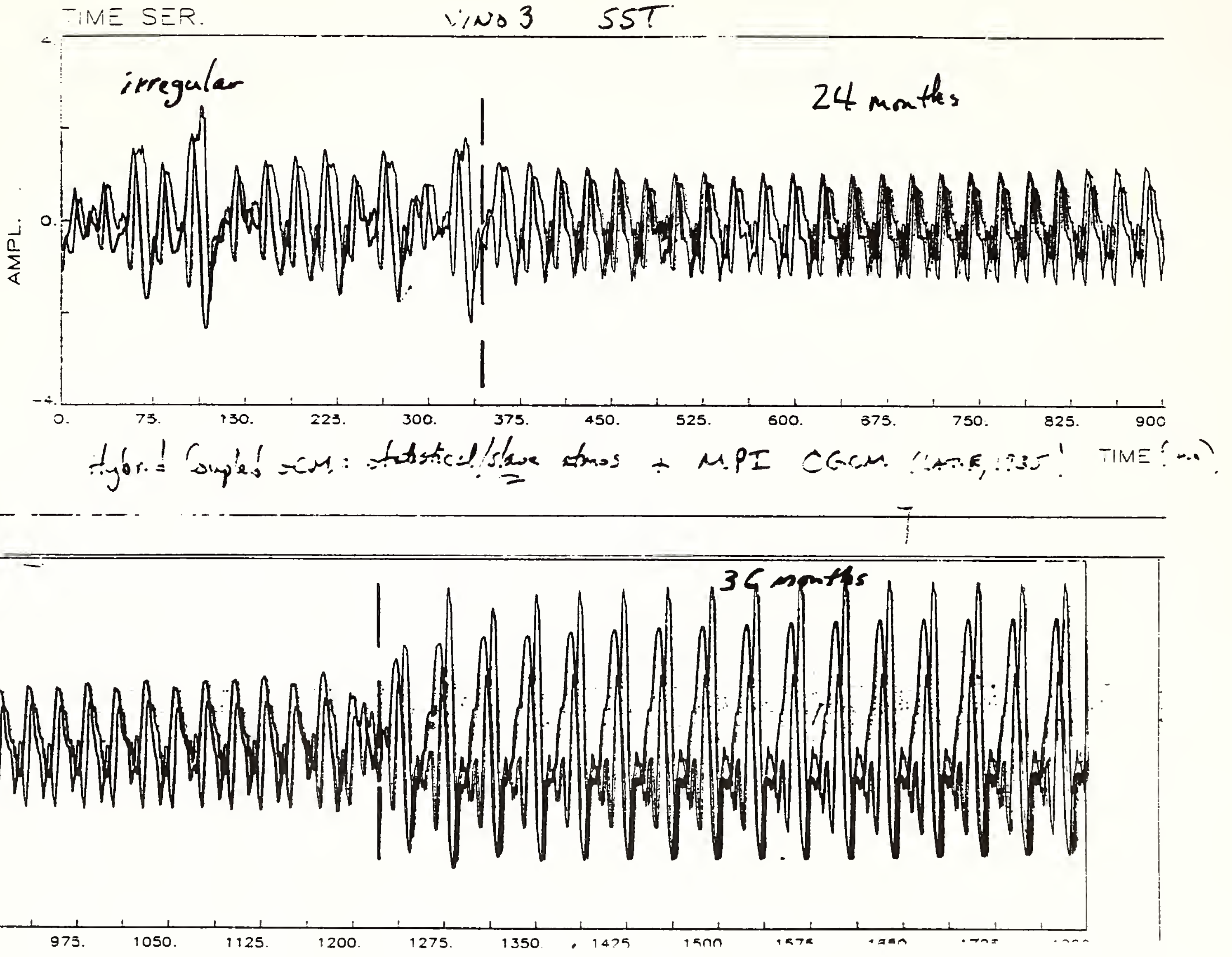

FIG. 1: POPS coefficient for HCM SST field over 1800 months of integration

# CONCLUSION

The QB variability has two related parts

PART I A slow, generally eastward A/S mode confined to the equatorial zone: A coupled O-A interaction

PART II An element of the "delayed action oscillator"

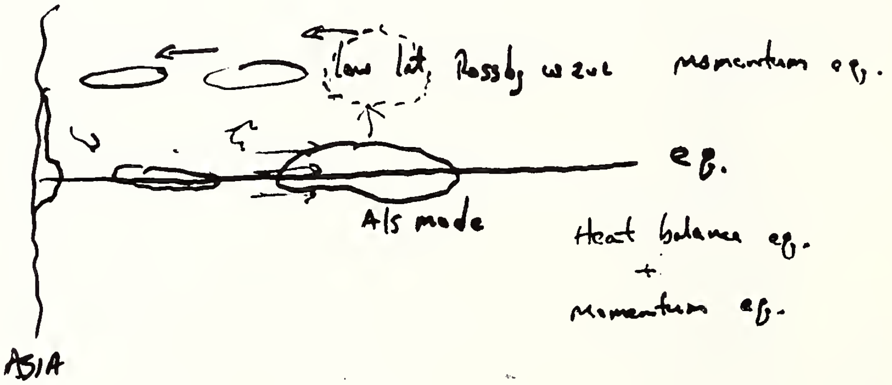

These ideas have been around in bits & pieces for some time.

FIG. 2: A schematic of the two elements of the tropical Pacific Quasi-biennial "normal mode"

# A Potential Vorticity Analysis of Interannual Atmospheric Variability

Martin P. Hoerling
*Cooperative Institute for Research in the Environmental Sciences*
*University of Colorado, Boulder, CO 80309*

## 1. INTRODUCTION

The condition that diabatic processes are the only source of the potential vorticity (PV) of an inviscid fluid makes it a particularly attractive property for studying the role of heat sources and sinks in the general circulation. In the presence of non-zero PV, a local source occurs due to vertical variations in heating. Horizontal advection effectively acts to redistribute the potential vorticity between its source and sink regions. However, since the irrotational flow is in part related to heating, a portion of the advective effect is itself diabatically forced. This relationship is particularly strong in isentropic coordinates where the irrotational mass circulation is identically equal to the vertical variation of the time-averaged heating. It is thus reasonable to treat the horizontal advection of PV by the irrotational isentropic mass circulation as an "effective" diabatic source.

Such an interpretation of the potential vorticity budget may be viewed as a generalization of Sardeshmukh and Hoskins' (1988) analysis of the kinematic vorticity budget. In analogy to their formulation of an effective barotropic Rossby wave source due to a horizontal distribution of divergence, a relation is developed herein for an effective baroclinic wave source due to a three-dimensional distribution of heating.

Diagnostic results are compared for potential and kinematic vorticity balances, and in particular with regard to understanding the interaction between tropical monsoons and extratropical circulation.

## 2. AN EFFECTIVE BAROCLINIC WAVE SOURCE DUE TO HEATING

The potential vorticity in isentropic coordinates is

$$P = (\zeta_\theta + f)/\rho J_\theta, \qquad (1)$$

where $\zeta_\theta$ is the isentropic kinematic vorticity, $f=2\Omega\sin\phi$, and $\rho J_\theta = -1/g\partial p/\partial\theta$ is the isentropic mass density.

The isentropic potential vorticity equation is derived from a combination of the mass continuity equation

$$\frac{\partial(\rho J_\theta)}{\partial t_\theta} + \nabla_\theta\cdot(\rho J_\theta\vec{V}) + \frac{\partial(\rho J_\theta\dot{\theta})}{\partial\theta} = 0, \qquad (2)$$

where $\dot{\theta}=d\theta/dt$ is the diabatic heating rate, and the kinematic vorticity equation

$$\frac{d(\zeta_\theta+f)}{dt} = -(\zeta_\theta+f)\nabla_\theta\cdot\vec{V}+\left(\frac{\partial\dot{\theta}}{\partial y}\frac{\partial u}{\partial\theta} - \frac{\partial\dot{\theta}}{\partial x}\frac{\partial v}{\partial\theta}\right) + \vec{k}\cdot\nabla_\theta\times\vec{F}, \tag{3}$$

where $\vec{F}$ is the friction force. Elimination of the velocity divergence terms between (2) and (3) with the definition of PV yields

$$\frac{dP}{dt} = P\frac{\partial\dot{\theta}}{\partial\theta} + \frac{1}{\rho J_\theta}\left[\left(\frac{\partial\dot{\theta}}{\partial y}\frac{\partial u}{\partial\theta} - \frac{\partial\dot{\theta}}{\partial x}\frac{\partial v}{\partial\theta}\right)+\vec{k}\cdot\nabla_\theta\times\vec{F}\right]. \tag{4}$$

As suggested in the Introduction, a diagnostic PV model for studying the effect of heating must represent the portion of horizontal PV advection that is explicitly coupled to diabatic processes. Through an expansion of the Lagrangian derivative and a multiplication by the isentropic mass density, (4) becomes

$$\rho J_\theta\frac{\partial P}{\partial t_\theta} + \rho J_\theta\vec{V}\cdot\nabla_\theta P + \rho J_\theta\dot{\theta}\frac{\partial P}{\partial\theta} = (\zeta_\theta+f)\frac{\partial\dot{\theta}}{\partial\theta} + \vec{k}\cdot\nabla_\theta\times\vec{F}, \tag{5}$$

where tilting has been neglected. The mass transport vector $\rho J_\theta\vec{V}$ is expressed in terms of rotational and irrotational components according to

$$\rho J_\theta\vec{V} = (\rho J_\theta\vec{V})_\psi + (\rho J_\theta\vec{V})_\chi. \tag{6}$$

With the steady-state assumption, the irrotational component of the mass transport is directly related to diabatic heating through the isentropic mass balance (2). A combination of (5) with (6) thus yields

$$\left(\rho J_\theta\frac{\partial}{\partial t_\theta} + (\rho J_\theta\vec{V})_\psi\cdot\nabla_\theta\right)P = S_P + \vec{k}\cdot\nabla_\theta\times\vec{F}, \tag{7}$$

where $S_P$ expresses the "effective baroclinic wave source" due to diabatic processes

$$S_P = -(\rho J_\theta\vec{V})_\chi\cdot\nabla_\theta P - \rho J_\theta\dot{\theta}\frac{\partial P}{\partial\theta} + (\zeta_\theta+f)\frac{\partial\dot{\theta}}{\partial\theta}. \tag{8}$$

$S_P$ is linked to the three-dimensional distribution of heating through the effects of (1) horizontal advection of PV by the irrotational isentropic mass transport, (2) vertical advection of PV by the diabatic mass flux, and (3) a vertically varying local heat source. Note that (8) is analogous to Sardeshmukh and Hoskins' (1988) effective source of Rossby waves due to divergence

$$S_\zeta = -\vec{V}_\chi\cdot\nabla_\theta(\zeta_\theta+f) - \dot{\theta}\frac{\partial\zeta}{\partial\theta} - (\zeta_\theta+f)\nabla_\theta\cdot\vec{V}. \tag{9}$$

It is important to recognize, however, that inferences on the diabatic forcing of circulation based on (9) are inherently confounded since only within near-equatorial latitudes do $\nabla_\theta\cdot\vec{V}$ and the associated $\vec{V}_\chi$ bear a close relation to heating. In contrast, the effective PV source is explicitly determined by the three-dimensional distribution of diabatic forcing globally.

## 3. SOME FEATURES OF THE CLIMATOLOGICAL PV BALANCE

The potential and kinematic vorticity balances are dervived from once-daily NMC global initialized analyses for the December-February periods of 1986-87, 1987-88 and 1988-89. Results are shown at 350 K (near 200 mb) corresponding roughly to the level of maximum outflow from tropical deep convection. Figs. 1a and 1b present the 3-year winter-mean distribution of the diabatic heating and the divergent mass transport, respectively. A non-local influence of the tropical convection is implied by the transport of low-PV air from tropics to extratropics by the divergent mass outflow.

An important feature of the midlatitude balance is that analysis of the effective baroclinic wave source reveals a large dynamical influence of the mass outflow from the tropical heat sources. This remote effect in the time-mean PV budget is comparable to the local effect of the midlatitude heat sources. Horizontal PV advection by the divergent flow attains maximum values near 30° latitude where the poleward mass circulation encounters the intense PV gradient along the tropopause break (Fig. 1c). A prominent sink by advection occurs nearly symmetric about the equator, and spans the extent of the Austral-Asian monsoon. Note in paticular that the contribution to decreasing PV over eastern Asia due to advection exceeds the local generation of PV associated with the continental heat sink (Fig. 1d), while both processes contribute equally to a decreasing tendency of PV over the North Pacific.

This PV perspective on tropical-extratropical interactions is to be contrasted with that derived from analysis of the Rossby wave source (Figs. 1e and f). Qualitatively similar results emerge from both budgets with regard to the inferred remote influence of the tropical monsoons. The subtropical sinks of potential and kinematic vorticity that occur through advection by the irrotational flow (Figs. 1c and 1e) are important effects in their respective budgets. In this regard, the diagnostics support the modeling results of Sardeshmukh and Hoskins (1988), who demonstrated that the extratropical response to tropical divergence is significantly altered by incorporating the divergent component of absolute vorticity advection in the Rossby wave source. Quantitatively, however, horizontal PV advection by $(\rho J_\theta \vec{V})_\chi$ exerts a proportionately larger effect in the PV budget than does horizontal absolute vorticity advection by $\vec{V}_\chi$ in the kinematic vorticity budget. The greater influence in the PV budget is due to the near discontinous meridional variation of potential vorticity near 30° latitude which acts to amplify the dynamical effect of divergent outflow from the winter monsoon.

## 4. ENSO-RELATED TROPICAL-EXTRATROPICAL INTERACTIONS

It is evident from the climatological budget results that the horizontal advective effect by the divergent flow is a useful diagnostic measure of tropical-extratropical interactions. Of particular interest is the extent to which this interaction varies interannually, thereby offering a perspective on the sensitivity of the extratropics to changes in tropical diabatic forcing. A major component of tropical interannual variability is the zonal shift of equatorial Pacific convection during ENSO. During the winter of 1986-87, heating was maximized over the equatorial dateline (Fig. 2a) associated with the warm phase of ENSO, while convection was maximized over the Maritime Continent during the winter of 1988-89 (Fig. 2b) associated with the cold phase of ENSO.

A dramatic zonal shift of the effective PV sink due to advection accompanies these shifts in tropical Pacific heating (Figs. 2c and d). During the warm phase of ENSO, upper level mass outflow is intense near the dateline which leads to a maximum PV sink in midlatitudes over the North and South Pacific Oceans. During the cold phase of ENSO, upper level mass outflow is confined to the far western Pacific which leads to a maximum PV sink over eastern Asia and Australia. Comparitively little interannual variability of advection by the divergent flow is seen in the kinematic vorticity budget (Figs. 2e and f). As a first approximation, this process appears quite insensitive to the zonal redistribution of tropical convection.

These different impressions of the interannual variability stem from the condition that the PV budget explicitly incorporates the mass redistribution that is fundamental to the baroclinic response to heating. In contrast, the kinematic vorticity budget captures only the barotropic dynamics. It is well known that an essential feature of the tropical atmospheric response to El Niño-related heating anomalies is a zonal redistribution of mass along the equatorial Pacific. During the warm phase, this Southern Oscillation is manifested in upper isentropic layers as a decrease in the mass density (associated with a lowered tropopause) over the suppressed convective regime in the western Pacific, and an increase in the mass density (associated with an elevated tropopause) over the enhanced convective regime over the eastern Pacific. As such, the anomalous *mass divergence* and its associated irrotational mass transport will be more intimately related to the anomalous diabatic heating than the anomalous *velocity divergence* and its associated irrotational velocity. Thus, in addition to the distinctions between the climatological budgets of potential and kinematic vorticity discussed earlier, the above results reveal significant differences in the corresponding anomaly budgets, especially with regard to interannual variability in tropical-extratropical interactions.

## 5. CONCLUDING REMARKS

The current study has attempted to combine the attributes of an isentropic perspective of the general circulation especially regarding the thermodynamics of monsoonal circulations (see Johnson, 1989), with the dynamical insight offerred by application of potential vorticity principles (e.g. Hoskins et al., 1985). In addition to lending insight on the role of the climatological heating in maintaining the time-mean circulation, the diagnostic model described herein appears useful in understanding interannual variability of the circulation in relation to anomalous tropical heating. The PV budget results agree favorably with empirical and numerical studies on tropical-extratropical interactions. In particular, a comparison of the potential vorticity dynamics during extreme phases of the Southern Oscillation has revealed major changes in patterns of tropical-extratropical interactions, a result less evident from a conventional vorticity budget analysis.

## 6. REFERENCES

Hoerling, M. P., 1991: Diabatic sources of potential vorticity in the general circulation. Submitted to *J. Atmos. Sci.*

Hoskins, B. J, M. E. McIntyre and A. W. Robertson, 1985: On the use and significance of isentropic potential vorticity maps. *Quart. J. R. Met. Soc.*, **111**, 877-946.

Johnson, D. R.,1989: The forcing and maintenance of global monsoonal circulations: An isentropic analysis. *Advances in Geophysics*, B. Saltzman, Ed., Academic Press, **31**, 43-316.

Sardeshmukh, P. D., and B. J. Hoskins, 1985: The generation of global rotational flow by steady idealized tropical divergence. *J. Atmos. Sci.*, **45**, 1228-1251.

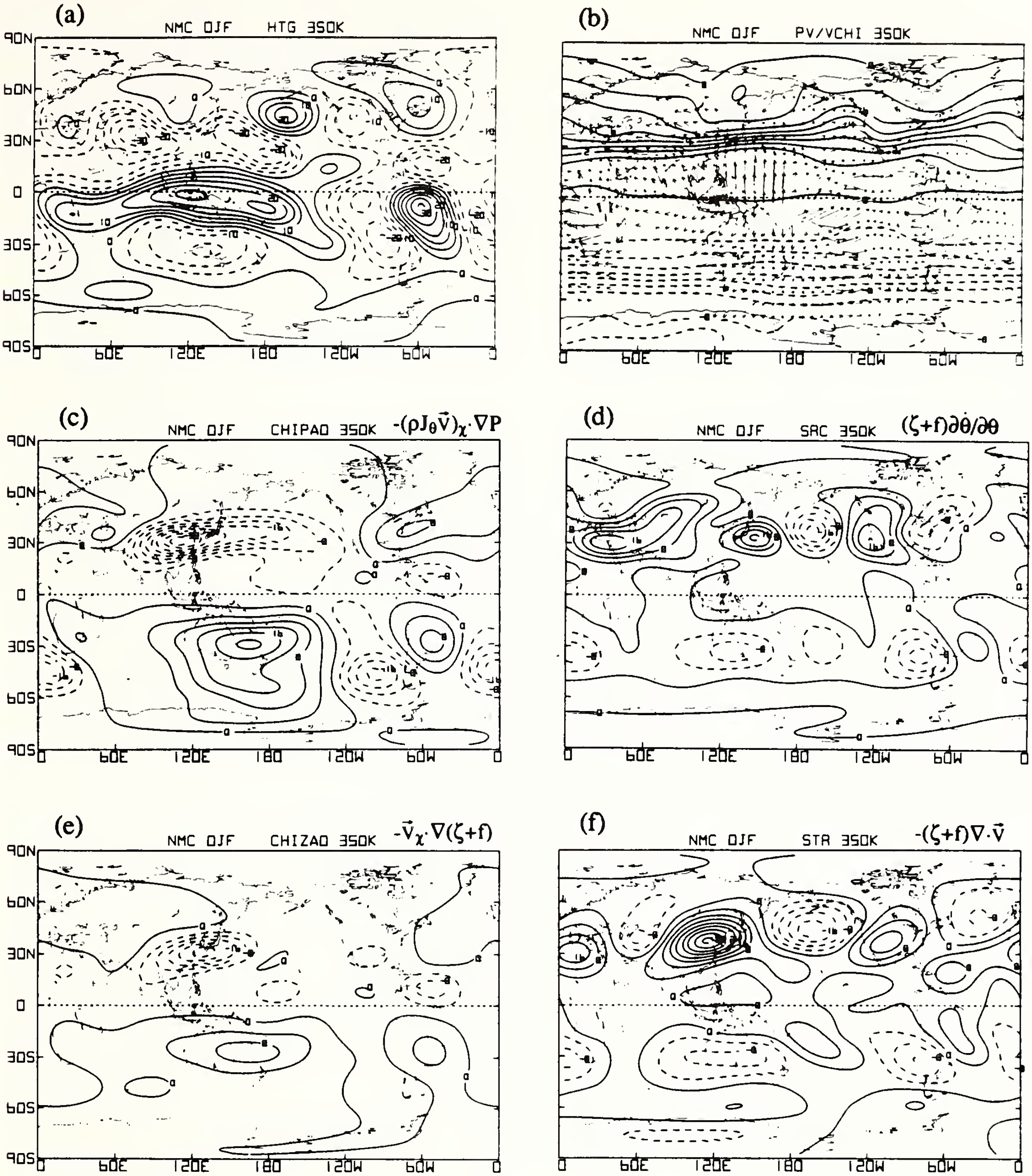

(a)
NMC DJF HTG 350K
(b)
NMC DJF PV/VCHI 350K
(c)
NMC DJF CHIPAD 350K $-(\rho J_\theta \vec{V})_\chi \cdot \nabla P$
(d)
NMC DJF SRC 350K $(\zeta+f)\partial\dot{\theta}/\partial\theta$
(e)
NMC DJF CHIZAD 350K $-\vec{V}_\chi \cdot \nabla(\zeta+f)$
(f)
NMC DJF STR 350K $-(\zeta+f)\nabla \cdot \vec{V}$
90N
60N
30N
0
30S
60S
90S
0
60E
120E
180
120W
60W
0

Fig. 1. DJF 3-year mean distributions of (a) 350 K heating (K day$^{-1}$), (b) 350-355 K potential vorticity ($10^{-6}$ kg$^{-1}$ m$^2$ s$^{-1}$ K) and irrotational mass transport vectors. DJF mean contributions to the 350-355 K potential vorticity budget by the (c) horizontal advection of PV by the irrotational mass transport, (d) local diabatic source. DJF mean contributions to the 350-355 K kinematic vorticity budget by the (e) horizontal advection of absolute vorticity by the divergent velocity, (f) local stretching. Panels (c)-(f) are contoured every 4 x $10^{-11}$ s$^{-2}$. Fields filtered to emphasize wavelengths greater than 6000 km.

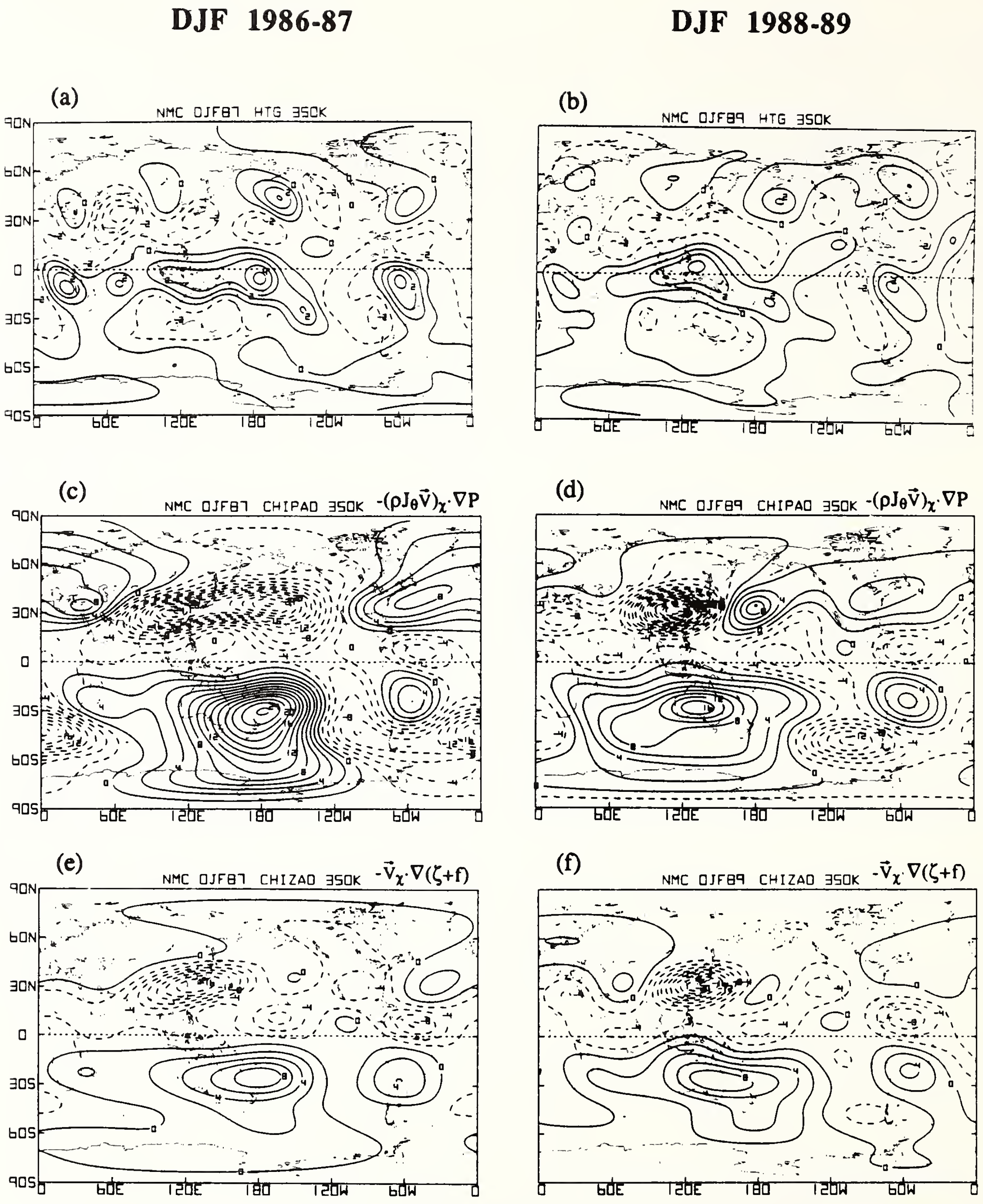
DJF 1986-87
DJF 1988-89
(a)
NMC DJF87 HTG 350K
(b)
NMC DJF89 HTG 350K
(c)
NMC DJF87 CHIPAD 350K $-(\rho J_\theta \vec{V})_\chi \cdot \nabla P$
(d)
NMC DJF89 CHIPAD 350K $-(\rho J_\theta \vec{V})_\chi \cdot \nabla P$
(e)
NMC DJF87 CHIZAD 350K $-\vec{V}_\chi \cdot \nabla(\zeta+f)$
(f)
NMC DJF89 CHIZAD 350K $-\vec{V}_\chi \cdot \nabla(\zeta+f)$
90N
60N
30N
0
30S
60S
90S
0
60E
120E
180
120W
60W
0

Fig. 2. DJF distributions of (a),(b) 350 K heating (K day$^{-1}$); (c),(d) horizontal advection of PV by the irrotational mass transport; (e),(f) horizontal advection of absolute vorticity by the divergent velocity. Left-side panels are for DJF 1986-87 coinciding with the warm phase of ENSO. Right-side panels are for DJF 1988-89 coinciding with the cold phase of ENSO. Panels (c)-(f) are contoured every 4 x $10^{-11}$ $s^{-2}$. Fields filtered as in Fig. 1.

# TEDAZ: A New Look at ENSO Cycle Teleconnections

Eugene M. Rasmusson
Cooperative Institute of
Climate Studies
Department of Meteorology
University of Maryland
College Park, MD 20742

Kingtse C. Mo
Climate Analysis Center
NMC/NWS/NOAA
Washington D. C. 20233

## 1. INTRODUCTION

Elongated bands of cloudiness extending diagonally in an eastward and poleward direction from the deep tropics into the subtopics and middle latitudes are a ubiquitous phenomenological feature of satellite visible and IR observations. These 'tropical extratropical cloudbands" (TECB) occur throughout the tropics except over the cold Atlantic and eastern Pacific. Many authors (Kuhnel, 1989; McGuirk et al. 1987) have identified TECBs as a prime indicator of tropical extratropial interaction. According to Anderson and Oliver (1970) and others, they occur when an upper tropospheric trough and wind maximum approach the equator and couple with the zone of deep convection. Similar features can also been found in monthly mean outgoing longwave radiation (OLR) climatology and in OLR 1-5 day synoptic variance and the interannual variance (Lau and Chan 1988). We suggest that the interannual variance may reflect modulation of this activity on the ENSO time scale.

## 2. ENSO cycle patterns and TEDAZ

The dominant features of the ENSO cycle teleconnection patterns over the Pacific-Atlantic sector include belts of upper troposphere divergence anomalies which coincide with the well documented pattern of OLR anomalies. We will refer to the eastward and poleward extensions of these anomalies as tropical extratropical divergence zones (TEDAZ). This banded structure of ENSO cycle anomalies is a reflection of the eastward and poleward extension of equatorial precipitation anomalies into the subtropics and extratropics, and therefore has the appearance of direct links between anomalous tropical convection and the anomalous extratropical circulation.

We plotted here the difference maps of 200 mb streamfunction (Fig.1), divergence (Fig.2), velocity potential (Fig.3) and vorticity source S (Fig.4) between warm and cold phases of the 1986 -89 ENSO cycle during the NH winter Janaury to March . Fig.5 shows the OLR difference map between 1987 JFM and 1989 JMF , while the corresponding sea surface temperature (SST) difference map is given in Fig.6. From these charts, we synthesize information into an observational description of the coupling which take place between the anomalous equatorial convection and the NH 200 mb subtropical - midlatitude circulation during JFM. The primary ingredients of the coupling as deduced from this analysis, supplemented and supported by analyses of the 1982-83 warm episode (Rasmusson and Arkin, 1985) are summarized below:

1. The enhanced equatorial convection associated with an eastward migration of SST greater than about $28^{0}$C was located primarily between $160^{0}$E-$150^{0}$W.

2. Although part of the anomalous 200 mb divergent outflow from this convection was in the nature of an anomalous Walker circulation to the western Pacific, a more significant outflow was directed northward into higher latitudes between $160^{0}$E -$160^{0}$W.

3. The subsiding branch of this anomalous Hadley outflow was centered near $30^{0}$N in the same longitude belt.

4. While there was little in the way of a vorticity source directly associated with the equatorial convection outflow, there was a large source generated by the 200 mb convergence associated with the subsiding branch of the anomalous Hadley circulation.

5. Significant rotational flow anomalies appeared in the region and downstream of this vorticity source. These include:
(a) enhanced westerlies with a split in the anomalous flow. The northern branch curls around the anomalous cyclonic circulation in the Gulf of Alaska. The southern branch constitutes the enhanced subtropical westerlies across the Gulf of Mexico into the Atlantic.
(b) an equatorial enhancement of 200 mb synoptic scale variability apparently associated with the enhanced westerlies.

6. At the eastern end of the enhanced equatorial convection, the anomalous westerly flow and eddy activity penetrate to very low latitudes. We suggest that an interaction takes place between westerly disturbances and the enhanced tropical convection which leads to a northeastward extension of the anomalous convection across Mexico into the Gulf of Mexico and Atlantic.

7. The TEDAZ extending from the eastern equatorial Pacific across Mexico into the Gulf of Mexico and the western North Atlantic is associated with a region of anomalous upward motion and outflow. The compensating downward branch for this regional circulation appears to extend from the Amazon Basin eastward across the low latitude North Atlantic. In a broad sense, this is in opposition to the climatological regional Hadley circulation, and is associated with slightly weaker westerlies in the entrance region of the subtropical jet over the Atlantic during

the warm phase of this cycle. This regional divergent circulation links the well documented ENSO cycle wintertime precipitation anomalies over Mexico, the southeastern US and Gulf of Mexico with those of opposite sign over northeast South America (Ropelewski and Halpert, 1987,1989). This is in contrast to the usual picture, which associates the low latitude South American-Atlantic anomalies more directly with the Pacific anomalies through an anomalous Walker circulation.

8. While there is little upper troposphere vorticity directly generated by the convective anomalies within about $15^o$ of the equator, the increasing Coriolis parameter can result in significant vorticity anomaly source in the subtropical branches of the anomalous Hadley circulations and in the extratropical extensions of the TEDAZs.

In the Southern Hemisphere, TEDAZs are most directly associated with the equatorial convection anomalies linked to the shifts of SPCZ, which result in positive and negative precipitation anomalies that extend southeastward across the central Pacific during the SH winter. In the NH winter, the dominant TEDAZs are associated with the diminished convection over the western Pacific anomalous convection.

## REFERENCES

Anderson, R. K., and V. J. Oliver, 1970: Some examples of the use of synchronous satellite pictures for studying changes in tropical cloudiness. Proc. Sym. on Ttropical Meteorology, , Honolulu, Amer. Meteor. Soc. E Xii 1-6.

Kuhnel, I. 1989: Tropical extratropical cloudband climatology based on satellite data Intl. J. Climatol, **9**, 441-463

Lau K. M. and P. H. Chan 1988: Intraseasonal and interannual variations of tropical convection : a possible link between 40-50 day oscillations and ENSO ? J. Atmos. Sci, **45**, 2718-2743

McGuirk, J. P, A. H. Thompson and N. R. Smith, 1987: Moisture bursts over the tropical Pacific ocean Mon. Wea. Rev, **115**, 787-798.

Rasmusson, E. M., and P. A. Arkin, 1984: Interannual climate variability associated with the El Nino/Southern Oscillation Coupled Ocean -Atmospere Models, J. C. Nihoul ED. Elsevier, Amsterdam, 697-725.

Ropelewski, C. F. and M. S. Halpert, 1989: Precipitation patterns associated with the high index phase of the Aouthern Oscillation J. Climate, **2**,268-284.

------------- and --------------, 1987: Global and regional scale precipitation patterns associated with the El Nino/ Southern Oscillation Mon. Wea. Rev, **114**, 1606-1626

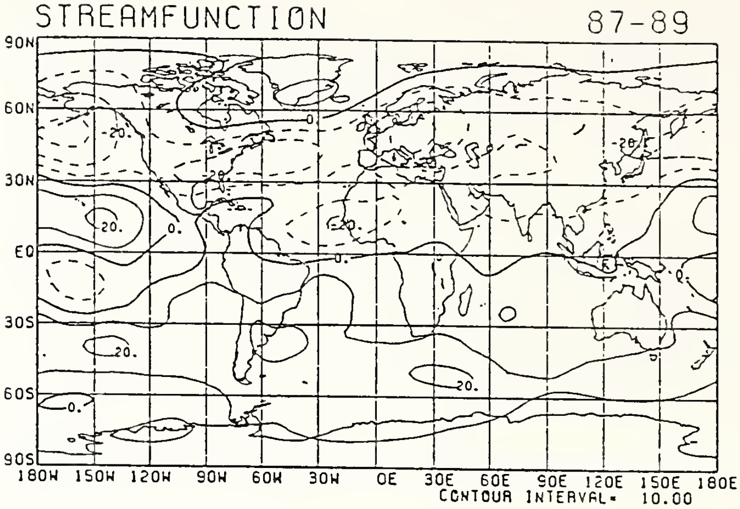

Figure 1: Warm minus cold phase 200 mb streamfunction differences for JFM, contour interval $1.E+07 m^2/sec$. Negative contours are dasned.

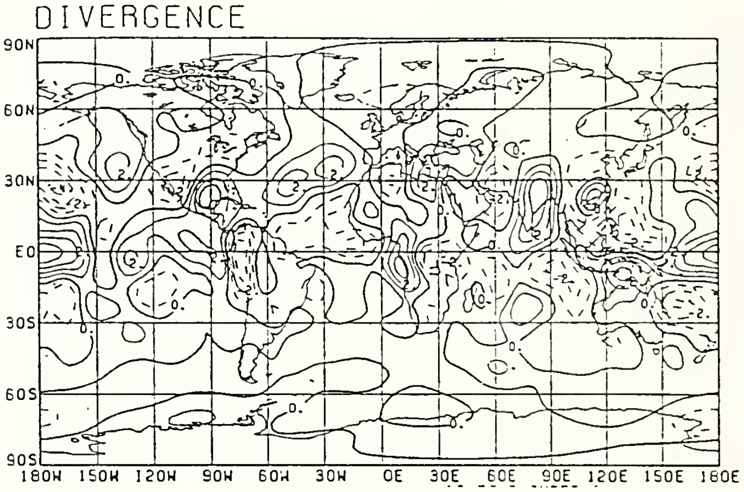

Figure 2: Same as Fig.1, but for divergence. Contour interval 1.E-06/sec

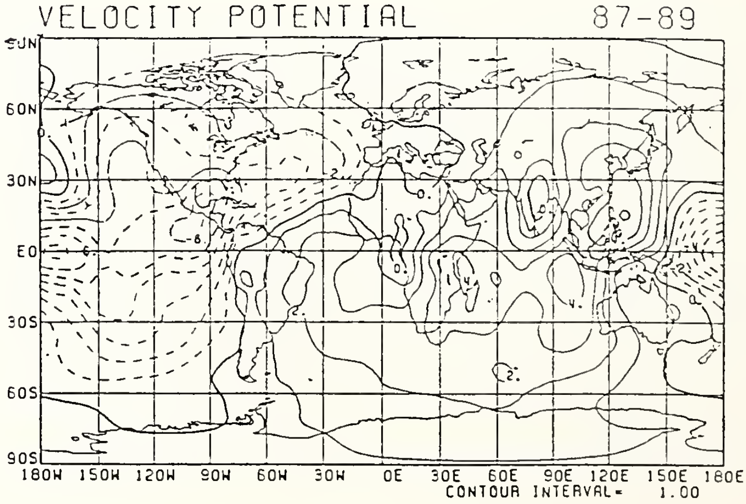

Figure 3: Same as Fig.1, but for velocity potential. Contour interval $1.E+06\ m^2/sec$

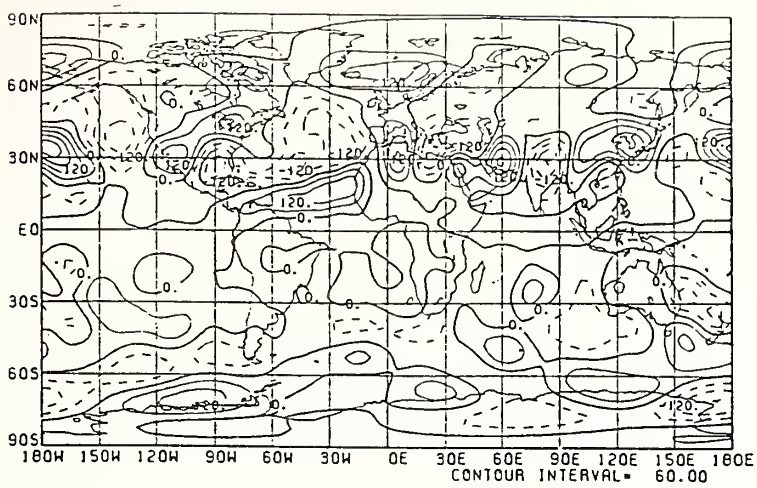

Figure 4: Same as Fig.2, but for vorticity source S . Contour interval 6E-11/sec

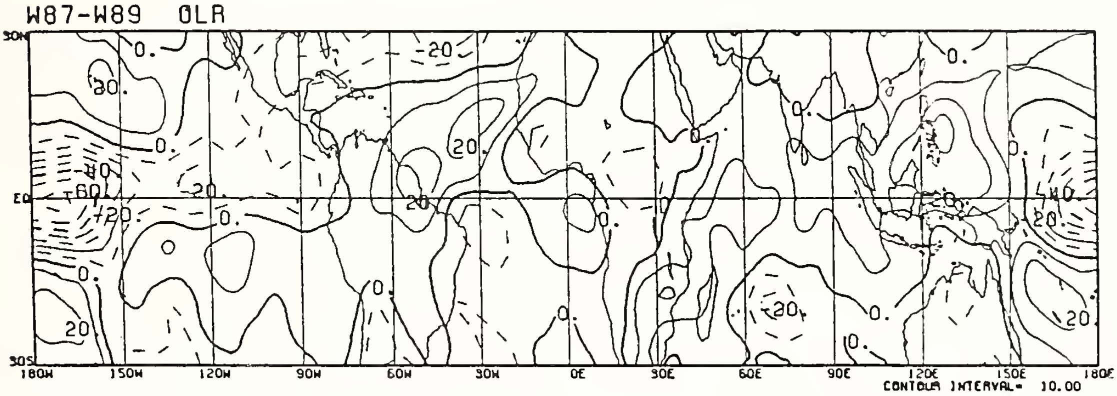

Figure 5: Warm minus cold phase OLR difference for JFM. Contour interval 10W/$m^2$. Negative contours are dashed

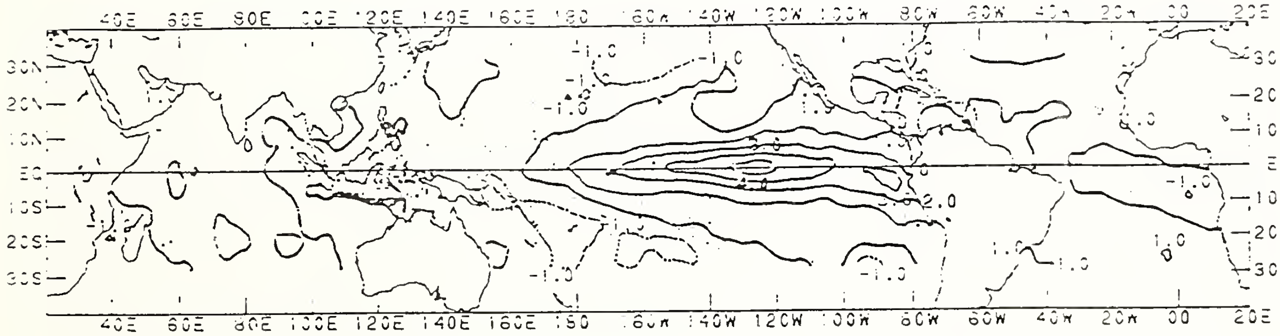
40E 60E 80E 100E 120E 140E 160E 180 160W 140W 120W 100W 80W 60W 40W 20W 00 20E
30N
20N
10N
EQ
10S
20S
30S

Figure 6: Warm minus cold phase SST difference for JFM. Contour interval 1C.

# TEDAZ 2 A Second Look at Tropical and Extratropical Circulation Anomalies

Kingtse C. Mo and Vernon E. Kousky

Climate Analysis Center
NOAA/NWS/NMC
Washington D. C. 20233

## 1. Introduction

In the previous paper, Rasmusson and Mo studied the 200 mb circulation anomalies and the associated vorticity budget during recent extremes in the Southern Oscillation (1987-1989). They described the linkages between the equatorial Pacific convection anomalies and extratropical circulation in terms of regional Hadley cells and tropical-extratropical divergence anomaly zones (TEDAZs). Their analyses were based on recent extremes in the Southern Oscillation. The immediate question is whether or not TEDAZs are also the principal extratropical response to convective anomalies for other ENSO years or for variability with time scales shorter than those associated with the Southern Oscillation.

In this paper we focus on the linkages between the tropical and extratropical circulation anomalies having time scales greater than 10 days. The data used are pentad mean 250 mb streamfunction and outgoing long wave radiation (OLR) over the period 1979-1990. The principal modes of anomalous 250 streamfunction are computed and are related to anomalous OLR, which is used as a proxy for deep tropical convection.

## 2. First EOF pattern: Zonally symmetric mode

Figure 1 displays the first northern winter EOF. The pattern for the first NH summer EOF is the same. For the winter and summer data , it explains 22% and 19% of the total variance, respectively. The pattern is dominated by a zonally symmetric component. The zonally asymmetric circulation shows a signal generally associated with extremes in the Southern Oscillation, with large loadings concentrated in the tropics and subtropics from $30^{\circ}$S to $30^{\circ}$N. For positive amplitudes of this mode, easterlies are found in the tropical Pacific and strong westerlies extend from the tropical Atlantic eastward across Africa and into the Indian Ocean. The asymmetric part of EOF 1 shows an anticyclonic couplet (positive S-PC 1 for the warm episode) straddling the equator in the Pacific, which is consistent with the eastward displacement of the west Pacific warm pool and its associated convection during ENSO years. There is also a cyclonic couplet over the Atlantic that indicates a strengthening of the climatological cyclonic couplet in that area (Rasmusson and Mo 1991). In the NH, this pattern is similar to the correlation map between equatorial SST anomalies averaged over the region from the date line to the South American coast, and 500 mb height anomalies (Wallace and Jiang 1983).

The S-PC 1, obtained by projecting all pentad data onto EOF 1, is plotted in Fig. 2a. An examination of S-PC 1 reveals rather high amplitude high frequency fluctuations superposed on the slowly evolving ENSO-related variations. When we subject S-PC 2 to singular spectrum analysis , it shows that the intraseasonal frequency variations in S-PC 1 are related to the 30-60 day oscillations.

Figure 2b shows the OLR anomalies (OLRA) averaged over the box $5^oS$-$5^oN$ and $160^oE$-$160^oW$ without any filtering or smoothing. There is a noticeable out-of-phase relationship between OLRA (Fig. 2b) and S-PC 1 (Fig. 2a). The correlation between the two series is -0.41, which is statistically significant at the 99% level according to the formula given by Sciremammano (1979). This suggests that the zonally symmetric pattern is physically related to anomalous convection in the equatorial Pacific. To obtain the global OLR anomaly pattern, which is related to the zonally symmetric circulation pattern, we correlated S-PC 1 with OLRA pentad maps for DJF (Fig. 3). On average, the correlation has to be 0.23 (0.30) or greater to be statistically significant at the 95% (99%) level. Figure 3 shows the following pattern: for positive S-PC 1, there is relative dryness (positive OLRA) over Indonesia, the Philippines, the Indian Ocean and the equatorial Atlantic, and enhanced convection (negative OLRA) in the tropical Pacific east of $150^oE$. There is also a strong South Pacific Convergence Zone extending from the central tropical Pacific southeastward toward the coast of Chile and an enhanced South Atlantic Convergence Zone. In the NH, there is some indication of a cloud band extending from the Gulf of Mexico east-northeastward through the North Atlantic, which is consistent with the TEDAZ pattern. This pattern also appears in the NH summer, but the correlations are weaker. There is also considerable similarity related to extremes in the Southern Oscillation, and it matches the pattern of anomalous rainfall found during ENSO years obtained by Ropelewski and Halpert (1987).

## 3. EOF 2 : the TEDAZs signal

The NH winter EOF 2 pattern (Fig. 4a) explains 4.9% of the total variance. There is no similar pattern in the JJA season, so this is basically a NH winter pattern. The third EOF explains 3.5% of the total variance. To avoid possible degeneracy, we performed varimax rotation using the first 5 EOFs. Together they explain 38.9% of the total variance. The first rotated EOF pattern is again the zonally symmetric pattern, and the TEDAZs pattern appears as rotated EOF 4 (Fig. 4b), which explains 4.1% of the total variance.

There is a great deal of similarity between rotated REOF 4 and unrotated EOF 2 from the western Pacific eastward into the Atlantic. Both patterns have large loadings located in the NH and the tropics. The NH features in the western hemisphere for both patterns bear a remarkable resemblance to the streamfunction pattern associated with the tropical-extratropical patterns observed during recent extremes in the Southern Oscillation . There is also considerable symmetry between the SH and NH features in both EOFs in the Pacific for the latitude band $30^{o}$n-$30^{o}$S.

To study the relationship between TEDAZs and convection in the tropics, we made composite maps based on extremes in the T-PC for S-PC 2 and S-RPC 4. Dates where a given T-PC is larger in absolute value than 1.6 times its own standard deviation were selected. We then averaged 250 mb streamfunction anomalies and OLR anomalies keyed to those dates to form composites. We also made composites for both fields for the three pentads before and after the selected dates in order to study the lag and lead relationships among signals.

The composite 250 mb streamfunction and OLR anomalies for negative S-RPC4 indicate a ENSO related low frequency signal. Composites for streamfunction and OLR anomalies keyed to the negative extremes of S-PC 2 are given in Figs. 5 and 6, respectively. The corresponding composites for positive S-RPC 4 are essentially the same. Two pentads before the S-PC 2 reaches its minima, the cloud bands located in the Pacific ($160^{o}$E-$160^{o}$W, 0-$30^{o}$N) are already well-organized with an accompanying trough at the same location (Figs. 5a and 6a). At the same time, there is enhanced convection over the maritime continent and Indian Ocean and relative dryness in northern Australia. There is also enhanced convection over northern South America and the tropical North Atlantic. Comparing the pattern for a lead of two pentads (Fig. 5a) with the simultaneous pattern (Fig. 5b), it is evident that the subtropical westerlies increase with time at most longitudes. At the same time, the anomalous convection strengthens over northern South America and negative OLR anomalies extend eastward into the Atlantic, while in the Pacific the cloud bands begin to dissipate. Two pentads later, the cloud bands in the Pacific dissipate (Fig. 6c), but the TEDAZs signal (Fig. 5c) is still evident.

For the NH summer, the TEDAZs pattern also appears as EOF 2. It shows a extension of the SPCZ to higher latitudes of the

South Pacific and an out-of-phase relationship between middle and high latitudes. Composites indicate that, as expected, this pattern is related to tropical convection. The PCs associated with EOF 2 contain 60 day oscillations, which may be related to variability of the Asian monsoon.

## REFERENCES

Rasmusson, E. M., and K. C. Mo, 1991: Linkage between 200 mb tropical and extratropical circulation anomalies during the 1986-1989 ENSO cycle. Submitted to *J. of Climate*.

Ropelewski, C. F., and M. S. Halpert, 1987: Global and regional scale precipitation patterns associated with the El Nino/ Southern Oscillation. *Mon. Wea. Rev.*, **115**, 1606-1626.

Sciremammano, F., 1979: A suggestion for the presentation of correlations and their significance levels. *J. Phys. Oceanogr.* **9**, 1273-1276.

Wallace, J. M., and Q. R. Jiang, 1987: On the observed structure of the interannual variability of the atmosphere/ocean climate system. *Atmospheric and Oceanic Variability*, Roy. Meteor. Soc. H. Cattle, ED., 17-43.

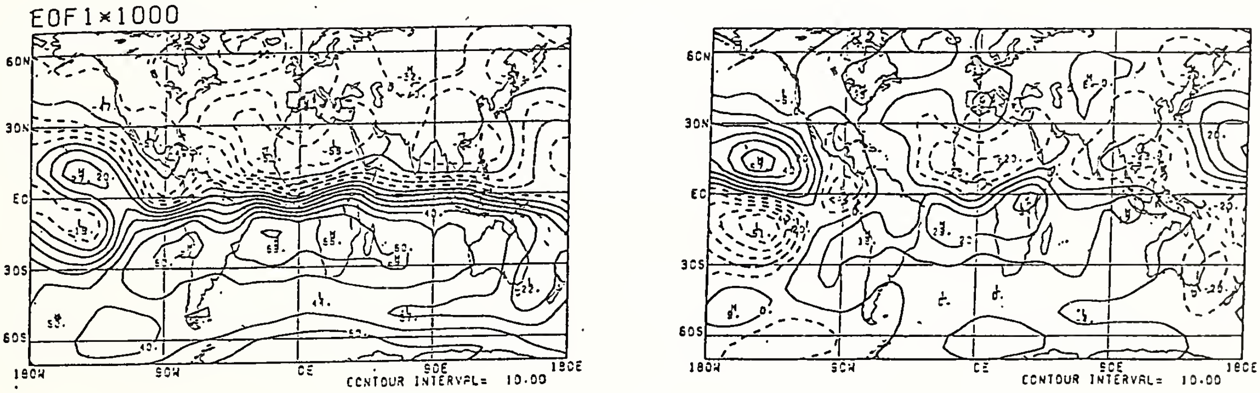

Figure 1 (a) Spatial EOF 1 pattern for the NH winter. Contour interval 10 x $10^{-3}$. Negative contours are dashed.

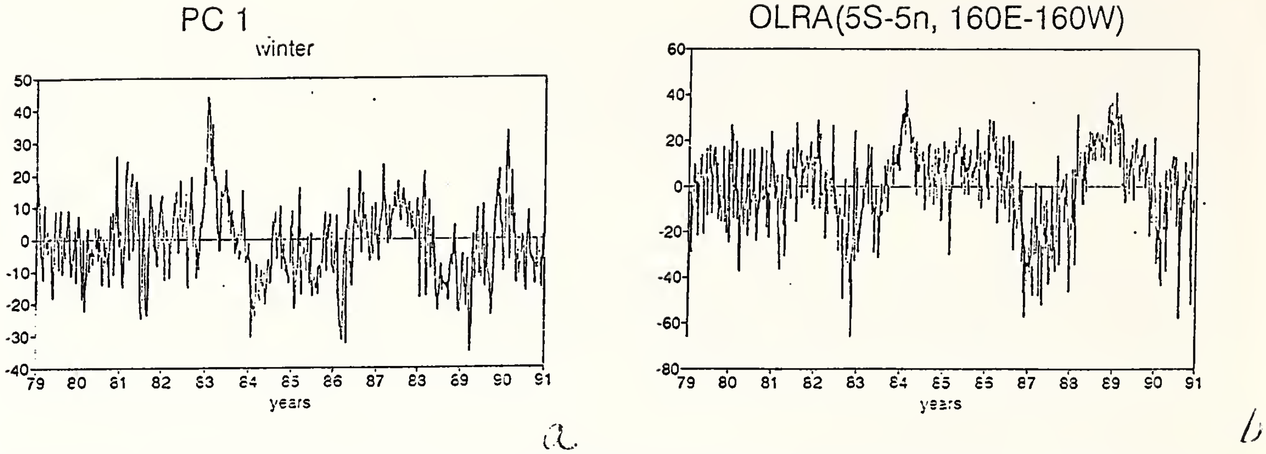

Figure 2 (a) S- PC 1 associated with the NH winter EOF 1. and (b) pentad OLR anomalies averaged over $5^{\circ}$S-$5^{\circ}$N and $160^{\circ}$E -$160^{\circ}$W.

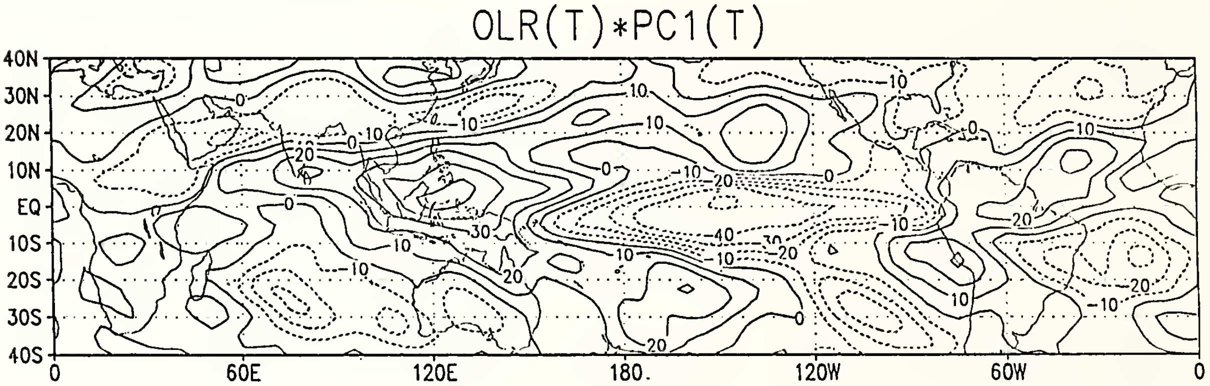

Figure 3 Correlation*100 between NH winter S-PC 1 and OLR anomalies for the winter season (DJF). Contour interval 10

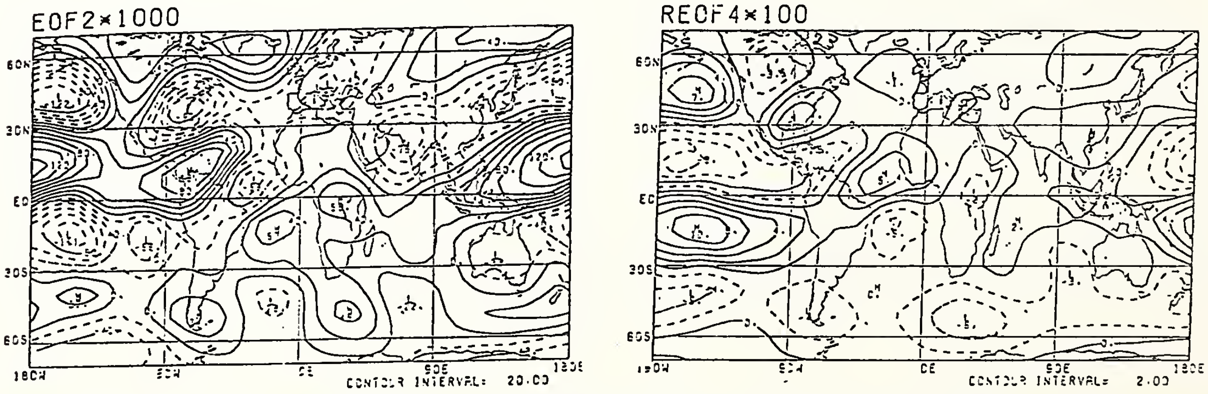

Figure 4 (a) Spatial EOF 2 pattern for the NH winter. Contour interval 20x$10^{-3}$. and (b) rotated spatial EOF 4. Contour interval 2*10 $^{-2}$.

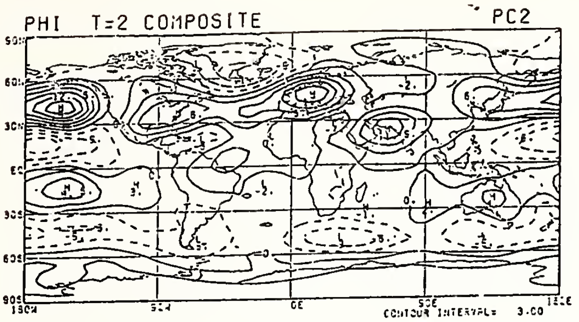

5a

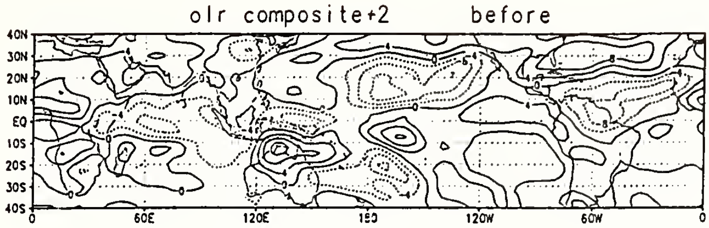

6a

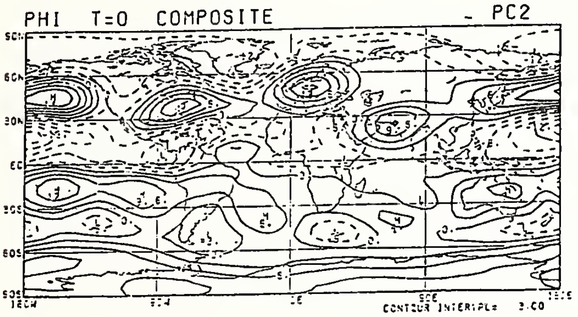

5b

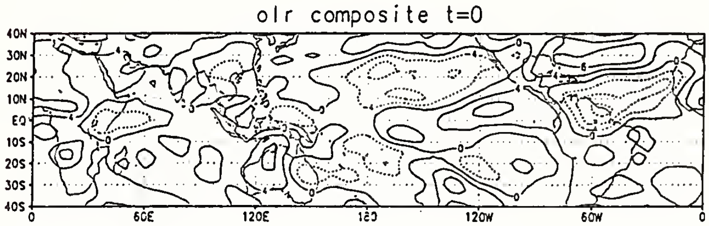

6b

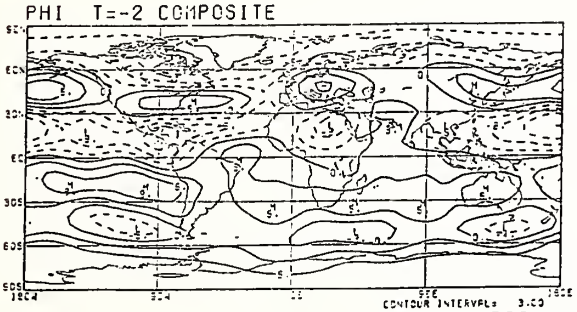

5c

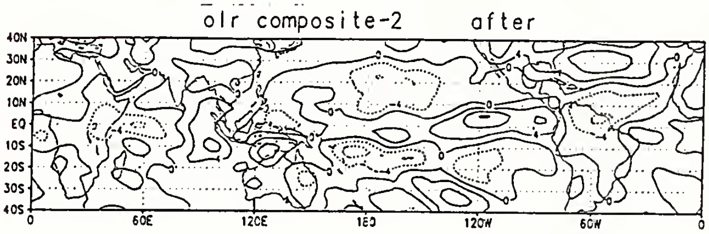

6c

Figure 5 Composites of 250 mb streamfunction anomalies keyed to (a) 2 pentads before, (b) simultaneous with, and (c) 2 pentads after negative S-PC2 extremes. Contour interval 4 x $10^6$ $m^2s^{-1}$.

Figure 6 Same as Fig 5., except for OLR anomalies. Contour interval 4 $Wm^{-2}$.

# ENSO's Precipitation Signature in the U. S.
# Are Wet Days Wetter or More Frequent?

Edward S. Epstein
CAC/NMC/NWS

## 1. Introduction.

Ropelewski and Halpert (1986) (RH) found that warm events in the equatorial Pacific were accompanied by, among other signatures, heavier than normal winter precipitation in an extensive region of the southeastern United States surrounding the Gulf of Mexico. They also found that summer precipitation was enhanced in warm event years in the great basin of the US. In an effort to define better the nature and extent of these phenomena, both to understand their physical origin and as an aid in extended (monthly and seasonal) forecasting, we have analyzed daily precipitation data extending back to 1900 in terms of the frequency of precipitation (in pentads) and the amounts of precipitation conditional on its frequency. We examine and contrast low (SOI) index (warm events) and high index (cold events) years and ask if seasonal precipitation (in the summer and winter seasons defined in RH) is anomalous under either or both ENSO conditions. We also assess the geographic extent within the contiguous United States of these phenomena. The data are daily precipitation amounts at 138 long term Historical Climatological Network--Daily (HCN) stations. We have included in our analysis all but the 22 of these stations for which the data did not begin until after 1910.

## 2. Method.

The analysis involved harmonic representations of the frequencies of zero, one, and two or more days with precipitation in a five-day period, and also of the median amounts of precipitation per five days when only one day in five was wet (at least .01 inches) or two or more days in five were wet (Epstein, 1989). The harmonic representations covered a two-year ENSO cycle, beginning in July of the year preceding the nominal year (i.e. year -1), and ending with June of year +1. Separate calculations were made for warm event years and cold event years. Four harmonics were calculated, i.e. periods of 24, 12, 8 and 6 months.

Ropelewski and Jones (1987) identified, in the period from 1900 to 1988, 27 years as warm event years, and 17 as cold event years. These, listed in Table 1, were the basis of our calculations. We then repeated the calculations for 100 random specifications of 27 warm and 17 cold event years in the period 1900-1988. The statistics that we examined for each station, based on the harmonic representations, were (1) the seasonal (October of year 0 through March of year +1, and April through October of year 0) mean probabilities of wet pentads (defined as two or more wet days in five; (2) the seasonal mean of the five-day median precipitation of wet periods; and (3), as a proxy for total precipitation, the contribution to the total precipitation of wet periods (the integral, over the season, of the product of the probability of a wet pentad and the median amount given the pentad is wet).

We examined the number of randomly selected sets of years that produce statistics that are exceeded by those based on the set of years given in Table 1. These are numbers that can range from 0 to 100. We also looked at the numerical values of the statistics to assess their practical significance.

## 3. Results.

Table 2 contains a count of the numbers of stations out of 116 for which exceedences totaled 0 or 100, 1 or 99, 2 or 98, and 3 or 97. If the years listed in Table 1 were indistinguishable, with respect to precipitation, from a random set of years, then the expected numbers in this table would be 2.3. The expected total over all four categories under those null conditions is 9.2. The counts of exceedences pertaining to the summer response to cold events are about those one would expect by chance. There is no overall, or 'field' significance in this category and one cannot argue strongly for attaching significance to individual stations. The only other category for which field significance is questionable is the conditional precipitation amounts in the warmer months of warm event years. In contrast, the winters of cold event years are extremely wet or extremely dry (counts less than 4 or more than 96) at 28 of the 116 stations.

The results confirm in many ways those of RH, but they also lead to additional insights and conclusions. Figure 1 gives the numbers of exceedences of the proxy total precipitation for the given warm event set of years over those of the randomly chosen year-sets for the winter periods. Isopleths are drawn for 1, 5, 10, 90, 95, and 99. There is a large region in which the total winter precipitation is enhanced during warm events. This corresponds roughly to the southeastern region identified by RH, although it is confined more to the Gulf coast in the southeast and extends further west and north than RH portray. There are additional indications of wetter than normal conditions during warm event winters throughout the southwest, in coastal California, and in the northeast. There is evidence of dryness in the central Appalachians and along the continental divide between Montana and Idaho.

Figures 2 and 3 offer insight into the relative roles of frequency and intensity of precipitation. The extension to the southwest and the response in the northeast are largely dependent on greater amounts of rain when wet periods occur. In contrast the phenomena in the southern high plains and in the northern Rockies are associated with enhanced and diminished probabilities of wet periods, respectively.

During summers of warm event years, the probability of wet periods is enhanced over large regions of the southwest including the Great Basin region identified by RH (see Figure 4). Also in evidence is a tendency for fewer wet periods during warm event summers in the middle Atlantic states from Maryland to South Carolina.

Table 2 indicates that the largest number of stations showing anomalous results relate to the probability of wet periods during the winter of cold event years. Figure 5 is a map of those exceedences. All 11 stations in Texas, Oklahoma and New Mexico had smaller mean frequencies in the winters of cold years than in any of the random sets of years. The dry signal in the winter of cold event years is supported in the immediate vicinity of the Gulf of Mexico by decreases in conditional amounts (Figure 6), but is largely a phenomenon of frequency of wet periods elsewhere. Wet conditions in the northern Rockies during warm event winters are also largely a frequency phenomenon.

These responses are not only statistically impressive. They are also impressive quantitatively. Some examples for the winter period are given in Table 3. Note, for example, the implications of the proxy total winter precipitation that we compute for Albany, TX, to be twice as great in warm event years than in cold event years. There are substantial variations in the relative roles of frequency and conditional amounts.

We have used 'winter' and 'summer' seasons as previously defined in RH. The results would have been more dramatic (but statistically unsound) if we had chosen the season after examining the data. Figure 7 shows the harmonic fits to the Blue Hill, MA, data for the median precipitation in wet periods for warm and cold event years. Note the difference extending from the fall of year 0 to the spring of year 1. The +'s and x's indicate the individual pentad values that went into the harmonic analysis, + for warm event years and x for cold event years. The consistency of the higher precipitation amounts during wet periods associated with warm events is very much in evidence. The regional pattern to this seasonality of the ENSO effect on precipitation needs careful study.

## 4. Conclusions.

The relative roles of frequency of precipitation and the amounts conditional on precipitation events present a complex pattern. Clearly there are some very real differences seasonally, regionally, and between warm and cold events. Understanding these differences is a challenge.

## REFERENCES

Ropelewski, C.F., and M.S. Halpert, 1986: North American precipitation and temperature patterns associated with the El Niño/Southern Oscillation (ENSO). Mon. Wea. Rev., 114, pp. 2352-2362.

_________ and P.D. Jones, 1987: An extension of the Tahiti-Darwin Southern Oscillation Index. Mon. Wea. Rev., 115, pp. 2161-2165.

**Table 1.** Years during which the Tahiti-Darwin Southern Oscillation Index remained in the lower or upper 25% of the distribution for 5 months or longer.

Low index (warm event) years

1900, 1902, 1905, 1911, 1913, 1918, 1919, 1923, 1925, 1926, 1939, 1940, 1941, 1946, 1951, 1953, 1957, 1963, 1965, 1969, 1972, 1976, 1977, 1982, 1983, 1986, 1987

High index (cold event) years

1904, 1909, 1910, 1916, 1917, 1924, 1928, 1938, 1950, 1955, 1956, 1964, 1970, 1971, 1973, 1975, 1988

**Table 2.** Counts of exceedences, by statistics based on ENSO high and low index years, of statistics from random sets of years.

| | | | Number of Exceedences | | | |
|---|---|---|---|---|---|---|
| ENSO Category | Season | Statistic | 0/100 | 1/99 | 2/98 | 3/97 |
| warm event | summer | prob 2+ | 7 | 3 | 4 | 5 |
| (low index) | | cond. amt. | 2 | 3 | 3 | 1 |
| | | total (proxy) | 5 | 4 | 4 | 3 |
| warm event | winter | prob 2+ | 5 | 9 | 5 | 3 |
| (low index) | | cond. amt. | 6 | 4 | 4 | 4 |
| | | total (proxy) | 10 | 12 | 3 | 2 |
| cold event | summer | prob 2+ | 5 | 1 | 3 | 2 |
| (high index) | | cond. amt. | 3 | 5 | 0 | 3 |
| | | total (proxy) | 1 | 4 | 4 | 1 |
| cold event | winter | prob 2+ | 20 | 6 | 4 | 1 |
| (high index) | | cond. amt. | 3 | 5 | 4 | 3 |
| | | total (proxy) | 19 | 3 | 3 | 3 |

**Table 3.** Some quantitative examples of the ENSO signature in terms of winter precipitation. Numbers in parentheses in the number of times, out of 100, that the statistic exceeded a similar calculation for a random assignment of years to warm and cold event categories.

| Station | event | prob. wet pentad | conditional amount | proxy total precip |
|---|---|---|---|---|
| Apalachicola. FL | warm | 0.40(100) | 1.08(100) | 15.8(100) |
| | cold | 0.27(0) | 0.95(51) | 9.4(3) |
| Albany, TX | warm | 0.20(83) | 0.79(98) | 6.0(99) |
| | cold | 0.13(0) | 0.61(16) | 3.0(0) |
| Biloxi, MS | warm | 0.41(91) | 1.25(100) | 18.5(100) |
| | cold | 0.36(14) | 0.91(1) | 12.2(0) |
| Blue Hill, MA | warm | 0.60(25) | 0.85(100) | 18.7(100) |
| | cold | 0.63(92) | 0.68(3) | 15.9(15) |
| El Dorado, KS | warm | 0.28(98) | 0.54(53) | 5.9(96) |
| | cold | 0.20(0) | 0.61(91) | 4.5(12) |
| Fortine, MT | warm | 0.45(3) | 0.27(24) | 4.5(0) |
| | cold | 0.53(97) | 0.30(80) | 5.9(100) |
| Napa, CA | warm | 0.41(68) | 1.05(98) | 16.3(92) |
| | cold | 0.42(76) | 0.77(0) | 12.1(5) |
| San Jon, NM | warm | 0.13(100) | 0.42(68) | 2.1(99) |
| | cold | 0.07(0) | 0.36(13) | 1.1(0) |

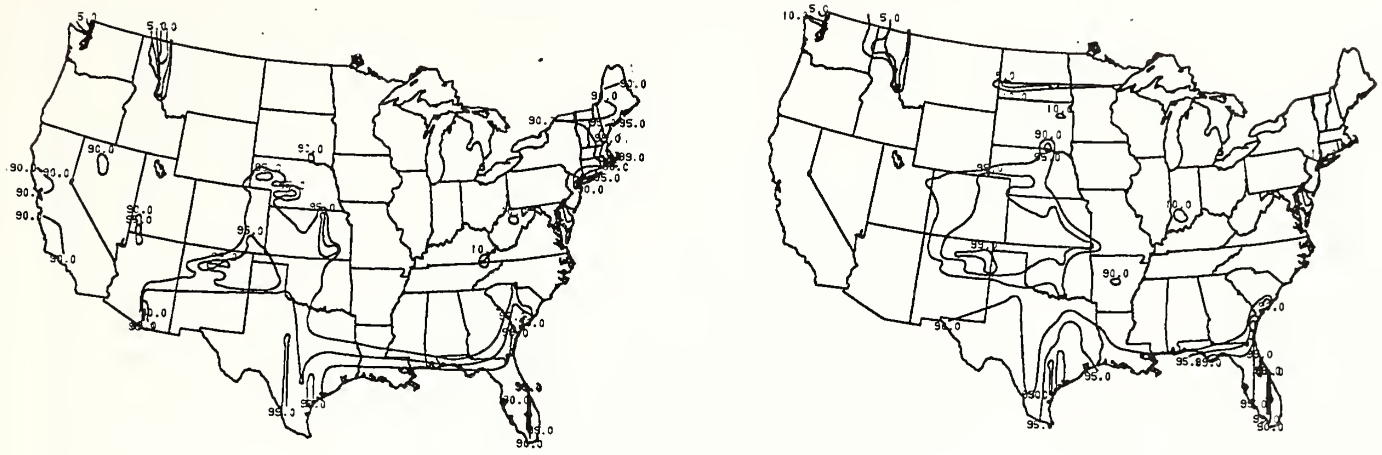

WARM / WINTER / CONTRIB TO TOTAL

WARM / WINTER / PROB WET

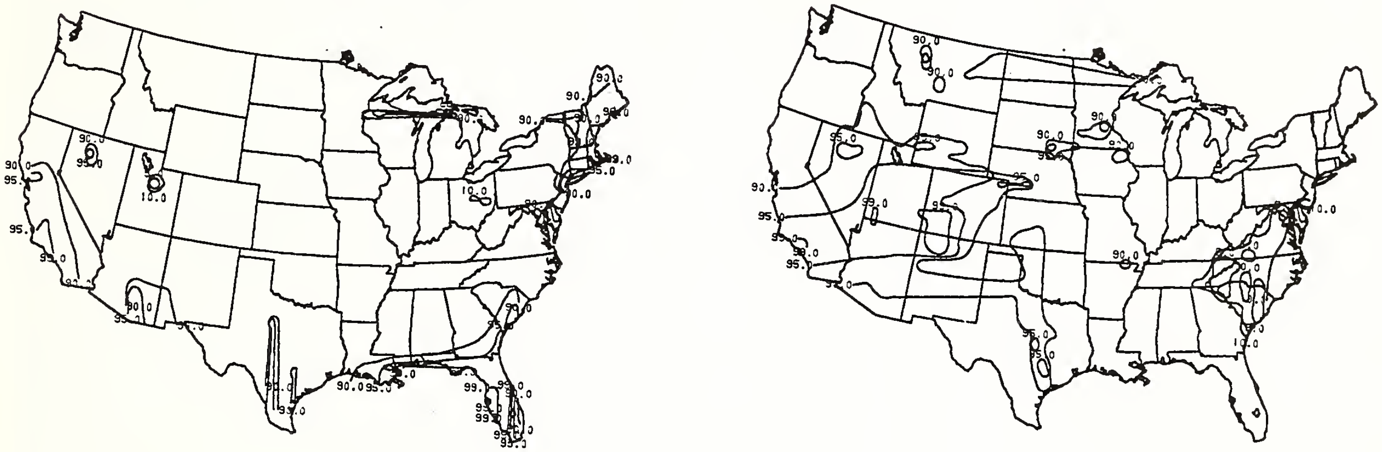

WARM / WINTER / AMOUNT IF WET

WARM / SUMMER / PROB WET

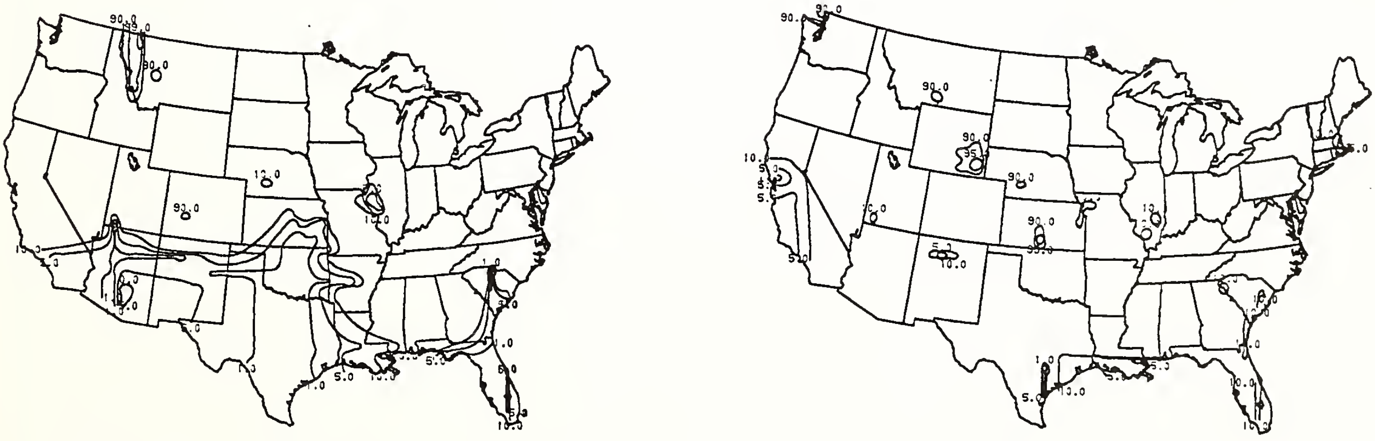

COLD / WINTER / PROB WET

COLD / WINTER / AMOUNT IF WET

Figures 1 through 6. Numbers of random sets of years, out of 100, for which the indicated statistic was exceeded by the statistic calculated on the basis of years given in Table 1.

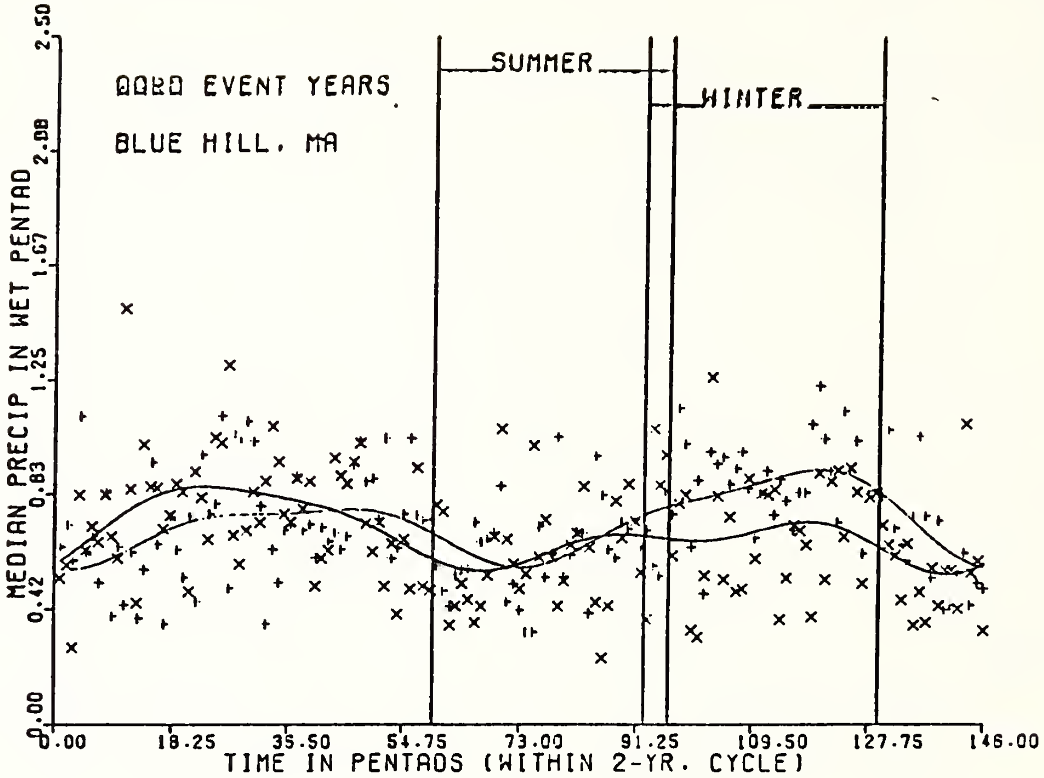

Figure 7. Superimposed graphs of harmonic fits for warm and cold event years for Blue Hill, MA. The x's and +'s are the pentad-by-pentad data on the basis of which the harmonic fit was calculated for cold event and warm event years respectively.

# Seasonality in ENSO scale variability

Muthuvel Chelliah
Climate Analysis Center, NMC, NWS, NOAA, Washington DC

## 1. Introduction

The work described here is essentially a continuation of the work reported in the previous workshop. In order to understand the new results to be reported here and to establish the connection, a brief recapitulation (without figures) of last year's work is necessary. In the last workshop, the results from an investigation of the tropical/tropical and tropical/extratropical teleconnections (interactions) in the low frequency time scale, using rotated joint principal component analysis (JPCA) of monthly outgoing longwave radiation (OLR) and 200 & 800 mb vorticity anomalies, were reported (Chelliah, 1991, Proceedings of 15th Annual Climate Diag. Workshop, Asheville, NC, October 29 - November 2, 1990, pp 149-154). That analysis included all seasons, i.e., all twelve calendar months, of the year from 1975 through 1989 (excluding calendar year 1978, when OLR data was not available for the last ten months of the year). Of the top five rotated eigenmodes (or principal components) from the JPCA, the leading mode that was not shown was associated with the changes in the global data assimilation system (GDAS) at NMC. The second and third modes, termed respectively the 1982/83 mode and the 'canonical ENSO' mode, described the spatial patterns on the ENSO time scale of the tropical (especially Pacific) convection changes along with the upper and lower level vorticity changes and the associated time series. Note that the main reason for calling the 1982/83 mode so, is because the spatial loadings corresponding to this mode represents the very unusual much farther eastward shift in convection in the tropical Pacific during the 1982/83 ENSO. Even though this mode is termed the 1982/83 mode, the time series corresponding to this mode indicates that the feature - convection in the far eastern Pacific, was also present during 1986/87 ENSO event. Unlike the second and third mode, where the OLR patterns are characterized by an east-west dipole in the Indian, Pacific Ocean regions the fourth eigenmode is characterized by a north-south oriented dipole in the central Pacific. It was noted that this mode was associated with the maximum vorticity changes over the north American continent. The fifth mode (not shown in last year's proceedings) relates the changes in the intensity of the northern Pacific intertropical convergence zone (ITCZ) to the vorticity changes. It should be noted that except for the leading eigenmode, each of the other four modes considered above was associated with some aspect of the ENSO phenomenon, including both the warm and cold events in the analysis period, and all of these modes were described in detail in last year's report.

## 2. Results

The above analysis is now updated to include data through May 1991. In order to examine the seasonal dependence of the various eigenmodes to the winter and summer seasons the joint PC analysis is repeated separately for extended winter (Nov-Dec-Jan-Feb-Mar) and summer (may-jun-jul-aug-sep) seasons only. It has to be reminded that the analysis region for OLR anomalies is the deep tropics ($20^{O}$N-$20^{O}$S) and for vorticity anomalies it is from $40^{O}$S to $40^{O}$N. The leading five eigenmodes from the winter case were exactly the same as the leading five modes from the all-season case (described above), even though the ordering of the modes is now different. The numerical ordering of the leading five modes from the winter case is now as follows, where the number in parentheses refer to the corresponding mode number from the all-season case : 1) the 1982/83 mode (2), 2) the mode with the north-south oriented dipole in OLR anomalies (4), 3) the mode that reflects the changes in GDAS analysis procedures (1), 4) canonical ENSO mode (3) and 5) the mode related to the changes in the ITCZ (5). The consistency between the tropical convection anomalies and the upper & lower level vorticity anomalies has already been pointed out. Unlike winter case, there are only three (out of five) common modes between the summer case and all-season case. These three modes are namely 1) the mode that was related to the analysis changes in GDAS, 2) the canonical ENSO mode, with the convection anomalies exhibiting an east-west dipole centered over the Indian ocean/western Pacific region and 3) a mode similar to the 1982/83 mode (from the all-season case) with large OLR loadings over the eastern tropical South Pacific Ocean. Interestingly, the notable second mode in the winter case, which was characterized by a north-south oriented dipole in OLR anomalies east of the dateline, did not have its counterpart during summer.

Figs. 1,2 and 3,4 belong respectively to the winter and summer seasons. In these figures, we have shown for each season, the 1982/83 mode and the canonical ENSO mode. The seasonal dependence of the other common mode between the two seasons, namely the mode that was related to the GDAS changes is not shown here in the interest of space. For each mode in figures 1 through 4, there are four panels shown and they are, respectively from the top, the time series, the spatial loadings of OLR, 200 mb and 850 mb vorticity. While interpreting these diagrams, note that the sign of either the loading pattern or the time series by itself is arbitrary and only the product of the signs of these two quantities (loadings and time series) determine the actual sign of the anomalies for a given variable. Even though the same two modes were present in the all-season case, since the winter and summer seasons differ on either side of the equator, the seasonality of the two modes is described clearly in these figures with a marked tendency for these low frequency modes to be biased towards the winter hemisphere with stronger loadings. Other differences that can be seen between the two seasons include the lack during summer of a strong west center in the east-west dipole of OLR anomalies in the 1982/83 mode, but the same west center is present over the Indian ocean/western Pacific region in the dipole corresponding to the canonical mode. Particularly, this difference implies the following: i.e, during the summer of a regular (canonical phase) warm event, the east-west Walker circulation is such that the rainfall over India and the equatorial Indian ocean is reduced as convection is increased in the central equatorial Pacific along with a stronger north Pacific ITCZ. However, if enhanced convection moves to far eastern equatorial Pacific, Indian monsoon rainfall appears to be unaffected. Associated with ENSO, further differences can also be found over south America between winter and summer.

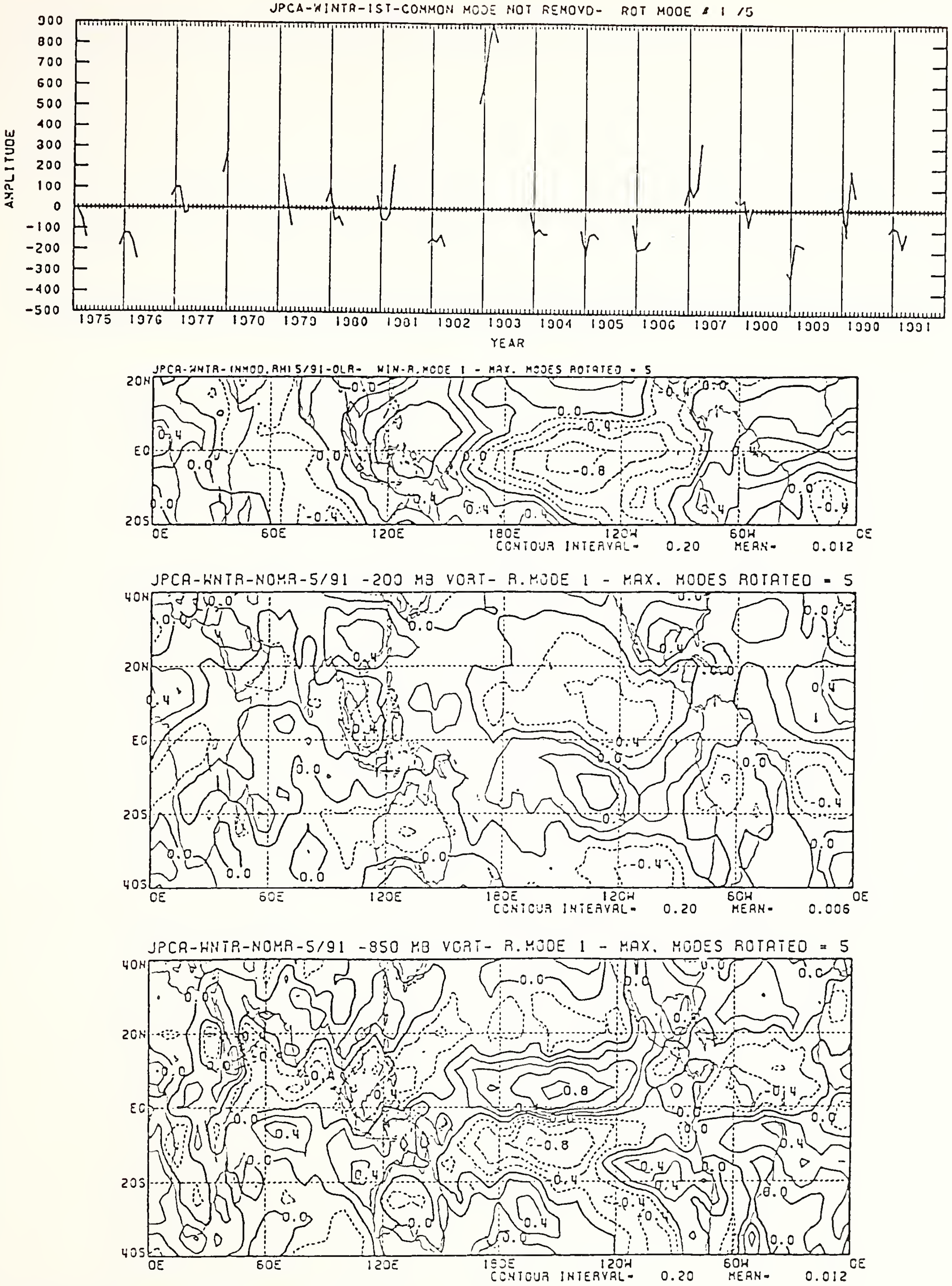

Fig. 1 '1982/83 mode' from joint analysis for winter months only.

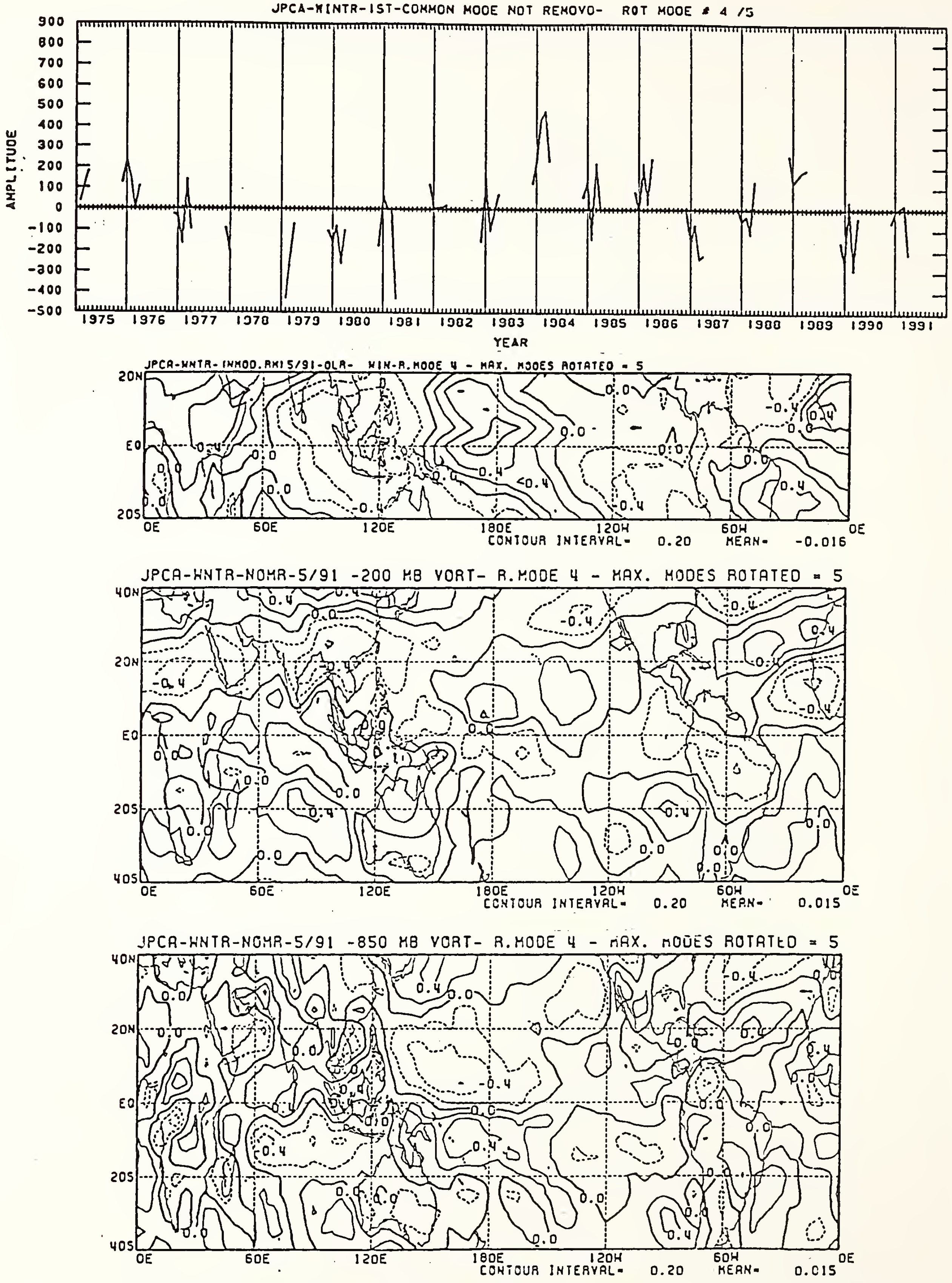

Fig. 2 'Canonical ENSO mode' from joint analysis for winter months only

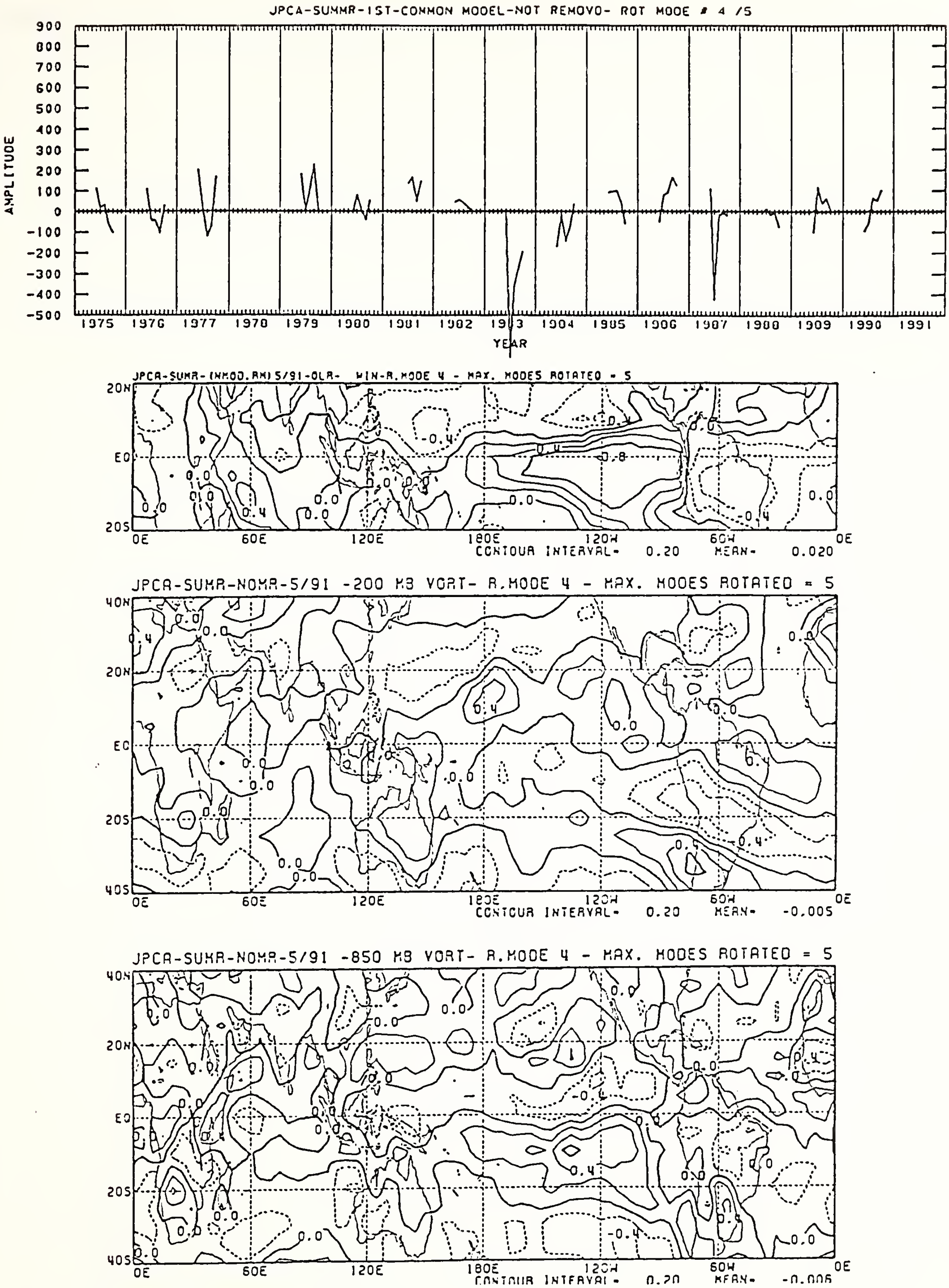

Fig. 3 '1982/83 mode' from joint analysis for summer months only.

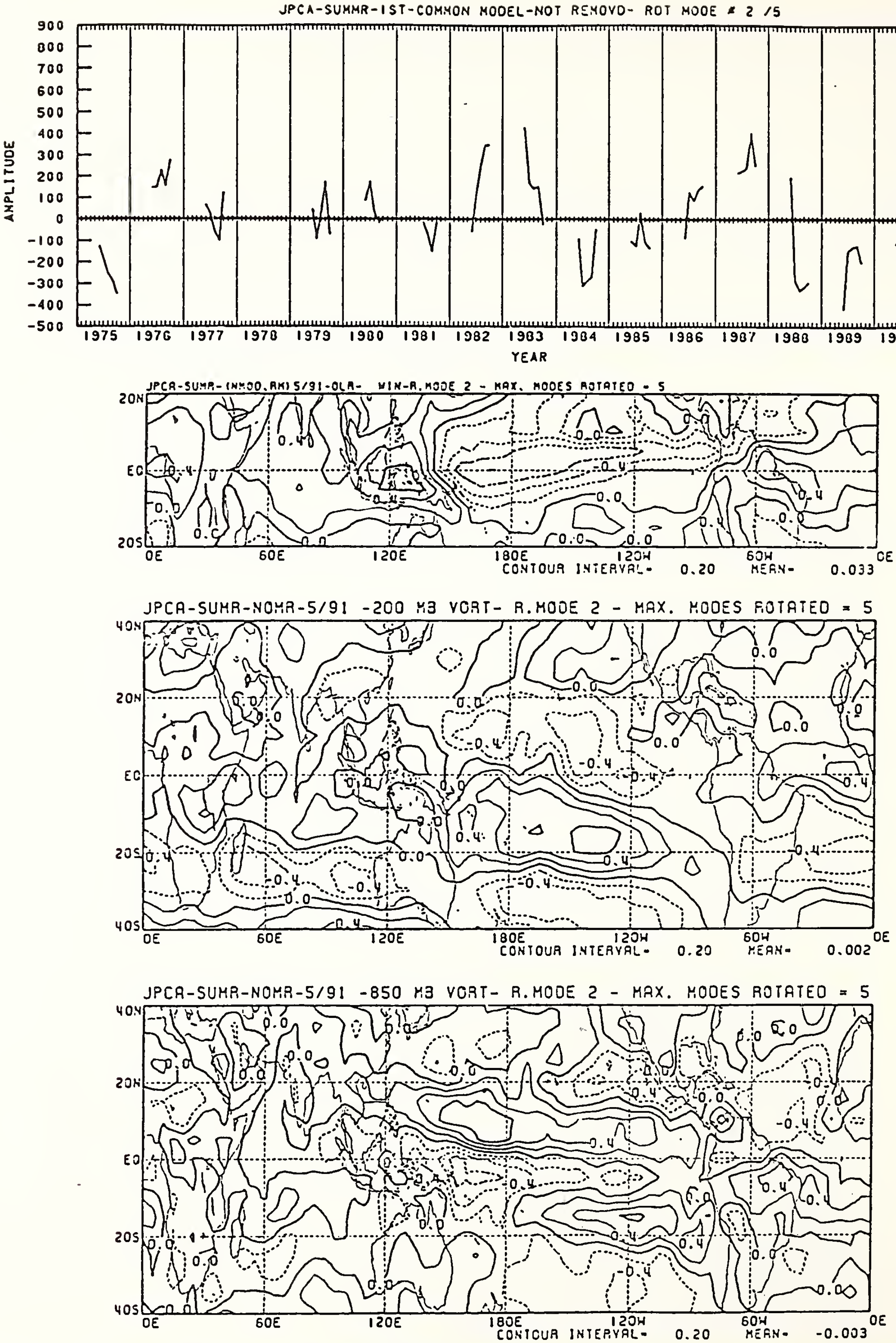

Fig. 4 'Canonical ENSO mode' from joint analysis for summer months only

# Resonant Modulation of Nordeste Precipitation by Tropical Atlantic and Pacific Sea Surface Temperatures

Kenneth R. Sperber* and Sultan Hameed†

**Program for Climate Model Diagnosis and Intercomparison*
*Atmospheric and Geophysical Sciences Division*
*Lawrence Livermore National Laboratory*
*Livermore, CA 94550, USA*

†*Institute for Terrestrial and Planetary Atmospheres*
*State University of New York*
*Stony Brook, NY 11794, USA*

1. Introduction: In teleconnection studies of regional precipitation we need to understand how the remotely connected climatic variables interact to produce the observed variations of precipitation. The work of several authors over the past decades has established that precipitation variations over a number of regions are associated with changes in sea surface temperature (SST) in the different oceans (Hastenrath and Heller 1977, Lamb 1978, Lough 1986, Folland *et al.* 1986, Ropelewski and Halpert 1987, Nicholson and Entekhabi 1987, Aceituno 1988). One such region is the Nordeste in Brazil, which is known for its large interannual fluctuations in rainfall (Hastenrath and Heller 1977) as seen in Figure 1a. Here we investigate the relationship of these precipitation variations and COADS (Woodruff *et al.* 1987) SSTs during March and April, the months during which the Nordeste receives the bulk of its precipitation, for the period 1950–1985. Their relationship, indicated by the correlation coefficients in Figure 1b, are in general agreement with the studies of Hastenrath and Heller (1977) and Lamb *et al.* (1986) which show that increased Nordeste precipitation occurs with a warm tropical south Atlantic and a cold tropical north Atlantic, as well as the result of Ward *et al.* (1988) showing a negative relationship between tropical Pacific SSTs and Nordeste precipitation. For each of the three regions in Figure 1b we calculate the mean March–April SST time series, which we will utilize to explain the time scales of variation of Nordeste precipitation. SST data from only within these significantly correlated regions are used because we expect their averages to preserve the temporal variations that are coherent with Nordeste precipitation.

2. Time Scales and Phases of Variability: As shown by the Fourier spectrum in Figure 2a, the variability of Nordeste precipitation is dominated by only a few time scales. During the period of study, 1950–85, the dominant variance is contained near periods of 3.6 years (the quasi–triennial oscillation, QTO), 6 years, and 9–12 years, with a small contribution from the quasi–biennial oscillation (QBO). Hastenrath and Kaczmarczyk (1981), Chu (1984) and Lamb *et al.* (1986) have also found these time scales to be important in Nordeste precipitation, although the relative amplitudes of the peaks are found to be different in different periods of record. Such differences are to be expected from the non–stationary characteristics of climate in time and space. For example, Hastenrath and Kaczmarczyk (1981) in their analysis of the 1921–72 Nordeste precipitation found the QBO to be more prominent. Figures 2b, 2c and 2d show, respectively, the spectra of the average SSTs in the north Atlantic, the south Atlantic

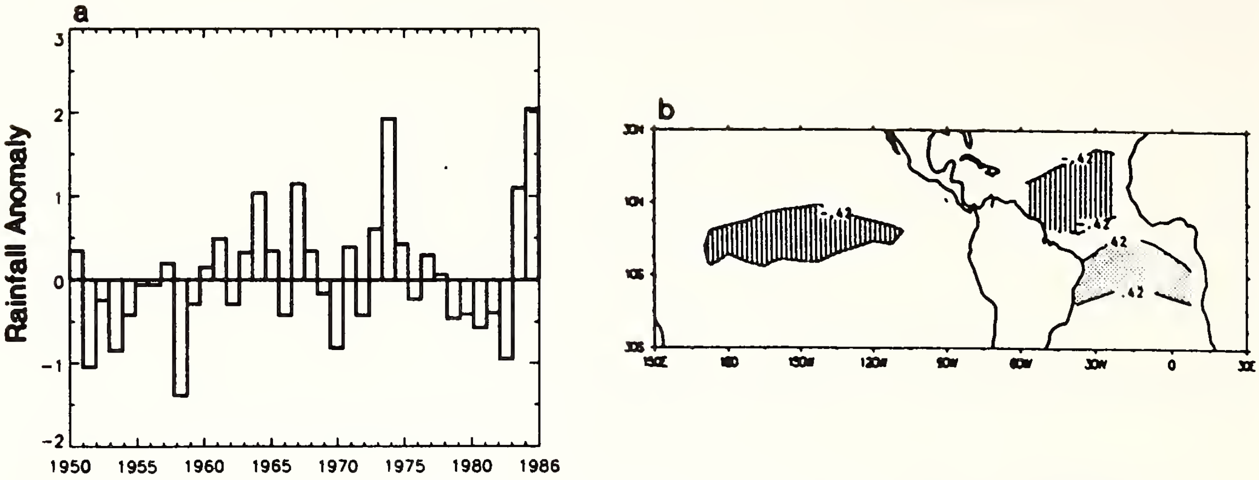

Figure 1. a) 1950–85 Nordeste precipitation index (based on the work of Nobre, and Hastenrath) b) March–April correlation of COADS SST with a Nordeste precipitation index (1950–1985). Positive correlation indicates below normal SST during drought. |R|=0.42 corresponds to the 99% confidence level.

and the Pacific subregions. We see that the ocean basins share subsets of the time scales of Nordeste precipitation, each in a different combination, in addition to having their own particular time scales. While each of the oceanic regions contain significant power at the 12 year period and in the 5–6 year interval, the Pacific and the north Atlantic are the main contributors to the QTO, while the northern and southern Atlantic are apparently responsible for the QBO signature. Additionally, as shown in Table 1, we note that the phases of the most dominant time scales of SST in each of the ocean basins are not generally coherent, and tend to differ from those in precipitation. For example, Figure 3a shows the QBO signals in the northern and southern Atlantic SSTs. These SST signatures tend to be out of phase with each other and their envelope structures (a sensitive indicator of phase as a result of the once per year samping) are disjoint relative to each other and to that of the QBO signature of precipitation (shown as the solid line in Figure 3b). These preliminary results cast doubt on the possibility of a causal link between the SSTs and precipitation on the time scales represented by these frequencies.

To address this quandry we utilize the information obtained in Figure 1b. This figure shows that the Nordeste precipitation is positively correlated with the south Atlantic and negatively correlated with the north Atlantic. Thus we subtract the SST time series of the north Atlantic from the SST time series of the south Atlantic, and compute the Fourier spectrum of the resulting difference; it is shown in Figure 2e. We notice that this spectrum is somewhat more like the precipitation spectrum, Figure 2a, than either of the two Atlantic Ocean spectra in Figures 2b and 2c. Variance of the 6 year period in Figure 2e is comparable to that of the 3.6 year period, as in the precipitation spectrum (Figure 2a), and the 5.1 year period of the south Atlantic does not appear in the difference spectrum. Moreover, we see in Table 1, fourth line from the bottom, that the difference spectrum phases of all the periods

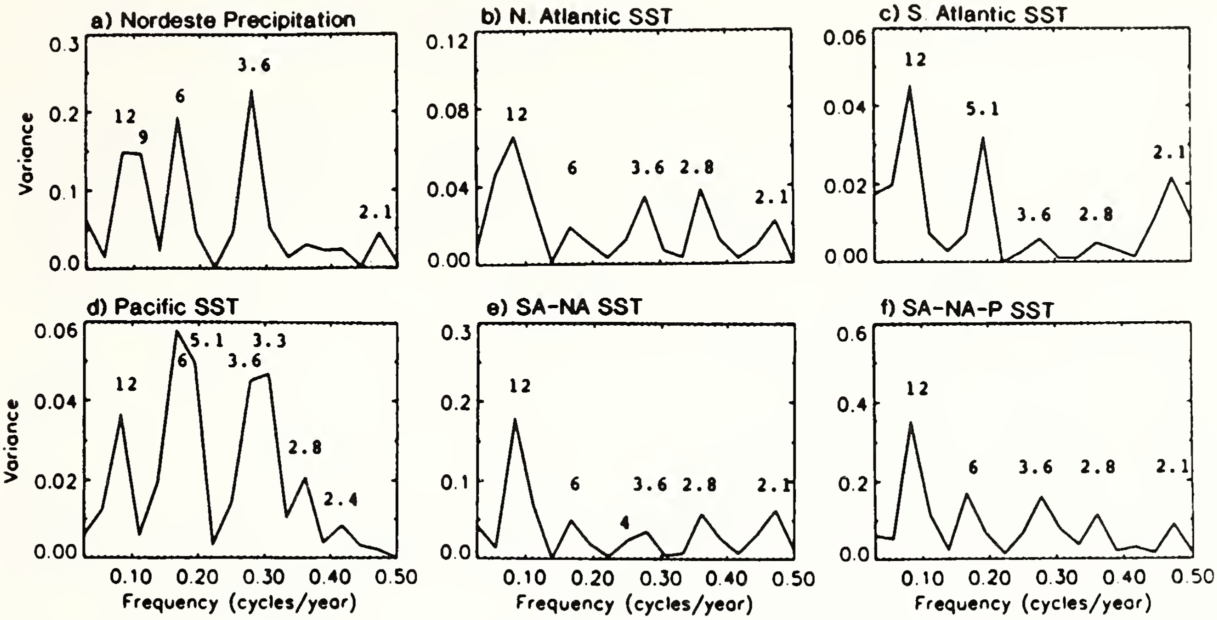

Figure 2. Fourier spectra (1950–1985) of a) Nordeste precipitation index b) northern Atlantic SST c) southern Atlantic SST d) Pacific SST e) (south Atlantic – north Atlantic) SST f) (south Atlantic – north Atlantic – Pacific) SST. The ordinates of the SST spectra are in (°C).[2]

| Period (Years) | 12.0 | 9.0 | 6.0 | 5.1 | 4.0 | 3.6 | 3.3 | 2.8 | 2.4 | 2.1 |
|---|---|---|---|---|---|---|---|---|---|---|
| Time Series | | | | | | | | | | |
| Nordeste Precip. | 52.3 | 57.0 | 55.2 | 53.8 | 52.5 | 52.7 | 51.3 | 51.7 | 52.1 | 50.2 |
| (SA - NA - P) SST | 52.3 | 56.6 | 55.2 | 54.5 | 52.0 | 52.8 | 51.5 | 51.3 | 52.3 | 50.2 |
| (SA - NA) SST | 61.9 | 56.6 | 54.7 | 53.7 | 52.2 | 52.8 | 51.2 | 51.5 | 52.2 | 50.3 |
| Pacific SST | 51.0 | 56.7 | 55.6 | 55.0 | 51.7 | 52.8 | 51.6 | 51.0 | 50.0 | 50.2 |
| N. Atlantic SST | 50.7 | 56.7 | 54.7 | 55.0 | 52.1 | 53.1 | 51.5 | 51.3 | 52.1 | 50.4 |
| S. Atlantic SST | 61.0 | 56.2 | 54.7 | 53.2 | 52.5 | 52.0 | 50.3 | 51.8 | 52.3 | 50.1 |

Table 1. Phases of the frequencies in the Fourier spectra shown in Figure 2a–f are given here as the time of the first maximum of the wave (the first minimum for the Pacific SST and North Atlantic SST since they are negatively correlated with precipitation). For example, 55.2 in the table stands for 1955.2.

except 12 years are within one–half year of their values in Nordeste precipitation given in the top line. Thus we obtain confirmation of the suggestion of Lamb *et al.* (1986) that it is the thermal gradient of the tropical Atlantic SSTs that influences the phases of the Nordeste

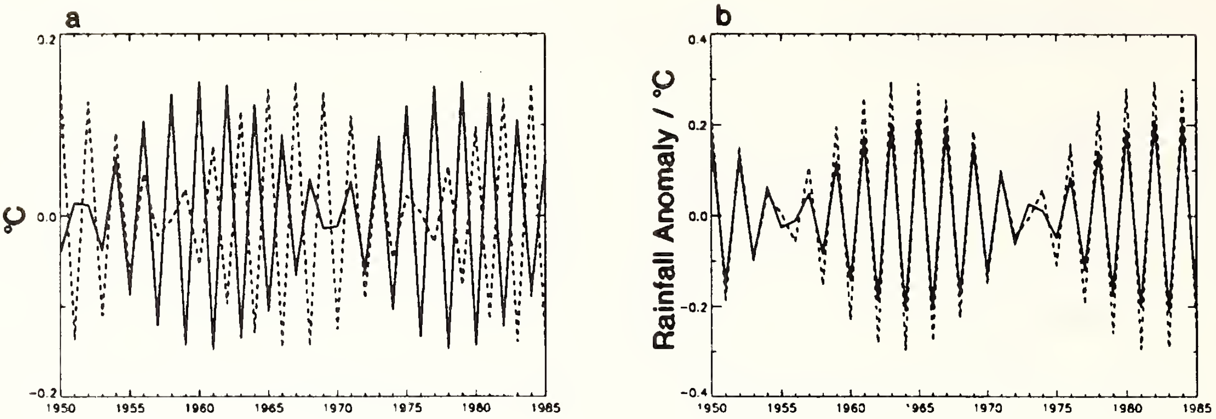

Figure 3. a) QBO waveforms of a) north Atlantic SST (solid line) and south Atlantic SST (dashed Line) b) Nordeste precipitation (solid line) and (south Atlantic – north Atlantic – Pacific) SST (dashed line).

precipitation, rather than the fluctuations of the SSTs in the individual ocean basins. However, the agreement is further improved when we incorporate the information in Figure 1b about the negative correlation between Nordeste precipitation and Pacific SSTs. We now construct the composite SST time series (south Atlantic - north Atlantic - Pacific) and compute its Fourier spectrum, shown in Figure 2f. Here we see that in comparison with Figure 2e, the amplitudes of the 6 year and 3.6 year oscillations have gained relative to the 12 year period and the QBO, and Figure 2f bears greater similarity to the precipitation spectrum of Figure 2a than any of the component spectra. When we compare the phases of the composite SST (Table 1, second line from the top) and the precipitation we see that the 12 year period is now phase locked; there is a deterioration of the phase agreement at periods of 5.1 and 4.0 years, but these periods contain insignificant power in the precipitation and composite SST spectra. These phase relationships suggests that the Walker circulation and the tropical Atlantic circulation interact on time scales of ~12, 9, 6, 3.6, and 2.1 years to modulate the track of the Intertropical Convergence Zone in the Atlantic and the amount of rain received in Nordeste during March–April. As an example, we demonstrate this phase locking in Figure 3b by showing the composite SST and precipitation QBO waveforms. The phase locking between the curves indicates that the variations of the SSTs in the three ocean basins resonate with the Nordeste precipitation.

3. Inter–frequency Resonant Modulation: Since both the 6 year and 3.6 year periods carry substantial variance in SSTs, we expect that their maxima and minima occurring together, as they do every 18 years, are likely to have a significant impact on Nordeste precipitation. In Figure 4a, the solid line shows the waveform of the 6 year wave in the composite SST series and the dashed line gives the waveform of the 3.6 year period in the same data. We notice that both waves have amplitudes of ~0.4°C; thus significant perturbations of the ocean heat flux to the atmosphere are likely to take place when the two waves are in phase, such as in

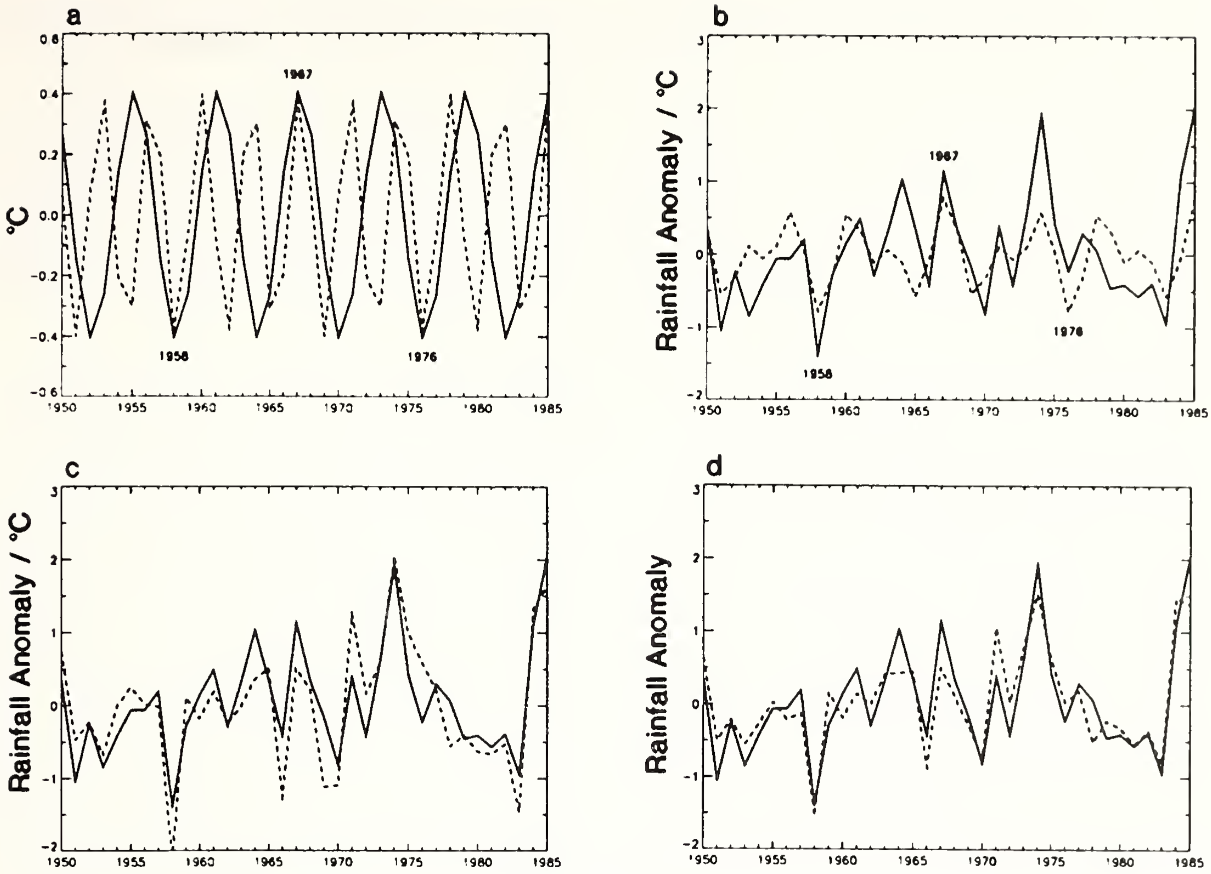

Figure 4. a) Waveforms of the composite SST 6 year period (solid line) and the QTO (dashed line) b) Nordeste precipitation index (solid line) and the sum of the composite SST 6 year and QTO waveforms from (a) (dashed line) c) Nordeste precipitation index (solid line) and the (south Atlantic - north Atlantic - Pacific) SST (dashed line) d) Nordeste precipitation index (solid line) and the multiple regression predicited precipitation.

1958, 1967, 1976 and 1985. The sum of the two waves in Figure 4a is reproduced as the dashed line in Figure 4b and compared with the raw Nordeste precipitation index shown as the solid line. We note the impact of just these two waves in producing the precipitation minima of 1958 and 1976 and the maxima of 1967 and 1985. These extrema in precipitation are preceeded and followed by 1–2 years of constructive interference of the two SST waves during which the precipitation tends to transit from and to the opposing phase. In Figure 4a the two waves are seen to be nearly out of phase in the intervals 1952–55, 1961–64, 1970–73 and 1979–82. The destructive interference of the two waves is reflected in smaller fluctuations of precipitation during these periods. Figures 4a and 4b illustrate the simplicity of the precipitation variations in a region where it is dominated by a few time scales. Further improvement of the agreement between the precipitation curve in Figure 4b and the composite SST results when waves of the other dominant frequencies are included as shown in Figure 4c. In this case the composite SST series explains 72% of the varaince in the precipitation. Further improvement results when multiple regression of the precipitation and the three SST time series is performed. Multiple regression indicates that the SST variations explain 80% of the precipitation variability, with the improvement occurring during 1968–70 and 1974–77.

Acknowledgments. We wish to thank Dr. Karl Taylor for helpful discussions, Dr. Tim Barnett for providing the gridded COADS SST data and Dr. David Rowell for providing the Nordeste precipitation index. This work was performed under the auspices of the Department of Energy Environmental Sciences Division by the Lawrence Livermore National Laboratory under contract W-7405-ENG-48 and grant DEFG0285ER60314A007 to the State University of New York at Stony Brook.

## References

Aceituno, P., 1988: On the functioning of the southern oscillation in the South American sector. part 1: surface climate. *Mon. Wea. Rev.*, **116**, 505–524.

Chu, P.-S., 1984: Time and space variability of rainfall and surface circulation in the Northeast Brazil–tropical Atlantic sector. *J. Meteoro. Soc. Japan*, **62**, 363–370.

Folland, C. K., Palmer, T. N. & Parker, D. E., 1986: Sahel rainfall and worldwide sea temperatures, 1901–1985. *Nature* **320**, 602–607.

Hastenrath, S., and L. Heller, 1977: Dynamics of climatic hazards in Northeast Brazil. *Quart. J. Roy. Meteoro. Soc.*, **103**, 77–92.

Hastenrath, S., and E. B. Kaczmarczyk, 1981: On spectra and coherence of tropical climate anomalies. *Tellus*, **33**, 453–462.

Lamb, P. J., 1978: Large–scale tropical Atlantic surface circulation patterns associated with subsaharan weather anomalies. *Tellus* **30**, 240–251.

Lamb, P. J., R. A. Peppler, and S. Hastenrath: 1986: Interannual variability in the tropical Atlantic. *Nature*, **322**, 238–240.

Lough, J. M., 1986: Tropical Atlantic sea surface temperatures and rainfall variations in subsaharan Africa. *Mon. Wea. Rev.* **114**, 561–570.

Nicholson, S. E. & Entekhabi, D., 1987: Rainfall variability in equatorial and southern Africa: Relationships with sea–surface temperature along the southwest coast of Africa. *J. Clim. App. Meteoro.* **26**, 561–578.

Ropelewski, C. F. and M. S. Halpert, 1987: Global and regional scale precipitation patterns associated with the El Niño/southern oscillation. *Mon. Wea. Rev.*, **115**, 1606–1626.

Ward, M. N., S. Brooks, and C. K. Folland, 1988: Predictability of seasonal rainfall in the northern Nordeste region of Brazil. in *Recent Climatic Change: A Regional Approach*, **Chapter 21**, edited by S. Gregory, Belhaven Press, NY, 237–251.

Woodruff, S. D., R. J. Slutz, R. L. Jenne, and P. M. Steurer, 1987: A comprehensive ocean–atmosphere data set. *Bull. Amer. Meteoro. Soc.*, **68**, 1239–1250.

# Westerly wind anomalies in the central Pacific and rainfall episodes in central Chile

P. Aceituno and J. Rutllant
Department of Geophysics. University of Chile
Casilla 2777 Santiago - Chile

## 1. Introduction

The interannual rainfall variability along the subtropical west coast of South America during the rainy season in the austral winter is closely related to perturbations in the ocean-atmosphere system in the central Pacific. In particular, relatively wet (dry) conditions prevail during the negative (positive) phase of the Southern Oscillation (for a review about this relationship see Rutllant and Fuenzalida, 1990). Consistently with this SO-related climate anomaly, convection and precipitation is generally enhanced in the equatorial region around 180° during anomalously wet months in central Chile (Del Río, 1989; Aceituno *et al.*, 1989). Furthermore, major winter storms during the development phase of El Niño episodes are related to blocking in the southeastern Pacific (Rutllant and Fuenzalida, 1990). A recent study has shown that this circulation anomaly is associated to biennial and intraseasonal easterly propagating signals at midlatitudes in the Southern Hemisphere (Rutllant and Aceituno, 1991).

The purpose of this study is to examine the relationship between the circulation anomalies in the central Pacific and individual rainfall episodes in central Chile at the synoptical scale level, in order to obtain a better understanding of the physical aspects of this teleconnection.

## 2. Data

Three sets of data are used in this study. Monthly maps of OLR in the region 55°N- 55°S with a resolution 2.5° x 2.5° for the period 1974-1988; Southern Hemisphere ECMWF daily analyses (200 and 500 hPa height and 850 hPa wind) during 1980-1987; and daily rainfall and snow data at five stations in central Chile (La Serena, 30°S, 71°W; Puerto Oscuro, 31°S, 72°W ; Valparaíso, 33°S, 72°W; Lagunitas, 33°S, 70°W; and Santiago, 33°S, 71° W) between May and August, during 1980-87.

## 3. Results

Considering the available data, a daily index for circulation anomalies in the central Pacific was defined in term of the 850 hPa zonal wind, whose anomalies are closely related to changes in the convection regime. The average OLR distribution during June-July-August (Fig 1) and the difference between one OLR composite corresponding to wet months minus another for dry months in central Chile (Fig. 2) were considered to define the region where the zonal wind index was calculated. The selected area, (160°E-180°, 0-10°S) is in the western side of the region where enhanced convection is observed during anomalously wet months in central Chile (Fig. 2) and on the eastern side of the SPCZ. This assures that the wind index is highly sensible to eastward displacements of the equatorial convection in the central Pacific.

The daily wind index was calculated from ECMWF analyses by averaging the 850 hPa zonal wind at all grid points in the selected area (Fig. 1) for the period April-September during 1980-87. Its evolution during the austral winter in 1982 and 1987 is presented in Figs. 3 and 4. The interannual variability of low level zonal circulation in this region is mostly associated to the Southern Oscillation. Thus, the progressively weaker trades during 1982 (Fig. 3) indicate the developing phase of the major 1982-83 El Niño. A significant variability at the intraseasonal and even shorter time scales is also observed. The episodes of relatively weak easterlies or westerlies may be associated to enhanced convection in the equatorial region around 180° or to perturbations in the circulation at higher latitudes.

Daily snow accumulation at one station in the Andes (Lagunitas: 33 °S, 70° W, 2765 m a.s.l.) is used in Figs. 3 and 4 to describe the intensity and duration of winter storms. A preliminary analysis of all winter storms at this station during 1980-1987 in relation to the wind index suggested that they tend to coincide with episodes of relatively weak easterlies in the central Pacific. Examples are the rainfall episodes occurring around days 130, 170, 177, 198, 225, and 238 in 1982 (Fig. 3) and 149, 154, 195 and 225 in 1987 (Fig. 4).

An objective analysis was designed to test this preliminary result. To eliminate most of the interannual and intraseasonal variability, an exponential filter was applied to the wind index (Essenwanger, 1986; p. 183, coefficient a = 0.10). Positive and negative wind anomalies were calculated with respect to the filtered series. The rainy days were defined as those for which more than 1 mm of rain was measured in at least one out of four selected stations in central Chile (La Serena, 30°S; Puerto Oscuro, 31°S; Valparaiso, 33°S; and Santiago, 33°S). Rainfall in this part of the world is mostly associated with the passage of cold fronts and accordingly these stations show a high degree of coherence with respect to the occurrence of rainfall episodes.

The ratio (N+)/(N-) between the total number of rainy days coinciding with positive wind anomalies (N+) and those with negative ones (N-) were calculated, for the entire period 1980-87. The ratio (I+)/(I-) between the sum of positive wind anomalies (I+) associated with rainy days and the sum of negative ones (I-), also associated with rainy days, was as well determined. Similar ratios were calculated with the wind index lagged with respect to rainfall. For lag = +1 rainfall occurrence during the period 1 May-31 August was compared with the wind index during the period 2 May-1 September. For lag = -1 the same period for rainfall was compared with the wind index during the period 30 April - 30 August .

Figure 5 shows that for lag 0 and +1 the ratios (N+)/(N-) and (I+)/(I-) are significantly larger than those expected by chance. In fact, when all days are considered, regardless of the occurrence of rain, the ratios (N+)/(N-) and (I+)/(I-) are around 0.9 and 1.0, respectively. This confirms that there is a significant tendency for a simultaneous occurrence of westerly wind anomalies in the central Pacific and rainfall episodes in central Chile. A Monte Carlo test, based on the empirical distributions of duration of storms and intervals between them, for all winters in the years 1980-87, was used to estimate the upper and lower 5% limits of the distribution of ratios (N+)/(N-) and (I+)/(I-) that could be obtained by chance, when rainfall episodes are randomly generated (Fig. 5).

A preliminary analysis of the Southern Hemisphere 500 and 200 hPa height fields revealed that the majority of the episodes of westerly wind anomaly in the central Pacific were associated with negative height anomalies in the domain of the south Pacific subtropical high, combined with positive height departures in the southeastern Pacific at higher latitudes. This blocking structure is similar to that described in Rutllant and Fuenzalida (1989) for major winter storms during the El Niño years. Therefore, the quasi-instantaneous teleconnection described here seems to be related to coherent fluctuations of extratropical height fields in the Southern Hemisphere, associated to enhanced convection in the central Pacific. Similar quasi-instantaneous teleconnections involving rainfall should exist in other regions, in association with observed syncronous changes in the tropical convection and the extratropical geopotential height fields (Lau and Phillips, 1986, Ferranti *et al.*, 1990). Since rainfall episodes in central Chile tend to occur during a particular phase of intraseasonal easterly propagating signals at midlatitudes in the Southern Hemisphere (Rutllant and Aceituno, 1991) it is a matter of further investigation to compare these signals with the intraseasonal anomalies in the tropical convection.

## 4. Acknowledgments.

This research was supported by Projects Fondecyt 89-1140 and DTI E2830e-8922. OLR and rainfall data were kindly provided by the Climate Analysis Center (NOAA/USA) and Dirección Meteorológica de Chile, respectively. Wind and height analyses were obtained from ECMWF. The authors acknowledge the technical assistance of Ricardo Pizarro, Mauro Huenupi and Aldo Montecinos.

## 5. References

Aceituno, P., A. del Río, and J. Rutllant, 1989: Rainfall anomalies in the subtropical west coast of South America. Part I: relationships with SST and convective activity over the Central Pacific. pp 162-166 in Extended Abstracts: Third Int. Conf. on S. Hemisphere Meteor. and Ocean., Nov. 13-17 1989, B. Aires. Amer. Meteor. Soc., 444 pp.

Del Río, A., 1989: Estudio de algunos aspectos físicos que contribuyen a la variación interanual de la precipitación en Chile Central. Engineering School. University of Chile, 71 pp.

Essenwanger, O.M., 1985: Elements of Statistical Analysis. World Survey of Climatology Vol. 1B, Elsevier, 424 pp.

Ferranti, L., T.N. Palmer, F. Molteni, and E. Klinker, 1990: Tropical-extratropical interaction associated with the 30-60 day oscillation and its impact on medium and extended range prediction. *J. Atmos. Phys.*, **47**, 2177-2199.

Lau, K-M. and T.J. Phillips, 1986: Coherent fluctuations of extratropical geopotential and tropical convection in intraseasonal time scales. *J. Atmos. Phys.*, **43**, 1164-1181.

Rutllant, J., and H. Fuenzalida, 1990: Synoptic aspects of the Central Chile rainfall variability associated with the Southern Oscillation. *Int. J. of Climatology*, **11**, 64-76.

Rutllant, J., and P. Aceituno, 1991: Southern Hemisphere circulation signals in connection with winter rainfall forecasting in central Chile. Internal Report IC/91/64. International Centre for Theoretical Physics. Trieste - Italy, 20 pp.

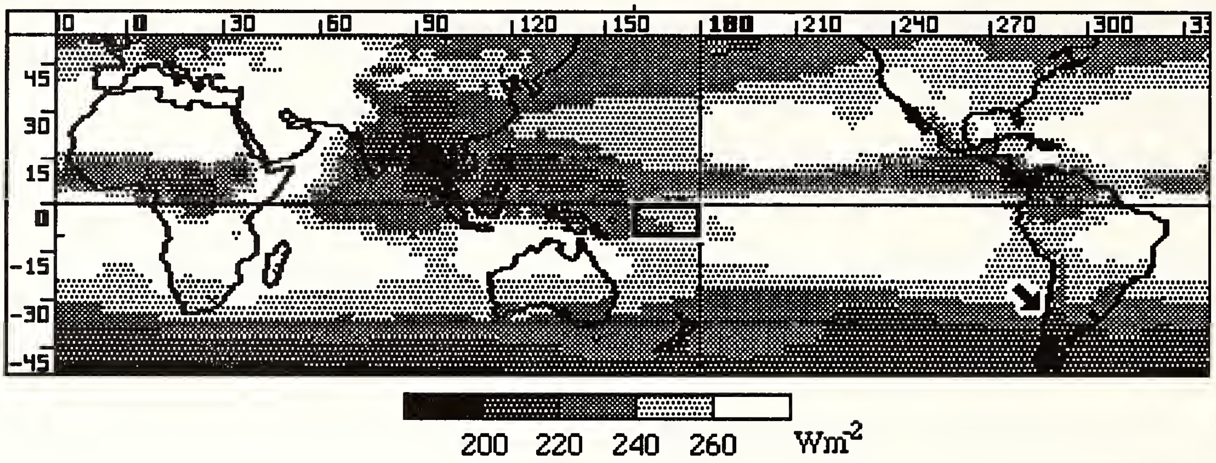

Fig. 1. Average OLR for June-July-August. The rectangle in the central Pacific indicates the area where an index for the 850 hPa zonal wind was calculated from ECMWF daily analyses. The arrow points to the region in central Chile where rainfall episodes were studied.

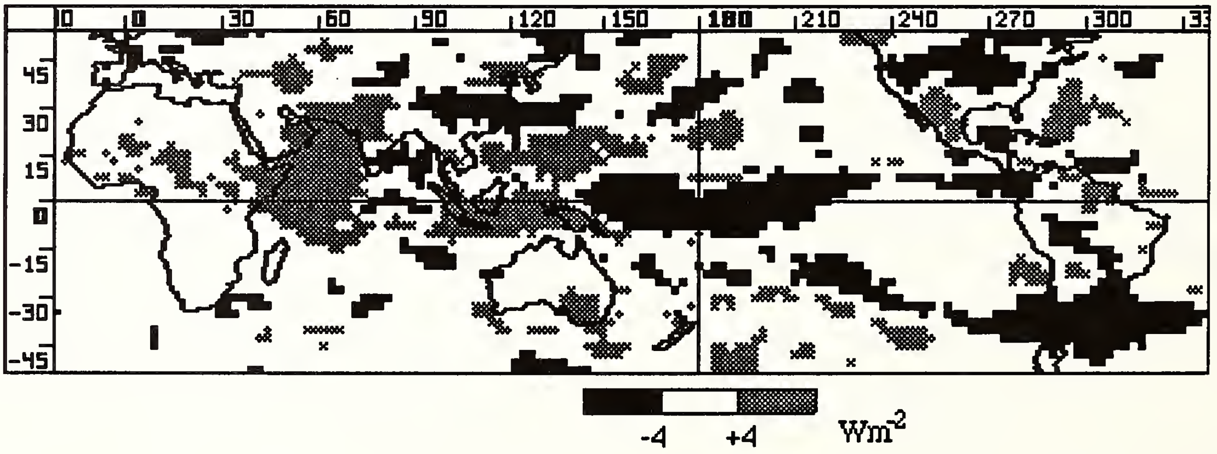

Fig. 2 Difference between one OLR composite corresponding to wet months minus another for dry months in central Chile, selected from June, July and August of the years 1974-88. Dry months are Jul. 74, Jul. 76, Jun. 79, Aug. 84, Aug. 85, Jul. 86, Jun. 88 and Jul. 88. Wet months are Jun. 74, Jul. 77, Aug. 79, Jun. 82, Aug. 82, Jul. 84, Jul. 87, and Aug. 87 (adapted from Del Río, 1989).

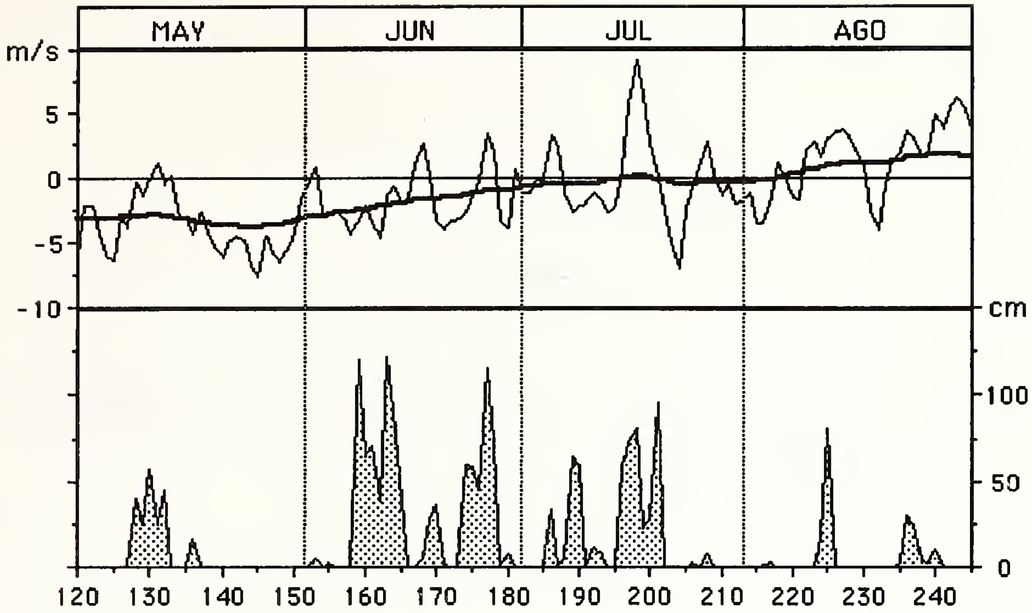

Fig. 3. Daily zonal wind at 850 hPa in the central Pacific (see Fig 1) from ECMWF analyses and snow accumulation at Lagunitas (33°S, 70° W, 2765 m a.s.l.) during May-August 1982. The heavy line in the upper part represents the zonal wind smoothened with an exponential filter (Essenwanger, 1986, p. 183; a= 0.10).

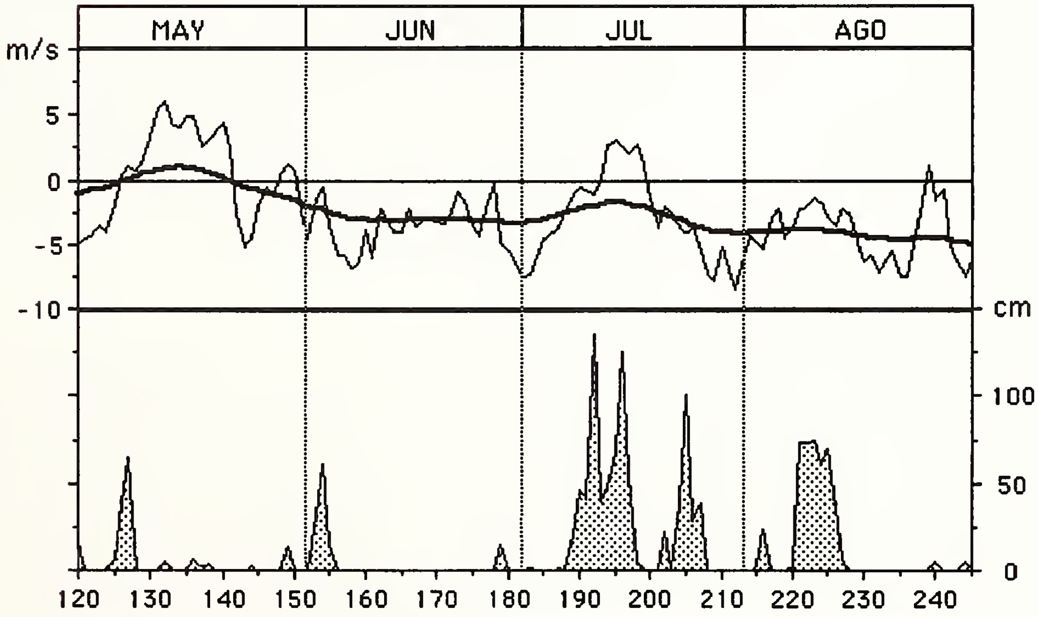

Fig. 4 Id. to Fig. 3 but for May-August 1987.

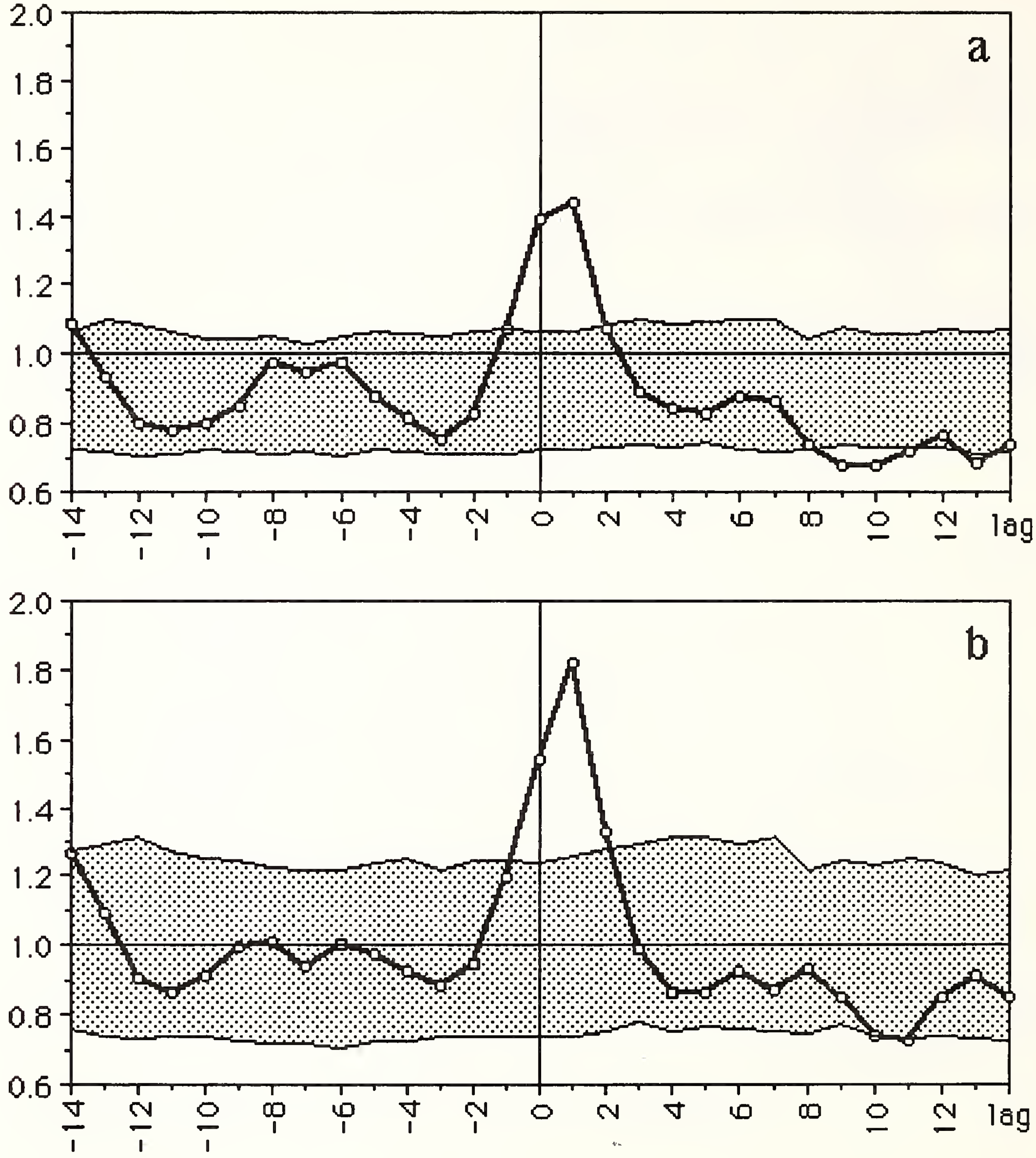

Fig. 5 a. Ratio between the number of rainy days associated with positive wind anomalies *versus* those associated with negative wind anomalies during May-August for the years 1980-87; b. Ratio between the integrated positive wind anomalies *versus* the absolute value of integrated negative wind anomalies for rainy days during the same period. Wind anomalies are defined as the residue after applying a high-pass filter to the original index of 850 hPa zonal wind in the central Pacific (see Figs. 3 and 4). Lag is expressed in days with positive values indicating that rainfall leads the wind. Values inside the dot raster could be obtained by chance according to a Monte Carlo test described in the text.

# Angular Momentum Variability Using Climate Data Sets

David A. Salstein and Richard D. Rosen
Atmospheric and Environmental Research, Inc.
840 Memorial Drive, Cambridge, MA 02139

## 1. Introduction

Angular momentum is a three-dimensional measure of the state of the Earth system. Because of its conservative nature, its components are important diagnostic parameters on a variety of time scales. We concentrate here on the axial component of atmospheric momentum relative to the Earth, i.e. that portion due to the zonal winds, which can be defined (see Rosen and Salstein, 1983) as an integral over the mass of the atmosphere between a low level, 1000 mb, and a high level, for example, 100 mb:

$$M^W = \frac{2\pi a^3}{g} \int_{100}^{1000} \int_{-\pi/2}^{\pi/2} [u] \cos^2 \phi \, d\phi dp \qquad (1)$$

Here $[u]$ is zonal mean zonal wind, $a$ radius of the Earth, $g$ acceleration due to gravity, $\phi$ latitude, and $p$ pressure. To the extent that atmosphere and solid Earth form a two-body system, changes in atmospheric angular momentum are related to those in the length of day, l.o.d., after removing appropriate tidal terms, by a simple proportionality:

$$\Delta l.o.d. = \frac{l.o.d.}{\omega_\circ I} \Delta M^W = 1.68\text{x}10^{-29} \Delta M^W \qquad (2)$$

Here $\omega$ is the mean rotation rate and $I$ the axial moment of inertia of the Earth, respectively. This relationship has been shown to be largely valid on a wide range of time scales at least between about 10 days and a few years (Rosen et al., 1990). Besides examining global momentum values, this study will report on its zonal and regional decomposition within belts and latitude-longitude sectors.

## 2. Climate Data Sets for Momentum Studies

a. Geodetic Sets Because of the close relation between atmospheric angular momentum and Earth rotation, geodetic l.o.d. data sets on a variety of time scales can be used as proxies for globally integrated atmospheric momentum. During the past couple of decades accurate, high time-resolution space-based data have become available from techniques such as very long baseline interferometry (VLBI), which measures the orientation of Earth relative to distant extragalactic radio sources. Prior to the current era, annual values of l.o.d. data derived from optical techniques, especially that of observing lunar star occulations, are available for the period since the 1600s; these data have errors small enough to be useful for our proxy purposes since about 1860 (Salstein and Rosen, 1986). Interestingly, this historical data set has shown that years with El Nino-Southern Oscillation (ENSO) events had significantly larger values of l.o.d. than non-ENSO years (Fig. 1), and this expected relationship validates the l.o.d. series as a useful index of global momentum variability.

b. Meteorological Sets A variety of atmospheric data sets has been used for studying angular momentum. Relevant quantities have been computed from global analyses of winds produced operationally from the world's major weather centers. These values are derived from systems that have been improving over the years since the first global analysis was performed in 1976, at NMC. Such momentum quantities are currently being collected, distributed, and archived in near-real time at a specialized data center, the Sub-bureau for Atmospheric Angular Momentum of the International Earth Rotation Service, for the purposes of assessment, forecast evaluation, geophysical study, and navigational support (Salstein and Kann, 1991). In addition, the torques that dynamically link the solid Earth to the atmosphere due to surface stress and orographic pressure forcing can be computed from operational analyses; the means to do so within the model framework are currently under development at NMC (White, 1991).

Climate analyses will be useful in preparing consistent momentum data sets less subject to the heterogeneities of the operational series. Such analyses are being planned at NMC for the Climate Data Assimilation System (CDAS), and its historical counterpart, the Reanalysis effort. Angular momentum values from a prototype CDAS data, run spectrally at T80 resolution and archived at R30 for July 1989, are compared with NMC GDAS (Global Data Assimilation System) values for the same period (Fig. 2). The availability of 6-hourly data form this CDAS sample is useful to demonstrate a diurnal signal relevant to high frequency studies of Earth rotation. Further experiments assessing the needed spatial resolution for CDAS will be performed when appropriate data sets are available.

General circulation models are useful in studying atmospheric angular momentum variability in a number of contexts. For example, Rosen and Gutowski (1991) examine the response of momentum within models to a doubling of atmospheric $CO_2$ content. Their work, for example, showed a tropospheric momentum decrease in each of the two solsticial seasons that is comparable to the difference in momentum between the two seasons. Models can also provide a mechanism to study the Earth-atmosphere torques mentioned earlier (e.g., Boer, 1990).

A number of specialized instruments have been developed, or are proposed, to determine torque-related stresses or improved measurements of winds. These include satellite-based scatterometers and the Special Sensor Microwave Imager (SSM/I), already deployed, as well as the Laser Atmospheric Wind Sounder (LAWS) proposed for the late 1990s. The instrument, though, that has taken the most widespread measurements of winds during the last several decades and operates *in situ* is the rawinsonde, results from which are discussed below.

## 3. Momentum from Operational NMC Analyses and the Oort Rawinsonde Network

Winds from the rawinsonde network were collected primarily from the Northern Hemisphere since 1958, and globally since 1963, by A. H. Oort of the Geophysical Fluid Dynamics Laboratory/NOAA. Monthly analyses based on these winds, described by Oort (1983), were supplied to us to study momentum variations more regionally. The temporal coverage of the rawinsonde analyses predates the NMC global analyses by over a decade. When the NMC and rawinsonde-based values of global momentum are compared (not shown here), the agreement is generally good on most time scales; however, the Oort values are somewhat weaker, probably resulting from an underestimate of the jet exit regions over the subtropical oceans. Once a low-pass filter that eliminates variability on annual and shorter time scales is applied to the two global sets, their agreement at interannual scales is apparent (Fig. 3).

To study regional sources of momentum variability, the angular momentum data were decomposed into a series of values at a set of 46 equal-area latitude belts designed by Rosen and Salstein (1983). This NMC belt data set was subjected to running mean filters by Dickey et al. (1991), to reveal the low frequency propagation of features from low latitudes poleward in both hemispheres. These authors' striking result shows, for example, a tropical precursor of the 1983 ENSO maximum that had a strong subtropical momentum signal in both hemispheres. Other positive and negative momentum anomalies had similar precursors, some 2-2 1/2 years in advance.

A novel aspect of the Oort station-based data set is its lengthy record. During the overlap period with NMC, the latitudinal distribution of momentum in time is similar to that of the NMC data. The zonal belt distribution back to 1958, filtered with our low-pass filter, is shown in the time-latitude plot of Fig. 4. Here we see the poleward propagation, mentioned above, occurring on time scales of about one to two years, especially throughout the late 1960s and early 1970s; these are marked by the chevron pattern of the (subjectively drawn) straight propagation lines.

To examine the geographical distribution of momentum from the Oort monthly station data, we divide the globe into 276 sectors that are equally spaced in 23 latitude bands and 30 degrees in longitude. As a first step we have taken the low-pass filtered series of momentum in each sector and subjected the set to a straightforward empirical orthogonal function (EOF) decomposition in the manner of Salstein et al. (1983). The first global eigenvector mode, shown in Fig. 5, is largely of one sign over the globe with centers over the subtropics of the North and South Pacific oceans. Small areas of opposite sign appear over North America, North Africa, and far northern Asia.

Peaks of the associated time series shown during 1963-89 are contemporaneous with ENSO warm years. The portion of this mode over the tropical Pacific, as well as its temporal variability, are reminiscent of Arkin's (1982) mode containing anomalously strong winds during ENSO events.

Further modes contain (i) a strong center south of Africa (which may be spurious), and (ii) a contrast between low latitudes and the subtropics/ middle latitudes of both hemispheres. Discussion of these modes, as well as other principal component techniques designed to examine spatial propagation, will be given elsewhere.

## 4. Summary

Atmospheric angular momentum is a parameter whose global integral may be inferred from independent geodetic data sets during both our era and in the past. It is also connected to the large-scale ENSO phenomenon because of enhanced westerly momentum anomalies over widespread regions. A variety of data sets exist or are planned that are useful in studying global angular momentum, including geodetic (length of day) observations, operational and climate analyses, general circulation model results, specialized wind and stress observations, and the global rawinsonde network.

Operational analyses depict poleward propagation of interannual momentum anomalies (Dickey et al., 1991). When the rawinsonde set analyzed by Oort is used to compute atmospheric angular momentum, its global integral is in relatively good agreement with operational NMC analyses after a suitable low-pass filter is applied. Furthermore its latitudinal distribution over the 31-year record reveals that the poleward propagation pattern has occurred repeatedly during this period. An eigenvector analysis contains a dominant Pacific mode that is strong in ENSO years, a possibly spurious high southern latitude mode, and a mode with contrasting behavior between the tropics and extratropics.

*Acknowledgments*. We thank A.H. Oort of NOAA/GFDL for supplying his rawinsonde-based wind analyses, J.O. Dickey of JPL for giving us her results from the NMC latitude belts, and K.C. Mo for sending preliminary CDAS data. This work was supported by the National Science Foundation under Grant ATM-8911293 and by the NOAA Climate and Global Change Program under Grant NA16RC0114-01.

## References

Arkin, P., 1982: The relationship between interannual variability in the 200 mb tropical wind field and the Southern Oscillation. *Mon. Wea. Rev.*, **110**, 1393-1404.

Boer, G.J., 1990: Earth-atmosphere exchange of angular momentum simulated in a general circulation model and implications for the length of day. *Geophys. Res. Lett.*, **95**, 5511-5531.

Dickey, J.O., S.L. Marcus, and R. Hide, 1991: manuscript in preparation.

Oort, A.H., 1983: *Global atmospheric circulation statistics, 1958-1973.* U.S. Dept. of Commerce, NOAA Professional Paper 14.

Rosen, R.D., and W. J. Gutowski, 1991: Response of zonal winds and atmospheric angular momentum to a doubling of $CO_2$. Submitted manuscript.

Rosen, R.D., and D.A. Salstein, 1983: Variations in atmospheric angular momentum on global and regional scales and the length of day. *J. Geophys. Res.*, **88**, 5451-5470.

Rosen, R.D., D.A. Salstein, and T. M. Wood, 1990: Discrepancies in the Earth-atmosphere angular momentum budget. *J. Geophys. Res.*, **95**, 265-279.

Salstein, D. A., and D. M. Kann, 1991: Developments at the sub-bureau for atmospheric angular momentum of the IERS. *Proceedings of the AGU Chapman Conference on Geodetic VLBI: Monitoring global change.* U.S. Dept. Commerce, NOAA Tech. Report NOS 137 NGS 49, 228-237

Salstein, D.A., and R.D. Rosen, 1986: Earth rotation as a proxy for interannual variability in atmospheric circulation, 1860-present. *J. Clim. Appl. Meteorolog.*, **25**, 1870-1877.

Salstein, D.A., R.D. Rosen, and J.P. Peixoto, 1983: Modes of variability in annual hemispheric water vapor and transport fields. *J. Atmos. Sci.*, **40**, 788-803.

White, G.H., 1991: Mountain and surface stress torques in NMC analyses. *Proceedings of the AGU Chapman Conference on Geodetic VLBI: Monitoring global change.* U.S. Dept. Commerce, NOAA Tech. Report NOS 137 NGS 49, 262-269.

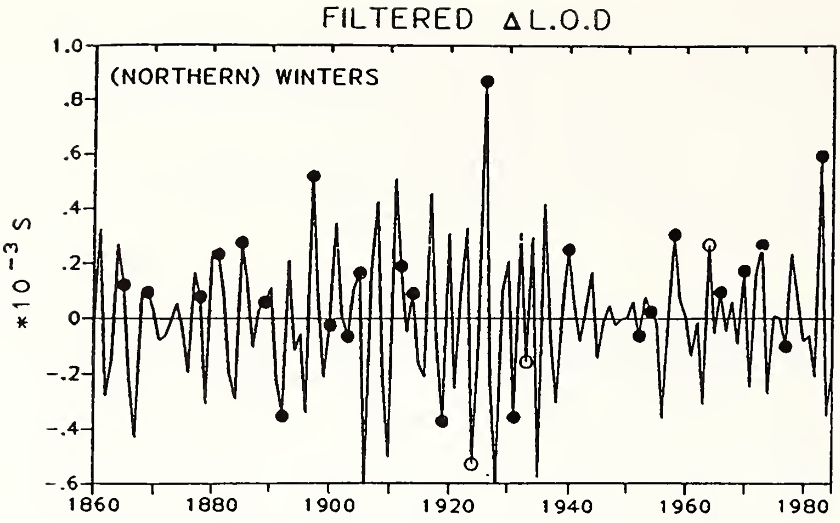

Fig. 1. Time series of high-pass filtered values of the length of day for northern winters during 1860-1985. Dots mark those winters that fall at the end of a year containng a well-defined ENSO warm event. [From Salstein and Rosen, 1986]

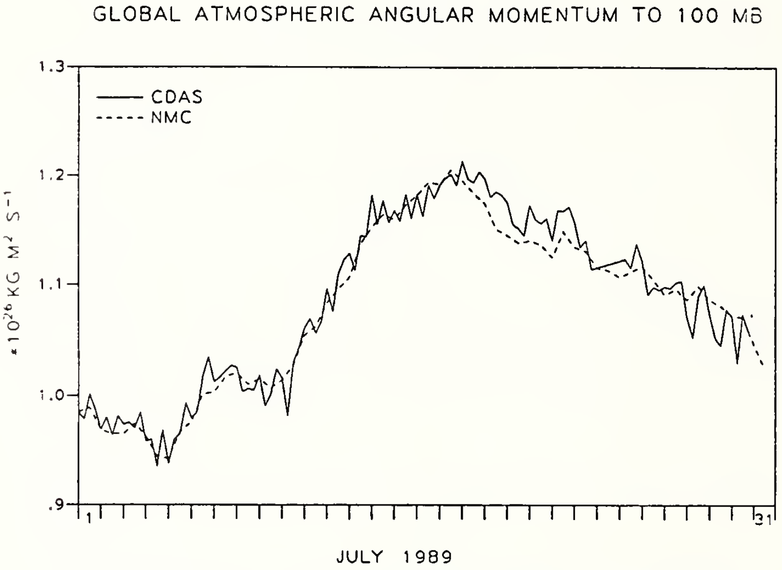

Fig. 2. Global atmospheric angular momentum from the CDAS protoype analysis, and the NMC GDAS analysis for July 1989.

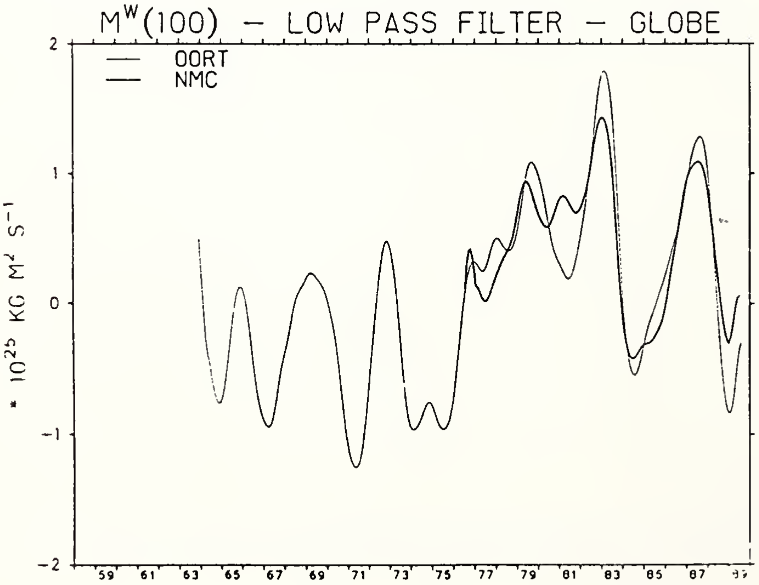

Fig. 3. Global atmospheric angular momentum placed through a low-pass filter centered at 15 months and smoothed. The means of each series have been adjusted so that they are equal during the overlaps period of the NMC and Oort analyses.

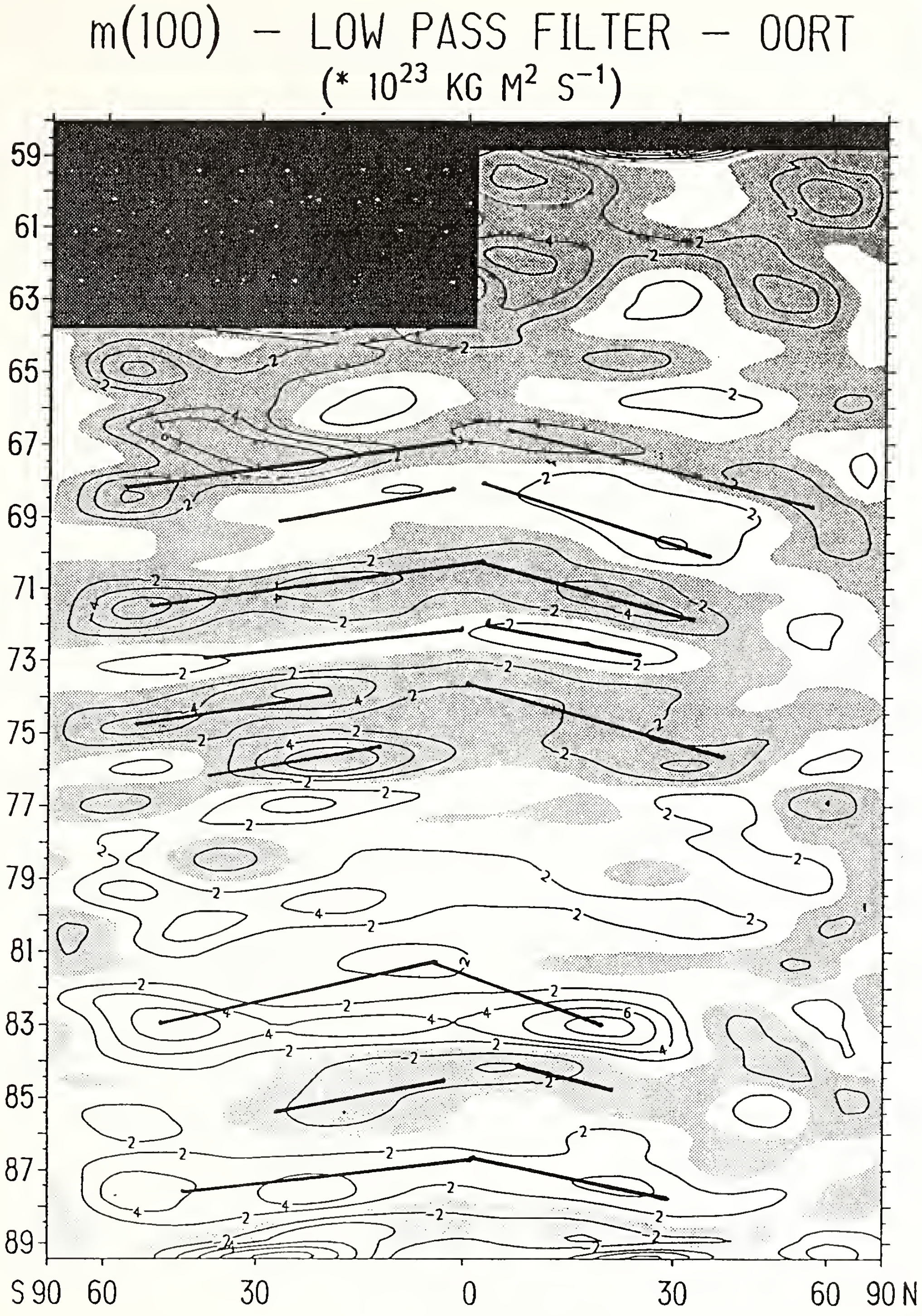

Fig. 4. Momentum in zonal belts based on the Oort station analyses after applying a low-pass filter centered at 15 months and smoothing. Subjectively drawn lines show poleward propagation of positive and negative anomalies. Light grey areas contain negative values. Dark grey area indicates times when data are unavailable.

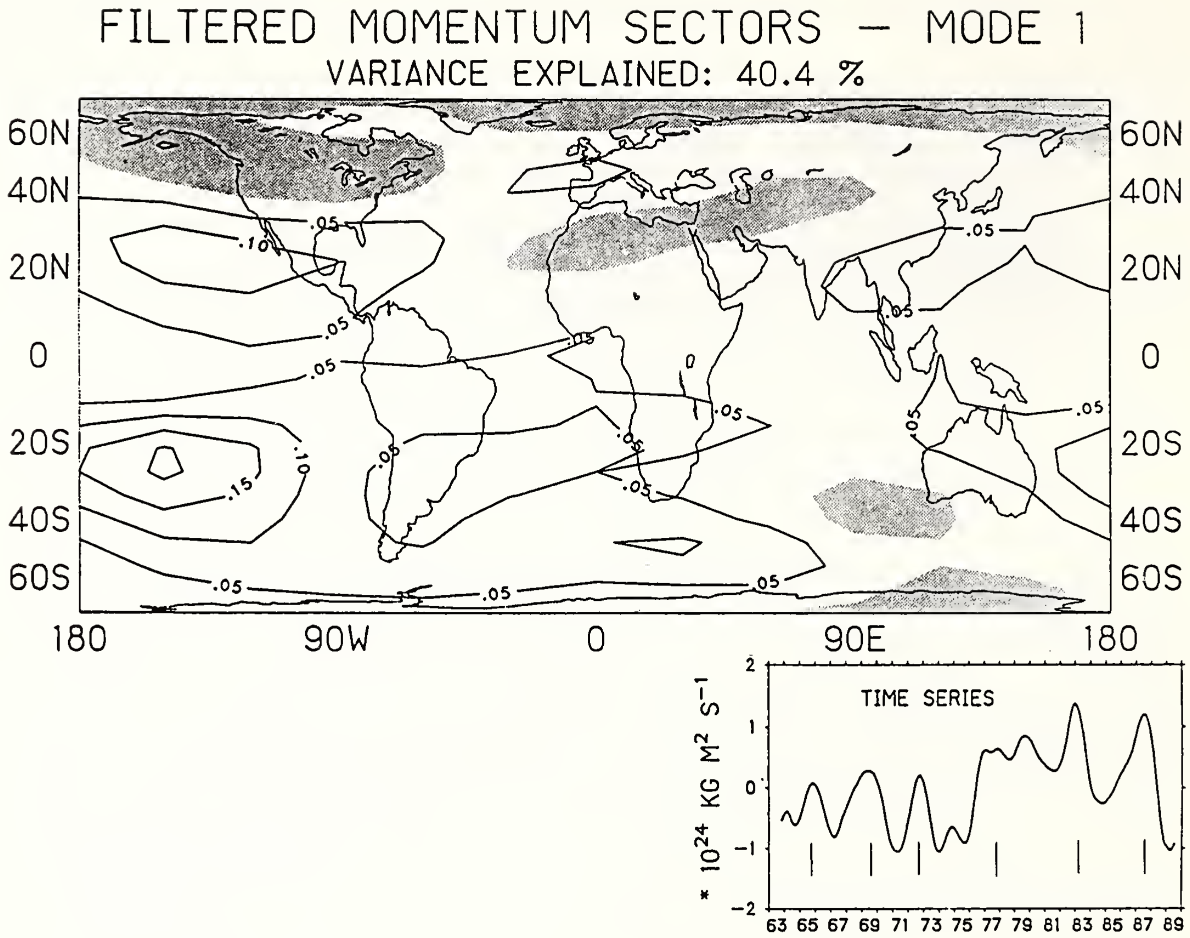

Fig. 5. First empirical orthogonal function (non-dimensional) showing variability of momentum in sectors from the Oort station analysis and associated time series with ENSO occurrences marked as vertical lines.

# The Atmospheric Angular Momentum Budget during a Madden-Julian Oscillation

Klaus Weickmann
NOAA/ERL/CMDL/Climate Research Division
325 Broadway R/E/CG2
Boulder, CO 80303

and

Prashant Sardeshmukh
CIRES, Campus Box 449, University of Colorado
Boulder, CO 80309-0449

## 1. Background

The angular momentum of earth-atmosphere system is conserved for intraseasonal time scales greater than about 10 days (Hide et al., 1980; Rosen et al., 1990). Surface tangential and normal stresses must therefore accompany 30-60 day atmospheric angular momentum (AAM) variations and provide for the exchange of angular momentum between the atmosphere and the solid earth. Madden (1987,1988) and Kang and Lau (1990) have proposed that forcing of 30-60 day AAM changes is related to frictional stress variations that occur over the Pacific Ocean. These stresses are thought to be directly related to Madden Julian Oscillation (MJO) convective activity occurring over Austral-Asia as in a Gill (1980) model. Questions of whether these oceanic surface stresses can be quickly (< 3 days) communicated to the solid earth prompted Ghil and collaborators (Jin and Ghil, 1991) to suggest that mountain torques associated with a topographic instability could also account for the AAM oscillations. Oscillations driven by such a mechanism have been obtained in a general circulation model (GCM). In this study, we examine the complete AAM budget for a 65 day period during the 1984-85 winter to help clarify the observed relationship between the torques and the AAM anomalies.

## 2. Budget Computations

A one-time step integration (Klinker and Sardeshmukh, 1992) of the NCAR Community Climate Model (CCM1), initialized with daily observed NMC data, is used to obtain the basic variables for the budget calculations including the surface frictional stress. The CCM Processor is then used to compute the terms in the budget. The observed tendency of AAM is obtained by daily differencing of the observed AAM data. The processes that can change the relative AAM are the pressure torque, the frictional torque, the coriolis torque and the relative AAM transports. Since we have vertically integrated, the coriolis torque is very small being about an order of magnitude smaller than the other terms.

## 3. Results

Fig. 1 shows the Northern Hemisphere (NH), Southern Hemisphere and global AAM for July 1984 - June 1985. The case study period is bracketed by vertical lines and includes one of a series of lower frequency oscillations (~60-80 day period) that followed the 1982-83 ENSO. The event is phase-locked to the seasonal cycle in the sense that the increase of AAM coincides with seasonal intensification of the NH subtropical jet streams and the onset of the Australian monsoon. The length of day (LOD) data is shown as an inset curve below the global AAM curve and corresponds well with the NMC AAM data. The top inset curve shows the AAM evolution as predicted by the computed torques. A systematic error in the torques results in a large discrepancy between the predicted and observed AAM by the end of the period. We have determined this is due, in part, to errors in the computation of the pressure gradient force around mountains and related errors in the pressure torque. The low frequency variations, however, are well captured by the computed torques and we will therefore focus on these variations by examining the anomaly AAM budget for the event.

### 3a. Time mean budget

Fig. 2 shows the time mean balance for the vertically and zonally integrated relative AAM budget. The balance is consistent with the classical idea that there is a source of AAM in the tropics associated with friction acting on the surface easterlies, that this momentum is transported out of the tropics into mid-latitudes and that it is returned to the solid earth as friction acts on the mid-latitude surface westerlies. The northward momentum transport is dominated by transient eddies which account for approximately 65% of the total eddy transport during northern winter. The balance emphasizes that there is a close link between the momentum transports and the tropical surface flow.

The difference between the two curves (not shown) is much larger than the observed tendency over the 65 day period and illustrates the budget imbalance described for the predicted AAM curve seen in Fig. 1. The imbalance is particularly large in the latitude band containing the Tibetan Plateau.

### 3b. Time varying budget

#### 1. Global integrals

Fig. 3a shows the globally integrated AAM tendency and total torque anomaly as a function of time during the 65 days. For a global integral, the transports are identically zero and the global AAM tendency must equal the sum of the frictional and pressure torque. The total torque anomaly corresponds reasonably well with the observed AAM tendency . In contrast to the total 65-day mean budget, the sign of the torque anomaly generally agrees with the sign of the anomalous AAM tendency throughout the period. This agreement is consistent with the correspondance between the low frequency variations predicted by the torques and the observed low frequency variations (Fig. 1).

Fig. 3b shows the breakdown of the total torque in Fig. 3a into the individual frictional and mountain torque. The relationship between the two can described with reference to the observed tendency in Fig. 3a. During the period of large AAM increase, the frictional torque starts increasing first going from near zero around day 14 to large positive values around days 21-27. The pressure torque, however, also contributes as it goes rapidly from large negative values on day 19 to large positive values on day 30. The tendency and total torque both peak around day 30 and the mountain torque continues moderately positive until day 40. Global AAM also peaks around day 40 and thereafter the negative AAM tendency is primarily associated with a negative frictional torque anomaly.

#### 2. Zonal integrals

The contribution from different latitude bands to the global frictional and mountain torque described above can be seen in time-latitude diagrams in Figs. 4a and 4b respectively. For the vertically and zonally integrated budget, the balance is between the total torque (Fig. 4c = sum of Fig. 4a and 4b) and the divergence of momentum transport (Fig. 4d). The difference between the two (Fig. 4c - Fig. 4d) represents the computed AAM tendency as determined by the budget calculations and is shown in Fig. 4e. In the last panel (Fig. 4f), the observed relative AAM tendency is shown and can be compared with the computed tendency. The agreement is surprisingly good with most features evident in both panels. In particular, the positive tendency period is well captured by the budget as is the negative tendency period. The agreement suggests it is reasonable to examine the terms that contribute to the computed tendency in some detail.

The total torque anomaly in Fig. 4c largely represents the frictional torque (Fig. 4a) although the mountain torque makes a significant contribution around day 30. In general, the mountain torque is locally smaller (Fig. 4b) but since there is less cancellation of zonal anomalies its global integral is comparable to that of the frictional torque (Fig. 3b). Subtle changes in the regions covered by easterly or westerly surface wind stress anomalies and in the mountain torque anomaly contribute to the global integral seen in Fig. 3a. To provide a perspective on the size of these changes, the days with the largest negative and positive global torque anomaly are marked on Fig. 4c. The torque anomaly in the tropics, e.g., along 15°N, corresponds closely with these maxima in the global torque anomaly.

To first order the total torque anomaly shows a similar pattern as the divergence of momentum transport anomaly. The difference between the two, however, (Fig. 4e) is of the same order as the values themselves and, broadly speaking, can be ascribed to the transports leading the torques. Thus, just prior to the positive tendency period, the anomalous momentum divergence that was maximized near 35°N on day 7 shifts southward to near 25°N on day 21. This shift is then followed by an increase in the positive torque which reaches a maximum on day 29 and coincides with a major rearrangement of the transports. Similarly, after a period where the transports and torques again are nearly in balance, the transport pattern abruptly breaks down and the mid-latitude surface flow anomalies weaken as the torque pattern persists. In the tropics, an imbalance develops earlier as anomalous transport out of the tropics and weaken trades lead to a negative AAM tendency there.

## 4. Discussion

The positive pressure and frictional torques both develop during the period that tropical convection is intensifying over the western Pacific Ocean not shown). An examination of the regional contributions to the Fig. 4 zonal integrals (not shown) indicates that the southward shift in the momentum transports at day 21 is primarily associated with tilted wave structures over North America and the Atlantic Ocean. The associated momentum sink forces a regional increase in the surface flow near 15°N which contributes to the positive frictional torque that peaks about day 26. A secondary contribution comes from east of the Phillipines presumably in response to the intensifying convection to the south. The positive mountain torque is predominantly due to pressure changes around the Himalayas as high pressure is favored on their eastern slopes. These results illustrate the complex nature of the torques that force the AAM changes including the possibility of remote links between tropical convection, momentum transports and changes in the surface wind.

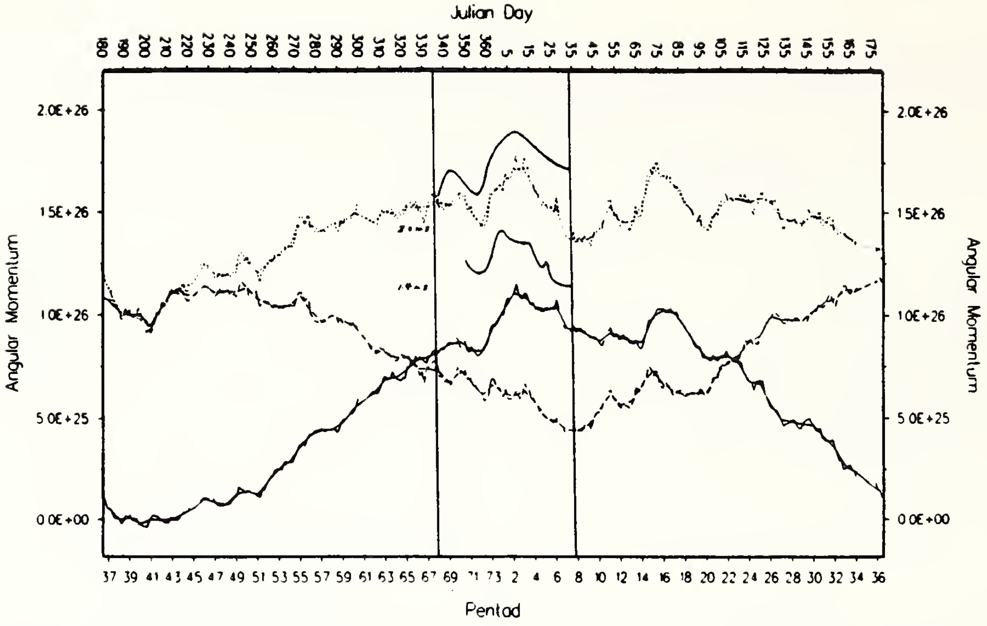

Fig. 1 The global (dotted), Northern Hemisphere (solid) and Southern Hemisphere (dashed) relative atmospheric angular momentum (AAM) for daily and pentad data for the period July 1984 to June 1985. The bottom abscissa has labels in pentads from 37 (June 30-July 4) to 36 (June 25-29) and the top has labels in Julian day. The top inset curve is the relative AAM "predicted" by the computed torques (see text) while the bottom inset is the length-of-day. The units on the ordinate are kg $m^2$ $s^{-1}$.

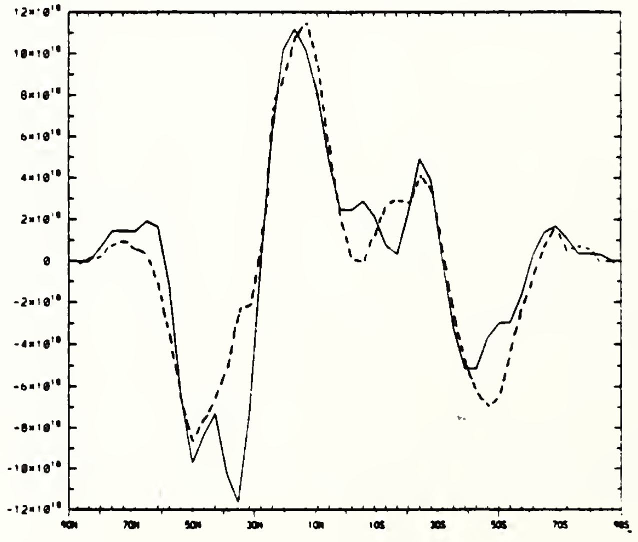

Fig. 2 The primary budget balance for the time mean, zonally and vertically integrated flow. The solid curve is the total momentum flux divergence while the solid curve is the total (frictional and mountain) torque. The maximum momentum divergence of ~12x$10^{18}$ Hadleys (kg $m^2$ $sec^{-2}$) at ~18°N corresponds to a vertically integrated, zonally averaged zonal wind tendency of ~-1 m $s^{-1}$ $day^{-1}$. This can be balanced by a zonally averaged surface stress of ~1 dyne $cm^{-2}$ (0.1 N $m^{-2}$).

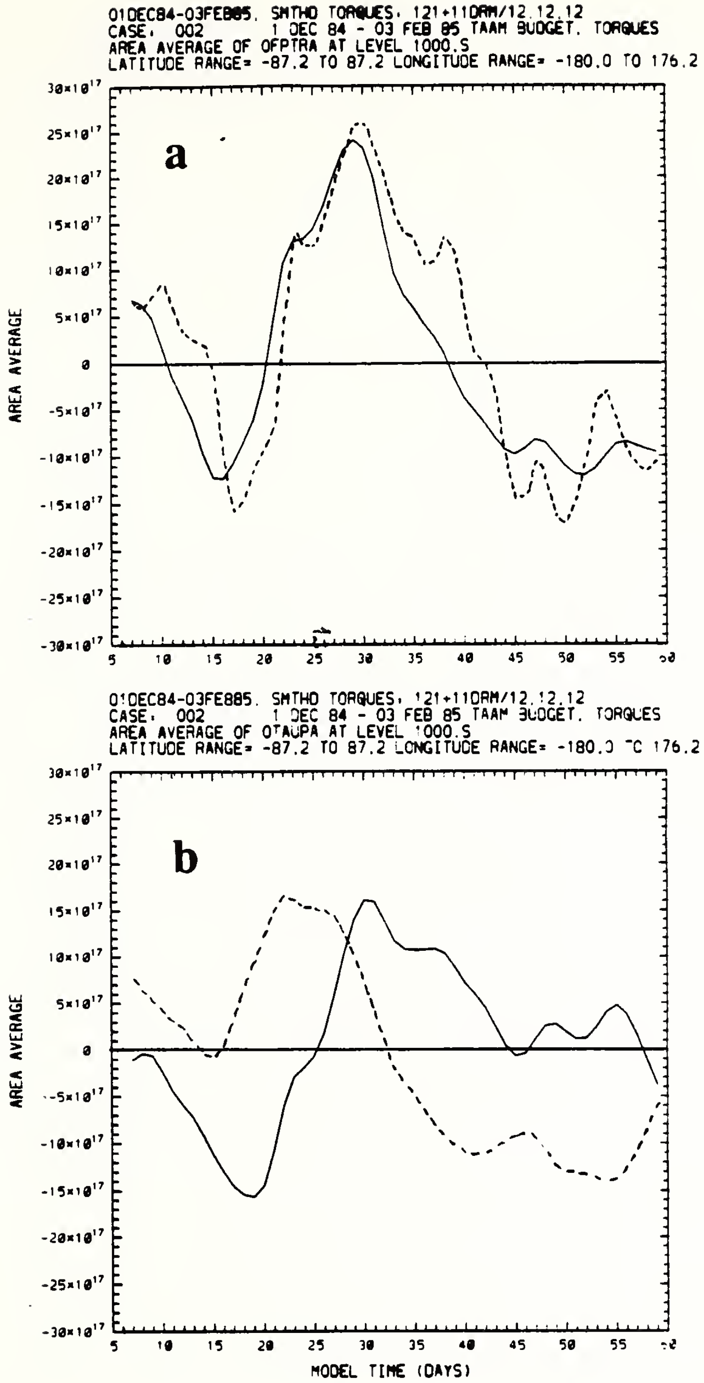

Fig. 3 a) The observed (dashed line) and budget-computed (solid line) anomalous tendency of global relative atmospheric angular momentum from day 7 (7 December 1984) to day 59 (28 January 1985). The budget-computed curve is the sum of b) the frictional torque (dashed line) and the mountain torque (solid line). The daily fields have been temporally smoothed with a 1-2-1 and an 11-day running mean filter as well as spectrally truncated from T31 to T12 before integration.

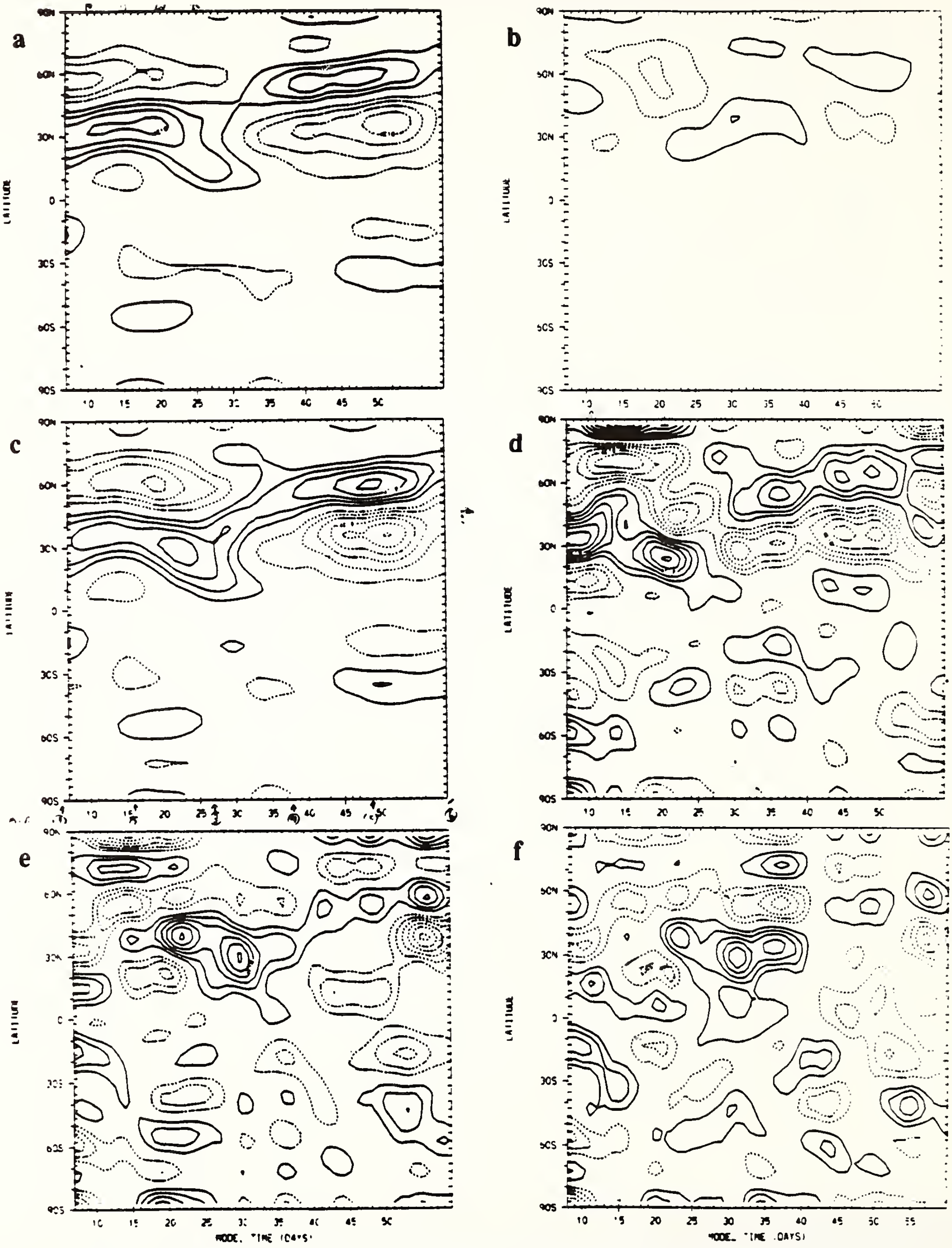

Fig. 4 Time-latitude plots of the anomalous vertically and zonally integrated a) frictional torque, b) mountain torque, c) total torque [a plus b] , d) momentum flux divergence, e) computed relative atmospheric angular momentum (AAM) tendency [c minus d] and observed relative AAM). On all panels, the contour interval is $1.0 \times 10^{18}$ kg $m^2$ $s^{-1}$, negative contours are dashed and the zero contour is omitted.

# ATMOSPHERIC ENERGY FLUXES ALONG THE PACIFIC-NORTH AMERICAN ARC

Neil E. Sargent and Amir Shabbar
Climate Diagnostics Research Group
4905 Dufferin St., Downsview Ont. M3H 5T4

Hoskins and Karoly (1981) found that in theory barotropic wave groups emanating from tropical sources follow paths which arc through the mid-latitudes. These paths are reminiscent of the anomaly pattern of highs and lows known as the Pacific-North American (PNA) pattern which can be interpreted as arcing out of the Pacific, over western Canada and down across North America to a point southeast of the continent. Numerous studies (e.g. van den Dool, Feng and Murphree 1990) have confirmed this behaviour in barotropic and shallow water models. This paper reports on a search for direct evidence of such wave groups in data from daily European Centre for Medium-Range Weather Forecasting (ECMWF) analyses for the period 1980-86.

The approach taken will be to extract from the full flow that component of it which can be characterized as the barotropic component. We then derive equations for evaluating the energy flux associated with this component of the full flow. The assumption then is that if standing (i.e. monthly mean) wave patterns form a zero frequency portion of a wave group then they are established and maintained by transient motions forming non-zero frequency portions of that group. We will be examining energy fluxes of the barotropic component of flow which are due to transients (deviations about the monthly mean). This approach avoids problems in the tropics where the quasi-geostrophic definitions of Eliassen-Palm and Plumb fluxes break down.

It is first necessary to derive equations for a barotropic component of the full flow. Starting from the primitive equations in pressure coordinates and assuming a barotropic horizontal wind $\overline{\mathbb{V}(\phi,\lambda,\mathrm{p},\mathrm{t})}^{p}$ and $\omega(\mathrm{p}=0)=0$ leads to the conclusion $\mathrm{T}(\phi,\lambda,\mathrm{p},\mathrm{t})=\Theta(\mathrm{t})\left(\frac{\mathrm{p}}{\mathrm{p_0}}\right)^{\kappa}$, $\omega=\frac{\omega_s\,\mathrm{p}}{\mathrm{p}_s}$ and the equations

$$\frac{\partial\overline{\mathbb{V}}^{p}}{\partial \mathrm{t}} + \overline{\mathbb{V}}^{p}\cdot\nabla\overline{\mathbb{V}}^{p} + \mathrm{f}\hat{\mathbf{k}}\times\overline{\mathbb{V}}^{p} + \nabla\overline{\Phi}^{p} + (\overline{\Phi}^{p}-\Phi_s)\nabla\ln \mathrm{p}_s = \overline{\mathbb{F}}^{p} \tag{1}$$

$$\frac{\partial\Theta}{\partial \mathrm{t}} = \overline{\left(\frac{\mathrm{p_0}}{\mathrm{p}}\right)^{\kappa}\frac{\mathrm{Q}}{\mathrm{c}_p}}^{p\phi\lambda} \tag{2}$$

$$\frac{\partial \mathrm{p}_s}{\partial \mathrm{t}} + \nabla\cdot \mathrm{p}_s\overline{\mathbb{V}}^{p} = 0 \tag{3}$$

$$\overline{\Phi}^{p} - \Phi_s = \frac{\mathrm{R}\Theta}{\kappa+1}\left(\frac{\mathrm{p}_s}{\mathrm{p_0}}\right)^{\kappa} \tag{4}$$

where standard meteorological notation is used, $\overline{\mathrm{X}}^{p}\equiv\frac{1}{\mathrm{p}_s}\int_0^{\mathrm{p}_s}\mathrm{X}\,d\mathrm{p}$, $\overline{\mathrm{X}}^{\phi\lambda}$ is the horizontal average of X and $\mathbb{F}$ and Q are sources of momentum and heat respectively. (1)-(4) indicate that the barotropic component of the flow that they describe can be extracted from the full flow by suitable averaging operations. They can be further combined in the usual manner to form an equation for the energy budget of that barotropic component:

$$\frac{\partial(K+E)}{\partial t}+\nabla\cdot\overline{\mathbb{V}}^{p}(K+\frac{p_s\overline{\Phi}^{p}}{g}+E)-\frac{\Phi_s}{g}\nabla\cdot p_s\overline{\mathbb{V}}^{p}=\overline{\mathbb{V}}^{p}\cdot\int_0^{p_s}\mathbb{F}\,\frac{dp}{g}+\frac{R}{(1+\kappa)}\left(\frac{p_s}{p_0}\right)^{\kappa}\overline{\int_0^{p_s}\left(\frac{p_0}{p}\right)^{\kappa}\frac{Q}{c_p}\frac{dp}{g}}^{\phi\lambda} \tag{5}$$

where $K=\frac{p_s}{g}\frac{\overline{\mathbb{V}}^{p}\cdot\overline{\mathbb{V}}^{p}}{2}$ and $E=\int_0^{p_s}c_pT\,\frac{dp}{g}=\frac{p_s}{g\kappa}\,(\overline{\Phi}^{p}-\Phi_s)$. (5) identifies $\mathbb{E}_b\equiv\ \overline{\mathbb{V}}^{p}(K\ +\ \frac{p_s\overline{\Phi}^{p}}{g}\ +\ E)$ as the vertically integrated flux of energy due to barotropic motions. The comparable term for the full flow is $\mathbb{E}_f=\int_0^{p_s}\mathbb{V}(\frac{\mathbb{V}\cdot\mathbb{V}}{2}\ +\ \Phi\ +\ c_pT)\frac{dp}{g}$. Note that $\mathbb{E}_f$ includes $\mathbb{E}_b$. Furthermore $\mathbb{E}_b=\mathbb{E}_{bm}+\mathbb{E}_{bt}$ and $\mathbb{E}_f=\mathbb{E}_{fm}+\mathbb{E}_{ft}$ where the subscript m indicates terms due to the monthly mean flow and the subscript t those due to transients about that mean flow.

Hoskins and Karoly's idea, now, is that transient parts of barotropic wave groups (whose energy flux is $\mathbb{E}_{bt}$) originating in the central Pacific establish standing parts of those groups along the PNA arc. Is there any evidence of this in the observed $\mathbb{E}_{bt}$? Annual mean fields of $\mathbb{E}_{bt}$ and $\mathbb{E}_{ft}$ are closely meridional with no sign of preference for energy flux along the PNA arc. However their monthly anomalies do commonly show this arc. Varimax rotated empirical orthogonal functions (EOFs) of $\mathbb{E}_{bt}$ and $\mathbb{E}_{ft}$ anomalies show that the EOFs accounting for the most variance in $\mathbb{E}_{ft}$ and the second most variance in $\mathbb{E}_{bt}$ exhibit a broad sweep of transient energy fluxes out of the central Pacific and across North America. The second EOF of $\mathbb{E}_{bt}$ , shown in Fig. 1, is derived from anomalies for all months of the year and has been truncated to a T6 resolution to bring out the broad features.

This arc pattern is suggestive of a connection between $\mathbb{E}_{bt}$ and PNA anomalies but a more direct test is to covary the $\mathbb{E}_{bt}$ field with some function of the PNA index I as computed by the method of Wallace and Gutzler (1981). Since the idea is that $\mathbb{E}_{bt}$ is involved in the growth or decay of the PNA pattern it makes sense to covary $\mathbb{E}_{bt}$ with the time derivative $\frac{dI}{dt}$ of the PNA index. The covariance of $\mathbb{E}_{bt}$ with $-\ \frac{dI}{dt}$ (in Fig. 2) again shows an arc pattern out of the central Pacific and across North America, albeit not as complete a pattern as that of the EOF in Fig 1. The interesting thing to note, though, is the sign of the covariance; a positive flux $\mathbb{E}_{bt}$ out of the central Pacific and across North America does not strengthen PNA patterns but rather weakens them.

We hope to extend this work to even more clearly identify the mechanisms of the PNA. In particular we wished but have so far been unable to identify a single source forcing region in the Pacific. The global extent of the patterns shown in Figs. 1 and 2 suggest this may be difficult.

## References

Hoskins, B. J., and D. J. Karoly, 1981: The steady linear response of a spherical atmosphere to thermal and orographic forcing. *J. of Atmos. Sci.* **38**, 1179-1196.

van den Dool, H., J. Feng and T. Murphree, 1990: Dynamic calculation of teleconnections. Proceedings of the Fifteenth Annual Climate Diagnostic Workshop, Asheville, U. S. Department of Commerce, 520-527.

Wallace, J. M., and D. S. Gutzler, 1981: Teleconnections in the geopotential height field during the Northern Hemisphere winter. *Mon. Wea. Rev.* **109**, 784-812.

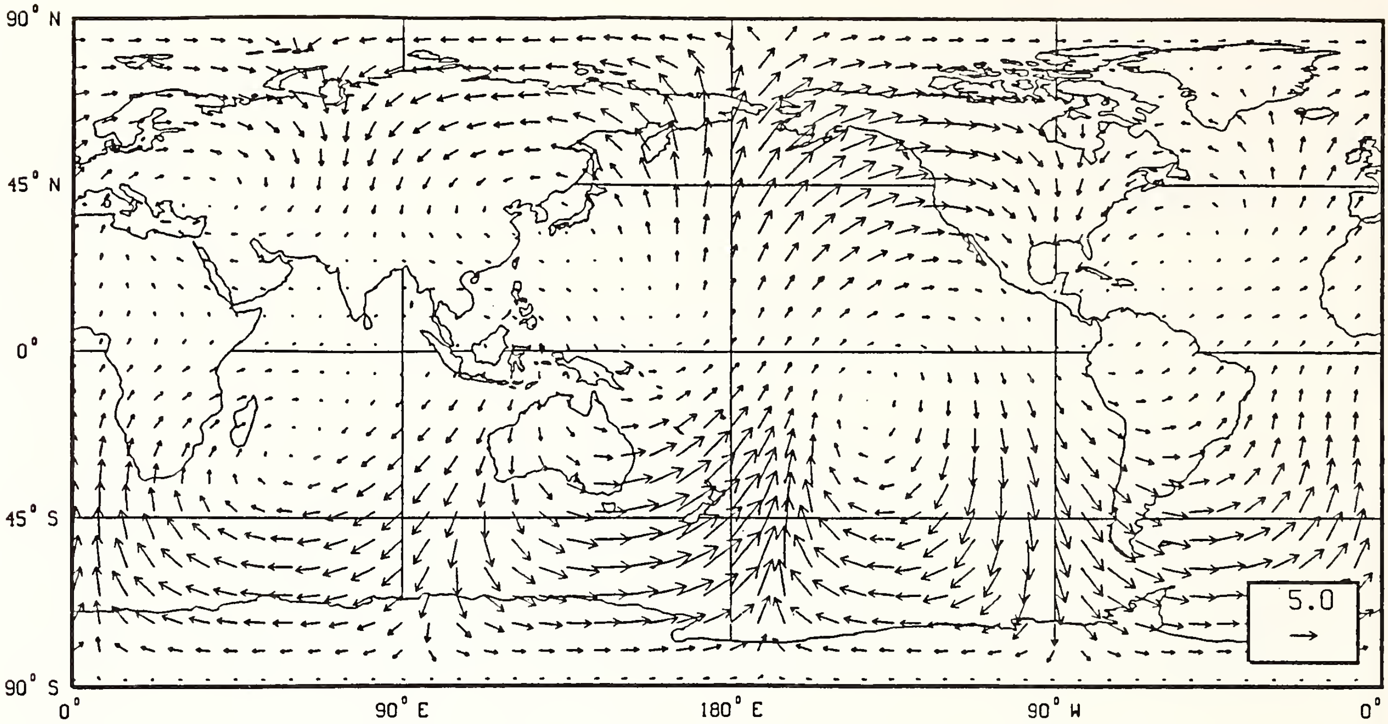

Fig. 1. EOF #2 of monthly anomalies in the barotropic component energy flux $\mathbb{E}_{bt}$ due to deviations of flow from monthly means over the period Jan 1980-Dec 1986. The EOF has been truncated at T6.

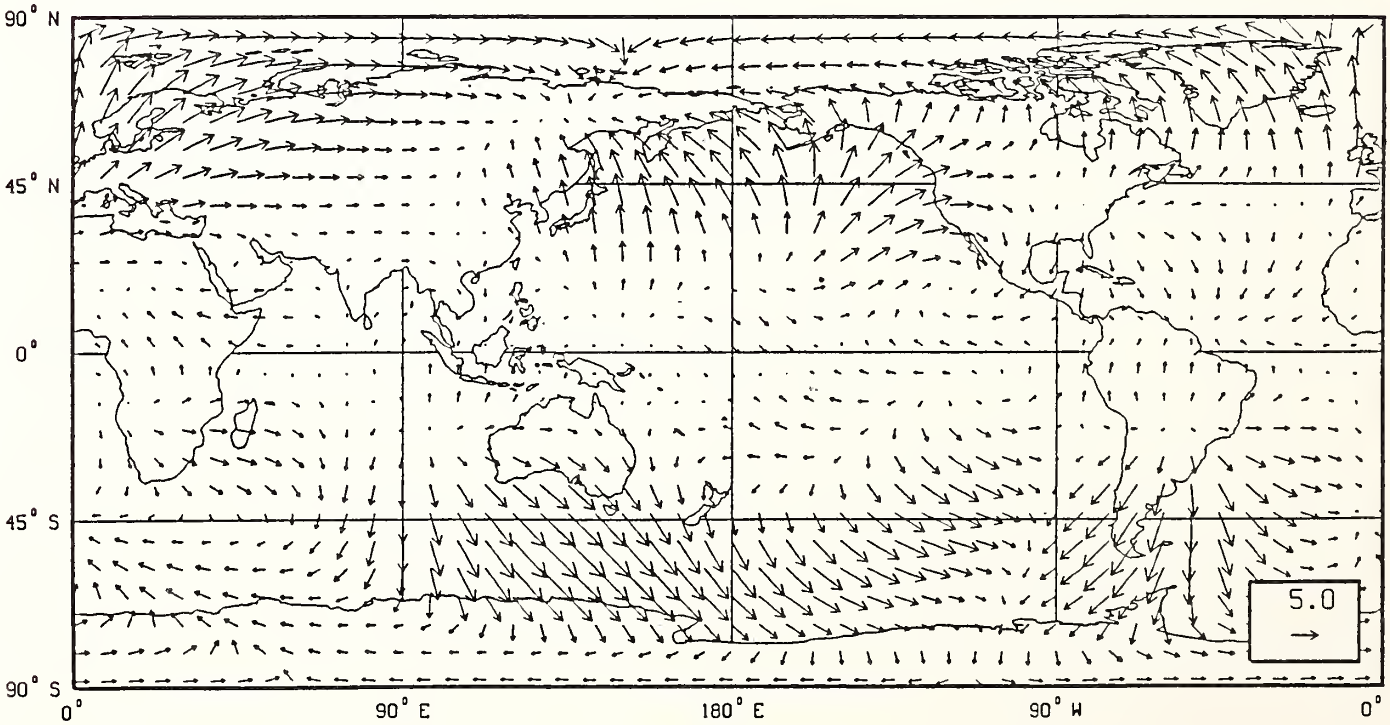

Fig. 2. Covariance of $\mathbb{E}_{bt}$ with $-\frac{dI}{dt}$ where I is the PNA index computed from monthly means according to Wallace and Gutzler. The covariance has also been truncated at T6.

# VERTICAL MOTIONS OVER CHRISTMAS ISLAND: OBSERVATIONS BY THE 50 MHZ PROFILER

John R. McAfee, Kenneth S. Gage, and George C. Reid
Aeronomy Laboratory
National Oceanic and Atmospheric Administration
Boulder, CO 80303

*Introduction*: Direct measurements of vertical motions are possible through the use of wind profiling Doppler radars. The Aeronomy Laboratory Wind Profiler on Christmas Island is a 50 Mhz clear air Doppler radar with a 100mx100m phased array antenna producing three narrow beams, one vertical and two at 15° off vertical in the E-W and N-S planes. A profile of velocities is produced for each of these beams during an approximate seven minute period, producing over 200 profiles per day. The resolution is 600 meters, which gives the vertical beam a useful height coverage of 1.8 to 24.6 kilometers in steps of 0.6 km. The system is designed for continuous, unattended operation.

Christmas Island (2°N, 157°W), located in the equatorial dry zone of the central Pacific, is a large coral atoll with a high point of only 14 meters, limiting possible orographic effects on the local background wind. Typically there is little rainfall except during the warm phase of the Southern Oscillation when convection moves eastward from the western Pacific. During the 44 month period between April, 1986 and November, 1989, the profiler operated virtually uninterrupted, making this data set amenable to analysis in a climatological sense. Although the time covered is less than four years, it does contain a nearly complete ENSO cycle. In this study we present the results of an analysis of vertical velocities observed at Christmas Island during the period 1986-1989.

*Daily Analysis*: Determining mean vertical motions is complicated by the fact that vertical velocities are dominated by short-period internal gravity waves with typical rms amplitudes of 10-20 cm $s^{-1}$. Since we are looking for mean motions of $\sim$1 cm $s^{-1}$, it is necessary to average large amounts of data. A typical "well-behaved" set of data for day 139 of 1987 is shown in Figure 1 in both the plot at the bottom left and at the top. This data, basically confined to the range ±30 cm $s^{-1}$, has already been modified by removing those values with either signal-to-noise ratios less than -16 db or spectral widths less than 12.5 cm $s^{-1}$. In the graph at the lower right the solid vertical line at about 210 is the total available number of data points for the day and the dashed (middle) curve represents the remainder of the data after the removal just mentioned. Additional data in the form of outliers are removed until the standard deviation falls below 12.5 cm $s^{-1}$. The solid curve in the top graph is the resulting mean profile for the day and the total number of values used to determine that mean is shown in the lower right plot as the dotted curve.

There is considerable variability in the daily profiles, but not to the extent seen during a day. Figure 2 is an example of the 31 daily profiles from January, 1988. Most of the values are now confined to a spread of 3 or 4 cm $s^{-1}$ and it is now possible to recognize a somewhat typical profile. A downward motion of around one cm $s^{-1}$ is evident in the middle troposphere between about 4 and 12 km. Below this, from 2 to 4 km, the values are more positive. In the upper troposphere, the velocities become positive, peaking around 15 or 16 km and then lessening to where it becomes difficult to follow a trend in the noise.

*Long -Term Analysis*: In order to look at the behavior for periods longer than a day, it is convenient to average the daily profiles for months. The profiles for the 44 months of April, 1986 through November, 1989 are shown in Figure 3. The variability has become smaller and the "typical" profile mentioned previously is now more apparent . The temporal behavior is shown in Figure 4, a contour plot using the same data as that shown in Figure 3. The dashed curves represent negative (downward) velocities. The consistency of both the upward motion near 3 km, the downward motion in the 4 to 12 km range, and the upward motion in the 14 to 18 km region is quite apparent. The most striking variation on this time scale can be seen above 18 km where an oscillation is evident. A period of about 2 years and downward phase propagation is consistent with a QBO link .

An annual variation based on this limited four year set of data is difficult to discern in Figure 4, but is apparent in Figure 5, a contour plot of the annual average vertical velocity . The upward motion near 3 km has a maximum in June and a minimum in January. The downward motion in the middle troposphere maximizes in February and is smallest in August, with the upward motion at the tropopause acting in an opposite sense. The amplitudes run from about .5 to 1.5 cm $s^{-1}$.

The annual behavior may be removed from the data set in order to look more closely at the interannual behavior. The 44 monthly profiles are again shown in Figure 6 where the mean annual cycle has been removed. The remaining variability is fairly constant within one cm $s^{-1}$ up to about 18 km. Above this level it increases, probably mostly due to the QBO-like feature. The distribution also becomes skewed, with more frequent but smaller upward values. The corresponding contour plot is shown in Figure 7. Besides the obvious QBO-like feature, an ENSO-like signal may be seen near 10 km with more upward motion in early 1987 (warm event) and more downward motion in early 1989 (cold event). The opposite behavior is evident near 15 km.

*Concluding Remarks*: Measurements of vertical velocities at Christmas Island with the Aeronomy Laboratory Wind Profiler during the time period 1986-1989 have shown several important features:

1) The motion in the 2-4 km region is most often upward with a summer maximum. This may be an effect of clouds or particulates at the top of the boundary layer.

2) The vertical velocity is downward through much of the troposphere (4-12 km), consistent with clear air radiative cooling.

3) Upward vertical motions measured at the tropopause contradict the popular "stratospheric fountain" concept .

4) The lower stratosphere shows a definite QBO-like feature.

*Acknowledgments*: The Christmas Island wind profiler is supported by the U.S. TOGA Project Office. This research has been supported in part by the National Science Foundation under Agreement No. ATM-8720797.

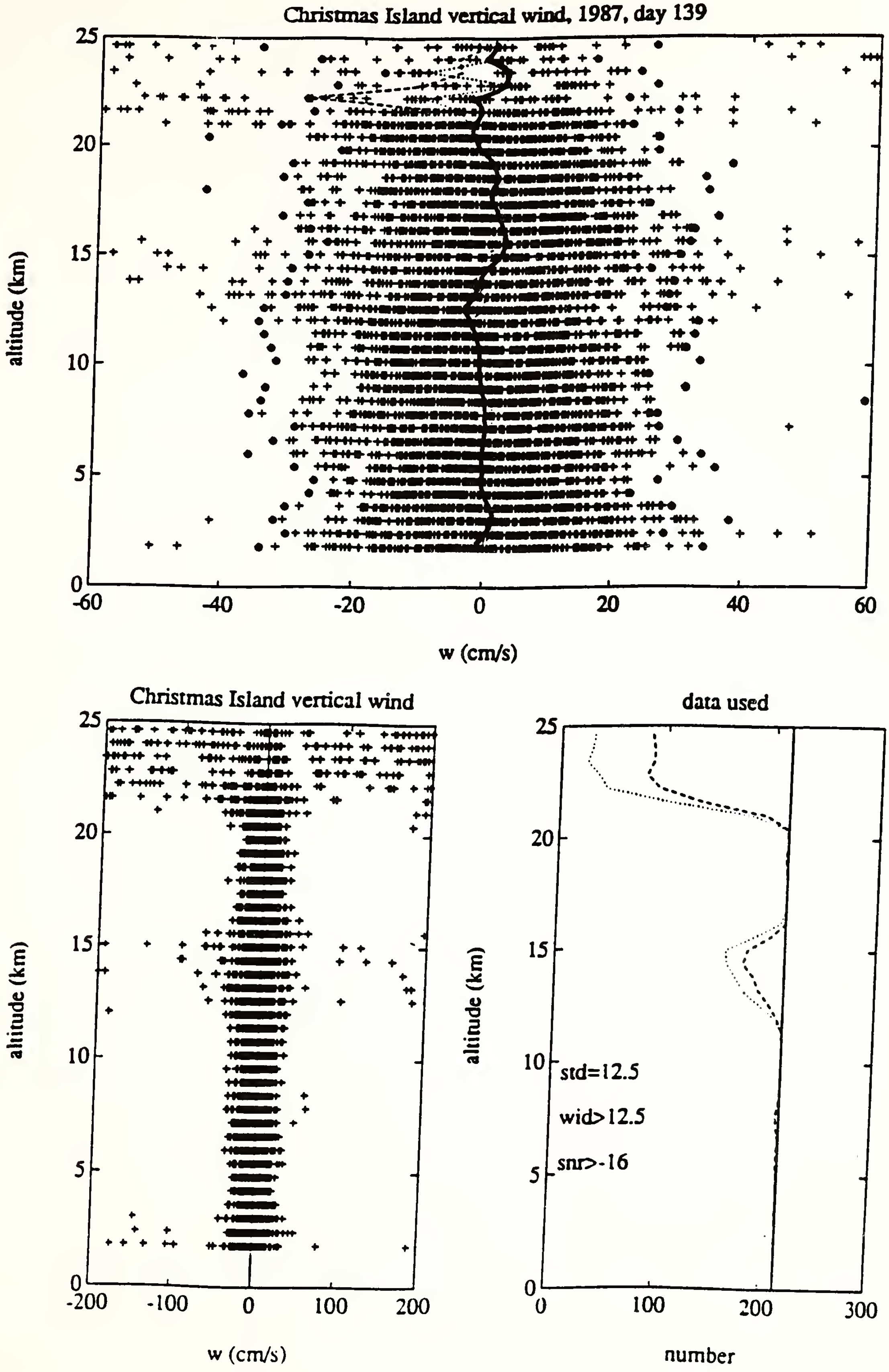

Figure 1. Example of vertical velocities during a day.

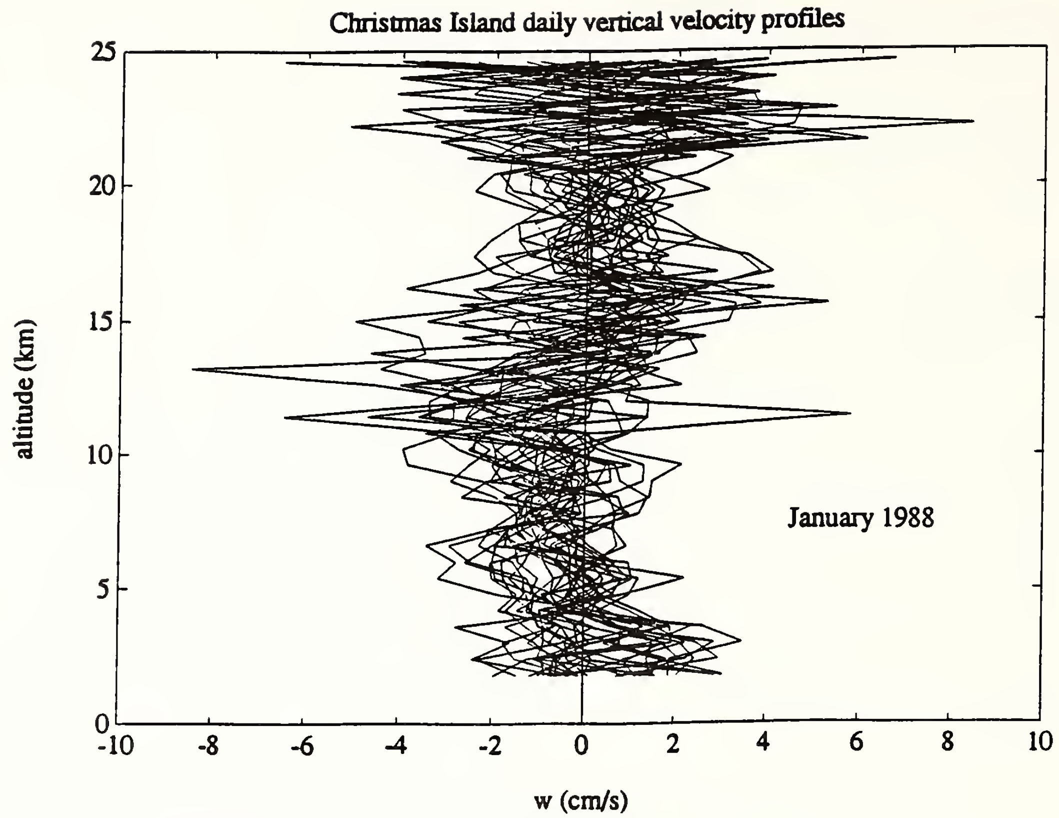

Figure 2. Example of daily average vertical profiles during one month.

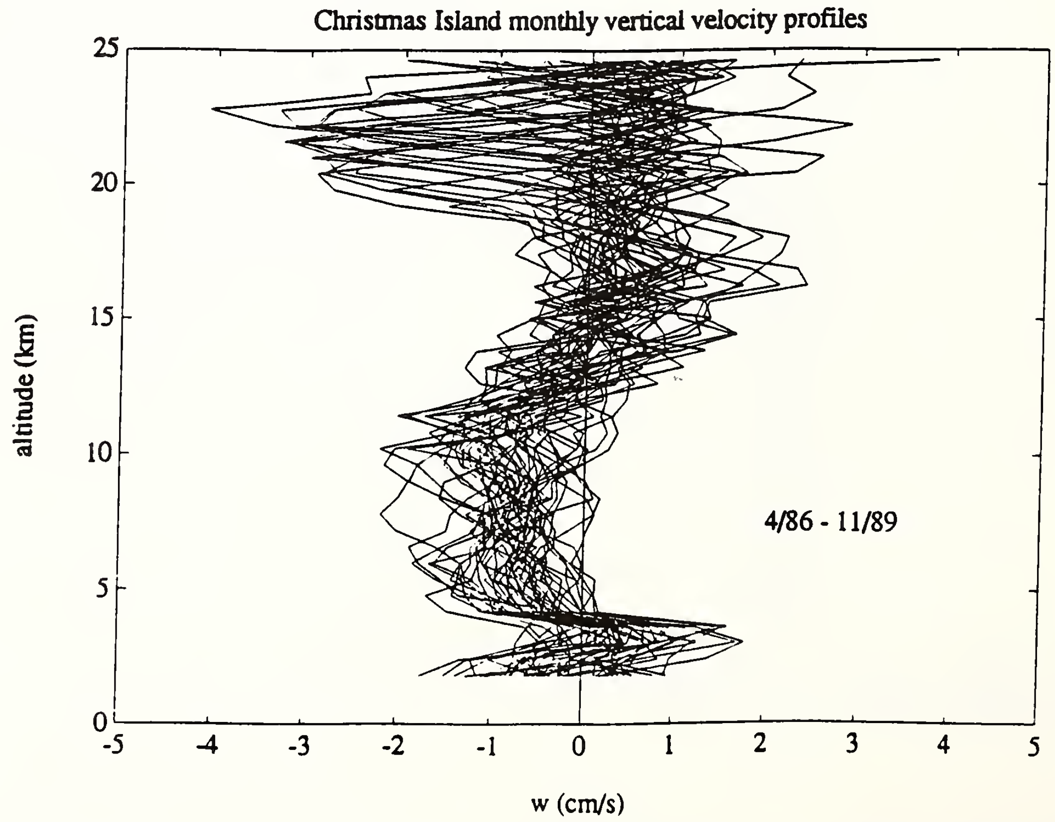

Figure 3. Monthly averaged vertical profiles for April, 1986 through November, 1989.

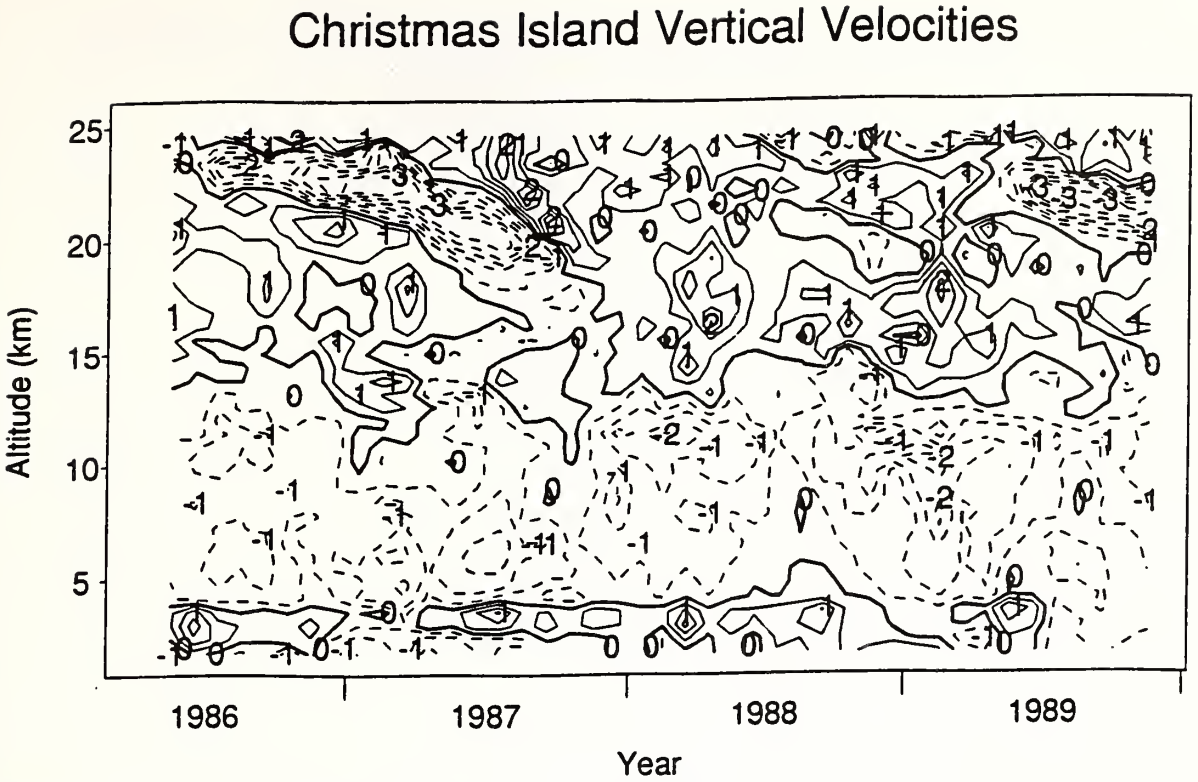
Christmas Island Vertical Velocities

Figure 4. Contour plot of monthly averaged vertical velocities for April, 1986 through November, 1989.

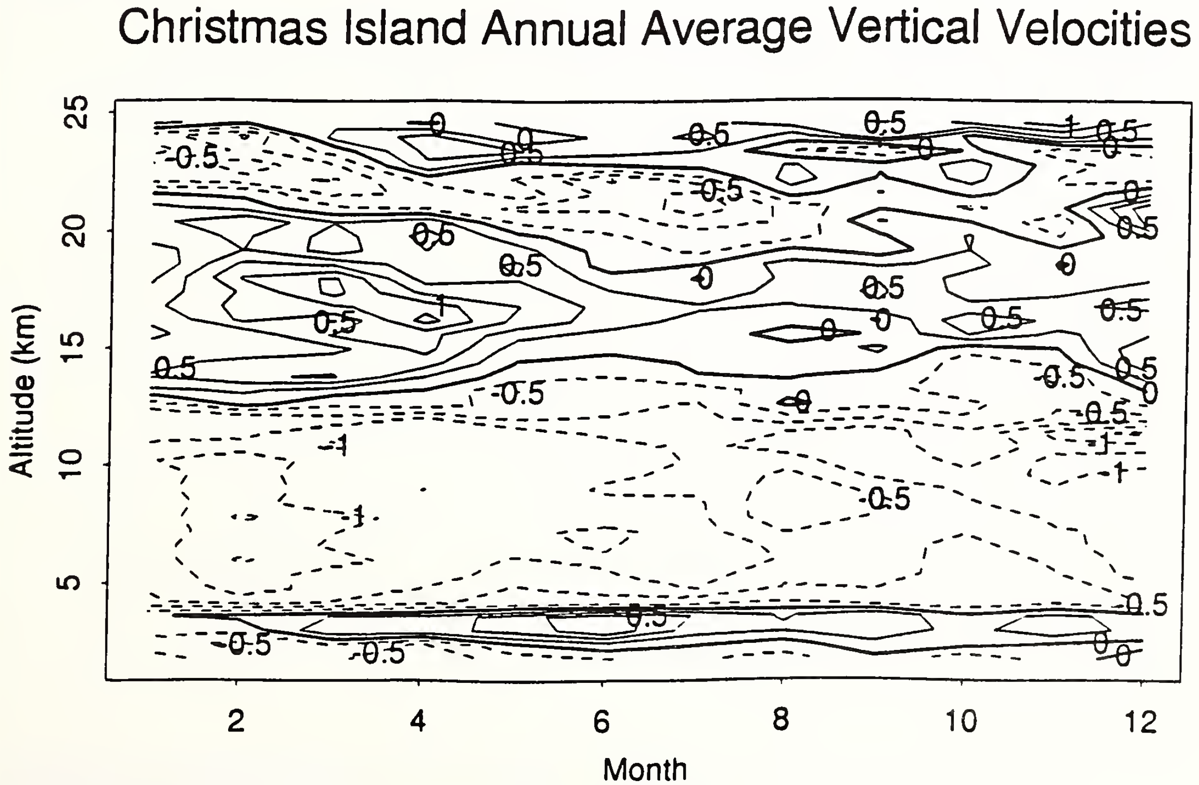
Christmas Island Annual Average Vertical Velocities

Figure 5. Contour plot of the mean annual behavior based on 1986-1989 data.

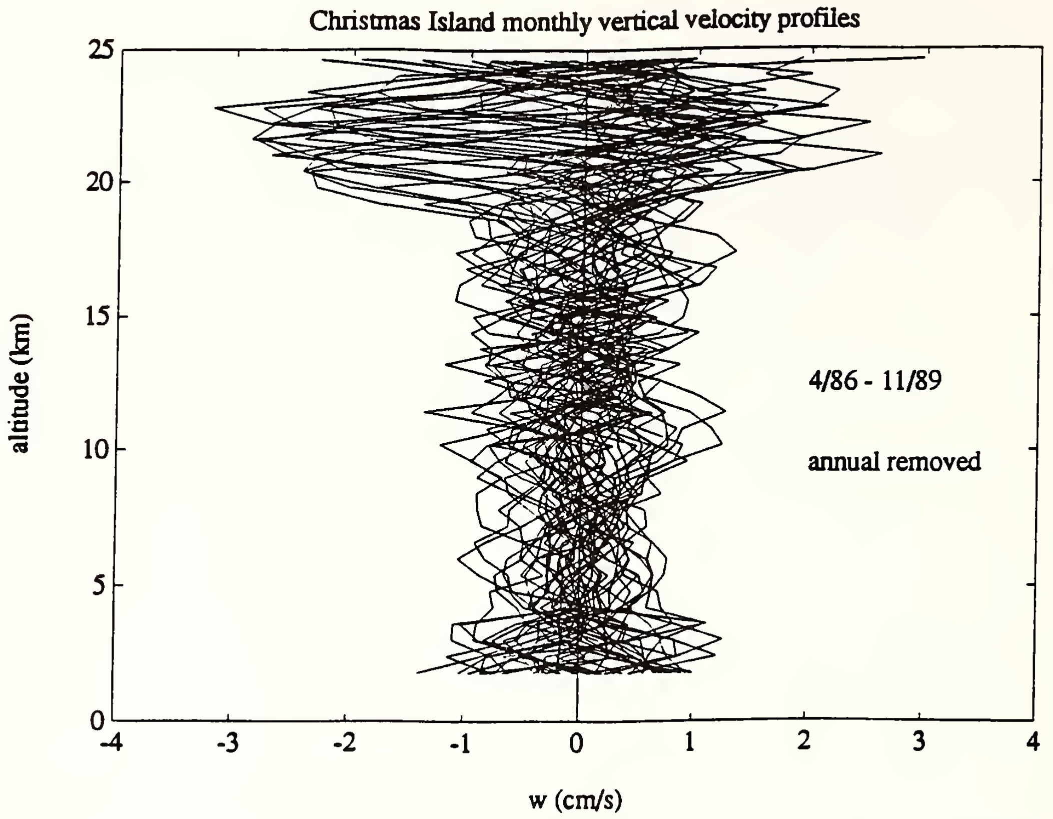

Figure 6. Monthly averaged vertical profiles for April, 1986 through November, 1989 with the annual removed.

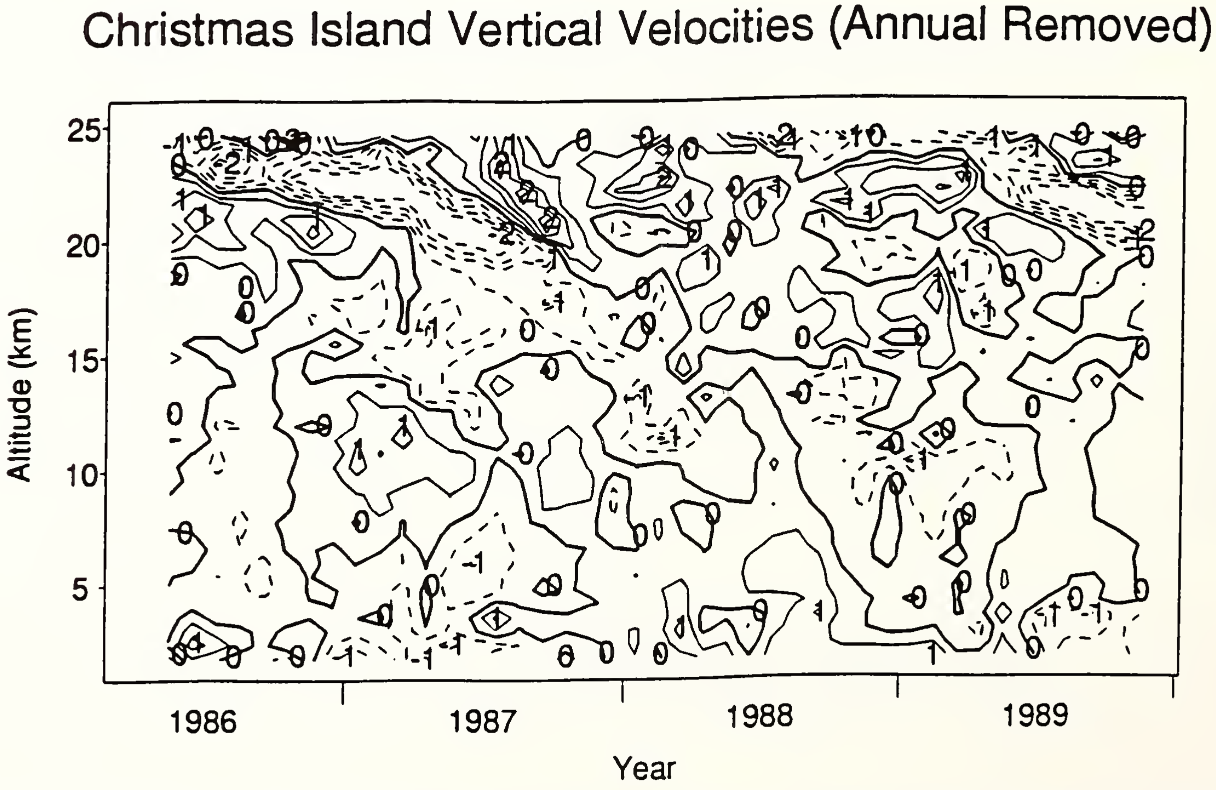

Figure 7. Contour plot of monthly averaged vertical velocities for April, 1986 through November, 1989 with the annual removed.

# A First Look at Annual and Interannual Variability of Tropospheric Diurnal and Semidiurnal Oscillations using the Christmas Island Wind Profiler

Christopher R. Williams, Susan K. Avery,
Cooperative Institute for Research in Environmental Sciences,
University of Colorado at Boulder

John R. McAfee and Kenneth S. Gage
NOAA Aeronomy Laboratory
Boulder, Colorado

For the past four months, we have been analyzing the diurnal and semidiurnal wind oscillations in the troposphere and lower stratosphere using the Christmas Island 50 MHz wind profiler (2°N, 157°W). It is generally believed that diurnal and semidiurnal wind oscillations are generated in the troposphere and stratosphere then propagate vertically growing in amplitude until breaking in the mesosphere. We are interested in understanding how these oscillations are generated and how they are related to cloud physics, convection, precipitation, and other climatological processes. This paper will briefly discuss some interesting and not yet completely understood results from our analysis as well as future directions of our research.

## Data Analysis Techniques

The Christmas Island Wind Profiler is part of a Pacific network of radars being used to study the lower tropical atmosphere. This radar generates doppler radial wind velocities from three beams (one vertical, two 15° off Zenith to the North and East) approximately every 7 minutes. The lowest and highest heights are 1.8 and 25.5 km with a range resolution of 0.6 km. These radial winds were averaged into hourly orthogonal winds (Zonal, Meridional, and Vertical) for the nearly continuous data set from April 1986 to November 1989. The four year data record was band-pass filtered about the diurnal period. The filtered data were compressed into a 'Mean Day' by taking the statistical mean of the wind occurring in each hour of the day. The standard deviation of the mean of this mean day was determined by dividing the standard deviation of the bandpassed data record by the square root of the number of days in the data record.

The Semidiurnal Mean Day was calculated using these same techniques except the band-pass filter was centered about 12 hours.

## Vertical Phase Structure

The Zonal Diurnal Mean Day and associated standard deviation of the mean for the four year record is shown in Figure 1. Notice the vertical phase structure of this oscillation and the apparent vertical wave length of about 14 km. The Zonal Semidiurnal Mean Day and associated standard deviation for the four year record is shown in Figure 2. This oscillation has a very long vertical wave length. The phase appears constant for the first 14 km of the troposphere. The maximum standard deviation of the mean for both diurnal and semidiurnal mean days is approximately 0.03 $ms^{-1}$ and occurs near 14 km. The vertical wave lengths for both the diurnal and semidiurnal oscillations are consistent with theoretical wave lengths for the migrating diurnal and semidiurnal winds. By analyzing the winds at only one physical location, we can not determine the zonal structure of these oscillations. In the future, we will perform spatial analyzes between Tropical Pacific wind profilers.

## Diurnal Band-Pass Power vs. Time

The Mean Day analysis technique compresses the four year data record into 24 hours for phase structure analysis. This type of analysis does not give temporal variations of power. Therefore, the monthly zonal power in the diurnal bandpass winds were calculated.

The Monthly Zonal Diurnal Bandpass Power for the four year data record at 11 km (near typical 250 mbar level) is shown in Figure 3. Also shown in Figure 3 is the Monthly Zonal Mean Wind at 11 km. These signals have been smoothed with a 5 month running average. There is a significant increase of the Monthly Zonal Diurnal Bandpass Power during the Fall-Winter of 1988-1989. The cause of this increase is not understood and further investigation will determine whether this is the result of larger amplitude migrating oscillations or the generation of short duration (1-2 week) non-migrating oscillations.

## Surface Pressure and Wind Correlations

The surface pressure at Christmas Island has been recorded nearly continuously since January 1987. The observed diurnal and semidiurnal surface pressures were compared with theoretically derived migrating surface pressures. There was excellent agreement between the observed and theoretical surface pressures (not shown).

Using the Equations of Motion on a frictionless rotating sphere, the surface winds as a result of the surface pressure oscillations can be calculated. The semidiurnal surface winds were calculated and are shown in Figure 4. Also in Figure 4 are the observed semidiurnal winds at the lowest resolvable height of 1.8 km. The calculated Meridional wind under-estimates the observed Meridional wind. This is a short coming of the frictionless model which predicts zero Meridional wind at the equator. There is very good agreement between the Zonal theoretical and observed winds.

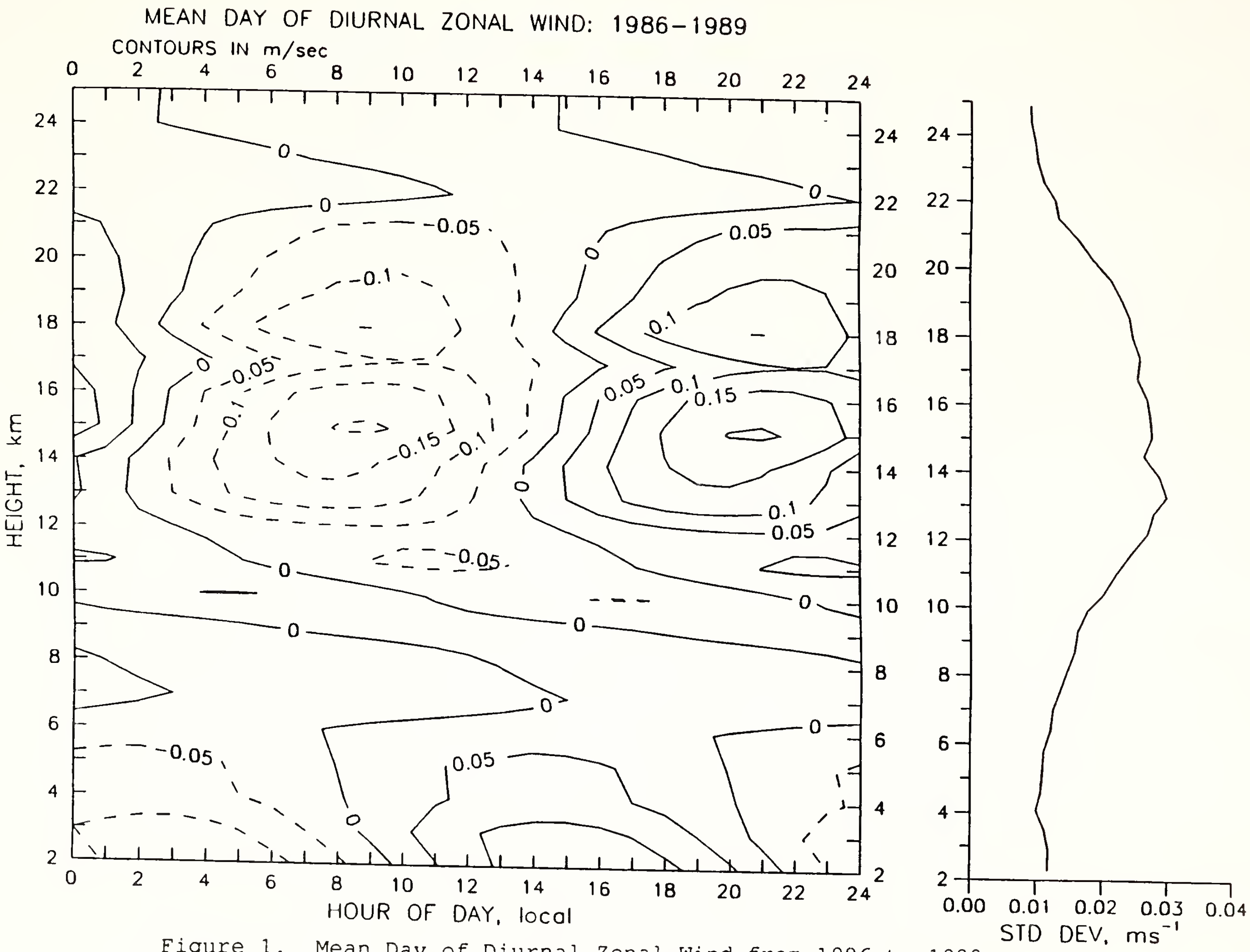

Figure 1. Mean Day of Diurnal Zonal Wind from 1986 to 1989. Contours are in 0.05 ms$^{-1}$, solid (dashed) are Westerlies (Easterlies). Standard Deviation of the mean is in ms$^{-1}$.

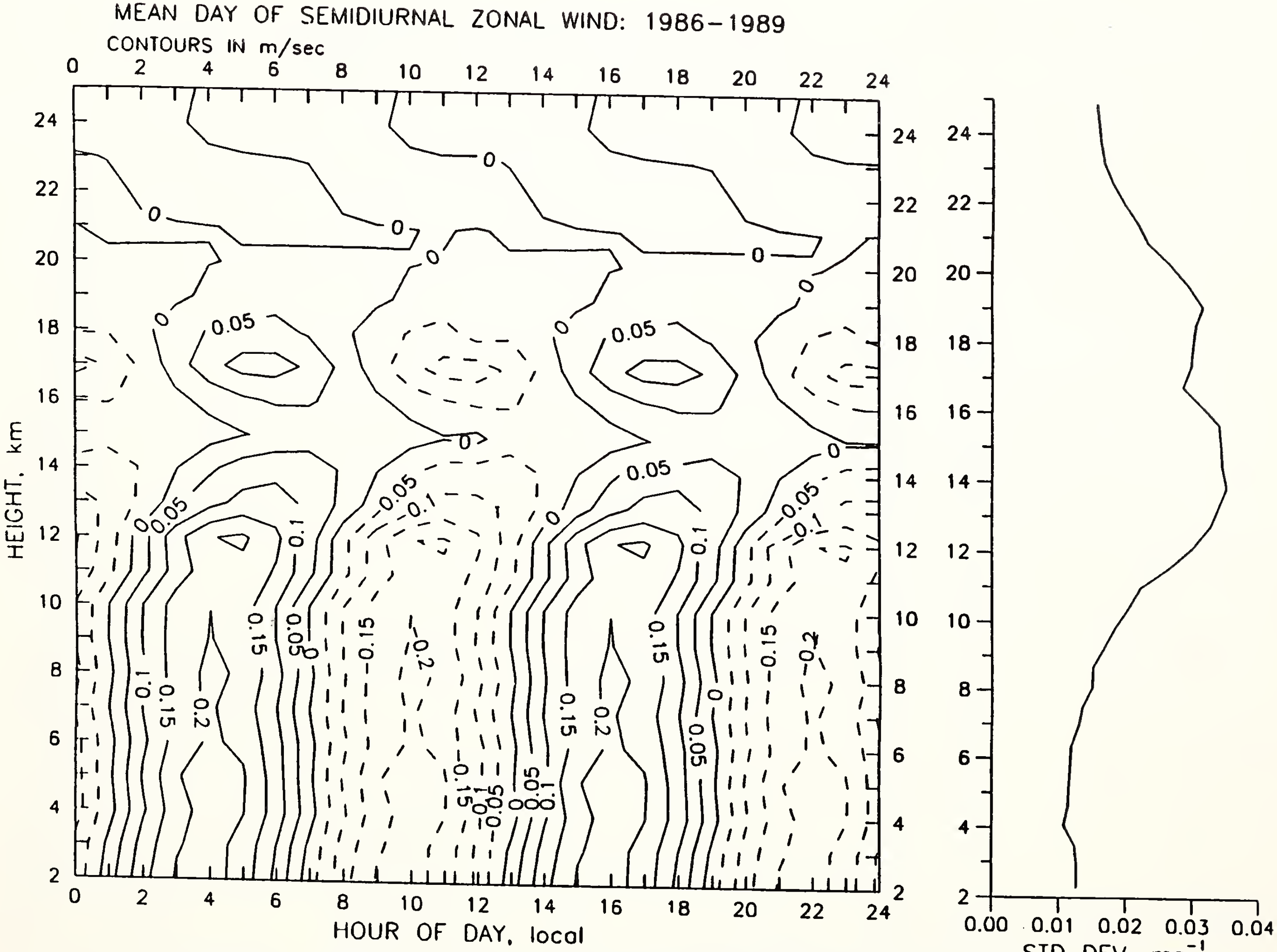

Figure 2. Same as Figure 1, except for Semidiurnal Zonal Wind.

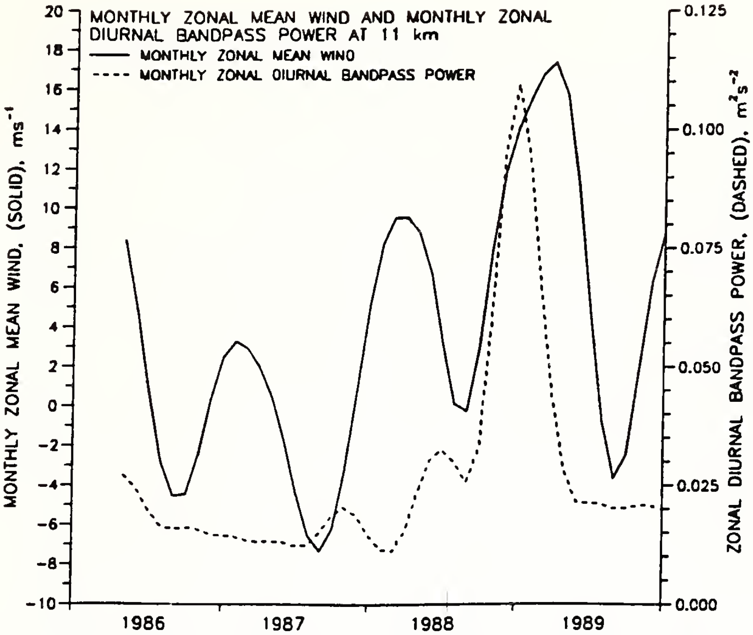

Figure 3. Monthly Zonal Diurnal Bandpass Power (dashed) and Monthly Zonal Mean Wind (Solid) both at 11 km.

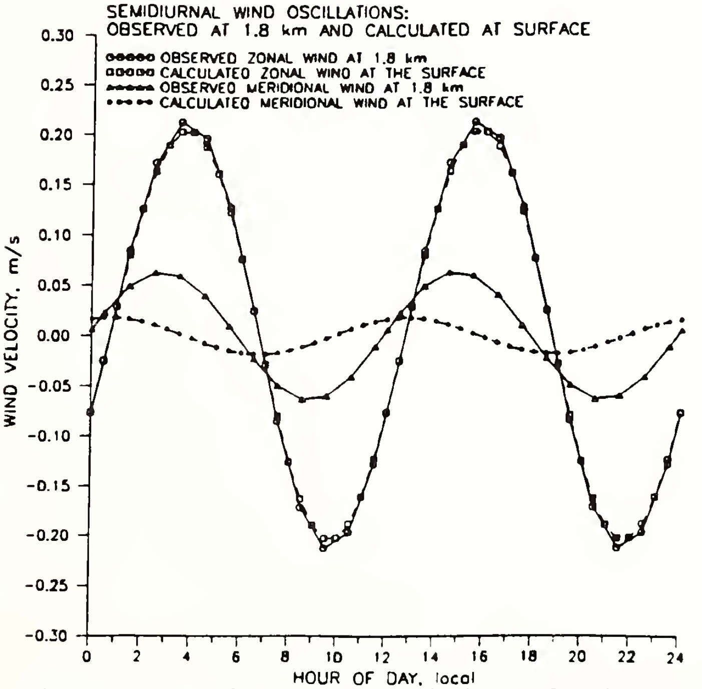

Figure 4. Observed Semidiurnal Wind at 1.8 km and calculated Semidiurnal Wind at the Surface.

# DIAGNOSIS OF A BLOCKING EPISODE OVER THE SOUTH-CENTRAL SOUTH PACIFIC

Gerald D. Bell
World Weather Bldg. Rm 605
Climate Analysis Center W/NMC52
5200 Auth Rd
Camp Springs MD 20746

The purpose of this study is to examine observationally the low frequency (background) mid-tropospheric flow structure and evolution during the persistent phase (April-June 1991) of a blocking episode over the high latitudes of the central and eastern South Pacific.

Individual monthly mean 500 mb heights and anomalies for the period April-June 1991 (Fig. 1) show a meridional dipole of persistent height anomalies over the central and eastern South Pacific, flanked by persistent negative anomalies both upstream over New Zealand and downstream over the Scotia and Weddell Sea's. The wave pattern over the South Pacific intensifies during May (Figs. 1c,d) and June (Figs. 1e,f), with strong flow diffluence observed throughout the central South Pacific the entire period. The three-month mean height anomaly pattern during this period exhibits marked asymmetries (Fig. 2a), with strong mean diffluence and maximum meridional flow speeds located upstream of the block. The implication is that much of the flow structure immediately upstream of the mean block position is strongly associated with intermonthly (IM) time scale variability (periods greater than 30 days) in this case. Moreover, both the structure and evolution of the blocking episode is strongly coupled with IM fluctuations. The contribution from IM fluctuations to the observed positive height anomaly over the mean block position at the time of maximum block intensity, for example, is greater than 75% (Figs. 3a,b).

A variance analysis suggests that the distributions of intermonthly and intra-monthly (periods 10-25 days) height field variability are markedly different with respect to the mean ridge axis during the blocking episode. IM fluctuations (Fig. 2b), for example, dominate the height field variability over the mean block position and over the mean downstream trough position. Intra-monthly fluctuations (Fig. 2c), on the other hand, dominate the height field variability upstream of the mean block position, and within the southern branch of the split flow both equatorward of and downstream of the mean block position. A future investigation will examine the influence of the interactions between these two frequency bands on the evolution of the IM flow during the blocking episode.

The general structure of the IM height anomaly field during the blocking event is summarized with a one-point correlation map centered on the mean block position (Fig. 4a). IM fluctuations are strongly simultaneously correlated (absolute magnitudes are larger than .85) throughout the middle and high latitudes of the Southern Hemisphere the entire period (Fig. 4a), with the overall correlation pattern strongly resembling the monthly mean anomaly fields (Fig. 1). The temporal evolution of the IM anomaly pattern is isolated by computing one-point lagged covariances for lags between +20 days and -20 days, centered on the mean block position. All covariance values are then normalized by the standard deviation (i.e., by the expected positive IM anomaly) over the mean block position. The resulting normalized covariance maps (Fig. 4b-f) reflect the expected IM anomaly pattern at a given lag, provided that the expected positive lag-zero IM anomaly exists over the mean block position. These analyses summarize the evolution of the IM anomaly field during the blocking episode, since corresponding correlation coefficients (not shown) are very large for all lags. The flow pattern is highly asymmetric about the ridge axis at lag -20d (Fig. 4b). The flow then becomes increasingly symmetric about the ridge axis over the next 20 days (Figs. 4c,d), and amplification is maximized within and upstream of the block position. Thereafter, the strongest meridional flow, along with the region of anomaly intensification, is found downstream of the block (Figs. 4e,f). This evolution reflects the apparent propagation of a jet through the mean ridge axis, with maximum ridge intensity observed when the jet is centered within the ridge crest. The ridge then weakens as the jet moves toward the downstream trough. Consequently, the IM anomaly field undergoes a well-defined life cycle in the block region which resembles the symbiotic relationship between jets and waves during baroclinic wave evolution.

In summary, the persistent phase (April-June 1991) of a blocking episode which dominated the Southern Hemisphere circulation for more than three months has been examined. Five well-defined periodic fluctuations in amplitude, corresponding to individual blocking events, are evident. Intermonthly (IM) fluctuations (periods greater than 30 days) are strongly simultaneously correlated during the period, suggesting that the blocking episode occurs in conjunction with strongly coherent low frequency fluctuations which extend around the hemisphere. These IM fluctuations contribute substantially to both the structural and temporal evolution of the 500 mb height field during the blocking episode. Normalized lagged covariance analyses reveal that the IM fluctuations exhibit a well-defined life cycle in the block region. This life cycle resembles that of a baroclinic wave during baroclinic wave evolution, and appears to reflect energy propagation through the block region on the IM time scale.

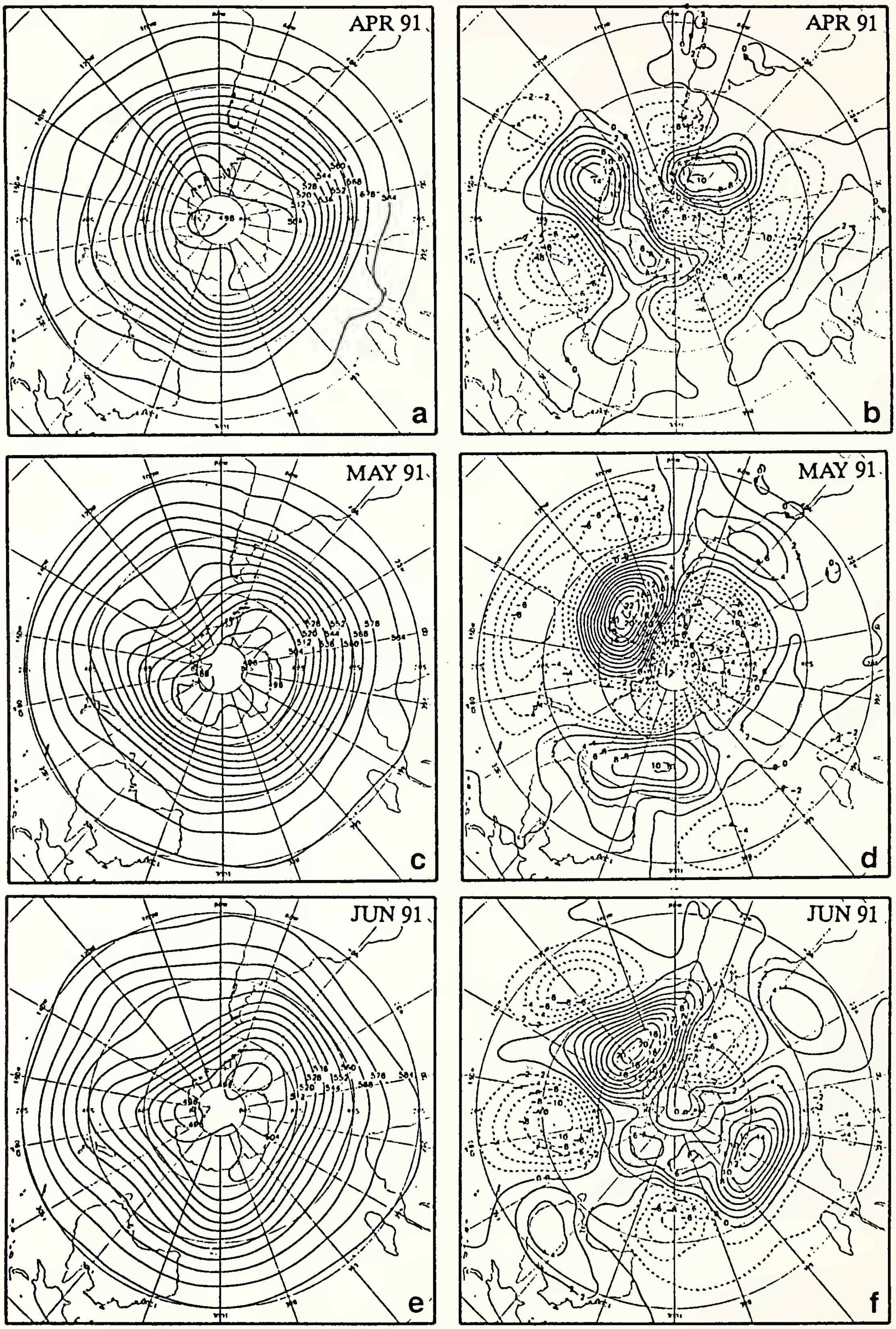

Fig. 1. Monthly mean 500 mb heights (interval is 80 m) and anomalies (interval is 20 m) for (a,b) April 1991, (c,d) May 1991 and (e,f) June 1991, respectively.

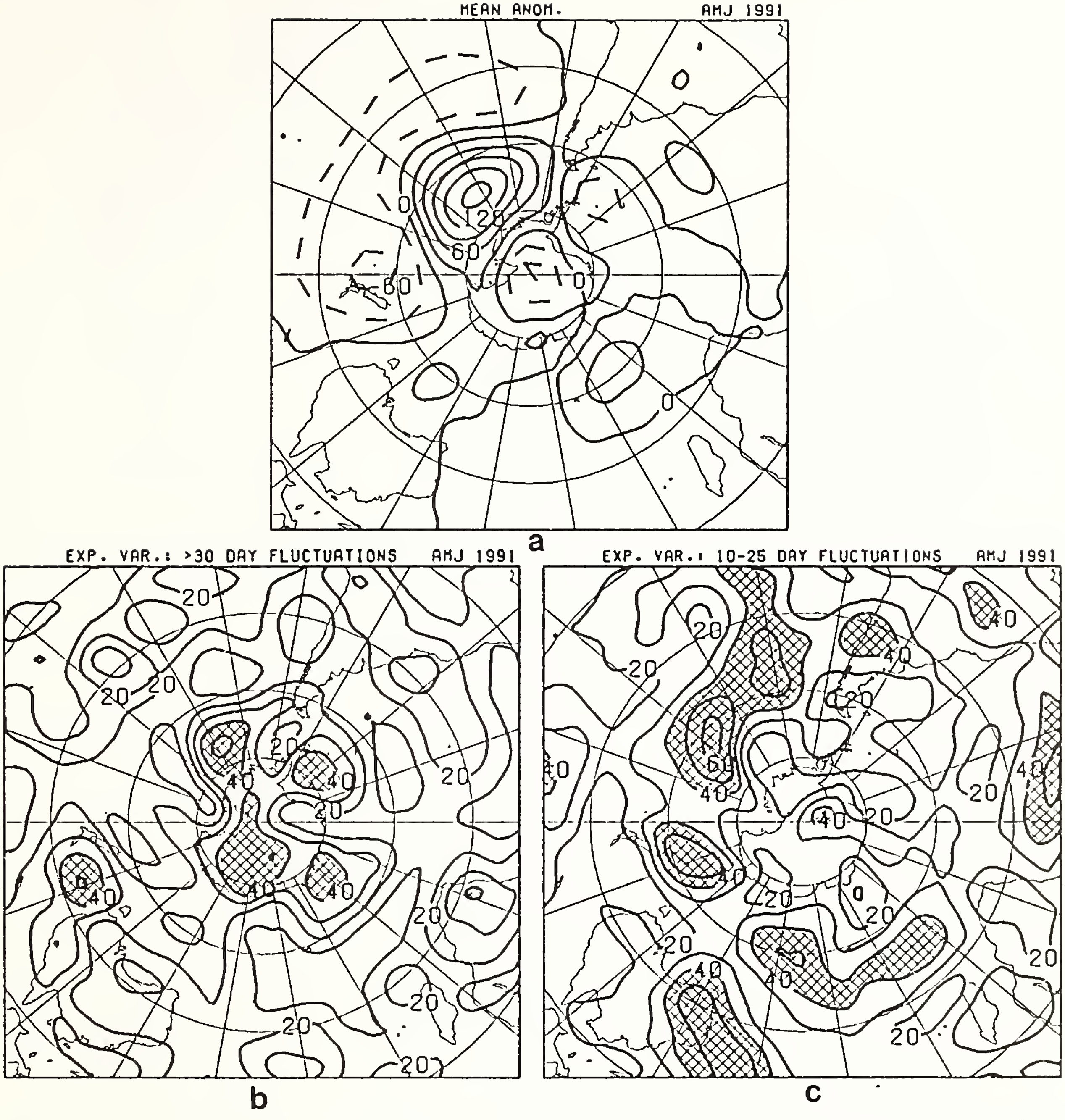
MEAN ANOM.
AMJ 1991
0
120
60
-60
0
0
a
EXP. VAR.: >30 DAY FLUCTUATIONS
AMJ 1991
20
40
b
EXP. VAR.: 10-25 DAY FLUCTUATIONS
AMJ 1991
20
40
60
c

Fig. 2. (a) Three-month mean 500 mb height anomaly during April-June 1991 (interval is 30 m). (b) Ratio of intermonthly height variance (periods greater than 30 days) to the total height variance. (c) Ratio of intra-monthly height variance (periods 10-25 days) to the total height variance. The period mean height is removed in all computations. Contour interval in (b) and (c) is 10 percent. Ratios larger than 40% are shaded.

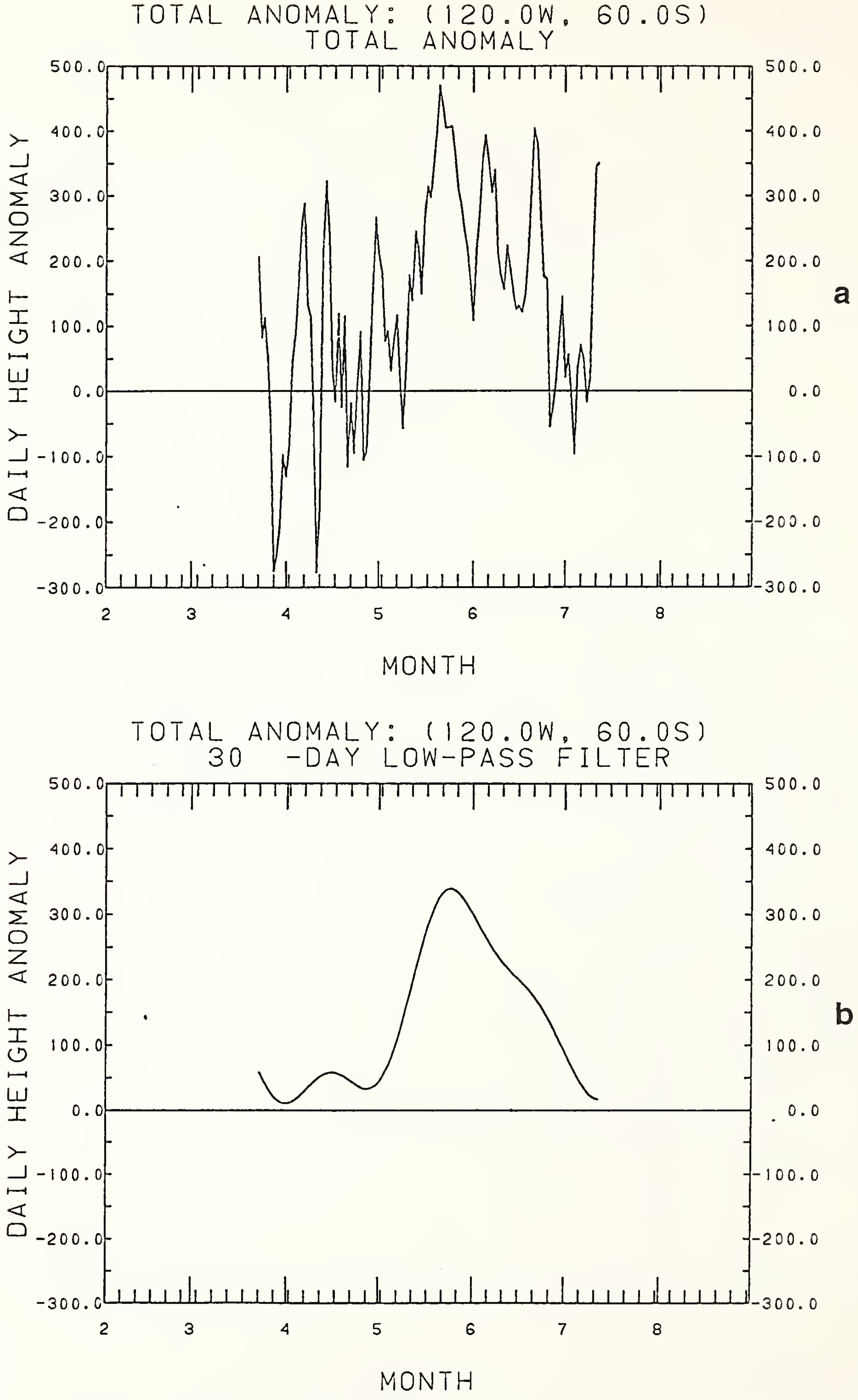

Fig. 3. Time series of daily (a) total height anomalies and (b) intermonthly (periods greater than 30 days) height anomalies during April-June 1991. Units of anomalies are meters.

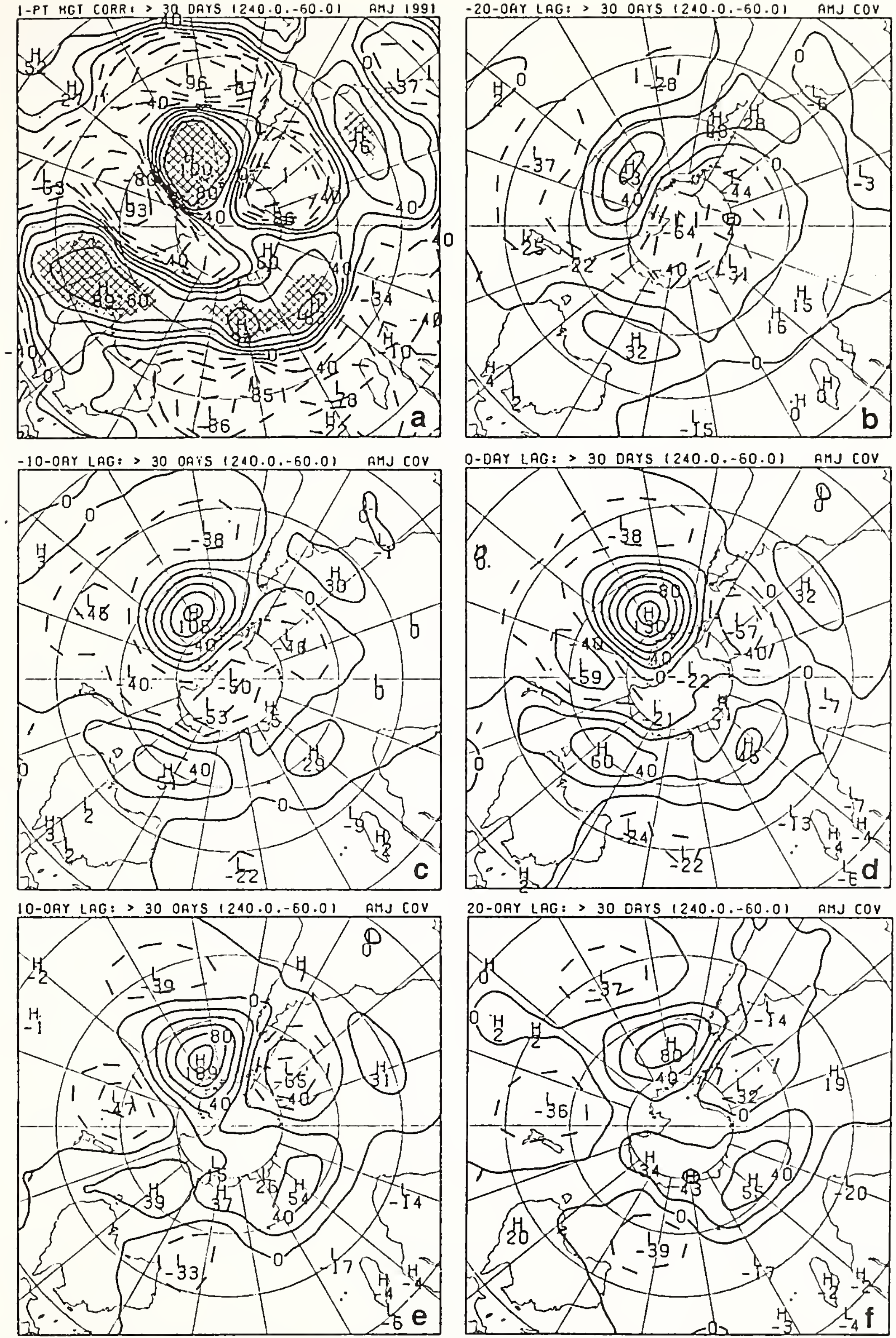
1-PT HGT CORR: > 30 DAYS (240.0,-60.0) AMJ 1991
-20-DAY LAG: > 30 DAYS (240.0,-60.0) AMJ COV
-10-DAY LAG: > 30 DAYS (240.0,-60.0) AMJ COV
0-DAY LAG: > 30 DAYS (240.0,-60.0) AMJ COV
10-DAY LAG: > 30 DAYS (240.0,-60.0) AMJ COV
20-DAY LAG: > 30 DAYS (240.0,-60.0) AMJ COV
a
b
c
d
e
f

Fig. 4. (a) One-point correlation map (periods greater than 30 days) centered on the mean block position (interval is 20, positive correlations greater than 75% are shaded). One-point normalized covariance analyses of intermonthly fluctuations (see text) centered on the mean block position for the following lags: (b) -20 d; (c) -10 d; (d) 0 d; (e) 10 d; and (f) 20 d. Contour interval is 20 m in panels (b)-(f).

# ESTABLISHMENT,MAINTENANCE AND BREAKDOWN OF A BLOCKING REGIME

Wilbur Chen
Climate Analysis Center
NMC/NWS/NOAA
Washington, DC 20233

## 1. Introduction

Atmospheric motions fluctuate with a wide range of temporal and spatial scales. The slowly varying large-scale flows can somtimes deviate greatly from the climatological means. Among the large weather anomalies, the middle latitude persistent blocking phenomenon is perhaps most striking. An abrupt transition from a quasi-stationary zonal flow regime to a prominent, 30 days long blocking flow was observed over the North Atlantic during November-December 1989. The breakdown of the blocking regime was also as swift as its onset. The mechanisms of regime transition and blocking maintenance were diagnosed by various techniques, with both Eulerian and Lagrangian viewpoints.

## 2. Description of regimes

On average, the 1989/90 northern winter does not deviate much from the climatological normal (not shown). However, a careful examination reveals a few drastic shifts of weather regimes within this season, resulting in tremendous changes in the regional, short-term climate. As shown in Fig. 1, a strong zonal flow is observed over the North Atlantic from November 1 to 11. It is followed by a prominant, 30 days long blocked regime. Another transition to an even stronger zonal flow is then observed. Each of these regimes displayed a very high degree of stability from day to day (not shown). An outstanding feature of this season is the very sudden transition between weather regimes. As shown in Fig.2, with the 540 and 570 dam contours, the flow over the North Atlantic was still very zonal on November 9. But, with only 3 days of transition, a clear ormaga blocking became firmly established. The breakdown of the blocking flow was as rapid as its establishment. As shown in Fig. 3, the 552 dam contours indicate blocking configuration for December 5, 6, and 7, while those of December 11, 12, and 13 show a very strong zonal flow over the North Atlantic. The transition, again, takes only 3 days to accomplish.

## 3. Upstream mean flow influence

The relationship of Atlantic blocking to time-mean flow over the Rockies was investigated first. In Fig. 4, we see similar anomalous flows over the Rockies (4a,4b), yet the flow configuration over the North Atlantic are entirely different. Similar disagreement can also be observed in Fig. 4c and 4d. On the other hand, Fig.4b and 4c show different anomalous flow over the Rockies, but, the same highly blocked flows over the North Atlantic. Therefore, the upstream mean flow resonant interaction with mountains does not seem to be the likely mechanism for the regime transitions observed in this case. This is in good agreement with earlier finding of Hoskins and Sardeshmukh (1987).

### 4. Transient Eddy forcing

Eddy covariance was then diagnosed to assess the transient eddy forcing of the time-mean flow. As shown in Fig. 5, the E-vectors of Hoskins et al.(1983) converge strongly into the blocked region and decelerate the westerlies there, signifying eddy feedback to help maintain the dipole blocking regime.

### 5. Transitions of regimes

During transition period, Lagrangian perspective with a daily sequence of isentropic potential vorticity (IPV) maps was diagnosed. Hoskins et al. (1985) have discussed in detail the use and significance of IPV charts. In the absence of diabatic process, the potential vorticity is advected on isentropic surfaces. They use this conservation concept to illustrate the dynamics of several synoptic systems including the development of a characteristic Atlantic block. They point out that the essential ingredient of a blocking anticyclone is a large poleward excursion of low IPV air from the lower latitudes ahead of a slowly moving, meridionally elongated trough. Furhter discussions on block formation can also be found in Shutts (1986) and Hains and Marshall (1987).

Prior to establishment of blocking, the ambient flow field was found to be diffluent over the North Atlantic (Fig. 6). It helped stretch the embedded disturbances meridionally (Shutts' eddy straining mechanism, 1983), resulting in large amount of vorticity and temperature exchanges between the low and high latitudes, overturning the normal north-south IPV gradient and establishing the blocking configuration. Figure 7 shows the series of daily IPV charts for Nov 9 to 15. The contour interval is 1 PV unit. The region between 2 and 3 PV unit is hatched, representing the likely tropopause position. The region with value greater than 3 unit is shaded representing the likely region for stratospheric air. On November 10 and 11, the depression over the North Atlantic became more meridionally elongated. It brought southward a lot of high IPV air while helped, in the following few days, sweep up poleward a lot of low IPV air from the lower latitudes. Meanwhile, the depression over the eastern North America acted sequentially in a similar way. With excursions of IPV air, the depressions also brough about exchanges of temperature between the high and low latitudes (not shown). During the subsequent two days, the excursions became deeper and the high IPV air accompaning the southward moving depression was on the brink of being cutoff. On November 14, the cutoff was complete and two blubs of low IPV air joined togather to become a vast pool of low IPV air. On November 15, while the low IPV air occupied the blocked area, the high IPV air is clearly seen to occupy the region south of it.

The dynamical process this series of charts reveals emphasizes the interactions of the transient eddies with the time-mean flow. The transient eddies become meridionally elongated, assisted likely by the diffluent background flow, bring in large excursions of air between low and high latitudes, and result in reversing the normal north-south gradient of the IPV air distribution, and thus establish and maintain the dipole blocking configuration.

Prior to breakdown of the blocking regime, the diffluence in the ambient flow field diminished dramatically (Fig. 8). Instead of being stretched meridionally, a depression became longitudinally elongated (Fig. 9). It pierced through the blocked region with high IPV air and prevented low IPV air from being swept to the blocked region. Without replenishment of new low IPV air, the old low IPV air in the blocked area gradually dissipated and the block disappeared accordingly. In this case, a new regime with a very strong quasi-stationary zonal flow became firmly established.

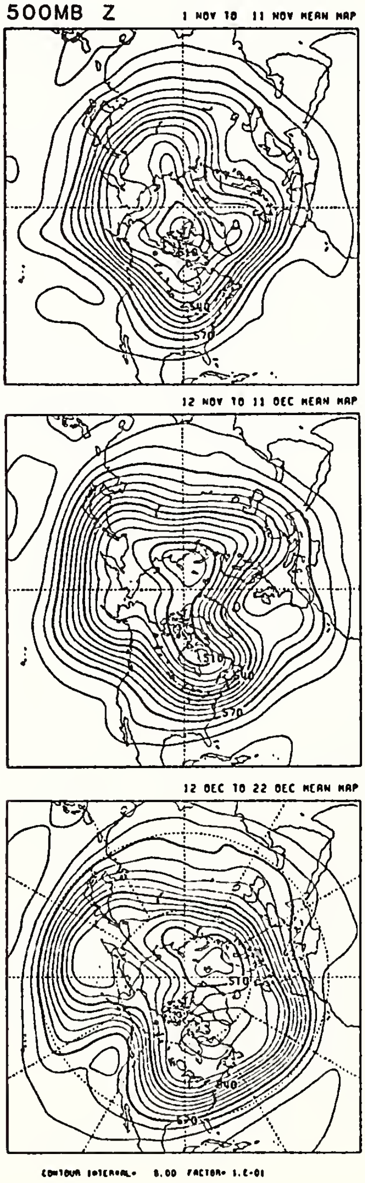
500MB Z
1 NOV TO 11 NOV MEAN MAP
510
540
570
12 NOV TO 11 DEC MEAN MAP
510
540
570
12 DEC TO 22 DEC MEAN MAP
510
540
570
CONTOUR INTERVAL= 6.00 FACTOR= 1.E-01

**Fig.1.** Mean 500mb geopotential height contours for period prior to (a), during (b), and after (c) the blocking circulation regime. Contour interval is 6 dam.

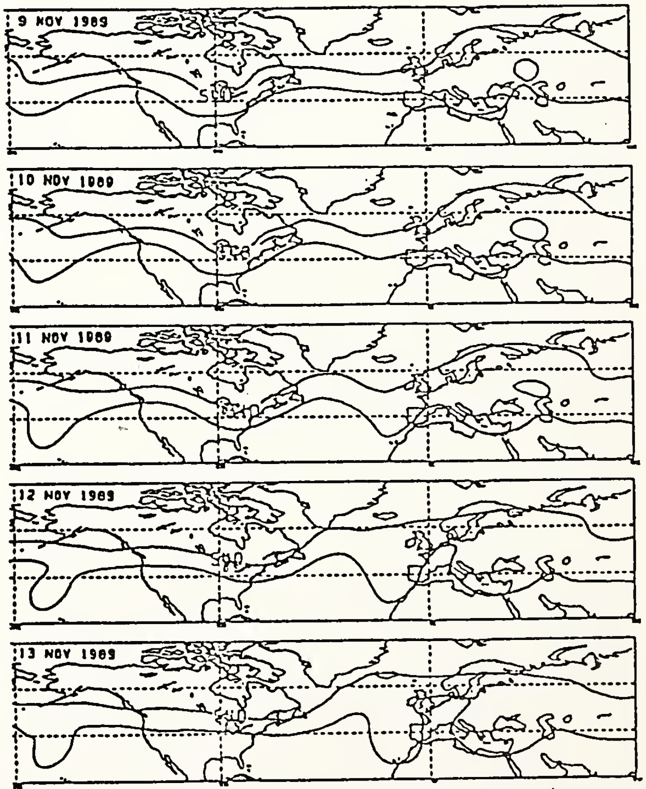

Fig.2. 540 and 570 dam Z contours at 500mb. A three-day running mean filtering has been applied to each contour.

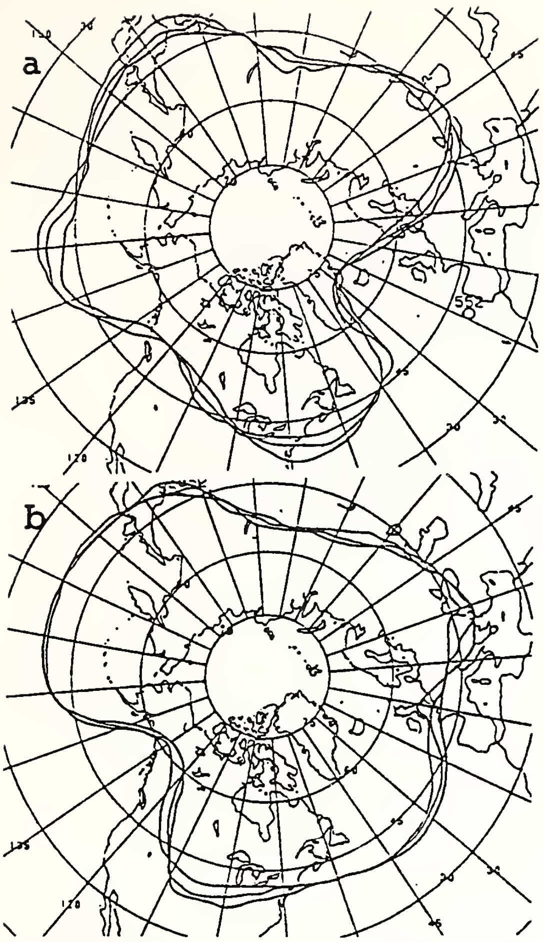

Fig.3. Daily 500mb 552 dam Z contours for December 5-7 (a), and December 11-13 (b). A three-day running mean filtering has been applied to each contour.

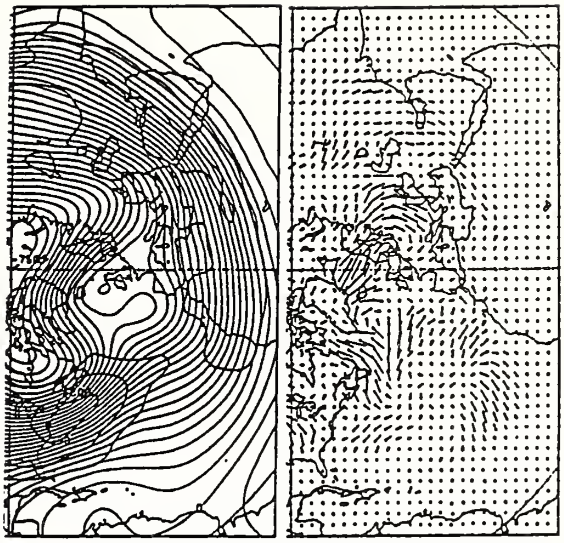

Fig.5. 250mb streamfunction and wind speed (darker contours that begin at 25 m and increase with interval of 10 m). Right-hand panel : the corresponding localized E-P flux pseudo vectors at 250mb level. The scaling vector is not shown.

Fig.4. 500mb Z anomalies for four consective periods. The anomaly contour interval is 60 m. Positive anomalies above 120 m are shaded. Negative anomaly contour are dashed.

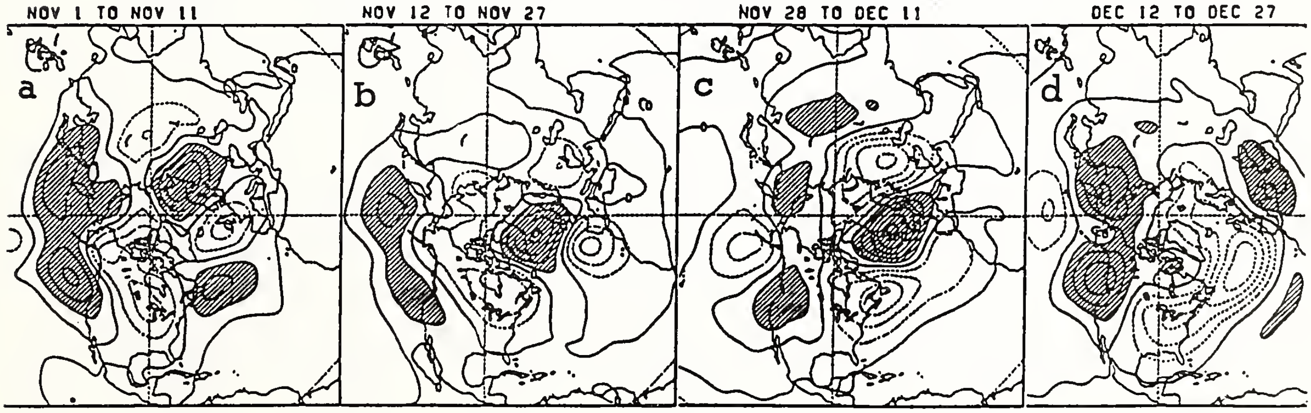

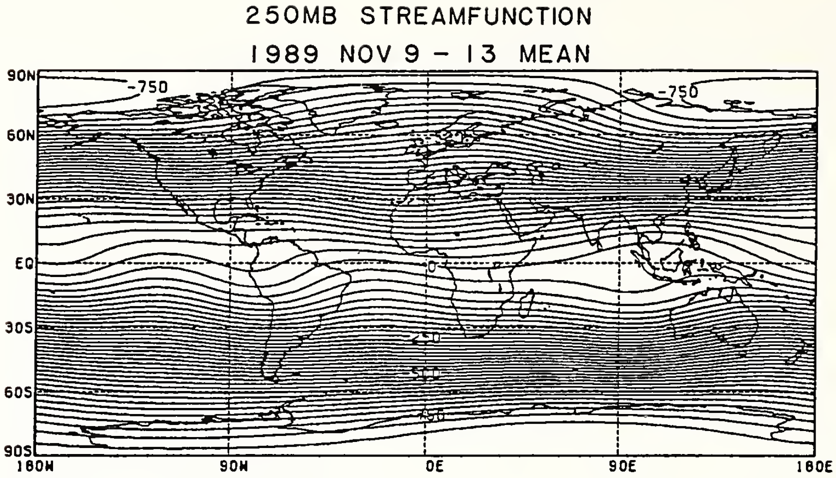

Fig.6. Spatially filtered large-scale streamfunction at 250mb, mean of November 9-13. Shown are those spherical harmonic components with two-dimentional wavenumbers less than 6. Contour intervals are 25xE-6 1/sec.

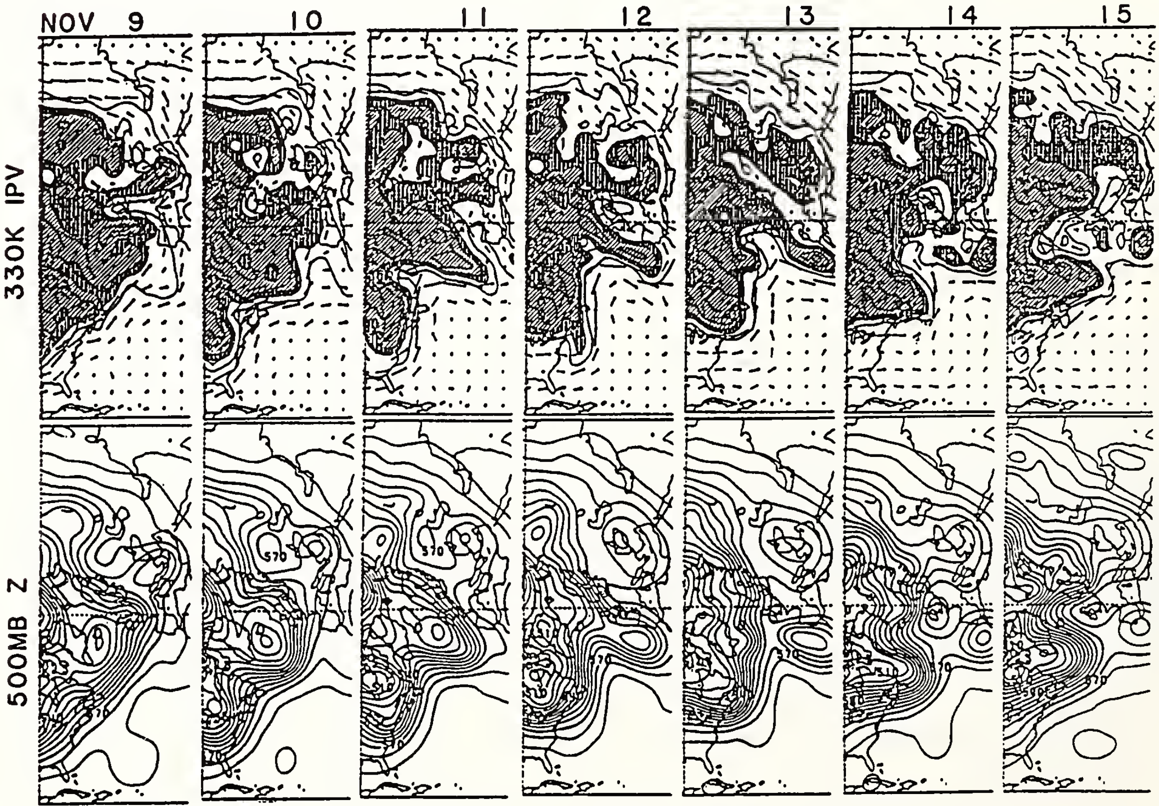

Fig.7. Series of daily charts of 330K IPV and 500mb Z in 1989.

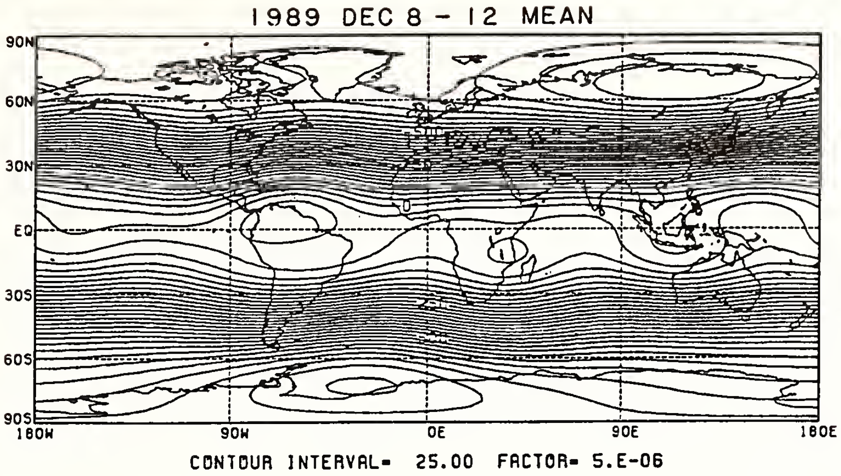

Fig.8. Same as figure 6 except for December 8-12.

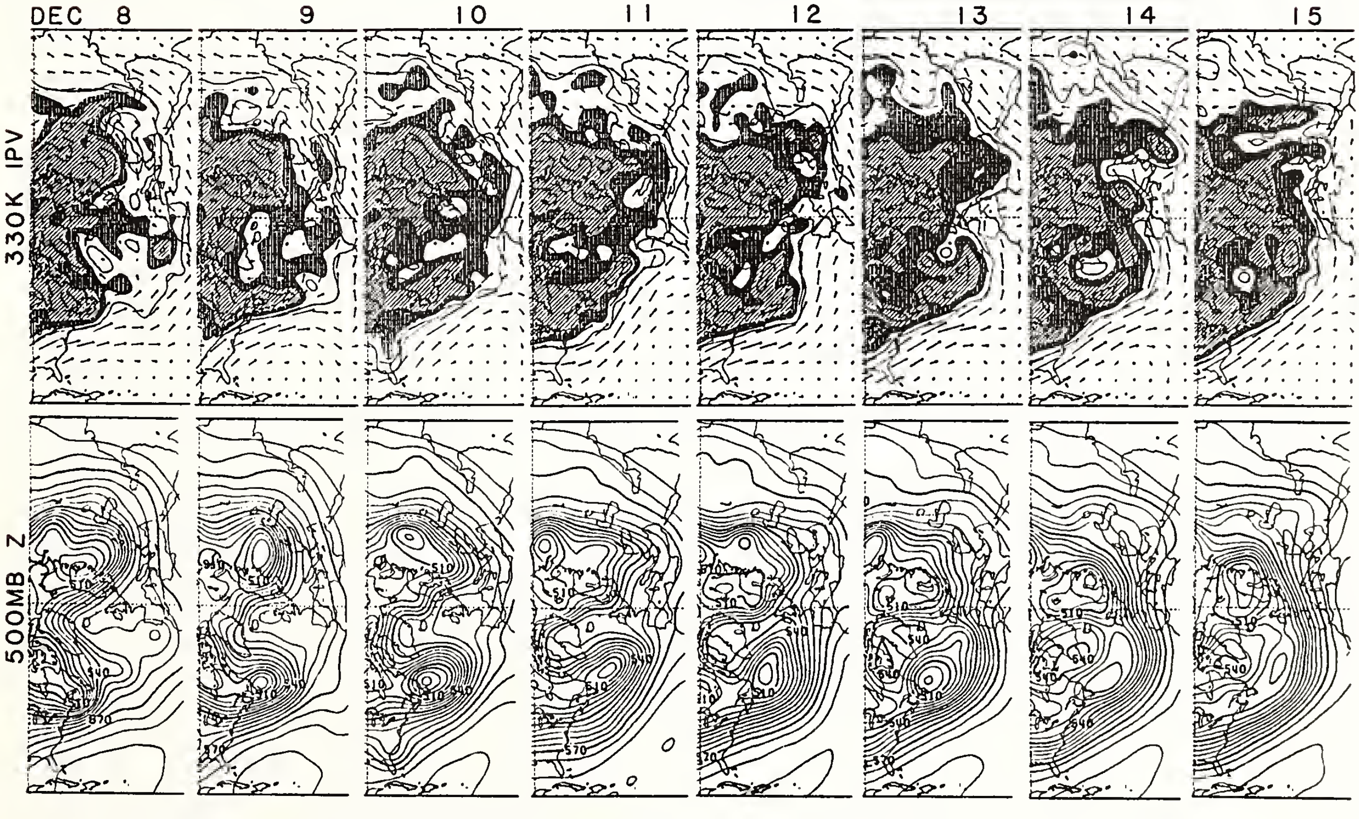

Fig.9. Same as figure 7 except for period December 8-15, 1989.

# SENSITIVITY OF UCLA ATMOSPHERIC GENERAL CIRCULATION MODEL SIMULATIONS TO DIFFERENT GLOBAL SEA SURFACE TEMPERATURE DISTRIBUTIONS

Tomoaki Ose[1], Carlos R. Mechoso[1] and David Halpern[2]

[1] *Department of Atmospheric Sciences, University of California, Los Angeles*

[2] *Jet Propulsion Laboratory, California Institute of Technology, Pasadena*

## Introduction

Two non-identical observational datasets for monthly-mean SST are available starting 1979. One is COADS (Comprehensive Ocean-Atmosphere Data Set), which is derived from ship observations. Another is HIRS/MSU (High Resolution Infrared Sounder/ Microwave Sounding Unit) SST dataset, which is derived from NOAA operational satellite measurements. The question arises on how these differences affect our view of the current climate and the detection of climate change. In this paper, we address these questions by contrasting simulations performed with the UCLA atmospheric general circulation model (AGCM) using the COADS and HIRS/MSU SST datasets in the boundary conditions.

## Description of the AGCM experiments

We focus on January 1979 and compare ensembles of UCLA AGCM simulations in the perpetual-January mode using HIRS/MSU and COADS SST distributions. In addition, we consider three SST distributions consisting of COADS for January 1979 in selected regions, and of climatology elsewhere. This is done to analyze similarities and differences between the atmospheric response to regional and global SST anomalies.

We use the 9-layer, 5º long by 4º lat version of the AGCM. Each ensemble of simulations consists of five 30-day periods from 210-day integrations. The results are shown as anomalies, i.e. departures from those obtained with the climatological distribution of SST.

## HIRS and COADS

The departures from the January climatology of HIRS and COADS SST for January 1979 are shown in Figs.1 (a) and (b), respectively. In the Northern Hemisphere, there is pattern similarity between Figs.1 (a) and (b). Except for the extratropics of the Northern Hemisphere, COADS anomalies are very small.

Figures.2 (a) and (b) show 500mb geopotential height anomalies obtained using COADS, and their statistical significance with t-value, respectively. Figs.3 (a) and (b) are those corresponding for HIRS. COADS SSTs produce highly significant geopotential height anomalies in the mid-latitudes of the Northern Hemisphere. The zonally-asymmetric structure of these anomalies is similar to the first EOF in the control simulation (see Fig.4a). We will show later that these atmospheric anomalies are explained mainly by the SST anomalies in the East Pacific.

HIRS SSTs produce different geopotential height anomalies in the mid-latitudes of the Northern Hemisphere than COADS SSTs. The zonally-asymmetric structure of the HIRS anomalies is similar to the second EOF in the control simulation (Fig.4b). In the Southern Hemisphere, HIRS SSTs produce more significant geopotential height anomalies than COADS SSTs.

### Regional SSTs from COADS

We study the atmospheric response to three regional SSTs anomalies, obtained from COADS (see Fig. 5). The corresponding experiments are called ATCOADS, EPCOADS and WPCOADS, respectively. ATCOADS shows a region of strong positive anomalies in geopotential height east of the SST anomalies (see Fig. 6). This pattern is similar to that obtained by Palmer and Sun (1985) with a region of warm SST anomalies confined to the North Atlantic. The geopotential height anomalies obtained in ATCOADS, however, do not resemble those obtained in COADS, even in the Atlantic basin.

The pattern of geopotential height anomalies obtained in both EPCOADS and WPCOADS (see Figs. 7 and 8, respectively) have many similarities with that obtained in COADS. Although SST anomalies in EPCOADS are weak compared with those in ATCOADS and WPCOADS, the atmospheric response in EPCOADS shows extended regions of strong anomalies with comparatively high statistical significance both in the mid-latitudes and in the tropics. The results of WPCOADS have small statistical significance in general.

### Summary

There are important differences between the atmospheric circulations simulated with the UCLA AGCM using the HIRS and COADS SSTs for January 1979. This result emphasizes the need for accurate global SST datasets in climate studies. The GCM response to SST anomalies seems to be connected with the modes of variability in the control simulation with the climatological distribution of SST. Regional and relatively weak SST anomalies (particularly those in the eastern Pacific) can have a global impact on the atmospheric circulation.

**Acknowledgments.** We are grateful to J.A.Spahr of UCLA and R.D.Haskins of NASA/JPL for programming assistance. This reserch was supported by NASA/JPL under Contract Number 958658.

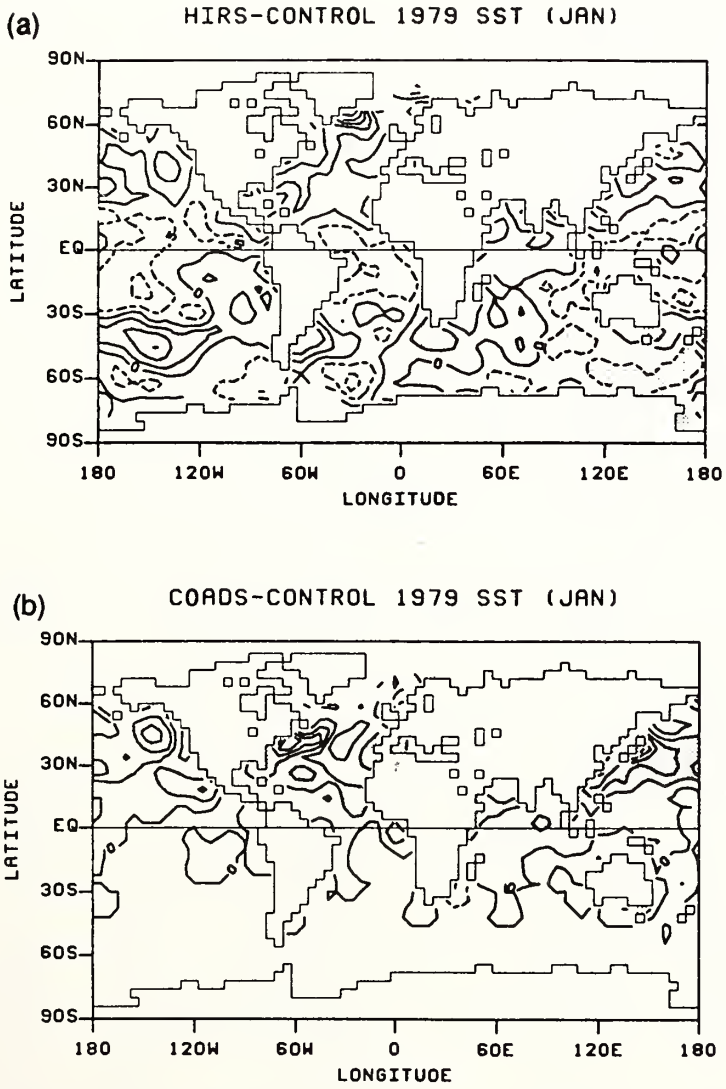

Fig.1. (a) HIRS SST anomalies, and (b) COADS SST anomalies. Contour interval is 0.5ºC.

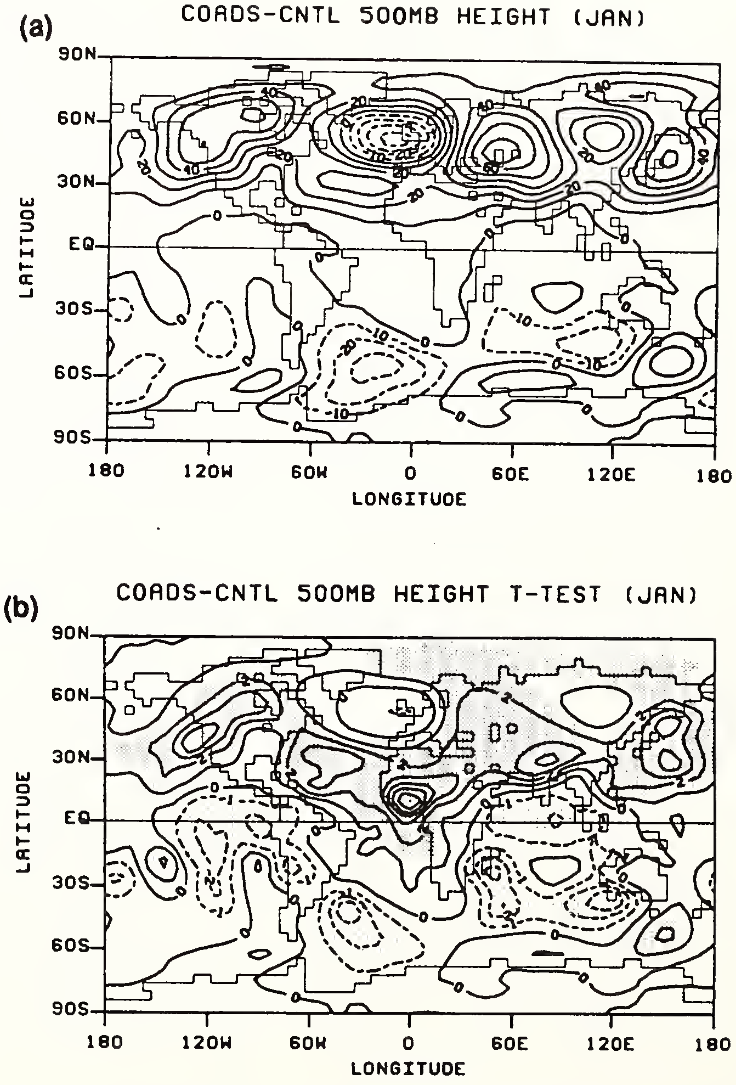

Fig.2. (a) Geopotential height anomalies at 500mb obtained in COADS. (b) t-statistics. The t-values for 80%, 90% and 95% significance are 1.40, 1.86 and 2.31, respectively.

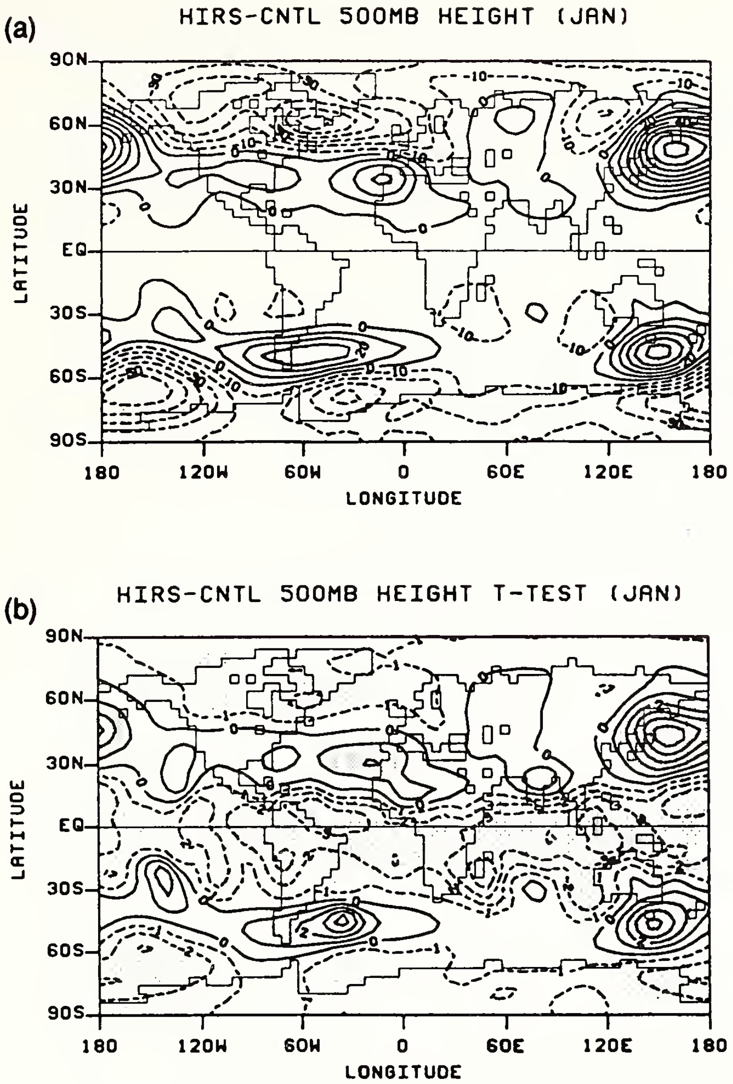

Fig.3. Same as in Fig.2 except for HIRS.

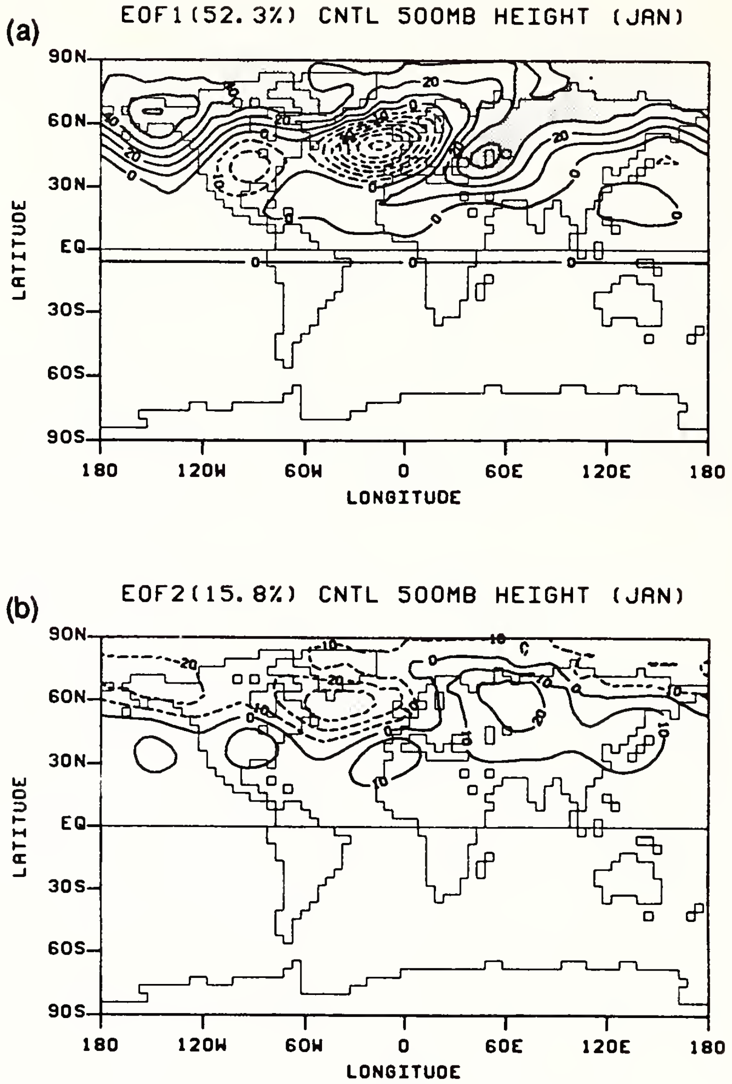
(a)
EOF1(52.3%) CNTL 500MB HEIGHT (JAN)
LATITUDE
LONGITUDE
90N
60N
30N
EQ
30S
60S
90S
180
120W
60W
0
60E
120E
180
(b)
EOF2(15.8%) CNTL 500MB HEIGHT (JAN)

Fig.4. (a) The first EOF of geopotential height at 500mb obtained from the control run. (b) The second EOF. Contour interval is 10m.

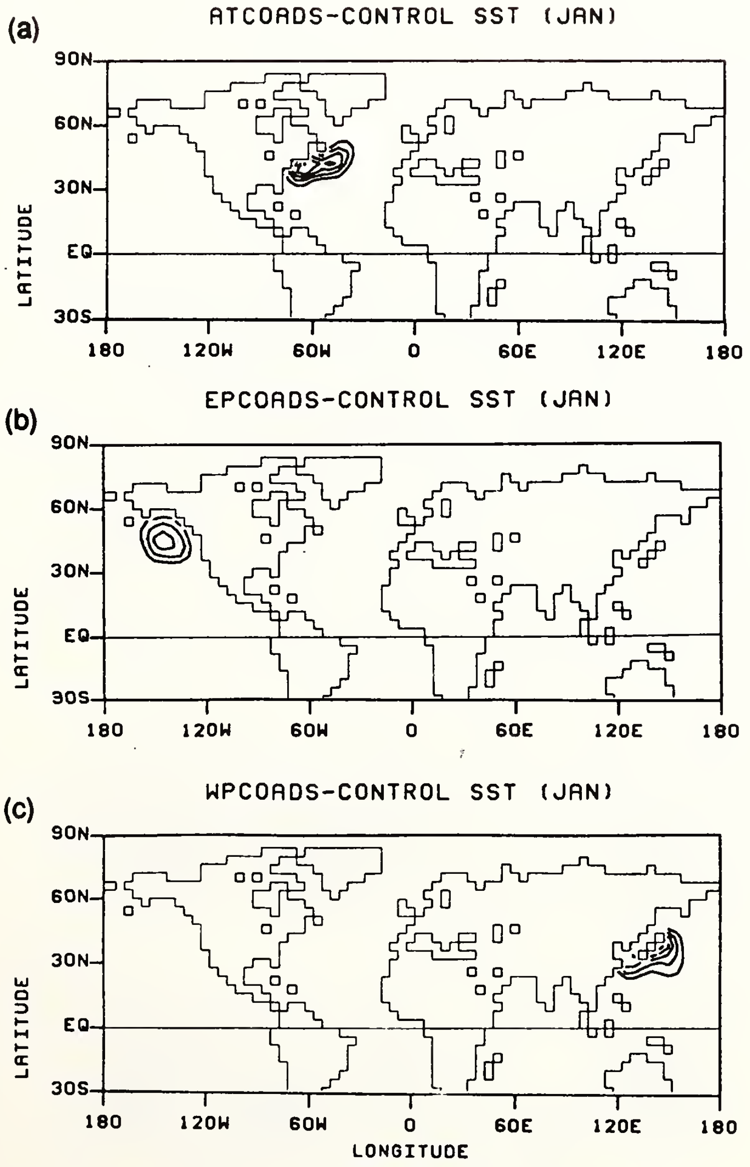
(a)
ATCOADS-CONTROL SST (JAN)
(b)
EPCOADS-CONTROL SST (JAN)
(c)
WPCOADS-CONTROL SST (JAN)
LATITUDE
90N
60N
30N
EQ
30S
LONGITUDE
180
120W
60W
0
60E
120E
180

Fig.5. Same as in Fig.1, except for (a) ATCOADS, (b) EPCOADS, and (c) WPCOADS.

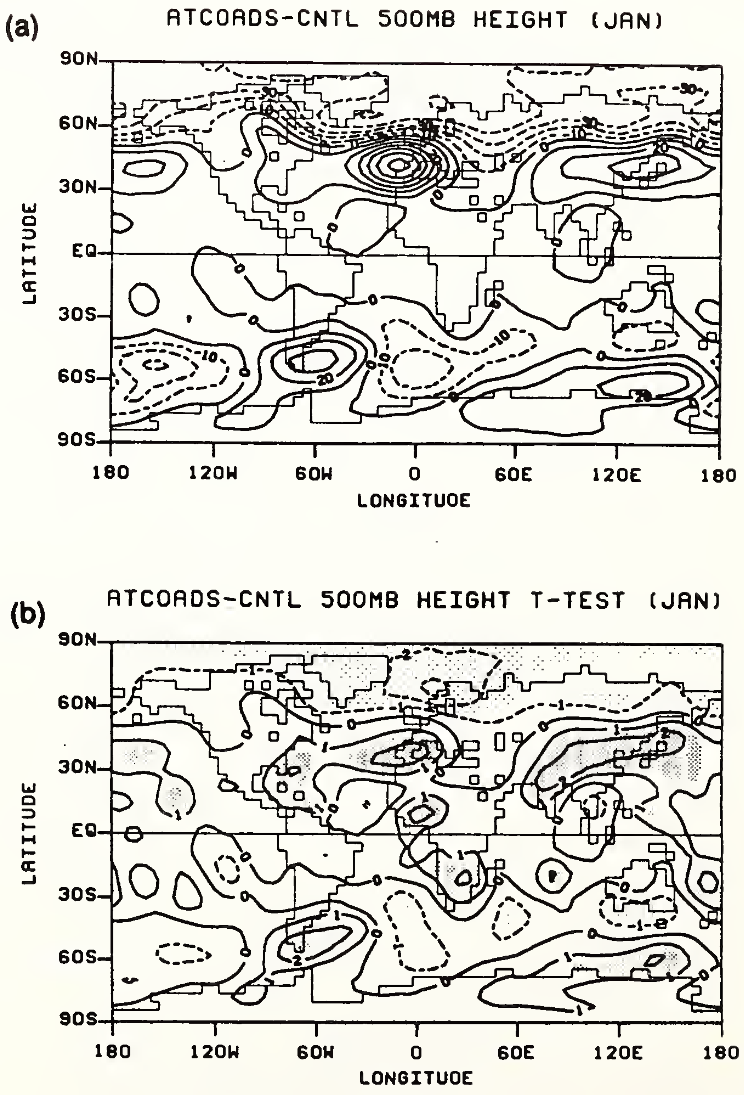

Fig.6. Same as in Fig.2, except for ATCOADS.

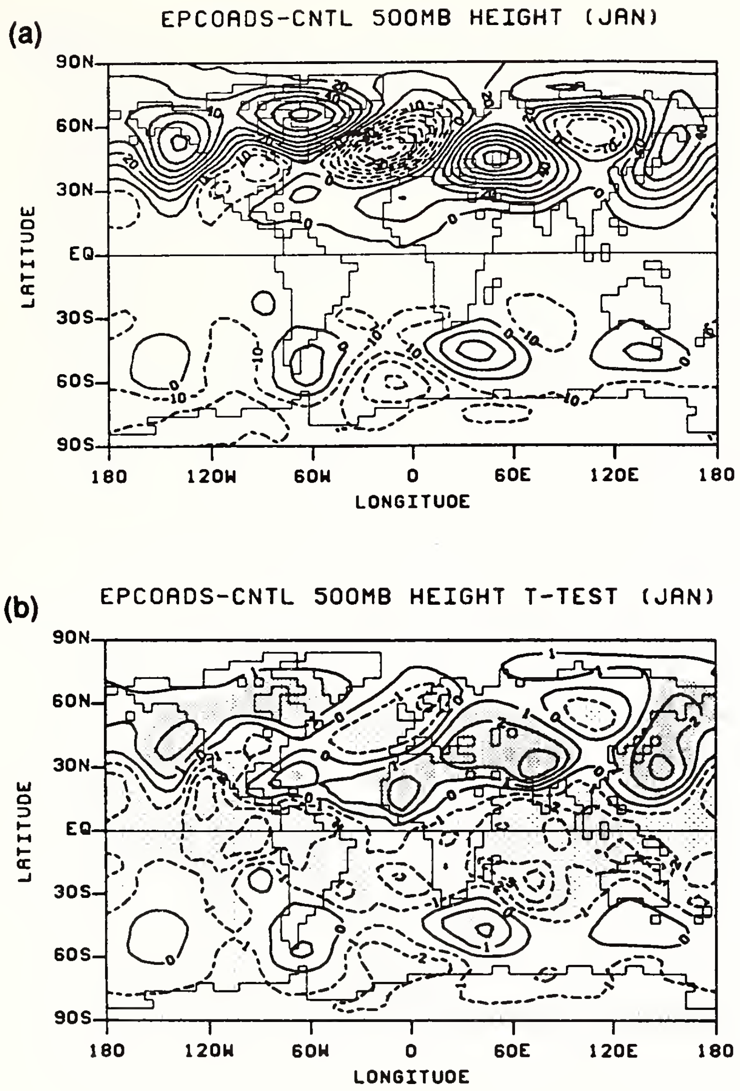
(a) EPCOADS-CNTL 500MB HEIGHT (JAN)

(b) EPCOADS-CNTL 500MB HEIGHT T-TEST (JAN)

Fig.7. Same as Fig.2, except for EPCOADS.

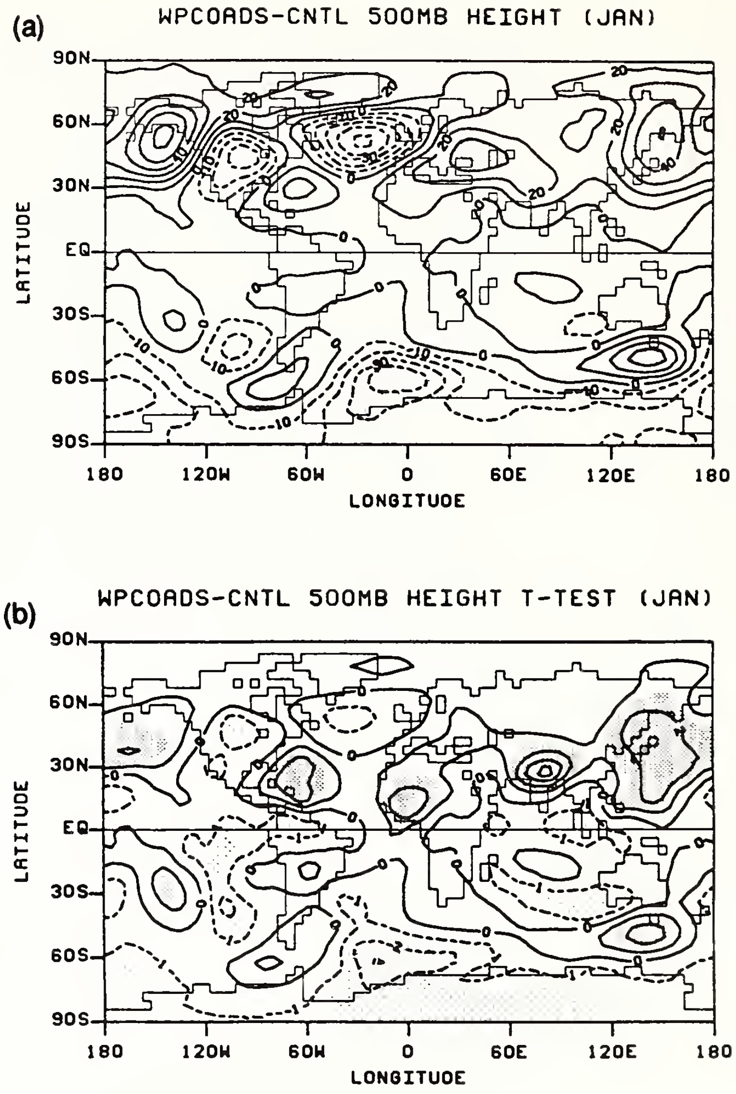
(a) WPCOADS-CNTL 500MB HEIGHT (JAN)

(b) WPCOADS-CNTL 500MB HEIGHT T-TEST (JAN)

Fig.8. Same as in Fig.2, except for WPCOADS.

# MODELING THE SEASONAL DEPENDENCE OF THE NORTHERN HEMISPHERE 40-DAY OSCILLATION

Christopher Strong, Feifei Jin and Michael Ghil
Department of Atmospheric Sciences, University of California
Los Angeles, CA 90024-1565

## 1. INTRODUCTION

During the last decade, considerable research has addressed low-frequency (LF) variability of the atmosphere, and in particular, the 30-60 day oscillation discovered by Madden and Julian (1971, 1972). Theoretical studies of the tropical intraseasonal oscillations have focused mainly upon the dynamical instability of coupled moist processes (Lau and Phillips, 1986). More limited attention has been focused on the 30-60 day oscillations occurring in the extratropics. Low-frequency oscillations with periods of 30-60 days have been identified in 700 mb geopotential height data over the Northern Hemisphere middle latitudes (Ghil and Mo, 1991a). These and other recent observations (Dickey *et al.*, 1991) reveal that LF oscillations in the intraseasonal band of the NH middle latitudes are quite robust. Though the low-frequency oscillations are not as apparent in the Southern Hemisphere extratropics, they still exist (Ghil and Mo, 1991b; Dickey *et al.*, 1991). The significance of the extratropical intraseasonal oscillations, and the impact of extratropical circulations on the tropics, or vice-versa, imply that the dynamical origin of extratropical LF oscillations can be quite complex (Ferranti *et al.*, 1990; Magaña and Yanai, 1991). The possible contribution of a nonlinear instability to the interactions of nonzonal flow with topography has been emphasized by Ghil (1987). Legras and Ghil (1985), and Tribbia and Ghil (1990), suggest that topographic instability which leads to multiple equilibria in models such as Charney and DeVore (1979) could generate LF oscillations in the intraseasonal bands. Jin and Ghil (1990) more comprehensively illustrate the relevance of oscillatory topographic instability (OTI hereafter) in models of the Legras and Ghil type.

Recent observational studies indicate further that episodic intraseasonal oscillations in the NH extratropics are most likely to occur in and around the winter season (Knutson and Weickmann, 1987; Ghil and Mo, 1991a; Dickey *et al.*, 1991; Kimoto *et al.*, 1991). The relevance of OTI to the origin of low-frequency oscillations is further explored here with a model similar to Legras and Ghil (1985), with a more realistic configuration of forcing. The central focus of this study, however, is to study the role of the seasonal cycle in intraseasonal oscillations by prescribing an annual cycle in the forcing of the model. As an extension, an idealized tropical forcing related to the Madden-Julian oscillation is prescribed in the model to investigate its possible impact on the LF variability (LFV) of the NH extratropics and atmospheric angular momentum (AAM).

## 2. MODEL DESCRIPTION

### *a. Governing Equations*

The atmospheric model used in this study is one of equivalent-barotropic flow forced by a zonally-symmetric stress and dissipated by surface friction:

$$\frac{\partial}{\partial t}\left(\Delta - L_R^{-2}\right)\psi + J\left(\psi, \Delta\psi + f\left(1 + \frac{h}{H}\right)\right) = -\alpha\Delta\left(\psi^{*} - \psi\right) - \nu\Delta^{2}\psi. \qquad (1)$$

Here, $\psi$ is the streamfunction, $h$ is the topographic height and $H$ is the scale height of the atmosphere. A relaxation forcing is introduced into the right-hand side with a characteristic time scale $\alpha^{-1}$. The forcing streamfunction $\psi^*$ can be considered as a zonal flow driven directly by differential heating in an idealized purely zonal circulation. $L_R$ is the external Rossby radius. A very small viscous term, $\nu$, is also included. $\Delta$ is the horizontal Laplacian. The horizontal coordinates in the spherical model are the longitude $\lambda$ and the sine of latitude $\mu = \sin\theta$. The following scaling is incorporated:

$$\begin{array}{llll} h = Hh' & t = t'/\Omega & L_R = a\Gamma^{-1} & f = 2\Omega\mu \\ \alpha = \Omega\alpha' & \nu = \Omega a^2 \nu' & \psi = a^2\Omega\psi' & \psi^* = aU\psi^{*\prime}. \end{array} \tag{2}$$

Using (2) and dropping the primes, the nondimensional form of Eq. (1) can be written as

$$\frac{\partial}{\partial t}\left(\Delta - \Gamma^{-2}\right)\psi + J(\psi, \Delta\psi + 2\mu(1+h)) = -\alpha\Delta\left(\rho\psi^* - \psi\right) - \nu\Delta^2\psi. \tag{3}$$

Here the non-dimensional number $\rho = U/a\Omega$, analogous to a Rossby number in the real atmosphere, measures the intensity of the forcing. In our model, this number parameterizes the zonal thermal forcing, due to the variation with latitude of net radiative heating, and the zonally-averaged effects of baroclinic eddies. A conventional spherical spectral transform method is used in the discretization of Eq. (3), with T21 resolution.

### b. *Forcing*

In the case under consideration, real Northern Hemisphere topography is used, along with a shifting jet at 250 mb obtained from ECMWF climatology as zonal forcing. It peaks around 35°N in winter and around 50°N in summer,with the annual cycle being approximated by

$$\rho\psi^* = \rho_1\left[\left(1+\cos\left(\frac{2\pi day}{365}\right)\right)/2\right]\psi_w^* + \rho_2\left[\left(1-\cos\left(\frac{2\pi day}{365}\right)\right)/2\right]\psi_s^*. \tag{4}$$

Here, $\psi_w^*$ denotes the winter jet, forced at intensity $\rho_1$, while $\psi_s^*$ denotes the summer jet, forced at intensity $\rho_2$.

## 3. INTRASEASONAL OSCILLATIONS IN THE MODEL

A typical five-year nondimensionalized AAM time series from a 100-year run (Figure 1a) indicates well-known features of a seasonal cycle, with superimposed high-frequency events in the summers, and episodic, intraseasonal activity in the winters. Power spectrum analysis (Figure 1b) shows clearly the usual red-noise signature of a chaotic time series, but two peaks stand out in particular: the intraseasonal peak, centered around 35-38 days, and a second peak around 13 days.

Figure 2 shows clearly the physical nature of the model oscillation. By taking from the model simulation nine winters in which episodic intraseasonal oscillations were present, the particular episodes, each around 35-45 days, were broken down into four distinct regimes: **1.** Zonal regime, in which 30-80 day filtered AAM shows a relative maximum and d(AAM)/dt = 0; **2.** descending regime, in which the filtered AAM shows a maximum rate of decrease with respect to time; **3.** blocked regime, in which AAM has reached a relative minimum and d(AAM)/dt = 0; **4.** ascending regime, in which AAM shows a maximum rate of increase with respect to time. Composing nine events' worth of each of the four categories from nine winters yields the phases (i) - (iv) of the oscillation. The zonal and blocked regimes indicate a dominant wavenumber-one structure, and it is noted that little or no mountain torque fluctuations are present. The *du/dt* term from mountain torque is computed, and clearly meanders close to the zero line. Across the hemisphere, net cancellation of the small regional decelerations and accelerations occurs. However, in the descending and ascending regimes, it is clear that the $\psi$ -anomaly patterns have shifted mainly to either side of the Rocky Mountains and Himalayas, producing a strong mountain torque which tends to decelerate the atmosphere in the descending regime, and accelerate the atmosphere in the ascending regime. Here, a dominant wavenumber-two and wavenumber-three structure is present. The corresponding peaks associated with the torque appear clearly in the *du/dt* term, the peaks being well correlated with the greatest root-mean square NH topography shown in the dashed line. Finally, the composite exhibits a distinct standing pattern for the oscillation. The four stages illustrated in the figure bear considerable similarity to the composite patterns in 700 mb observed height anomalies associated with those modes dominated by intraseasonal standing components (Ghil and Mo, 1991a).

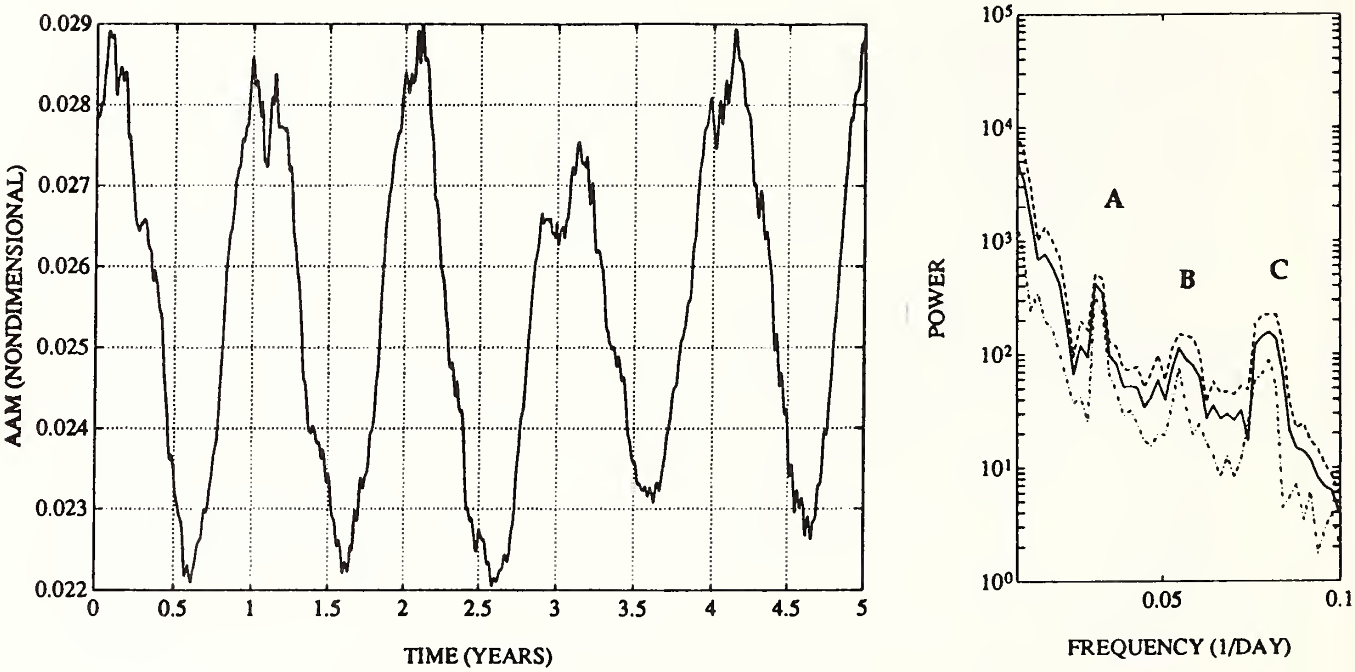

(a)

(b)

**Figure 1. (a) Five-year nondimensionalized AAM time series. (b) Power spectrum analysis of the AAM time series between 10 and 100 days. Peak A: 35-38 days; peak B: 16-19 days; peak C: 12-14 days.**

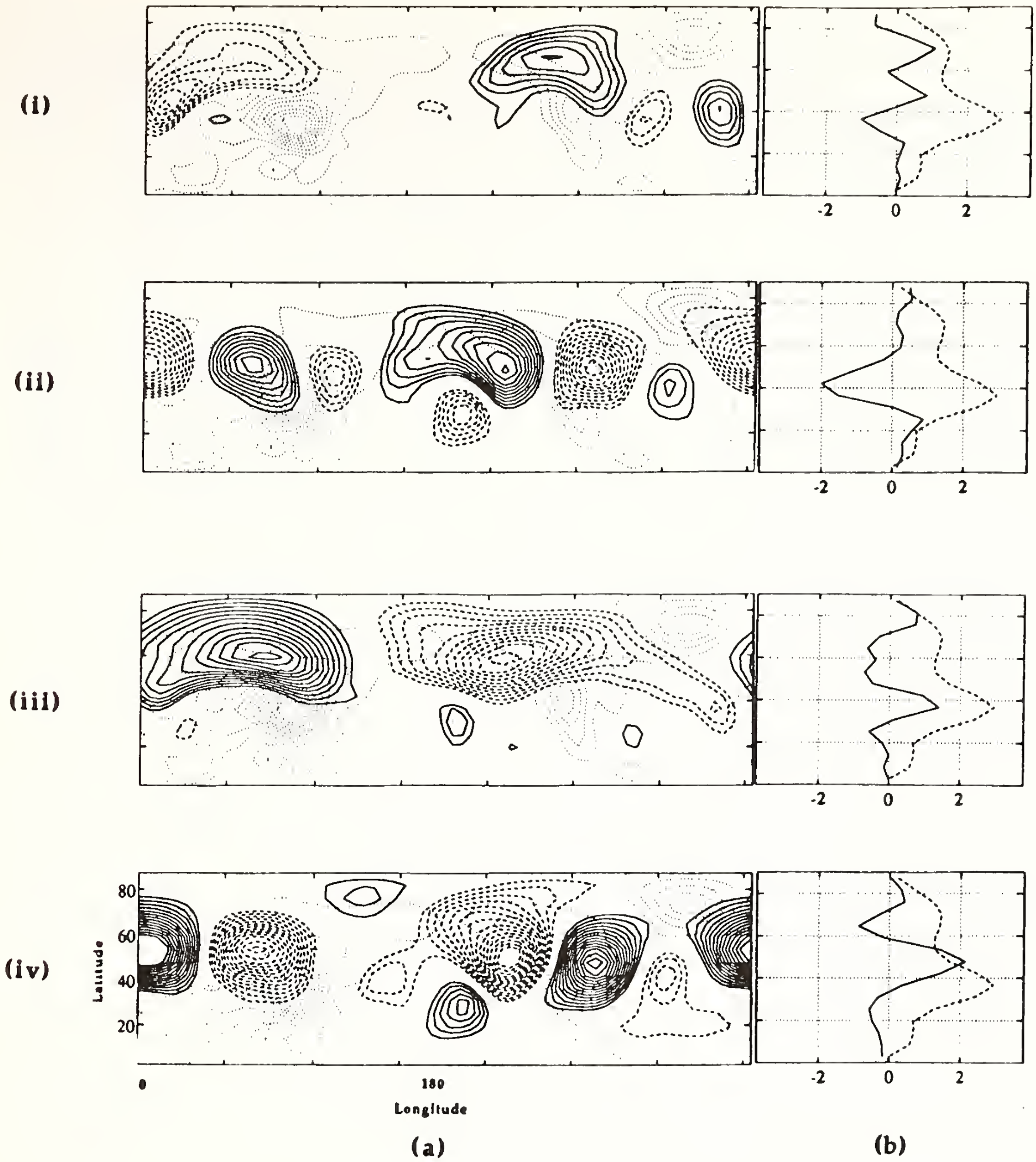

**Figure 2. (a) Nine-year composite: ψ-anomaly fields for four stages of characteristic winter episodes. Negative anomalies shown in dashed lines, real NH topography shown in dotted lines. (i) Zonal regime; (ii) descending regime; (iii) blocked regime; and (iv) ascending regime. Anomaly contour: $1*10^{-4}$ $m^2$ $s^{-1}$.**
**(b) Acceleration of zonal mean *u* (solid line), and RMS topography (dashed line). Units of abscissa: $10^{-6}$ m $s^{-2}$.**

## 4. EFFECTS OF TROPICAL FORCING RELATED TO MJO

The Madden-Julian oscillation (MJO) has long been recognized as a major source of intraseasonal variability over the tropics and has great influence on the circulations of the extratropics (Ferranti *et al.*, 1990). To study the possible impact of MJO in the context of our simple model, a vorticity source term is introduced to mimic the effects of divergence induced by convection around 300 mb. This source term $S$ is taken as

$$S = f_o D. \qquad (5)$$

Centering the vorticity source region between 70°E and 170°E, and ±10° latitude, the region was allowed to propagate eastward between the boundaries and change from upper-level convergence to upper-level divergence over a 40-day period. Equivalent-barotropic Rossby-wave propagation between the tropics and extratropics gives essentially a linear view of the linkage between oscillating phenomena in the tropics and middle latitudes (Sardeshmukh and Hoskins, 1988; Hoskins and Jin, 1991). One would expect, therefore, either constructive or destructive interference to occur with the oscillations induced by OTI over the NH extratropics.

Figure 3a displays the five-year AAM time series in which this tropical forcing has been switched on, using as initial conditions the last day's total streamfunction of Figure 1a. The time series again shows a clear tendency for an intraseasonal modulation of the winter seasons, and the corresponding power spectrum analysis of AAM, Figure 3b, indicates some interesting features. First, there has been a shift of the intraseasonal peak in Figure 1b from 35-38 days to a period ~ 40-43 days. Additionally, the power spectral density of the new intraseasonal peak has increased relative to the previous peak, indicating a more vigorous signal. A look at the dynamics of the winter composite shows a clear enhancement of the mountain torque accelerations/decelerations in the ascending/descending regimes of the model's oscillation. Therefore, this idealized tropical forcing related to the MJO has some constructive impact on the intraseasonal oscillations in the NH extratropics. Further study of the prescription of this tropical forcing in the model, as well as its impact, is under investigation.

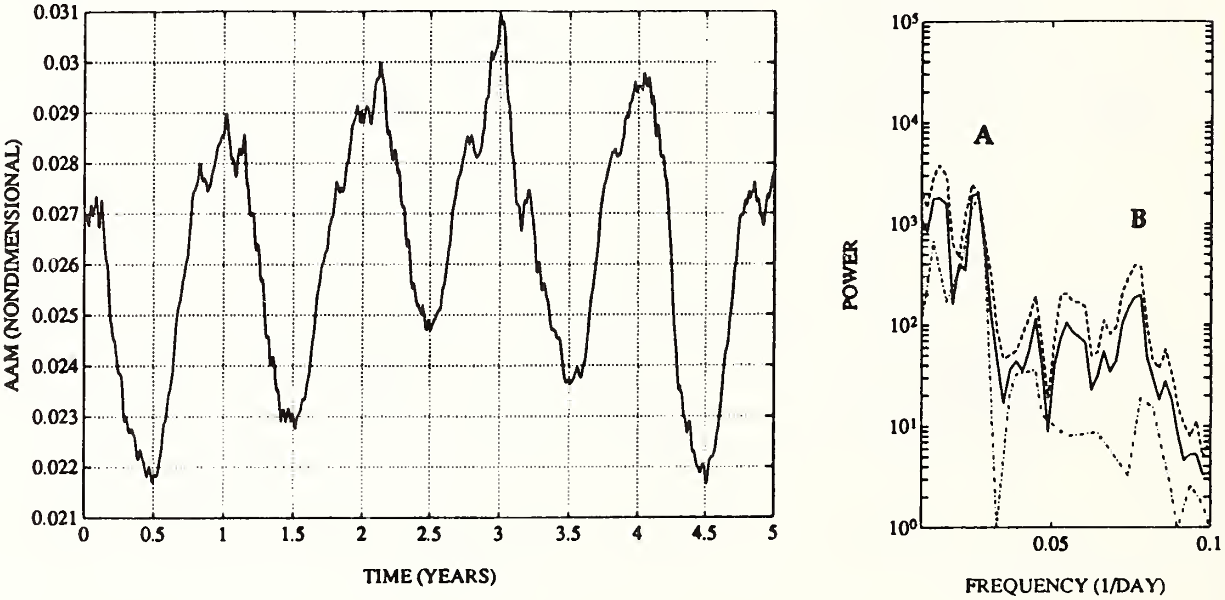

(a) (b)

**Figure 3. (a) Five-year nondimensionalized AAM time series, with MJO included in the model. (b) Power spectrum analysis of the AAM time series between 10 and 100 days. Peak A: 40-43 days; peak B: 12-14 days.**

## 5. CONCLUSIONS

In summary, the study of this barotropic model has led to the following results:

- Time-dependent solutions with seasonal forcing are still chaotic in structure.
- Episodic intraseasonal oscillations occur mainly in the winter, and are weaker in the summer.

- The dominant period associated with the oscillatory exchange of AAM with the solid earth via mountain torque is about 40 days.
- Spatially, the $\psi$ -anomaly patterns showed a clear standing nature.
- A clear association exists between mountain torque acceleration or deceleration and the stage of the oscillation.
- Idealized tropical forcing related to the Madden-Julian oscillation has some constructive impact on NH extratropical LFV.
- Oscillatory topographic instability is one important mechanism in initiating episodic intraseasonal oscillations in the NH middle latitudes.

**Acknowledgments.** This work has been triggered by conversations with Klaus Weickmann. It was supported by NSF grant ATM90-13217 and NASA grant NAG5-317.

## REFERENCES

1. Dickey, J.O., M. Ghil, and S.L. Marcus, 1991: Extratropical aspects of the 40-50 day oscillation in length-of-day and atmospheric angular momentum. *J. Geophys. Res.*, in press
2. Ferranti, L., T.N. Palmer, F. Molteni, and E. Klinker, 1990: Tropical-extratropical interaction associated with the 30-60 day oscillation and its impact on medium and extended range prediction. *J. Atmos. Sci.*, **47**, 2177-2199.
3. Ghil, M., 1987: Dynamics, statistics, and predictability of planetary flow regimes. *Irreversible Phenomena and Dynamical Systems Analysis in the Geosciences*, C. Nicolis and G.Nicolis, Eds., D.Reidel, 241-283.
4. Ghil, M. and K. Mo, 1991a: Intraseasonal oscillations in the global atmosphere. Part I: Northern hemisphere and tropics. *J. Atmos. Sci.*, **48**, 752-779.
5. Ghil, M. and K. Mo, 1991b: Intraseasonal oscillations in the global atmosphere. Part II: Southern Hemisphere. *J. Atmos. Sci.*, **48**, 780-790.
6. Hoskins, B.J., and F.-F. Jin, 1991: The initial value problem for tropical perturbations to a baroclinic atmosphere. *Quart. J. Roy. Meteor. Soc.*, **117**, 299-317
7. Jin, F.-F. and M. Ghil, 1990: Intraseasonal oscillations in the extratropics: Hopf bifurcations and topographic instabilities. *J. Atmos. Sci.*, **47**, 3007-3022.
8. Kimoto, M., M. Ghil, and K.-C. Mo: Spatial structure of the 40-day oscillation in the northern hemisphere extratropics. Eighth Conference on Atmospheric Waves and Stability, Denver, CO, Oct., 1991, pp. 115-116.
9. Knutson, T.R., and K.M. Weickmann, 1987: 30-60 day atmospheric oscillations: composite life cycles of convection and circulation anomalies. *Monthly Weather Review*, **115**, 1407-1436.
10. Lau, K.-M. and T.J. Phillips, 1986: Coherent fluctuations of extratropical geopotential height and tropical convection in intraseasonal time scales. *J. Atmos. Sci.*, **43**, 1164-1181.
11. Legras, B., and M. Ghil, 1985: Persistent anomalies, blocking and variations in atmospheric predictability. *J. Atmos. Sci.*, **42**, 433-471.
12. Madden, R.A., and P.R. Julian, 1971: Detection of a 40-50 day oscillation in the zonal wind of the Tropical Pacific. *J. Atmos. Sci.*, **28**, 702-708.
13. Madden, R.A., and P.R. Julian, 1972: Description of global-scale circulation cells in the tropics with a 40-50 day period. *J. Atmos. Sci.*, **29**, 1109-1123.
14. Magaña, V., and M. Yanai, 1991: Tropical-midlatitude interaction on the time scale of 30 to 60 days during the northern summer of 1979. *J. Climate*, **4**, 180-201.
15. Sardeshmukh, P.D., and B.J. Hoskins, 1988: The generation of global rotational flow by steady idealized tropical divergence. *J. Atmos. Sci.*, **45**, 1228-1251.
16. Tribbia, J.J., and M. Ghil, 1990: Forced zonal flow over topography and the 30-60 day oscillation in atmospheric angular momentum. NCAR Ms. 0501/89-5, 26 pp.

# Intraseasonal Oscillation and Response to Sea Surface Temperature Anomalies in a Linear Tropical Atmospheric Model

Jia-yuh Yu and J. David Neelin
Dept. Atmospheric Sciences, University of California
Los Angeles, CA 90024-1565

## 1. Intraseasonal oscillation

The tropical intraseasonal oscillation (or Madden-Julian oscillation), characterized by global-scale eastward propagation of zonal wind and convection, dominated by wavenumber 1, is the strongest intraseasonal signal found in the tropospheric atmosphere. A large number of studies have indicated that the mechanism responsible for the Madden-Julian oscillation (MJO) involves interaction between the large-scale circulation and cumulus convection. Kelvin wave-CISK was first suggested by Lindzen (1974) as a likely mechanism responsible for the MJO and numerous papers have followed this hypothesis. We use a simple linear primitive equation model with the Betts-Miller (1986) convective adjustment parameterization of sub-grid scale convective processes and analyze the convective-dynamical modes both analytically and numerically, with special emphasis on the intraseasonal mode. Using perturbation expansions in the small parameter $\tau_c$, the relaxation time scale of cumulus convection, analytical results show that a single vertical mode obeys special balances that allow slowly-propagating deep convection. For Kelvin-wave meridional structure, the zeroth order eigenvalue is

$$\lambda = -\frac{1}{2}(\epsilon_m + \frac{\epsilon^*}{A^*}) - iCk \tag{1}$$

where

$$C = \{\Delta M - \frac{1}{4k^2}(\epsilon_m - \frac{\epsilon^*}{A^*})^2\}^{1/2}$$

is the Kelvin wave phase speed and the minus sign before the imaginary part denotes eastward propagation. $\epsilon_m$ and $\epsilon^*$ are momentum and collective thermal damping coefficients respectively. $k$ is the zonal wavenumber and $A^*$ is an unitless constant determined by the mean thermodynamic basic state. $\Delta M$ corresponds to the gross moist static stability discussed by Neelin and Held (1987) which represents the net static stability, including moist effects, felt by this mode. It is given by lengthy integral expressions (not shown) involving the basic state static energy and moisture profiles and is positive for reasonable basic states. Thus this slow Kelvin mode is propagating as long as the gross moist stability term overcomes the damping effects. An estimate of $C$, using (10 days)$^{-1}$ damping coefficient and a typical observed tropical mean basic state, yields a period of about 37 days for wavenumber one. Figure 1 shows the vertical profiles of normalized pressure velocity, latent heating and moisture sink for this intraseasonal Kelvin mode. These are similar to the MJO structures appeared in many GCMs and observations. Equation (1) also shows that this intraseasonal mode is stable in the presence of friction and its decay rate is independent of wavenumber. The lack of scale dependence in the decay rate is due to the fact that our perturbation expansions only hold for sufficiently small wavenumbers.

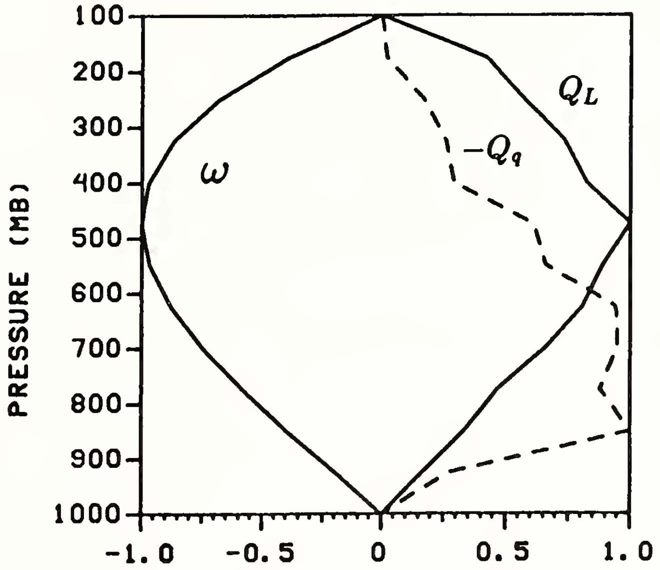

Figure 1: Vertical profiles of normalized pressure velocity ($\omega$), latent heating ($Q_L$) and moisture sink ($-Q_q$) for the intraseasonal Kelvin mode reconstructed from the analytical solution.

When the evaporation-wind feedback mechanism is added, the dispersion relation (1) becomes

$$\lambda = -\frac{1}{2}(\epsilon_m + \frac{\epsilon^*}{A^*}) + \frac{1}{\sqrt{2}} Ck\sqrt{(1 + F^{*2}C^{-4}k^{-2})^{1/2} - 1}$$

$$-i\frac{1}{\sqrt{2}} Ck\sqrt{(1 + F^{*2}C^{-4}k^{-2})^{1/2} + 1} \qquad (2)$$

where $F^*$ is the evaporation constant in units of Joul $\mathrm{kg}^{-1}\mathrm{m}^{-1}$. It is clearly seen from (2) that the eastward-moving Kelvin wave is destabilized by the inclusion of evaporation-wind feedback while the period decreases with increasing $F^*$. As noted in Neelin *et al.* (1987), the growth rate asymptotes to a constant value at large $k$

$$\lambda \rightarrow -\frac{1}{2}(\epsilon_m + \frac{\epsilon^*}{A^*}) \qquad (3)$$

so there is no strong scale selectivity in this dispersion relation, although at least it avoids selecting the smallest scales, as is common in CISK models.

Figure 2 shows the e-folding rate as function of wavenumber for this intraseasonal mode from numerical results for finite cumulus adjustment time, $\tau_c$ = 2 hours. Even though this mode is stable for all wavenumbers in the absence of evaporation-wind feedback, it does show that planetary-scale waves are decaying much slower than higher-wavenumber waves, giving strong scale selectivity. When the evaporation-wind feedback is included, within a reasonable range of magnitude, only planetary-scale (wavenumber 1 or 2) waves are selectively destabilized with e-folding times of O(10 days), which is consistent with observations.

The above properties concur with previous studies that the interaction of convection with large-scale dynamics can produce slowly propagating modes consistent with the MJO. However, they lead us to conclude that the CISK mechanism is unlikely to be responsible for destabilizing the MJO in general circulation models (GCMs) using convective adjustment and very possibly in the real atmosphere. It is more likely that large-scale disturbances are maintained by feedback mechanisms, such as the evaporation-wind feedback, that increase the enstropy of the boundary layer (or decrease the static stability of the troposphere) or are decaying modes stochastically forced from the extratropics or by convective "noise".

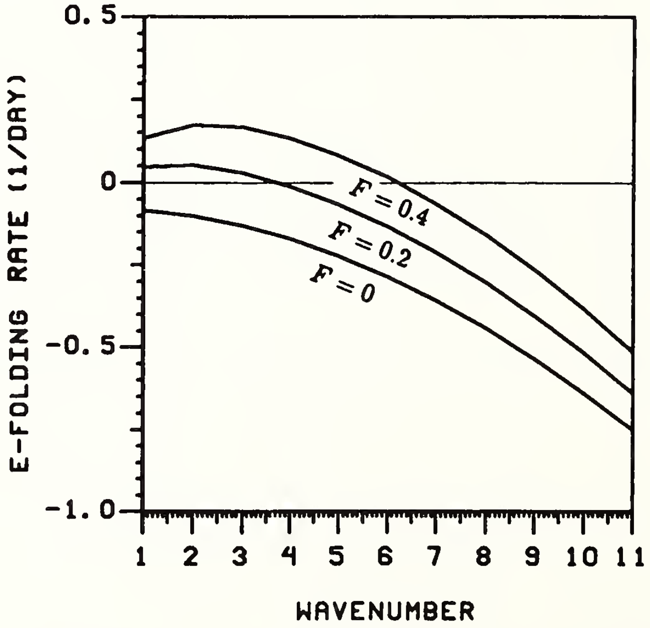

Figure 2: The e-folding rate of the intraseasonal mode as function of wavenumbers for different values of the evaporation constant. The unit of the evaporation constant ($F$) here is mm day$^{-1}$ (m/s)$^{-1}$ which has a slightly different definition than $F^*$ in equation (2).

## 2. Response to sea surface temperature anomalies

The fluctuations in the tropical atmosphere with planetary spatial scale and interannual time scale are undoubtedly highly correlated to sea surface temperature (SST) variations. The El Nino/Southern Oscillation (ENSO) is a typical example of the global-scale air-sea interaction involving warming of SST over the eastern Pacific Ocean. Understanding the physical mechanisms which control the response of the atmosphere to the lower boundary thermal forcing resulting from SST anomalies is useful because it can provide information about tropical variability which might lead to improvement of current AGCMs and atmosphere-ocean coupled models. By including SST anomalies in the evaporation and sensible heating terms in the boundary layer and dropping the time-dependent terms, we can use the same model to study the steady-state response of tropical atmosphere to SST forcing.

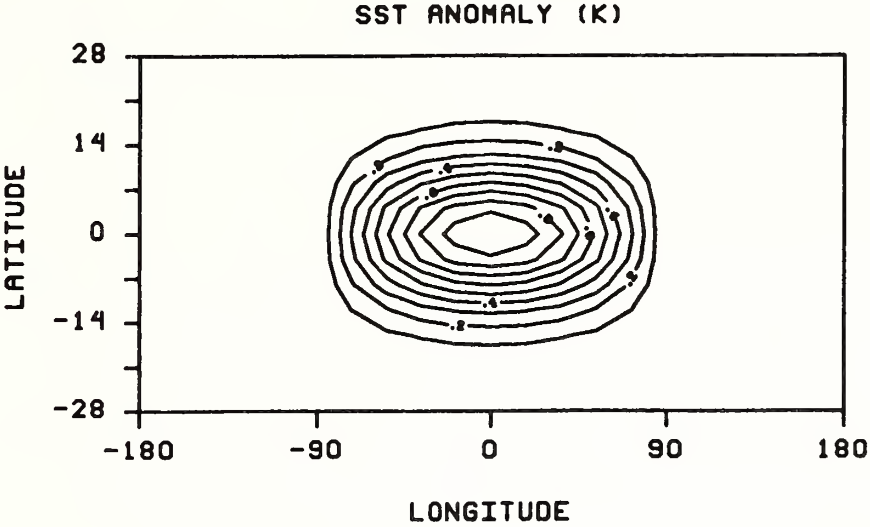

Figure 3: Idealized sea surface temperature anomaly used to forced the atmospheric model. The maximum amplitude is $1^0$ K located at the center of the domain.

Figure 3 is the idealized SST anomaly, with maximum amplitude of $1^0$ K in the domain center, used to forced the model. Figure 4 shows the atmospheric precipitation anomalies and low-level (962.5 mb) wind response. The upper panel of Fig. 4 is the case with both zonal and meridional momentum damping rates of $(1 \text{ day})^{-1}$. We find that the precipitation anomalies are almost in phase with the SST forcing, with maximum amplitude of about 2 mm $\text{day}^{-1}$. It is also noted that the precipitation response in the west is broader than that in the east and this zonal asymmetry is what one expects qualitatively from equatorial wave dynamics. Meanwhile, two negative anomalous precipitation centers are found in the subtropics which result from the downward branches of meridional cells similar to local Hadley cells in these regions. The low-level wind shows eastward-decaying, Kelvin-wave-like response to the east of the maximum heating center and strongly-damped, zonal-wind-dominated response to the west. Significant meridional wind response is also found in the region just poleward of the maximum heating.

The lower panel of Fig. 4 is the case with very small zonal momentum damping rate, $\epsilon_u = (100 \text{ days})^{-1}$. A significantly different but interesting feature is found in this case. The maximum precipitation anomaly (ITCZ) splits into two centers at $\pm 4^0$ latitudes and is no longer in phase with SST forcing. The amplitudes of the maximum precipitation anomalies are slightly higher than in the former case, about 2.5 mm day$^{-1}$, due to stronger moisture convergence in the boundary layer. Meanwhile, stronger negative precipitation anomalies are found in the west associated with weaker negative precipitation anomalies in the east, suggesting intensification of Walker circulations in this case. The low-level wind shows strong Kelvin-wave response to the east of the maximum heating and two Rossby-wave-like circulations to the west of heating. The split ITCZs are apparently associated with this intensified Rossby-wave-like response characterized by convergence/divergence maxima away from the equator.

While further analytical work is necessary to clarify the dynamics of this phenomenon, it is clear that split ITCZs *can* be produced under convective adjustment, contrary to examples currently available in the literature (Atusi and Hayashi, 1991; Hess *et al*, 1991), at least when zonally-asymmetric forcing is included.

## REFERENCES

Atusi N., and Y. Hayashi, 1991: Behaviors of the cumulus activity and the structures of the circulations in the "aqua planet" model. Part I. The structure of the super clusters. submitted to *J. Meteor. Soc. Japan.*

——, and ——, 1991: Behaviors of the cumulus activity and the structures of the circulations in the "aqua planet" model. Part II. Large scale structures and evaporation-wind feedback. submitted to *J. Meteor. Soc. Japan.*

Betts, A. K., 1986: A new convective adjustment scheme. Part I: Observational and theoretical basis. *Quart. J. Roy. Meteor. Soc.,* **112**, *677-691.*

—, and M. J. Miller, 1986: A new convective adjustment scheme. Part II: Single column tests using GATE wave, BOMEX, ATEX and artic air-mass data sets. *Quart. J. Roy. Meteor. Soc.,* **112**, *693-709.*

Hess, P. G., D. S. Battisti, and P. J. Rasch, 1991: The maintenance of the intertropical convergence zones and the large-scale tropical circulation on a water covered earth. *J. Atmos. Sci., accepted.*

Lindzen, R., 1974: Wave-CISK in the Tropics. *J. Atmos. Sci.,* **31**, *156-179.*

Neelin, J. D., I. M. Held, and K. H. Cook, 1987: Evaporation-wind feedback and low-frequency variability in the tropical atmosphere. *J. Atmos. Sci.,* **44**, *2341-2348.*

—, and I.M. Held, 1987: Modeling tropical convergence based on the moist static energy budget. *Mon. Wea. Rev.,* **115**, *3-12.*

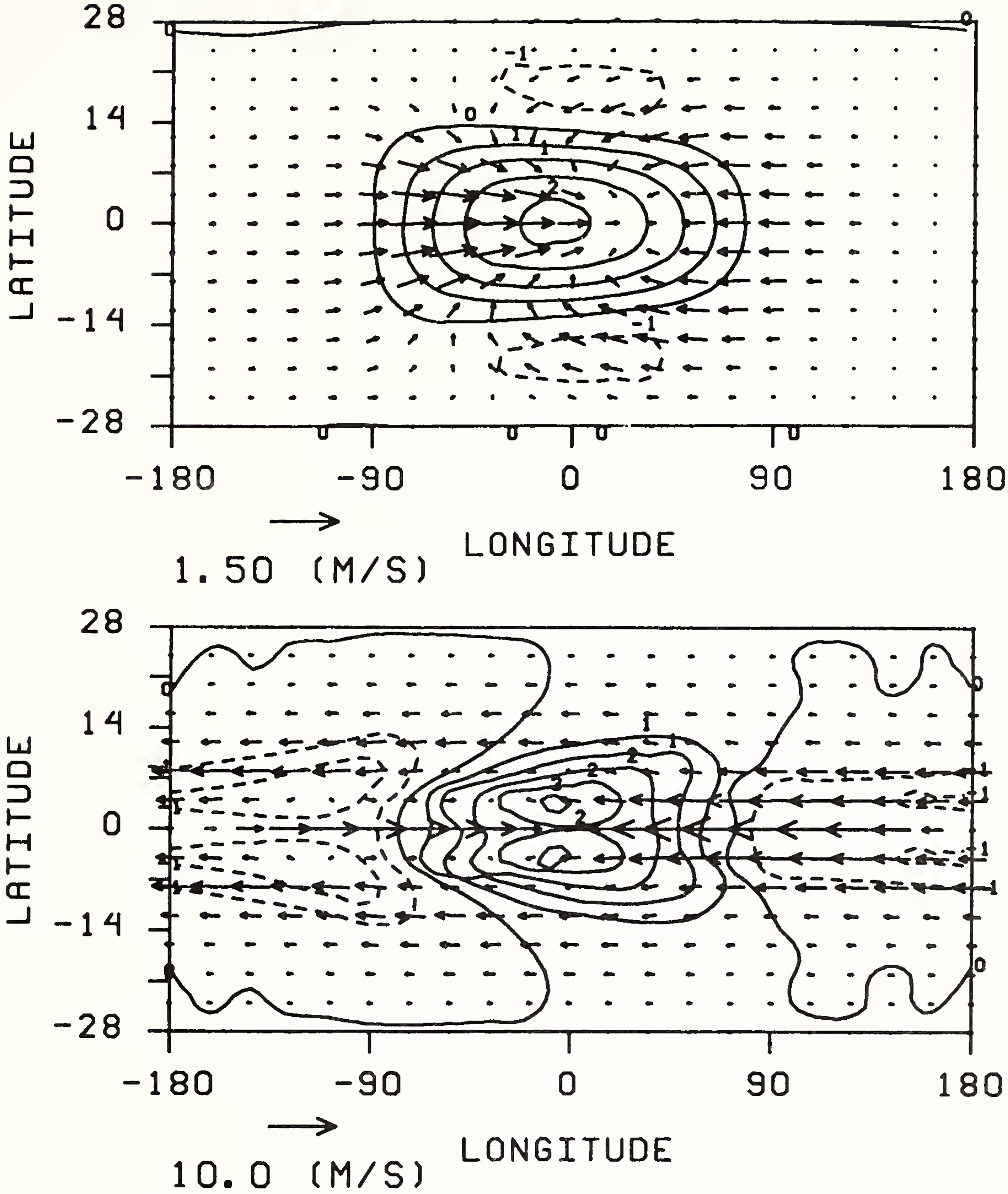

Figure 4: Atmospheric precipitation and low-level wind response. The upper panel is the case where both u-momentum damping coefficient ($\epsilon_u$) and v-momentum damping coefficient ($\epsilon_v$) are (1 day)$^{-1}$ and the lower panel shows the case of $\epsilon_u$ =(100 days)$^{-1}$ and $\epsilon_v$ =(10 days)$^{-1}$. The precipitation anomalies are shown by contours with solid (dashed) lines denoting positive (negative) anomalies. The contour interval is 0.5 mm/day in both cases. The arrows represent the low-level wind response at 962.5 mb.

# Upper Level Waves and Ozone Patterns During the 1986-1989 Austral Springs

J. Nogués-Paegle, K. C. Mo* and K. P. Callahan
Department of Meteorology, University of Utah
Salt Lake City, Utah 84112

*Climate Analysis Center, NMC/NOAA, Washington, D.C., 20233

This paper seeks to document the intrannual variability of planetary waves in the lower stratosphere of the Southern Hemisphere using height and ozone gridded fields for the years 1986 through 1989. Gridded NMC analysis and Nimbus 7 TOMS Grid-T Version 6 data for September 15 through December 15 for 1986, 87, 88 and 89 are used to quantify the relationships between these fields. The calibration method for the TOMS data is dicussed in McPeters et al. (1990). These four years include the anomalous circulations of the 1987 and 1988 austral springs, when the circumpolar vortex exhibits very late and early demises, respectively.

The large interannual variability of the four years chosen for study complicates interpretation of EOF patterns based on the four austral springs. Therefore, we opted to compute the EOF's for each year separately, and to use the resulting structures to describe the dominant patterns of horizontal variability for the different years. The horizontal domain extends from 30°S to 80°S for a 5°by 5°latitude-longitude grid. Covariances were area weighted. The EOF analysis is done on the anomalies (difference of daily values from the seasonal time average) for the total column ozone and the zonally asymmetric component of the height field. Certain pairs of EOF patterns are in quadrature with each other, representing oscillations.

The EOF analyses reveal three different pattern types. These, in general, describe the seasonal trend, a quasi-stationary or eastward propagating wavenumber 1 (period 30 to 45 days) and a fast moving wavenumber 2 pattern (period 10-20 days). The wave patterns maximize at about 60°S with meridional half wavelengths of 30°latitude. We focus here on the wavenumber one pattern which exhibits significantly different behaviour during years of strong and weak polar vortices. A more complete discussion which also includes other wavenumbers is given in Nogués-Paegle et al. (1992).

The dominant wavenumber one patterns are represented by the EOFs shown in Figs. 1 through 4 for the years 1986 through 1989. During 1986 (Fig. 1), both ozone and height patterns describe a traveling wave with a period of 36 days. This is apparent in the time series (Fig. 1e and f) that show the propagation of the two components of the wave pattern which are in quadrature with each other. The correlation coefficient between EOF 2 for ozone and EOF 1 for 50 mb heights is -0.81. Inspection of Fig. 1 a, c and g reveals that this negative correlation coefficient is due to air with low ozone values in troughs and high ozone values in ridges.

The year 1987 (Fig. 2) is quite different from the other four years. There is no well defined wavenumber 1 pattern among the first four leading EOF's for the height field. The largest wavenumber 1 components are found for the ozone EOF 2 and the 50 mb height EOF 1 (Fig. 2a and b).The correlation coefficient between the two principal components is .75, with the two time series mostly in phase (Fig. 2e).

EOFs for 1988 are shown in Fig. 3. The ozone field has more of a wavenumber 1 structure than the height field, but both principal components (PC) evolve approximately in phase during October and November. The time series reflect the prevailing quasi-stationary character of this pattern. The correlation coefficient between the ozone and height principal components is .8. The year 1989 exhibits the highest correlation coefficients between the ozone and 50 mb height patterns Those with dominant wavenumber 1 components are shown in Fig. 4. The correlation coefficients between the EOF 2/EOF 3 between ozone and 50 mb heights are . 93 and .84, respectively.

This study has shown that 50 mb height and ozone EOFs display, in general, similar patterns and are highly correlated. This implies that undulations of the 50 mb height fields mantain the integrity of the polar vortex, keeping air with low ozone content within the boundaries of the polar low. The wavenumber 1 patterns exhibit eastward propagation with periods of 30 days or longer (1986, 1989) or it is quasi-stationary (1988). This wave is very weak during 1987, a year with low ozone values which persisted into summer. The year 1987 was also characterized by an unusually strong polar vortex which persisted through spring.

### *Acknowledgements*

This investigation was supported by NASA grant NAG-527 to the University of Utah and by USAF/AWS support to K. Callahan. The ozone data was kindly provided by the Ozone Processing Team of NASA/Goddard Space Flight Center.

### *References*

McPeters, R.D., and the NASA Ozone Processing Team, 1990. Results of calibration of Nimbus 7 TOMS Ozone data using the pair justification technique. In Digest of topical meeting on optical remote sensing of the atmosphere., Vol 4. 413-416.

Nogués-Paegle,J., K. C. Mo and K. P. Callahan, 1992: Low stratosphere waves during the 1986-1989 austral springs. Submitted to Tellus.

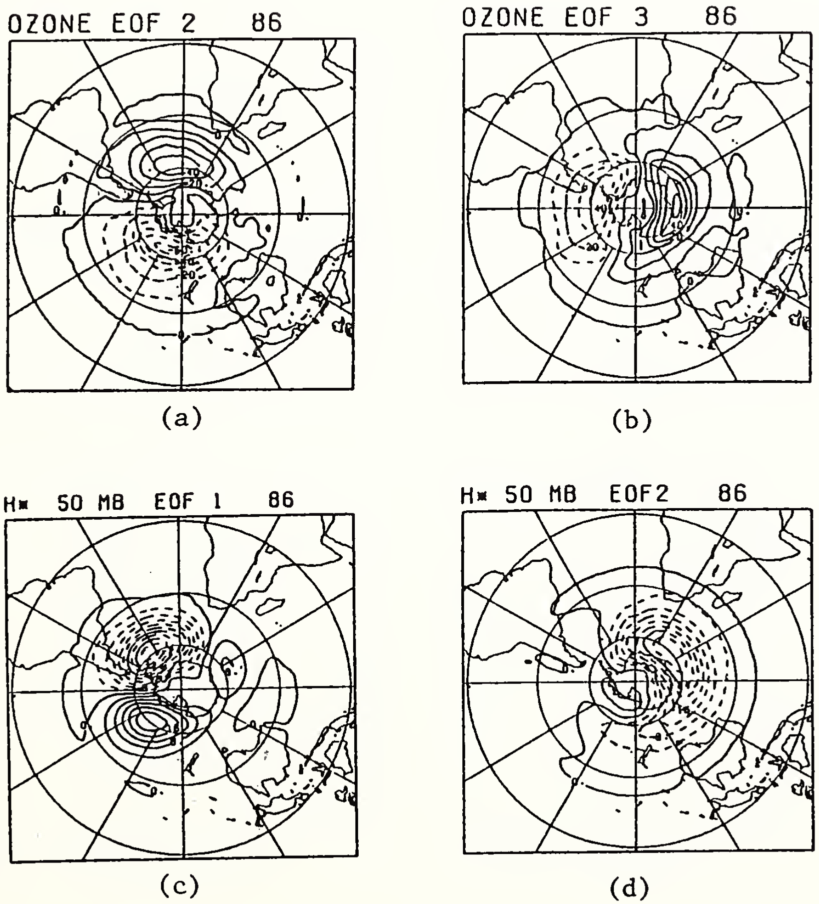

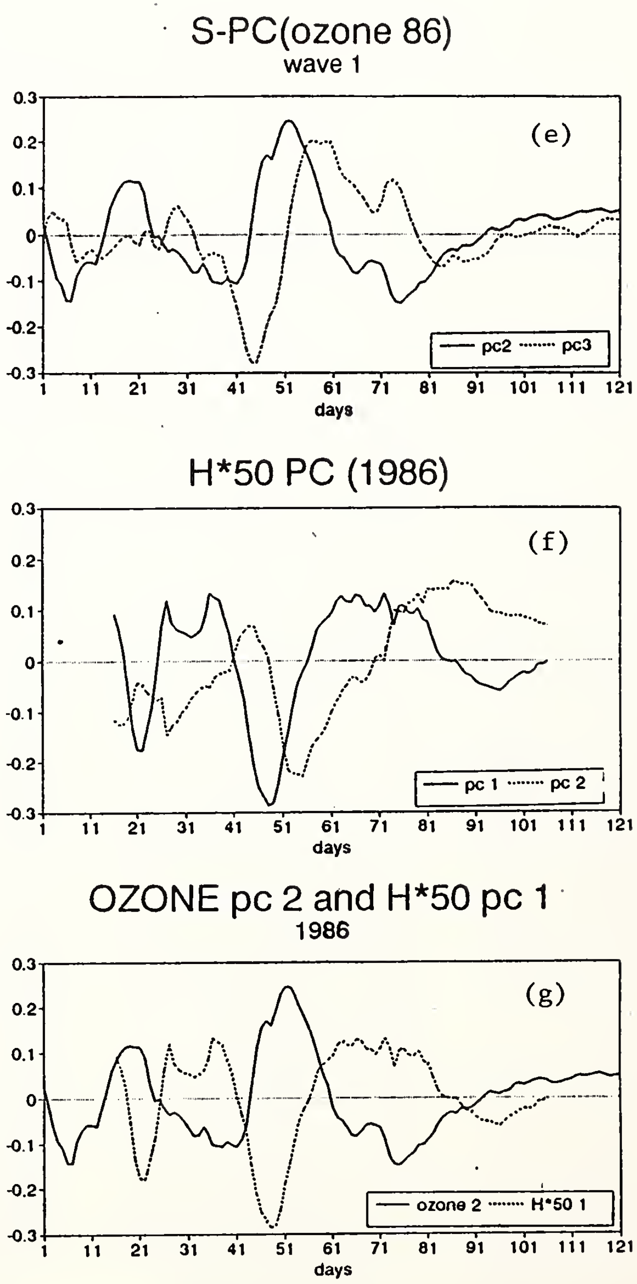

Fig. 1. Empirical orthogonal functions (EOF) as indicated in the figure, for 1986. These exhibit dominant wavenumber 1 patterns. The ozone EOFs are contoured every 100 DU. These represent 17.4% (a), 13.5% (b), 29.6% (c) and 26.7% (d) of the total variance. Time series of principal components are shown in (e), (f) and (g).

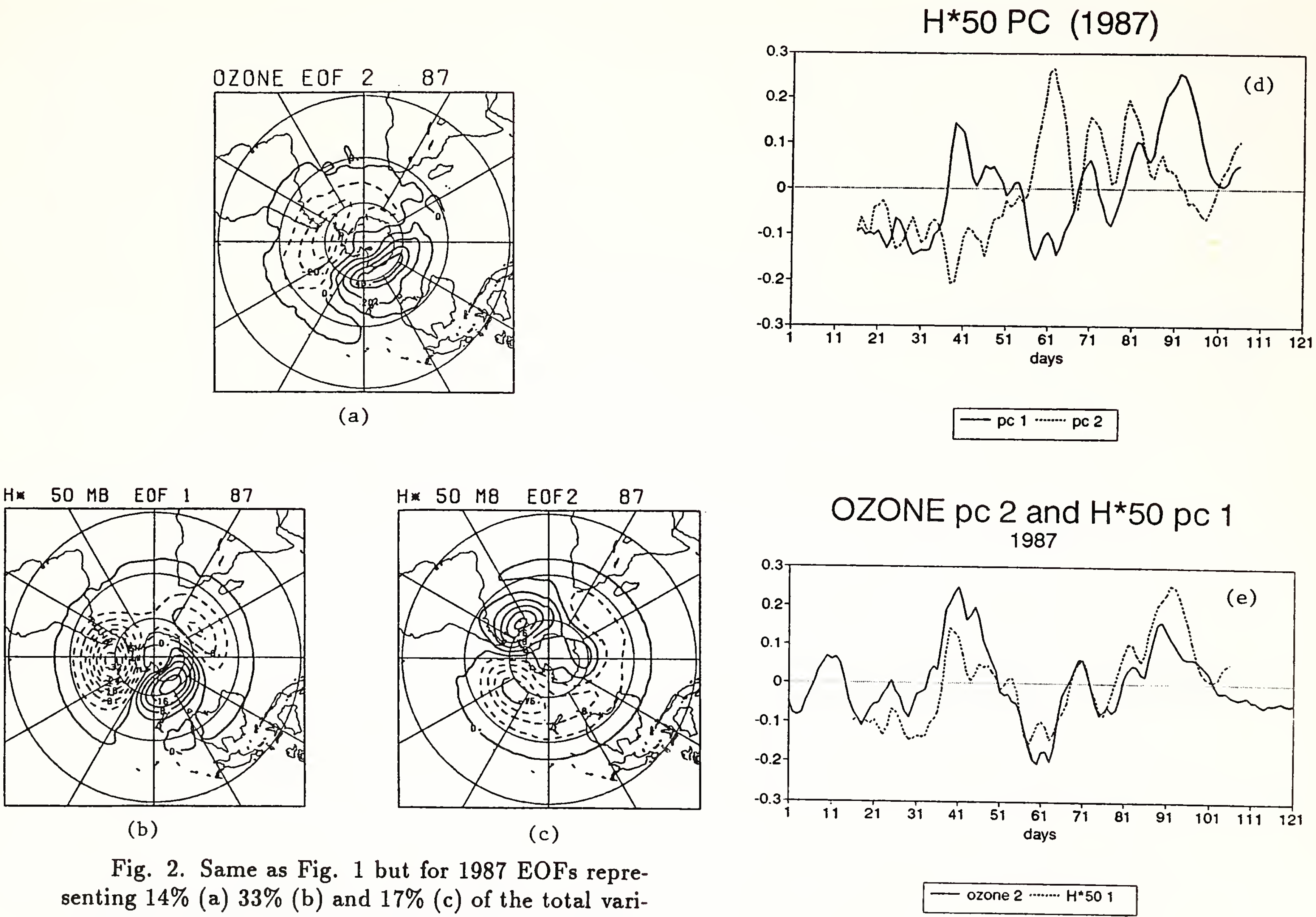

Fig. 2. Same as Fig. 1 but for 1987 EOFs representing 14% (a) 33% (b) and 17% (c) of the total variance. Time series of principal components are shown in (d) and (e).

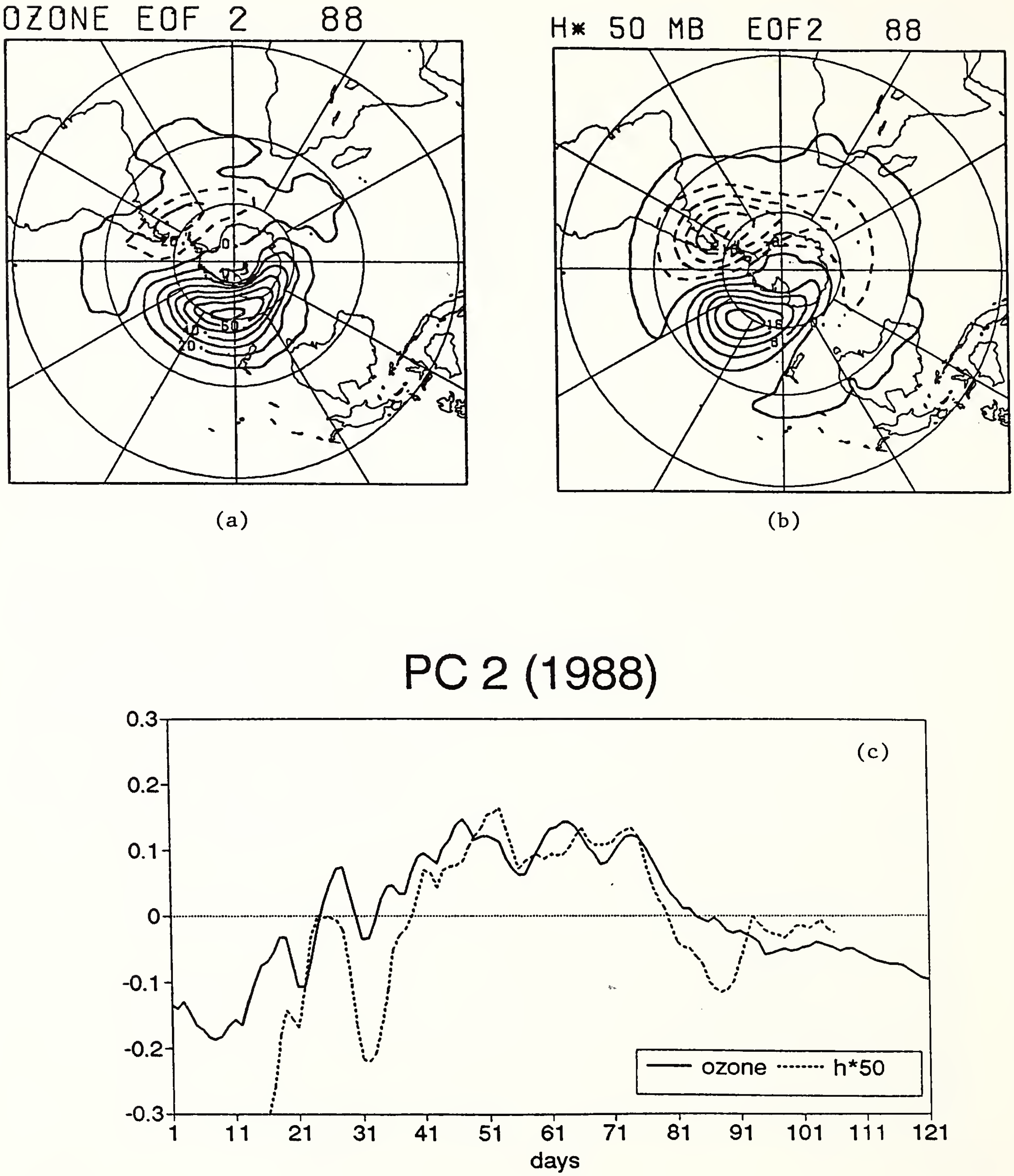
(a)
(b)

Fig. 3. same as Fig. 1 but for the second EOF for 1988 representing 17.2% (a) and 17.7% (b) of the total variance. Time series of principal components are shown in (c).

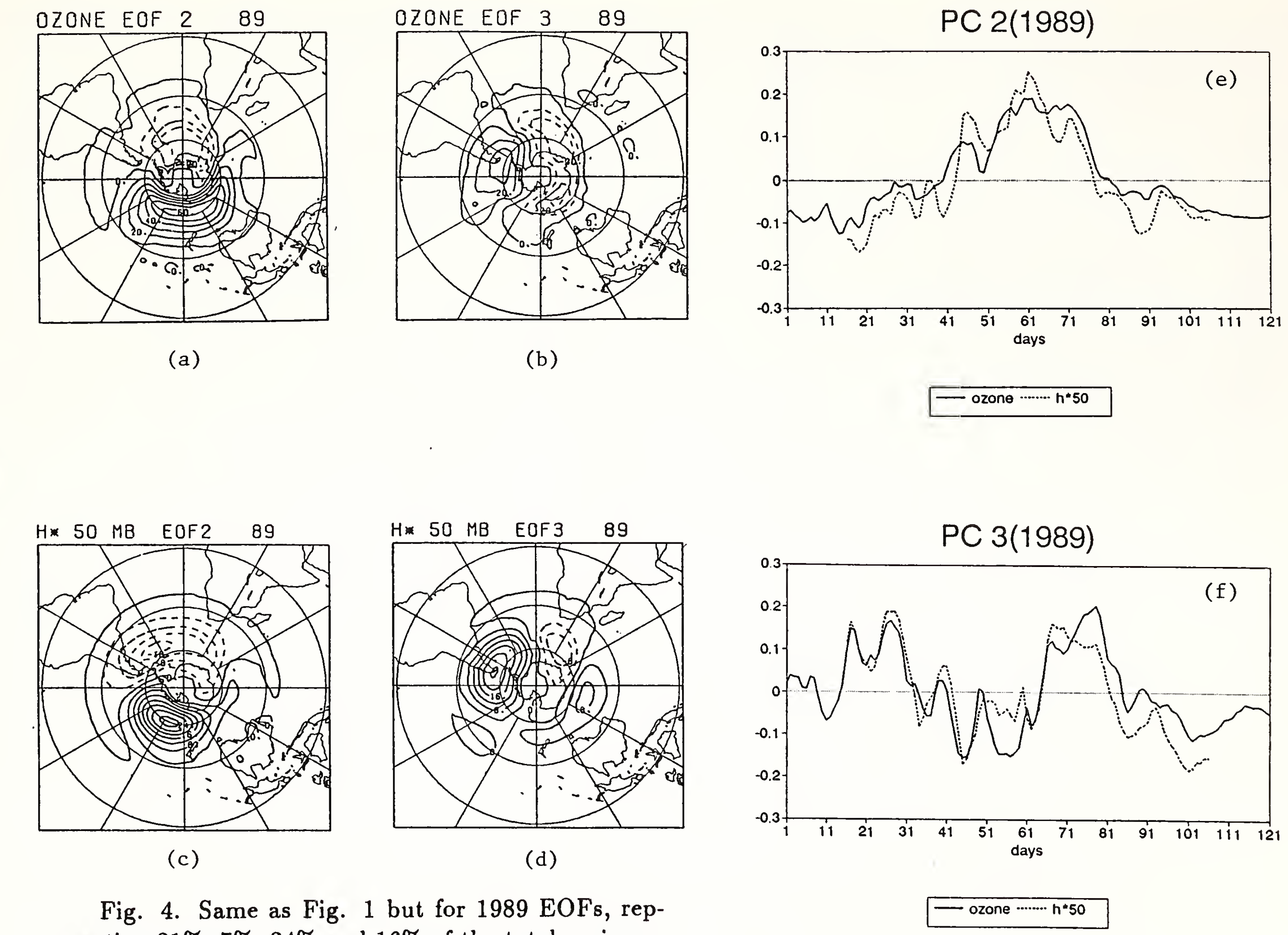

Fig. 4. Same as Fig. 1 but for 1989 EOFs, representing 21%, 7%, 24% and 16% of the total variance. Time series of principal components are shown in (e) and (f).

# QBO Modulation of Tropical Convection and ENSO Variability

William M. Gray, John D. Sheaffer and John A. Knaff
Dept. of Atmospheric Science, Colorado State University
Fort Collins, Colorado 80523

is report describes a hypothetical mechanism whereby the QBO of the tropical stratosphere articipate in triggering the onset of most El Nino and La Nina events. Rather than actually ng" the warm El Niño and cold La Niña modes, we propose that each of the two phases of the establish conditions favorable for the development of distinct modes of meridional anomalies distribution of deep convection over the equatorial West Pacific. When properly phased with nnual cycle, this rather modest QBO linked reconfiguration of regional convection initiates onal feedback processes which inturn affect the regional distribution of surface pressure, the c trade wind circulation and ultimately, ENSO. This sequence of events are diagramed in e 1, wherein QBO linked variations in the distribution of convection perturb the regional vest distribution of surface pressure, thence the trade winds, surface and internal ocean wave ty and eventually, SSTs in in the Eastern Pacific.

nvection penetrating into the lower stratosphere is frequently observed in the warm pool This penetrating convection can cause an additional small but significant warming of the stratosphere as rapidly rising air parcels overshoot their level of neutral buoyancy, entrain er stratospheric air and force compensating subsidence and warming effects. This additional stratospheric) warming creates a modest additional surface pressure decrease in regions of e deep convection, provided that the areas of stratospheric warming remain superposed over eas of upper tropospheric warming. This latter condition is possible if the difference in ntal wind direction and speed between the lower stratosphere and the upper troposphere is o great (i.e., weak vertical shear). Consequently, a convection linked process through which BO could either inhibit or promote regional anomalies of deep convective activity involves sting QBO linked distributions of vertical wind shear between approximately 200 mb and 50

ne occurrence of these linked QBO effects follows the highly variable spatial and seasonal ution of upper tropospheric–lower stratospheric vertical wind shear, which is shown for the al summer season in Figure 2. The time variation of this shear also occurs in a manner is consistent with important features of ENSO variability. Insert Box A in Figure 2 shows ross-tropospheric vertical wind shear in what we term "off–equator" areas which, in the al summer, lie between approximately 8 to 18°S. These off-equator areas in the Southern sphere include Northern Australia and much of the South Pacific Convergence Zone (SPCZ). diminished off-equator vertical wind shear is observed across the tropopause in the Area A North Australia and the SPCZ) region during the west-phase of the QBO. This diminished hase off-equator shear situation promotes deep convection and, thereby, a modest regional ive pressure anomaly with enhanced low level convergence further enhancing deep regional ctive activity. Note however that the QBO west-phase stratospheric winds in near-equator (i.e., ±7° latitude) shown in Boxes B and C of Figure 2 create a strong west-phase vertical situation which is nearly opposite that of the off–equator (Box A) region. Hence, a west condition of strong shear with inhibited deep convective activity occurs all along the equator, y tending to restrict deep convection near the equator to the warmest portions of the warm ndonesia area, but with low shear and enhanced convection favored in the off-equator areas. onfiguration of these surface pressure and precipitation anomalies, observed over the West c in association with the QBO west-phase, is shown in Fig. 3.

ne QBO east-phase conditions shown in Figure 2 create a diminished cross-tropopause vertical shear effect in the near-equator areas and thus promote conditions favorable to the eastward sion of deep equatorial convective activity along the equator. Enhanced east-phase equatorial ction expanding into the Central and East Pacific must lead to a systematic weakening of the Walker circulation. Note in Fig. 2, Box C, that a minimal vertical shear situation develops s the tropopause near the Dateline during the east–phase. This easterly QBO situation is likely favorable for enhanced eastward propagation of convective activity associated with the 30–60 day oscillation. This convection is presumably accompanied by enhanced low level westerly wind burst activity. Concurrently, deep east-phase tropical convective activity in the off-equator monsoon regions (Box A in Fig. 2) tends to be suppressed as a result of the strong (easterly) vertical zonal wind shear above the tropopause. The resulting diminished monsoon convection in the off-equator areas of the West Pacific leads to higher surface pressure in these areas, to lower pressures in the East Pacific and thus, to negative pressure anomalies in the Tahiti minus Darwin Southern Oscillation pressure Index (SOI). Hence, the resulting configuration of West Pacific precipitation and pressure anomalies in the QBO east-phase is just the opposite of the west-phase conditions in Fig. 3. These negative SOI anomalies then cause a further weakening of the Walker and equatorial trade wind circulations, leading to El Niño events.

During the past 40 years, 13 of 17 west-to-east QBO transitions were associated with a notable warming of East Pacific SSTs. The remaining four periods wherein the QBO turned easterly with no distinct warming occurred when the ENSO was either in or just concluding a prolonged warm event. As illustrated in Fig.4, a characteristic period of time, on the order of several years, is normally required for La Niña like processes to recharge the warm pool beyond the indicated threshold level, whereafter the ocean-atmosphere system is again unstable to east-phase QBO linked perturbations. Hence, this timing requirement explains why four historical QBO west-to-east transitions did not trigger sizable warmings.

Note also that the SOI reaches it annual maximum amplitude during the Austral summer (December-March) and then decreases rapidly to a July-August minimum. Hence, for an incipient El Niño to mature into a significant warm event, it may be important that the onset of El Niño promoting QBO east-phase effects coincide approximately with this annual weakening of the SOI. This idea is illustrated in Fig. 5 wherein the mean annual cycle of surface pressure at Tahiti and Darwin are contrasted with the anomaly conditions imposed by the onset of the QBO east-phase during the Boreal spring. These favorable aspects of a January to July concurrence of the QBO east-phase onset with the enhancement of an incipient warm event are entirely consistent the observed seasonality of both ENSO and the QBO variability. Longer term time variations of the phase association between the QBO and the annual cycle may thus be an additional factor in the three to seven year timing of El Niño events.

In summary, if deep convection linked tropospheric feedback effects in the tropical Pacific are tied to the lower stratospheric QBO, then the conditions they promote will occur over large areas and will persist for periods of time which are adequate to force changes in the tropical regional circulation (i.e., months to years). We find that the most likely process by which the QBO may modify and redistribute regional deep convection is through the contrasting effects of the east-phase versus west-phase vertical wind shear between the lower stratosphere and upper troposphere. This assertion is in agreement with the observed spatial and temporal variability of this shear. In regions where this vertical shear is strong, we also observe positive surface pressure anomalies and decreased deep convection (OLR) and precipitation. Conversely, in regions where this shear is weak, the opposite anomaly situations are observed. The resulting alteration of Pacific regional surface pressure (i.e., the SOI) due to the contrasting QBO effects influences the equatorial trade winds in a way entirely consistent with that required to produce the observed variations of the ENSO. Additional details of this mechanism and of observational evidence supporting the hypothesis are presented in two forthcoming reports; Gray *et al.*, in *Geophysical Research Letters* (in press) and in the *Journal of the Meteorological Society of Japan* (submitted, October, 1991).

*Acknowledgements.* This research was funded by the NS0000 NSF-National Science Foundation

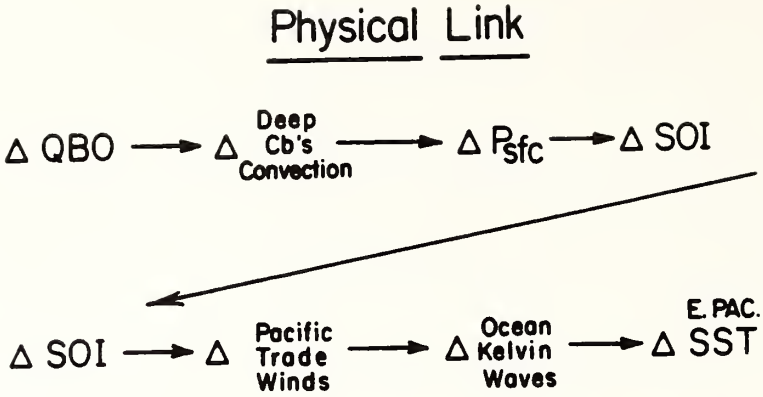

Fig. 1. Conceptual diagram of the sequence of event-associations which link the stratospheric QBO to ENSO variability by altering the distribution of intense convective activity in the tropical Pacific. The distribution of convection varies with the QBO east-phase in such a way as to cause negative values of the SOI, thereby leading to weaker trade winds, ocean Kelvin waves and an ENSO warm event. The reverse occurs with the QBO west-phase.

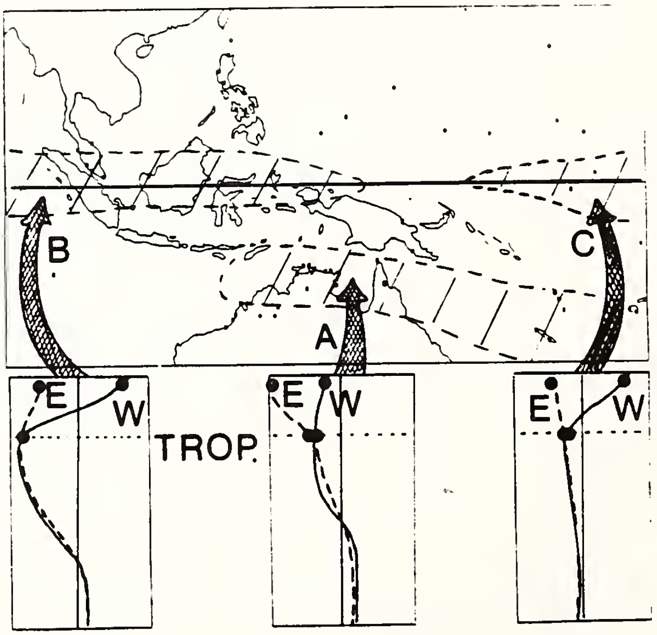

Fig. 2. Comparative QBO east-phase (E) and west-phase (W) representations of the basic differences in zonal wind profiles during the November-March portion of the annual cycle. Profiles are shown for areas near the equator in the far West Pacific (B) and near the Dateline (C), as well as off-the-equator in the SPCZ and in the Australian monsoon circulation (A). The "dots" on the profiles emphasize key differences in the vertical shear values between the upper troposphere and lower stratosphere.

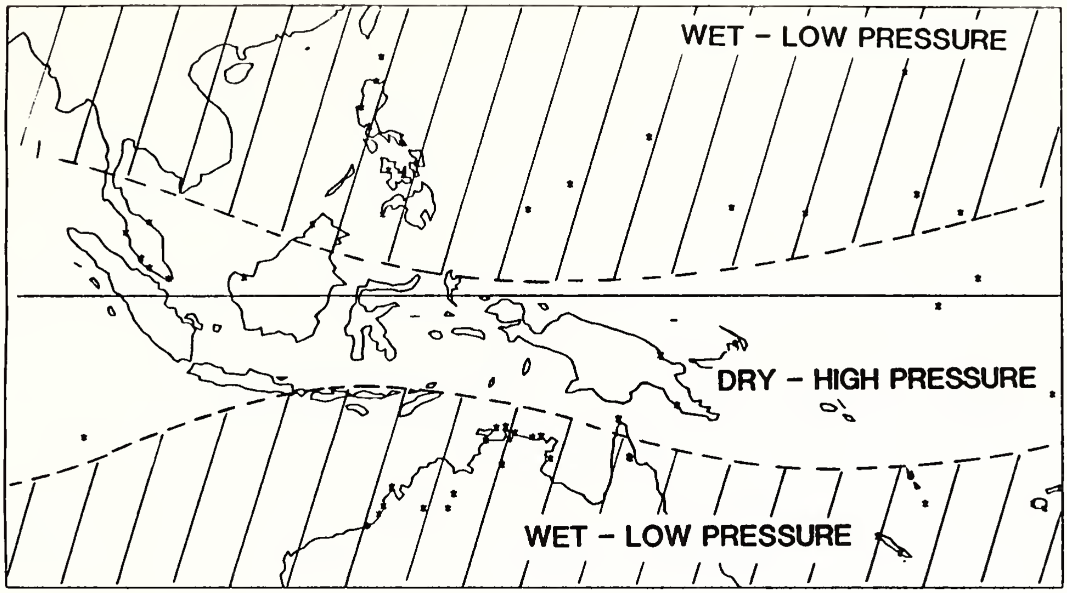

Fig. 3. Analysis of QBO linked precipitation and surface pressure anomalies at highly reliable stations (less than 5% missing data) in the tropical West Pacific and Eastern Indian Oceans. The figure shows the mean anomaly conditions for January, February, and March period. The analysis reflects average three-month values for ten west-to-east phase QBO transition years minus mean values for ten east-to-west QBO transition years. Off-equator areas of positive precipitation and negative pressure anomalies are cross-hatched.

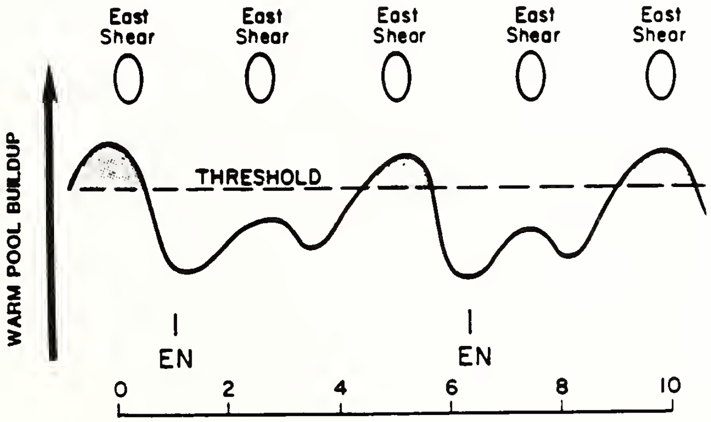

Fig. 4. Idealized response of the West Pacific warm pool to the effects of periodic easterly QBO shear events in the lower stratosphere (represented by small ovals). Heat storage in the warm pool slowly accumulates until a critical thresholds passed, often which the warm pool discharges as a warm event accompanying the destabilizing effects of the east-phase QBO on regional convective activity.

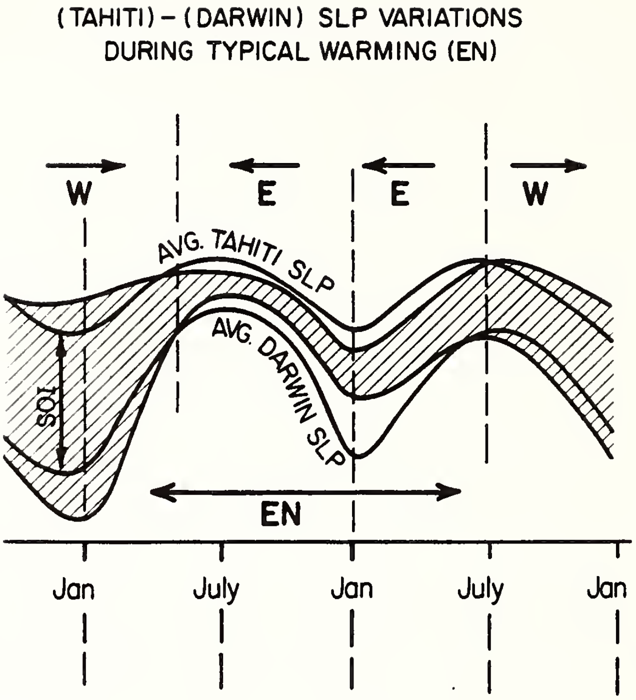
(TAHITI) – (DARWIN) SLP VARIATIONS
DURING TYPICAL WARMING (EN)
W
E
E
W
AVG. TAHITI SLP
AVG. DARWIN SLP
SOI
EN
Jan
July
Jan
July
Jan

Fig. 5. Contrast of the mean annual cycles of Tahiti and Darwin Sea-Level Pressure (SLP) versus those which attend the west (W) and east (E) phases of the QBO; the difference between the latter, QBO linked SLP being cross hatched in the figure. Starting from left, the QBO is westerly (strong SOI) in January, going easterly by July (weak or negative SOI) as an incipient El Niño intensifies.

# Annual and Interannual Variability of the Tropical Pacific during 1985-89

Xueliang Wang[1], Zhiyuan Dai[2]
James Carton[2], Eugene Rasmusson[2]
Climate Analysis Center
NMC/NWS/NOAA, Washington, DC 20233

## 1. **Introduction**

While knowledge of atmospheric variability advances quickly with enhanced observation and extensive modeling in recent years, understanding of spatial structure and temporal variation of large-scale ocean circulation are still rather preliminary due to lack of gridded oceanic data. An endeavor at the National Meteorological Center (NMC) during recent several years is implementation of an oceanographic data assimilation system (ODAS) by using a primitive equation ocean general circulation model (OGCM) from the Geophysical Fluid Dynamics Laboratory (GFDL) (Leetmaa and Ji, 1989). By use of grid data from the system, some low-frequency planetary-scale features over equatorial pacific are presented here.

## 2. **Data and Analysis**

The parameters used in this study are monthly averaged sea surface temperature (SST) and surface dynamic height (SDH) from NMC ODAS. Data domain covers the tropical Pacific from 130°E to 70°W between 20°S and 20°N. All quantities are available from 1985 to 1989. The resolution of data are 4° longitudes and 1° latitude.

The extended empirical orthogonal function (EEOF) analysis were applied to model SST and SDH. The time intervals of EEOF were 3 months. A varimax rotation was performed to EEOF eigenfunctions of SST in order to separate annual and interannual variabilities.

## 3. **Results**

During the five years from 1985 to 1989, Pacific ocean experienced the 1986/87 warm event and 1988 clod event. In order to investigate interannual variation along with seasonal change, we used total fields of SST and SDH. The EEOF analysis was able to separate two time periods into different modes.

Presented in Fig. 1 are principal components (PC) of the first 4 dominant EEOF modes for both SST and SDH. For SST field, the first pair of PCs (PC1 and PC2) describes annual cycle, which takes 64.4 percent of variance, and the second pair (PC3 and PC4) for interannual variability, which accounts for 17.6 percent of variance (Fig. 1a). However, it is immediately noticed that the

---

[1] Research and Data System Corporation, Greenbelt, MD
[2] Department of Meteorology, University of Maryland, College Park, MD

PC2 and PC3 are frequency contaminated with each other. PC2 is dominated by annual cycle but is confused with part of interannual frequency, and vise verse for PC3. We then submit these four EEOF modes to a varimax rotation and the resulted PCs are show in Fig. 1b. By comparison of Figs. 1a with 1b, it is clear that rotated EEOF of the SST cleanly separates interannual variability from mean annual cycle. The variance explained by individual modes is redistributed by shift of about one percent variance from interannual modes to annual ones. In fact, the spatial patterns before and after the rotation remain essentially same except the region of eastern Pacific cold tongue where the interannual and annual periods are coexisted and confused.

For SDH field, two periods were not apparently contaminated (Fig. 1c) so no rotation was performed. The first pair of PCs (PC1 and PC2) captures interannual variation and annual cycle mode comes next (PC3 and PC4). Next, we will describe evolution cycle of interannual and annual modes separately by showing the EEOFs only corresponding to Figs. 1b and 1c.

(1) Annual variation

The evolution of annual cycle of assimilated SST is captured by EEOF1 and EEOF2, as shown in Figs. 2a and 2b, respectively. Each EEOF contains three patterns corresponding three time steps to 0 month delay (upper panel), 3 months delay (mid panel), and 6 months delay (lower panel). As seen for PCs in Fig. 1b, PC1 and PC2 are nearly identical but with quarter phase difference. This is also true for EEOF1 and EEOF2 in Figs. 2a and 2b. Therefore, the pattern of EEOF1 at 3 months delay, denoted as EEOF1(3), is nearly identical to the pattern of EEOF2 at 0 month delay (EEOF2(0)), so does for EEOF1(6) and EEOF2(3). Hence, four patterns of EEOF1(0), EEOF1(3), EEOF1(6), and EEOF2(6) complete a cycle of seasonal SST change of the equatorial Pacific. According to PCs in Fig. 1b, EEOF1(0) corresponds to Feburary-March-April (FMA) pattern, EEOF1(3) for MJJ pattern, EEOF1(6) for ASO pattern, and EEOF2(6) for NDJ pattern. Basically, SST change delays seasonal cycle of solar radiation by two months, which agrees with literatures. It is interest to note that during transition phases, i.e., EEOF1(3) and EEOF2(6), the structure and variation of equatorial eastern Pacific cold tongue is well defined due to high resolution of the model. This feature is ill defined in any of observed SST field.

For the SDH field, the second pair of EEOFs, i.e., EEOF3 and EEOF4, depicts annual change as shown in Figs. 2c and 2d. The quarter phase difference is also evident in PCs (Fig. 1c) and EEOFs (Figs. 2c and 2d). Four patterns of EEOF4(0), EEOF3(0), EEOF3(3), and EEOF3(6) complete an evolution cycle of seasonal SDH variation of the equatorial Pacific. From the PCs in Fig. 1c, it is able to relate each pattern in Figs. 2c and 2d to a season. For example, patterns EEOF3(0) and EEOF4(3) are for northern summer (JJA), EEOF3(3) and EEOF4(6) for SON, EEOF3(6) for DJF, and EEOF4(0) for MAM.

The SDH variation is equivalent to change of oceanic current through the geostrophic balance. In the equatorial Pacific, there are four major currents, i.e., north equatorial current (NEC), south equatorial current (SEC), north equatorial counter current (NECC), and south equatorial counter current (SECC).

There are also some coastal currents, e.g., Peru current. The main feature described by EEOF3 and EEOF4 (Figs. 2c and 2d) reflects oceanic current variation responding to trade wind system. For example during the summer (EEOF3(0) or EEOF4(3)), southeasterly trades are strongest and push the current system northward. The SEC is displaced from its averaged position south of the equator to north of the equator. Similar shift can be seen for NEC, NECC, and SECC. Reversal occurs during winter (EEOF3(6) in Fig. 2c). During the transition seasons (EEOF3(3) in Fig. 2c and EEOF4(0) in Fig. 2d), east-west displacement of the currents dominates and coastal currents along central-south America responding to trades seems quicker than the open ocean currents.

(2) Interannual variability

Interannual modes of SST field are captured by EEOF3 and EEOF4 in Figs. 3a and 3b with corresponding PCs in Fig. 1b. Since 6 months delay is unable to describe the evolution of interannual changes, three patterns (corresponding three time steps) of each EEOF are very alike. Each EEOF basically reflects several extreme states (marked by black dots on PC3 and PC4 in Fig. 2b) of warm and cold events within the five years. For example, EEOF3s are the dominant patterns around beginning of 1986 (pre-ENSO phase), end of 1987 (ENSO mature-decay phase), and end of 1988 (La Nina mature-decay phase). EEOF4s dominate at beginning of 1987 (ENSO onset-mature phase) and mid of 1988 (La Nina onset-mature phase). These patterns are very much similar to the classic ENSO composites by Rasmusson and Carpenter (1982).

It is also interest to note the first appearance of SST change near Peru coast in EEOF3(3) in Fig. 2c. The anomaly propagates westward along the equator (EEOF3(6) in Fig. 2c). This feature suggests that the equatorial oceanic Kelvin wave activity is also evident in the model SST field.

The SDH variation on interannual time scale is essentially forced by the Pacific trade wind systems. Once again interannual SDH changes can be interpreted by variation of oceanic current systems. Shown in Figs. 3d and 3c are EEOF1 and EEOF2 of SDH field. EEOF1s are most important during the period from fall 1986 to fall 1987 (ENSO onset-mature phase) and the period from summer 1988 to summer 1989 (La Nina mature-decay phase). EEOF2s are predominant at the winter of 1986 (ENSO onset-mature phase) and over the period from winter of 1987 to fall of 1988 (ENSO decay-La Nina onset phase). The interannual variation of Pacific currents as revealed by EEOF1 and EEOF2 of SDH (Figs. 3c and 3d) agrees very well with the theory proposed by Wyrtki (1975) that the Pacific trades are primarily responsible for ENSO.

By comparison of interannual PCs of SST and SDH, we note that SST change delays SDH variation by one or two months. In other words, SDH field and current systems are more efficiently and directly forced by the surface winds and SST change evolves more oceanic thermal and dynamic processes.

## 4. **Conclusions**

The evolution of the annual cycle of model SST can be explained to a large extent in terms of seasonal changes in incoming solar radiation. The annual cycle of surface dynamic height is mainly determined by the meridional migrations of the Pacific northwesterly and southeasterly trade wind belts.

During the transition seasons, oceanic dynamic processes seem to play more important role. For example, variations of eastern Pacific cold tongue is well resolved in SST field during spring and fall, and intensity change of the Peru coastal current is also well captured in the SDH field.

On interannual time scale, both SST and SDH variations describe ENSO and La Nina evolutions. The SST change reflects slow migration of Pacific warm pool and effect of equatorial oceanic Kelvin wave propagation. The SDH variability is essentially related to oceanic current change which is forced by surface wind system.

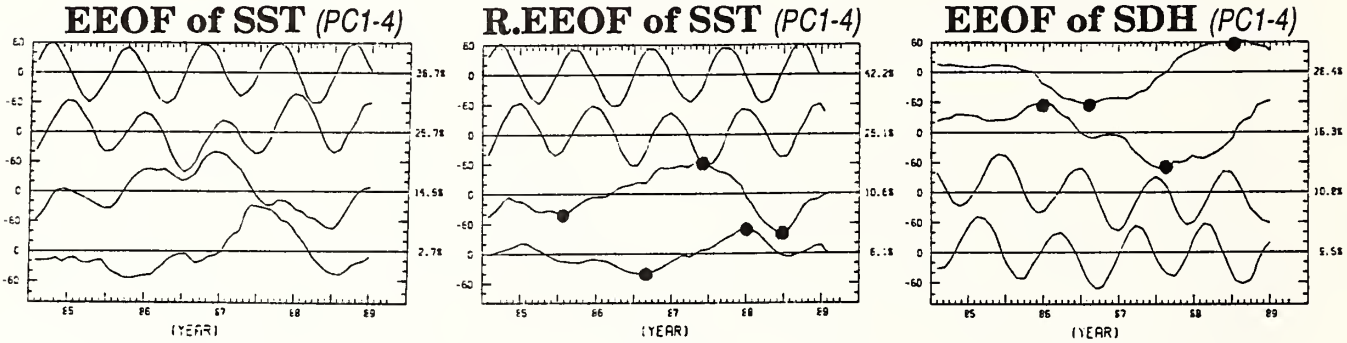

*Fig. 1a*

*Fig. 1b*

*Fig. 1c*

Fig. 1: The first four principal components (PC1, PC2, PC3, and PC4) of EEOF analysis. (a) for un-rotated EEOF of SST, (b) for rotated EEOF of SST, and (c) for un-rotated EEOF of SDH. Variance explained by each mode is also given. Black dots mark the extreme states discussed in the text.

Fig. 2: Annual EEOFs of SST and SDH. (a) for EEOF1 of SST, (b) for EEOF2 of SST, (c) for EEOF3 of SDH, and (d) for EEOF4 of SDH. Contour intervals are 5 units. Unit is arbitrary. Negative values are dashed.

Fig. 3: Same as Fig. 2 except (a) for EEOF3 of SST, (b) for EEOF4 of SST, (c) for EEOF1 of SDH, and (d) for EEOF2 of SDH.

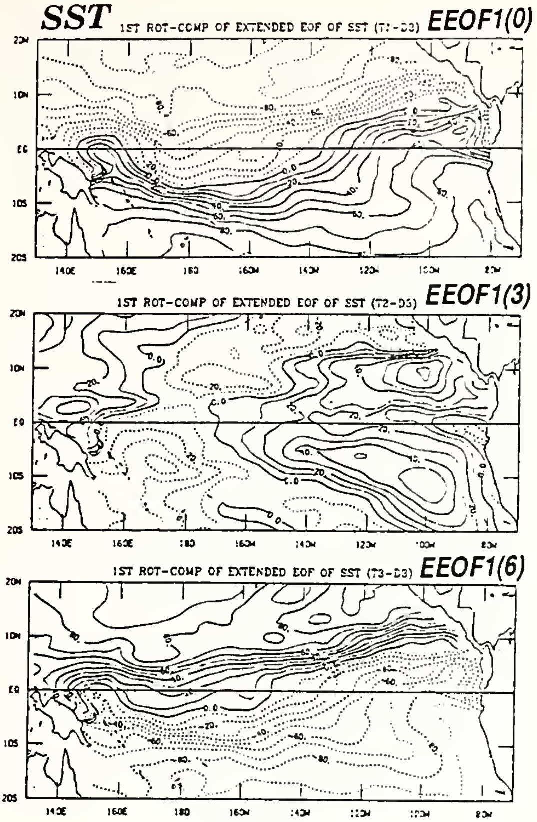
SST
1ST ROT-COMP OF EXTENDED EOF OF SST (T1-D3) EEOF1(0)
1ST ROT-COMP OF EXTENDED EOF OF SST (T2-D3) EEOF1(3)
1ST ROT-COMP OF EXTENDED EOF OF SST (T3-D3) EEOF1(6)
20N
10N
EQ
10S
20S
140E
160E
180
160W
140W
120W
100W
80W

*Fig. 2a*

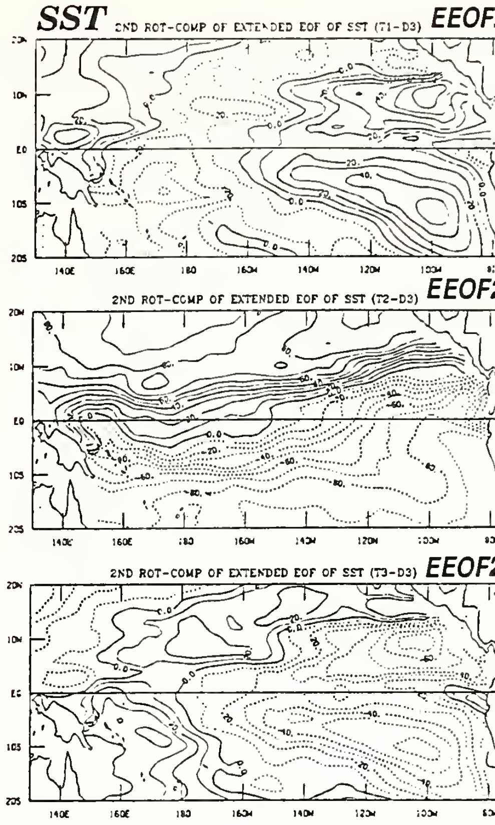
SST
2ND ROT-COMP OF EXTENDED EOF OF SST (T1-D3) EEOF
2ND ROT-COMP OF EXTENDED EOF OF SST (T2-D3) EEOF
2ND ROT-COMP OF EXTENDED EOF OF SST (T3-D3) EEOF2
20N
10N
EQ
10S
20S
140E
160E
180
160W
140W
120W
100W

*Fig. 2b*

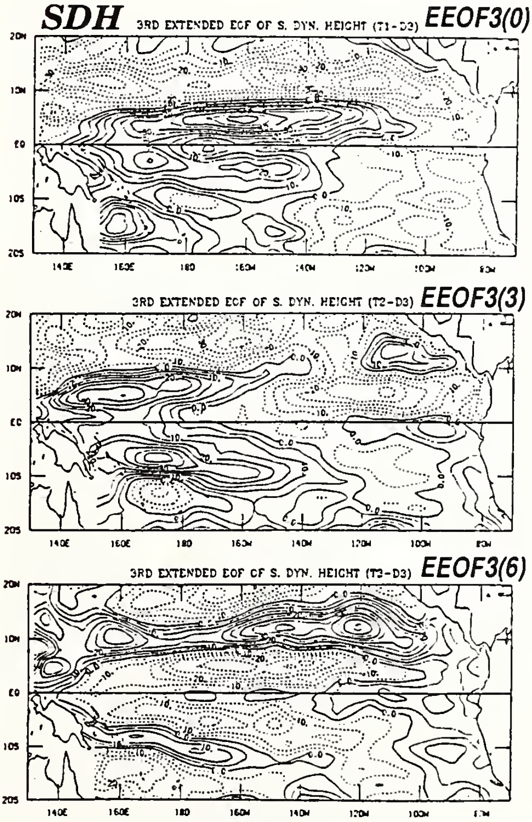
SDH
3RD EXTENDED EOF OF S. DYN. HEIGHT (T1-D3) EEOF3(0)
3RD EXTENDED EOF OF S. DYN. HEIGHT (T2-D3) EEOF3(3)
3RD EXTENDED EOF OF S. DYN. HEIGHT (T3-D3) EEOF3(6)
20N
10N
EQ
10S
20S
140E
160E
180
160W
140W
120W
100W
80W

*Fig. 2c*

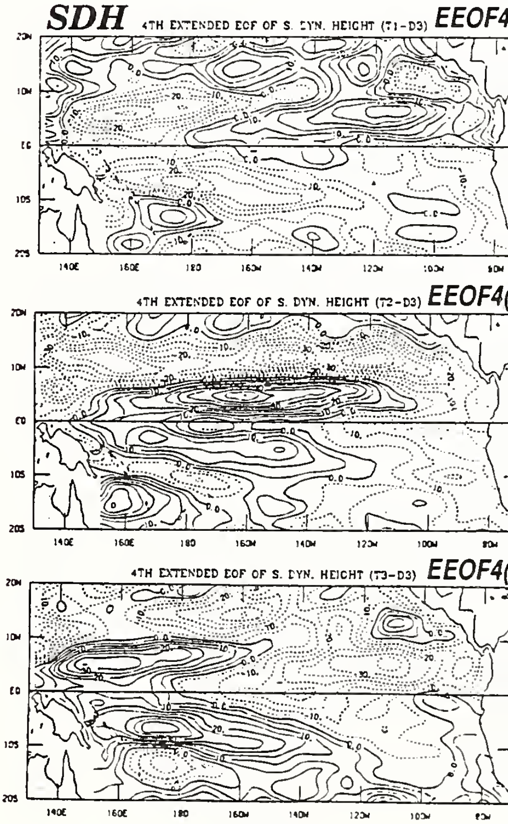
SDH
4TH EXTENDED EOF OF S. DYN. HEIGHT (T1-D3) EEOF4
4TH EXTENDED EOF OF S. DYN. HEIGHT (T2-D3) EEOF4
4TH EXTENDED EOF OF S. DYN. HEIGHT (T3-D3) EEOF4
20N
10N
EQ
10S
20S
140E
160E
180
160W
140W
120W
100W
80W

*Fig. 2d*

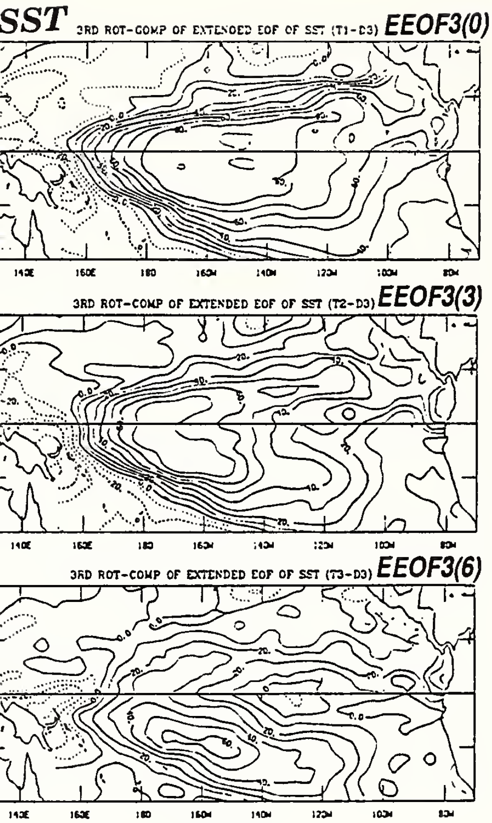
SST
3RD ROT-COMP OF EXTENDED EOF OF SST (T1-D3)
EEOF3(0)
3RD ROT-COMP OF EXTENDED EOF OF SST (T2-D3)
EEOF3(3)
3RD ROT-COMP OF EXTENDED EOF OF SST (T3-D3)
EEOF3(6)
140E
160E
180
160W
140W
120W
100W
80W

Fig. 3a

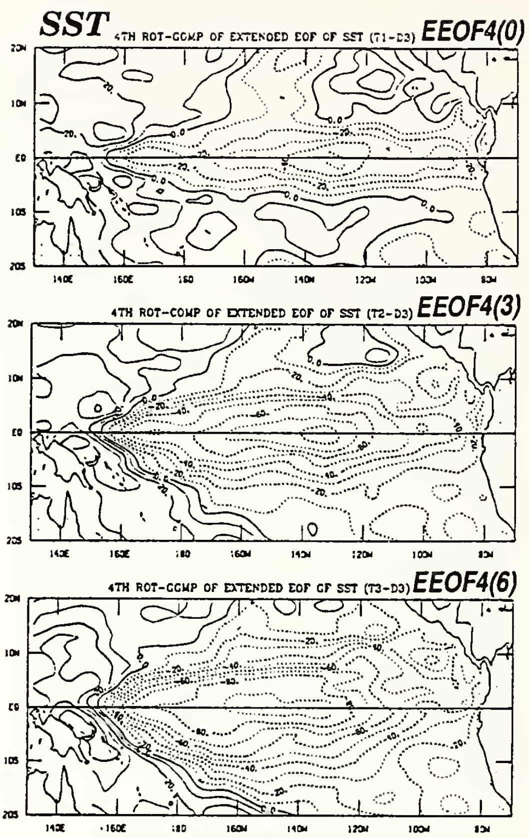
SST
4TH ROT-COMP OF EXTENDED EOF OF SST (T1-D3)
EEOF4(0)
4TH ROT-COMP OF EXTENDED EOF OF SST (T2-D3)
EEOF4(3)
4TH ROT-COMP OF EXTENDED EOF OF SST (T3-D3)
EEOF4(6)
20N
10N
EQ
10S
20S
140E
160E
180
160W
140W
120W
100W
80W

Fig. 3b

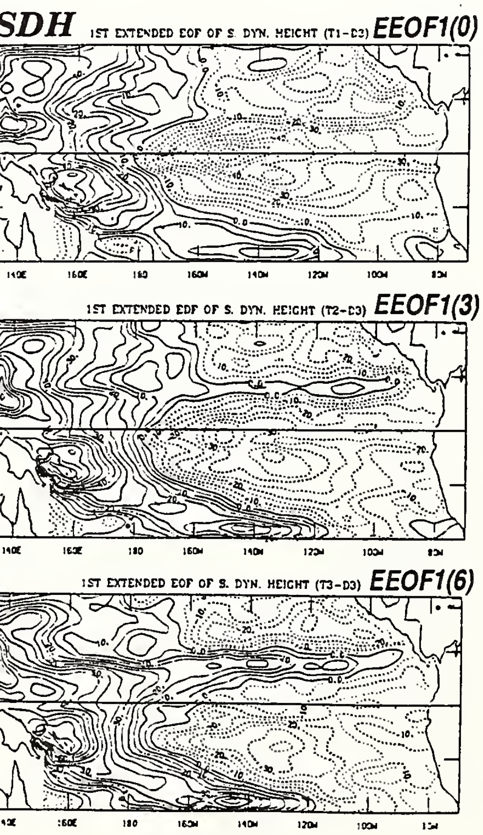
SDH
1ST EXTENDED EOF OF S. DYN. HEIGHT (T1-D3)
EEOF1(0)
1ST EXTENDED EOF OF S. DYN. HEIGHT (T2-D3)
EEOF1(3)
1ST EXTENDED EOF OF S. DYN. HEIGHT (T3-D3)
EEOF1(6)
140E
160E
180
160W
140W
120W
100W
80W

Fig. 3c

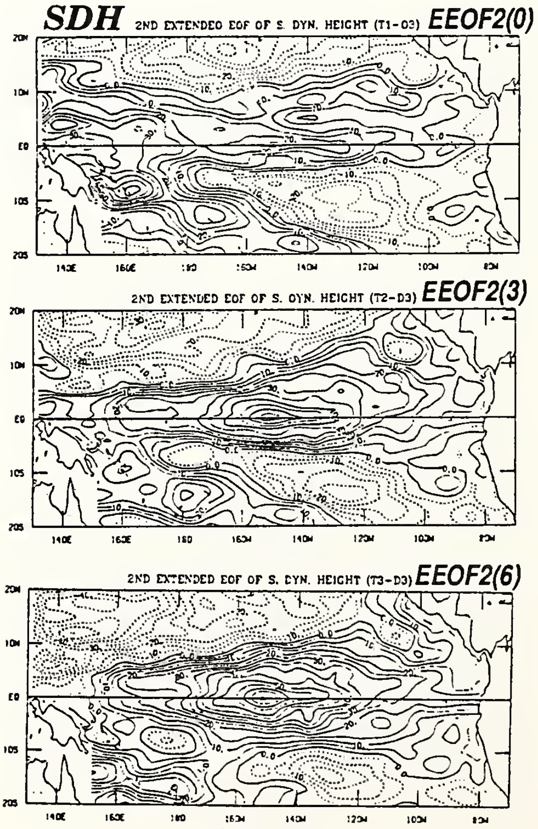
SDH
2ND EXTENDED EOF OF S. DYN. HEIGHT (T1-D3)
EEOF2(0)
2ND EXTENDED EOF OF S. DYN. HEIGHT (T2-D3)
EEOF2(3)
2ND EXTENDED EOF OF S. DYN. HEIGHT (T3-D3)
EEOF2(6)
20N
10N
EQ
10S
20S
140E
160E
180
160W
140W
120W
100W
80W

Fig. 3d

# Low Frequency Variability in Blended SST and Ocean Temperature Analysis

Thomas Smith, Muthuvel Chelliah, and Chester Ropelewski
Climate Analysis Center/NWS/NOAA

Some preliminary results of an ongoing tropical Pacific air-sea study are given. Under development at CAC are procedures to routinely do detailed analysis of coupled ocean/atmosphere model output and Pacific Ocean model and analysis products. The CAC analysis is complementary to analyses done by the NMC coupled-modeling group by it focus on climate diagnostics. Discussed here is analysis of blended SST anomalies (Reynolds, 1988), and cross-section temperature anomalies to 500 m depth from the operational Pacific Ocean analysis system (Leetmaa et al., personal communication). The sections are along the equator, and latitude vs depth sections, 20°N to 20°S, at 165°E and 110°W.

Blended SST monthly anomalies are taken from the COADS/ICE 1950-1979 climatology. The cross-section monthly anomalies are with respect to the 1985-1990 base period. The study period is February, 1985 to May, 1991. Rotated principal component (RPC) analysis was done on the Pacific SST anomalies. Rotated joint principal component (RJPC) analysis was done on the cross sections of ocean-temperature anomalies, all three jointly. The period used was the longest available period for both SST and ocean cross sections at the time of analysis. The period contains one warm event (the 1986/87 event), and one cold event (the 1988 event).

The SST 1st mode shows a symmetric Southern Oscillation warm event, cold event signal (Fig. 1a). It accounts for 33% of the total variance, by far the most important mode. First mode loadings are strong over a large area in the central Pacific, between about 20°S and 10°N. The maximum loading occurs in the Southern Hemisphere central Pacific. The western-Pacific signal is of opposite sign to the eastern-Pacific signal. The 2nd SST-anomaly mode (Fig. 1b) also indicates the warm and cold events, but the time series shows that the cold event has a larger amplitude in this mode. The 2nd mode accounts for 9% of the total variance. Higher modes account for lower fractions of the variance. The 2nd mode appears to represents an asymmetric component of the 1985-1990 SST oscillation, which is weaker than the symmetric component of the oscillation. Complementary SST analysis was done for this workshop by Wang et al.

In the analysis of the cross-section anomalies (Fig. 2), the 1st RJPC mode is symmetric in warm-cold events, and accounts for 26% of the variance. Along the equator, 1st mode upper-ocean loadings are maximum between 160°W and 110°W, the surface to 80 m. Near the eastern boundary, the positive loadings extend to greater depths, suggesting great changes in the mixed-layer depth. Beneath the positive 1st mode loadings are mostly negative loadings west of 120°W. The 165°E north-south section shows positive loadings near the equator in the upper 100 m, and negative loadings over most of the rest of the area, suggesting a transfer of heat towards the equator during the warm event and away during the cold event. The 110°W section has positive loadings almost everywhere, except between 5°N and 15°N, from near the surface to 350 m. The maximum positive loadings in the 110°W section are on the equator in the upper 100 m.

The 2nd RJPC mode of the cross-sections (Fig. 3), which accounts for 21% of the variance, has a larger amplitude for the warm event than for the cold event. The maximum occurs later than in the 1st mode, suggesting that this reflects conditions during the mature phase of the warm event. The east-west loadings are similar to the 1st mode's, except that the surface positive loadings are weaker and smaller in area, while the subsurface negative loadings are stronger and cover a larger area. The 165°E north-south section indicates cooling over a large region in the west Pacific during the mature phase of the warm event. In the eastern section, warming is indicated over most of the upper ocean. Exceptions are at the equator, where the undercurrent appears to have brought cooler waters eastward, and near 7°N associated with the counter current. The deep cooling north of the equator during the warm event, shown by both the 1st and 2nd mode, may reflect increased oceanic divergence in the region. The Northern Hemisphere trades were stronger than average during the boreal winter of 1986-87, and particularly strong for the winter of 1987-88 (CAC Bulletins). Strengthening trades and cooling near 7°N will also tend to increase the strength of the north equatorial current.

Future analyses will include RPC and RJPC analysis using NMC archived 850 mb winds and outgoing-longwave radiation over the Pacific, in addition to ocean temperatures. We intend to extract what additional information we can from the archived data, and develop analysis tools for later use. Planned for the near future at NMC is reanalysis of the Pacific Ocean, and a separate reanalysis of the global atmosphere. The reanalyses will use all available observations for assimilation, including observations which were not available to the original analysis. In addition, consistent oceanic and atmospheric models will be used throughout the reanalysis. That will eliminate problems in the currently archived data associated with gradual model modifications over time, and will yield a more complete and dynamically consistent data set for further analysis. Analysis of those data sets by our group should give a clearer understanding of ocean-atmosphere climatic variations. Also planned at NMC are completely coupled ocean-atmosphere analysis and forecast runs. Thus far the coupled model is still actively under development (as discussed in the workshop paper by Marsico et al.). Coupled runs will provide a dynamically consistent sources of information for our group's study of Pacific ocean-atmosphere coupling and the coupling's relation to climatic variation.

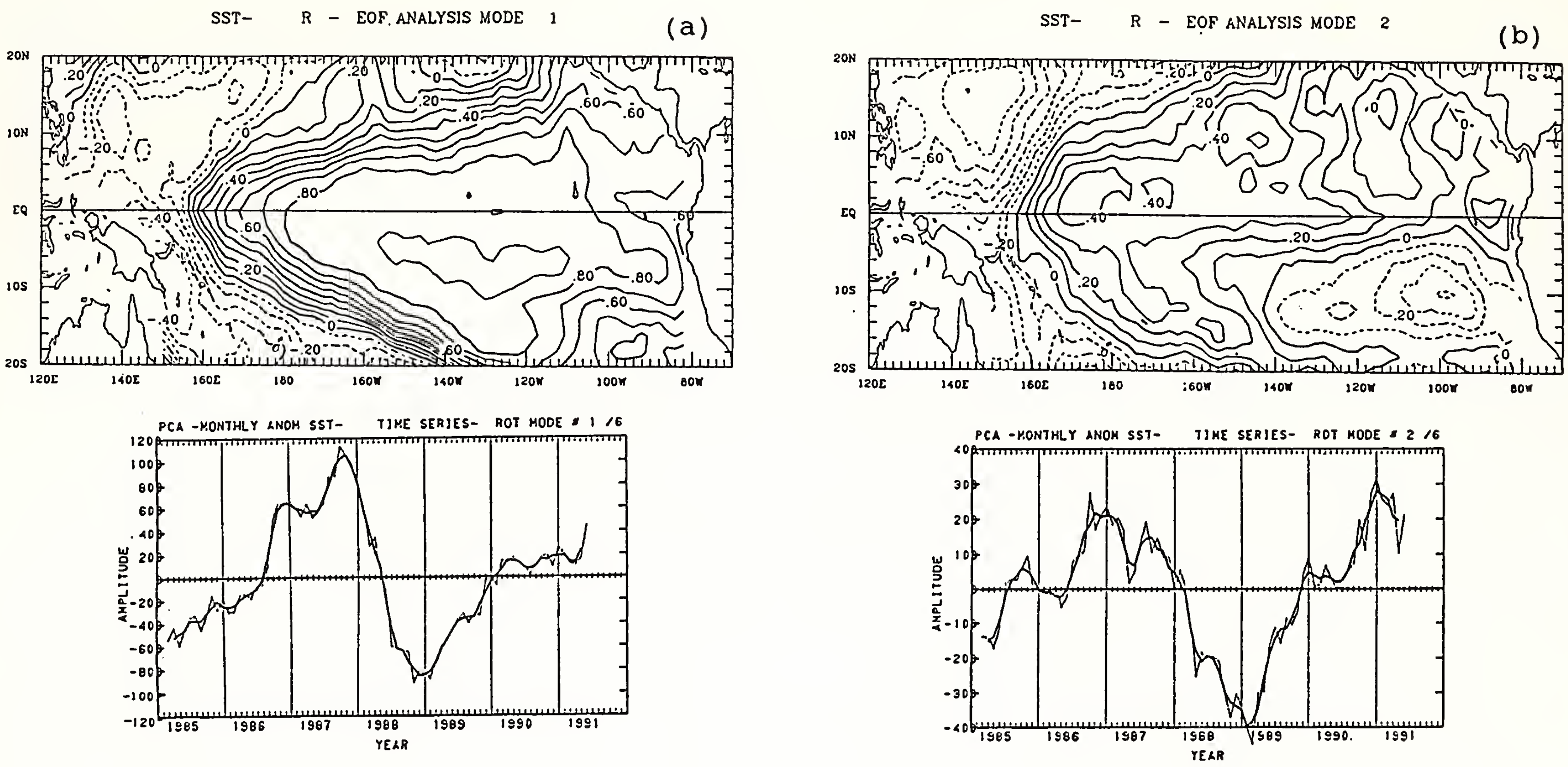

Fig. 1. Rotated principal component analysis of blended SST anomalies, Feb 1985 to May 1991. Shown are loadings and time series for the first mode (a), and for the second mode (b).

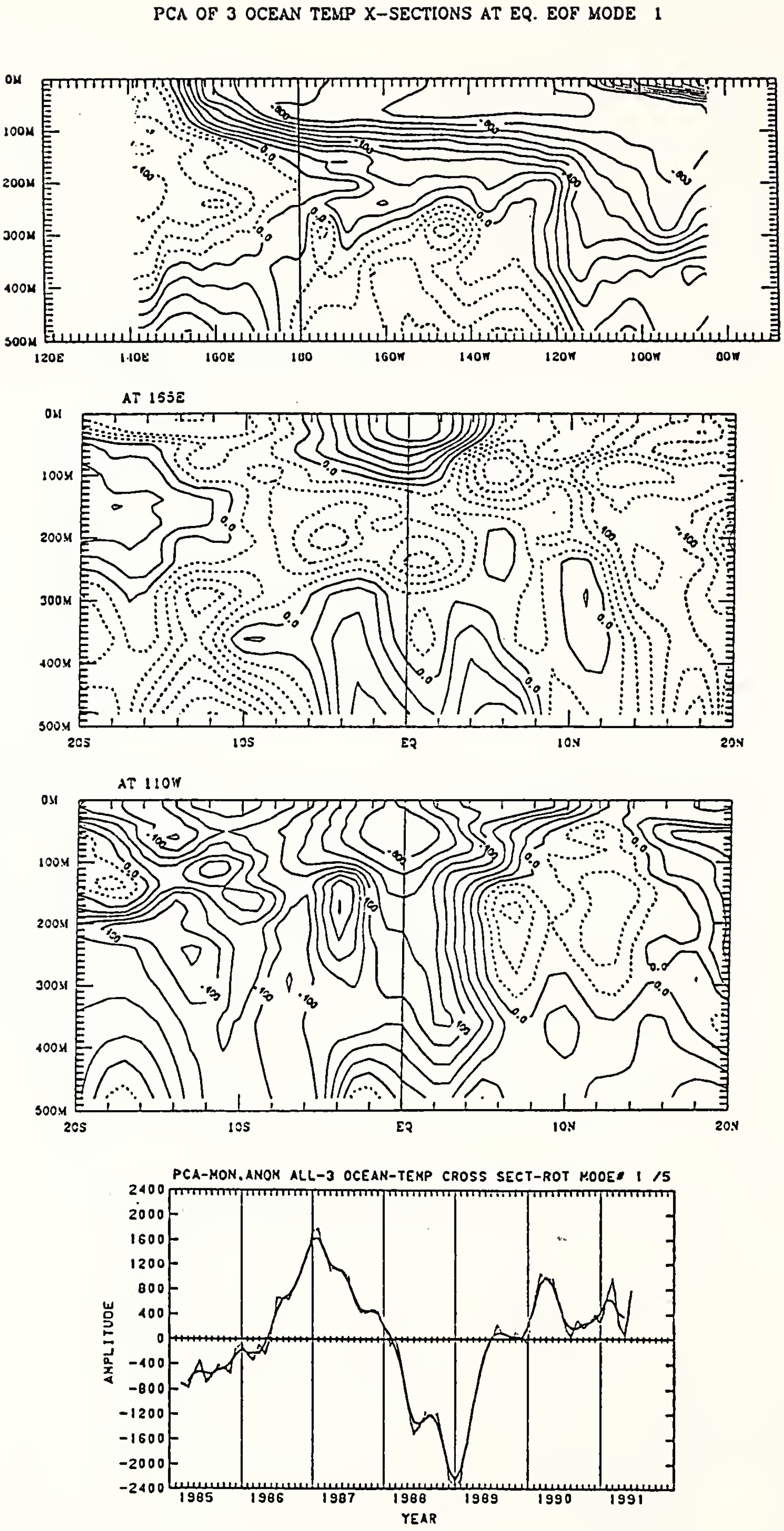

Fig. 2. Rotated joint principal component analysis of ocean temperature anomalies on cross sections. The sections are: east-west along the equator, north-south at 165°E and at 110°W. Shown is the first mode loadings and the associated time series.

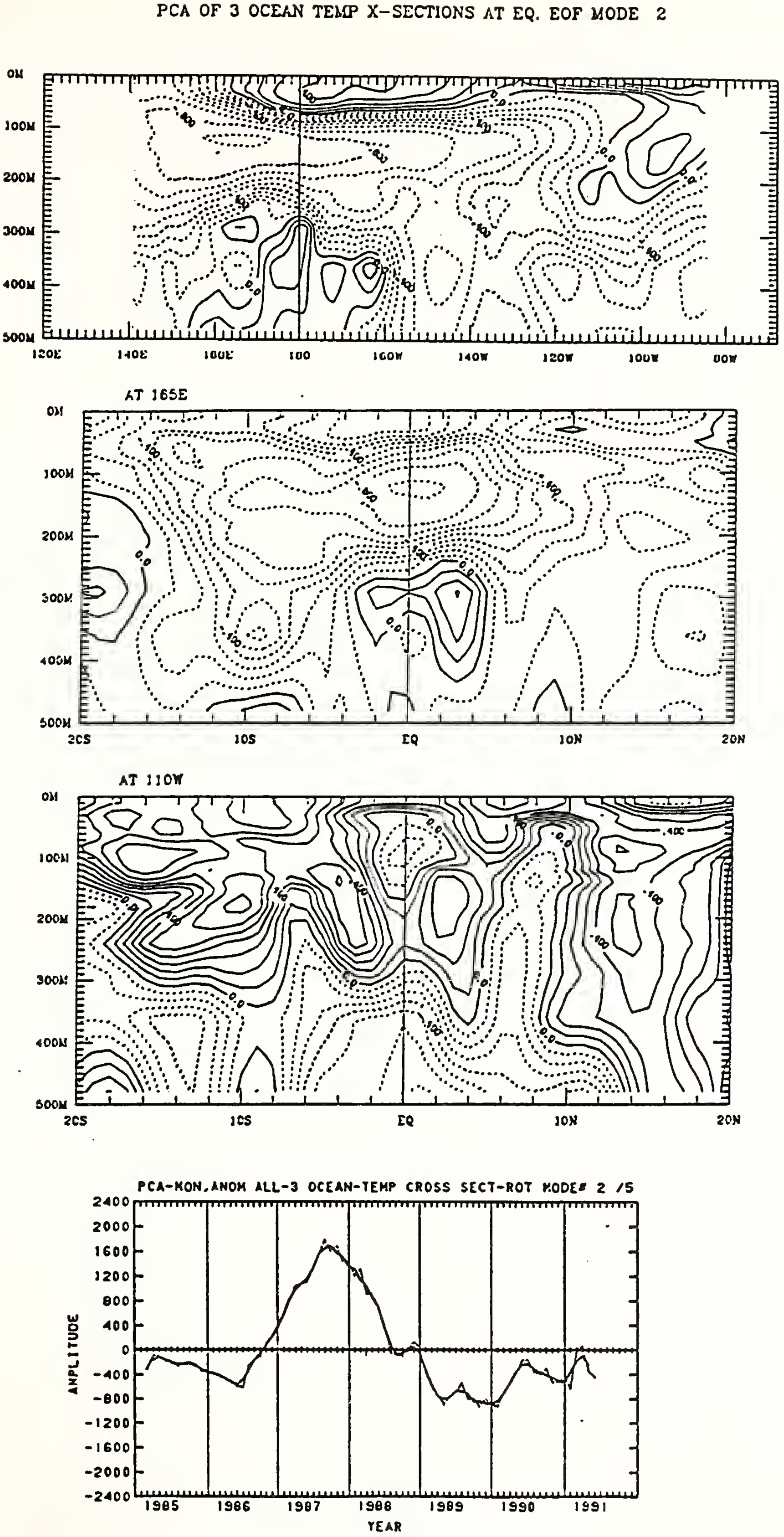

Fig. 3. As in Fig. 2, but for the second mode.

# Uncertainties in SST Analyses Due to Historical Changes in Data Distribution

Diane C. Marsico and Richard W. Reynolds
Coupled Model Project NMC/NWS/NOAA
Washington, D.C. 20233 U.S.A

Chester F. Ropelewski
Climate Analysis Center NMC/NWS/NOAA
Washington, D.C. 20233 U.S.A

Historical analyses of sea surface temperature (SST) fields depend on coverage provided by ships and (more recently) buoys. This data coverage is not constant with time. During the last one hundred years there have been shifts in the data distribution due to e.g., changes in trade, conversion from wind- to steam- driven ships and opening of canals. We will measure here the uncertainty involved in analyzing SST fields incurred by spatial sampling and observe how this uncertainty changes with time.

We chose for our initial study to look at three decades which have different ship track patterns (1880's, 1920's and 1970's) and two months (February and August) to sample the seasonal cycle. We acquired the monthly number of observations and mean observation location for each 2° box from the COADS (Comprehensive Ocean-Atmosphere Data Set) MSTG (Monthly Summary Trimmed Groups) gridded fields. Figure 1 shows the data distributions for August in the three decades of this study. In the 1880's (top panel), the most heavily traveled regions were in the North Atlantic and in the South Atlantic where ships proceeded around Cape Horn and Cape of Good Hope. In the Pacific the data is scattered with a data void in the western tropical Pacific. The 1920's (middle panel) show an increase in coverage in the North Atlantic and some well-defined ship tracks in the Pacific. The effects of the opening of the Panama Canal are evident in the new ship traffic in the canal region and a decrease in traffic around Cape Horn. The 1970's (lower panel) show an overall increase in coverage. Most of the oceans are well-covered with the exception of the Antarctic, the western South Atlantic and the eastern South Pacific. The 1970's are representative of the current *in situ* data coverage without satellite data.

In order to separate the effect of spatial variations in actual temperature from the effects due to sampling, we set the SST anomaly to 1°C for all observations. We analyzed the fields using optimum interpolation (OI) with a first guess of 0°C. The resulting fields have values ranging from 0°C to 1°C. This method effectively converts a given data distribution into a normalized SST field. A SST value near 1°C indicates that the data distribution was sufficient to produce a well-defined SST; a value near 0°C indicates no data.

Figure 2 shows the decadal means of the normalized SST for the three periods. As expected, the patterns resemble the data distributions in figure 1. Very small values are observed in the Pacific in the 1880's (top panel) with the exception of small regions with values of 0.6°C to 0.9°C off California and Mexico. The normalized SST gets stronger in the 1920's and 1970's. Still, the central tropical Pacific has only a modest value in the 1970's. The decadal means for February (figure 3) are similar to those for August but have a larger SST in the Antarctic in the southern hemisphere summer.

In order to estimate the effects of sampling on large scale mean SST anomalies, we separated the ocean into five basins and computed means. Figure 4 shows the mean result for each basin in August of the three decades. The North Pacific is close to perfect (mean normalized SST equals 0.93°C) in the 1970's but only has a mean value of .21°C in the 1880's. Thus, if the SST anomaly were constant at 1°C as we assumed, a time series of the mean SST for this region would show variations of up to 0.72°C (the difference between 0.93 and 0.21) simply due to sampling. Note also, despite the fact that the 1920's have more data globally than the 1880's, the 1880's are slightly better in the South Atlantic than the 1920's. The results for each basin are similar in February (not shown).

These results demonstrate that regional data distribution must be considered. Our goal, upon completion of this study, is to quantify, as a function of time and location, the error that can be expected with historical estimates of SST.

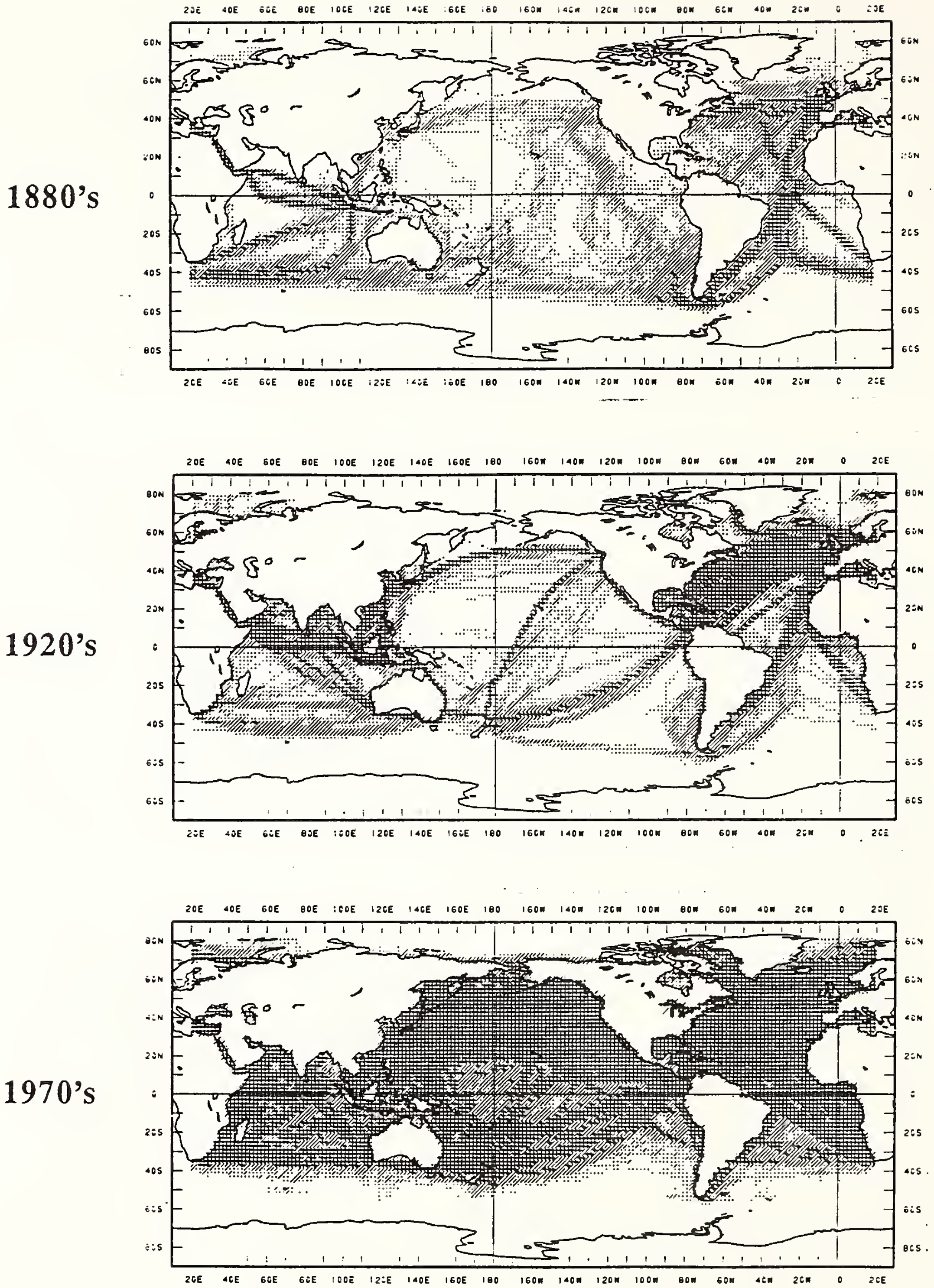
1880's
1920's
1970's
20E 40E 60E 80E 100E 120E 140E 160E 180 160W 140W 120W 100W 80W 60W 40W 20W 0 20E
80N 60N 40N 20N 0 20S 40S 60S 80S

Figure 1: The number of years in the decade with observations in August. Dots represent 2° boxes with obs in 1 to 3 years. Slashes represent 4 to 7 years. Plus signs represent 8 to 10 years.

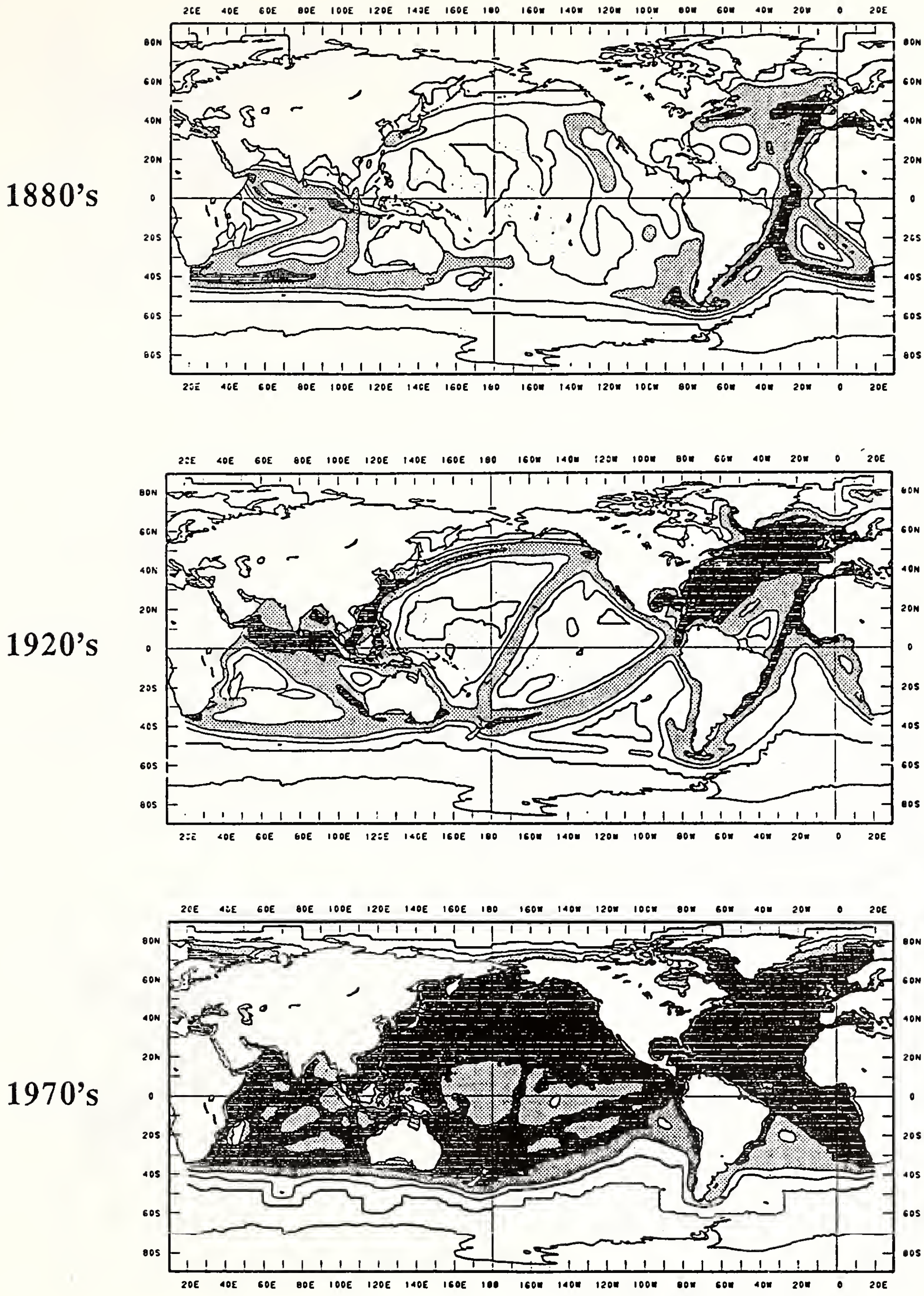
1880's
1920's
1970's
20E 40E 60E 80E 100E 120E 140E 160E 180 160W 140W 120W 100W 80W 60W 40W 20W 0 20E
80N 60N 40N 20N 0 20S 40S 60S 80S

Figure 2: Decadal means of normalized SST for August. Heavy contours are at 0°C. Light contours are at 0.3°C, 0.6°C, and 0.9°C. Regions between 0.6°C and 0.9°C are lightly shaded. Regions greater than 0.9°C are heavily shaded.

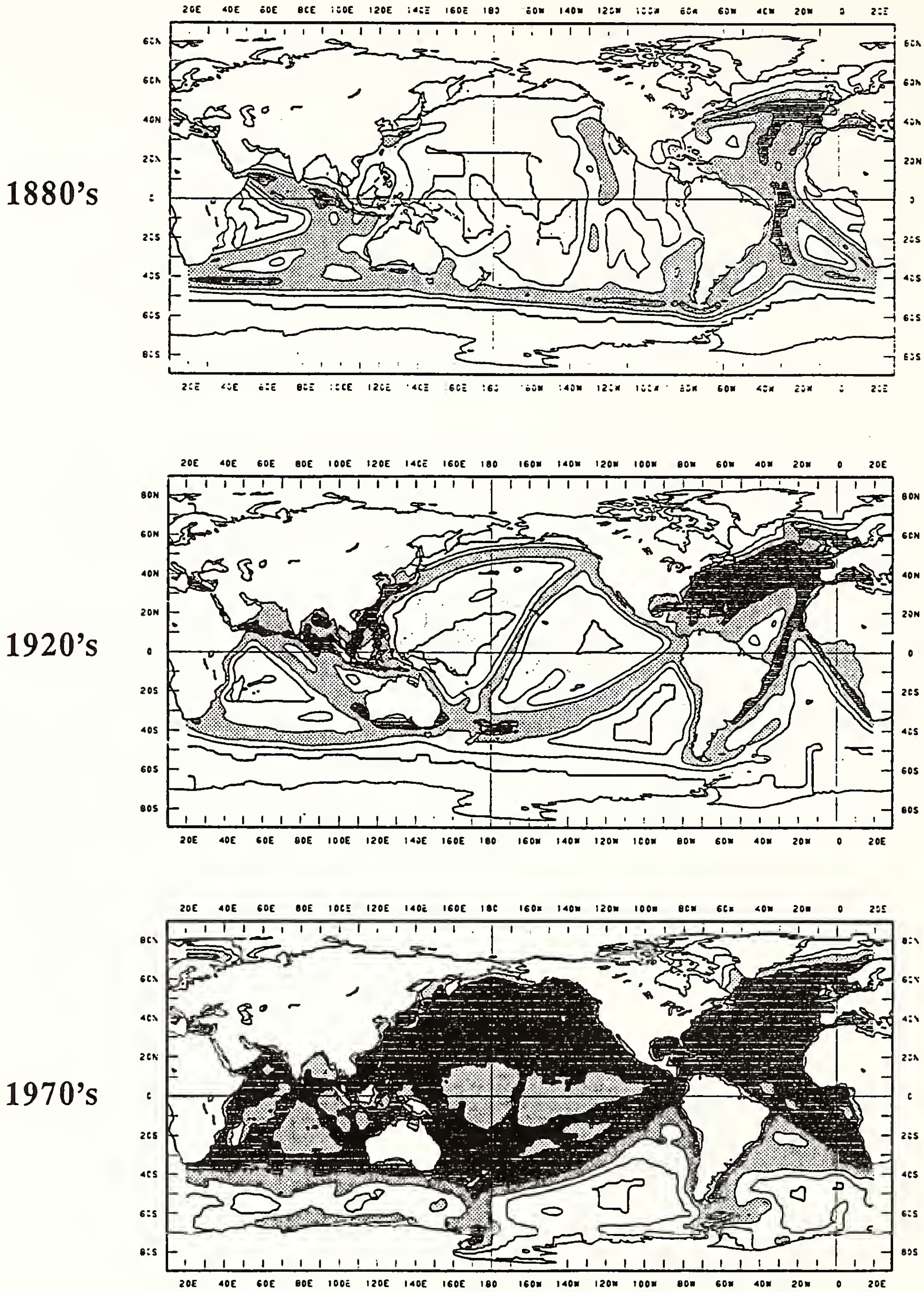
1880's
1920's
1970's
20E 40E 60E 80E 100E 120E 140E 160E 180 160W 140W 120W 100W 80W 60W 40W 20W 0 20E
80N 60N 40N 20N 0 20S 40S 60S 80S

Figure 3: Decadal means of normalized SST for February. Heavy contours are at 0°C. Light contours are at 0.3°C, 0.6°C, and 0.9°C. Regions between 0.6°C and 0.9°C are lightly shaded. Regions greater than 0.9°C are heavily shaded.

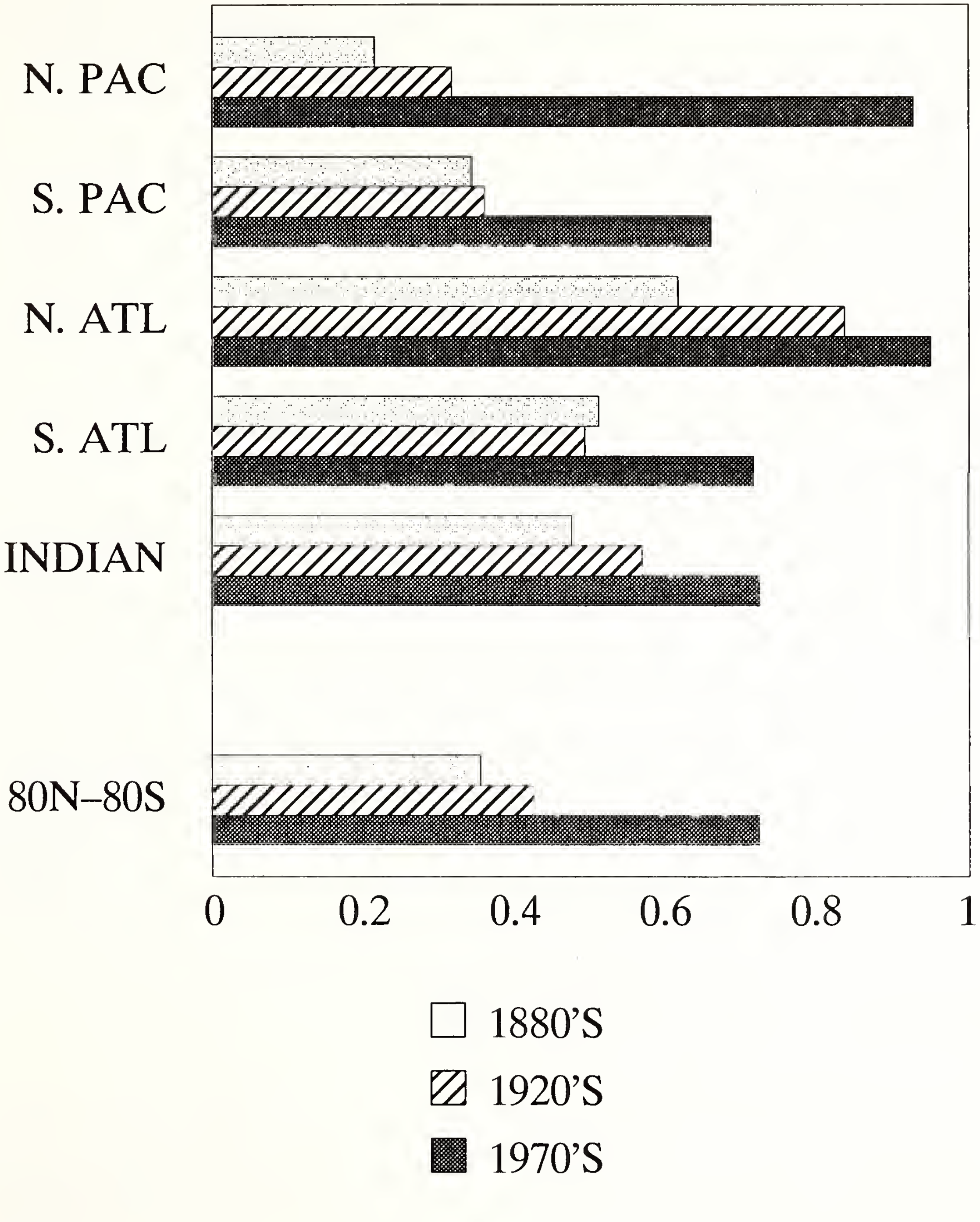

Figure 4: Decadal means of normalized SST (°C) for August averaged over each ocean basin. Ocean areas only. Each box is area-weighted.

# Comparison of Vertical Mixing Schemes for Ocean General Circulation Models

Chung-Chun Ma, Yi Chao, Carlos R. Mechoso
and William M. Weibel
*Department of Atmospheric Sciences, University of California, Los Angeles, CA 90024*

David Halpern
*JPL/Caltech, MS 300-323, 4800 Oak Grove Drive, Pasadena, CA 91109*

## 1 Introduction

Ocean general circulation models (OGCMs) are forced by fluxes of heat and momentum applied to the ocean surface. Vertical mixing by subgrid-scale turbulent processes plays a crucial role in distributing these forcings to the ocean interior. The vertical turbulent mixing is also important in determining the structure of the thermocline and the Equatorial Undercurrent. The parameterization of vertical mixing, therefore, is one of the key issues in oceanic modeling.

Models with simple mixing schemes using coefficients depending on the Richardson number have had reasonable success in modeling the thermal structure of the upper ocean (e.g., Philander *et al.* 1987). However, in these first-order closure schemes the turbulent fluxes are locally related to the mean flow. In particular, no transport effect on the turbulence fields is taken into account. Higher-order closure schemes have been designed to take into consideration the energetics of the turbulence (e.g., Mellor and Yamada 1974, 1982).

In this paper we analyze the sensitivity of simulations by an OGCM in the uncoupled mode to a first-order and a second-order turbulence closure schemes.

## 2 Model Description

The model we use in this study is the OGCM developed at the NOAA Geophysical Fluid Dynamics Laboratory (GFDL)/Princeton University by K. Bryan and M. D. Cox (Bryan 1969, Cox 1984). The model is based on the primitive equations with the Boussinesq approximation. Depth is used as the vertical coordinate. The top of the model is assumed to be a rigid lid.

The domain of the model is the tropical Pacific, from 130°E to 70°W in longitude, and 28°S to 50°N in latitude. In longitude the resolution is 1°. In latitude the mesh spacing is $\frac{1}{3}°$ between 10°S and 10°N, and decreases gradually polewards. There are 27 layers in the vertical, with a 10-meter resolution in the topmost 10 layers. The ocean bottom is at a constant depth of approximately 4150 m.

### 2.1 Forcing of the Model

The wind stress used to force the OGCM is obtained from the monthly wind stress climatology by linearly interpolating to daily values.

Concerning the determination of heat flux at the ocean surface, one of the methods follows Philander *et al.* (1987). In this case the short-wave solar heating and the long-wave radiation are assumed to be simple, zonally uniform distributions that approximate annual mean conditions. The sensible and latent heat fluxes are computed according to the bulk aerodynamic formulae from air temperature linearly interpolated from monthly climatology and the sea surface temperature (SST) produced by the OGCM.

Complementary to the method above, we also investigate the response of the OGCM to surface heat fluxes produced by the AGCM in an uncoupled simulation. In this case, the heat flux is taken from the monthly-mean fields obtained in a multi-year simulation with the 9-layer, coarse resolution (4° latitude by 5° longitude) version of the UCLA AGCM with prescribed SST corresponding to an observed monthly climatology.

### 2.2 Parameterization of Vertical Mixing

We consider two parameterizations of vertical mixing by subgrid-scale turbulence in the OGCM. A parameterization scheme that has been widely used in ocean models is that proposed by Pacanowski and Philander (1981). It is a first-order closure scheme, in which the eddy viscosity and diffusion coefficients are assumed to depend on the Richardson number. This scheme has been shown to give reasonable results in the tropical ocean when the ocean model is forced with observed wind stress and the heat flux parameterization described above (Pacanowski and Philander 1981).

The other scheme we consider is the Mellor-Yamada level $2\frac{1}{2}$ second-order closure scheme (Mellor and Yamada 1974, 1982; Rosati and Miyakoda 1988). In this scheme the turbulent kinetic energy and the mixing length are predicted. Therefore changes in the structure of turbulence due to advection, diffusion and generation by buoyancy and shear are taken into account.

## 3 Comparison of Simulations

### 3.1 Surface Heat Flux Estimated from Air Temperature

The OGCM was integrated for three years using the first- and second-order closure schemes (which we will call experiments OOK1 and OOK2, respectively). Both experiments started with an ocean at rest. The initial temperature and salinity correspond to the January

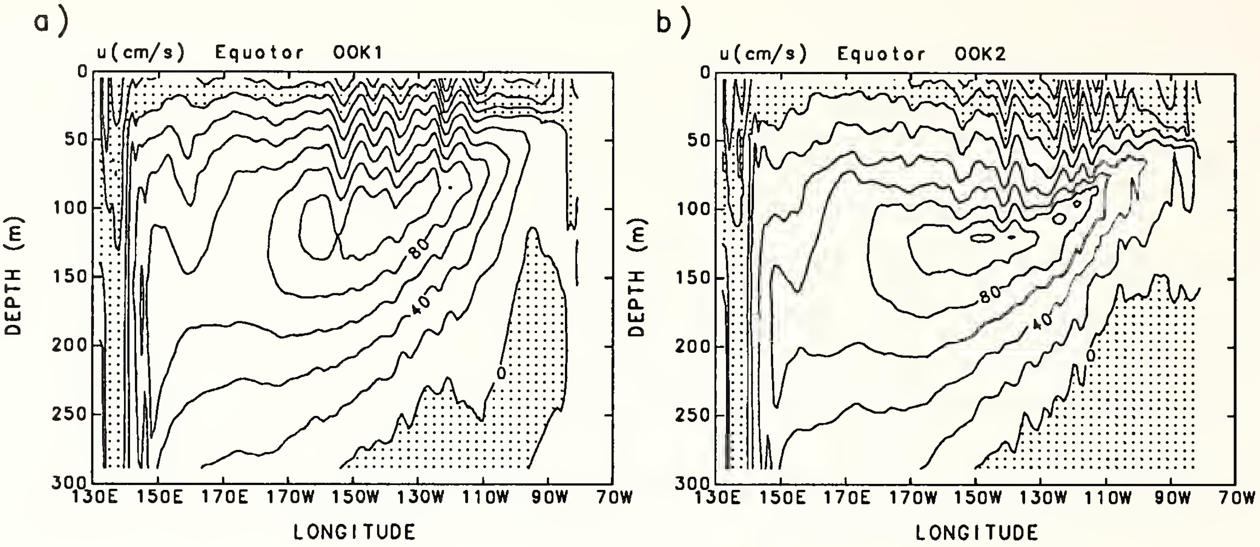

Figure 1: Cross-sections of zonal current along the equator in mid-July of year 3 from experiments (a) OOK1 and (b) OOK2. Contour interval is 20 cm $s^{-1}$. Regions with westward flow are shaded.

climatology. Experiment OOK1, therefore, is basically a repetition of the run made by Philander *et al.* (1987).

We find that, in general, there are no dramatic differences between simulations with the two mixing schemes. The Equatorial Undercurrent simulated in both experiments has comparable strength (Fig. 1). In OOK2 the Undercurrent core is slightly weaker and deeper, and shifted towards the west. Equatorial cross-sections of temperature are shown in Fig. 2. Figure 3 shows the time variations of zonal velocity at the equator and 139°W. Overall, the second-order closure scheme appears to produce stronger mixing in the tropics and the winter subtropics, as shown by the deeper mixed layer and the deepening and weakening in the core of the Equatorial Undercurrent. The difference in temperature structure is more readily seen in the eastern part of the ocean. Surface currents are also weaker in OOK2. The thermocline, however, is better-defined despite the apparent stronger mixing.

## 3.2 Surface Heat Flux from Uncoupled AGCM

The SSTs obtained with the two different mixing schemes using the heat flux from uncoupled AGCM simulations (experiments OAK1 and OAK2, respectively) are shown in Fig. 4. The wind stress used is the same as in OOK1 and OOK2. Between 20°N and 30°N, the temperature from both experiments is unrealistically high. It should be noted that the heat flux does not interact with SST in this set of experiments. When the sea surface warms up, the heat flux from the atmosphere does not adjust accordingly. In the case of OAK1, the mixing decreases as the Richardson number becomes large. In the case of OAK2, the buoyancy generation of turbulence decreases as the stratification becomes more stable. The turbulent vertical mixing becomes very inefficient due to the accumulation of heat near the

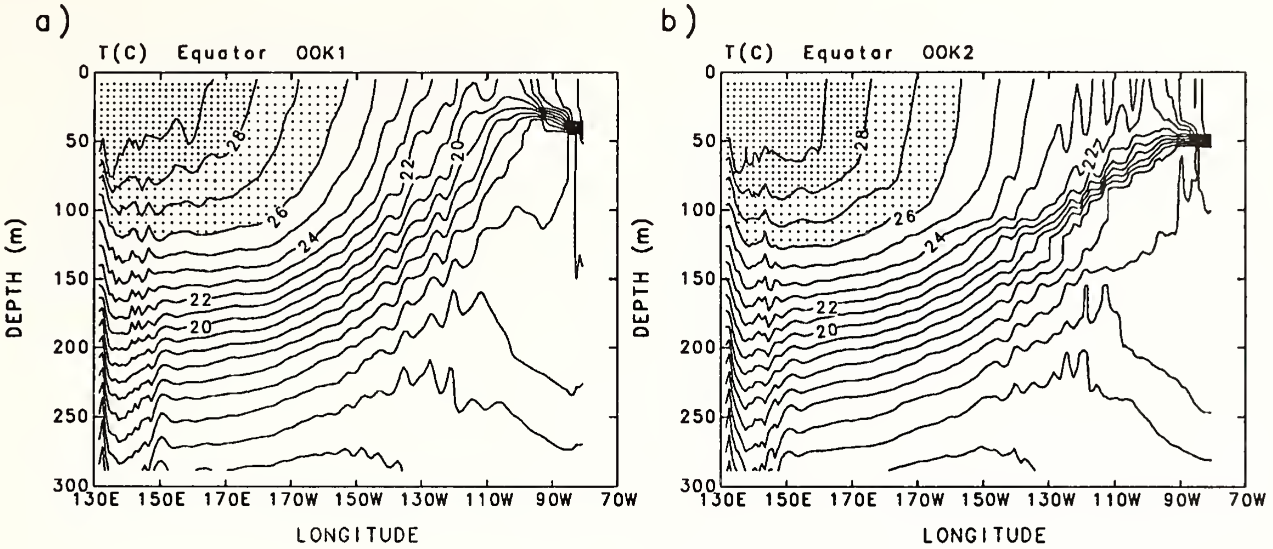

Figure 2: Cross-sections of temperature along the equator in mid-July of year 3 from experiments (a) OOK1 and (b) OOK2. Contour interval is 1°C. Regions with temperature higher than 26°C are shaded.

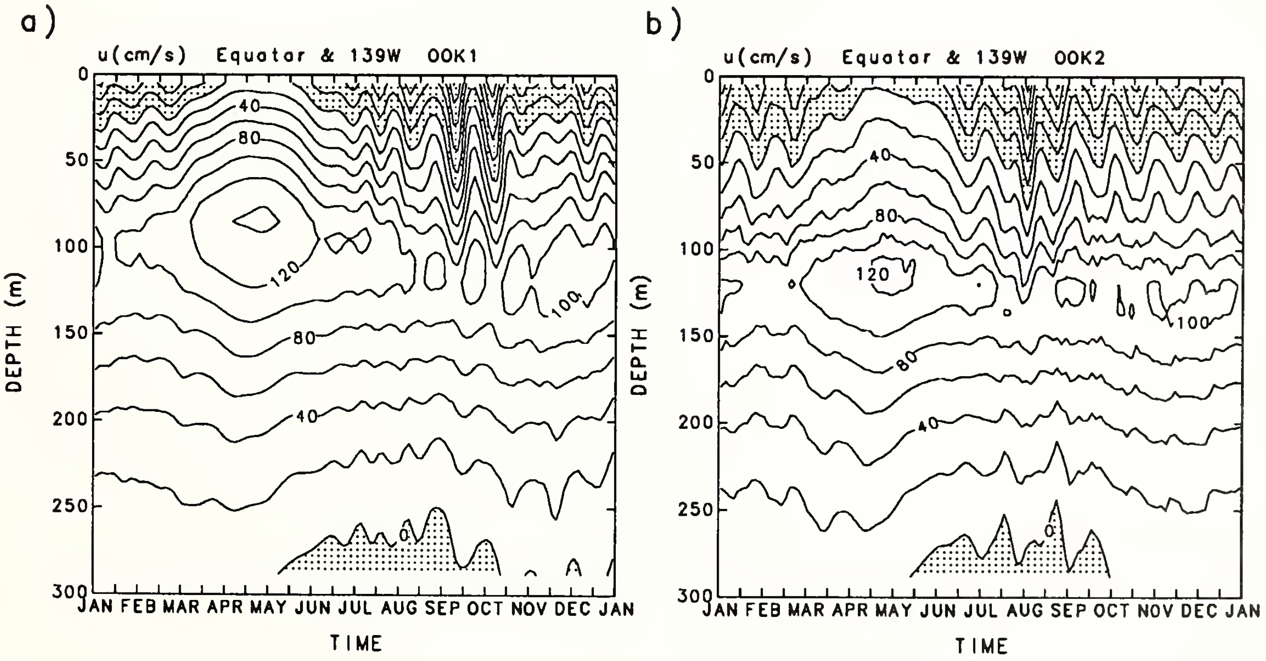

Figure 3: Time-depth plots of zonal velocity at the equator and 139°W for the third year of experiments (a) OOK1 and (b) OOK2. Contour interval is 20 cm s$^{-1}$. Regions with westward flow are shaded.

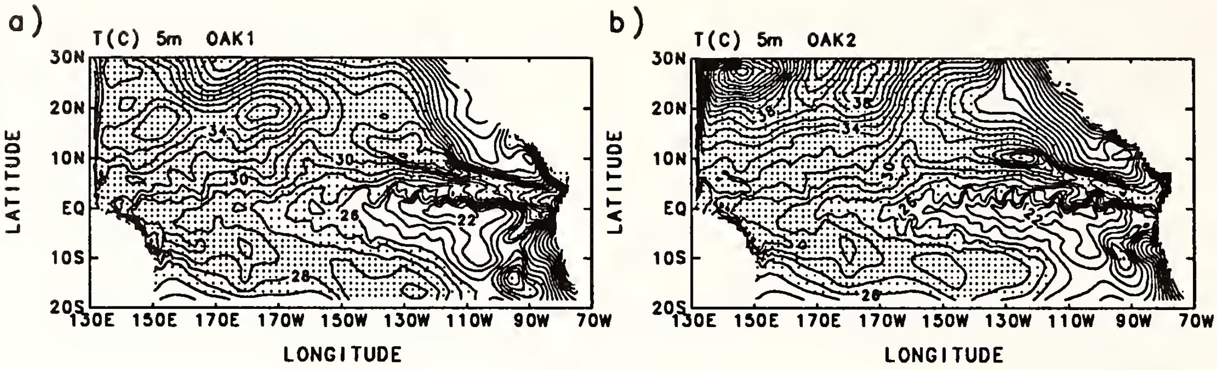

Figure 4: Sea surface temperature after six months of model integration for experiments (a) OAK1 and (b) OAK2. Contour interval is 1°C. Regions with temperature higher than 26°C are shaded.

surface. As a result the surface gets warmer. The positive feedback led to the unrealistic SST.

## 4 Conclusion

We examined simulations performed with an ocean GCM for the tropical Pacific Ocean with first-order and second-order turbulence closure schemes for vertical mixing. No dramatic differences were found between the results obtained with different mixing schemes. The second-order closure scheme in general gives stronger mixing in the tropics and the winter subtropics. The Equatorial Undercurrent, however, has comparable strength with either mixing scheme used. With the second-order closure scheme the model produces a better-defined mixed layer and a sharper thermocline.

When the heat flux produced by the uncoupled AGCM is used as forcing to the OGCM, the model produces unrealistically high SST in the summer subtropics. This suggests potential problems when the two models are coupled together. The last word, however, has to be given by the coupled simulation: Whether run-away processes take place and lead to a climate drift, or negative feedbacks result in a reasonable climatology for the coupled system. Those aspects are discussed in the paper by Mechoso *et al.*, in this volume.

*Acknowledgements.* This work was supported by ONR under Grant N00014-89-J-1845, NSF and DARPA under Cooperative Agreement NCR-8919038 with the Corporation for National Research Initiatives, NASA RTOP 518-21-13 to JPL, and JPL contract 958658 to UCLA. Model integrations were performed at the San Diego Supercomputer Center and the NASA Ames Research Center.

# REFERENCES

Bryan, K., 1969: A numerical method for the study of the circulation of the world ocean. *J. Comp. Phys.*, **4**, 347-376.

Cox, M. D., 1984: A primitive equation, 3-dimensional model of the ocean. GFDL Ocean Group Tech. Rep. No. 1.

Mellor, G. L., and T. Yamada, 1974: A hierarchy of turbulence closure models for planetary boundary layers. *J. Atmos. Sci.*, **31**, 1791-1806.

—–, and —–, 1982: Development of a turbulence closure model for geophysical fluid problems. *Rev. Geophys. and Space Physics*, **20**, 851-875.

Pacanowski, R. C., and S. G. H. Philander, 1981: Parameterization of vertical mixing in numerical models of tropical oceans. *J. Phys. Oceanogr.*, **11**, 1443-1451.

Philander, S. G. H., W. J. Hurlin, and A. D. Seigel, 1987: Simulation of the seasonal cycle of the tropical Pacific Ocean. *J. Phys. Oceanogr.*, **17**, 1986-2002.

Rosati, A., and K. Miyakoda, 1988: A general circulation model for upper ocean simulation. *J. Phys. Oceanogr.*, **18**, 1601-1626.

# Different Surface Wind Products in the Tropical Pacific and their Impacts on Oceanic Circulation

Yi Chao
Department of Atmospheric Sciences, UCLA, Los Angeles, CA 90024

In the ocean, there are too few routine observations to perform synoptic descriptions of the ocean general circulation. In order to measure the subsurface thermal structure, the Expendable Bathythermographs (XBTs) are collected along ship tracks, and sea level is measured at tide gauge stations from selected islands. These observations have very limited spatial and temporal coverage, so that it is difficult to use these data sets to depict the ocean general circulation. Satellite altimetry opens a new way of measuring sea surface height with increased spatial and temporal resolutions. Although sea surface height is a good surrogate for the thermocline depth or heat storage in the upper ocean, it is difficult to use to provide a 3-dimensional description of ocean circulation. To better utilize satellite altimeter data, it is necessary to combine them with 3-dimensional ocean general circulation models.

The purpose of this study is to explore how realistically an ocean general circulation model forced with observed winds can simulate in situ and remotely measured sea level variabilities. There are in general two types of surface wind products which can be applied to the ocean model. One product comes from subjective analyses of directly ship-measured winds, e.g., those from Florida State University (FSU). Another product comes from sophisticated four-dimensional atmospheric data assimilation systems at operational centers, such as the European Center for Medium-Range Weather Forecasts (ECMWF). Ship-measured winds are more accurate than those from atmospheric models, however their spatial interpolations in data sparse areas are somewhat arbitrary and their temporal resolution is usually one month. Winds from atmospheric models have better spatial and temporal resolutions, but they are strongly influenced by the bias of an atmospheric model. It is therefore difficult to decide which wind product should be used for ocean modeling studies, without quantifying their similarities and differences.

To understand differences between these two types of wind products, the ship-measured winds from FSU are compared with winds from ECMWF. The resolution of the FSU winds is $2^o$ longitude and latitude with a time interval of one month, and that of the ECMWF winds is $2.5^o$ longitude and latitude with a time interval of 12 hours. Figure 1 shows longitude-time plots of zonal wind stress at $5^o$N from FSU and ECMWF, respectively. At this latitude from 1987 to 1988, it is noted that there are strong seasonal fluctuations in the zonal wind stress. Seasonal variations are similar between the FSU and ECMWF wind stress, but their amplitudes are significantly different. The ECMWF wind stress is about 30% weaker than the FSU wind stress. In this study, a constant drag coefficient of 0.0014 is used for both wind fields. Given the fact that FSU winds are monthly mean and ECMWF are twice-daily, a more realistic drag coefficient formulation (Trenberth et al., 1989) will give even larger differences between the two wind fields.

It is expected that differences between the FSU and ECMWF winds will have significant impact on model-simulated dynamic height. The model used to perform the sensitivity studies is a tropical Pacific general circulation model described in Chao et al. (1991). The initial condition of the model was the climatological January distribution of temperature and salinity (Levitus, 1982). The climatological monthly mean surface wind stress of Hellerman and Rosenstein (1983) was used to spin up the model for 3 years by which time a quasi-equilibrium seasonal cycle was established in the upper ocean. Then monthly mean FSU winds or twice-daily ECMWF winds were applied to the model from January 15, 1986 to January 15, 1989. Surface dynamic height (dyn cm) is then calculated relative to 400 meters to compare with sea level observations from the TOGA Sea Level Center at University of Hawaii, which are treated as the ground truth for comparison purposes. Comparisons of model-simulated dynamic height using FSU and ECMWF winds and sea level are shown in Figure 2 at 12 selected tide gauge stations, and the statistics of the comparisons are displayed in Table 1. It is seen that seasonal and interannual fluctuations of sea level are reasonably reproduced in both simulations with comparable correlation coefficients with the observed sea level. Yet the amplitude of the ECMWF-simulated dynamic height is significantly smaller than that of the FSU-simulated dynamic height. The average standard deviation of the FSU-simulated dynamic height is 7.1 cm, which is close to that of the observed sea level of 9.8 cm; while that of the ECMWF-simulated dynamic height is only 5.5 cm.

In conclusion, a tropical Pacific ocean general circulation model forced with observed winds can realistically produce sea level variabilities as compared with tide gauge measurements. Ship-measured winds of FSU are significantly different from the ECMWF-analyzed winds. The amplitude of the ECMWF winds is about 30% weaker than that of the FSU winds. These differences in surface wind forcings produce significantly different model-simulated dynamic height, as compared with sea level measurements. Results indicate potential problems in using the ECMWF winds to assimilate satellite altimeter data into tropical Pacific general circulation models.

**Acknowledgements**: This work is supported by NASA RTOP 578-21-13 to JPL and by JPL Contract 958658 to UCLA. I am very grateful to Dr. David Halpern (JPL) and Professor Carlos R. Mechoso (UCLA) for their continuous encouragement. Computations were performed at NASA's Ames Research Center Numerical Aerodynamics Simulation Facility.

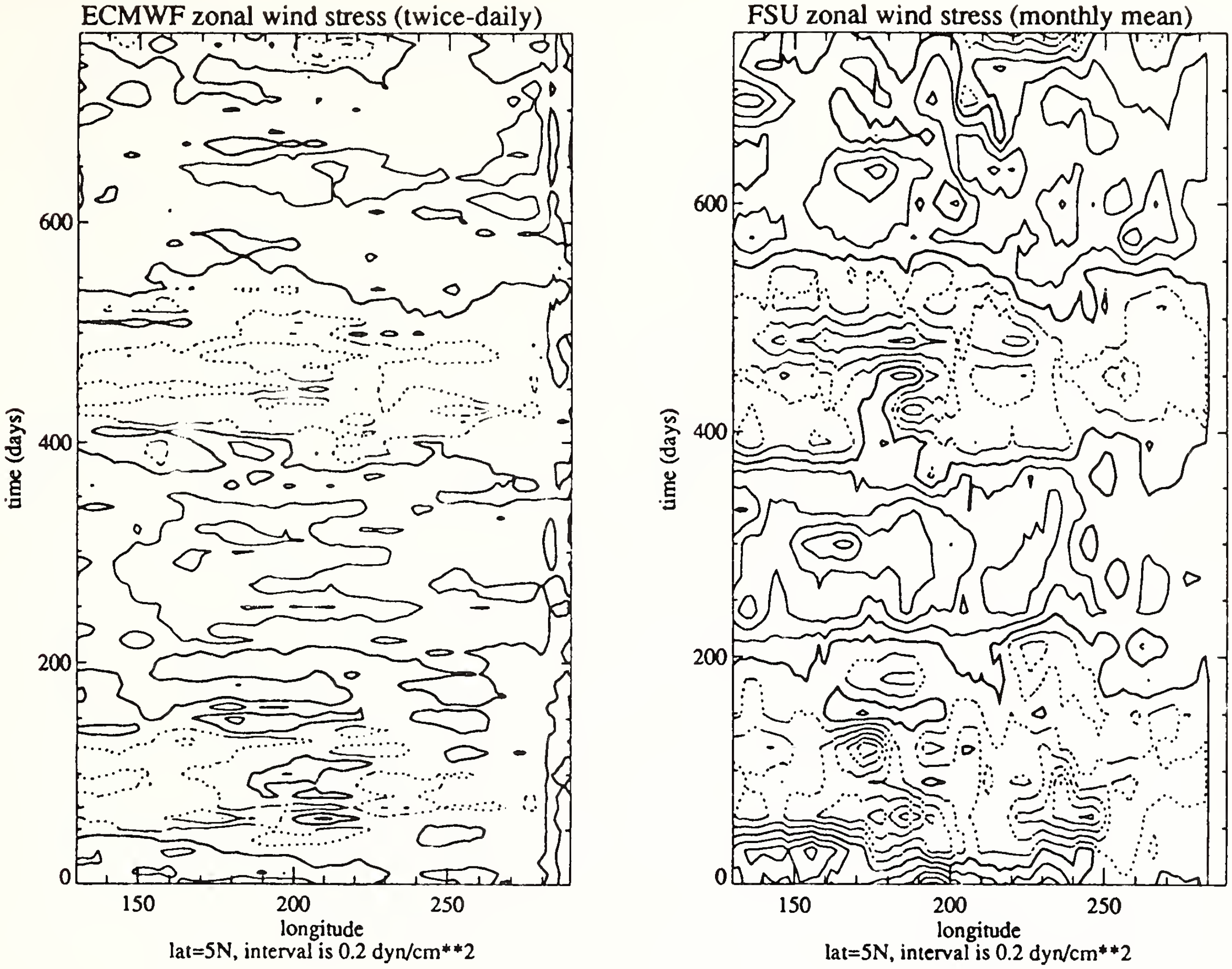

Figure 1 Longitude-time plots of zonal wind stress at $5^{o}$N, calculated from FSU and ECMWF analyses, respectively. Time goes from November 15, 1986 to January 15, 1989. The contour interval is 0.2 dyn/cm$^2$. The annual mean has been removed. Solid lines indicate westerly anomalies and dashed lines indicate easterly anomalies.

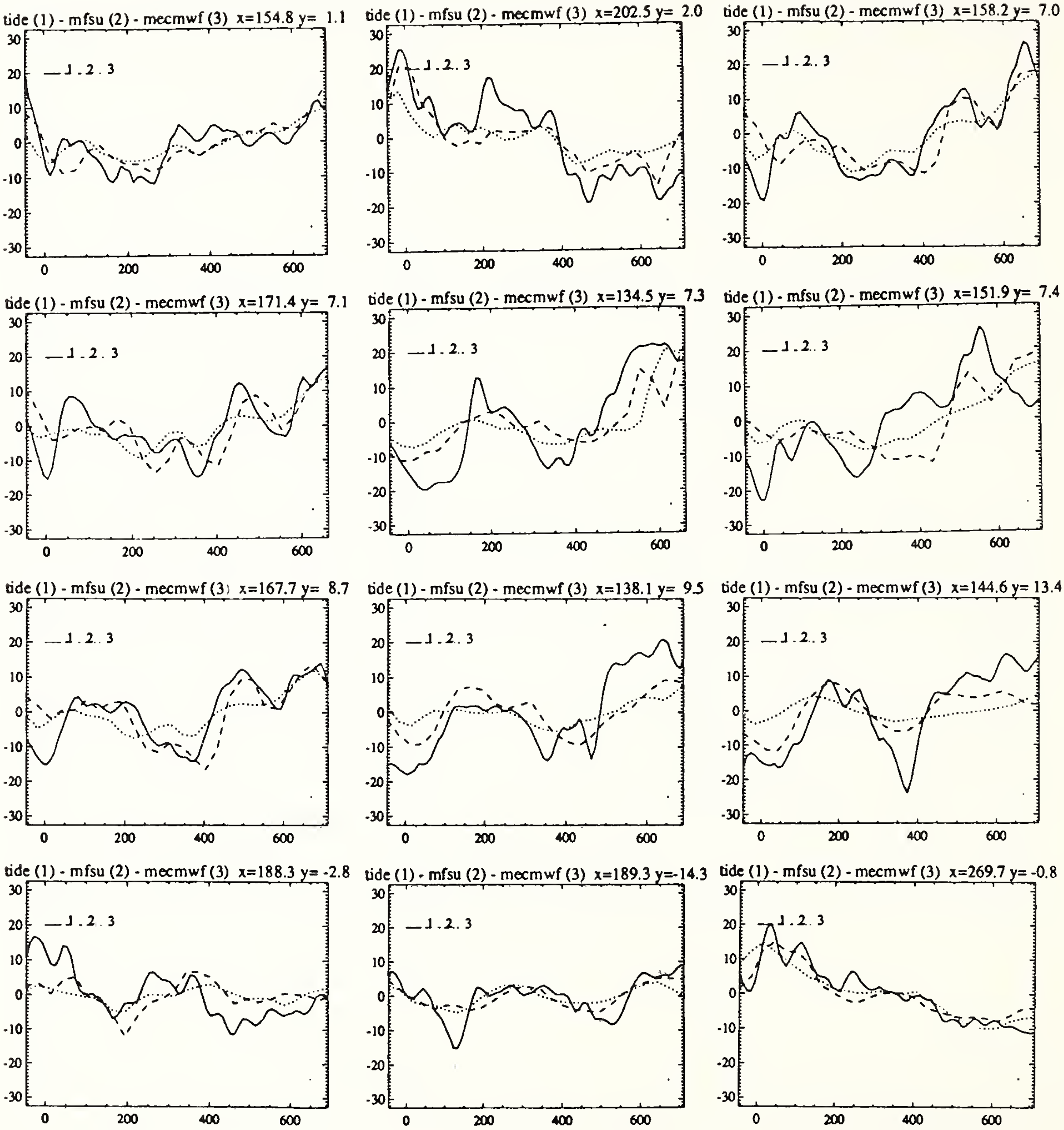

Figure 2 Time series of sea level anomalies at 12 selected tide gauge stations (x=longitude, y=latitude). Solid lines represent tide gauge measurements, dashed and dotted lines represent model simulations using the FSU and ECMWF winds, respectively. The unit is in cm.

Table 1 Standard deviations of sea level from tide gauge, the FSU and ECMWF simulations; correlation coefficients (tide gauge with the FSU simulation and tide gauge with the ECMWF simulation) at 12 selected stations and their corresponding averages. The unit is in cm.

| Location | S. D.(tide) | S.D.(fsu) | S.D.(ecmwf) | Corr(tide,fsu) | Corr(tide,ecmwf) |
|---|---|---|---|---|---|
| Kapingamarangi<br>154.8°E, 1.1°N | 6.6 | 6.3 | 4.4 | 0.74 | 0.72 |
| Christmas<br>157.5°W, 2.0°N | 11.9 | 7.8 | 4.8 | 0.86 | 0.86 |
| Ponape<br>158.2°E, 7.0°N | 11.0 | 9.1 | 7.8 | 0.77 | 0.89 |
| Majuro<br>171.4°E, 7.1°N | 8.3 | 7.3 | 5.7 | 0.62 | 0.71 |
| Malakal<br>134.5°E, 7.3°N | 13.5 | 8.3 | 8.2 | 0.78 | 0.69 |
| Truk<br>151.9°E, 7.4°N | 11.3 | 9.6 | 7.4 | 0.44 | 0.55 |
| Kwajalein<br>167.7°E, 8.7°N | 8.4 | 7.9 | 5.4 | 0.73 | 0.72 |
| Yap<br>138.1°E, 9.5°N | 11.4 | 6.0 | 3.3 | 0.72 | 0.72 |
| Guam<br>144.6°E, 13.4°N | 11.4 | 5.6 | 2.4 | 0.85 | 0.60 |
| Canton<br>171.7°W, 2.8°S | 7.0 | 3.9 | 1.9 | 0.39 | 0.37 |
| Pago Pago<br>170.7°W, 14.3°S | 5.5 | 3.2 | 2.4 | 0.75 | 0.74 |
| Santa Cruz<br>90.3°W, 0.8°S | 8.1 | 6.6 | 7.1 | 0.91 | 0.89 |
| Average | 9.8 | 7.1 | 5.5 | 0.71 | 0.71 |

# Coupled interaction in the equatorial eastern Pacific

**Ming Ji**
**Arun Kumar**
**Ants Leetmaa**

**Coupled Model Project**
**National Meteorological Center**

**NOAA**
**Washington D.C.**

## Introduction

A dedicated project was formed at the National Meteorological Center in March, 1991 to develop seasonal climate prediction capability using coupled ocean–atmospheric models. The atmospheric model we use is a T40 variation of the NMC's 1991 version of the Medium Range Forecast model (MRF91), the ocean model is developed at the NOAA's Geophysical Fluid Dynamic Laboratory (GFDL), it is a Pacific basin, high resolution muti–layer ocean GCM model. Currently our effort is focused on tuning the boundary layer parameterization of the atmospheric model to make it more suitable for climate prediction purpose and studying behaviors of both the atmospheric model and coupled model such as model climate, annual cycle, and interannual variabilities.

In the equatorial eastern Pacific ocean, the annual march of the ITCZ zone, a region of strong convection and rainfall, cross equator and the disappearance and reappearance of the equatorial cold tongue in SST is a result of strong coupled ocean atmosphere interaction. Study by Mitchell and Wallace (1991) using historical climate data of observed SST, OLR, sea level pressure (SLP), and surface wind suggests that this annual variation of SST and convection is essentially independent of the interannual basin scale variation of SST, namely the EL Nino–Southern Oscillation (ENSO) phenomena, instead, this is rather a coupled effect of the eastern Pacific region. Our study using tuned atmospheric model forced with climate SST show that the atmosphere model can reproduce the annual march of the convection zone similar to that of observed annual variations, and results of an 8 year coupled model experiment suggests that the cross equatorial circulation in the eastern Pacific region has weak link to the circulation further to the west.

## Discussion

a.) Tuning the atmospheric model.

This first obstacle we have to overcome is that the surface stress produced by short to medium range forecast model is too weak to force the ocean model for climate prediction purpose. This results an immediate relaxation of ocean thermocline, and the coupled system goes into an El Nino state. This is sometimes called a climate crash. Tuning of some atmospheric model boundary layer parameters can help to increase the surface stress and prevent severe climate crash from happening. Figure 1 show effects of tuning of the convective parameterization and diffusion of moisture and momentum fluxes of the atmospheric model. Figure 1a is monthly averaged surface stress over the Pacific basin for July 1990, figure 1b is monthly averaged rainfall (in mm/day) for the same month. Top panels in these figures are results from an untuned model, middle panels are results from a model with tuned convective parameterization only, and bottom panels are results of tuning of both convective parameterization and diffusion of moisture and momentum. Clearly, the strength of surface stress on the equator has increased significantly and the ITCZ zone becomes better organized as results of these tunings. This shows that the surface fluxes (heat and momentum) produced from the atmosphere mode, which are the fields that force the ocean, are very sensitive to the tuning of the atmospheric model boundary layer parameterizations, and therefore, it is important to properly tune the atmospheric model in order to achieve suitable surface fluxes for coupled models.

b.) Two year atmospheric model experiment forced with climate SST.

In this experiment, we forced the tuned atmospheric model (MRF91) with climate SST, and integrate the model for two years to study the annual variation of the tuned atmospheric model. Shown in figures 2–4 are changes of surface fields in the eastern Pacific region during spring transition season (March to May). Top panels of these figures are results from the model experiment, and bottom panels are results from observed climate data by Mitchell and Wallace(1991). Figure 2 show changes of surface stress and SST; figure 3 show changes of surface pressure(SLP) and surface wind, and figure 4 show changes of precipitation and surface wind. The OLR is used instead of precipitation in figure 4 in place of observed data since there is no historical observed precipitation data exist in the ocean. From these figures, we observe that the tuned atmospheric model behaves similar to observed spring transition season changes of the surface wind, surface pressure, surface wind and precipitation in response to the change of SST in the eastern Pacific region. This suggest that given climate SST, the tuned atmospheric model can simulate realistic annual cycle of the eastern Pacific which is result of strong coupled interaction. However, it remains a challenge to accomplish this by using coupled models with interactive SST.

c.) Eight year coupled model experiment

An eight year coupled model experiment was carried out to examine if our coupled model can display interannual variability similar to that of the El Nino–Southern Oscillation phenomena, and to study the annual cycle of the coupled model in the eastern Pacific region and its relationship to the basin scale interannual variation of the coupled system.

Shown in figure 5 is time variation of SST on the equator in the Pacific basin from the 8 year coupled integration (upper panel). We observe several important features from this figure. First, we observe that our coupled model does display robust annual cycle in the eastern Pacific and its amplitude is close to that of the climate SST (lower panel). Secondly, there is an initial warming trend of SST during the first year of the integration in the eastern Pacific. It takes about one and half to two years for SST to get back to normal. One possible cause of this initial warming is that there may be some imbalance between surface stress and initial ocean field which results to an eastward surge of warm water at the beginning of the integration, in other words, this could be indication of a mild climate crash; another possible explanation of the initial warming is that there may be climate signal (Calvin wave) exist in the initial ocean field which develops into this initial warming. Next, we observe that there is no apparent interannual time scale oscillation of SST, however, there is a gradual cooling of SST mostly evident in the western Pacific. The SST cools about 3 degree C. during the 8 year of integration in the western Pacific, in the contrary, if we ignore the initial warming of SST in the east, the SST in the eastern Pacific over the equatorial cold tongue region cools only about 1 degree C. during the same period. These feature lead us to conclude that although the coupled model failed to display ENSO like interannual variation of SST, it does suggest that the coupled interaction in the eastern Pacific is not strongly related to the event toward the west. As SST cools rather significantly in the western and central Pacific, the eastern Pacific annual cycle displayed little change except it amplitude.

In conclusion, we found that there is a strong coupled interaction in the eastern Pacific region which leads to robust annual cycle. This has been seen both from climate data study and from coupled model experiment. The interaction between monsoon–like cross equatorial circulation in the eastern Pacific and the Walker circulation seems to be weak, this interaction could be mainly in the form of modulation of the amplitude of the eastern annual cycle by conditions further to the west.

## References

Mitchell, T. P., and J. M. Wallace, 1991: On the Annual Cycle in Equatorial Convection and Sea Surface Temperature. submitted to J. Climate.

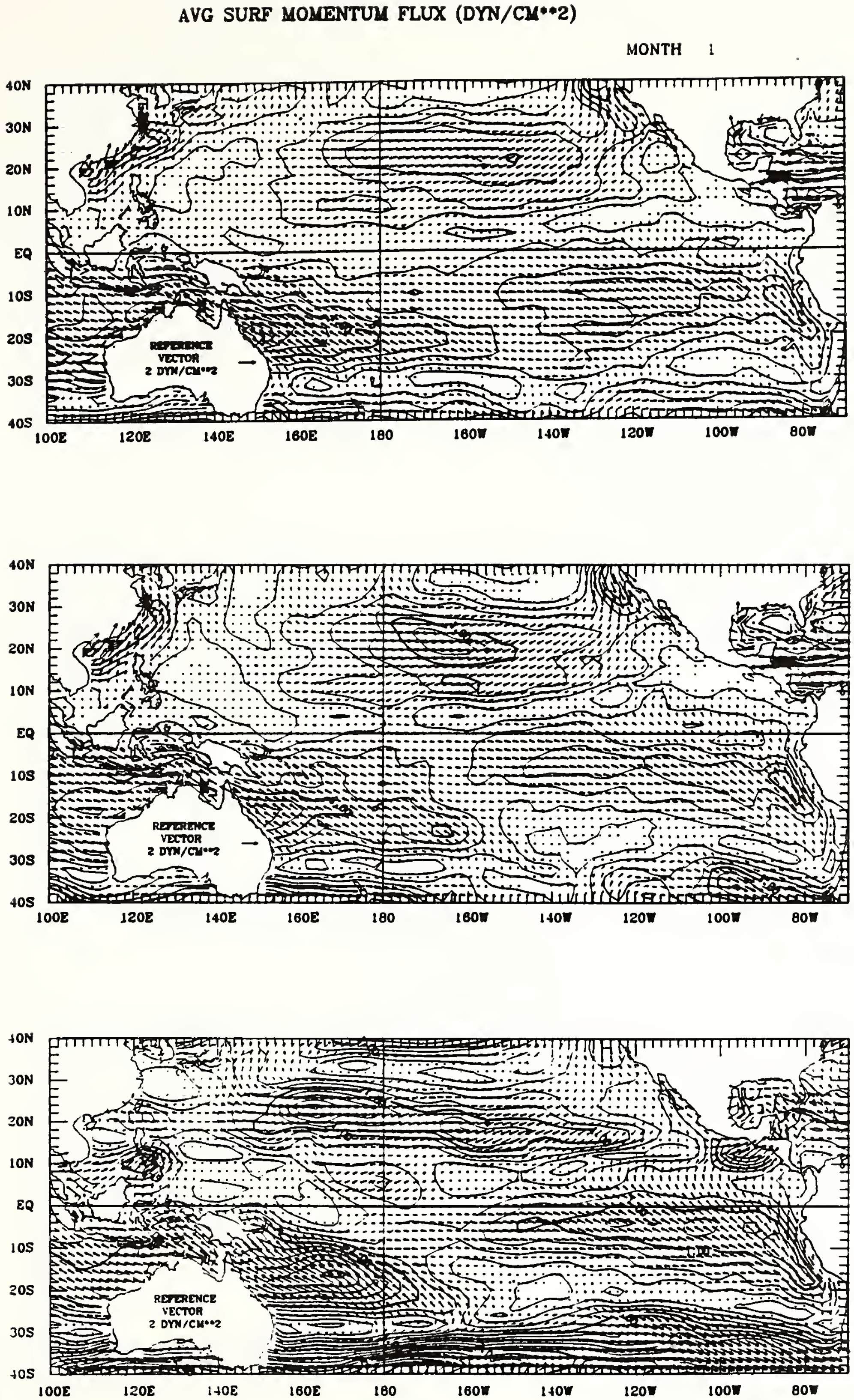

Figure 1a. Monthly averaged surface stress for July, 1990. The contour interval is 0.2 dyn./cm$^2$. (see text)

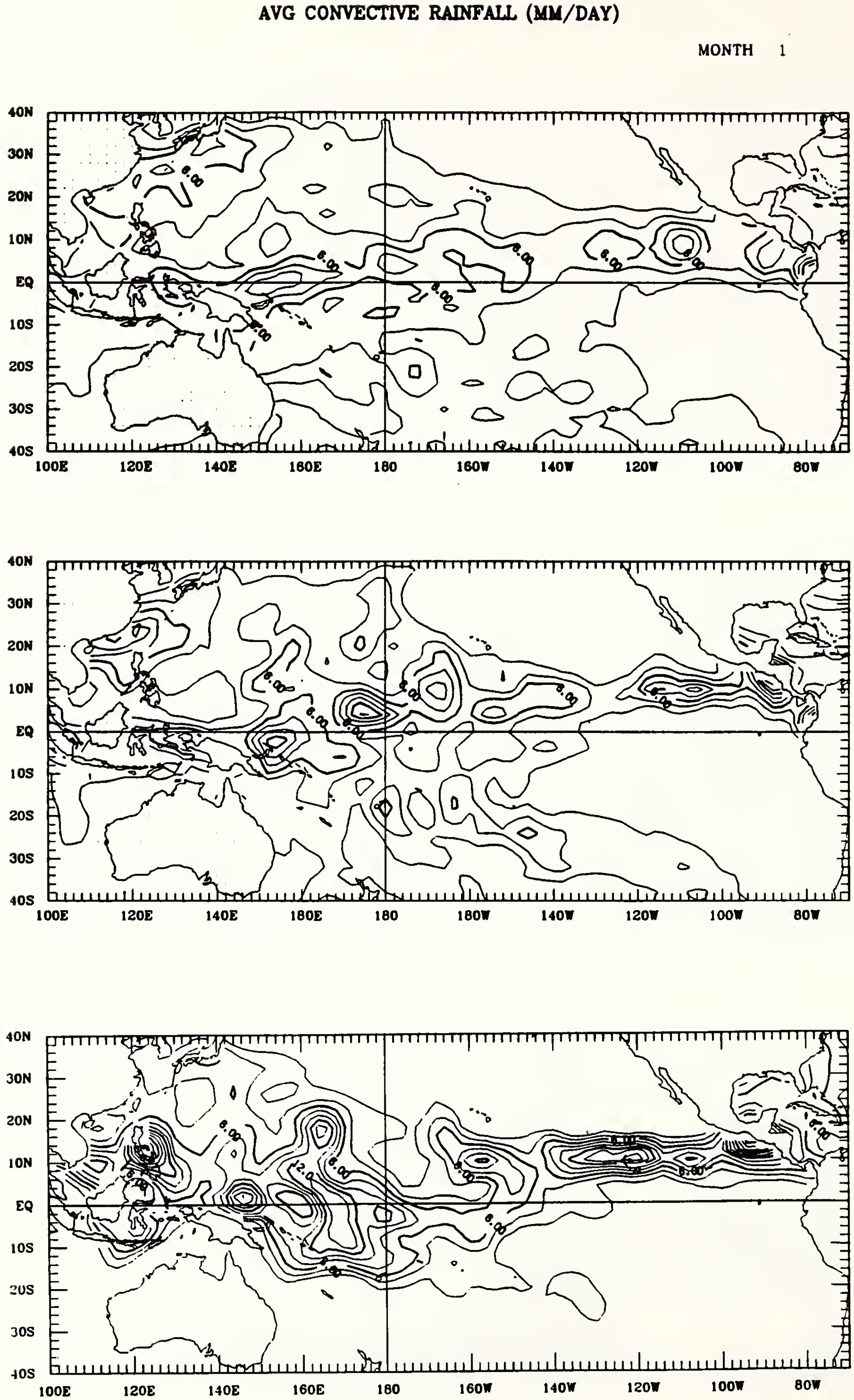

Figure 1b. Monthly averaged rainfall in the Pacific basin for month of July, 1990. Contour interval is 2mm/day. (see text)

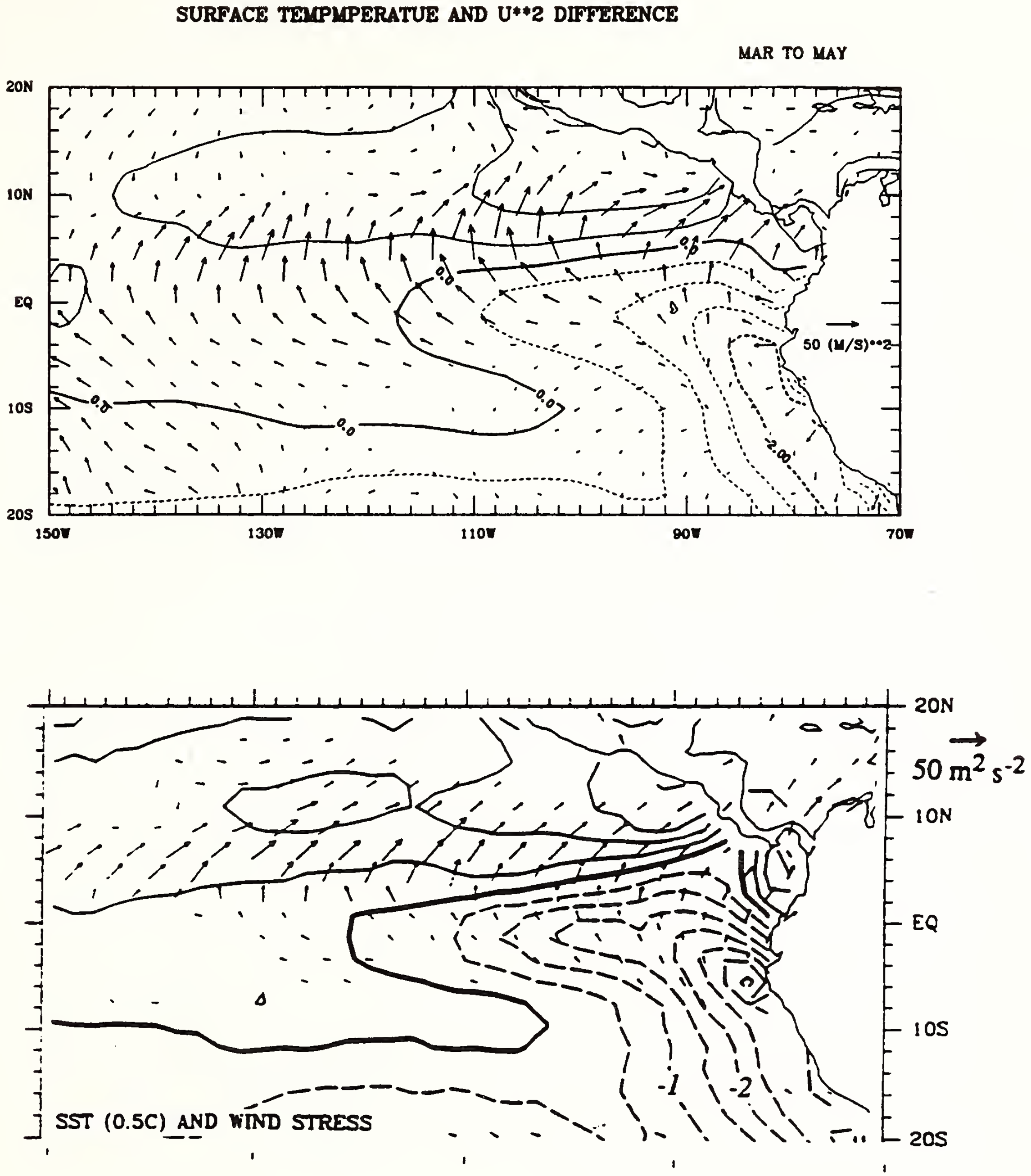
SURFACE TEMPMPERATUE AND U**2 DIFFERENCE

MAR TO MAY

SST (0.5C) AND WIND STRESS

Figure 2. March to May difference of monthly mean pseudo surface stress and SST. Contour interval for SST difference is 0.5 degree C.. Upper panel is average of 2 year atmospheric model results; lower panel is result from observed climate data by Mitchell and Wallace(1991).

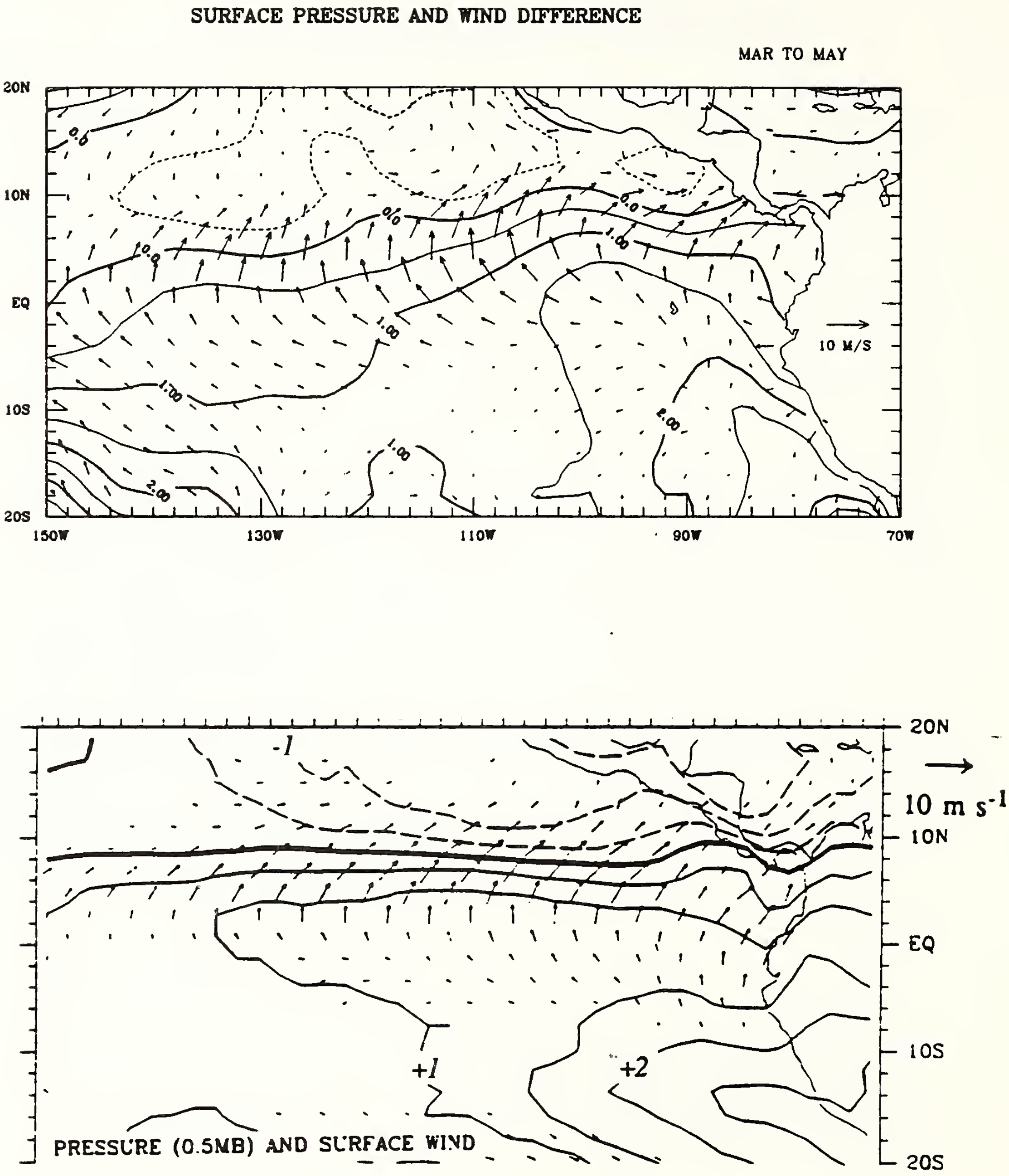

Figure 3. March to May difference of monthly mean sea level pressure (SLP) and surface wind. Contour interval for SLP is 0.5 hpa. Upper panel is average of 2 year model results, lower panel is result from observed climate data by Mitchell and Wallace (1991).

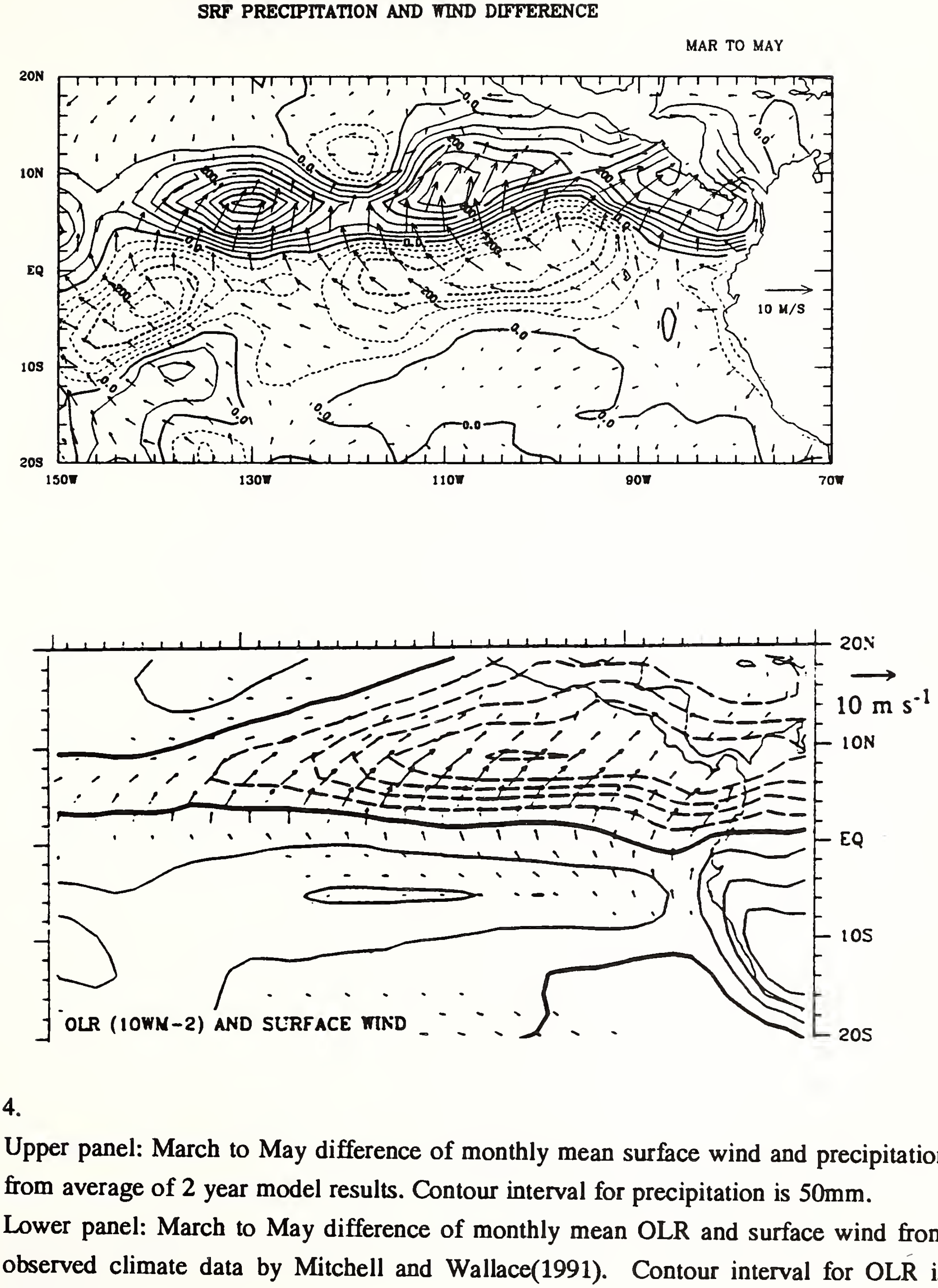

Figure 4.

Upper panel: March to May difference of monthly mean surface wind and precipitation from average of 2 year model results. Contour interval for precipitation is 50mm.

Lower panel: March to May difference of monthly mean OLR and surface wind from observed climate data by Mitchell and Wallace(1991). Contour interval for OLR is 10w/m$^2$.

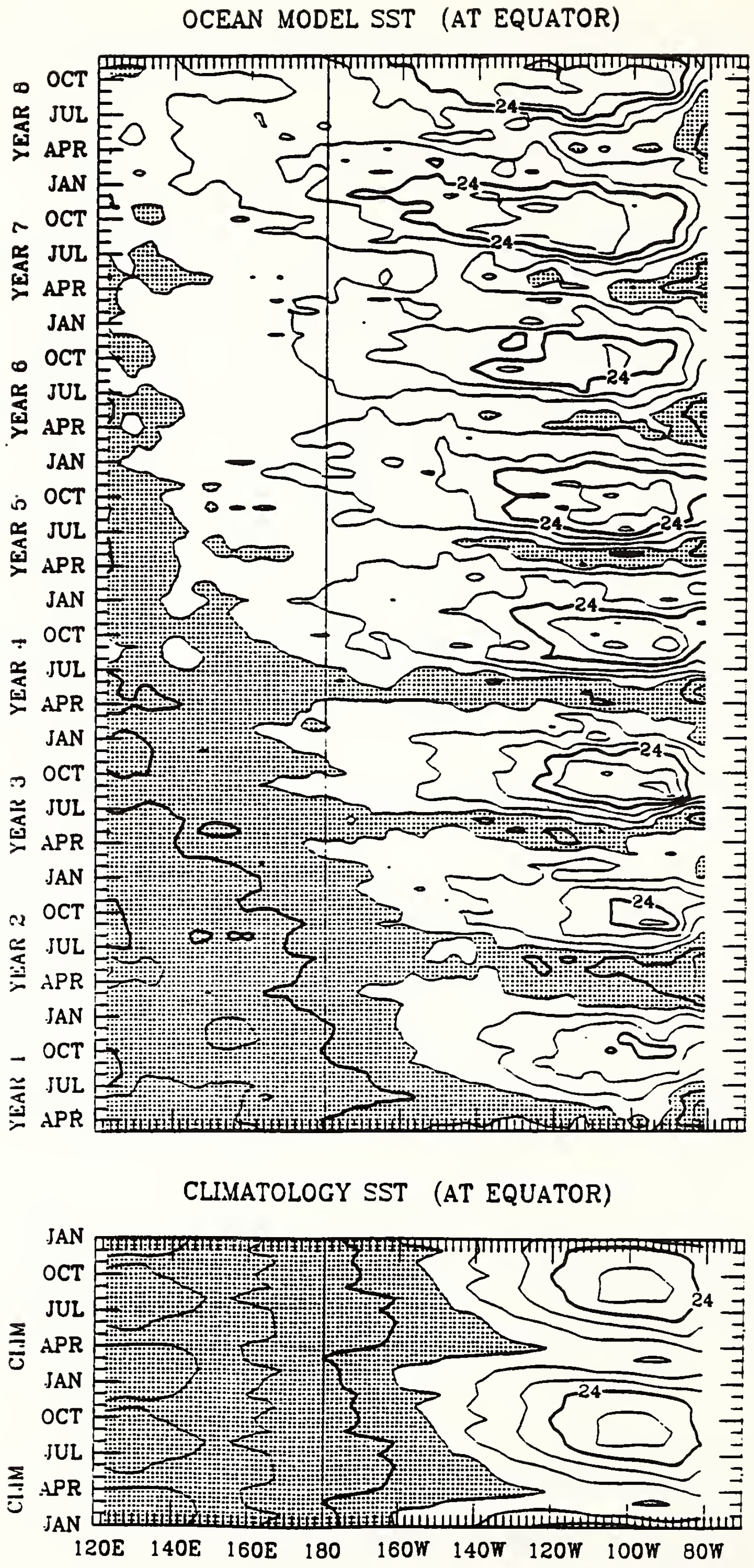

Figure 5. 8 year Time series of equatorial SST in the Pacific basin from coupled model experiment (upper panel); A 2 year example of time series of climatological equatorial SST in the Pacific basin (lower panel).

# THE OBSERVED GLOBAL LOW FREQUENCY VARIABILITY IN THE ATMOSPHERE-OCEAN SYSTEM FROM 1967 TO 1986

Jin-Song Xu
Max-Planck-Institut für Meteorologie

A combined data set including both atmospheric (sea level pressure, 700-mb and 200-mb zonal wind) and oceanic (sea surface temperature, Pacific sea level and Pacific subsurface temperature) parameters is used to study the large scale signals in the air-sea system on time scales of months to years and the air-sea interaction processes involved in these signals. For this purpose, two analysis steps are made. First the Principal Oscillation Pattern (POP) analysis, which can be interpreted as multivariate spectral analysis, is chosen to identify large scale coherent signals and their spectral features over the considered time period. As second step, it is attempted to specify the physical processes involved in each signal.

Six modes are found. Two modes are discussed here. The temporal evolutions of these modes are shown in Fig.1.

a) Mode 1: large scale process on month to month time scales

The atmospheric signal connected with this mode bears large resemblance to the PNA teleconnection pattern noted by Wallace and Gutzler (1981) (Fig.2a). In the SST pattern (Fig.2b), the anomalous anticyclonic flow in Fig.2a is indicated by the arrow. Because this mode is energetic mostly in the winter season, the negative (positive) SST anomalies in the regions of northwesterly (southeasterly) anomalies are likely produced by anomalous cold (warm) air advection. In Fig.1c, the negative sea level anomalies are located right below the center of the anomalous anticyclone. It appears that these sea level anomalies are generated by the inverse barometric effect.

The results suggest that the origin of this monthly time scale mode lies in the atmosphere, and the ocean reacts passively to the atmospheric anomalies.

b) Mode 2: large scale air-sea interaction process on decadal time scales

This mode is characterized by the simultaneous development of positive SST anomalies with the largest equatorial SST over the west Pacific (Fig.3a), and anomalous convection over the same region (Fig.3b). According to the POP concept, the signal, given by time series shown in Fig.1b and patterns shown in Figs. 3a and 3b describe a decrease of tropical SST and the strength of the ascending branch of the Walker Circulation over the west Pacific in the period from the end-sixties to the mid-seventies, and an increase of tropical SST and west Pacific convection since the mid-seventies. This result indicates an active air-sea interaction process in the tropics on decadal time scales.

The *tropical* signal is found to be associated with changes in the *extratropical* atmospheric and oceanic circulations. The extratropical atmospheric anomalies are dominated by zonal wind anomalies over the central North Pacific and zonal wind anomalies of opposite sign over the northern North Pacific at both the 700-mb and 200-mb (Fig.3b). The most coherent extratropical sea level signal is found along the coast of Japan with large positive values in the north and large negative values in the south (Fig.3c). Via geostrophic relation, these sea level anomalies are associated with changes of Kuroshio and Oyashio currents.

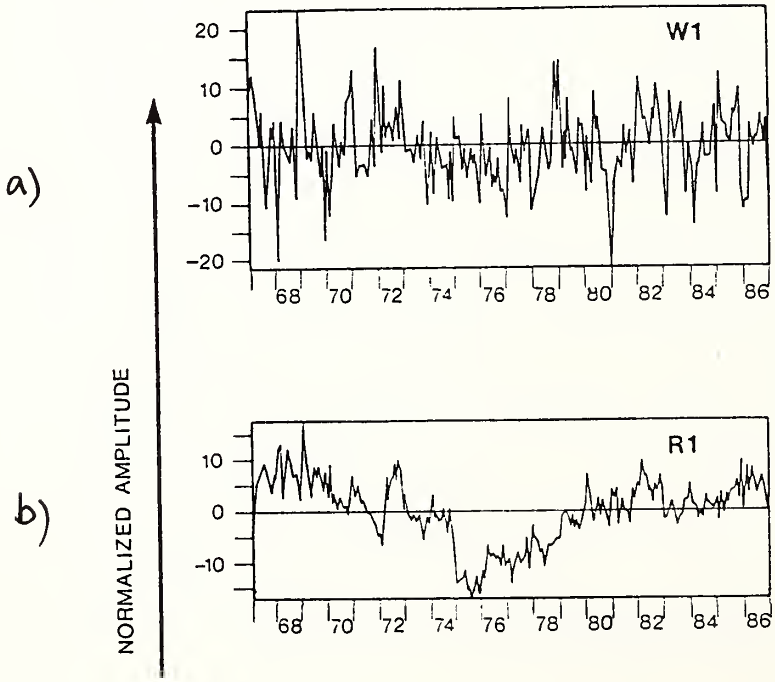

**Figure 1:** POP coefficient time series z(t) of a) the Mode 1, b) the Mode 2.

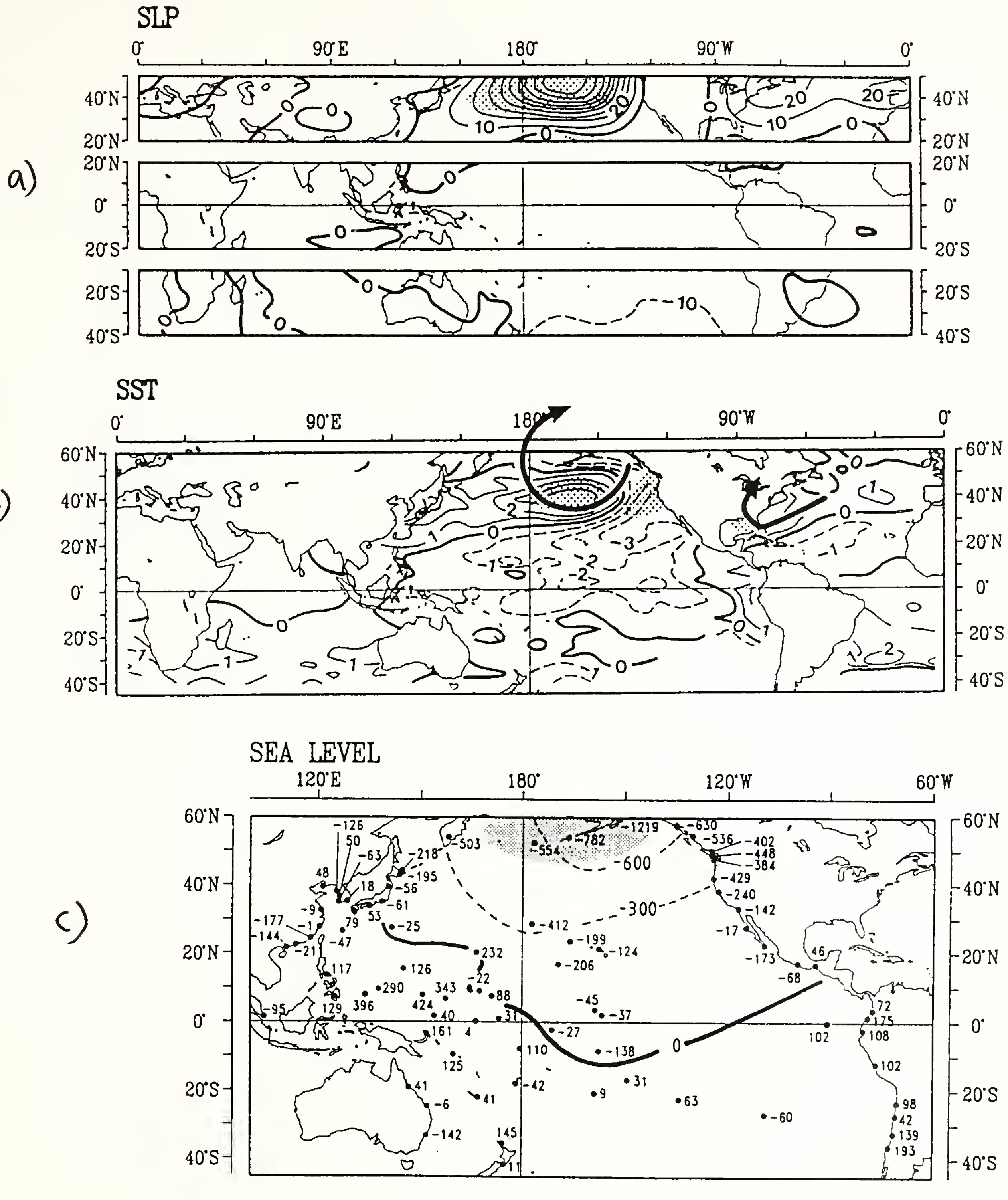

Figure 2: POP pattern **P** of the Mode 1 for a) SLP (in mb), b) SST (in °C), and c) sea level (in mm). Shaded areas indicate explained variance larger than 10% for SLP and larger than 5% for SST and sea level. The signal is given by z(t)·**P**.

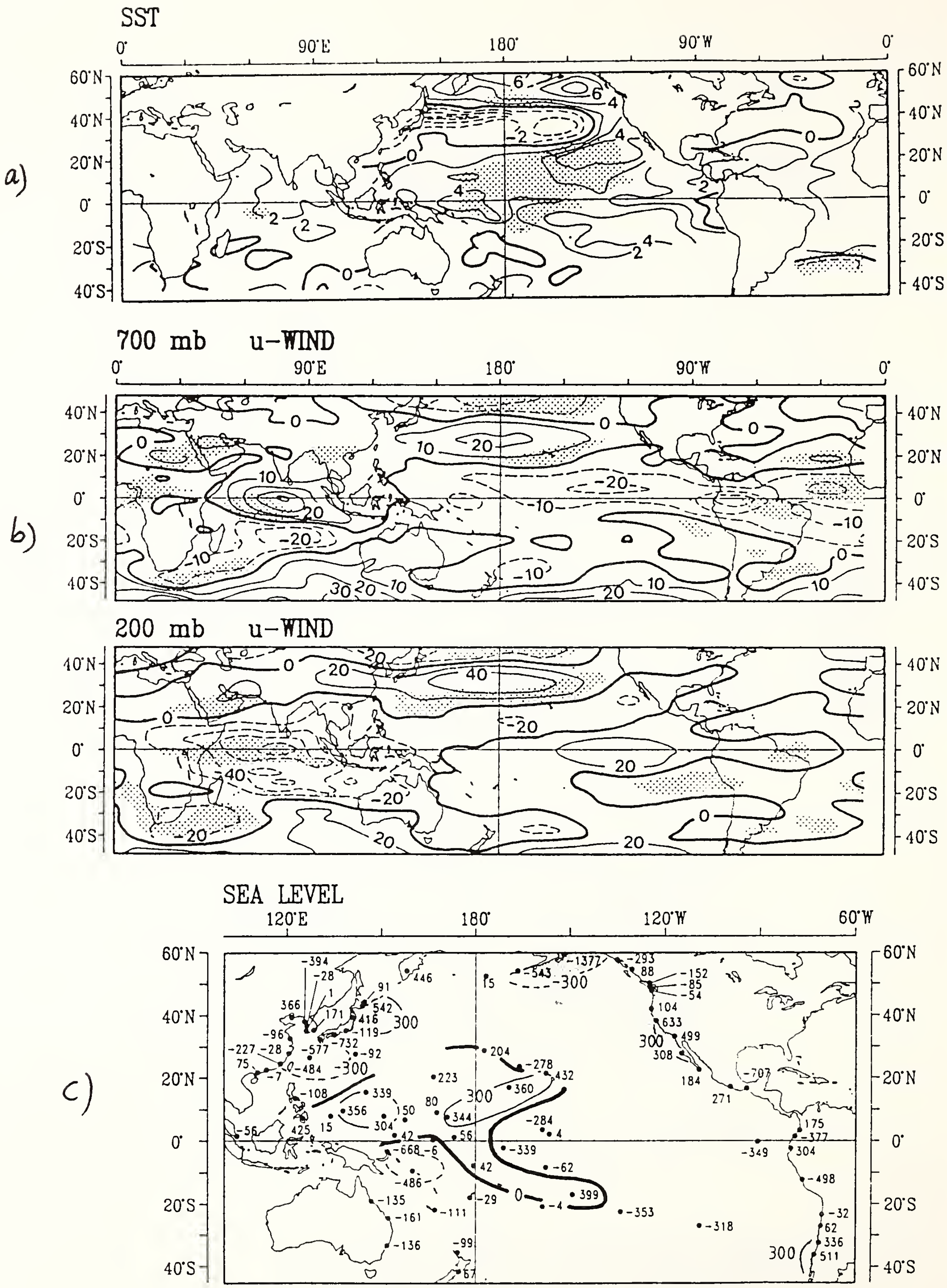

**Figure 3:** POP pattern P of the Mode 2 for a) SST (in °C), b) 700-mb and 200-mb zonal wind (in m/s), and c) sea level (in mm). Shaded areas indicate explained variance larger than 10%. The signal is given by z(t)·P.

# Simulations of the Seasonal Cycle with a Coupled Atmosphere-Ocean GCM

Carlos R. Mechoso, Chung-Chun Ma, John D. Farrara
and Joseph A. Spahr

*Department of Atmospheric Sciences, University of California, Los Angeles, CA 90024*

## 1 Introduction

Coupled atmosphere-ocean general circulation models (GCMs) are major assets for the study of climate phenomena on time scales from months to millennia. The atmospheric and the oceanic components of a coupled GCM (AGCM and OGCM, respectively) are both based on the primitive equations. These components may differ drastically, however, in the grids, methods used to discretize the equations, and in the parameterization of subgrid-scale processes. In general, the AGCM and OGCM components of current coupled GCMs were not originally designed to work as a single unit. Instead they are different codes that run separately, and periodically exchange boundary conditions representing continuity of momentum, energy and water fluxes.

In the uncoupled mode, AGCMs use prescribed boundary conditions in sea surface temperature (SST). Also in the uncoupled mode, OGCMs are forced at the surface by prescribed momentum and heat fluxes. These prescribed boundary conditions for each GCM can correspond to estimates from observed climatology, persistence, or the output from uncoupled simulations with the other GCM. Even with "observed" boundary forcing, the simulated atmospheric and oceanic circulations exhibit substantial differences from the observed, which are referred to as systematic errors. Once the AGCM and OGCM are coupled together, these errors can either amplify or decay as complicated feedbacks develop, since individual components are free from the constraints of prescribed boundary conditions.

In this paper, we analyze the climatology of a coupled GCM, inspect its systematic errors and investigate how sensitive these errors are to the parameterizations of several key processes in the surface energy balance of the coupled system. In the AGCM the parameterizations in question are those of long wave radiation, and sensible heat flux at the surface. In the OGCM, we consider different parameterizations of vertical mixing by turbulent processes, and the effect of penetration of short-wave radiative heating into the upper ocean. Specifically, we present selected results from multi-year integrations with a coupled atmosphere-ocean GCM using different parameterizations of the processes mentioned above. We show that the parameterization of long-wave radiation in the AGCM has a strong effect on the seasonal cycle produced by the coupled model.

## 2 The Models

The AGCM component of the coupled system is the UCLA GCM (see Suarez *et al.* 1983 and references therein). This is a finite-difference model with state-of-the-art parameterizations of convection, planetary boundary layer processes, and radiation. The version of the AGCM used in this study has 9 layers in the vertical with the top at 50 mb. The horizontal resolution is 4° latitude by 5° longitude.

The OGCM used in this study is the tropical-Pacific version of the GFDL ocean model. The reader is referred to the paper by Ma, Chao, Mechoso, Weibel, and Halpern (MCMWH) in this volume for further details.

Coupling between the models is synchronous with information exchanged each day. The AGCM provides the wind stress and heat fluxes to the OGCM, and the OGCM returns SST to the AGCM. Diurnal variations in these variables are averaged out in this coupling.

## 3 Summary of Parameterization of Subgrid-Scale Processes

We consider two parameterizations of long-wave radiation in the AGCM: 1) the K scheme, which follows Katayama (1972), and 2) the H scheme, which follows Harshvardhan *et al.* (1989). The major difference between the two schemes is that the H scheme includes a representation of the "continuum" absorption by water vapor, whereas the K scheme does not.

Two parameterizations of vertical mixing by subgrid-scale turbulence in the OGCM are considered: 1) the K1 scheme, which is a first-order closure scheme with mixing coefficients depending on the Richardson number (Pacanowski and Philander 1981), and 2) the K2 scheme, which is the Mellor-Yamada level $2\frac{1}{2}$ second-order closure scheme (Mellor and Yamada 1974, 1982), implemented as in Rosati and Miyakoda (1988). Further details can be found in MCMWH.

Comparison with observational studies suggested that the the sensible and latent heat fluxes calculated in the AGCM may be too small at low wind speeds. To test the impact of this discrepancy, we prescribed that when the wind speed is below 5 $\mathrm{m\,s^{-1}}$, the coefficient used to compute the flux is equal to that at 5 $\mathrm{m\,s^{-1}}$. In the OGCM, we allowed the penetration of solar radiation beyond the top layer according to the formula by Paulson and Simpson (1977). In this way, 27 percent of solar radiation is allowed to penetrate beyond the first layer of the OGCM, which is 10 m thick.

## 4 Coupled GCM Experiments

The initial conditions for the AGCM correspond to January 15 in a simulation with climatological SST that started several years earlier. The OGCM was started from initial

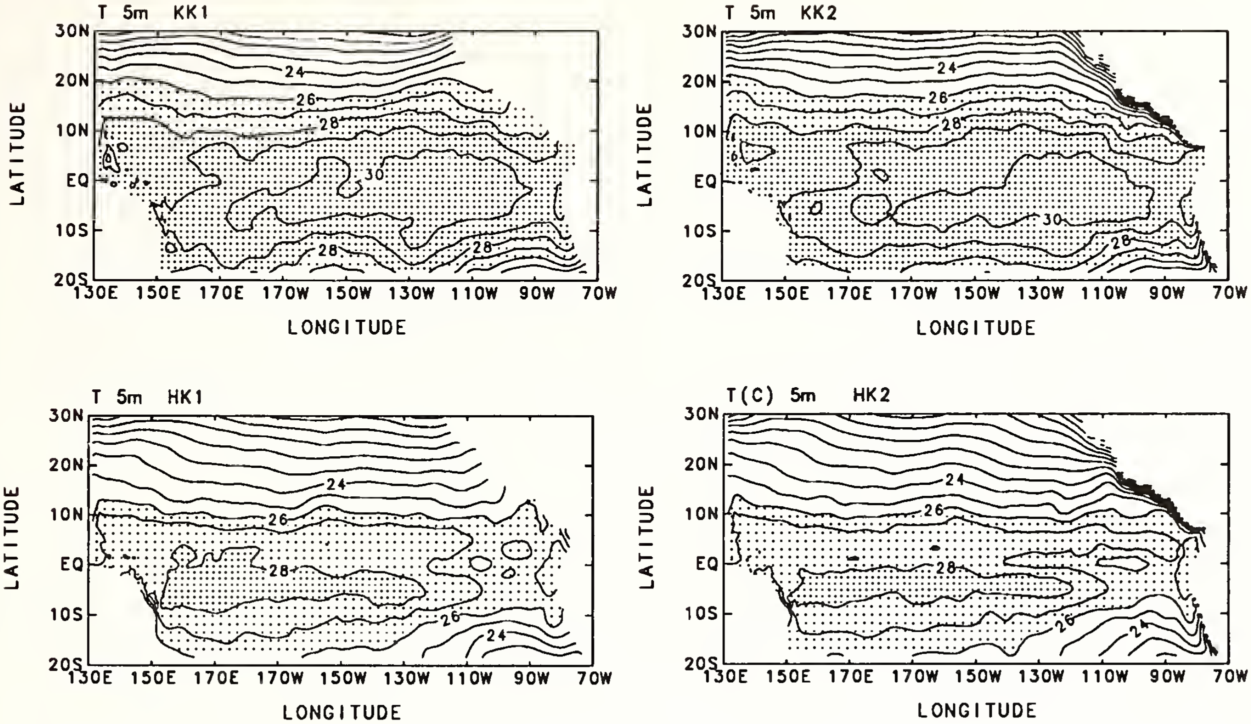

Figure 1: Simulated sea surface temperature after one year of model integration for experiments K-K1, K-K2, H-K1, and H-K2.

conditions corresponding to a state of rest with temperature and salinity distributions representing the January climatology. Integrations were carried out for different combinations of parameterizations of long-wave radiation in the AGCM and vertical mixing in the OGCM.

Significant differences between these integrations were observed after a few months. The simulated SST after one year of model integration is shown in Fig. 1 for four combinations of radiation schemes in the AGCM and vertical mixing schemes in the OGCM: K-K1, K-K2, H-K1 and H-K2.

With the K scheme for radiation used in the AGCM, a major adjustment process took place at the beginning of the simulation. Warm water surged eastward and most of the central equatorial Pacific ocean was covered with water warmer than 30°C throughout the integration. The simulation using the H scheme is significantly different. The cold tongue in the eastern Pacific is well simulated. The east-west temperature gradient is comparable to the observations in July, but slightly weaker in January. Overall, the simulated temperatures tend to be lower than the observed. Different parameterizations of vertical mixing in the OGCM do not have a qualitative effect on the results with either radiation scheme in the AGCM.

We have also carried out experiments without the minimum wind speed assumption in sensible heat flux calculations and the short-wave penetration in the OGCM. With the K scheme for radiation used in the AGCM, the climate drift of the coupled system occurs at an earlier stage in the simulation. The removal of short-wave penetration results in slightly higher temperatures in the subtropics.

The experiment H-K2 is being extended to study the interannual variability of the coupled model. The temporal variation of equatorial SST is shown in Fig. 2. In the first year of simulation, there is a relatively minor adjustment, with a clear cooling in the eastern Pacific. For the next eight years, the simulation displays a pronounced seasonal cycle with no significant climate drift. In the eastern Pacific, the cold tongue is strongest in the Northern Hemisphere summer. The temperature difference between the central and the eastern Pacific is comparable to the observations. In the western Pacific, however, the SST is slightly colder than observed, and the thermal gradient is weak.

## 5 Conclusion

We have presented a coupled atmosphere-ocean model based on the UCLA atmospheric GCM and the tropical-Pacific version of the NOAA GFDL/Princeton University OGCM.

We found that the coupled model is sensitive to the parameterization of long-wave radiation in the AGCM. With the parameterization by Katayama (1972), a strong adjustment process took place in the early stages of the simulation. The process resembles a strong El Niño, with warm waters flowing from west to east, convection moving from the western to the central Pacific, and the Trade Winds weakening in the equatorial Pacific. The system does not completely recover from that process and, after four years of integration, SSTs are still unrealistically high in the tropics, and the current and the thermal structure simulated by the OGCM are unrealistic.

With the parameterization by Harshvardhan *et al.* (1989), on the other hand, the coupled GCM achieves reasonable success in simulating outstanding features of the seasonal cycle in equatorial SST. Results include a gradient in equatorial SST of about 7°C between the cold tongue in the east and the warm pool in the west during the Northern Hemisphere summer; individual values at those locations are slightly colder than those observed.

Harshvardhan *et al.* (1989) suggested that "the impact of the continuum on the surface energy balance ... will become much more important in future coupled ocean-atmosphere models" than in AGCMs with prescribed SST. We concur with that. This sensitivity to the long-wave radiation parameterization is slightly reduced by allowing for penetration of short-wave radiation in the OGCM and modifying the calculation of sensible heat flux at the surface.

The results obtained so far for the simulated seasonal cycle with the coupled GCM are very encouraging. Integrations are being extended to evaluate the model's interannual variability.

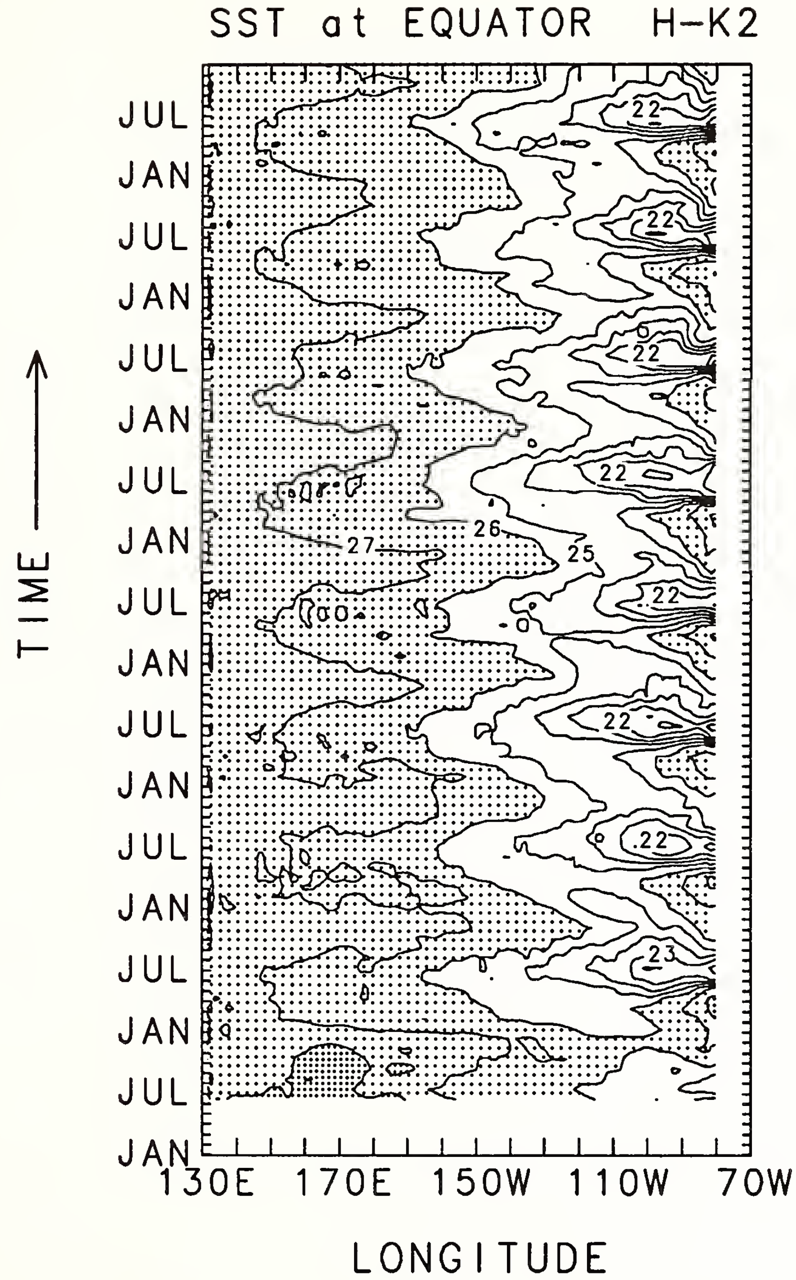

Figure 2: Time-longitude plot of SST on the equator for experiment H-K2. Time increases upwards. Contour interval is 1°C. Regions warmer than 26°C are shaded.

*Acknowledgements.* This work was supported by ONR under Grant N00014-89-J-1845, and NSF and DARPA under Cooperative Agreement NCR-8919038 with the Corporation for National Research Initiatives. Model integrations were performed at the San Diego Supercomputer Center.

# REFERENCES

Harshvardhan, D. A. Randall, T. G. Corsetti, and D. A. Dazlich, 1989: Earth radiation budget and cloudiness simulations with a general circulation model. *J. Atmos. Sci.*, **13,** 1922-1942.

Katayama, A., 1972: A simplified scheme for computing radiative transfer in the troposphere. Numerical Simulation of Weather and Climate, Tech. Rep. No. 6, Dept. of Meteor., University of California, Los Angeles, CA 90024, 77 pp.

Mellor, G. L., and T. Yamada, 1974: A hierarchy of turbulence closure models for planetary boundary layers. *J. Atmos. Sci.*, **31,** 1791-1806.

—, and —, 1982: Development of a turbulence closure model for geophysical fluid problems. *Rev. Geophys. and Space Physics*, **20,** 851-875.

Pacanowski, R. C., and S. G. H. Philander, 1981: Parameterization of vertical mixing in numerical models of tropical oceans. *J. Phys. Oceanogr.*, **11,** 1443-1451.

Paulson, C. A., and J. J. Simpson, 1977: Irradiance measurements in the upper ocean. *J. Phys. Oceanogr.,* **7,** 952-956.

Rosati, A., and K. Miyakoda, 1988: A general circulation model for upper ocean simulation. *J. Phys. Oceanogr.*, **18,** 1601-1626.

Suarez, M. J., A. Arakawa, and D. A. Randall, 1983: The parameterization of the planetary boundary layer in the UCLA general circulation model: Formulation and results. *Mon. Wea. Rev.*, **111,** 2224-2243.

# COUPLING AN OCEAN WAVE MODEL TO AN ATMOSPHERIC GENERAL CIRCULATION MODEL

Susanne L. Weber
Royal Netherlands Meteorological Institute
P.O.Box 201, 3730 AE De Bilt
The Netherlands

Hans von Storch
Max-Planck-Institute for Meteorology
Bundesstraße 55, 2000 Hamburg 13
F.R.Germany

Wind waves are an obvious feature of the interface between the atmosphere and the ocean. The fluxes through the interface are modified by the presence of waves on the interface. Therefore, ocean waves are of interest for climate studies, both for modeling of the atmosphere and the ocean separately and for modeling of the coupled ocean-atmosphere system. Recently, it has been proposed by Hasselmann (1990) to couple the atmosphere and the ocean through an explicit model of their interface: gravity and capillary waves which are generated by the wind on the ocean surface. In the present study we concentrate on one side of the ocean-waves-atmosphere system, namely the interaction between the atmospheric flow and the waves generated by it. Details can be found in Weber et al. (1991)

A coupled model, consisting of the WAM ocean wave model (WAMDIG, 1989) and the Atmospheric General Circulation Model ECHAM (Roeckner et al., 1989), is integrated over 390 days under perpetual July conditions. The wave model is forced by the AGCM wind stress, whereas the ocean waves modify the surface fluxes of momentum as well as latent and sensible heat. The coupling scheme is based on Janssen (1989). The surface fluxes are enhanced over newly generated, so-called *young* waves. Young waves are found after a change in the surface winds; if the situation is stationary the coupling becomes weak after 6-12 hours.

The wave fields which are generated by the coupled model are realistic, with time-mean wave heights of 3-4 m in the Southern Hemisphere storm track. Young waves are present in 20% of the time in the storm track, where the coupling is weak in the mean. Everywhere else the coupling is negligible. The enhancement of the surface fluxes in the storm track, due to the generation of young waves, exhibits a spatially and temporally highly variable pattern. The *time-mean* enhancement factor is extremely small.

The atmospheric circulation in the coupled experiment differs from the circulation in a control experiment only in the Southern Hemisphere storm track. The time-mean meridional gradient of the geopotential at 500 hPa has slightly steepened. The 2-15 days band-pass filtered variance, representative for baroclinic disturbances, has shifted poleward and has intensified at high latitudes (Fig. 1). The number of storms has increased by a few percent in the coupled experiment.

Young waves are generated mostly in the equatorward "frontal" area of a cyclone. The "front" denotes the position of strongest horizontal temperature gradient at 850 hPa. In that area the surface winds are strongest (20-25 m/s) and the wave heights are maximum (5-10 m). Due to the generation of young waves, the surface stress is enhanced (by a factor two at most) in the frontal area (Fig. 2). We hypothesize that the inhomogeneous distribution of surface roughness below a cyclone accelerates the poleward movement of a cyclone. At the same time the frequency, or intensity, of the storms is enhanced.

It is interesting to compare the results of the coupled experiment with an ACGM experiment, where the sea surface roughness was homogeneously enhanced (by a factor ten) in the Southern Hemisphere storm track. In this experiment the time-mean meridional gradient of the geopotential at 500 hPa as well as the high-frequency variance had *de*creased (Ulbrich et al., 1991). This is opposite to our findings. Apparently, the atmospheric circulation is sensitive to the strength and the spatial and temporal pattern of roughness enhancement.

The effect of ocean waves on the tropospheric circulation is of moderate relevance for the climatological mean circulation in the AGCM with the present resolution (T21). Going to higher resolutions the coupling would become stronger as the strength and the variability of the surface winds would become larger. The present experiment should be regarded as a test, which shows that ocean waves could be significant for future climate GCMs. It also shows that the path of an individual cyclone is affected by the presence of the wave field. Therefore, wave growth might be a significant process for weather forecasting.

**A full report can be found in:** Weber, S.L., H. von Storch, P. Viterbo and L. Zambresky, 1991: Coupling an ocean wave model to an atmospheric general circulation model. Max-Planck-Institut für Meteorologie Report 72.

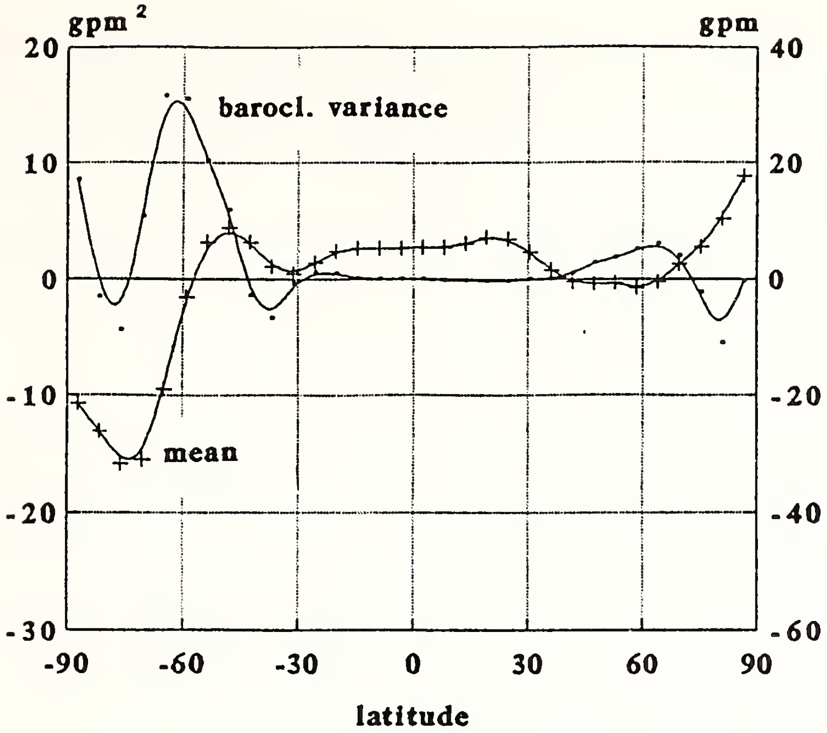

Fig. 1 The difference in the geopotential (in gpm) and in the 2-15 days band-pass filtered variance of the geopotential (in $(\mathrm{gpm})^2$) at 500 hPa between the coupled wave model- AGCM experiment and a control experiment (zonally averaged, mean over the last 360 days).

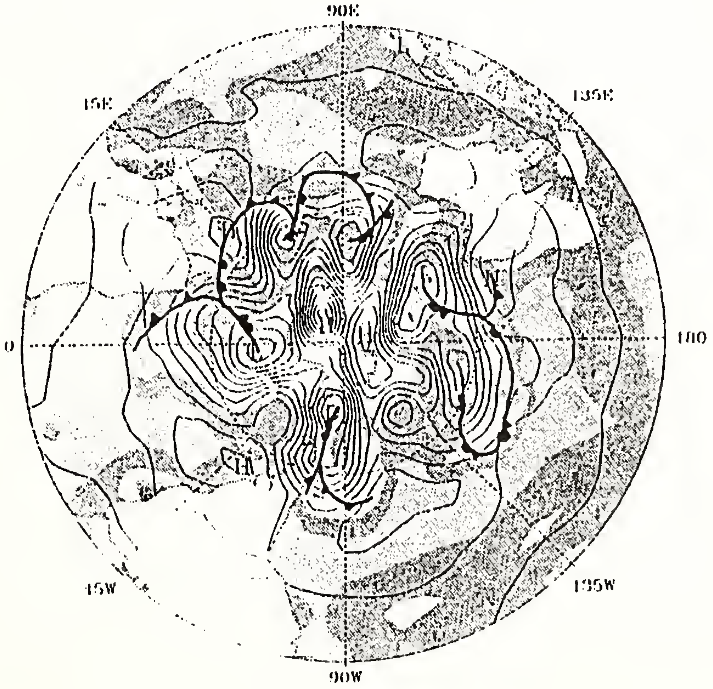

Fig. 2 The sea level pressure (isolines) and the ratio of the wave-induced stress to the total stress (shades) for a randomly chosen 12-hour interval (day 142, 0-12 UTC) in the coupled wave model-AGCM experiment. All values are 12-hourly means. The stress ratio denotes the strength of the coupling, with light shades indicating a 12-hourly mean roughness enhancement of 50-100%. The position of the "fronts", where the stress ratios tend to be relatively high, is indicated.

# Recent Changes in Atmospheric and Oceanic Anomaly Patterns Related to the Southern Oscillation

Vernon E. Kousky

NOAA/NMC/NWS
Washington, DC 20233

## 1. INTRODUCTION

A strong cold episode of the Southern Oscillation was observed in the tropical Pacific during 1988-1989. In association with the colder than normal sea surface temperatures, the tropical troposphere also cooled by as much as 3°C in the eastern equatorial Pacific. This cooling, although to a lesser degree, spread throughout the tropics, and was related to highly persistent anomalous circulation which dominated the mid-latitudes of both hemispheres during the period from late 1988 until late 1990.

In this paper we will document some of the anomalous atmospheric circulation features that were associated with the 1988-1989 cold Southern Oscillation episode.

## 2. RESULTS

The 1988-1989 cold episode in the tropical Pacific was the strongest cold episode since the early 1970's and one of the strongest in the last 50 years. Standardized sea surface temperature (SST) anomalies in the central equatorial Pacific were less than -2 at the height of the episode (Fig. 1a) accompanied by Southern Oscillation Index (SOI) values near +2 (Fig. 1b). The pronounced cooling of the equatorial SSTs was also accompanied by a strong cooling of the mid-troposphere throughout the tropics (Fig. 1c).

The evolution of the zonally averaged 500 mb temperature anomalies, for the period 1988-1991, is shown in Fig. 2a. Negative anomalies dominated the tropics from mid-1988 through early 1990. At the same time, negative temperature anomalies were also prevalent at very high latitudes with positive anomalies at mid-latitudes in both hemispheres. Consistent with this pattern of temperature anomalies, the lower mid-latitude westerlies were weaker than normal (easterly anomalies) and the high latitude westerlies were stronger than normal throughout the period (Fig. 2b). This pattern is stronger for zonally averaged temperature and zonal wind considering just the Pacific sector (150°E-110°W, Fig. 3). The persistence in the zonally averaged circulation features for DJF of 1988-89, 1989-90 and 1990-91 is especially evident in the Northern Hemisphere.

The spatial patterns of temperature anomalies, for the northern winter and summer seasons are shown in Figs. 4 and 5. Not only are the zonally averaged features persistent but it is evident from these figures that many of the regional circulation features are highly persistent as well. In each of the northern winter seasons (Fig. 4) a similar pattern of 500 mb temperature anomalies was observed over the North Pacific eastward to northern Europe.

## 3. CONCLUSION

The atmospheric circulation features described can be interpreted in the following manner. During cold episodes the equator-to-pole thermal contrast is weaker than in either normal or El Niño years. As a result, the main belt of westerlies contracts poleward in both hemispheres leading to easterly anomalies in the lower mid-latitudes and westerly anomalies at high latitudes. In the vicinity of North America, this results in a negative Pacific/North American pattern of anomalies with anomalous ridges in the Gulf of Alaska and over the East Coast, and an anomalous trough over western North America. These features are essentially the reverse of those observed during Pacific warm (ENSO) episodes.

## ACKNOWLEDGMENTS

The author wishes to thank John Kopman who helped in preparing the figures.

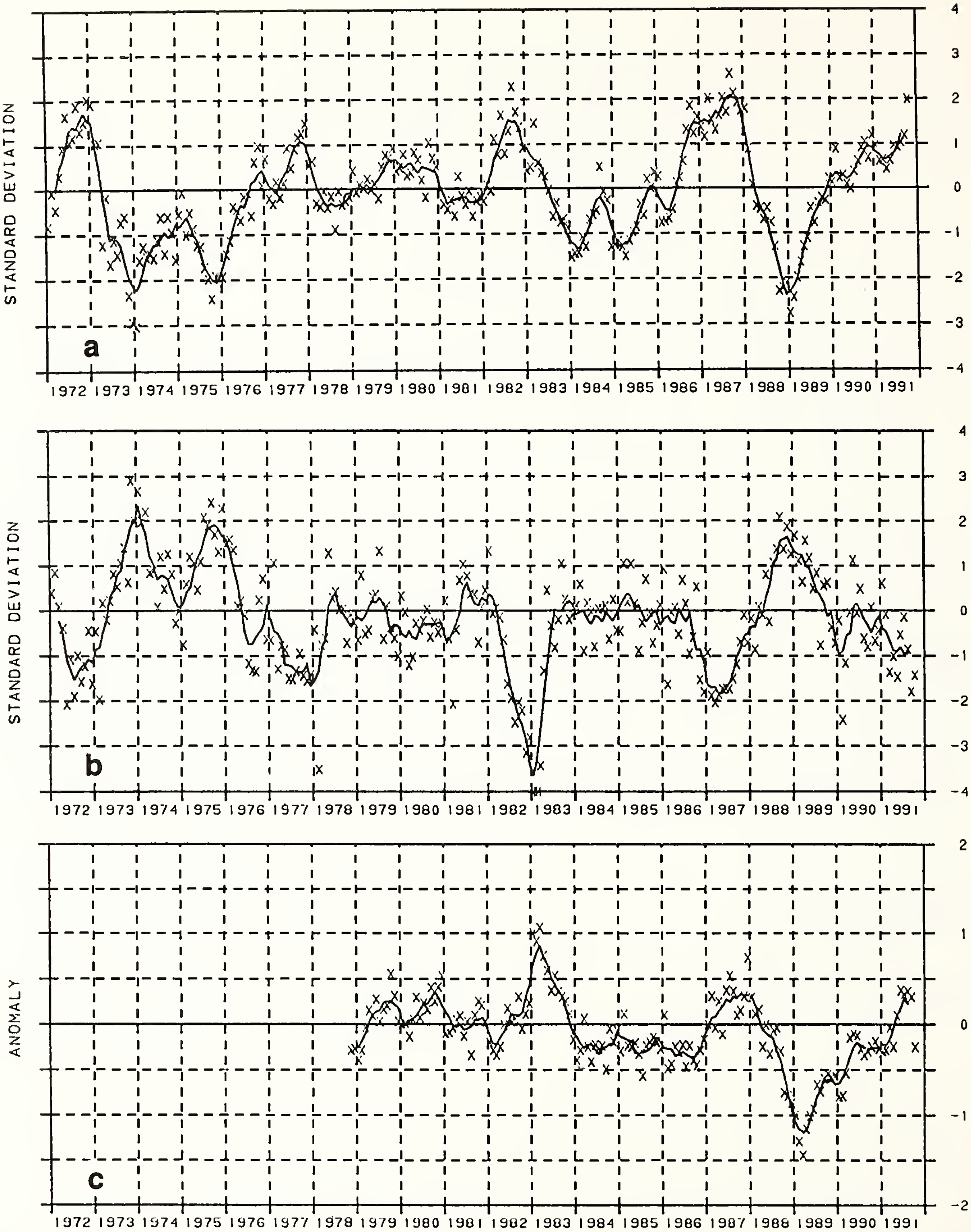

FIGURE 1 Time series of a) sea surface temperature anomalies for the equatorial portion of a ship track between Hawaii and Fiji, b) the Southern Oscillation Index, and c) the zonally averaged 500 mb temperature anomalies for the $20^{\circ}N$-$20^{\circ}S$ latitude band.

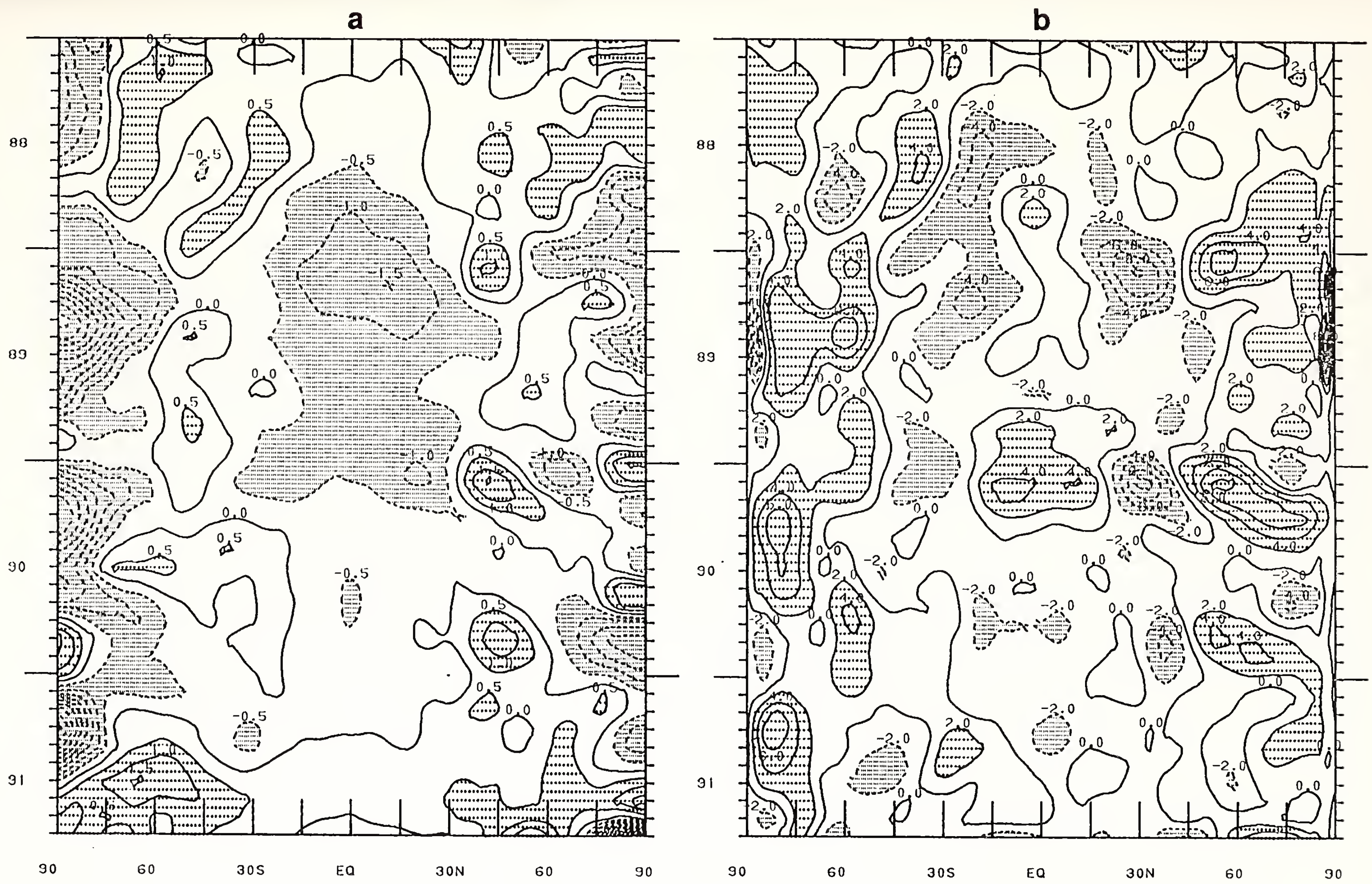

FIGURE 2 Time-latitude sections of a) zonally averaged 500 mb temperature anomalies and b) zonally averaged 200 mb zonal wind. Contour interval is 0.5°C and 2.0 $ms^{-1}$, respectively. Negative values less than -0.5 (-2.0) are shaded in (a) [(b)]. Positive values greater than 0.5 (2.0) are stippled in (a) [(b)].

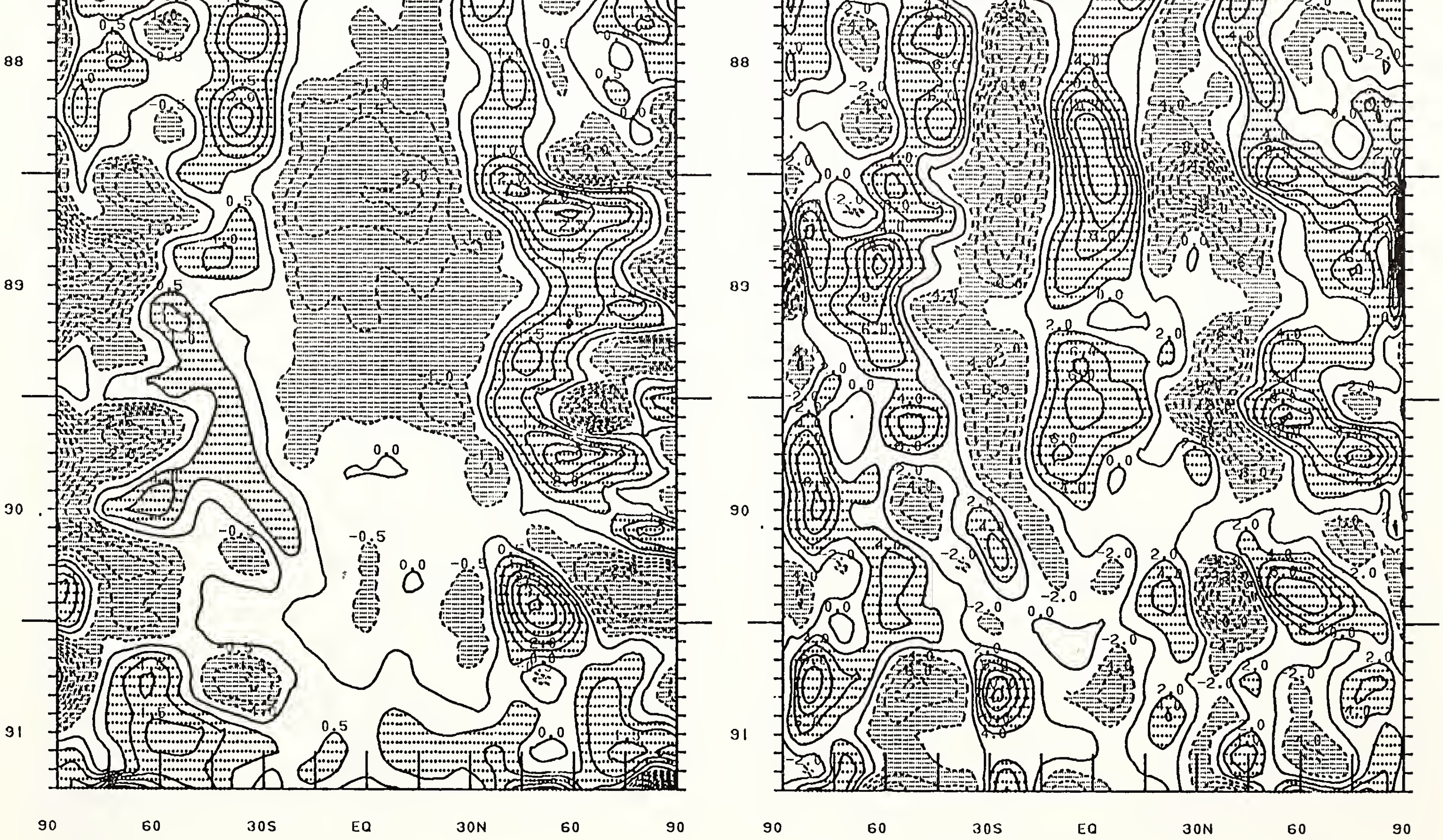

FIGURE 3 Same as Fig. 2, except temperature and zonal wind are averaged only for the Pacific sector ($150^{o}E-120^{o}W$).

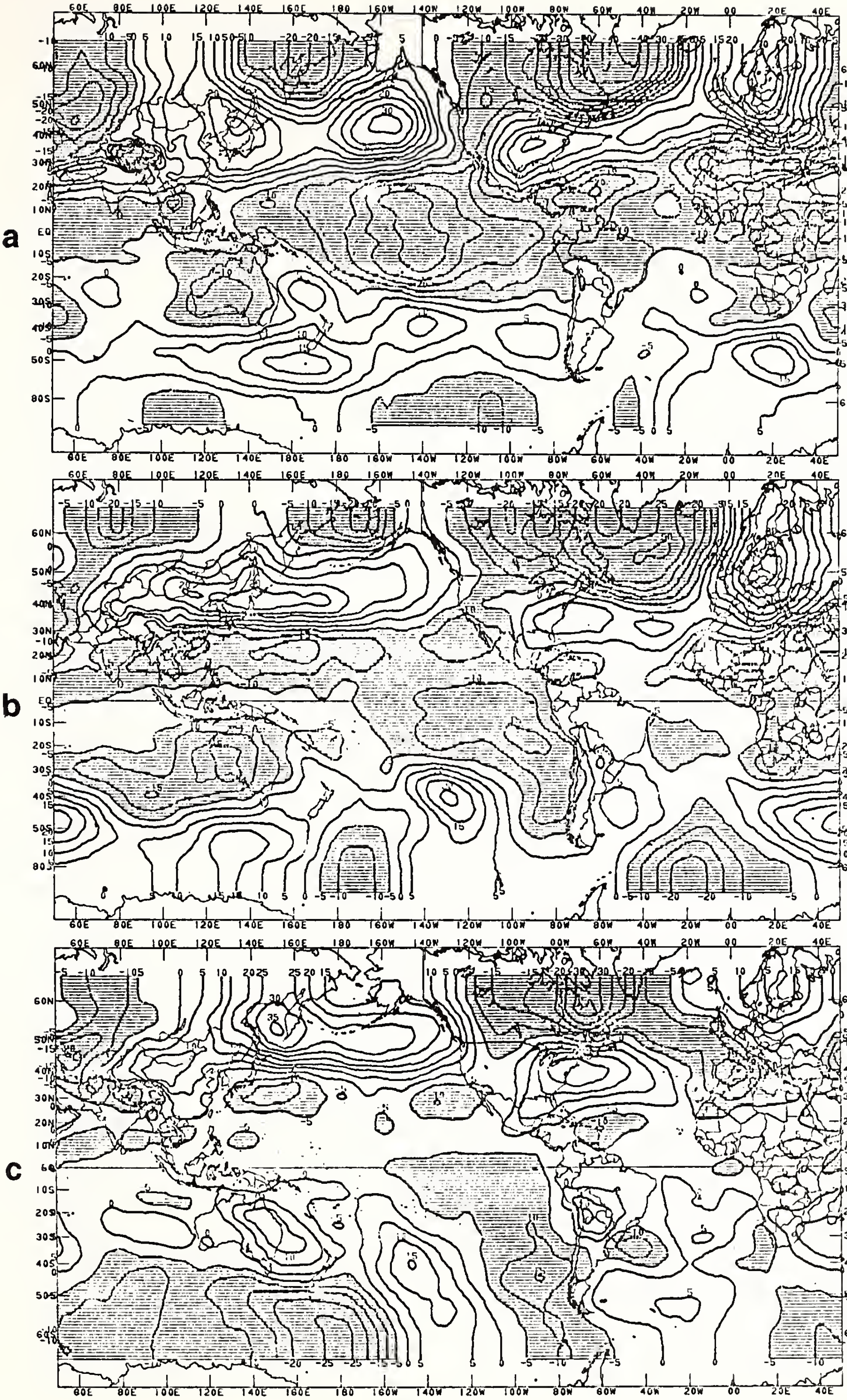
a
b
c
60E 80E 100E 120E 140E 160E 180 160W 140W 120W 100W 80W 60W 40W 20W 00 20E 40E
60N 50N 40N 30N 20N 10N EQ 10S 20S 30S 40S 50S 60S

Figure 4 Seasonal 500 mb temperature anomaly patterns for a
1988-89, b) 1989-90, and c) 1990-91. Contour int
is 0.5$^{o}$C. Values less than -0.5$^{o}$C are shaded.

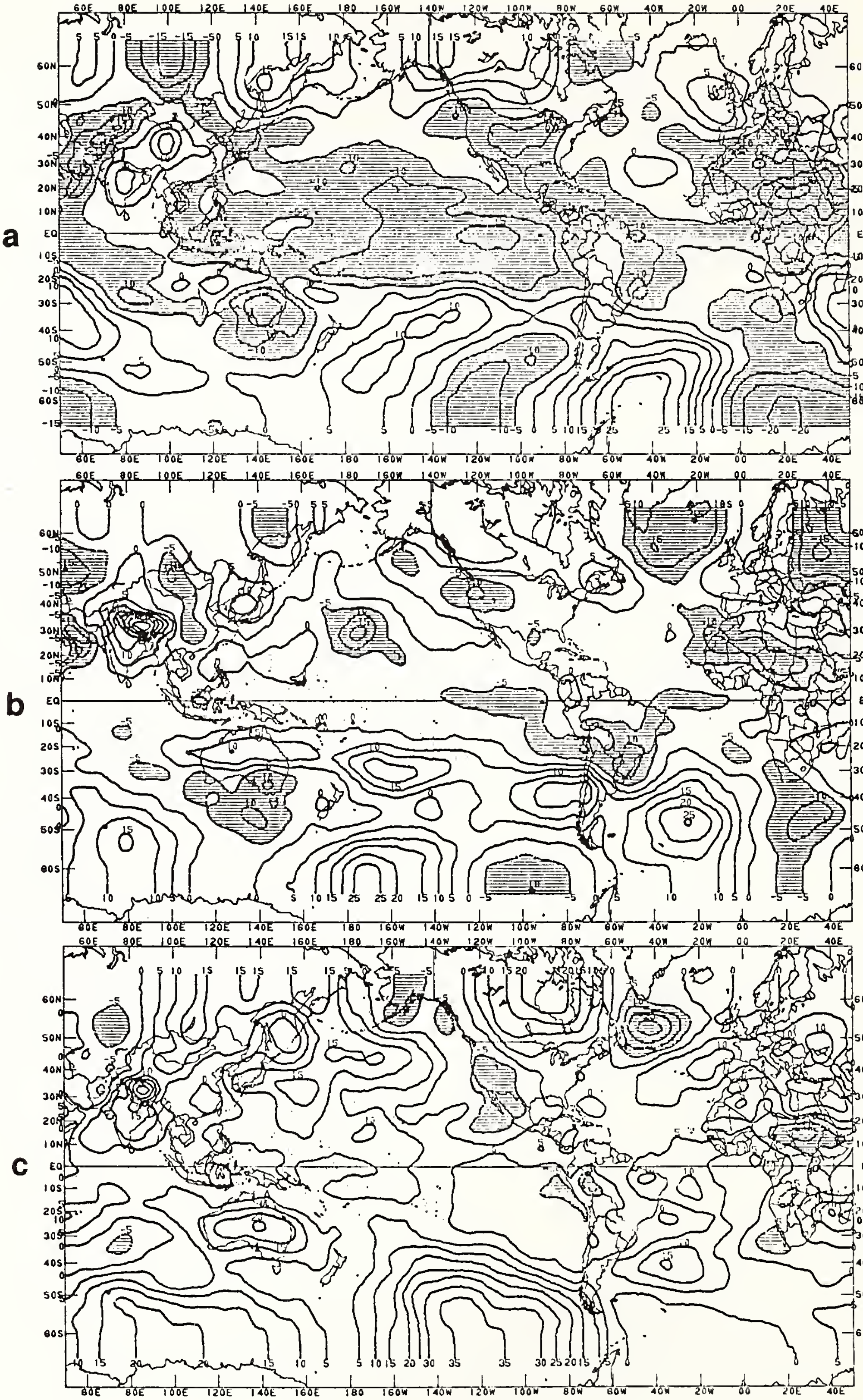
a
b
c
60E 80E 100E 120E 140E 160E 180 160W 140W 120W 100W 80W 60W 40W 20W 00 20E 40E
60N 50N 40N 30N 20N 10N EQ 10S 20S 30S 40S 50S 60S

Figure 5 Seasonal 500 mb temperature anomaly patterns for a) JJA 1989, b) 1990, and c) 1991. Contour interval is 0.5$^{o}$C. Values less than -0.5$^{o}$C are shaded.

# TEMPERATURE PATTERN VARIABILITY ON THE USSR TERRITORY IN 1931-1990

T.BELOKRYLOVA, O.BULYGINA, V.RAZUVAYEV

ALL-UNION RESEARCH INSTITUTE OF HYDROMETEOROLOGICAL
INFORMATION - WORLD DATA CENTRE
OBNINSK,USSR

## I. INTRODUCTION

During the last years climatic anomalies have been observed in some regions, whose scale suggests possibile climate changes. The periods 1931-1960 and 1961-1990 are of particular interest since they have been recommended by the WMO as the basic ones for determining climatic norms. Their values and empirical statistics, calculated for various periods, give important information on the climatic conditions in some regions for the last 60 years. The temperature pattern on the USSR territory during the last two 30-year periods is analysed in the paper.

## II. DATA

Air temperature monthly means for 243 USSR stations out of the baseline climate data set were used for analysis. Stations located outside large cities were chosen to create the baseline data set. About 38% of the stations are located in small towns and only 6% - in large cities with populations of over a million.

## III. RESULTS

Long-term air-temperature means were calculated for 1931-60 and 1961-90 for obtaining a comparative characteristic of the temperature pattern of two 30-year periods. The annual long-term air temperature mean for 1931-60 amounted to 1.2°C on the whole for the USSR territory . For the second 30-year period the mean annual temperature was 0.3°C higher. A comparison of the annual 30-year mean temperatures at individual stations showed, that it was only in the USSR northern areas that the mean annual temperatures for the last 30-year period were lower than in the period 1931-60. The difference between long-term means of annual mean air temperatures ($\bar{T}_{61-90} - \bar{T}_{31-60}$) is positive on the rest of the territory (Fig.1). The greatest differences between the long-term means are observed at the Arctic stations (-1.3°C ) and on the territory of Central Kazakhstan ( +1.2°C ), with the air temperature increase in 1961-90 mainly due to winter warming ( Table 1 ). Table 1 contains long-term mean air temperatures, averaged for two periods - cold ( November - March ) and warm ( April - October ).

TABLE 1

LONG-TERM AIR TEMPERATURE MEANS FOR THE USSR TERRITORY FOR 30-YEAR PERIODS

| Period | $\bar{T}_{1931-60}$ | $\bar{T}_{1961-90}$ | $\bar{T}_{1961-90} - \bar{T}_{1931-60}$ |
|---|---|---|---|
| Year | 1.2 | 1.5 | 0.3 |
| Cold | -11.4 | -10.7 | 0.7 |
| Warm | 10.2 | 10.2 | 0 |

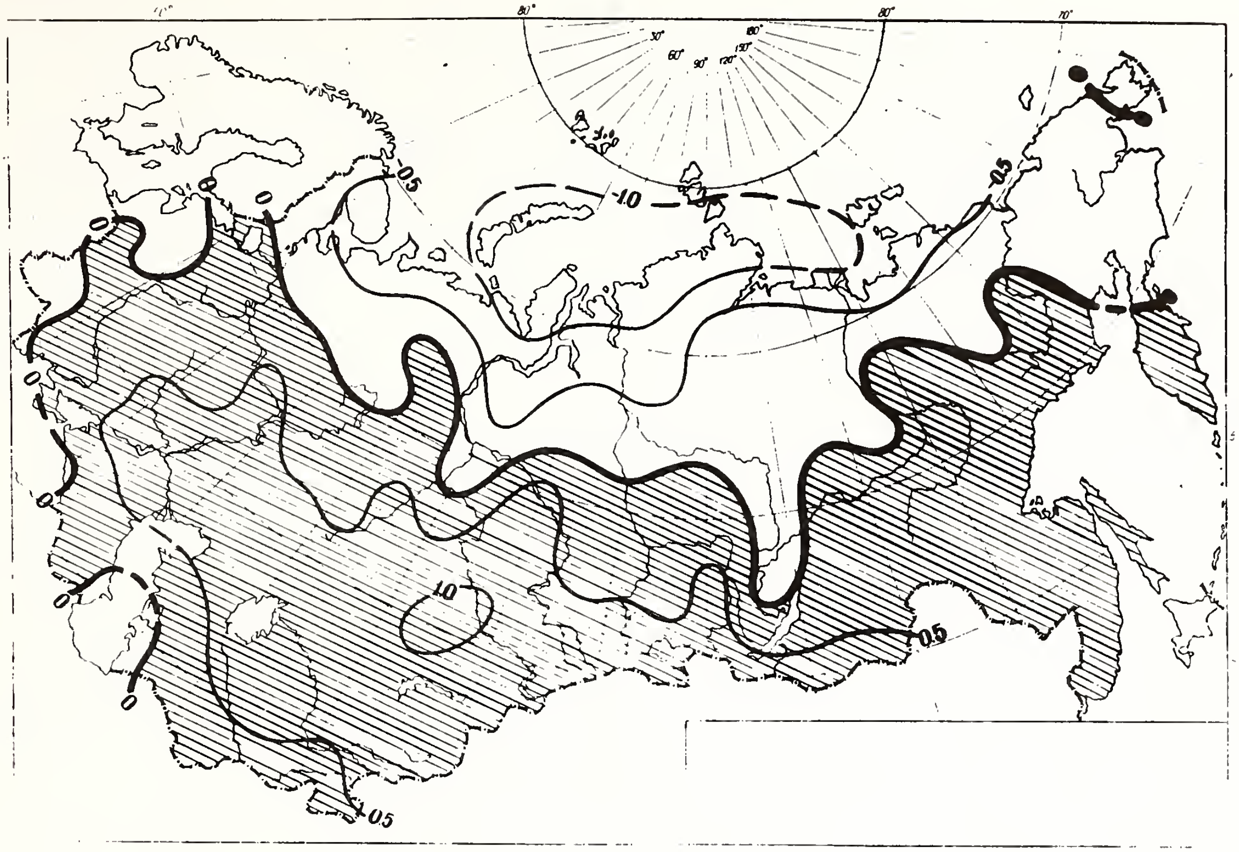

Fig.1. Difference between the long-term average values of annual air temperature in the period 1961-90 and 1931-60.

Averaging over the whole of the USSR territory yields a considerable smoothing of results. Similar calculations were therefore made for individual regions of the country. The territory was divided into three areas: the north area (north of 60°N ); the south - west area ( south of 60°N and west of 80°E ) and the south - east area. A decrease in the long -

term mean air temperature is only characteristic of the USSR north both in winter and summer of 1961-1990 ( Table 2 ) while an air temperature increase is characteristic of the southern area in the last 30-year period ( in the western area - by 0.9°C and in the eastern area - by 0.8°C ). Linear trend coefficients, calculated from data for the given periods, reveal an air temperature increase tendency , most essential in winter in the last 30-years in all selected areas (Table 2)

TABLE 2.

CHARACTERISTICS OF TEMPERATURE PATTERN IN THE USSR INDIVIDUAL REGIONS

| The USSR region | $\bar{T}_{61-90} - \bar{T}_{31-60}$ | | Linear trend coefficient , °/decade | | | |
|---|---|---|---|---|---|---|
| | | | 1931-60 | | 1961-90 | |
| | winter | summer | winter | summer | winter | summer |
| north | - 0.2 | -0.3 | -0.42 | -0.13 | 0.39 | 0.15 |
| south-west | 0.9 | 0.1 | 0.13 | -0.08 | 0.27 | 0.03 |
| south-east | 0.8 | 0 | -0.19 | -0.14 | 0.48 | 0.15 |

The linear trend coefficient amounted to 0.48°C / decade in winter in the south - west. It should be noted, that in spite of the fact that long-term mean air temperatures in the north areas are lower both in winter and summer in the last 30 years than in 1931-1960 the linear trend coefficient is positive amounts to 0.39°C / decade in winter. An air temperature decrease tendency ( $\beta$=-0.42°C / decade ) was observed during 1931-1960 ( Fig.2 )

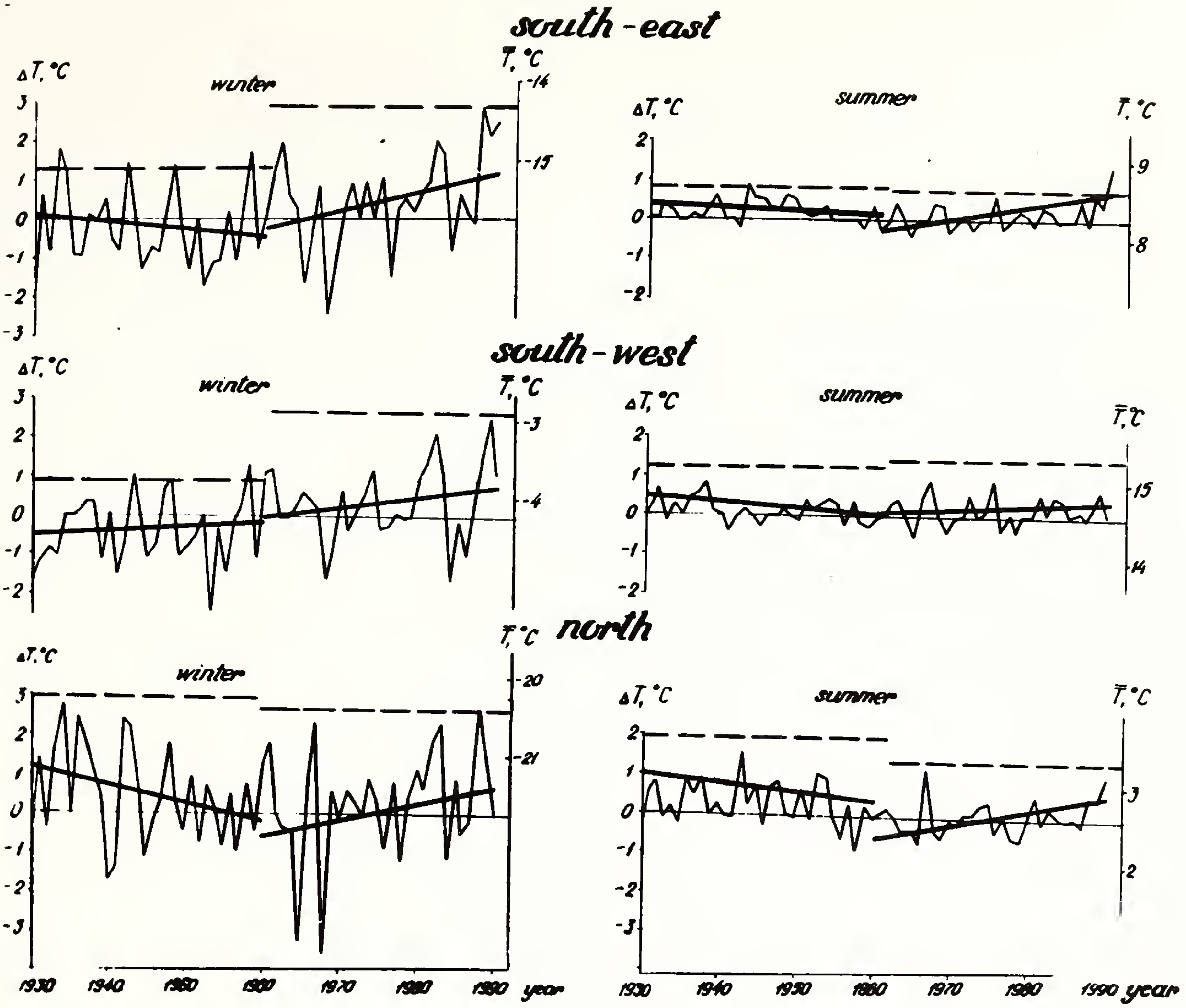

Fig. 2. Air temperature anomalies in cold and warm seasons of the year for the USSR various regions

----- - long-term mean air temperature in 1931-60 and 1961-90

_____ - linear trend coefficient ( °C / decade ) for two periods ( see values in the text )

## IV. CONCLUSION

A preliminary analysis of temperature pattern on the USSR territory shows, that practically in all areas within the USSR, with the exception of the northern areas, the mean temperature values for the last 30 years are higher than those for the preceding 30 years (1931-60). It is mainly due to temperature increase in winter. It is interesting to note that there exists a positive linear trend in the last thirty-year period irrespective of what the long-term air-temperature means of the two periods are. Further investigations, using precipitation, humidity and other data allows assessing the relationship of the observed temperature increase over the USSR territory with the global climate changes.

# TEMPERATURE ANOMALIES IN COLD PERIODS ON THE USSR TERRITORY

O.BULYGINA, N.KORSHUNOVA, V.RAZUVAYEV

ALL-UNION RESEARCH INSTITUTE OF HYDROMETEOROLOGICAL
INFORMATION - WORLD DATA CENTRE
OBNINSK, USSR

## I. INTRODUCTION

Studying extreme and anomalous weather phenomena presents both scientific and practical since an increase in the number of such phenomena in different regions can be treated as an indicator of climate change.

The temperature pattern of cold periods (November-March of 1988-89 and 1989-90), which were the warmest periods during the last hundred years within the USSR , is analysed in the paper.

## II. DATA

Mean monthly air temperature data for 243 stations with long data records for 1891-1991 were used for the analyses. The temperature anomalies were obtained with respect to norms calculated for 1951-1980.

## III. RESULTS

The years 1989 and 1990 were the warmest years for the last 100 years on the USSR territory. The mean annual air

air temperature was maximum in the whole period under consideration. The anomaly amounted to 5.0°C and exceeded $2\sigma$.

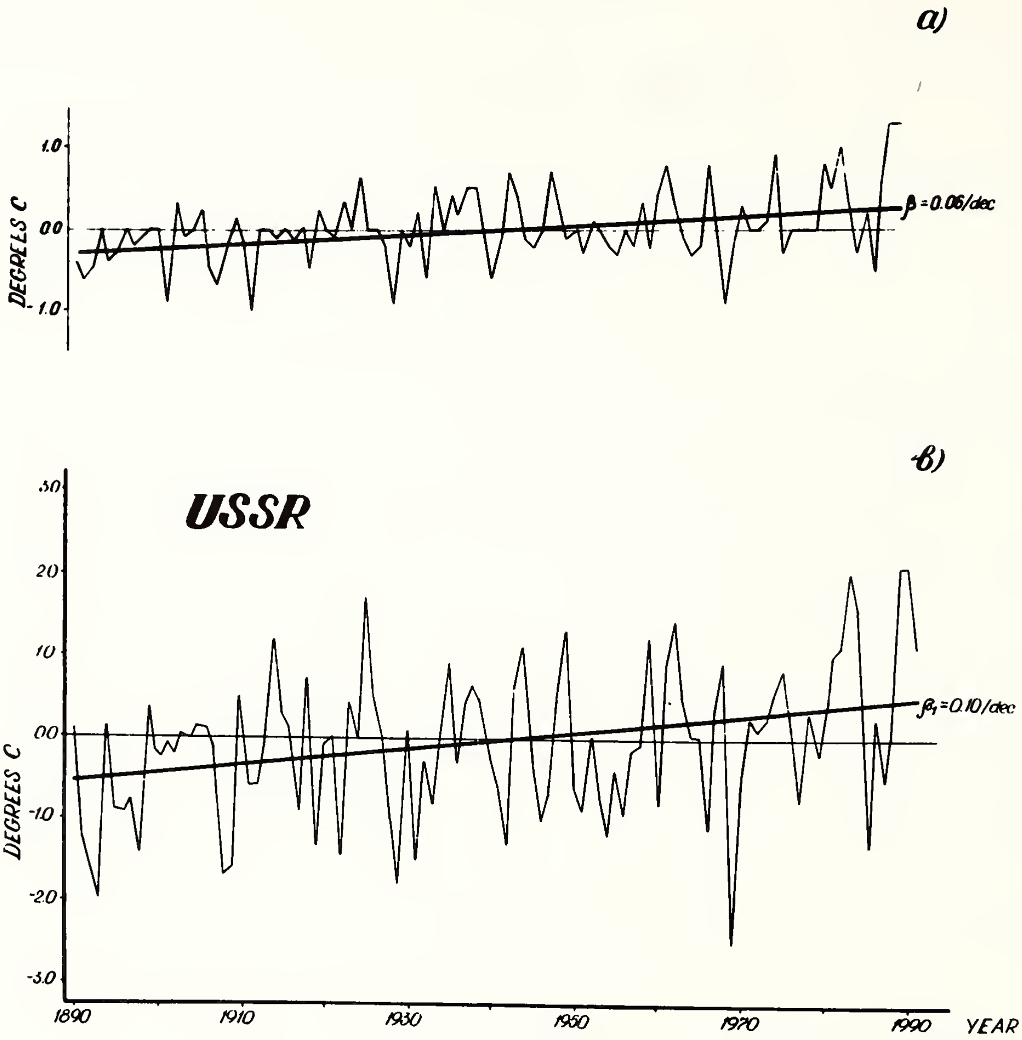

Fig. 1. Mean annual ( a ) and mean seasonal ( November-March ) ( b ) air temperature anomalies on the USSR territory. $\beta_1$ - linear trend coefficient, computed for the period 1890-1990
The anomalies were computed with respect to norms for 1951-80 for 243 stations

temperature anomaly for the whole of the USSR amounted to 1.3°C. It should be noted, that during the last decade there were three cases when the mean annual air temperature anomaly on the USSR territory either exceeded or amounted to 1°C while during the whole preceding period ( Fig. 1a ) no such anomalies were observed. The linear trend , calculated from a number of annual mean air temperature anomalies for 100 years ( the linear trend coefficient was $\beta_1$=0.06°C/decade ), is mainly due to the positive anomalies of the last years.

A comparative analysis of the temperature pattern in the warm ( April - October ) and cold ( November- March ) seasons of the year showed that it was in winter seasons that the largest positive anomalies were observed. The linear trend coefficient in the air temperature anomaly series averaged 0.10°C / decade ( Fig. 1b ) in the cold period on the USSR territory . Maximum seasonal anomalies for the last 100 years were obtained in the cold periods of 1988-89 and 1989-90 . They amounted to 2.1°C . As for the space distribution of the air temperature seasonal anomalies in the years under consideration positive values prevail on most of the USSR territory ( Fig. 2 ).In the cold period of 1988-89 the centre of maximum anomalies was observed in the central part of West Siberia, where seasonal temperatures exceeded the norm by 6-7°C. The next year seasonal temperature anomalies in this region decreased while in the European USSR they increased to 4°C ( Fig. 2 b ). To estimate the contribution of the monthly means to the formation of seasonal air temperature anomalies the mean air temperature anomaly series on the USSR territory in individual months of the season were considered . The largest positive anomalies were observed in February and March (Table 1), with February of 1989 being the warmest for the whole period of record ( 4°C anomaly ). As for the cold period of 1989-90 the largest anomalies were observed in March, when

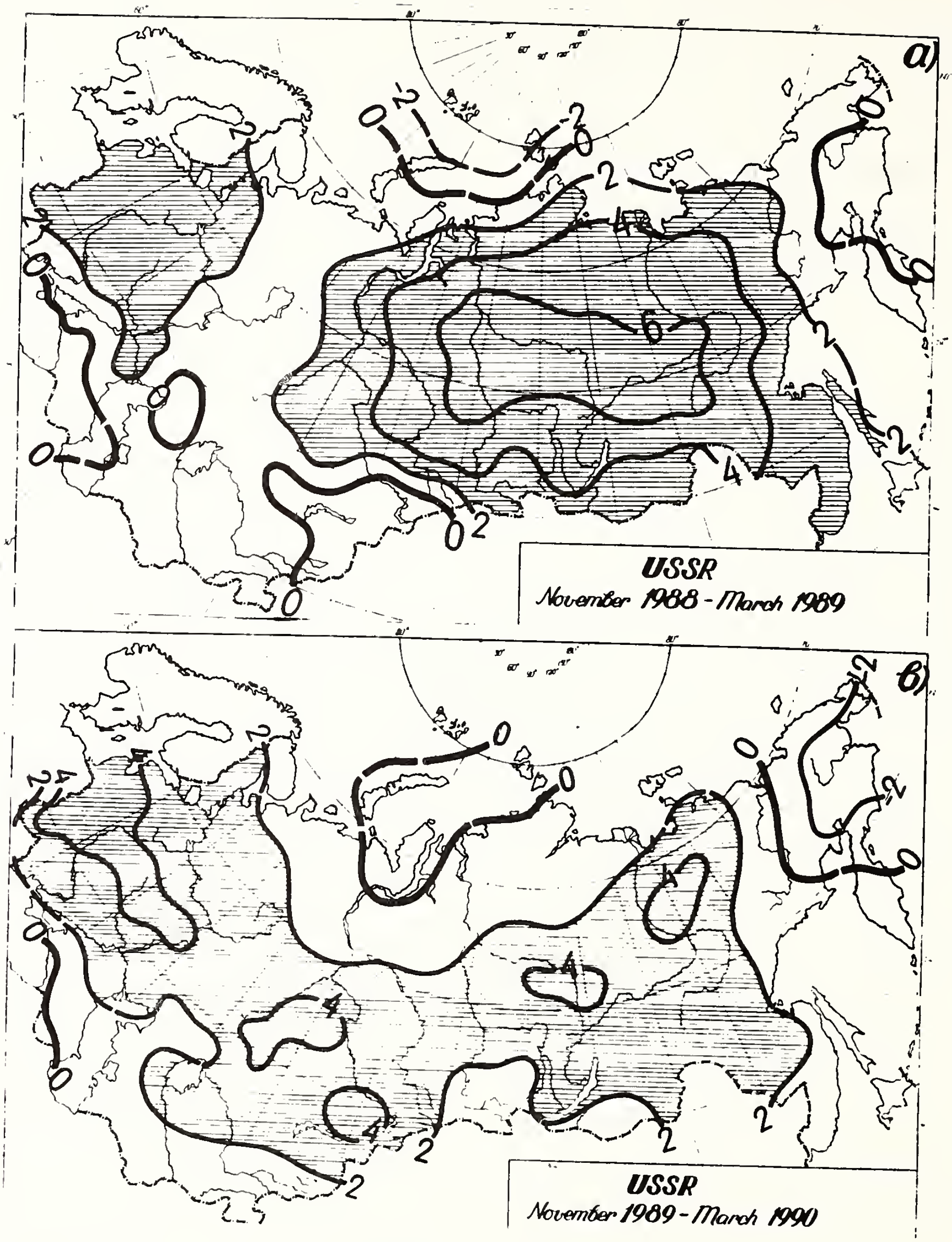

Fig. 2 Seasonal ( November-March ) air temperature anomalies ( with respect to norms for 1951-80 ) on the USSR territory in a) 1988-89, b) 1989-90
The hatched areas - seasonal anomalies exceed 2°C.

TABLE 1.

## MEAN MONTHLY AIR TEMPERATURE ANOMALIES IN THE COLD PERIODS ON THE USSR TERRITORY

| | November | December | January | February | March |
|---|---|---|---|---|---|
| $\sigma$ | 1.6 | 2.3 | 2.3 | 2.1 | 1.8 |
| 1988-89 | -0.4 | 1.7 | 1.8 | 4.0 | 3.7 |
| 1989-90 | 0.6 | 1.8 | -0.1 | 3.3 | 5.0 |

Concerning the space distribution of monthly temperature anomalies, in individual months the absolute maximum values were exceeded at many USSR stations. Absolute maximum temperatures exceeding $2\sigma$ were observed at a number of Siberian stations ( Minusinsk, Tura, Ust-Maya ) in March 1989. In the European USSR temperature anomalies were maximum in February 1990 ( Syktyvkar, Minsk, Arkhangelsk, Riga ) and March 1990 ( Kursk ). The station "Kursk" is to be mentioned in this connection, which was in the centre of maximum anomalies of the monthly mean air temperature for three months of the cold period in 1990. In January 1990 the monthly mean air temperature at the station approached its extremum while in February ( 0.1°C ) and March ( 3.4°C ) the monthly means exceeded the absolute maximum values for the whole period of record at the station. The monthly mean temperatures were slightly lower in February and March 1989 -0.7°C and 3.1°C, respectively. The temperature anomalies in these months exceeded $2\sigma$.

## IV. CONCLUSIONS

Anomalously warm winters, observed within the USSR in 1989-90, following one another ( the cold season of 1990-91 was also warm though less anomalous ) is an extraodinary event. Mean seasonal anomalies during the periods were maximum in the last 100 years. Anomalously warm winters, more frequent during the last years, the positive linear trend coefficients obtained for a number of the mean annual anomalies and air temperature anomalies in the cold period, can probably be considered as an indicator of climate change on the USSR territory.

# AFRICAN RAINFALL 1981-1990

S. Nicholson
Florida State University
Department of Meteorology
Tallahassee, FL 32306

This paper provides an update on the rainfall conditions which have prevailed over the African continent during the past two decades. The investigation utilizes the station network in Fig. 1; geographical regions of special interest are shown in Fig. 2. In view of the strong spatial coherence of African rainfall anomalies, time series for these eight regions serve to describe most of the continental-scale variability. Station and regional rainfall is calculated as in previous studies.

Rainfall for the eight regions in Fig. 2 is represented as time series of standardized spatially-averaged anomalies from the long-term mean (i.e., the mean over the entire length of record). A value of 1 thus represents an average regional anomaly of one standard deviation from the mean (Fig. 3).

Rainfall has been markedly below normal not only in the Sahel proper, but in adjacent semi-arid regions of West Africa as well (Fig. 3a). In the northern most sector, or Sahelo-Saharan zone, annual rainfall has exceeded the mean in only two years of the decade, 1988 and 1989. In the Sahel and Soudan zones, rainfall has not exceeded the long-term mean since 1969. In the wetter and more southern Soudano-Guinean zone the situation has been similar, with only 1978 exceeding the mean. These results are consistent with earlier analyses, which have shown a tendency for similar anomalies to prevail in these four zones. However, the humid Guinea Coast, which generally exhibited anomalies of the opposite sign, was also abnormally dry throughout both the 1970's and the 1980's.

In Eastern and Southern Africa, the situation has been markedly different (Fig. 3b). East Africa was generally abnormally wet during the 1980's, conditions which began about 1977. Rainfall fluctuations in the northern and southern Kalahari have continued to parallel each other, a characteristic demonstrated previously. They have also tended to parallel those in the Sahel as well. This was the case in the 1980s, when these regions were abnormally dry, but unlike the Sahel, Kalahari rainfall was above-average for the 1970s decade as a whole.

Figs. 4 and 5 show the mean decadal patterns of rainfall for the continent as a whole. Here, station data is presented, but averaged for 1° squares. Also, the values in this case represent a percent departure from the long-term mean. Rainfall was anomalous on a continetial scale during both decades. During the 1980s, rainfall was subnormal generally everywhere except in the low latitudes and in small sectors on the northern and southern extremes of the continent. In some individual years, such as 1983, rainfall was below the long-term mean over virtually the whole continent.

In the 1970s (Fig. 5) an unusual situation occurred; a clear opposition between northern and southern hemispheres is apparent. Rainfall was well above average in the southern subcontinent but well below average in the north. This pattern is not apparent in the major rainfall anomaly types determined previously with data prior to 1974. In fact, it was apparent in only a few individual years prior to the 1970s. This suggests a major change in the prevailing factors governing African rainfall variability.

Particularly unusual is the opposition between the Sahel and Kalahari, seen also in the time series of Fig. 3.. In the past the trends have tended to be parallel in the two regions, especially on decadal scales. It is interesting to note that if anomalies in the Sahel are calculated as a departure from recent 20-year means, the anomalies in the Sahel bear a much closer resemblence to those in the Kalahari (Fig. 6). The correlation coefficient r between the time series is .50, nearly as high as that between the two Kalahari series in Fig. 3b (r = .57). This provides some justification of the hypothesis (Nicholson, 1989) that the factors forcing interannual variability in the Sahel differ from those producing the long-term trends.

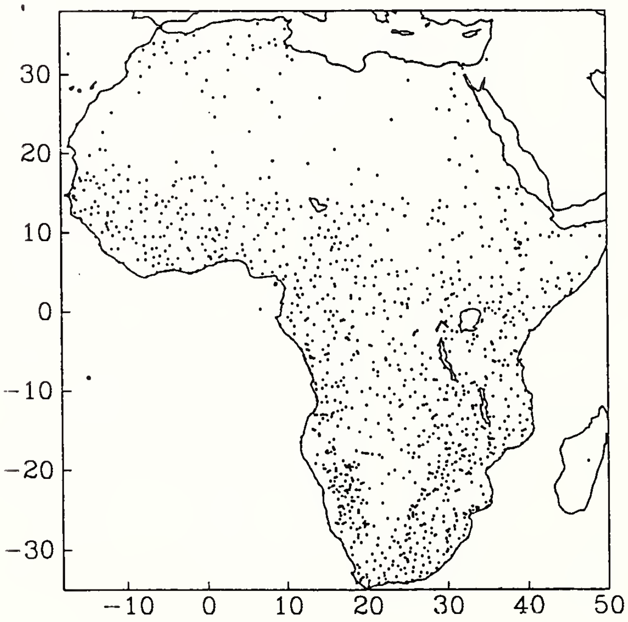

1. Map of rainfall stations.

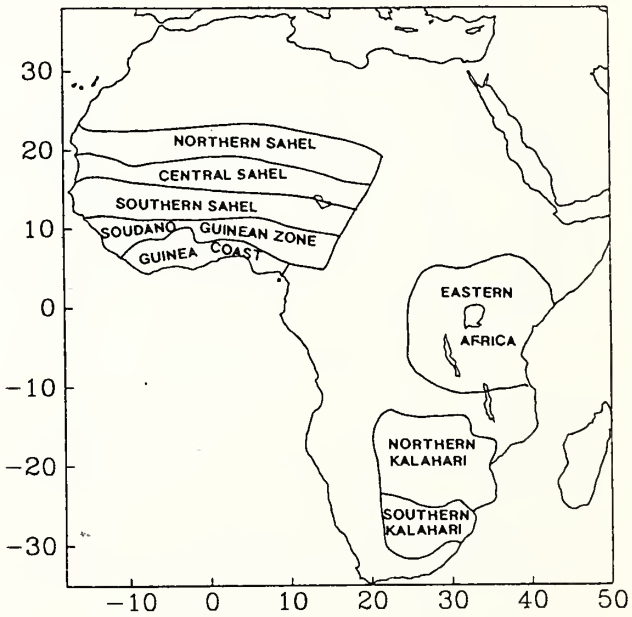

2. Geographical regions utilized in the analysis.

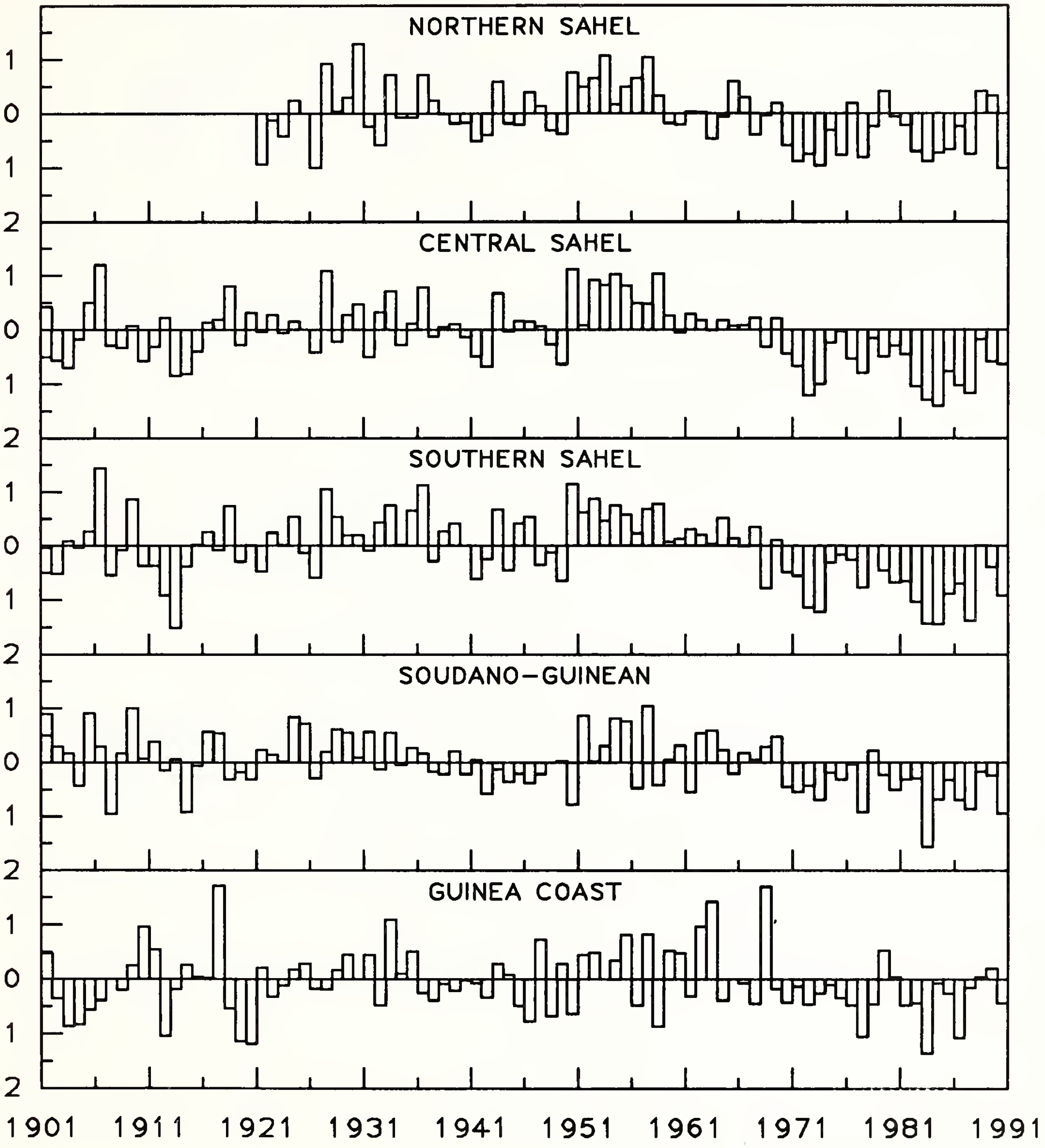

3a. Rainfall fluctuations in West Africa (1901 to 1990), expressed as a regionally-averaged standardized departure (departure from the long-term mean divided by the standard departure). Location of the five regions is indicated in Fig. 1.

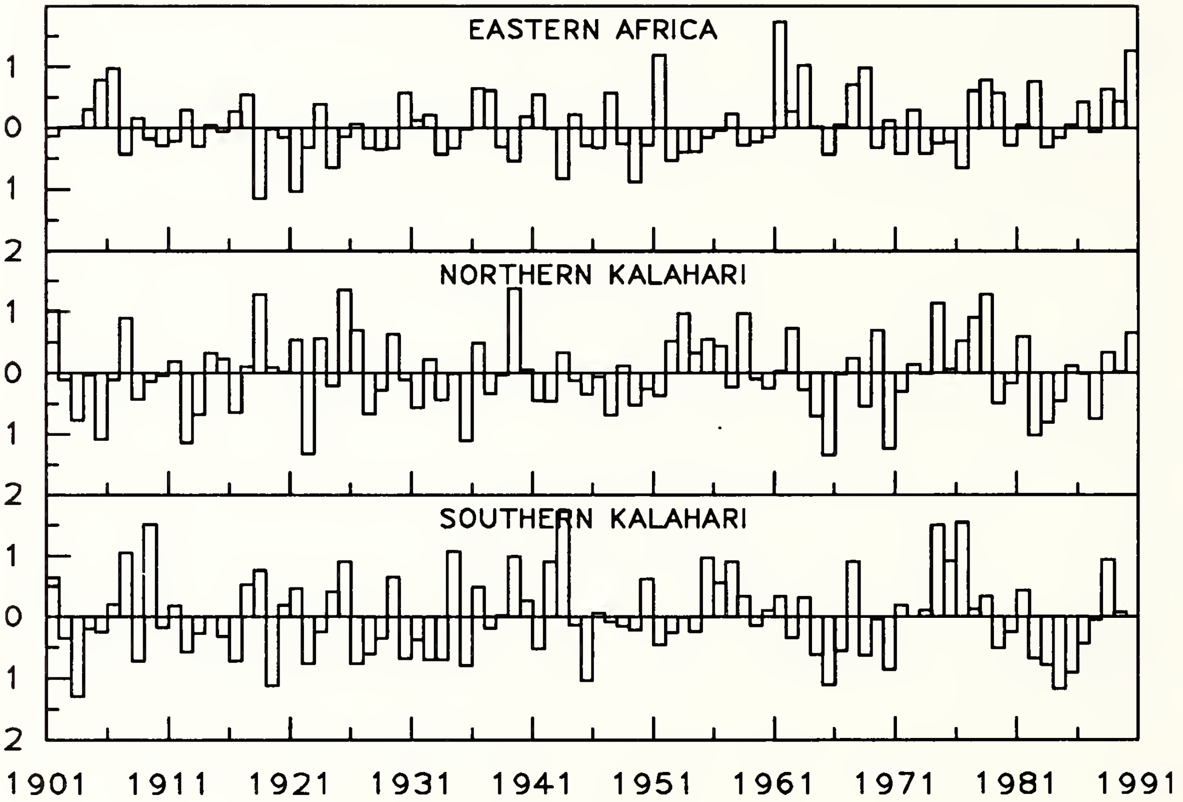

3b. As in Fig. 3a, but for regions of southern and eastern Africa.

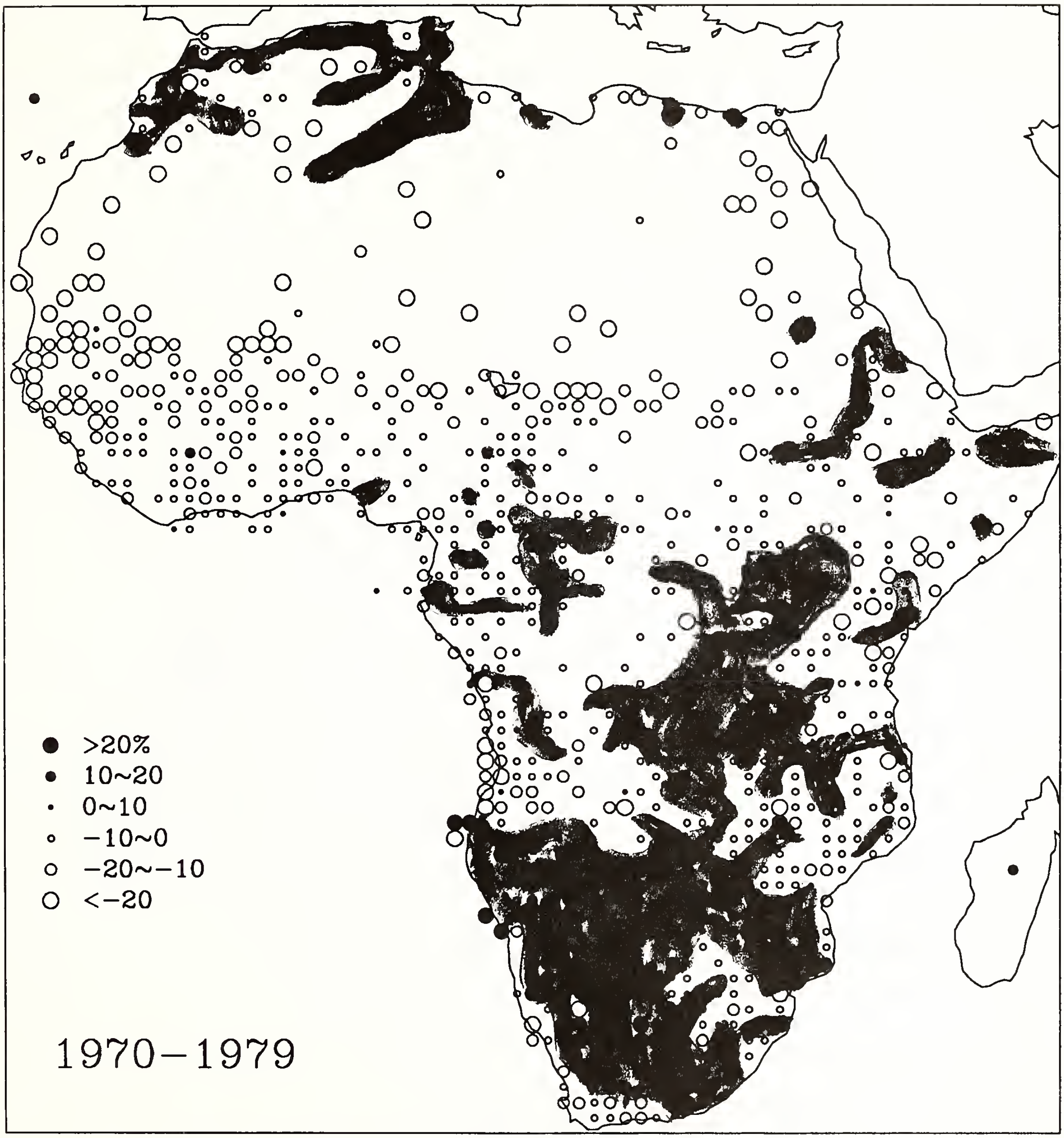

4. As in Fig. 5, but for 1970-79.

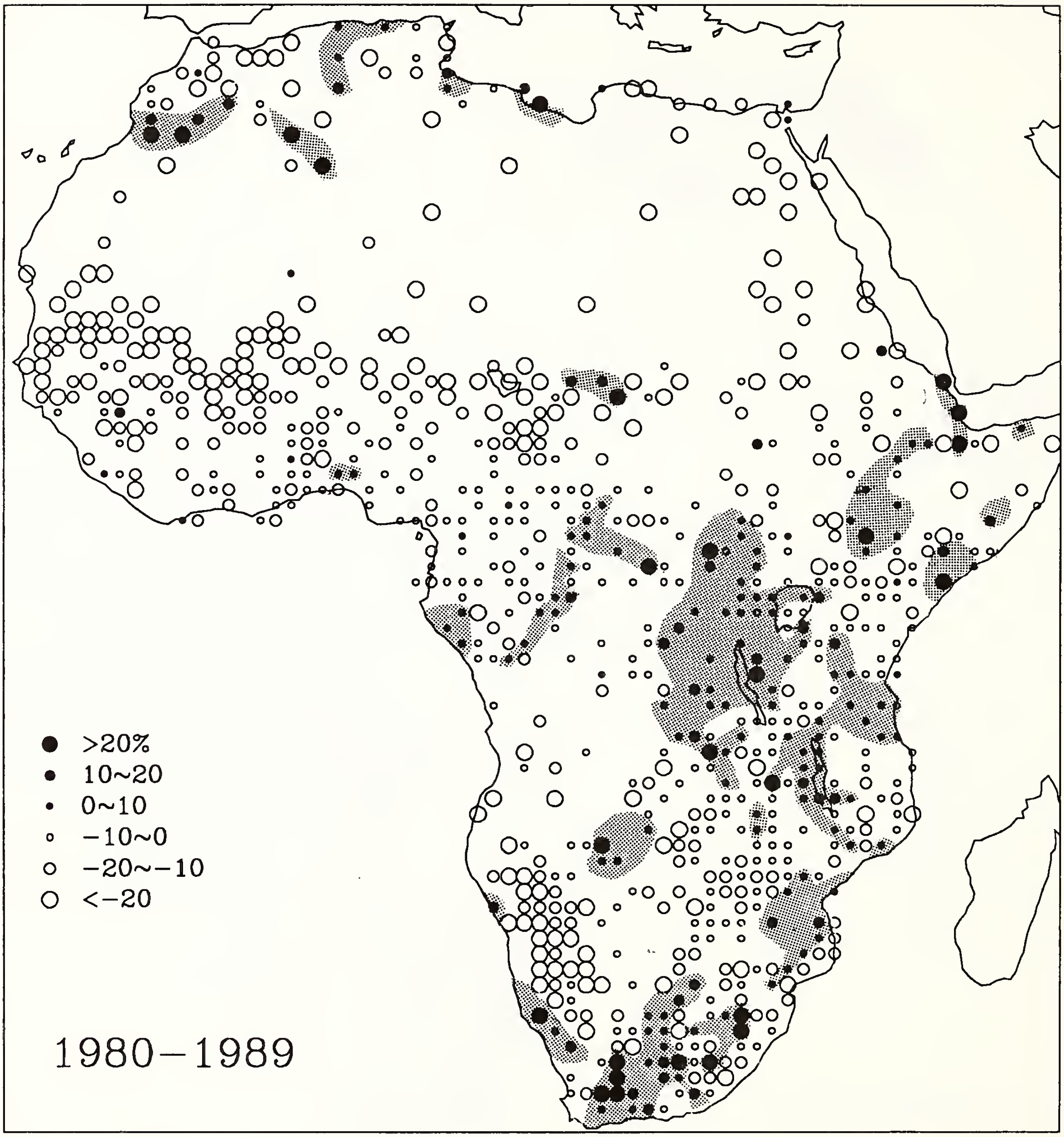

5. Mean rainfall for the decade 1980-89 (expressed as a percent departure from the long-term mean, with station data averaged over 1° squares).

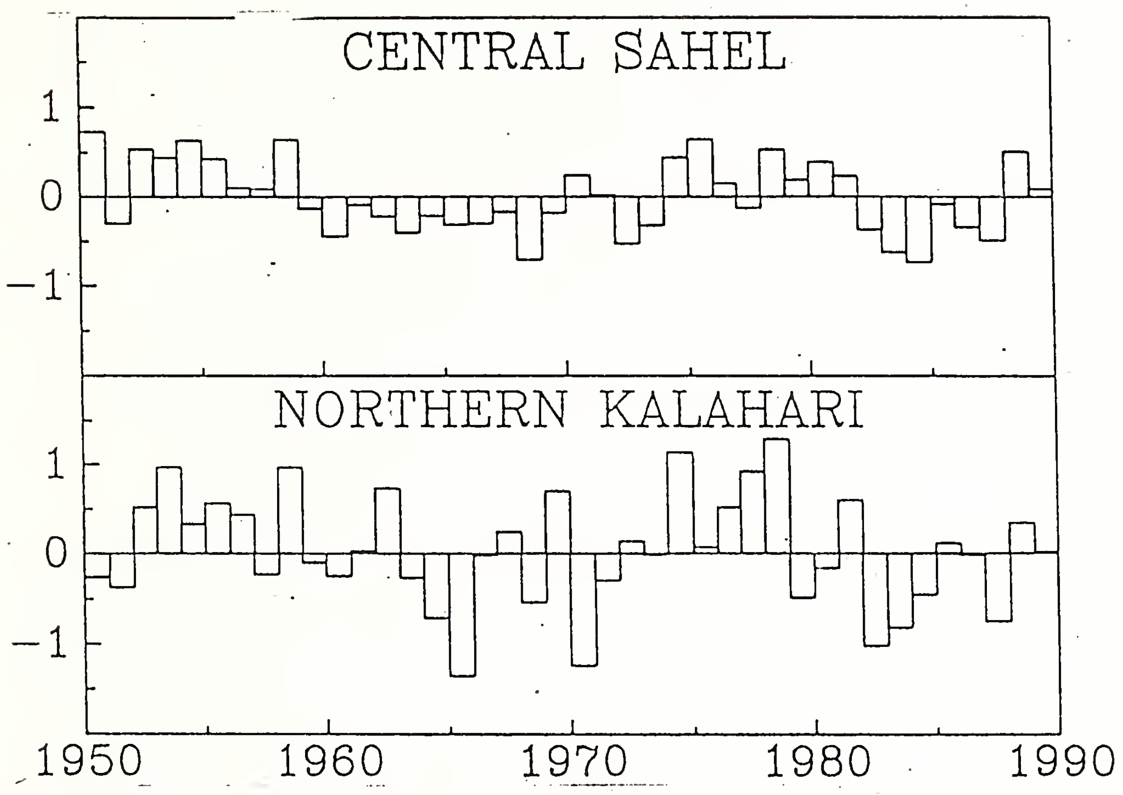

6. Rainfall for the period 1950 to 1990. The Kalahari series is as in Fig. 3. For the Sahel series, rainfall is expressed as in Fig. 3a, but with departures for 1950 to 1969 calculated from the mean for that 20-year period and with departures for 1970 to 1990 calculated from the mean for the 20 years 1970 - 1989.

# LARGE SCALE CLIMATE AND KUWAIT OIL FIRES. MODEL VERSUS OBSERVATIONS.

**Hans-F. Graf**
**Max-Planck Institut für Meteorologie**
**2000 Hamburg 13, Germany**

At the begin of the Gulf War, in early 1991, considerable scientific debate and public concern arose about the question whether or not the smoke from the burning oil wells might have a strong impact on global climate. Therefore, the response of the global climate system to burning oil wells in Kuwait was investigated in a series of numerical experiments using a coupled atmosphere-ocean general circulation model with an interactive soot transport model and extended radiation scheme (Bakan et al., 1991).

An advantage of the fully coupled model system used in this study is that all processes can be computed interactively. Thus the effect on the soot transport of the thermal uplift induced by warming in the layers of maximal soot concentration is automatically included, just as the inhibition of the vertical transport of soot due to the higher static stability established between the heated layers and the cooled surface. Similarly, the complete feedback chain describing the influence of the changed circulation on the precipitation distribution und thus on the soot washout rate, and thereby finally on the radiation perturbations driving the circulation change, is incorporated into a single model.

### Scenario

This study is restricted to the climatic impact of the burning wells on the global scale. Regional climate changes could not be studied in detail with the relatively coarse resolution (ca. $5^{o}$) of the available global models. All climate changes were computed relative to the long term climatology derived from an unperturbed control run. A number of soot injection experiments were carried out to address the many inherent uncertainties. The daily injection of 44.000 tons of soot in the standard scenario was assumed to begin on February 15 and continue until the end of the following January. The soot was introduced at a single gridpoint with constant mixing ratio into atmospheric levels between 65m and 1737 m (model layers 2 - 5). To allow for the sedimentation of large soot particles in the immediate vicinity of the source, the initial source strength was reduced by 15 %.

An a posteriori comparison with reality shows that this scenario really described a worst case. First of all the fires were gradually extinguished. At the end of October the last fire was blown out. Second, the estimated residence time of soot in the atmosphere (20 days) was by far too high. A value of less than 10 days has been observed. The amount of oil burned still is subject of debate, but the twofold daily pre-war production remains near the upper limit. Absolutely correct was the estimation of the injection height, one of the most important input parameters.

### Prediction versus observations

Observations have shown the **soot plume** to remain between 1 and 4 km height, with occasionally rising puffs up to 7 or 8 km during summer. This is in very good agreement with the model calculations.

The model predicted a decrease in surface **air temperature** on the order of $4^0C$ in the Gulf region. This high value could not be detected in monthly means of observations (Clim. Diagost. Bull., CAC 1991; Witterung in Übersee, DWD 1991). Outside this region the changes are small and mostly statistically insignificant. Those anomalies outside the Gulf which were of local statistical significance in the model computations could not be traced in the observations. Therefore, except some cooling in the vicinity of the Gulf region no indication is evident for any coincidence between thermal anomalies in the model and in nature.

Some evidence for an intensified **Indian Summer Monsoon** onset is seen in Figure 1 comparing our simulation (scenario 3) with year 9 of the control run, the year in which the soot forcing was introduced. There is no shift in the onset date. Similar anomalies were observed at the begin of the monsoon season of this year for the stations indicated in Figure 2, with amounts of the monsoon rain in the first monsoon month as never observed during the 30 year control period of 1931 to 1960 (a time when the Indian monsoon was generally strong). The stations in the southern part of India (Madras, Bangalore, Kozhikode, Minicoy, Trivandrum, Colombo and Hambantola) reported a mean of 186% of the normal June precipitation. The stations in Central India (Bombay,Poona, Hyderabat, Vishakhapatuam and Masulipatuam) still measured a mean of 150% of the mean June precipitation. Both positive anomalies were not due to single exceptionally strong rainstorms. The southern (central) stations had 19 (12) days with precipitation.

Fig.2: Stations used to study the Indian Monsoon onset (heavy dots)

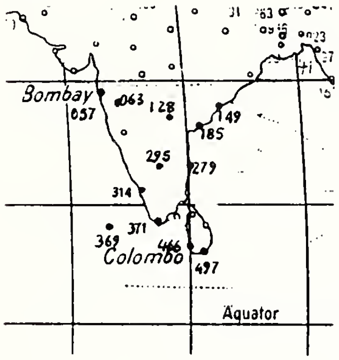

Figure 1: Time evolution of the Indian Monsoon. Shown is the time series of total precipitation at the gridpoint near the southern tip of India. Time axis starts with April 1. Year 9-ctrl is the year in the 20 year control run which was disturbed by the soot following scenario3 (see text)

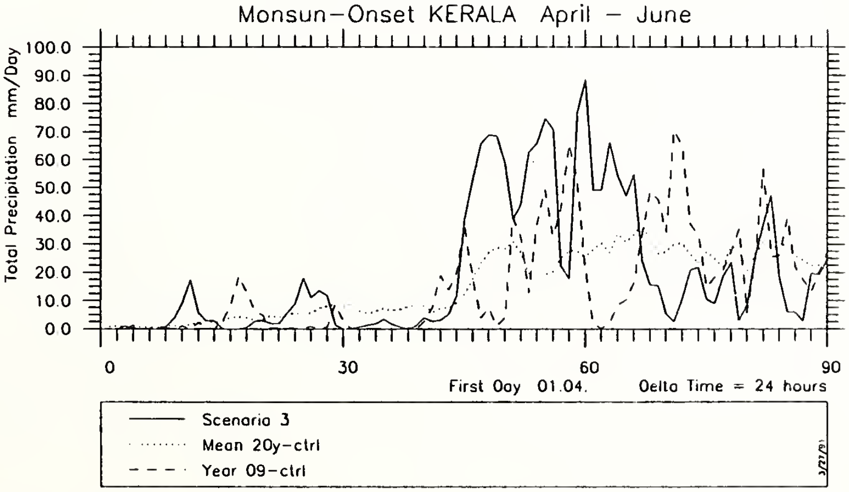

Literature: Bakan,S. et al., Nature, Vol.351, No. 6325, pp. 367-371, 30th May, 1991

# RECENT GLOBAL TEMPERATURE CHANGES: OZONE AND AEROSOL INFLUENCES

T.M.L. Wigley, P.D. Jones, P.M. Kelly, M. Hulme

Climatic Research Unit
University of East Anglia
Norwich NR4 7TJ, UK

Introduction: This paper serves two purposes. First, detailed information is provided on global-scale near-surface temperatures through October 1991 over land and August 1991 over the land-plus-oceans. An estimate is made of the annual-mean for 1991 based on these data and allowing for possible effects due to El Niño and the eruption of the volcano Pinatubo. Second, observational data are used to test two recently hypothesized mechanisms for influencing global-mean temperatures, the negative feedback due to ozone-related stratospheric cooling and the cooling effect of tropospheric aerosols. No evidence is found to support the former, while the data do show changes consistent with the latter.

Recent and predicted temperature changes: The Climatic Research Unit's land-plus-marine near-surface temperature data base (Jones and Wigley, 1990; Jones et al., 1991) is routinely updated with a roughly three-month delay due to data acquisition problems. Marine data are provided by the U.K. Meteorological Office as updates of the Bottomley et al. (1990) data set.

Monthly hemispheric temperature anomalies are shown in Figs. 1 and 2. Figure 1 shows land-only data through October 1991, with reference period 1951-70. Figure 2 shows combined land and marine data through August 1991, with reference period 1950-79. All records show only minor and non-significant trends over the period from January 1980, consistent with other data sets (see Folland et al., 1990). A marked warming trend is evident in both Northern Hemisphere records since late 1984, during which period extreme monthly anomalies occurred in December 1984 (cold) and March 1991 (warm). The latter is by far the warmest month on record. The warmth was associated with an unusually early retreat of the Northern Hemisphere's seasonal snow cover (Robinson et al., 1991).

On an annual-mean basis, 1990 was the warmest year in both the land-only and the land-plus-marine records (see Fig. 3 - this only shows part of the full record). For the monthly data available to August 1991, 1991 is slightly cooler than 1990, comparable to the second and third warmest years (viz. 1988 and 1987). What is the annual-mean value likely to be?

To estimate this, three factors need to be considered. First, annual-mean anomaly values correlate highly with average values over the first "n" months, where n = 1, 11. Correlations over 1901-90 between annual temperature anomalies and the anomalies for January, January-plus-February mean, January-to-March mean, etc. through to January-to-November mean (land-plus-marine data) are 0.824, 0.875, 0.919, 0.941, 0.955, 0.967, 0.977, 0.985, 0.989, 0.993 and 0.997. For the mean over January to August, the relationship with the annual mean is described by the regression equation

$$T_{ann} = 0.933\ T_{JtoA} - 0.003 \quad (n = 90,\ r^2 = 0.970)$$

Since $T_{JtoA}$ is 0.39, the estimated annual-mean temperature anomaly for 1991 is 0.36.

The second factor is the influence of the El Niño/Southern Oscillation (ENSO) phenomenon. Jones (1989) has shown that annual temperature deviations from the low-frequency changes (based on a 10-year Gaussian filter) correlate well with the Southern Oscillation Index (SOI) with SOI values lagged by six months (e.g., the 1991 anomaly is most strongly related to the SOI over July 1990 to June 1991, etc.). The low-frequency value for 1991 can be estimated by extrapolation to be 0.30°C. From the SOI data, the ENSO-related anomaly should be 0.04°C. Hence, the 1991 estimate becomes 0.34°C.

Neither of the above methods accounts for the effect of a randomly imposed external forcing factor. With the eruption of Pinatubo in the Philippines in June 1991, we have just such a factor. This should cause a cooling effect which should be superimposed on the above estimates. Based on Kelly and Sear (1984) and Sear et al. (1987) we might expect the influence of this volcanic eruption to be noticeable in the near-surface temperature data as early as two months after the eruption (i.e., August, 1991). The monthly temperature depression ($\Delta T$) can be estimated using the superposed epoch results of Sear et al. (1987), as given in the Table below (all temperatures in °C).

| Month after eruption | 0 | 1 | 2 | 3 | 4 | 5 | 6 |
|---|---|---|---|---|---|---|---|
| Actual month | J | J | A | S | O | N | D |
| Global $\Delta T$ ($\sigma$ units) | - | - | -0.5 | -1.0 | -1.2 | -0.7 | -0.7 |
| Monthly S.D. ($\sigma$) | - | - | 0.20 | 0.19 | 0.20 | 0.21 | 0.26 |
| Global $\Delta T$ (°C) | - | - | -0.10 | -0.19 | -0.24 | -0.15 | -0.18 |

The effect on the annual mean for 1991 should be one twelfth of the sum of the August through December $\Delta T$ values, viz. 0.07°C. We can allow for the fact that Pinatubo injected an unusually large amount of material into the stratosphere by inflating this value by 50%, to give a depression of 0.03°C.

If we now take the average of the partial-year regression and SOI-based estimates as a base level prediction (viz. $(0.36 + 0.34)/2 = 0.35$°C), then the estimated 1991 mean after allowing for Pinatubo is 0.28°C. This would still leave 1991 as an exceptionally warm year, fifth warmest in the full land-plus-marine record (after 1990, 1988, 1987 and 1983). This estimate ignores natural variability, and the relative small monthly volcanic signal could be obscured by this. We note that there is no evidence of anomalous cooling over the land masses up to the end of October. Given this, the final annual-mean for 1991 will probably be above the value estimated here.

Ozone depletion feedback effect: In the most recent assessment of halocarbon-related ozone depletion (WMO/UNEP, 1992) attention has been given to a possibly important feedback mechanism associated with stratospheric ozone depletion. Halocarbons have a direct and strong greenhouse effect which should cause warming of the lower troposphere. However, they also cause depletion of ozone in the lower stratosphere which leads to stratospheric cooling. It has been suggested that these cooler temperatures may lead to a change in the surface-troposphere radiation balance sufficiently large to offset the direct enhanced greenhouse effect of increasing halocarbon concentrations. While this effect is most pronounced at high latitudes, especially southern high latitudes, where ozone depletion is a maximum, the claim has been made that the stratospheric cooling would offset the halocarbon greenhouse effect on a global scale.

While a negative feedback on the surface-troposphere radiation balance is likely through this mechanism, whether or not there would be a noticeable temperature response at the surface is far less certain. The surface-troposphere result has already been misinterpreted on a number of occasions as implying a strong surface cooling, enough to counter-balance (or more) the halocarbon-induced component of greenhouse warming. If the surface cooling effect were significant, then one might already expect to see a relative cooling in the Antarctic (where ozone depletion is largest) during the months of September to November (when the main depletion occurs) relative to the rest of the year.

We test this hypothesis in Fig. 4. Ozone depletion has been noticeable only since 1978, and this has been accompanied by stratospheric cooling (Angell, 1988). However, there is no evidence whatsoever of any cooling during September to November relative to January to July (the transition months of December and August have been omitted from the analysis) since 1978 (or earlier). If anything, the relative trends are opposite to what one would expect under the stratospheric-cooling negative feedback hypothesis. Although a definitive statement cannot be made because of the large interannual variability of the temperature data, these results suggest that, if this feedback effect has a surface manifestation, then it is minor even at high latitudes.

Cooling due to tropospheric aerosols: The atmospheric concentration of sulphate aerosol derived from man-made emissions of $SO_2$ has increased significantly this century (see, e.g., Schwartz, 1988). Most of the increase in global $SO_2$ emissions has occurred since the mid-1950s. The relative increase in emissions may have had an amplified response in aerosol concentrations because of the increased use of tall stacks, which lead to longer atmospheric residence times and hence higher concentrations.

Increased aerosol levels cool the Earth in two ways. Over the oceans, where cloud condensation nuclei (CCNs) are less abundant, aerosols act as CCNs leading to more and smaller cloud droplets and, hence, increased cloud albedo (Charlson et al., 1987; Wigley, 1989). In cloud-free areas, Charlson et al. (1990, 1991) have shown that backscatter by sulphate aerosols significantly reduces incoming solar radiation. In both cases, more aerosols means a cooling effect. Wigley (1989) has estimated that the maximum radiative perturbation due to man-made, $SO_2$-derived aerosols over the Northern Hemisphere has been $-1.5Wm^{-2}$ this century. Charlson et al. (1991) estimate the clear-sky effect to be $-1.1Wm^{-2}$ this century averaged over the Northern Hemisphere. The effect is negligible in the Southern Hemisphere, since most $SO_2$ derives from Northern Hemisphere industrial sources. Can the aerosol effect be seen in the observational record?

To answer this question we first try to maximize the signal. We do this in two ways: first, by considering only the region where the aerosol effect is strongest, and, second, by considering only the time of the year when it is strongest. We restrict ourselves to the clear-sky effect only, noting that the cloud albedo effect is of much less certain magnitude (Charlson et al., 1990) and complicated by other cloud-related processes (Albrecht, 1989). To maximize the signal geographically, we choose the region given by Charlson et al. (1991) over which the signal exceeds $2Wm^{-2}$ (their Fig. 2b), and contrast this with the region south of 10°N (both hemispheres) where the effect is minimal. Note that it is important to eliminate areas north of 10°N in regions where the clear-sky aerosol signal is low, because these regions may be "contaminated" by aerosol-related cooling due to cloud albedo effects. To maximize the signal seasonally, we consider only the months June, July, August when the observed aerosol optical depth is largest (Husar and Patterson, 1980) and when the effect should be maximized on theoretical grounds. The data we use are from our own gridded land-plus-marine temperature data set.

The results are shown in Fig. 5. Since the 1950s, there has been a relative cooling in the strong-aerosol-effect region. Although this could simply be a manifestation of natural low-frequency variability (which the relative warming around 1920 must be), it is certainly qualitatively consistent with the hypothesis of a noticeable clear-sky aerosol effect.

Acknowledgements: This work was supported by the United States Department of Energy, Atmospheric and Climate Research Division.

## References

Albrecht, B.A., *Science* 245, 1227-1230 (1989).

Angell, J.K., *J. Climate* 1, 1296-1313 (1988).

Bottomley, M., Folland, C.K., Hsiung, J., Newell, R.E. and Parker, D.E., *Global Ocean Surface Temperature Atlas (GOSTA)*, U.K. Met. Office/MIT, 20pp + 313 Plates (1990).

Charlson, R.J., Lovelock, J.E., Andreae, M.O. and Warren, S.G. *Nature* 326, 655-661 (1987).

Charlson, R.J., Langner, J. and Rodhe, H., *Nature* 348, p. 22 (1990).

Charlson, R.J., Langner, J., Rodhe, H., Leovy, C.B. and Warren, S.G., *Tellus* 43AB, 152-163 (1991).

Folland, C.K., Karl, T.R. and Vinnikov, K.Ya., in, *Climate Change: The IPCC Scientific Assessment* (J.T. Houghton, G.J. Jenkins & J.J. Ephraums, Eds.), Cambridge University Press, 195-238 (1990).

Husar, R.B. and Patterson, D.E., *Ann. New York Acad. Sci.* 338, 399-417 (1980).

Jones, P.D., *Climate Monitor* 17, 80-89 (1989).

Jones, P.D. & Wigley, T.M.L., *Scientific American* 263, 84-91 (1990).

Jones, P.D., Wigley, T.M.L. and Farmer, G., in, *Greenhouse-Gas-Induced Climatic Change. A Critical Appraisal of Simulations and Observations* (M.E. Schlesinger, Ed.), Elsevier Science Publishers, Amsterdam, 153-172 (1991).

Kelly, P.M. & Sear, C.B., *Nature* 311, 740-743 (1984).

Robinson, D.A., Keimig, F.T. and Dewey, K.F., in *Proc. 15th Annual Climate Diagnostics Workshop*, NOAA, Washington D.C., 219-224 (1991).

Schwartz, S.E., *Nature* **336**, 441-445 (1988).

Sear, C.B., Kelly, P.M., Jones, P.D. and Goodess, C.M. *Nature* **330**, 365-367 (1987).

Wigley, T.M.L., *Nature* **339**, 365-367 (1989).

WMO/UNEP, *International Assessment of Ozone Depletion* (R.T. Watson and D.L. Albritton, Eds.), in press (1992).

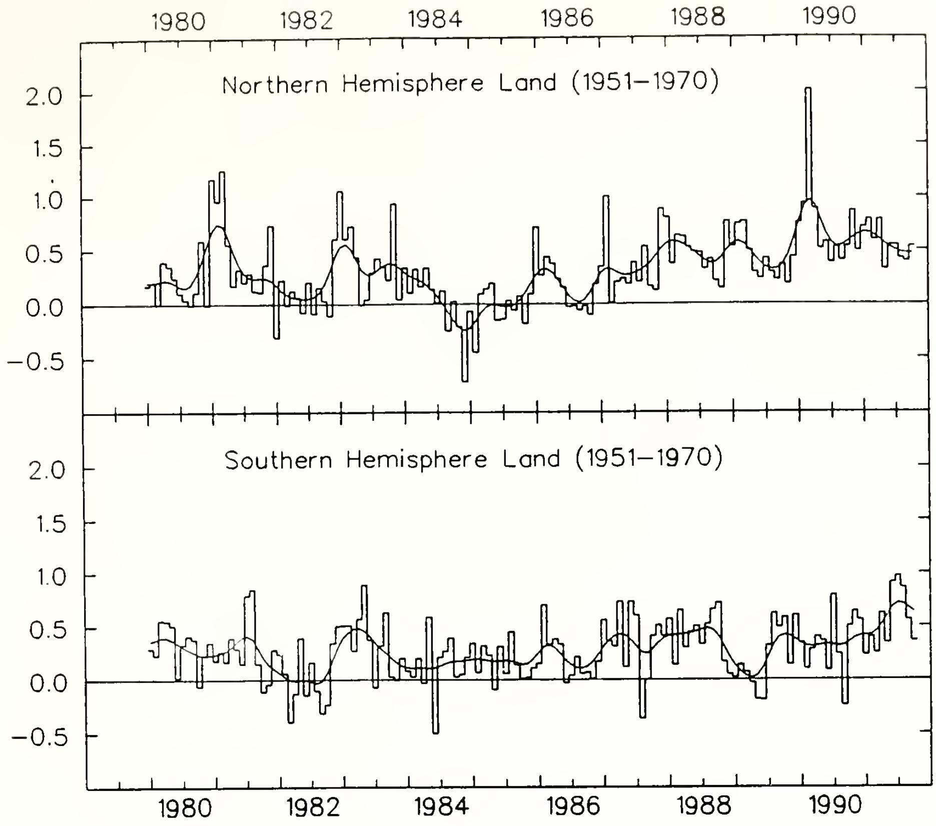

**Figure 1:** Average monthly land-based temperatures for Jan. 1980 to Oct. 1991. Reference period is 1951-70.

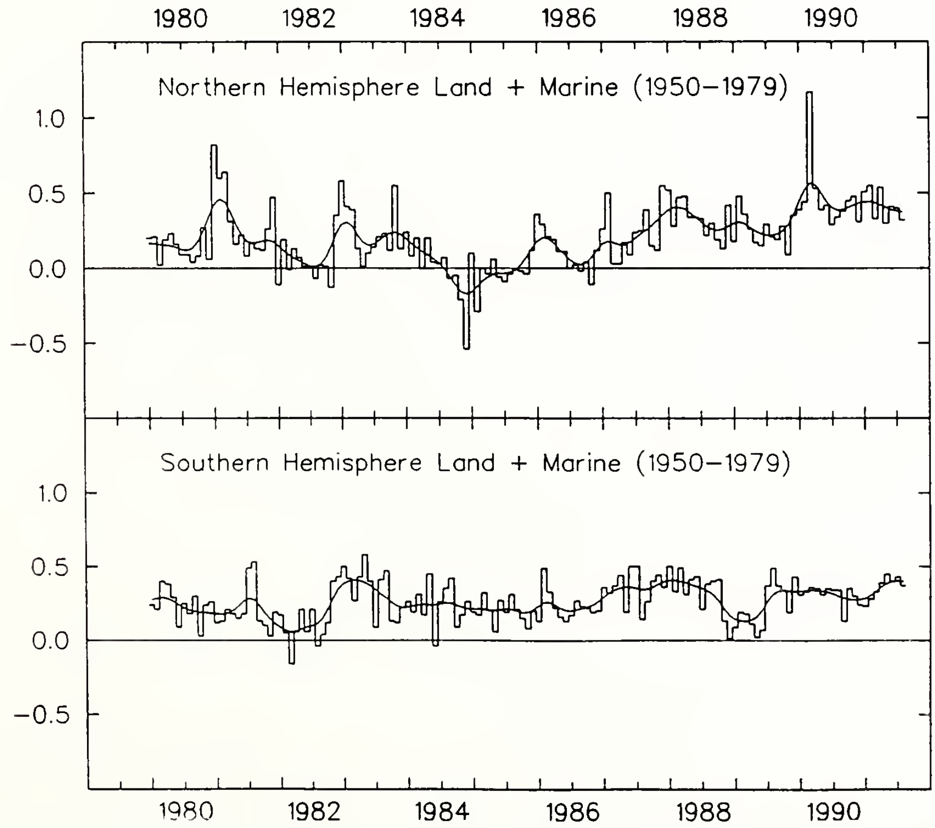

**Figure 2:** Average monthly land-plus-marine temperatures for Jan. 1980 to Aug. 1991. Reference period is 1950-79.

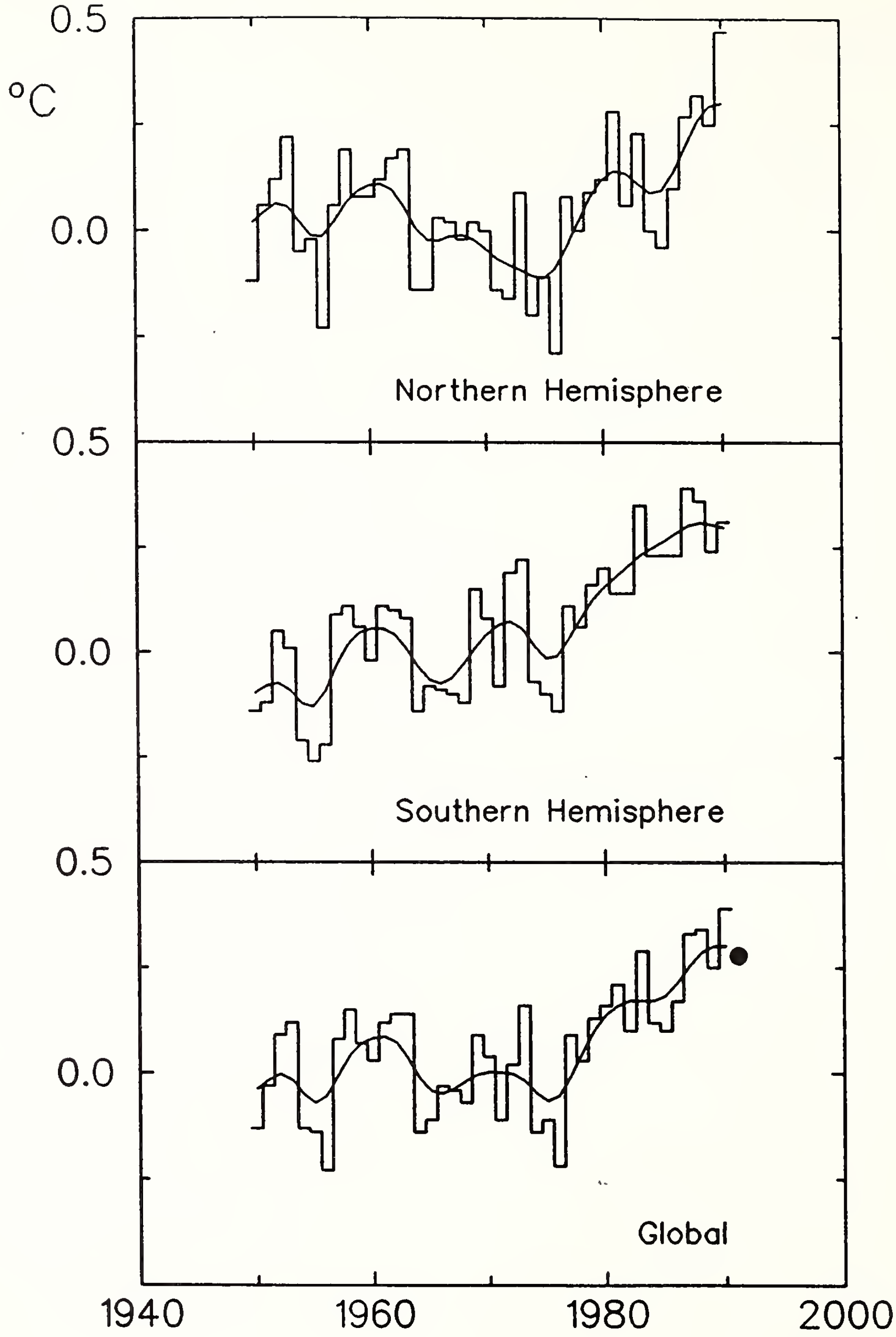

Figure 3: Land-plus-marine temperatures for the Northern Hemisphere, Southern Hemisphere and Globe, 1950-1990. Reference period is 1950-79. The dot shows the best guess value for 1991 for the globe.

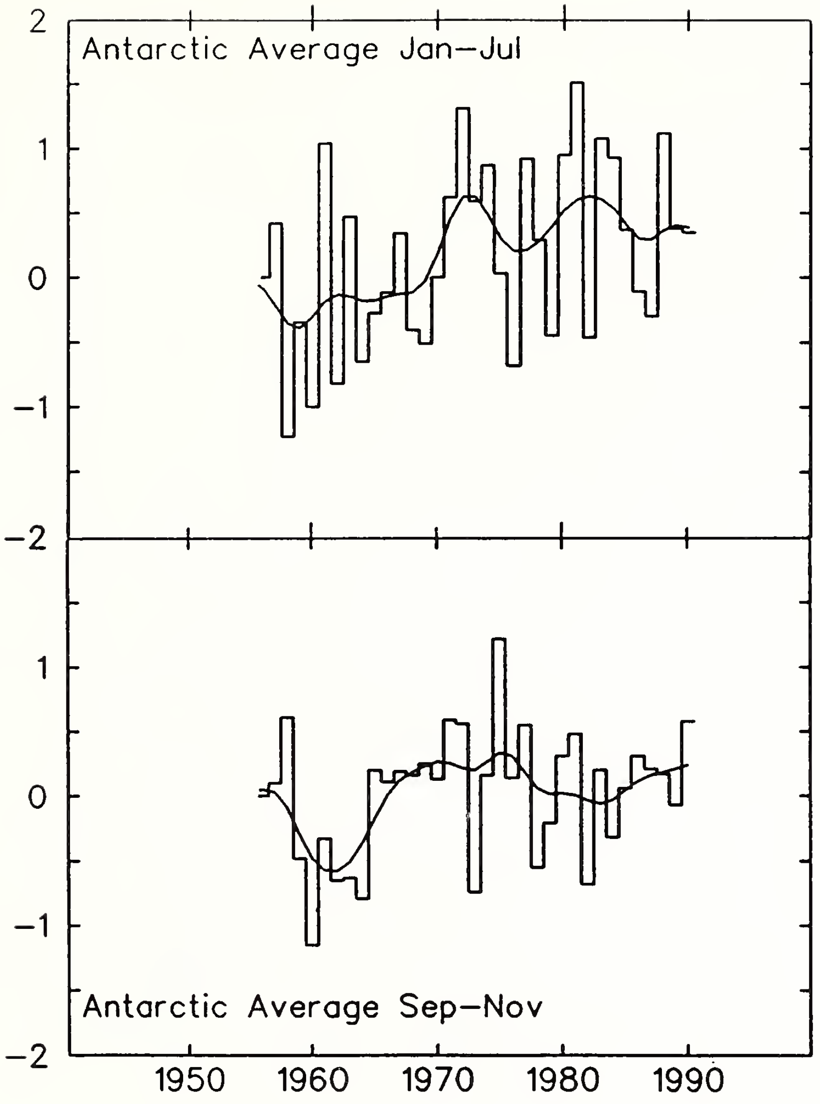

Figure 4: Antarctic (65-90°S) average temperatures for January to July (upper panel) and September to November (lower panel). Reference period is 1957-75.

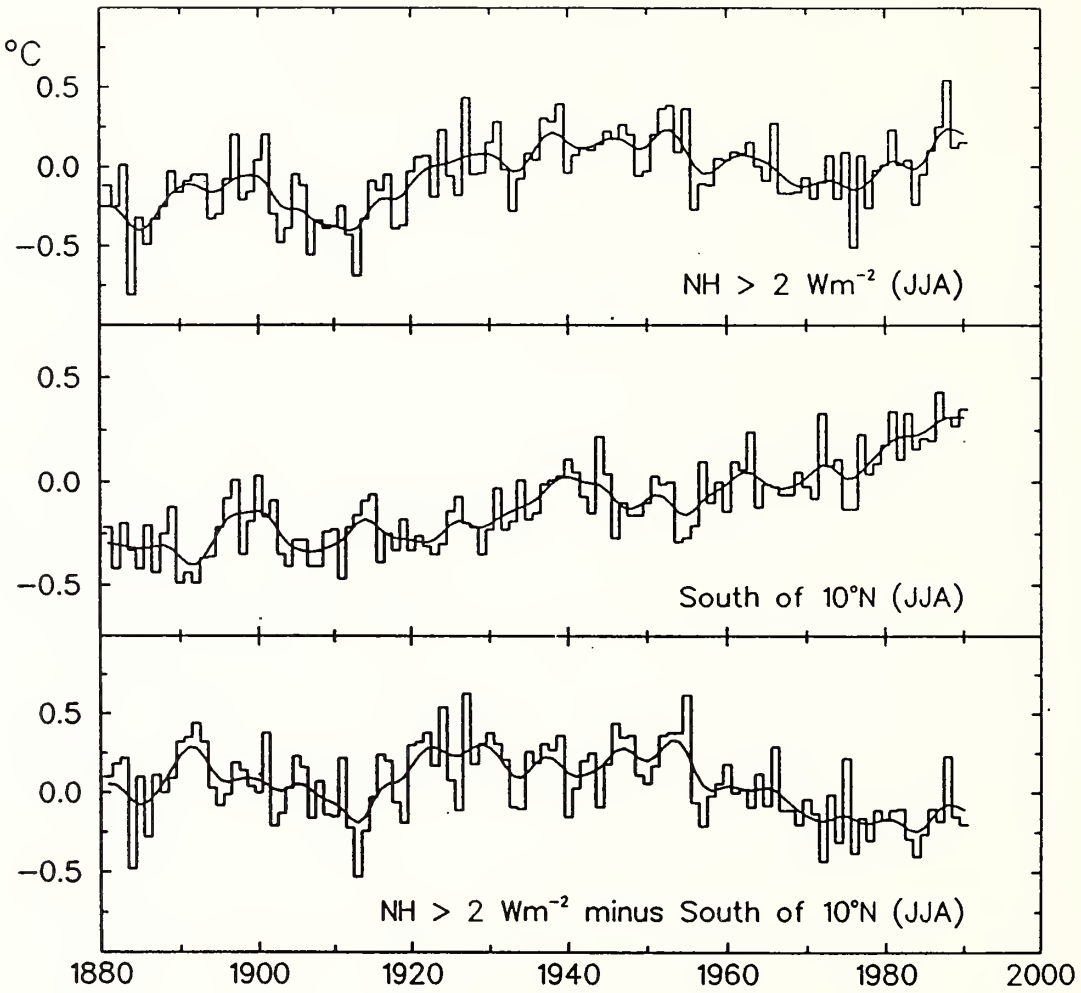

Figure 5: Observed temperature changes during June, July and August over two regions of the world: top panel, Northern Hemisphere areas where the calculated anthropic clear-sky aerosol-related increase of reflected flux to space exceeds $2Wm^{-2}$ (from Charlson et al., 1991, Fig. 2b); middle panel, the world south of 10°N, where the total aerosol effect should be negligible; and lower panel, the difference between the upper and middle time series.

# Greenhouse signal in the glacier recession on Mount Kenya

by

Stefan Hastenrath
Department of Meteorology
University of Wisconsin, Madison

The glaciers in the high mountains of the tropics are sensitive indicators of climatic change. With this motivation, a long-term monitoring program is being conducted on Mount Kenya (Hastenrath, 1984). The glaciers range mostly over 4600-5000 m, near the annual-mean elevation of the 0 °C isothermal surface, with the largest ice masses to the East due to the precipitation distribution. A radiation model incorporating shading by topographic obstacles and slope effects (Kruss and Hastenrath, 1987, 1990; Hastenrath and Kruss, 1988) indicates that increased solar radiation absorption resulting from reduced cloudiness was essential for the differential retreat rates of glaciers in the various portions of the mountain during 1899-1963. From a mapping of the glaciers at scale 1:5000 and with date September 1987 (Hastenrath et al., 1989) and the map at same scale of the January 1963 epoch (Forschungsunternehmen Nepal-Himalaya, 1967), the 1963-87 changes of all glaciers were reconstructed (Hastenrath et al., 1989). This provided the basis for a quantitative evaluation of climate and glacier variations.

In 1963-87 the total ice-covered area on Mount Kenya decreased at a considerably more rapid relative rate than during 1899-1987. Moreover, during 1963-87 surface lowering was essentially independent of the computed solar radiation (Fig. 2), with in fact the smallest values of ice thinning being associated with the largest incident solar radiation (Lewis and Gregory). Therefore, processes other than solar radiation must have been the controlling factors. Of particular interest here are the effects of changing atmospheric composition, environmental warming, and atmospheric humidity trends.

From January 1963 to September 1987, the average ice thickness change amounted to 14.51 m, or 59 cm per year. This translates to 50 cm liquid water equivalent per year. Given the latent heat of sublimation, $L_s = 284 \times 10^4$ $\mathrm{Jkg^{-1}}$, and of melting, $L_m = 33 \times 10^4$ $\mathrm{Jkg^{-1}}$, the energies required to dispose of this layer of ice amount to 46 $\mathrm{Wm^{-2}}$ for evaporation and 5.4 $\mathrm{Wm^{-2}}$ for melting.

A precipitation decrease of the required large magnitude is not borne out by stations on the Kenya highlands. Likewise ruled out are enhanced solar radiation resulting from reduced cloudiness, or atmospheric turbidity or a decrease of glacier albedo related to enhanced dust deposition or less snowfall, because these would lead to a differential thinning of the glaciers which is not observed.

Therefore, the consideration concentrates on the sensible and latent heat transfer $Q_s$ and $Q_e$, respectively, and the net longwave radiation LW. These can be estimated from bulk formulations containing as input temperature and specific humidity of the air, wind speed, as well as air density, surface temperature, and some constants (Hastenrath, 1984, p. 247-242; Budyko, 1974, p. 57-60; Sellers, 1965 p. 41); For the glaciers of Mount Kenya, Q, Q, and LW are of order 7, 20, and 70 $Wm^{-2}$, respectively. With reference to these background estimates, we examined the effect of small changes in environmental conditions on Q, Q, and LW, recognizing that the glaciers are in an elevation range near the annual-mean 0 °C isothermal surface and that the temperature of the glacier surface cannot rise above 0 °C. The estimated sensitivity of the glaciers to changes in air temperature and humidity plausible from observation is illustrated in Fig. 3.

This schematic diagram shows various lines of causality. Regarding LW, the effect of "thermal trapping" due to increasing "greenhouse" gases is from the literature (Dickinson and Cicerone, 1986) estimated at 0.5-1.0 $Wm^{-2}$. A cloudiness increase would affect solar radiation more substantially than LW. A 0.1-0.2 $gkg^{-1}$ increase in specific humidity translates into a reduction of LW by 0.2-0.4 $Wm^{-2}$. Concerning the effect of warming a temperature increase of order less than 0.2°C (Jones, 1988; Wolter and Hastenrath, 1989) would correspond to an increment in $Q_s$ of 1.4 $Wm^{-2}$ or less. Relevant to the latent heat implications are the findings (Hense et al., 1988) of a specific humidity increase in the layer 700-500 mb (Mount Kenya's glaciers around 580 mb) in the equatorial belt of 0.6 $gkg^{-1}$ over 1965-85. This has been related to the "global warming" and "greenhouse effect", and explained as a consequence of intensified sea-air interaction over the tropical oceans favored by an increase in sea surface temperature (Flohn and Kapala, 1989). In the well-ventilated upper reaches of Mount Kenya, moisture conditions are primarily controlled by advection. A specific humidity increment of 0.3 $gkg^{-1}$ would be sufficient to account, by itself, for the observed 1963-87 ice thinning. Changes in LW and cloudiness related to an increase of atmospheric humidity would act in the same sense but have a much smaller effect than the reduced $Q_e$.

In synthesis from these considerations, the following combination of climatic forcings is found most plausible to supply the energy of 5.4 $Wm^{-2}$ required to effect the observed ice thinning through melting: a longwave radiational contribution from "thermal trapping" of 0.5-1.0 $Wm^{-2}$; a warming of 0.0-0.2 °C, possibly in part caused by "thermal trapping", contributing through sensible heat transfer 0.0-1.4 $Wm^{-2}$; a warming of 0.0-0.2 °C, possibly in part caused by "thermal trapping", contributing through sensible heat transfer 0.0-1.4 $Wm^{-2}$; and a 0.1-0.2 $gkg^{-1}$ increase in specific humidity, possibly in part induced by atmospheric warming, which through latent heat transfer would make available 2-4 $Wm^{-2}$. The longwave radiational effect of this moisture increase is an order of magnitude smaller. All of the lines of forcing indicated in Fig. 3 may conceivably be steered by the "greenhouse effect". Of these, an increase in atmospheric water vapor content is found instrumental for the drastic wastage of Mount Kenya's glaciers over the past quarter century.

Acknowledgements:

This study was supported by National Science Foundation Grant EAR-9016657. The research is authorized by the Office of the President, Republic of Kenya.

## References

Budyko, M.I., 1974: Climate and life.
Academic Press, New York and London, 508 pp.

Dickinson, R. E., Cicerone, R. J., 1986: Future global warming from atmospheric trace gases.
Nature, 319 (6049), 109-115.

Flohn, H., Kapala, A., 1989: Changes of tropical sea-air interaction processes over a 30-year period.
Nature, 338 (6212), 244-246.

Forchungsunternehmen Nepal-Himalaya, 1967: Mount Kenya 1:5,000.
Kartographische Anstalt Freytag-Berndt und Artaria, Wien.

Hastenrath, S., 1984: The glaciers of equatorial East Africa.
Reidel, Dordrecht, Boston, Lancaster, 353 pp.

Hastenrath, S., Kruss P. D., 1988: The role of radiation geometry in the climate response of Mount Kenya's glaciers, Part 2: sloping versus horizontal surfaces.
J. Climatol., 8 (6), 629-639.

Hastenrath, S., Rostom, R., Caukwell, R. A., 1989: Variations of Mount Kenya's glaciers, 1963-87.
Erdkunde, 43 (3), 202-210.

Hense, A., Krahe, P., Flohn, H., 1988: Recent fluctuations of tropospheric temperature and water vapor content in the tropics.
Meteorol. Atmos. Phys., 38 (4), 215-227.

Jones, P. d., 1988: Hemispheric surface air temperature variations: trends and an update to 1987.
J. Climate, 1, 654-660.

Kruss, P. D., Hastenrath, S., 1987: The role of radiation geometry in the climate response of Mount Kenya's glaciers, Part 1: horizontal reference surfaces.
J. Climatol., 7 (5), 493-505.

Kruss, P. D., Hastenrath, S., 1990: The role of radiation geometry in the climate response of Mount Kenya's glaciers, Part 3: the latitude effect.
Int. J. Climatol., 10 (3), 321-328.

Sellers, 1965: Physical climatology.
University of Chicago Press, Chicago and London, 272 pp.

Wolter, K. E., Hastenrath, S., 1989: Annual cycle and long-term trends of circulation and climate variability over the tropical oceans.
J. Climate, 2, 1329-1351.

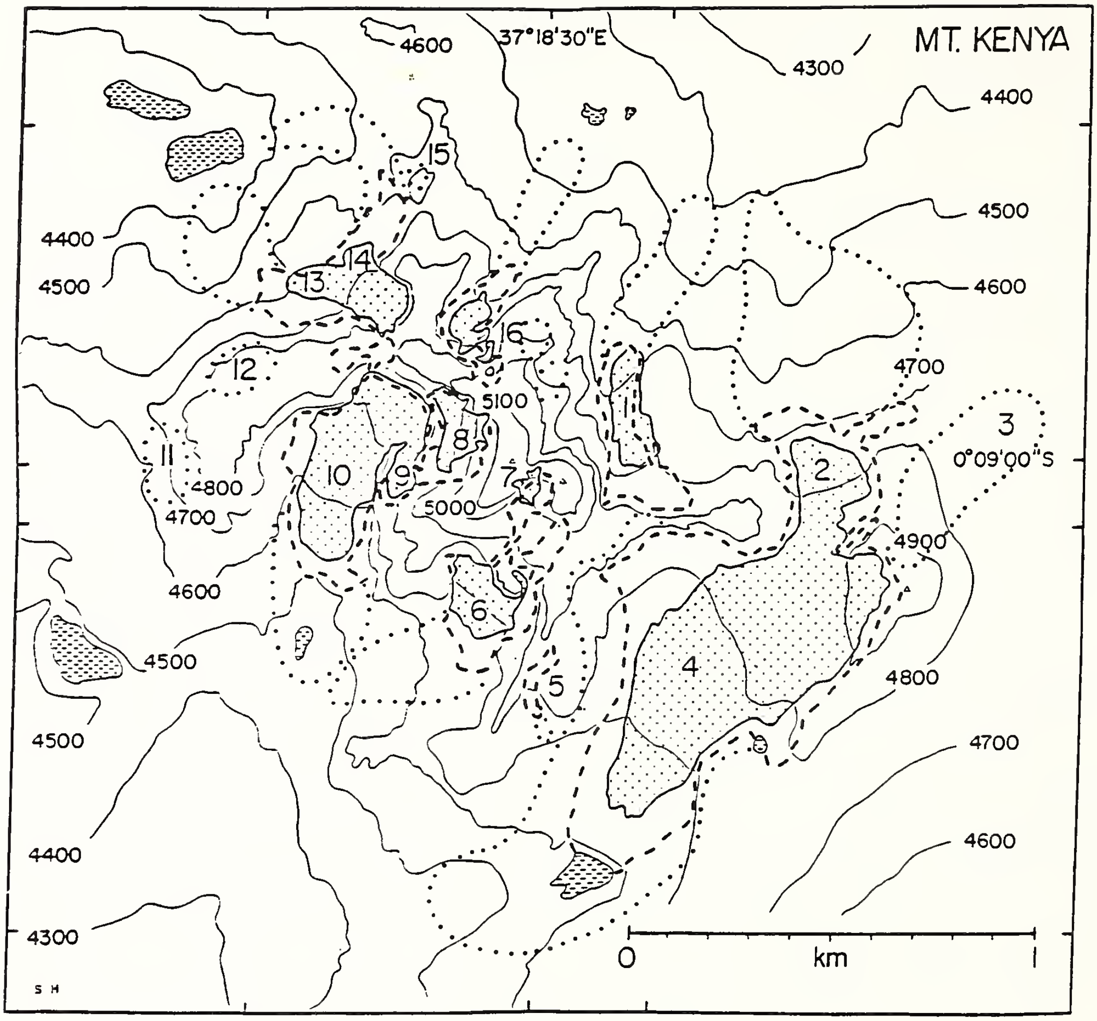

Figure 1. Map of Mount Kenya's glaciers. The ice extents in 1899, 1963, and 1987, are shown by dotted, broken, and solid lines, respectively. The key below lists for the North and South sides of the mountain and from West to East the names of the glaciers indicated in the map by numbers, with ** denoting glacier which disappeared in the course of 1963-87, and * ice entities which vanished prior to 1963. Scale 1:20,000 (sources: Forschungsunternehmen Nepal-Himalaya, 1967; Hastenrath et al., 1989).
North side: 12*NW Pigott, 13 Cesar, 14 Joseph, 15* Peter, 16 Northey, 17* Arthur, 18* Mackinder, 1 Krapf, 2 Gregory; South side: 11* Barlow, 10 Tyndall, 9 Heim, 8 Forel, 7 Diamond, 6 Darwin, 5** Melhuish, 4 Lewis, 3* Kolbe.

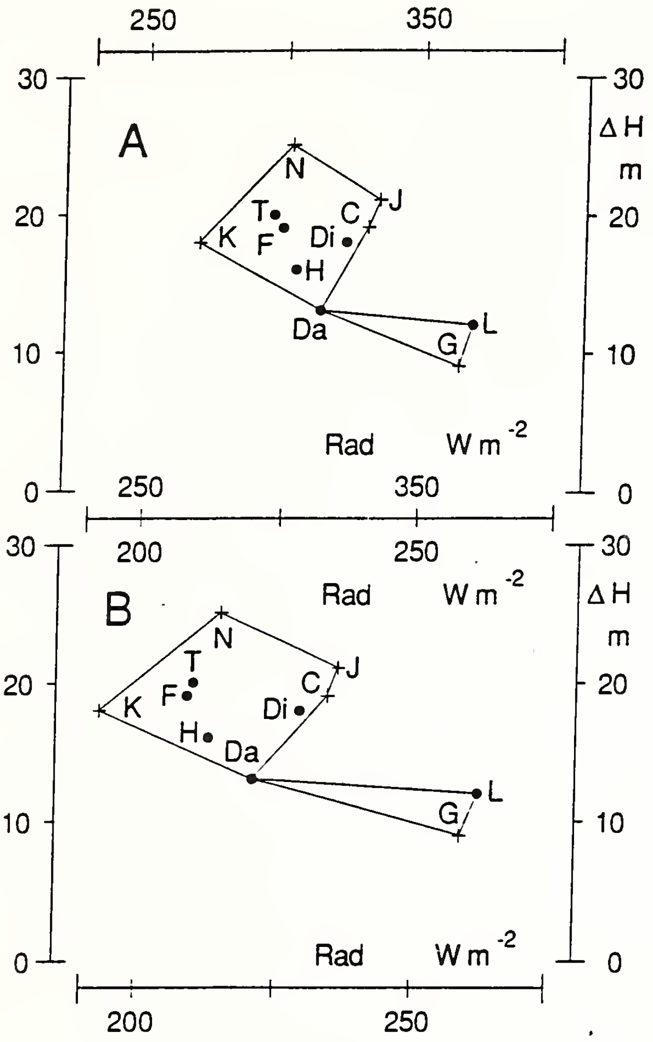

Figure 2. Surface lowering versus mean solar radiation (W $m^{-2}$) during 1963-87 for all glaciers. Crosses and dots indicate glaciers on the North and South sides of massif, respectively.
(a) clear sky;
(b) representative cloud conditions (cloudiness five tenths except for clear skies during mornings of the January/February and August dry seasons, topographic shading).

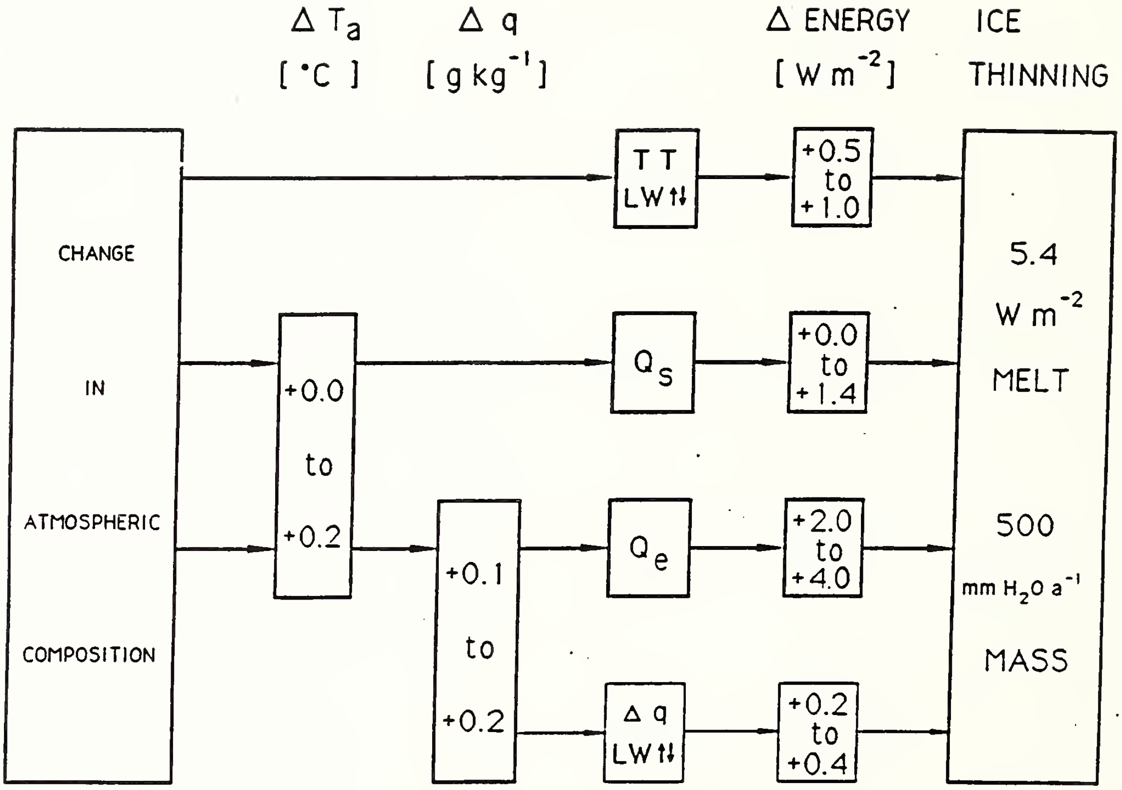

Figure 3. Schematic diagram of three "greenhouse"-induced climatic forcings contributing to the observed ice thickness change. Net longwave radiation due to thermal trapping (TT LW↑↓), downward-directed sensible heat flux $Q_s$, and upward-directed latent heat flux $Q_e$. $\Delta T_a$ and $\Delta q$ denote change in atmospheric temperature and specific humidity, respectively. Δ energy lists the corresponding change in the energy budget of the ice. Δq LW↑↓ indicates change in net longwave radiation related to humidity change; this latter causality chain is shown in thin print to indicate that it is considered to be of subordinate importance.

# Interannual and Interdecadal Variability of Surface-Air Temperatures in the United States

Michael D. Dettinger
U.S. Geological Survey
San Diego, California 92123-1135

Michael Ghil
Climate Dynamics Center, Department of Atmospheric Sciences and
Institute of Geophysics and Planetary Physics
University of California, Los Angeles
Los Angeles, California 90024-1565

Interannual and interdecadal variability of monthly mean surface-air temperatures in the conterminous United States was analyzed for the period 1910-87. Analyses were designed to address both temporal and large-scale spatial variability of temperatures across the entire area. The purpose of this paper is to describe briefly the dominant trends and periodic and quasi-periodic variations in the temperature record of the United States.

Surface-air temperatures used in these analyses are from the United States Historical Climatology Network data set (Karl et al., 1990). The 870 sites with serially complete records of monthly mean temperature during 1910-87 were selected from the data set. Because available sites in the Western States prior to 1910 were sparse, nationwide coverage earlier than this was judged to be impractical for the present study. Temperatures have been corrected for time-of-observation biases and effects of local urbanization (Karl et al., 1990). Monthly mean temperatures at each site were normalized by subtracting the normal temperature corresponding to that month of the year and dividing the difference by the standard deviation of monthly means for that month of the year at that site. The resulting temperature indices were interpolated onto a rectangular grid of 131 points separated by 2.5 degrees of latitude and 2.5 degrees of longitude, using an optimal-interpolation method (Yamamoto and Hoshiai, 1980); the method interpolates strictly on the basis of an assumed isotropic, homogeneous, and Gaussian spatial-correlation structure. A correlation distance of 150 km was assumed in the present study.

The matrix of temporal covariances between each pair of grid points was estimated from the 936 interpolated maps and decomposed to obtain spatial empirical-orthogonal functions (S-EOF's) that describe the spatial modes of large-scale temperature variation over the United States. The S-EOF's used in this study are unrotated, normalized eigenvectors and thus describe the maximum fraction of the temporal and spatial variability of observed temperatures in the fewest spatial patterns (Richman, 1986). The associated eigenvalues correspond to the amount of temperature variance describable by S-EOF's. Maps of the first five S-EOF's are shown in figure 1; they account for 85 percent of the temperature variance. These five S-EOF's were selected for subsequent temporal analysis because they stand above the largest break in a plot of log-eigenvalues against S-EOF number, and thus are most clearly above the noise level in the data (Richman, 1986). S-EOF 1 represents temperature variations that affect the entire domain in the same sense (simultaneously), S-EOF 2 represents east-west temperature differences, S-EOF 3 represents north-south temperature differences, S-EOF 4 represents center-to-coastal temperature differences, and S-EOF 5 represents differences between northwest-southeast and northeast-southwest temperatures. Such simple divisions commonly occur in limited-area S-EOF analyses (Richman, 1986) and probably do not reflect individually the influence of physical processes. However, the goal here was not to identify each individual S-EOF with a separate process but rather to identify large-scale trends and oscillations in the entire temperature record. Consequently, the patterns shown are discussed herein without rotation. In the interests of completeness, the first 10 S-EOF's were rotated orthogonally to arrive at a set of "natural" temperature divisions of the region. The rotated S-EOF's (not shown) corroborate the broad patterns discussed here and provide some additional detail as to the locations and magnitudes of the temperature oscillations discussed later in this paper.

The principal-components (S-PC's) associated with each of the five S-EOF's were then determined. These dimensionless time series are the strengths (amplitudes) in each month's temperature map of each of the five S-EOF's. The resulting series had strong high-frequency variability and were smoothed using moving averages developed through an initial application of Singular Spectrum Analysis (SSA) with a 12-month window. SSA is a form of temporal empirical-orthogonal function (T-EOF) analysis (Vautard and Ghil, 1989). SSA identifies tly random parts of the time-series variations and can be used to separate these from organized short-cillations present and from trends or oscillations with longer periods than the data window used. tion of SSA with a 12-month window to the S-PC series identified the longer-than-annual variations in es and all shorter term variations were removed. About 79 percent of the variability in the five leading ries was found to be shorter than annual. This high-frequency component was removed in order to he interannual and interdecadal components of variability.

smoothed S-PC series (fig. 2) then were subjected to a more detailed analysis using SSA with a 25-year SSA is very responsive to oscillatory signals and tends to separate them into individual components, s, according to the lag-correlation structure of the series rather than by testing a set number of frequency Vautard and Ghil (1989) recognized that purely periodic components identified by SSA ideally appear of T-EOF's with equal eigenvalues. For a linear oscillation, the pair of T-EOF's will be a sine and For nonlinear oscillations, the pair can differ in shape from sinusoidal (for example, boxcar or sawtooth ppear), but the T-EOF's still will be in quadrature with each other. T-EOF pairs that have large and qual eigenvalues were identified in the S-PC's, and their periodic nature was verified. Large eigenvalues fined as standing out above the background of selectively low-frequency noise (red noise) in plots of log-ues against T-EOF number (not shown here). The periodic nature of the paired EOF's was verified by ning that the lag-cross-correlations of the T-EOF's and their corresponding T-PC's were high (greater out 0.9) at lags equal to odd integers times one-quarter of their apparent periods. Because SSA does ematically search among a specified set of frequencies, the temporal components identified must be ly analyzed following SSA to determine precisely the frequencies that SSA has isolated. The frequencies riods) of the various oscillations identified by SSA with a 25-year window were determined by using the per method of spectral analysis (Thomson, 1982).

results of these SSA and spectral analyses of the leading S-PC's of the temperature indices are ized in table 1. Trends listed in the table are those temporal components of the S-PC's that vary more han the 25-year window used. The oscillatory components isolated by SSA and listed in the table nly appear to be mixes of a few harmonics. All the listed components stand above the red-noise und on plots of log-eigenvalue against T-EOF number. Trends (if present) are listed first, and the term oscillatory components are listed in the order of the magnitude of their overall contributions to the ty of the smoothed S-PC series. In most cases, a single temporal component listed in the table izes contributions of several T-EOF's. The major trends and oscillatory components listed in table 1 are d in the remaining paragraphs, starting with longest term components and ending with several interannual ons that contribute the most variability (among the many interannual oscillations detected).

trends listed in table 1 actually appear to be irregular oscillations with 30- to 60-year periods rather than monotone increases or decreases. The trend associated with S-EOF 1 (which is a weighted average of tures in the United States favoring the central States) consists of about 0.4°C warming during 1915-35, l by a somewhat-oscillatory temperature decline of about 0.3°C until the mid-1970's, followed since by g. The warming trend since the 1970's has been slower than that during 1915-35. The warming during is evident in all regions, whereas the cooling and much of the warming of the national average since 1935 sult of many differing, site-specific trends. This largest-spatial-scale trend is in general agreement with -term variations of global-average temperatures described by Ghil and Vautard (1991)--except that the temperatures for the United States do not reflect the net warming since 1910 found in the global s. The trend in S-EOF 2 consists of a weak oscillation with about a 28-year period. SSA of the PC series OF 3 (north-south temperature differences) yields no long-term trend. The trend of S-EOF 4 appears oscillation with a period of about 50 to 60 years. The smoothed PC series for S-EOF 5, however, shows increase in temperatures in the southwestern and northeastern parts of the United States relative to the tures in the northwest and southeast--in addition to an oscillation of about 60 years.

ak interdecadal oscillations are found in some of the PC series. A 23-year oscillation is detected by SSA ast-west seesaw of temperatures described by S-EOF 2. This 23-year oscillation amounts to about 0.2°C he S-EOF reaches maximum amplitude. The signal is significantly correlated at zero lag with the 23-year on identified by Ghil and Vautard (1991) in the global-average temperature series--applying mmano's (1979) significance test at a 95-percent level. Analysis of the PC series from rotated S-EOF's, reserve more spatial detail than the unrotated patterns, suggests that this oscillation may be strongest ìreat Basin and the Southwestern United States.

Table 1.--Descriptions of leading temporal components of the smoothed spatial-principal components (S-PC's) for the first five spatial empirical-orthogonal functions (S-EOF's)

[Percent of variance refers to percent of spatial and temporal variance of temperature indices contributed by indicated S-EOF and its unsmoothed S-PC's. Parentheses enclose the percent of variance contributed by smooth S-PC's. Components were determined by singular-spectrum analysis with a data window of 25 years. Oscillation periods were estimated using the multi-taper spectral method of Thomson (1982). Order of components defined in text.]

| S-EOF | Percent of variance | Temporal components |
|---|---|---|
| 1<br>(Whole region) | 39 (7) | • Trend (about 60-yr oscillation)<br>• 5.4-yr oscillations<br>• 10.4-yr oscillation |
| 2<br>(East-west) | 27 (6) | • Trend (about 28-yr oscillation)<br>• 3.3-yr oscillations<br>• 1.7-yr oscillations<br>• 2.3- and 23-yr oscillations |
| 3<br>(North-south) | 10 (3) | • No Trend<br>• 2.2-yr oscillations<br>• 9.2-yr oscillations<br>• 1.8-, 2.7-, 3.9-, and 5.7-yr oscillations |
| 4<br>(Center-coasts) | 5 (1) | • Trend (50- to 60-yr oscillation)<br>• 7.8- to 8.0-yr oscillations<br>• 2.0-yr oscillations<br>• 9.6-yr oscillations (stronger after 1945) |
| 5<br>(Checker-board) | 4 (1) | • Trend (about 60-yr oscillation)<br>• 2.2-yr oscillations<br>• 8.0- and 25-yr oscillations<br>• 9.2-yr oscillations |

A 10.4-year oscillation is found in S-EOF 1, amounting to about 0.1°C at its maximum in the center of the continent. The cross-correlation coefficient between this signal and annual sunspot numbers is only -0.6 (which is due to their shared 10-year periods and which is significant at less than a 70-percent level). van Loon and Labitzke (1988) proposed that sunspot-related temperature variations should take the form of east-west variability (during the western phase of the quasibiennial oscillation--QBO) and, possibly, an in-phase relation nationwide during the eastern phase of the QBO. The present analysis finds no trace of this oscillation in the east-west variations and an out-of-phase relation in the national averages (S-EOF 1). Our out-of-phase relation, however, is in keeping with the simplest global response that might be expected from the measured decreases in total solar irradiance with increased sunspot activity (Wilson et al., 1981).

The east-west seesaw of temperatures (S-EOF 2) has two dominant interannual 'tones' in the form of complicated mixes of 3.3- and 1.7-year signals. Together (and on the broadest spatial scale), these oscillations reflect regular variations with a fairly constant amplitude envelope of slightly more than 1°C, peak to peak. Analysis of PC series from rotated S-EOF's indicates that the 3.3-year oscillation may take the form of a strong oscillation in the Western States (strong relative to the weaker variations at this frequency in the Eastern States).

In contrast, the 1.7-year oscillation seems to be strongest across the southern half of the United States (with a gradual shift in phase from west to east).

The north-south temperature variation (S-EOF 3) is dominated by a single 2.2-year sinusoidal oscillation with a remarkably constant amplitude--about 0.7 ° C at its extreme grid points. This oscillation was previously reported by Rasmusson et al. (1981). Analysis of the PC series from rotated S-EOF's indicates that the oscillation is widely distributed over the United States. This oscillation does not seem to be directly related to other QBO's in either the tropics or high latitudes. For example, the amplitude envelope of the sum of the various components with strong 2.2-year periodicities is not significantly correlated with the amplitudes of the quasibiennial components of El Niño (comparing with results from Keppenne and Ghil, 1991). Neither is the envelope correlated with the QBO detected by Trenberth and Shin (1984) in the progression of Northern Hemisphere sea-level pressures. S-EOF 5 (the checkerboard distribution of temperature variations) also displays a strong 2.2-year oscillation.

In the analysis of spatial and temporal variability of surface-air temperatures, the combination of spatial EOF analysis and temporal analysis by SSA has proved to be a sensitive and robust approach. A wide range of interannual and interdecadal temperature oscillations can be detected in climatic data for the United States. This approach allows the spatial and temporal characteristics of these oscillations to be broadly described using data-adaptive filters in both space and time. Among the oscillations detected by this method in the temperature record of the United States are a number of oscillations at frequencies that also are important in the global-mean temperature series analyzed by Ghil and Vautard (1991); examples include 23-, 5.4-, and 3.3-year oscillations as well as the long-term (28 to 60 years) variations around the warming trend found in the latter data set. Despite the demonstrably wide range of sensitivity of the present analysis, the only large-scale net trend detected in the temperature record of the United States is a weak, long-term warming of the northeast and southwest relative to the southeast and northwest.

Acknowledgments. It is a pleasure to thank R.M. Thorne for suggesting the Wilson et al. (1981) reference. This work was partly supported by DOE grant W/GEC0014 (through the National Institute for Global Environmental Change) and a Guggenheim Fellowship to Michael Ghil.

---

References

Ghil, M., and Vautard, R., 1991, Interdecadal oscillations and the warming trend in global temperature time series: Nature, v. 350, p. 324-327.

Karl, T.R., Williams, C.N., Jr., and Quinlan, F.T., 1990, United States Historical Climatology Network (HCN) serial temperature and precipitation data: Carbon Dioxide Information Analysis Center, Oak Ridge National Laboratory, Oak Ridge, Tennessee, ORNL/CDIAC-30, NDP-019/R1, 374 p.

Keppenne, C.L., and Ghil, M., 1991, Adaptive spectral analysis and prediction of the Southern Oscillation Index: Proceedings, 15th Annual Climate Diagnostics Workshop, National Climate Analysis Center, NOAA, Asheville, North Carolina, p. 30-35.

Rasmusson, E.M., Arkin, P.A., and Chen, W.Y., 1981, Biennial variation in surface temperature over the United States as revealed by singular decomposition: Mon. Wea. Rev., v. 109, p. 587-598.

Richman, M.B., 1986, Rotation of principal components: J. Climatology, v. 6, p. 293-335.

Sciremammano, F., Jr., 1979, A suggestion for the presentation of correlations and their significance levels: J. Phys. Ocean., v. 9, p. 1273-1276.

Thomson, D.J., 1982, Spectrum estimation and harmonic analysis: Proceedings of the IEEE, v. 70, p. 1055-1096.

Trenberth, K.E., and Shin, W.K., 1984, Quasi-biennial fluctuations in sea level pressures over the Northern Hemisphere: Mon. Wea. Rev., v. 112, p. 761-776.

van Loon, H., and Labitzke, K., 1988, Associations between the 11-year solar cycle, the QBO, and the atmosphere. Part II: Surface and 700 mb in the Northern Hemisphere in winter: J. Climate, v. 1, p. 905-920.

Vautard, R., and Ghil, M., 1989, Singular spectrum analysis in nonlinear dynamics, with applications to paleoclimatic time series: Physica D, v. 35, p. 395-424.

Wilson, R.C., Gulkis, S., Janssen, M., Hudson, H.S., and Chapman, G.C., 1981, Observations of solar irradiance variability: Science, v. 21, p. 200-202.

Yamamoto, R., and Hoshiai, M., 1980, Recent change of the Northern Hemisphere mean surface air temperature estimated by optimum interpolation: Mon. Wea. Rev., v. 107, p. 1239-1244.

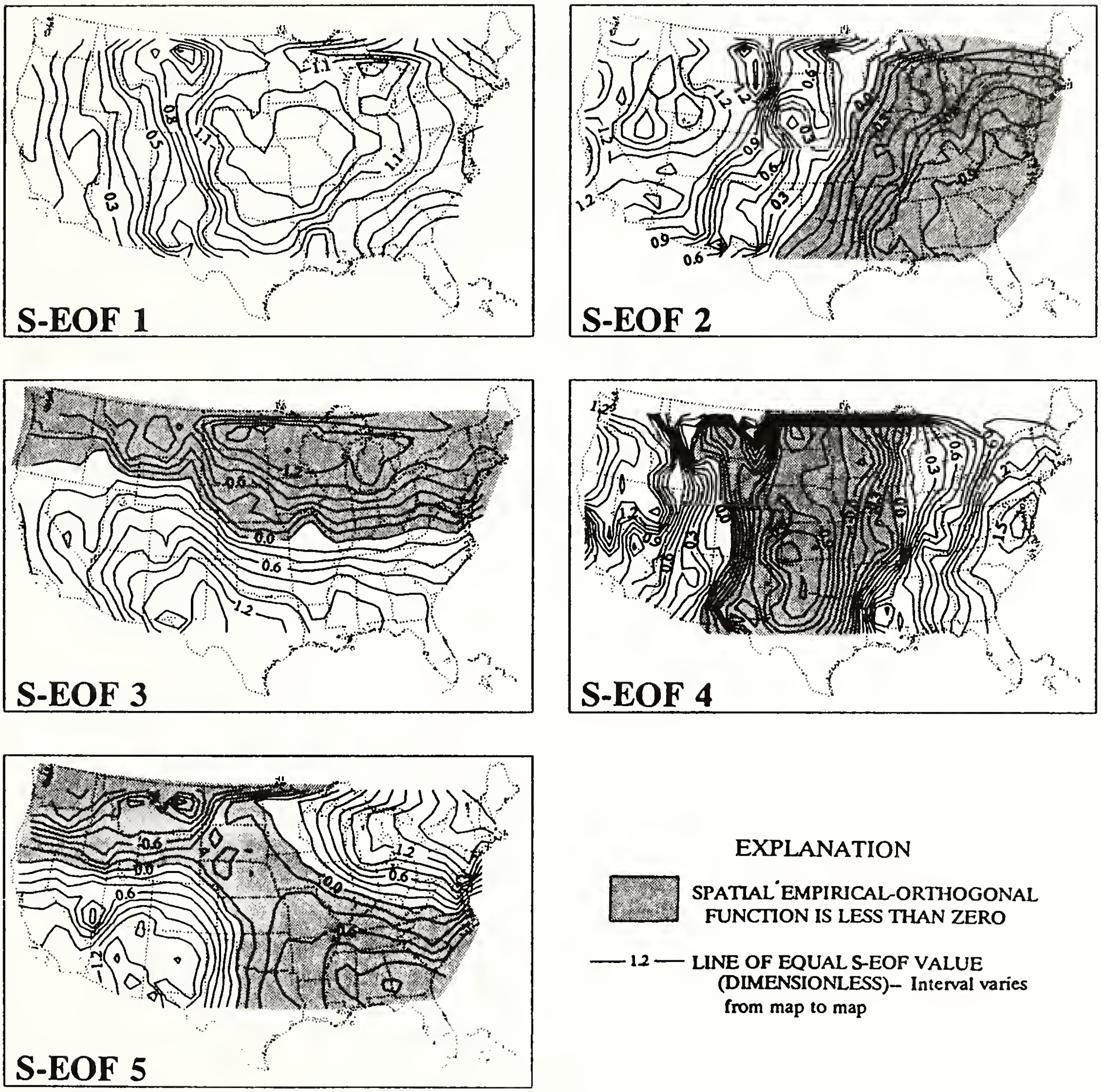
S-EOF 1
S-EOF 2
S-EOF 3
S-EOF 4
S-EOF 5
EXPLANATION
SPATIAL EMPIRICAL-ORTHOGONAL FUNCTION IS LESS THAN ZERO
1.2 LINE OF EQUAL S-EOF VALUE (DIMENSIONLESS)-- Interval varies from map to map

Figure 1. Spatial empirical-orthogonal functions (S-EOF's) of gridded temperature indices, 1910-87, normalized to unit vector length, times 10.

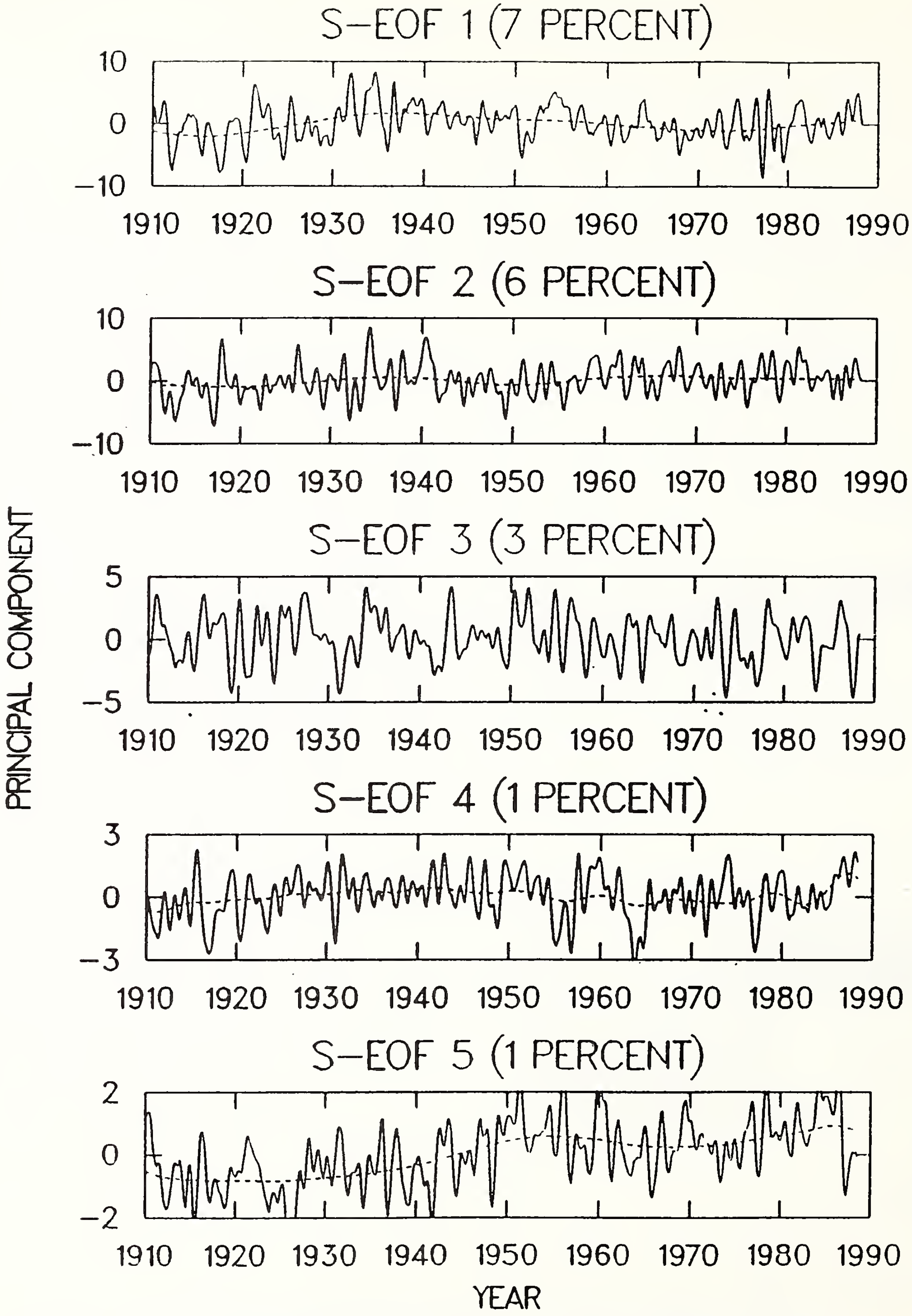

Figure 2.--Graphs of smoothed principal-component series for leading spatial empirical-orthogonal functions (S-EOF's) of gridded temperature indices, 1910-87. Smoothed series contribute the percentages of total variance shown in parentheses. Temporal components with periods longer than 25 years (listed as trends in table 1) are shown as dotted curves.

# SEASONAL CYCLE OF INSOLATION AND CLIMATE CHANGE

George Kukla
Lamont-Doherty Geological Observatory of Columbia University
Palisades, New York 10964 USA

and

Thomas Karl
NOAA/National Climate Data Center
Applied Climatology Branch
Federal Building
Asheville, North Carolina 28801 USA

Past climate fluctuations and the Earth orbital perturbations have common frequencies (Kukla et al., 1981). Shifts to cold global climate occurred repeatedly at times of June or July perihelion combined with high obliquity. The physical mechanism through which the insolation would move the climate system into a glacial stage however still remains unknown. This is unfortunate because the interglacial/glacial transitions were by far the most prominent shifts in the environment and climate of the last million years. If we do not understand them, how much trust can we place in the predictions of global circulation models which analyze the $CO_2$ impact on the future world?

Rind et al. (1989) tried to model the onset of a last glaciation in a GISS general circulation model by appropriately modified insolation forcing. In the model the climatic impact of decreased insolation in autumn was fully compensated by the correspondingly increased insolation in spring. That means that a season or a zone which would display higher sensitivity to insolation forcing than the rest of the world has not been found. This task is crucial (Kukla, 1975), because the orbital perturbations affect only the distribution of solar radiation within the seasons and within the latitudinal bands, without significantly changing the global annual totals (cf. Appendix). Correct identification of the sensitive season and zone is the key to solving the Milankovitch problem.

We are here reporting a few observations which may indicate the existence of such a sensitive season and area. The important element of the coupling may reside (1) in the phase shift between the seasonal cycle of insolation on one hand and the water vapor greenhouse effect on the other hand, and (2) in the different amplitude of the greenhouse cycle over land as compared to that over the ocean.

As known, the primary source of the earth's heating is the solar shortwave radiation. However, the earth's surface would be about 20°C colder without the water vapor, the main greenhouse gas in the atmosphere, which slows down the escape of the long wave radiation (heat) back to space. We have examined the seasonal variation of the atmospheric water vapor (precipitable water - Wp) concentrations using the dew point temperature at the 850 mb level (DP850) as a proxy (Fig. 1). Apart of representing reasonably well the seasonal Wp changes, the DP850 also closely correlates with the mean temperature of the corresponding atmospheric level (Fig. 2). At most stations inspected we have found a pronounced seasonal cycle with a minimum in spring and maximum in late summer and autumn. The amplitude of the seasonal wave in the northern middle latitudes is approximately twice as large over land than over the oceans and is delayed by approximately 1-2 months behind the insolation cycle (fig. 3). As a result of this lag, the surface heating efficiency of the shortwave radiation on clear days in autumn is considerably greater than in spring because of substantially higher amounts of water vapor in the atmospheric column. The difference is more pronounced in the Northern Hemisphere due to the dry atmospheri in winter and spring over land (Fig. 3). The largest seasonal asymmetry (and thus the greatest potential sensitivity to Milankovitch mechanism) occurs in the DP850 gradients between the land and the oceans, especially in the middle northern latitudes (Fig. 3).

In order to approximately quantify the impact of the greenhouse effect on the surface heating, we compared the mean monthly 850 mb dewpoint temperatures (DP 850) from the Navy/Air Force atlas with the greenhouse forcing over the oceans as measured from satellites by Raval and Ramanathan (1989). We also compared the dewpoints with the zonal mean surface net radiation computed for two degree latitudinal belts between 38 and 68°N across USSR (Barashkova et al., 1961). We obtained an empirical weighing factor $G_{dp} = 1 + [ln\ DP850 - ln\ 248] \times 10.97$, which approximately represents the efficiency added to the shortwave forcing of surface temperatures by the atmospheric greenhouse (Fig. 4). When weighted by this factor, the global mean "effective insolation" forcing of surface temperatures peaks in July over land and in January over the oceans (Fig. 5).

How does the seasonal cycle of water vapor relate to the Milankovitch mechanism? At approximately the 21st of each month the insolation distribution is symmetrical around the solstices (cf. Appendix). Neglecting the relatively small difference due to the precession, the insolation distribution on top of the atmosphere around the 21st of May is approximately the same as around the 21st of July. March pairs with September, January with November and so on. Figure 6 shows the difference in dewpoint temperature (and thus, approximately in the greenhouse forcing) for the months so paired at selected stations in the Northern Hemisphere. Obviously the difference between the fall and the spring is the largest. The departures are about twice as large over the land than over the oceans. Figure 5 shows the corresponding differences in the mean insolation efficiency index for the oceans and land.

In this context the regression analysis made by Berger et al. (1981) is of interest. A highly significant negative correlation was found between the 400 thousand year long paleoclimatic record in the deep sea sediments and the past March insolation. The highest positive correlation was found for September. Correlations with other months had low significance. There are several physical mechanisms which we think could explain the correlation. First, the strong insolation in September coupled with the weak one in March can maximize the heating efficiency of northern lands because of the peak greenhouse forcing in autumn (Fig. 6). Second, the strong March insolation coupled with a weak one in September could lead to increased water vapor transport to the northern snow fields and thus to the increase of surface albedo. Third, the high September and October insolation can speed up the dissipation of the Southern Hemisphere pack ice. The most important unknown in this respect are the changes of cloud cover, not considered in our exercise. Increased cloud albedo in a moister atmosphere could counterbalance the greenhouse effect.

It is unrealistic to expect that the insolation of any single month at any single latitude could adequately represent the Milankovitch forcing throughout the developing glacial cycle. On that ground alone, we can conclude that the mid-June insolation at 65°N is not the best representative of the extraterrestrial forcing of the global climate system. The August at 75°N would be a considerably better choice, since it reflects the time lag of the water vapor cycle behind insolation, and the large seasonal amplitude of insolation and precipitable water as well as the high sensitivity to obliquity in the high northern latitudes (Fig. 7).

We are continuing the study and plan to perform tests with the appropriately modified climate models. This is because a successful simulation of the glacial onset will have to take into account many feedbacks operating in the climate system such as the snow-ice albedo, clouds, ocean thermohaline circulation, etc. (Berger et al., 1990; Broecker and Denton, 1989). However, the seasonal march of atmospheric greenhouse effect is undoubtedly an important missing link in the chain of processes connecting orbital perturbations with terrestrial climates.

## REFERENCES

Barashkova, E. P., Gayersky, V. L., Dyachenko, L. N., Lugina, K. M. & Pivovarova, Z. I. Gidrometeorizdat, Leningrad (1961).

Berger, A., Guilot, S., Kukla, G. & Pestiaux, P. Geol. Rundschau **70**, 748-758 (1981).

Berger, A., Gallee, H., Fichefet, T., Marsiat, I. & Trico, Ch. Global and Planetary Change **3**, 113-124 (1990).

Berger, A. & Lutre, M.F. Quat. Sci. Rev. **10**, 297-317 (1991).

Broecker, W. S. & Denton, G. H. Geochimica Cosmochemica Acta **53,** 2465-2501 (1989).
Crutcher, H.L. and J.M. Meserve. NAVAIR 50-1C-52 Published by Direction of Commander, A Naval Weather Service Command, Washington, D.C. (1970).
Imbrie, J., J.D. Hays, D.G. Martinson, A. McIntyre, A.C. Mix, J.J. Morley, N.G. Pisias, W.L. Prell and N.J. Shackleton. In: A.L. Berger and others (Eds.), Milankovitch and Climate, Part I. Reidel Publishing Co., Boston, 169-305 (1984).
Joint U.S. Navy/U.S. Air Force Climatic Study of The Upper Atmosphere. Prepared by Naval Oceanography Command Detachment, Asheville, N.C. NAVAIR 50-1C-2, AWS/TR-89/002 (1989).
Kukla, G.J. Nature **253,** 600-603 (1975).
Kukla, G., Berger, A., Lotti, R. & Brown, J. Nature **290,** 295-300 (1981).
Lott, A.G. NOAA Tech. Report NWS20 (1976).
Raval, A. & Ramanathan, V. Nature **342,** 758-761 (1989).
Rind, D., Peteet, D. & Kukla, G. J. Geophys. Res. **94,** 12851-12871 (1989).

## FIGURE CAPTIONS

Figure 1. Relation between the 500, 700 and 850 mb mean monthly dew point temperature and precipitable water in the lowest 500 mb of the atmosphere in cm. For International Falls. Data from Crutcher and Meserve (1970) and Lott (1976).

Figure 2. Relation between the mean monthly air temperature and dew point at the 850 mb level at four US stations. Data from Crutcher and Meserve (1970).

Figure 3. Seasonal march of the mean monthly 850 mb dew point temperatures. Separately for the oceans and land of the two hemispheres. From the charts in the Navy/Air Force 1989 atlas, areally weighted (surface data at elevations above 850 mb).

Figure 4. Insolation efficiency obtained as a multiple of the insolation income I on top of the atmosphere (Berger and Lutre, 1991) and of the greenhouse forcing factor $G_{dp}$ (cf. text), compared with zonal mean monthly net radiation income over USSR (Barashkova et al., 1961) between 38° and 68°N in kcal $cm^{-2}$ (Barashkova et al., 1961).

Figure 5. Mean global insolation efficiency index for the oceans and the continents. Data centered at 21st of each month and areally weighted. Vertical bars show the difference between the autumn and spring months pairs with approximately equal insolation income to the top of the atmosphere.

Figure. 6. Difference of the DP850 in centigrades between the months paired by equal insolation for selected Northern Hemisphere stations. Data centered at 21st of each month. Stations: ALert, HEjsa, Int. Falls, San Antonio, MAlakal, SHeyma FUnchal and YAp and their latitude. Recalculated to be centered at 21st of each month. Data from Crutcher and Meserve (1970).

Figure 7. Mid-month August (~21st) insolation on top of the atmosphere at 75°N during the past 150 thousand years compared with the SPECMAP average oxygen isotope record in deep sea sediments which reflects the varying volume of ice stored on land. Increasing ice volume toward left (Imbrie et al., 1984).

## ACKNOWLEDGEMENTS

The research was in part supported by the grant DE-FG02-85ER60372D of the Carbon Dioxide Research Program, Office of Health and Environmental Research, ER72, U.S. Department of Energy.

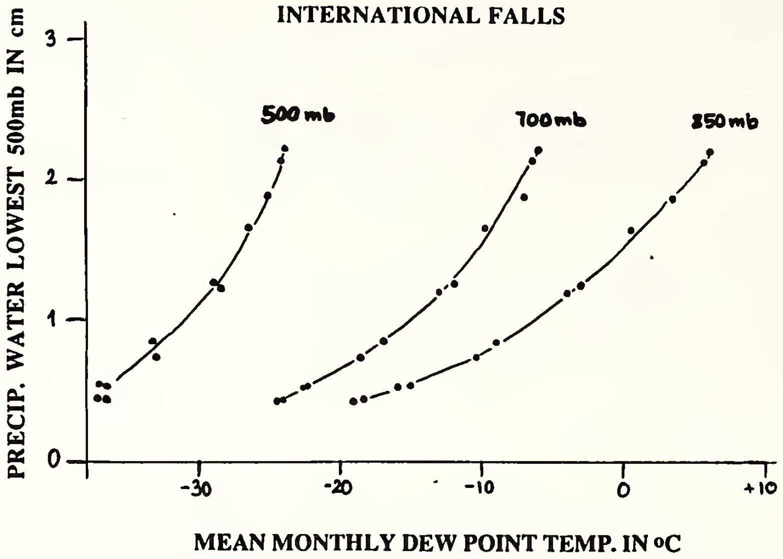

FIG. 1.

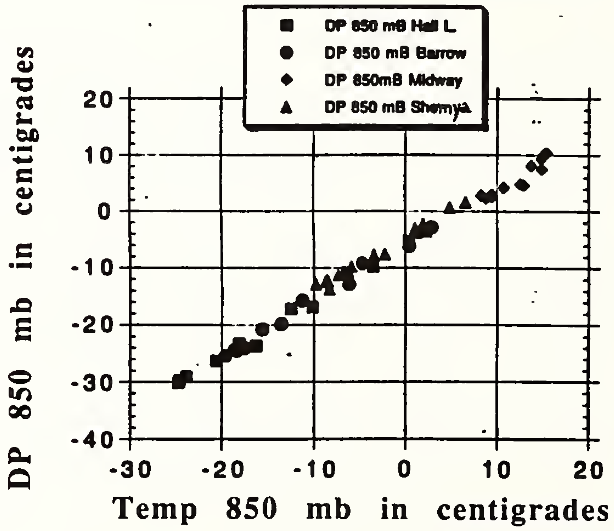

FIG. 2.

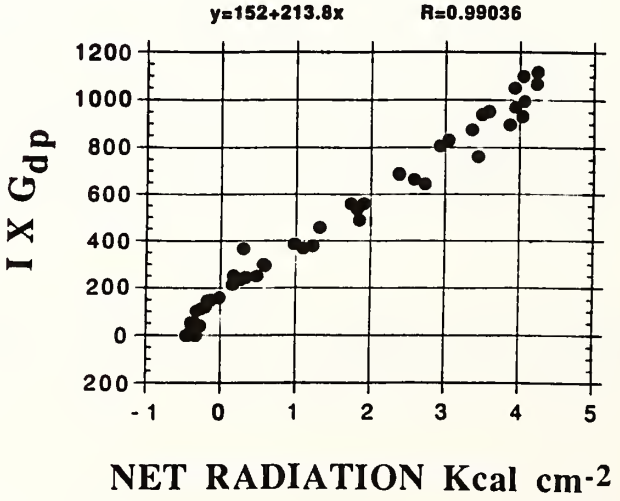

FIG. 4.

FIG. 3.

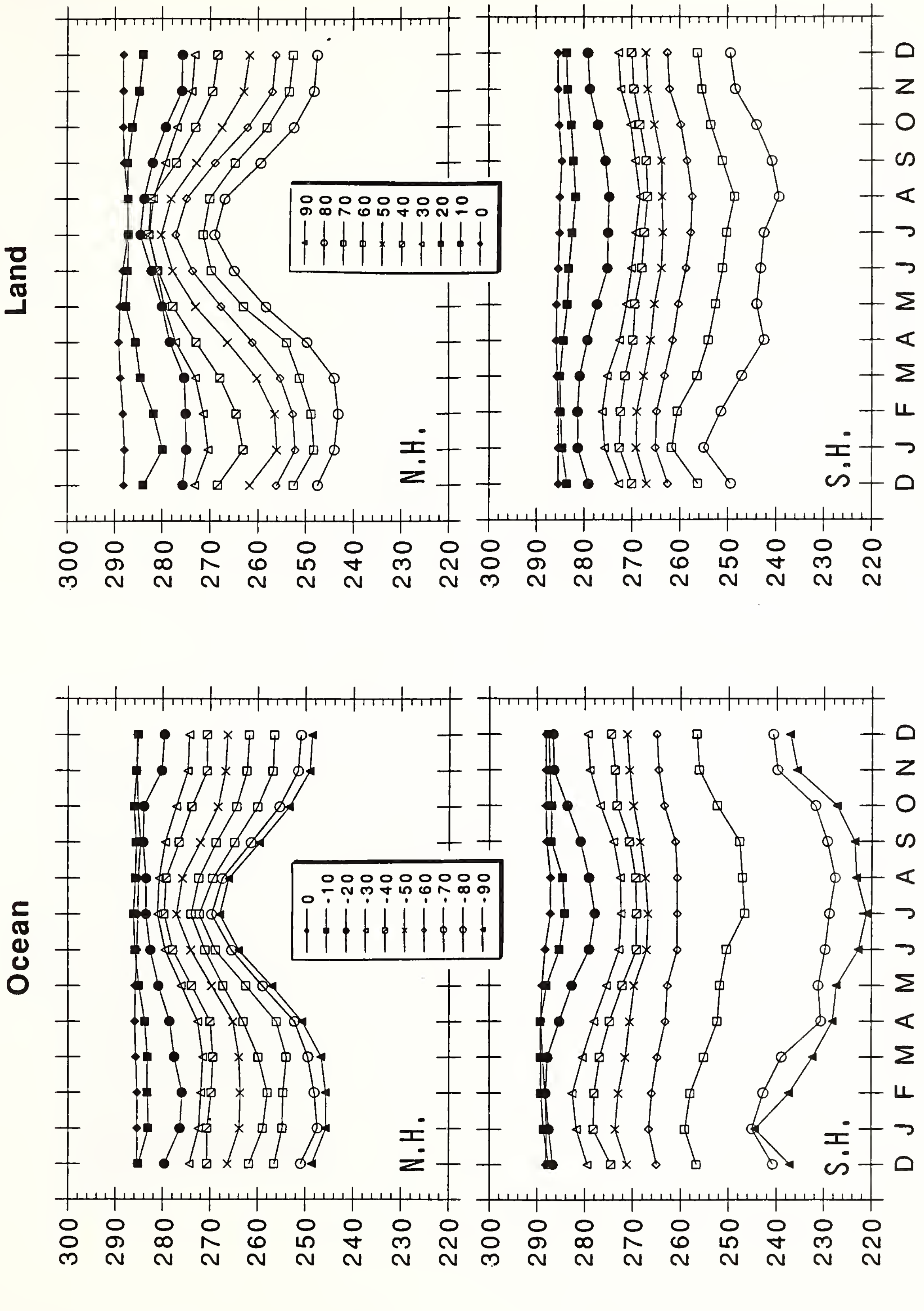

Land
Ocean
N.H.
S.H.
300
290
280
270
260
250
240
230
220
D J F M A M J J A S O N D
90
80
70
60
50
40
30
20
10
0
-10
-20
-30
-40
-50
-60
-70
-80
-90

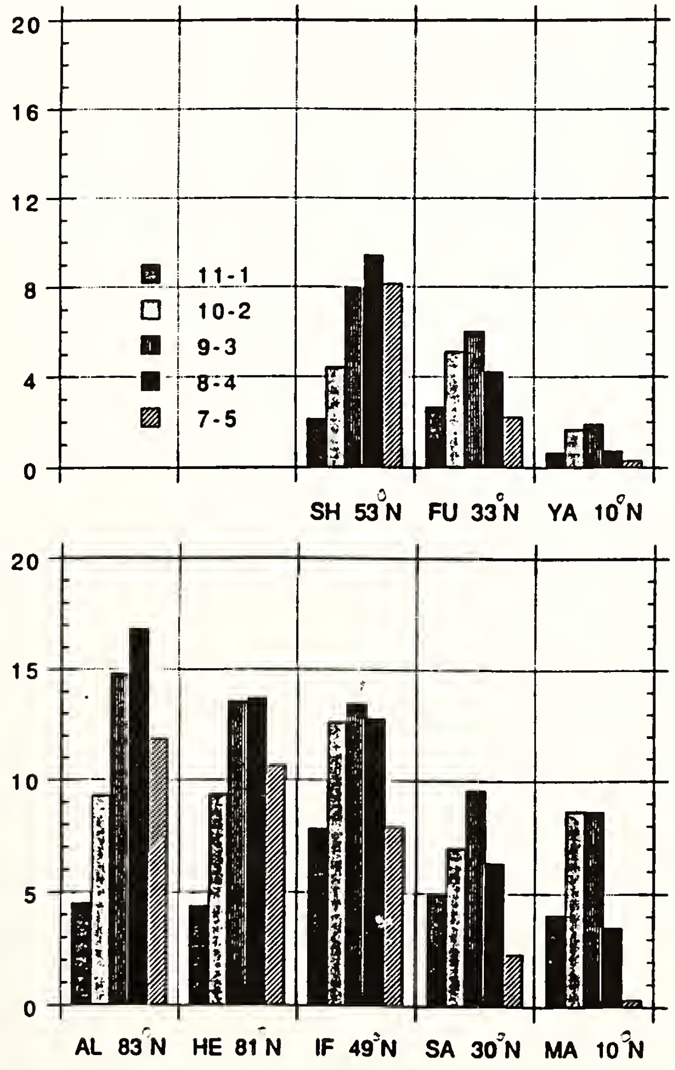

Fig. 6.

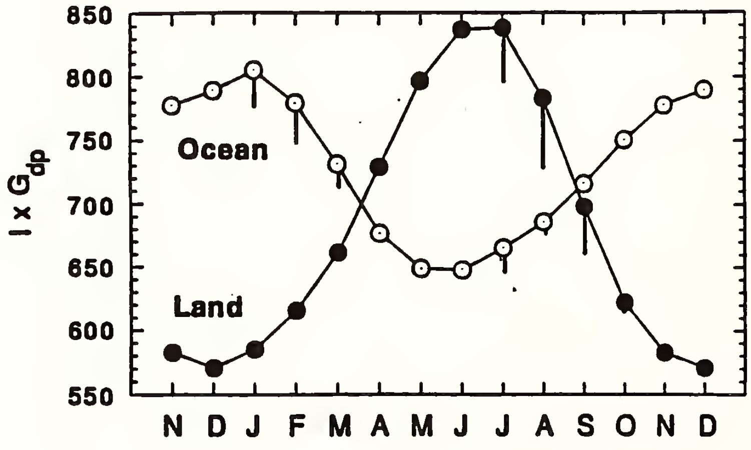

Fig. 5.

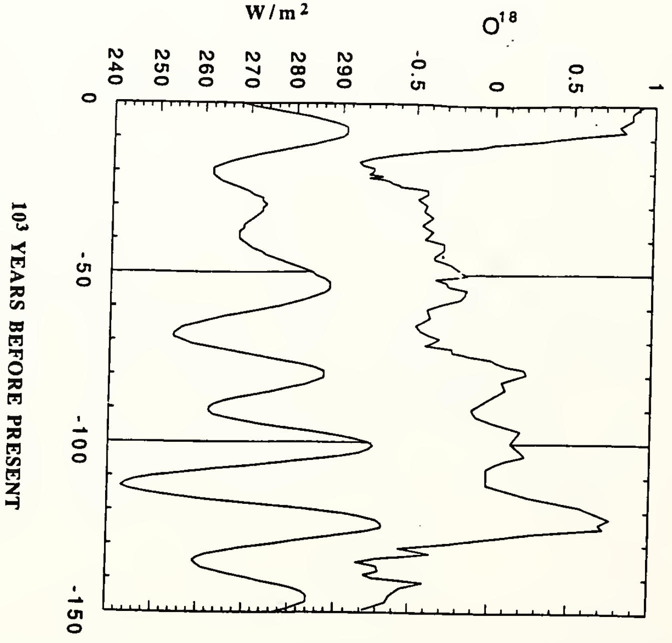

Fig. 7.

## APPENDIX

## NOTES ON MILANKOVITCH MECHANISM

Insolation received on top of the atmosphere depends on the sun-earth distance and on the inclination of the earth rotational axis to the plane of the orbit.

Since the orbit is not circular but elliptical, the sun-earth distance and therefore the intensity of solar rays changes through the year. It is today strongest in early January when the earth is closest to the sun (so-called perihelion) and weakest in early July when the earth is furthest from the sun (so-called aphelion).

The time in the seasonal cycle at which the planet gets to perihelion slowly changes. Two thousand years from now it will be in February; some 4 thousand years from now in March; about 6 thousand years from now in April, and so on. This wander, called the precessional cycle is completed on the average once every 23 thousand years (cf. Fig. 1).

The Earth's orbit becomes more circular and less elliptical in a so-called eccentricity cycle which on average is about 90 thousand years long. The intensity of solar radiation at perihelion is much greater than at aphelion when the eccentricity is large, but small when the eccentricity is low and the orbit approaches circular shape.

The earth's equator is tilted 23.4 degrees against the plane of the orbit (so-called obliquity). As a result the sun at the summer solstice is 23.4 degrees above horizon over the North Pole and at the winter solstice over the South Pole. The high latitudes of both hemispheres receive more insolation when the tilt is high. The opposite holds for the equatorial belt which receives most insolation when the tilt is low (Fig. 2). Most recent high tilt peaked at 9 thousand years ago, and the low 29 thousand years ago. The next low will come 10 thousand years from now.

Figure 3 shows the intensity of the solar beam reaching the top of the atmosphere at the solstices, equinoxes and approximately at the 21st of each of the remaining months. The values are shown for the last 20 and the next 10 thousand years. The insolation intensity (or the "instant solar constant", so to say) is strongest today in early January and lowest in July. It is close to the annual average and to the true solar constant in early April and October. Note that 6 thousand years ago, at the peak of the Holocene interglacial, the September insolation was strongest and the March insolation weakest. The opposite occurred 18 thousand years ago at the peak of the last glacial and will happen about 5 thousand years from now.

George Kukla
Lamont-Doherty Geological Observatory
of Columbia University
Palisades, New York 10964 USA

## FIGURE CAPTIONS

Figure 1. Succession of the earth's position in its orbit around the sun during the precession cycle. The closest approach, perihelion is today at the beginning of January. Furthest position, aphelion, in July. In about 2 thousand years the perihelion will be in February and perihelion in August.

Figure 2. Tilt controls the noon solar angle through the seasons. It is currently 23.44 degrees. Sun shown in its summer (and winter) solstice positions.

Figure 3. The intensity of solar beam reaching the top of the earth's atmosphere around the 20th of each month for the past 20 and future 10 millenia. It is today highest in early January and lowest in July. Compare with Figure 1.

FIG. 1.

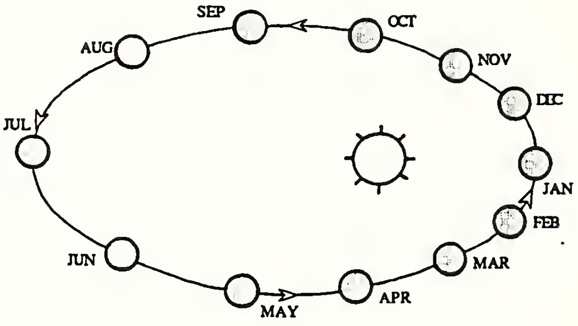

Precession

FIG. 2.

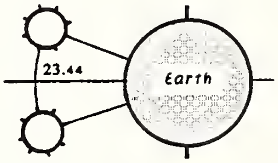

Tilt

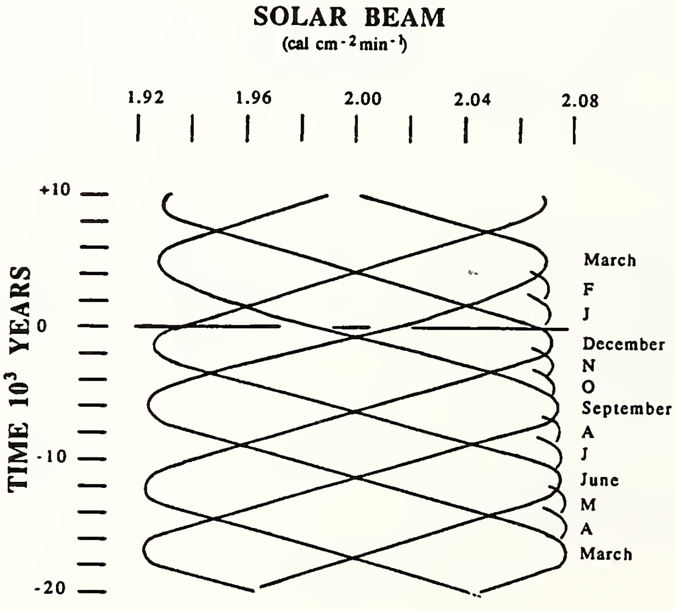

FIG. 3.

# Climatic Zones of the United States Deduced From Temperature and Precipitation Data

ROBERT G. FOVELL AND MEI-YING C. FOVELL
*Department of Atmospheric Sciences*
*University of California, Los Angeles*

## 1. Introduction

There have been many attempts to classify or discern climate types or clusters. Most have entailed *a priori* specification of climate types, like the famous Koeppen classification. An alternate approach would be to allow the data to group into their own, "natural" clusters. The first step is to identify "primitive" (influential) variables most responsible for determining climate type; temperature and precipitation are the most obvious candidates. Next, a tool is needed to perform the grouping. We choose to use *cluster analysis*, a technique much more widely employed in other fields such as biology and psychology, but is becoming more common in atmospheric sciences.

## 2. Brief summary of cluster analysis

The idea of cluster analysis is to take $n$ objects (such as meteorological stations) and group them into $m < n$ clusters which provide a valid summary or simplification of the objects by objective means. Three tasks need to be performed. First, we need to identify the important variables and objects. Second, some measure of similarity or dissimilarity is needed; this is the concept of *distance* between objects. Third, a strategy for recomputing distances among objects is needed once a merger has been made.

There are two basic types of "hard" cluster analysis, hierarchical and partitioning; both produce nonoverlapping clusters. The former, which is employed herein, starts with $n$ clusters, each containing one object. The two most similar clusters are fused together into one cluster. The distances between the new cluster and the remaining clusters are recomputed. The many hierarchical clustering methods differ greatly in how these new distances get computed. The process is continued until one all-inclusive cluster is created. The picture that is created looks like a tree (or "dendogram"). Finally, the results are inspected to determine the best place to "draw the line". If it is drawn too early, there will be too many objects to represent a useful simplification. As the clustering continues, however, cluster which are more and more dissimilar will be forced to merge. Near the end of a clustering, objects that may be as dissimilar as apples and oranges will be forced to to join together. In cluster analysis, the fusion of an apple and an orange creates a *lemon*.

The advantage of hierarchical clustering is that, because of its tree-like structure, it is easy to identify subclusters within clusters. This makes the "number of clusters" problem less serious. The major disadvantage is that the clustering at each step is constrained by what has been done at previous levels of clustering. The partitioning approach avoids this disadvantage by recomputing a totally new solution for each clustering level desired. This makes if difficult (if not impossible) to identify subclusters, however, and has the additional disadvantage of being dependent on the initial selection of observations to act as cluster "seeds".

One commonly used measure of distance is the *Euclidean distance*. The Euclidean distance between two objects $i$ and $j$ in a multivariate case with $m$ variables is given by:

$$d_{ij} = \sum_{k=1}^{m} \left( x_{ki} - x_{kj} \right)^2$$

lt, all *m* variables are combined equivalently; this may be a very bad assumption.

## and data processing

ata set used herein comes from the National Climate Data Center (NCDC) and consists of means of monthly average temperature and total precipitation (24 variables total) for the te divisions (CDs) of the conterminous United States. Note there is *no time dimension.* art our clustering project by trying to determine what can go *wrong*, so that we are aware of rouble points and biases that, if not unconfronted, may overly influence or even outright the results. We have identified three separate sources of bias. First, *methodological bias*, the quirks or characteristics of the clustering method chosen. After a survey of the literature, we decided upon the group average linkage method. Second, there might be *s* in the data set, due to its shape, resolution and/or finiteness. In the NCDC CD data set for rminous U.S., the sizes of the CDs are quite variable, ranging from quite small in the east to gly large in much of the interior west. More important is the missing data which lies outside cal boundaries of the U.S.. This situation is at least superficially analogous to the condition boundaries in fluid dynamics problems. In reality, clusters forming in New England, if rained by the lack of data, may well wish to cross over the political border and fuse with Canada. Without the Canadian data, the clusters which are formed in that area will likely omogeneous and realistic. The same problem exists elsewhere in the data domain, in the Southwest and Florida regions.

nost difficult source of bias may be *information bias.* The original input variables are d, and therefore contain redundant and/or mixed information. However, the Euclidean as well as other related measures (such as correlation coefficients), is "stupid". There is no m of squares" principle in cluster analysis like there is in regression analysis. Therefore, if les are identified, but 9 of them are really only saying the same thing (i.e., represent the ic information component), then distance measures calculated on the 10 variable data set erwhelmingly determined by the information component which is counted 9 times. This is the variables are similarly scaled, another problem with the distance measure.

nedial measure for information mixing and redundancy is *principal components analysis* Herein, the "PCs" are the rearranged variables and the values of these new variables at the on points are the "scores". These scores naturally scale to zero mean and unit variance. ir variances are the same, each component contributes equally (in an average sense) in the computations. Therefore, implicit in the use of PCA is the assumption that there exists in ata legitimate, nonoverlapping information components which are *equally important.*

pplied PCA on our 24 variable data set. First, the data were standardized by *data type* to nce to eliminate scaling problems but preserve as much as possible of the seasonal cycle on. A covariance matrix was constructed and three components were extracted. These ounted for 94% of the original variance. One component represented annual average ure (22% of variance), because the 12 temperature variables had large and rather uniform in this PC. The other two, explaining the bulk of the variance, could be characterized as month) and summer (5 month) precipitation, respectively. Orthogonal rotation on the PCs fect on the distance computations so long as each PC's scores scale to unit variance.

## reference clustering solution

olution we term the "reference clustering" is presented in Fig. 1. Some available test based on ratios of the between and within cluster sum of squares, suggest that 15 clusters the data, among other possibilities. The 15 cluster solution is shown. The number of problem is less acute in a hierarchical clustering owing to the feasibility of identifying rs. Most of the clusters are areally extensive and spatially cohesive, except in the Pacific st. One cluster was a single member "isolate" (South Carolina's first CD). The cluster in east had acquired the CDs adjacent to the Gulf and Atlantic coasts in the last step.

The huge Interior West cluster illustrates some of the problems with cluster anal cluster was formed from two smaller clusters several steps earlier (see Fig. 2). As a cluster has no annual cycle in precipitation, but this is misleading. The western meml distinct winter maximum in precipitation, while the eastern CDs in the Rockies have maximum. After averaging, the annual cycle disappears. The fusion of objects in a data entails an information loss.

## 5. Robustness of the identified clusters

We have a clustering solution, and now we need to determine how good it is. The v clustering is limited if it turns out that the clusters are very sensitive to perturbations in the clustering method. We subjected our reference clustering to a host of perturbations changing the clustering method, using raw data instead of PCA processed data, using PC weighting the scores by variance explained (creating "EOF scores") instead of allowing th to unit variance, redoing the PCA clustering with a different number of component comparing results between our original data set and one that was objectively gridded, ar designed to detect and eliminate suspect data points. These tests, taken as a whole, served that the least stable clusters in the reference clustering were those in the Northeast and Pla

Figure 3 shows how the clusters in this problem region realigned after one suspect dat isolate in the reference clustering (South Carolina CD#1) was dropped prior to PC proce raw data. The change wrought on the processed data set by the deletion of this point was but was sufficient to totally alter the spatial orientation of the two clusters in this zone. this area, the clusters were unchanged from those identified in the reference solution encouraging. Also, we have determined that latent bias owing to irregularly spaced CDs set is not a major obstacle. We have not been able to test for latent bias due to missing da likely to be quite important in some areas of the U.S..

The disadvantage of using raw (unprocessed but scaled) data is the presence of redun mixed information. The disadvantages of PCA processed data are that the components a to be equally influential (each is unit variance), and thus the PCA needs to be truncate small components exert an untoward influence on the distance measures. These distan obviously converge to a stable value as additional components are added.

One alternative to this problem might be to weight each variable according to the explains in the data, creating "EOF or variance weighted scores". This appears to solv truncation problem, but raises two other disturbing problems. First, the distance compu not invariant under orthogonal rotation, which raises the spectre of nonuniqueness. Sec test problems, we found that variance weighting the scores allows redundant informatio into the cluster analysis, despite the fact that the component variables are still uncorrel employing variance weighting created a clustering which compared well to our reference the most part, with the exception that borders and cluster areal sizes were changed.

## 6. Conclusions

We have used cluster analysis in an attempt to discern natural climate clusters which in a multivariate data set for the conterminous United States. We have seen that how t processed prior to the computation of the distance measures is a very important and diff The reason for this is that cluster analysis is critically dependent on the poorly and n defined concept of distance. Some of the clusters identified were more robust to data a perturbations than others. In addition, there is really no reason to believe the cluster boun be hard or nonoverlapping. We believe that if it is applied with a clear understan shortcomings, cluster analysis may be a useful tool which also could be applied to othe both collected and simulated, to help assess how climate types and statistics could cha future.

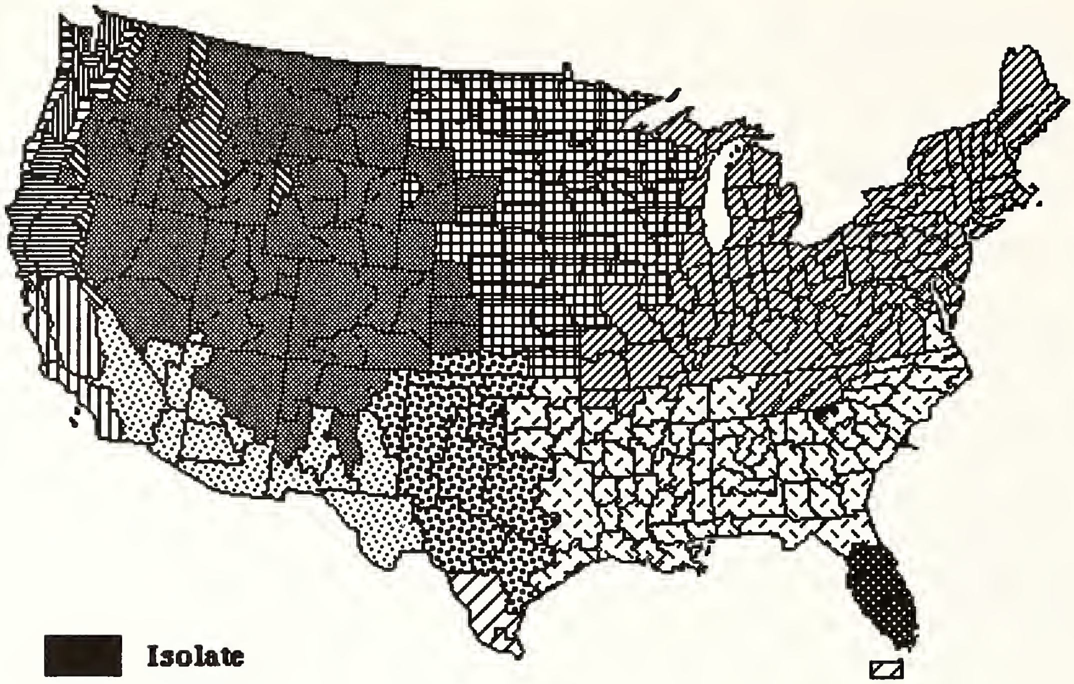

FIGURE 1 - The "reference clustering" at the 15 cluster level, conducted upon PCA processed data.

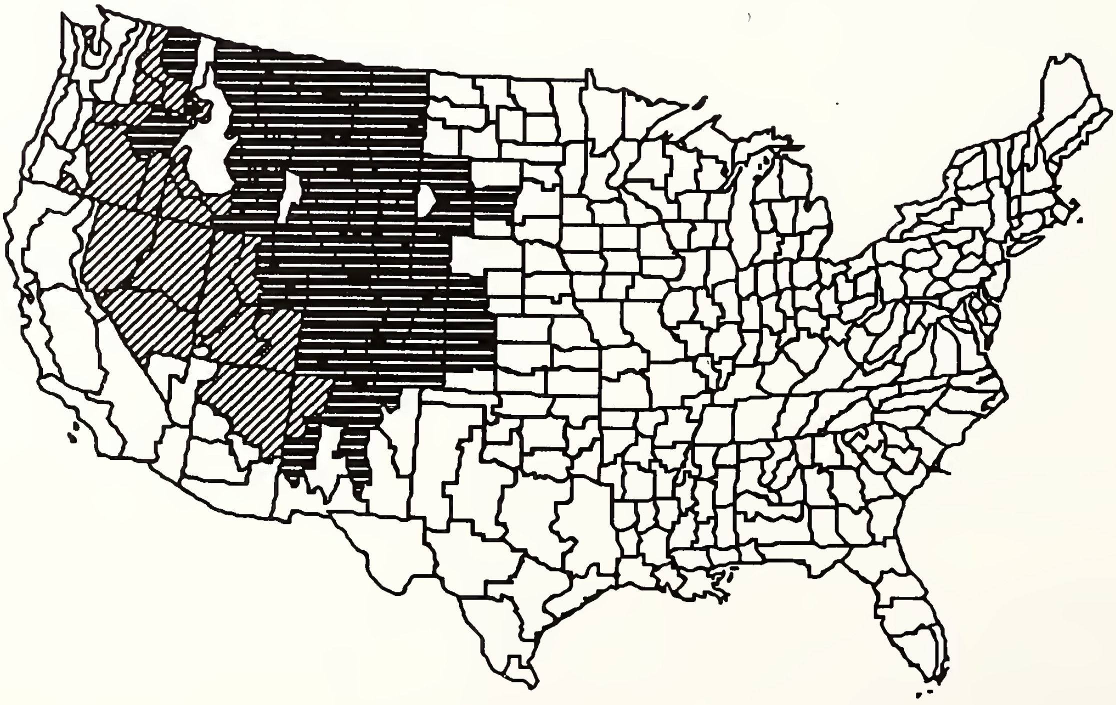

FIGURE 2 - Subgroups of the Interior West cluster, which had fused at the 19 cluster level.

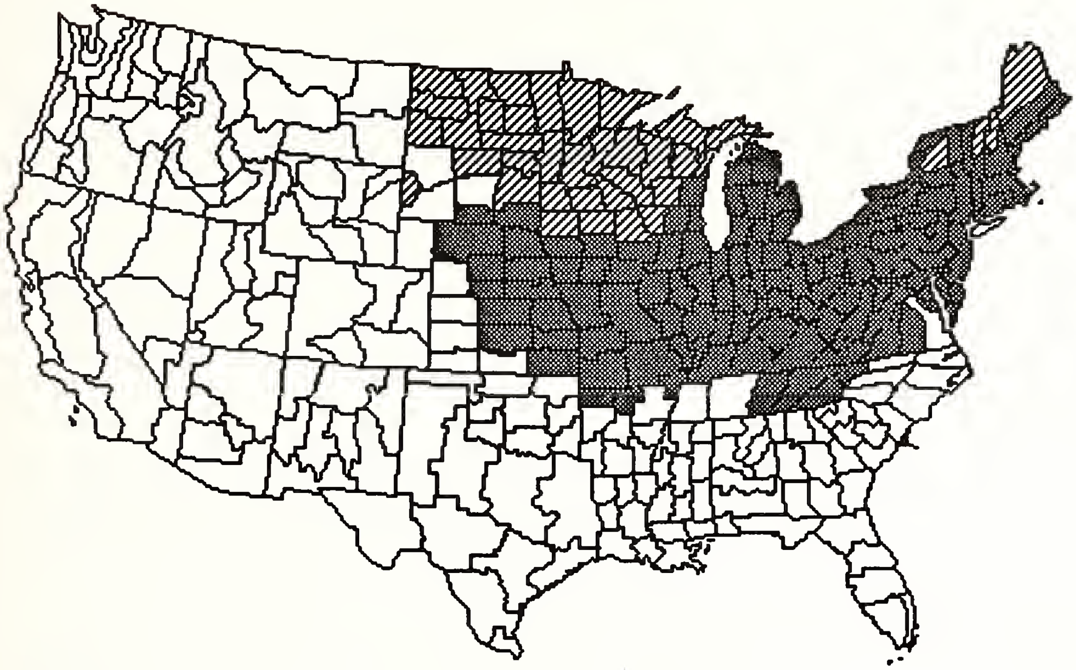

FIGURE 3 - Reorientation of clusters in the Northeast-Plains zone when the CD South Carolina #1 was deleted prior to PCA processing of the raw (scaled) data. Clusters not shown did not change.

# A Circulation-Based Consistency Check for Trends in Surface Temperature

Edward A. O'Lenic  Huug van den Dool
NOAA/NWS/CAC

and

William H. Klein
Department of Meteorology, University of Maryland

## I. Introduction.

In the course of routinely producing 30-day forecasts of temperature at the Climate Analysis Center, we have, for many years used the method of Klein(1983) to compute, or **specify**, temperatures for stations at the earth's surface using forecast anomalies of 700mb height as predictors. In order to evaluate recent biases in the temperatures, this technique has also been routinely run in a diagnostic mode, i.e., **observed** 700mb height anomalies are used to specify temperatures(s) which are then compared with observed surface temperatures(o). The difference, or residual, s-o, between the specified and observed temperatures at the stations of interest are typically plotted on a map for evaluation.

During the last several years we have noticed a consistent negative bias(s-o negative) in the surface temperatures specified by this technique(using **only** 700mb height as predictor) over much of the contiguous United States. Figure 1 shows a map of this quantity for a recent 30-day period. It is important to note that this map corresponds to the error in temperatures specified from **observed** 700mb height anomalies in comparison to **observed** surface temperatures. Throughout this paper the specified surface temperatures referred to are computed in this diagnostic mode.

Initially, we decided to investigate whether the time series of spatially averaged surface temperature residual maps contained a trend over the recent past. Subsequently, it has become clear that this work also presents the opportunity to examine the feasibility of using the surface temperature residuals as a consistency check on surface temperatures, provided that the circulation regimes which characterize the monthly time scale in the late 1980s to 1991 are essentially the same as those which characterized the training period of the data from which the specification equations were derived(1948-81).

One final goal of this study is to test the influence of urbanization and station movement upon the set of 109 U.S. stations used. To do this we asked Pamela Hughes of the National Climatic Data Center, Asheville, N.C., to choose a subset of stations from among the 109 to correspond to stations likely to be minimally biased. She provided us with the set of 24 stations listed in Table 1. We compared the results of the study using all 109 stations with results using only the 24 stations.

The data used in this work includes:

1. monthly mean surface air temperature(MMSAT) at 109 U.S. stations from January 1950 through September 1991;

2. an "unbiased" subset of the 109 U.S. stations for the same time period;

3. monthly mean 700mb height anomalies(MMZDN) for the Northern Hemisphere, from January 1950 through September 1991, on a 358 point nearly equal area grid;

4. training data consisting of MMSAT(109 stations) and MMZDN (358 points) from 1948-1981.

## II. Method

The multiple regression equations used to compute the MMSAT from MMZDN (Klein, 1983) are derived by minimizing

$$\sum_{j=48}^{81} (T_O(j,m) - T_S(j,m))^2 (1)$$

by choosing appropriate coefficients $a_n$, where

$$T_s(j,m) = \sum_{n=1}^{N} a_n Z_n(j,m)\,, (2)$$

n= index of admitted gridpoints, in order of admission,
j= year
m= month
N= total number of gridpoints admitted(approximately 3-4) chosen by forward screening.

Since the specified temperatures tend to be conservative estimates of the observed, their distribution tends to be more narrow than for observed. In order to mitigate this tendency, we inflate the specified temperatures by normalizing them by the multiple regression correlation coefficient, $\rho$, for the station in question as follows,

$$T_s^*(j,m) = \frac{T_s(j,m)}{\rho}\,. (3)$$

Hereafter, we drop the superscripted * and simply refer to the inflated specified temperatures as the specified temperatures.

Specified temperatures were computed from observed MMZDN from January 1950 through September 1991 over the U.S. at 109 stations. The map of stations is shown in fig. 2. Also shown is the 24 station subset of the 109 which were classified as "unbiased" with respect to urbanization and station relocation. The time series of spatially averaged, specified MMSAT is shown in fig 3a, while the observed MMSAT, averaged in the same manner, is displayed in fig 3b. Both time series were subjected to a 13-point running mean.

From fig 3 it is clear that the specified temperatures capture a remarkable amount of the variation of the observed temperatures on both annual and interdecadal time scales. These variations include the long downward trend from 1955 to 1970, the subsequent upward trend which continues to the present, and many of the large year-to-year swings seen throughout the record. The large differences in 1950-51 and 1957-58 may well be due to surface processes not accounted for in the development of the regression equations. The moderately large negative bias of the specified MMSAT beginning in 1988 is what initially attracted our attention to this problem.

The recent bias in the specified MMSAT is more easily seen in fig. 4, which shows the residual (s-o). Beginning in mid-1988, there has been a negative bias which reached nearly $-0.5_{o}$C by the end of the record. It is also apparent from fig. 4 that this trend is little different from that which occured from mid-1956 to mid-1958, a portion of the record which falls within the dependent data. Thus, it is unlikely that the current trend is extraordinary.

Also plotted on fig. 4 is the curve corresponding to the spatially averaged s-o residual based upon the 24 station subset of the 109 U.S. stations. The marked agreement between the two curves indicates that, for our purposes at least, the 109 station dataset is adequate and is little affected by biases due to urbanization and station relocation. This result, and the fact that the specified MMSAT tracks the observed so well(fig.3) indicate that the trend in observed MMSAT is probably real.

## III. Summary and Conclusions

We have compared two 40-year long time series of U.S. MMSAT, one observed and one specified by multiple linear regression from observed 700mb height anomalies over the Northern Hemisphere. We find that, despite small errors in both datasets, observed and specified MMSAT are remarkably similar on both annual and interdecadal time scales. A comparison of specified-minus-observed residuals from a 109 station set and a 24 station subset, chosen such that biases due to urbanization and stations relocation are minimized, indicates that biases in the results derived from the 109 station set are relatively unaffected by these biases. We further conclude that the observed trend in MMSAT is real, but not very different from other large trends in the 40-year record.

It is interesting to note that the recent downward trend in the residual is the kind of behavior we would expect in the early stages of a warming of surface air temperature due to an increase in greenhouse gases, provided that the circulation regimes present at 700mb during recent years are essentially the same as those which were present during the time period from which the data used to develop the specification equations, 1948-1981, were taken. If so, the technique we have described my provide a new method for checking the consistency of surface air temperature.

## References

Klein, W.H., 1983: Objective Specification of Monthly Mean Surface Temperature from Mean 700mb Heights in Winter. Mon. Wea. Rev., 111, 674-691.

Table 1

The 24 station subset of the 109 U.S. stations

| # | WMO# | State | Location |
|---|---|---|---|
| 1 | 72208 | South Carolina | Charleston Municipal |
| 2 | 72241 | Florida | Tallahassee Municipal |
| 3 | 72250 | Texas | Brownsville International |
| 4 | 72270 | Texas | El Paso International |
| 5 | 72280 | Arizona | Yuma International |
| 6 | 72306 | North Carolina | Raleigh-Durham |
| 7 | 72327 | Tennessee | Nashville Metropolitan |
| 8 | 72344 | Arkansas | Fort Smith Municipal |
| 9 | 72374 | Arizona | Winslow Municipal |
| 10 | 72425 | West Virginia | Huntington Tri-State |
| 11 | 72451 | Kansas | Dodge City Municipal |
| 12 | 72483 | California | Sacramento Executive |
| 13 | 72486 | Nevada | Ely, Yelland |
| 14 | 72514 | Pennsylvania | Williamsport-Lycoming County |
| 15 | 72546 | Iowa | Des Moines Municipal |
| 16 | 72562 | Nebraska | North Platte, Lee-Bird |
| 17 | 72576 | Wyoming | Lander, Hunt |
| 18 | 72617 | Vermont | Burlington International |
| 19 | 72635 | Michigan | Grand Rapids, Kent |
| 20 | 72681 | Idaho | Boise Municipal |
| 21 | 72712 | Maine | Caribou Municipal |
| 22 | 72745 | Minnesota | Duluth International |
| 23 | 72764 | North Dakota | Bismarck International |
| 24 | 72781 | Washington | Yakima Air Terminal |

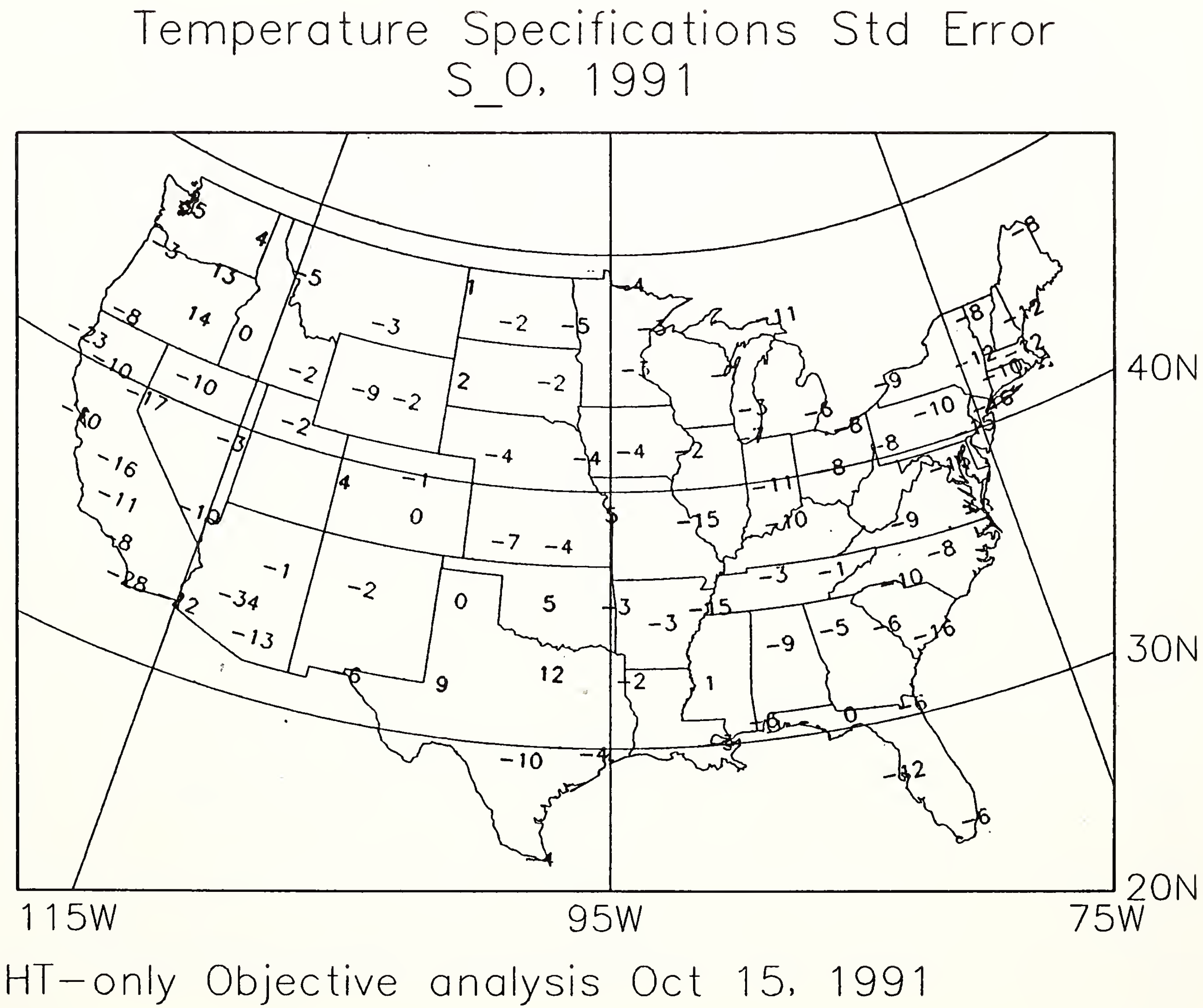
Temperature Specifications Std Error
S_0, 1991
40N
30N
20N
115W
95W
75W
HT—only Objective analysis Oct 15, 1991

1. Residuals(standardized error), specified-minus-observed, of monthly mean surface air temperature for mid-September to mid-October 1991. Values are in tenths.

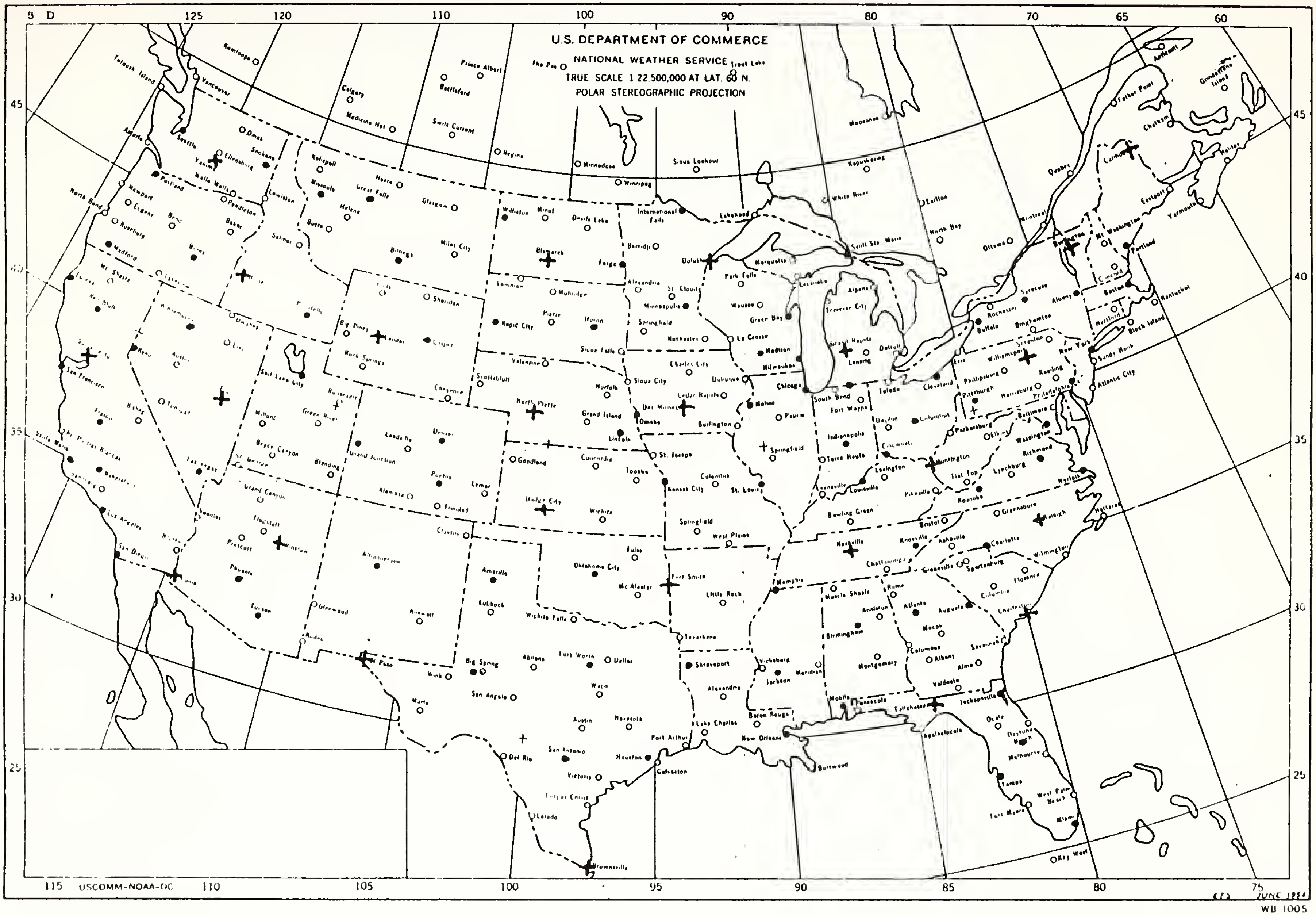

2. Locations of 109 U.S. stations(dots and crosses). Crosses are 24 station subset of the 109.

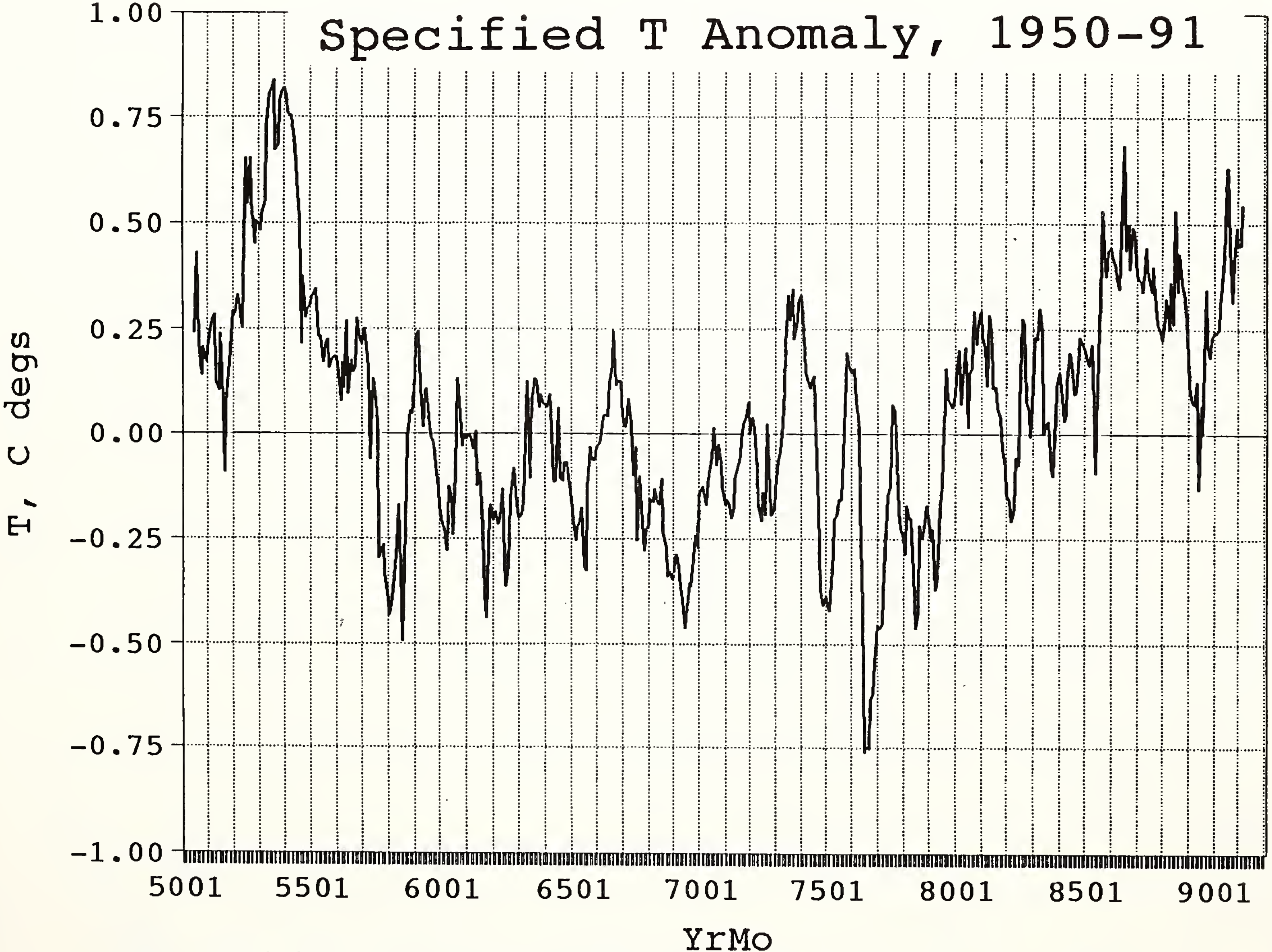

3a. Specified monthly mean surface air temperature anomaly, 1950-1991, in centigrade degrees. Values plotted are the monthly 109 station average beginning July, 1950 and ending March, 1991. Data for January, 1950 to September, 1991 were subjected to a 13-point(including the central time) running mean prior to plotting.

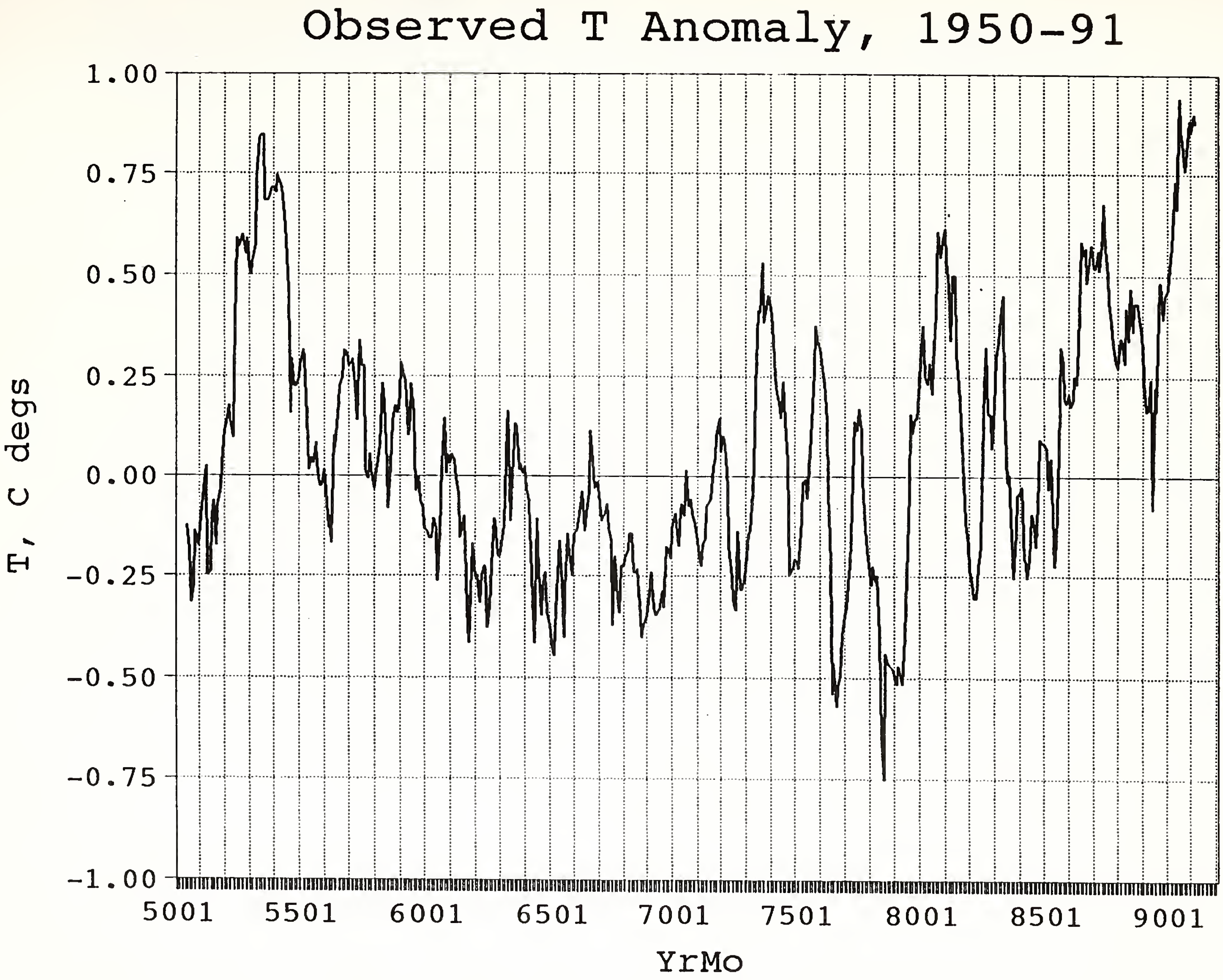

3b. Same as fig. 3a, but for observed temperature.

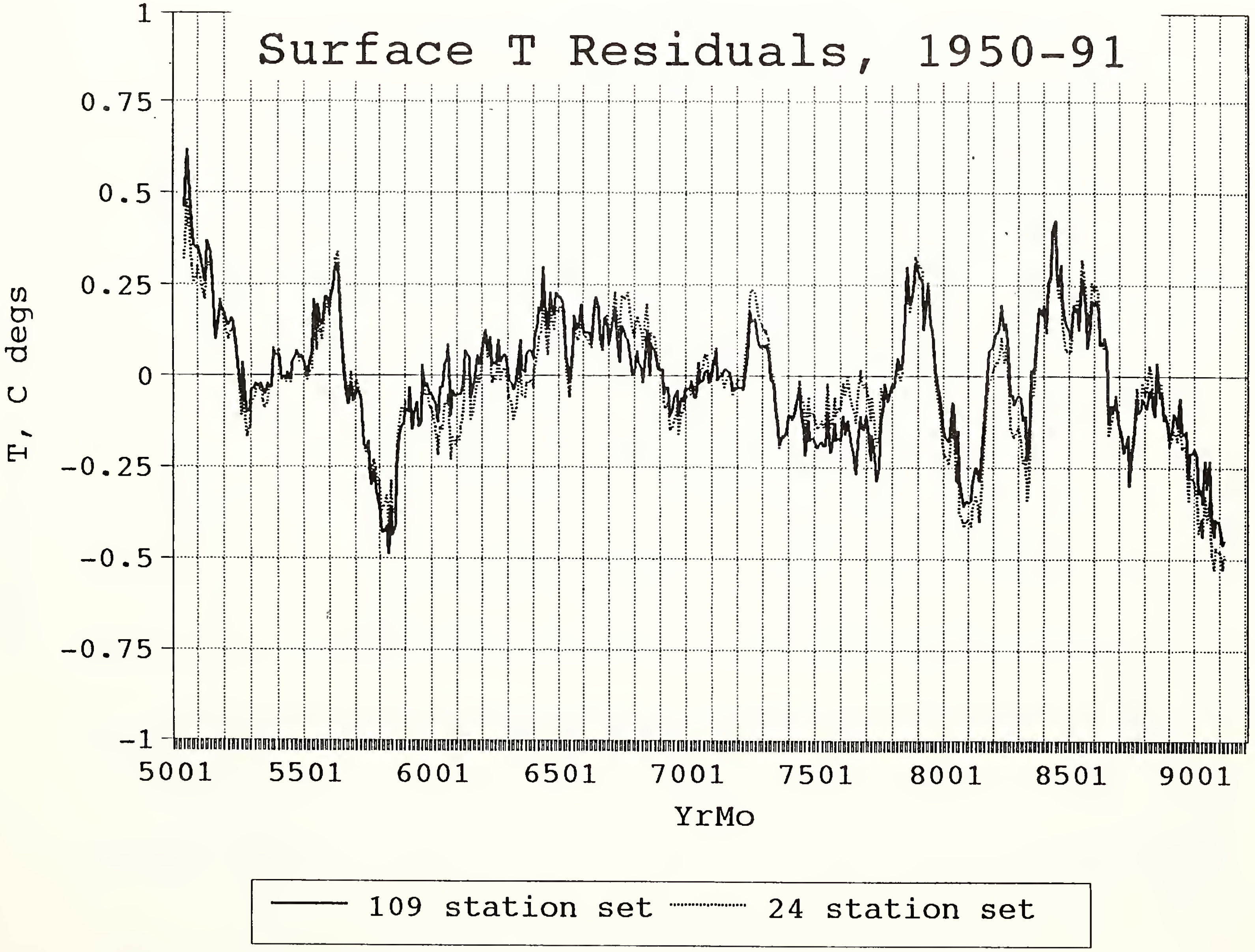

4. Residuals, specified-minus-observed, of MMSAT, 1950-1991, in centigrade degrees. Solid line is for 109 stations, dotted line is for a 24 station "unbiased" subset.

# Interannual Oscillations and the Sea Level Rise

Yurdanur Sezginer and Michael Ghil
Climate Dynamics Center, Department of Atmospheric Sciences and
Institute of Geophysics & Planetary Physics, University of California
Los Angeles, California 90024-1565

During the past few decades, scientists have focussed attention on the possibility of sea level rise due to the influence of global warming and have analyzed sea level height data. Even though methods used in the estimation of the global sea level rise and the selected station data were different, all studies predicted sea level rise in a range of 1-3mm/yr (Gornitz et al.,1982; Barnett, 1983; Barnet, 1984; Peltier and Tushingham 1989; and Douglas 1991). In this study , relative sea level height (RSLH) data have been analyzed on a monthly basis to identify the global sea level rise and interannual oscillations superimposed on it.

There are several factors affecting the sea level on different time and space scales. Real changes in sea level result from differences in atmospheric pressures, winds, ocean currents, temperature or salinity of seawater. In relation with the above factors, the thermal expansion of the oceans and the melting of polar ice sheets and temperate mountain glaciers change the sea level. On the other hand, vertical land movements contaminate sea level records because tide gauge instruments are attached to the land, and they measure sea level variations with respect to the land. Thus RSLH records include both the real changes in the ocean level and the fictitious changes due to the vertical land movements resulting from post glacial rebound (PGR) or tectonic processes. Therefore, relative sea level will show a rise in regions where the land is subsiding; likewise a fall in regions where the land is lifting. Elimination of the vertical land movements from RSLH records is essential to study the real changes of the sea level.

The RSLH data set which is organized by the Permanent Service for Mean Sea Level consists of monthly means of sea level heights at 846 stations measured between 1808 and 1987. The variability of sea level due to atmospheric forcing on time scales of years to decades can become as big as the current observed sea level rise (Sturges, 1987). The longer records can help to minimize the influence of atmospheric forcing on sea level trends. Therefore, stations which have records longer than 20 years, with no more than 20% of the monthly data missing are selected in this study. Prior to the analysis, each RSLH time series is examined graphically to detect some obvious problems (e.g. distinct jumps, irregular changes between the means of successive portions of the data, etc.). Then either doubtful portions of the data are omitted or the station is totally excluded from the data set. As a result of these modifications a total of 183 stations are found proper for further analysis. The data gaps present in the selected stations are filled by a random deviate having the same mean and standard deviation as the corresponding month.

The statistical technique used in this study is Singular Spectrum Analysis (SSA) discussed by Vautard and Ghil (1989). This method has been applied to several distinct data sets by Rasmusson et al. (1990), Ghil and Mo (1991ab), and Ghil and Vautard (1991), Keppenne and Ghil (1991), Vautard et al. (1991); it has been shown to be superior to conventional spectral analysis methods for short, noisy time series. The narrow peaks obtained by conventional methods appear as pairs of eigenvalues in SSA and the eigenfunctions and principal components corresponding to these eigenvalues are in quadrature with each other. The embedding dimension M, which is the ratio of the window size to the sampling interval, reflects the amount of significant information one hopes to retain, subject to the statistical confidence one needs to achieve (Vautard and Ghil, 1989). In order to choose the optimum M, we tested the stability of the eigenset and the statistical confidence for various values of M. We found that M=81 is suitable for our purposes.

Figure 1 shows the first 50 normalized eigenvalues of RSLH data in decreasing order for Talara in Peru. The 95% confidence interval is calculated as in Vautard and Ghil (1989). The thick line shows the cumulative variance explained by the eigenvalues. The first two eigenmodes are very distinct

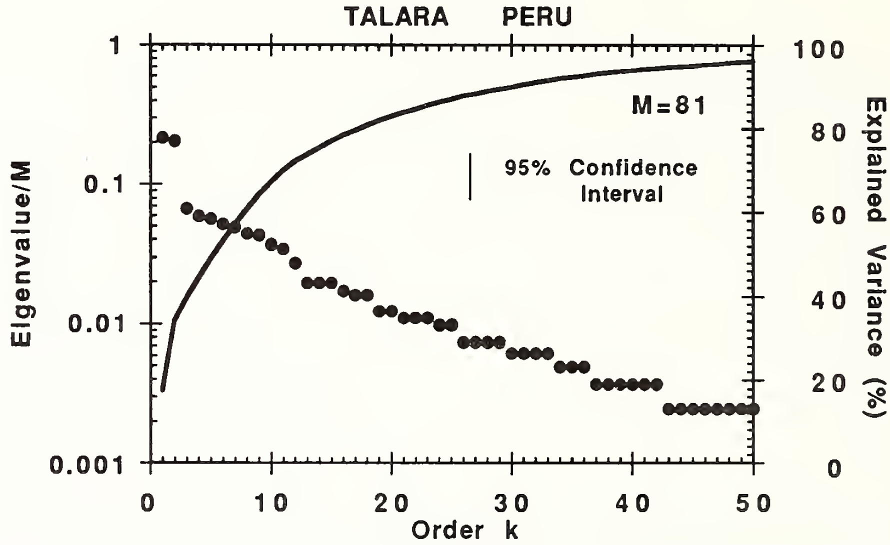

FIG.1. Singular spectrum of relative sea level height (RSLH)data. Embedding dimension M=81 is used.

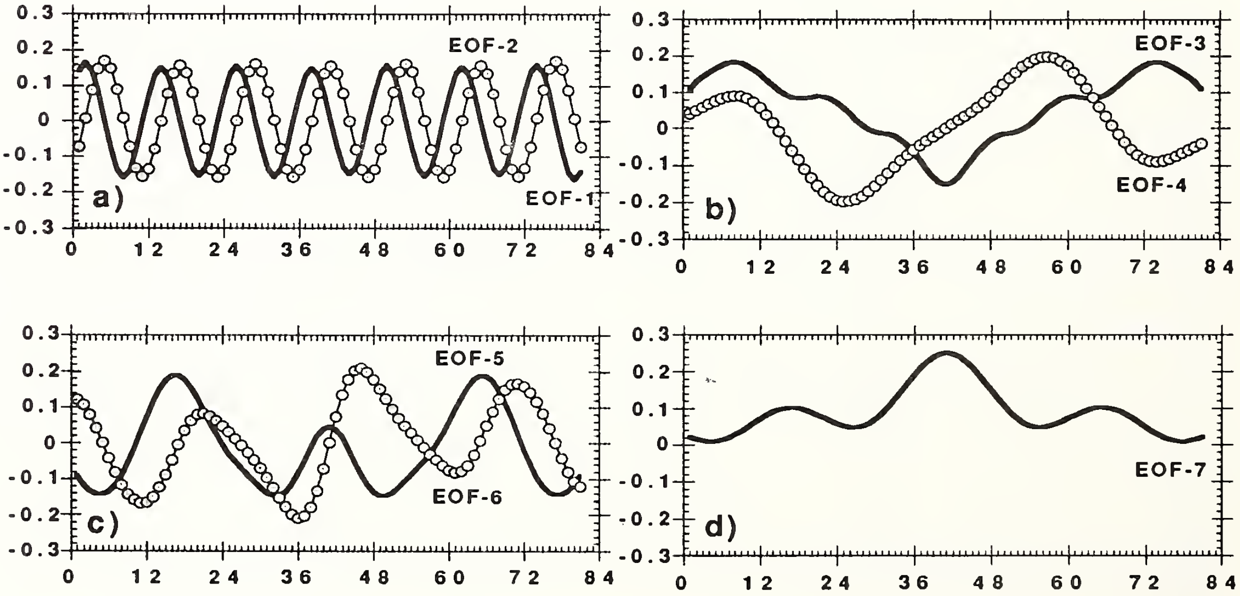

FIG. 2. a-d The seven leading eigenvector for M=81. The first pair is associated with 34% of the variance, the second pair with 10.3%, the third pair with 8.8%, and the seventh EOF -which shows very-low-frequency variability- with 4%.

from the rest and account for 34% of the total variance. A change in the slope of the singular spectrum occurs at k=12. The first 12 eigenmodes capture almost 72.7% of the variability of RSLH data. Higher-order eigenmodes are considered to be part of the noise floor. Figures 2a-d show the eigenvectors corresponding to the eigenvalues 1-7. The eigenvalues 1 and 2 are very close, and the corresponding eigenfunctions are in quadrature, as expected. Figure 2a shows that the eigenmodes 1 and 2 form an oscillatory mode corresponding to the annual cycle. EOF3-4 and EOF5-6 represent interannual oscillations with periods of 60 months and 24 months, respectively. EOF7 is not symmetric with respect to the zero line, and it represents a running mean superimposed on a biennial type signal. It might be related with a trend or with very-low frequency variability which cannot be resolved by the window length of 81 months.

We decomposed all RSLH time series into EOFs and Temporal Principal Components (T-PCs). Our analyses show that the SSA captures oscillations, secular trends and noise by different eigenmodes. In order to determine periods associated with the significant eigenmodes, we used Blackman-Tukey analysis with a Tukey window (Jenkins and Watts, 1968). The spectra of the T-PCs reveal that most of the principal components have a large peak in one frequency band and a white-noise background. We reconstructed the RSLH time series by using the T-PCs which correspond to very-low-frequency variability, or to periods of 18-30 months or 36-60 months, to study long-term sea level change or ENSO-type variability (not shown here), respectively. Trends are calculated by applying linear regression analysis to the filtered time series based on the lowest-frequency T-PCs. Figure 3 illustrates the reconstructed data from the eigenmode 7 (low-frequency variability component) and the linear trend for Talara. The observed sea level at Talara is rising with a rate of 0.5 mm/yr. On the other hand, predicted land rise in this region is 0.4 mm/yr (Tushingham and Peltier, 1991). Therefore eustatic sea level rise in Talara is 0.9 mm/yr.

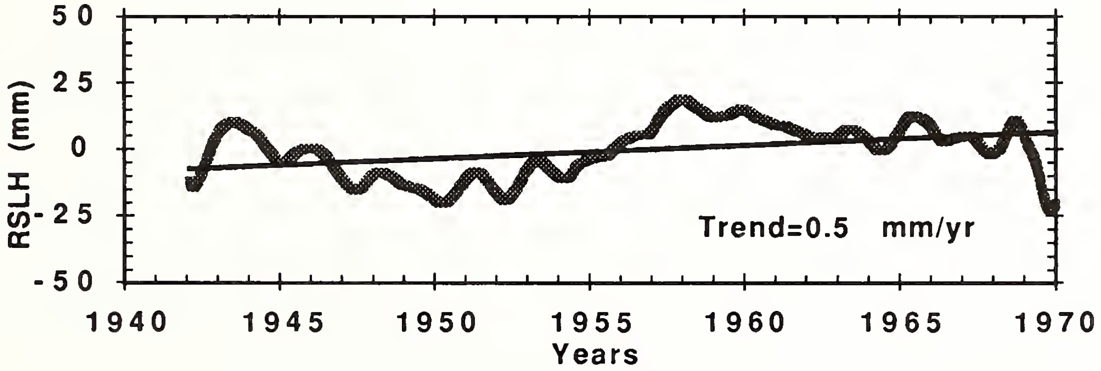

FIG. 3 Reconstructed sea level height data at Talara from the very-low-frequency eigenmodes. The thin straight line corresponds to the result of linear regression analysis.

There were two major continental ice sheets located over Canada and Northwestern Europe at the peak of the last glacial episode ( 18,000 yrBP). These ice sheets completely melted 7,000 yrBP, and contributed around 100 m to sea level rise . Although the melting process was completed thousands of years ago, the land along the east coast of America is still being uplifted, and the northwest coast of Europe is subsiding due to isostatic rebound. A global model based on the physics of the deglaciation and isostatic readjustment process was presented by Tushingham and Peltier (1991). We remove the isostatic PGR effects by using the ICE-3G model of Tushingham and Peltier. With PGR corrections, we observed that the RSLH trends are indeed distributed more uniformly over the globe than the trends without PGR corrections.

Since the data are sparsely distributed over the globe, a global sea level trend calculated by simply averaging the station trends would exhibit a strong bias. Therefore the data sites are divided into 10 regions according to geographical location, and the number of subregions in each ocean basin is selected so as to be proportional to the size of the basin. In order to enhance the coherence of the trends, nonrepresentative trends in each subregion are taken out of the data set. The results are summarized in Table 1. The global sea level trend is found to be 1.8±0.28 mm/year with PGR corrections.

TABLE 1. Regional mean trends and their standard deviations N shows the number of stations in each region.

| | Region | N | Trend (mm/yr) |
|---|---|---|---|
| Pacific Ocean | 1 | 6 | 1.8 ± 1.2 |
| | 2 | 4 | 1.5 ± 0.6 |
| | 3 | 5 | 2.0 ± 0.5 |
| | 4 | 9 | 1.9 ± 1.3 |
| | 5 | 11 | 1.6 ± 0.9 |
| Atlantic Ocean | 6 | 13 | 1.9 ± 1.0 |
| | 7 | 26 | 1.6 ± 0.9 |
| | 8 | 40 | 1.2 ± 1.4 |
| | 9 | 5 | 2.1 ± 0.8 |
| Indian Ocean | 10 | 3 | 2.2 ± 0.4 |
| Global Trend | | 122 | 1.8 ± 0.3 |

Our analyses on the oscillatory part of the data set show a quasi-biennial mode and a low-frequency variability with periods of four or five years in the equatorial Pacific region. These modes appear correlated with the El Nino-Southern Oscillation, and will be reported in detail elsewhere.

*Acknowledgments.* It is a pleasure to acknowledge useful discussions with T.P. Barnett, B. Douglas, C.L. Keppenne, and K. Mo. This work was supported by DOC/NOAA grant, NA16RC0058.

**References**

Barnett, T. P. (1983) Recent changes in sea level and their possible causes. *Clim. Change* , **5**, 15-38.

Barnett, T. P. (1984) Estimation of "global" sea level change: a problem of uniqueness. *J. Geopys. Res.*,**89**, 7980-7988.

Douglas, B. C. (1991) Global sea level rise. *J. Geopys. Res.* ,96,6981-6992.

Ghil, M. and K. Mo (1991a) Intraseasonal oscillations in the global atmosphere. Part I: Norhern hemisphere and tropics. *J. Atmos. Sci.*, **48**, 752-779.

Ghil, M. and K. Mo, (1991b) Intraseasonal oscillations in the global atmosphere. Part II: Southern hemisphere. *J.Atmos. Sci.*, **48**, 780-789.

Ghil, M. and R. Vautard (1991) Interdecadal oscillations and the warming trend in global temperature series. *Nature*, **350**, 324-327.

Gornitz, V., S. Lebedeff and J. Hansen (1982) Global sea level trends in the past century. *Science*, **215**, 1611-1614.

Jenkins, G. M. and D. G. Watts (1968) *Spectral Analysis and its Applications*. Holden-Day, 525pp.

Keppenne, C. L. and M. Ghil (1991) Adaptive spectral analysis and prediction of the southern oscillation index. *J. Geopys. Res.*, submitted.

Peltier, W. R. and A. M. Tushingham (1989) Global sea level rise and the greenhouse effect: Might be connected?. *Science*, **244** , 806-810.

Rasmusson, E. M., X. Wang and C. F. Ropelewski (1990) The biennial component of ENSO variability. *J. Mar. Sys.*, **1**, 71-96.

Sturges, W. (1987 ) Large-scale coherence of sea level at very low frequencies. *J.Phys. Oceanogr.* **17**, 2084-2094.

Tushingham, A. M., and W. R. Peltier (1991) ICE 3-G: A new global model of late pleistocene deglaciation based upon geophysical predictions of post glacial relative sea level change. *J. Geopys. Res.*, **96**, 4497-4523.

Vautard, R. and M. Ghil (1989) Singular spectrum analysis in nonlinear dynamics, with application to paleoclimatic time series. *Physica D* , **35**, 395-424.

Vautard, R., P. Yiou and M. Ghil (1991) Singular spectrum analysis: A toolkit for short chaotic time series. *Physica D* , submitted.

# A Comparison of the Stationary Wave Responses in Several GFDL Increased CO2 GCM Experiments

*John R. Lanzante*
*AOS Program, Princeton University*
*Princeton, NJ 08542*

A comparison of the responses in several GFDL increased CO2 GCM experiments was conducted. In the past emphasis has been directed towards *surface and near surface* parameters and *zonally averaged* effects. In light of this, the objective here was to examine the *regional* aspects of the atmospheric circulation *away from the surface.* The initial work reported here involves only the eddy (zonally asymmetric) component of 200 mb geopotential height.

This study attempts to answer the question: "Do the models (GFDL GCM's) suggest anything with regard to regional circulation changes?". [What should we look for in observed data?] The expectation was that *regional* changes should occur in response to a change in the *zonally symmetric* basic state induced by increased CO2. The major interest here is in the extratropics of the Northern Hemisphere during the winter (DJF) and summer (JJA) seasons.

The 5 model experiments (see Table 1 for abbreviations and a summary of the characteristics) were run by the Climate Dynamics Group at GFDL and were kindly made available by Dr. Suki Manabe. Four of these were equilibrium experiments in which CO2 is doubled while the other is a transient scenario in which CO2 was increased by 1% per year. Each of the 5 increased CO2 experiments (denoted 2xco2 for equilibrium runs or +1% for the transient) has a corresponding control run (1xco2 or +0%) of the same length. The equilibrium runs have 10 years of data (except for R30EQFIXCLD which has 5) while for the transient run 100 years were analyzed.

The control runs for the three r15 experiments produce reasonably realistic stationary wave climatologies during DJF. As an example see Fig. 1 for the DJF control from the transient simulation. The phases of all of the r15 control runs are quite similar although the amplitudes vary somewhat; compared to the real world the North American wavetrain is a bit weak and displaced westward (by about $10^{o}$). The r30 climatologies (not shown) are much less realistic during DJF; as a result their responses (which are less consistent) are not emphasized.

The response to increased CO2 was analyzed in terms of the eddy height difference (experiment minus control). Although the difference fields for the r15 runs are all distinct they have features in common. The difference field for decade 10 (years 91-100) of the transient run (Fig. 2) typifies the r15 runs. There is a tendency for the r15 difference fields in the sector from the central Pacific eastward through the Atlantic to be out of phase with climatology, indicating *diminished stationary wave amplitude.* Also, the largest eddy height changes tend to be *rises in the vicinity of Greenland.*

An assessment of the statistical significance of the responses was made using a t- test of the difference between the experiment and control means. A more rigorous and complicated nonparametric scheme which was considered was not employed at this time because of concerns with the small sample size and problems with the transient model run. The ocean model used in the transient experiment has a numerical instability which leads to catastrophic collapse when the model is run for many hundreds of years. Although the transient model data analyzed here is *probably* not much affected, it is nevertheless suspect; fortunately, the major aspects of the transient response are seen in the equilibrium runs as well.

T-score maps for each of the experiments were examined. For DJF it appears qualitatively that only the response for decade 10 of the transient experiment *might* pass a field significance test. Given the similarities of the responses it is felt that the problem may be that during DJF the natural variability is sufficiently large that a 10 year sample is simply not large enough to produce significant results given the strength of the increased CO2 signal. In order to highlight the features common to the different experiments the t-score fields for the three r15 runs were averaged and the result is shown in Fig. 3. The most prominent feature is the positive center over Greenland and its associated di-polar structure in the North Atlantic. This feature is reminiscent of the North Atlantic Oscillation pattern and implies a weakened jet in the trough exit region.

The summer (JJA) response is more highly significant (most maps *appear* to be field significant) perhaps due to the lower natural variability then. The JJA t-score field averaged over all five experiments (Fig. 4) depicts a *wave #1 response ~ 45-65$^{o}$N* with eddy height rises (falls) over the Pacific (Eurasia). Even the r30 runs show this aspect to some extent.

The nature of the evolution of the DJF response during the transient run is depicted by the time series of eddy height averaged over the area near Greenland (20-80$^{o}$W, 60-80$^{o}$N) shown in Fig. 5. Although the decade averages (dark, horizontal lines) appear to rise from year 50 onward, the rise is subtle and not monotonic. Furthermore, several of the larger decade means occur early in the run. Thus, although the effect *seems* to be evidenced in decade 10, the considerable natural variability and the fact that the response is evidenced *at the very end* of the time series tempers the confidence of this inference.

The transient response during summer (Fig. 6) is much clearer (than during winter). The JJA index (Pacific minus Europe eddy height at 55$^{o}$N) appears to trend upward over the entire 100 year sample. An important aspect is the fact that a noticeable increase may be evidenced after only 40 years; this suggests that it may be possible to detect such a response (if it occurs in nature) with the ~ 40 years of upper air data currently available.

The clarity (and implied greater potential predictability) of the summer response compared to winter is perhaps explained by Tim Barnett's argument that a response which is not similar to any naturally occurring modes of variability will yield a higher signal to noise ratio. The summer response found here appears to be of this type in contrast to the winter response pattern which resembles the low frequency North Atlantic Oscillation anomaly pattern.

At this point the principal conclusions of this study are as follows:
(1) The small sample sizes and large natural variability during winter (DJF) degrade the significance estimates. The numerical instability in the ocean model used for the transient runs is another reason for concern. Nevertheless, the main response features are reasonably consistent for the r15 runs. Hence the inferences made for the winter must be considered tentative.
(2) The small sample size is apparently less of a hindrance during summer (JJA) due to smaller natural variability. Here the levels of statistical significance are high.
(3)During winter the models *seem to suggest* (a) diminished stationary wave amplitude from the central Pacific eastward to the Atlantic and (b) eddy height rises in the vicinity of Greenland.
(4)During summer (JJA) eddy height changes occur at ~ 45-65$^{o}$N in a wave #1 pattern with rises in the Pacific and falls over Eurasia.
(5) Detection of the JJA response may be easier than for DJF due to a clearer transient evolution which appears to be noticeable after only 40 years.

| abbrev. | resltn. | clouds | ocean | scenario | # yrs. |
|---|---|---|---|---|---|
| R15EQFIXCLD<br>1xco2<br>2xco2 | r15 (4.5 lat 7.5 lon) | fixed | 50m slab (qflux) | equilibrium (2xco2) | 10 |
| R15EQVARCLD<br>1xco2<br>2xco2 | r15 | variable | 50m slab (qflux) | equilibrium (2xco2) | 10 |
| R30EQFIXCLD<br>1xco2<br>2xco2 | r30 (2.25 lat 3.75 lon) | fixed | fixed (clim.) | equilibrium (2xco2) | 5 |
| R30EQVARCLD<br>1xco2<br>2xco2 | r30 | variable | fixed (clim. + r15 diff) | equilibrium (2xco2) | 10 |
| R15CSGCO2<br>+0%<br>+1% | r15 | variable | ocm (coupled model) | transient (+1%/yr) {yr. 0 = 1958 co2} | 100 |

TABLE 1 - Characteristics of the 5 GCM experiments. The (4) equilibrium experiments in which a step function doubling of the CO2 is introduced are composed of the combinations of two atmospheric resolutions (r15 or r30) and two cloud schemes (fixed or variable). The fixed scheme uses a zonally averaged climatology from observed data; in the variable scheme the model determines the clouds. The r15 equilibrium runs employ a 50 m slab ocean (which has atmosphere/ocean heat fluxes but no ocean circulation); a statistical correction (heat flux) is used to prevent unrealistic increases (decreases) in the tropical (extratropical) ocean temperature in the absence of any ocean circulation. To reduce computing costs in the r30 equilibrium runs the SST's follow a seasonal cycle based on an observed climatology for the fixed cloud scheme; for r30 with variable clouds the SST difference *from the r15 runs* (variable minus fixed cloud scheme) is added to the r30 fixed cloud SST. In the transient scenario CO2 was increased by 1% per year; the r15 (variable cloud) atmosphere was coupled to an ocean circulation model.

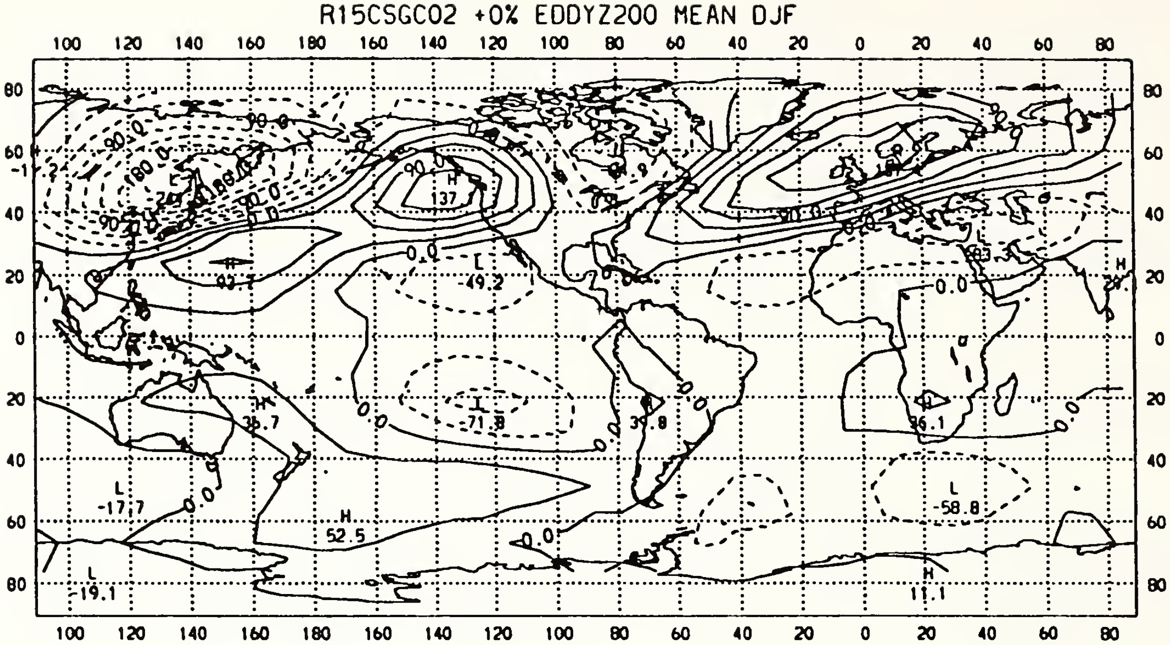

FIGURE 1 - The DJF control climatology for the transient experiment. Contours of 200 mb eddy height are given every 30 m; negative contours are dashed.

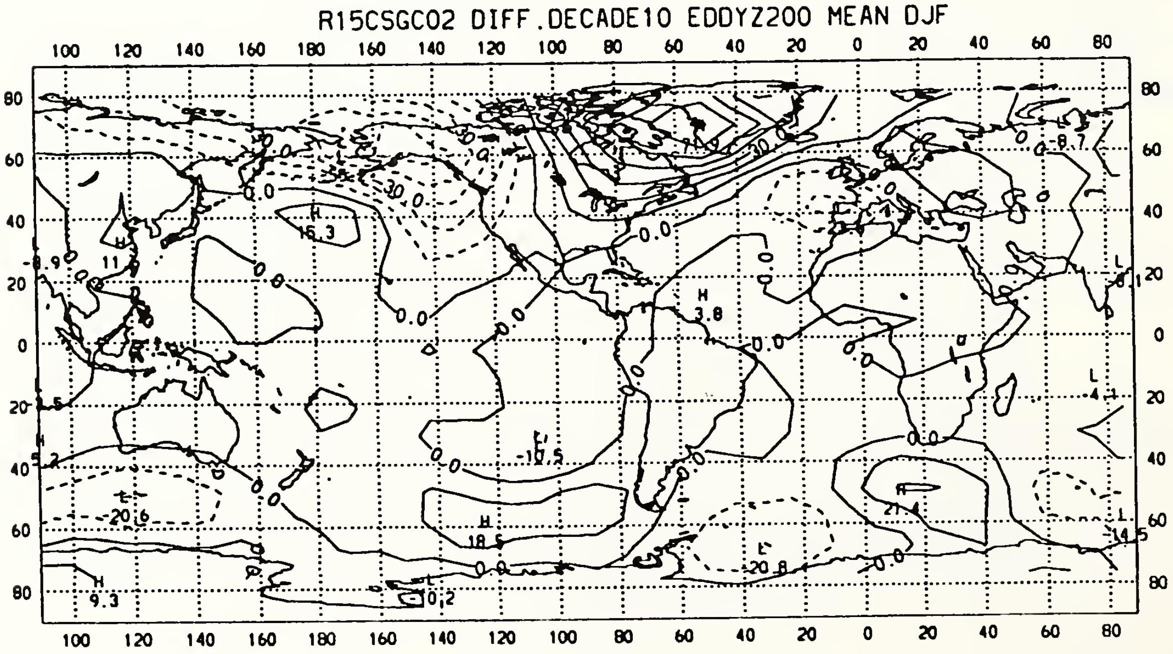

FIGURE 2 - The DJF difference field (experiment minus control) for decade 10 (years 91-100) of the transient experiment. Contours of 200 mb eddy height difference are given every 10 m; negative contours are dashed.

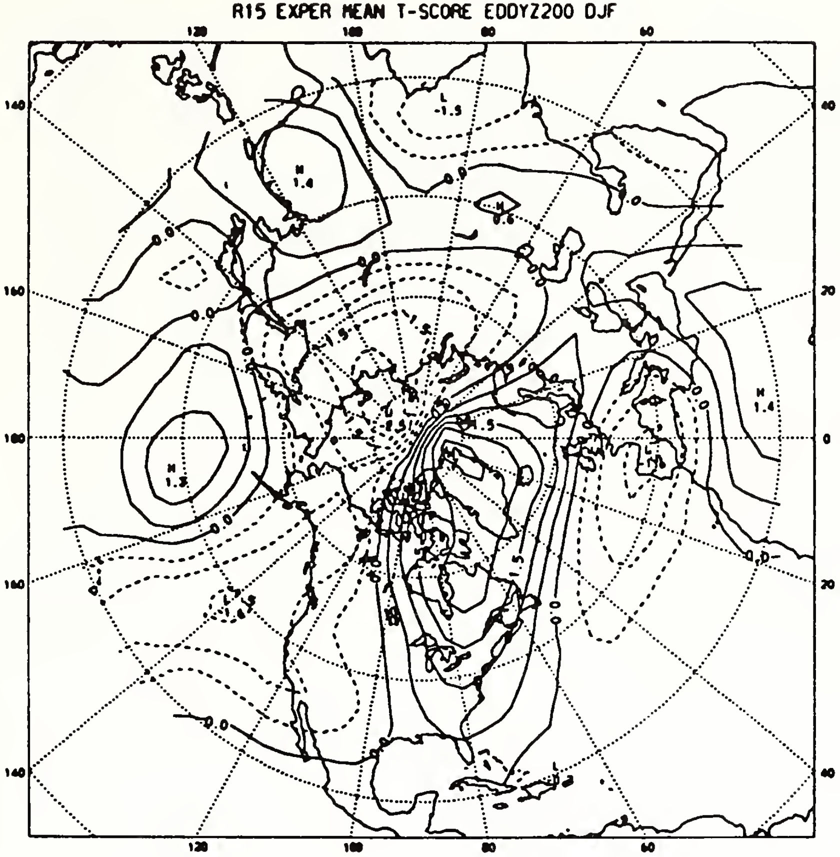

FIGURE 3 - The DJF t-score field (for experiment minus control) averaged over the three r15 runs (using only decade 10 for the transient run). Contours of t are given every 0.5; negative contours are dashed.

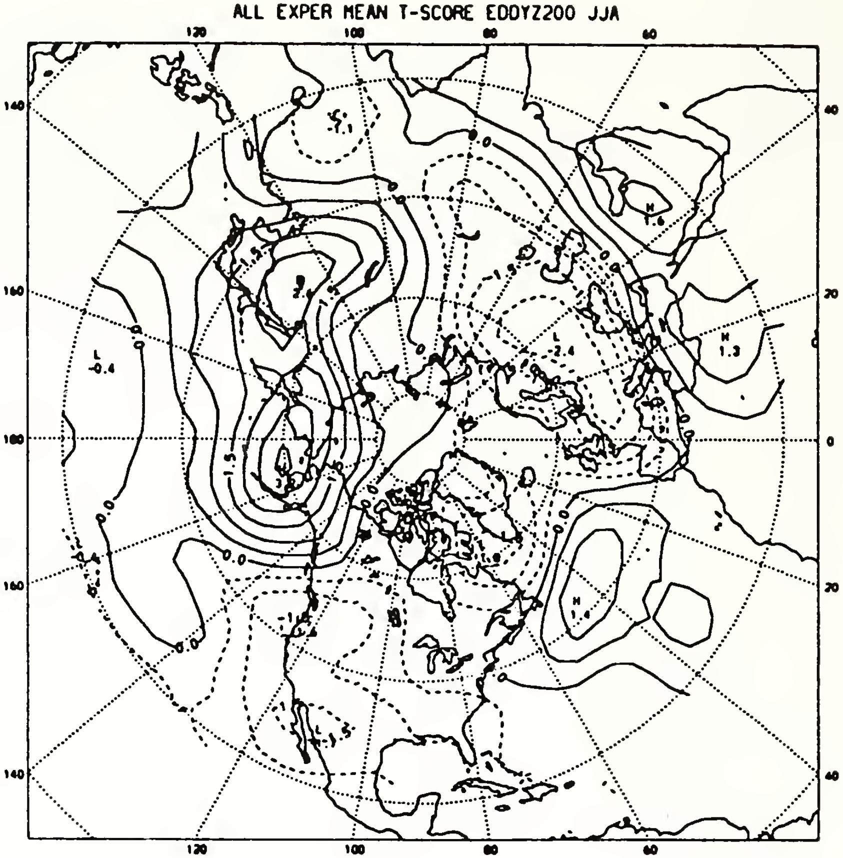

FIGURE 4 - Same as Fig. 3 except for JJA and averaged over all five experiments (using only decade 10 from the transient run).

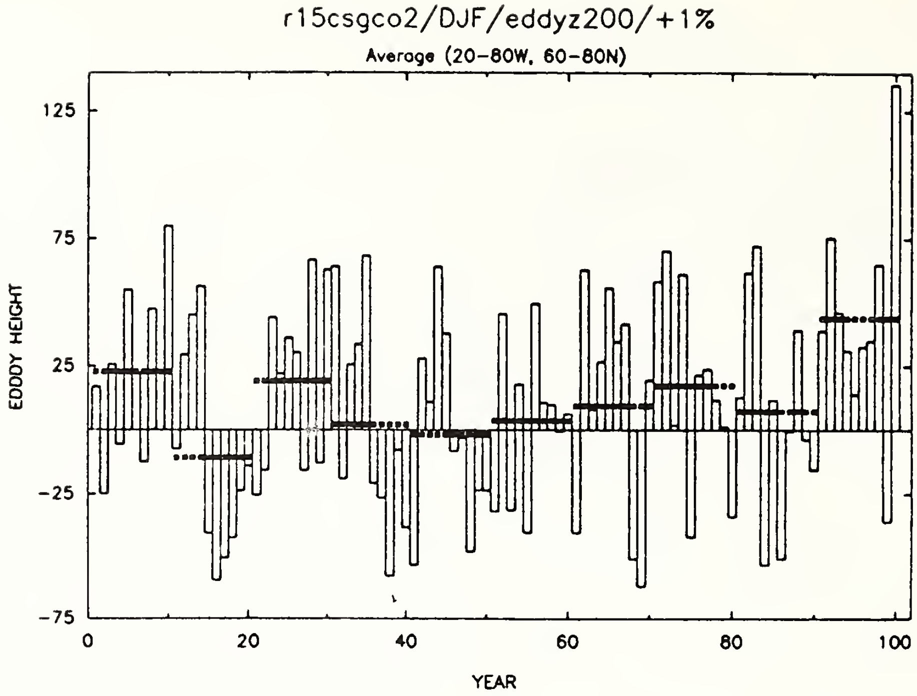

FIGURE 5 - Time series of DJF index (200 mb eddy height averaged over 20-80°W, 60-80°N) from the 1st 100 years of the transient experiment. Dark horizontal lines are decade averages.

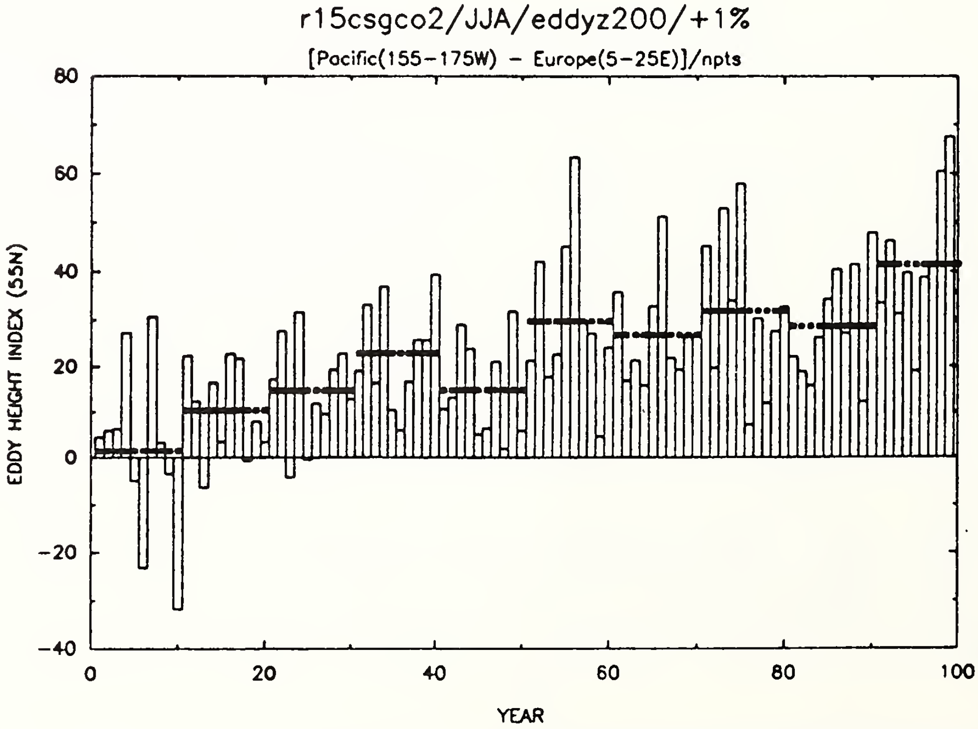

FIGURE 6 - Same as Fig. 5 except for the JJA index (200 mb eddy height difference at 55°N: 155-175°W minus 5-25°E).

# INTERANNUAL VARIABILITY IN A 10-YR RUN OF THE NMC MODEL: GLOBAL AND HEMISPHERIC MEAN SURFACE TEMP, PRECIP AND PRECIPITABLE WATER

H. M. van den Dool
Climate Analysis Center
Washington D.C. 20233

## 1. INTRODUCTION

The model integrated is a T40 version of the global spectral model used operationally at NMC for weather forecasting out to 10 days. The model has 18 vertical levels in sigma coordinates. A complete documentation can be found in NMC (1988), with updates by Kalnay et al (1990), and Kanamitsu et al (1990).

This model was integrated for 10 years (3653 days), starting from initial conditions on July, 31, 1990. The external boundary conditions were as follows. Solar radiation was updated every day according to the astronomical calendar. The snow depth, soil moisture, sea-ice and sea surface temperature were updated every day according to their known climatologies.

The run was made to assess this Numerical Weather Prediction's model capability to simulate the mean climate, the annual cycle and variability in various frequency bands (Van den Dool, Saha and Toth 1991). Here we present only a few global and hemispheric mean quantities which are often discussed in climate meetings.

As far as external conditions are concerned we went through 10 identical annual cycles. Year-to-year variability can hence be entirely attributed to the model's internal dynamics, or climate "noise". In nature, the total observed variance can symbolically be written as

$$\underset{\text{observed}}{\sigma^2} = \underset{\text{"noise"}}{\sigma^2} + \underset{\text{true climate change}}{\sigma^2}$$

From observation we know only the l.h.s. We here present model estimates of the noise term, albeit from a possibly rather imperfect model and from only a 10 year experiment. By comparing noise and observation one can surmise how much signal is left for true climate change in the observations.

## 2. GLOBAL MEAN TEMPERATURE, PRECIPITATIPION AND PRECIPITABLE WATER

Fig.1 shows a time series of 0Z global mean surface temperature (T) at each of the 3653 days. One can see 10 annual cycles, the highest T occurring in NH summer. Interannual variability is quite obvious. Notice for instance the very cold fifth year where T is about 0.5 degree C colder than in the other years, see sct 3.

Fig.2 shows a time series of global mean precipitation (P). A nice chaotic looking trace appears, averaging out to a reasonable 2.9 mm/day, and varying between 3.3 and 2.5 mm/day. It is probably hard to see any seasonality from Fig.2, but in fact there is. In Fig.3 we show the monthly mean precipitation. Climatologically, the model rainfall is highest/lowest in May/October, amounting to 2.97 and 2.86 mm/day. The evaporation has a similar annual cycle, but with higher amplitude. Also shown, in Fig. 3 is the difference (E-P).

Fig. 4 shows time series of 10 values of annual mean global mean T and P. Discarding the first year (spin-up/climate drift), we see that with so much space-time averaging T and P vary within narrow bands only. T varies less than 0.1 C, which is little compared to observations of this kind. Remember though that T is prescribed over 70% of the surface of the earth. P varies only 0.05mm/day. This seems awfully constant, but there are no trustworthy observations to compare to. Clearly 10 years is not enough to discuss climate trends as produced by a model like NMC's. We note however the lack of any apparent persistence in the anomalies in Fig.4. A far redder spectrum is required to produce interdecadal T changes of any magnitude. This would imply the role of interaction with the lower boundary (missing in the model) as an agent for interdecadal climate change.

In Fig.5 we show a time series of the last five years of the global mean precipitable water (w). This quantity peaks at about the same time as T, i.e. in NH summer. Yr-to-yr variability appears to be on the order of a few tenths of a millimeter. Note that the model atmosphere, which is too cold, has at least 5 mm too little water content.

Table 1 shows the interannual standard deviation of monthly mean T, P, and w as a function of the spatial averaging domain. Only the last 5 years are used here (not including the cold year 5). Each estimate is therefore based on 60 cases. Not surprisingly the standard deviation is largest over the smaller domains. We estimate that just over NH land the standard deviation for T would have been in access of 0.3 degree C.

## 3. THE COLD FIFTH YEAR

Fig. 6 shows the distribution of the monthly mean temperature anomaly in January of year 5. Anomaly here means departure from the 10-yr model mean for January. As can be seen both the North American and Eurasian continent are very cold with anomalies down to -7 and -8 degree C. In other years anomalies of this magnitude also occur, but never of the same sign over so much of the NH land. Remember that there is no feedback from anomalous snow-cover; the cold is entirely due to advection. Given that the SST has zero anomaly, by construction, the global mean T, as seen in Fig.1, varies interannualy according to what happens over NH land mostly. The anomalies in yr 5 are very large also in comparison to observation. Jones (1990) showed the March 1990 anomaly T map in the previous workshop to illustrate one of the largest positive anomalies seen to data. (We live in a warm decade and we sometimes suspect the Greenhouse increase to be the reason.) Except for the sign, Fig.6 looks very similar to March 1990, both in pattern and magnitude. Perhaps the field seen in Fig.6 is a natural mode of the system. Perhaps March 1990 was natural variability too.

Fig. 7 shows a 500 mb flow pattern right around the start of the cold spell at January, 4 in yr 5. A huge block appeared over the east Pacific, which was to persist for a long time. The zonal flow is displaced towards the south at almost all longitudes. Apparently, this single weather event causes sizable variations in quantities that we normally like to associate with climate.

## 4. CROSS-CORRELATION BETWEEN T, P AND W.

Table 2 shows simultaneous cross-correlations based on the 60 monthly anomalies of the last 5 yrs. We see that with the exception of the SH mid- and high latitudes, higher T is associated with higher w. Higher w correlates significantly with higher P, but only in the tropics. Even if deemed significant the T,w and w,P correlations are not high. T and P do not appear to correlate linearly at all. Thus the atmospheric moisture feedback, which is often quoted as the primary amplifier of a CO-2 induced Greenhouse, can only weakly be seen in these interannual monthly variations. From a slighty different perpective the atmopsheric water load (w) and precipitation have sometimes been mentioned as parameters to study the temperature change induced by increased greenhouse gases in an indirect manner (Elliot and Gaffen 1991). For instance a warmer climate is often quoted to be wetter as well (faster global mean hydrology) in many of the model projections of an enhanced Greenhouse climate. All such correlations appear to be rather small in our natural variability experiment.When introducing a lag/lead of one month, none of the above correlations is significantly different from zero.

## 5. CONCLUSION

Even with fixed lower boundary conditions, i.e. no anomalies in SST, soil moisture, snow and sea ice, a 10-yr run with the NMC model was able to produce occasional anomalies in near surface temperature that are, over land, as large as those observed in the real world.( The simulation of interdecadal trends can obviously not be addressed with just a 10-yr run. So we are not concluding that the general rise in observed temperature, 0.5 degree C since the 19-th century, can be the result of internal dynamics of the atmosphere only.) The temperature anomalies are associated with synoptic events, blocking for instance that seem reasonable. We found only mild evidence for the coupling between temperature and the hydrological cycle in the model run.

| | T | P | w |
|---|---|---|---|
| globe | 0.05 | 0.01 | 0.08 |
| $\varphi > 0$ | 0.09 | 0.03 | 0.12 |
| $\varphi < 0$ | 0.04 | 0.03 | 0.11 |
| $\varphi >$ 30N | 0.15 | 0.04 | 0.11 |
| $\varphi <$ 30S | 0.06 | 0.03 | 0.11 |
| Tropics | 0.03 | 0.03 | 0.13 |

Table 1. Standard deviations of domain averaged T, P and w, in units of C, mm/day and mm. Based on monthly mean data of the last 60 months of model run.

| | TP | Tw | wP |
|---|---|---|---|
| globe | 0.19 | 0.32* | 0.14 |
| $\varphi > 0$ | 0.01 | 0.20 | 0.43* |
| $\varphi < 0$ | 0.05 | 0.25* | 0.36* |
| $\varphi >$ 30N | -0.07 | 0.49* | 0.17 |
| $\varphi <$ 30S | 0.01 | 0.03 | 0.15 |
| Tropics | 0.17 | 0.35* | 0.43* |

Table 2. Simultaneous correlation between T, P and w. Asterisk indicates significance. Based on monthly mean data of the last 60 months of model run.

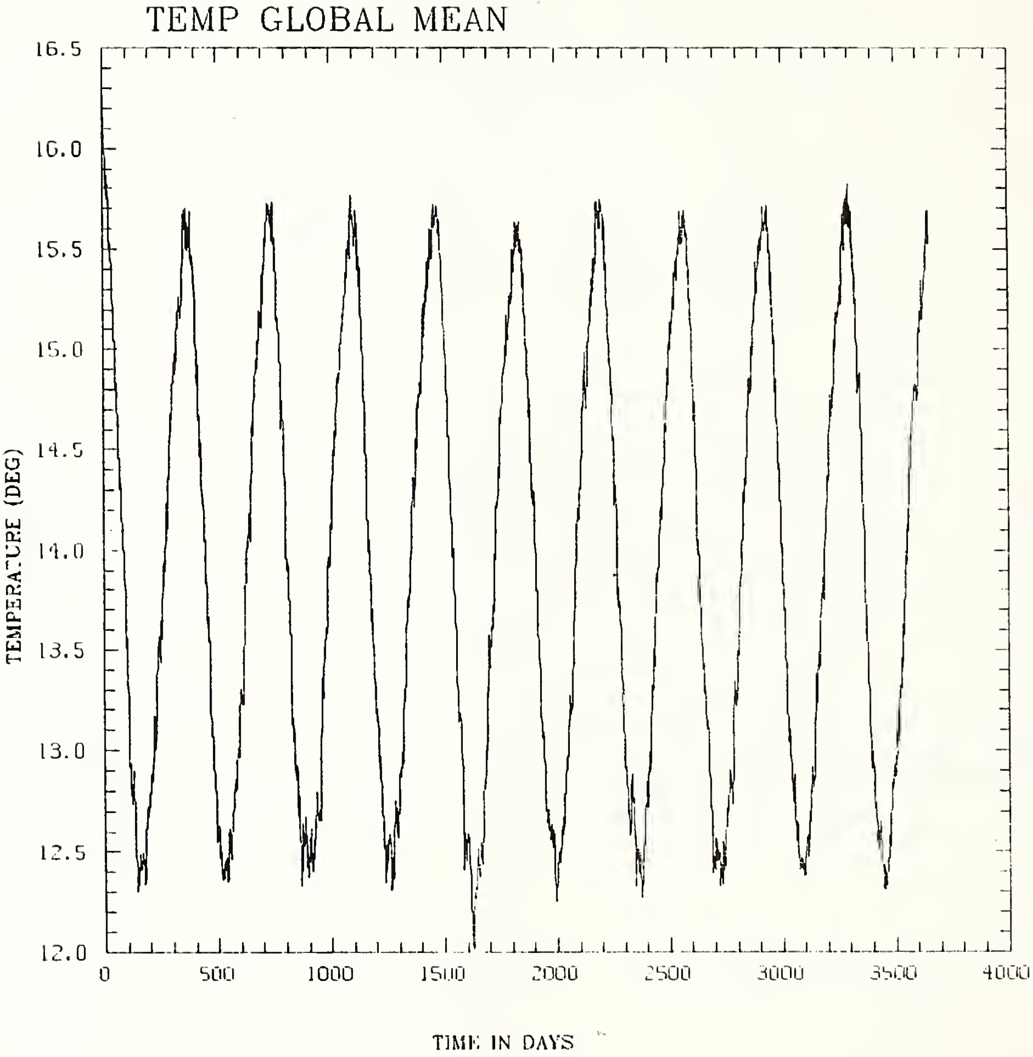

Fig.1 The global mean temperature at 0Z at each day in the ten year integration.

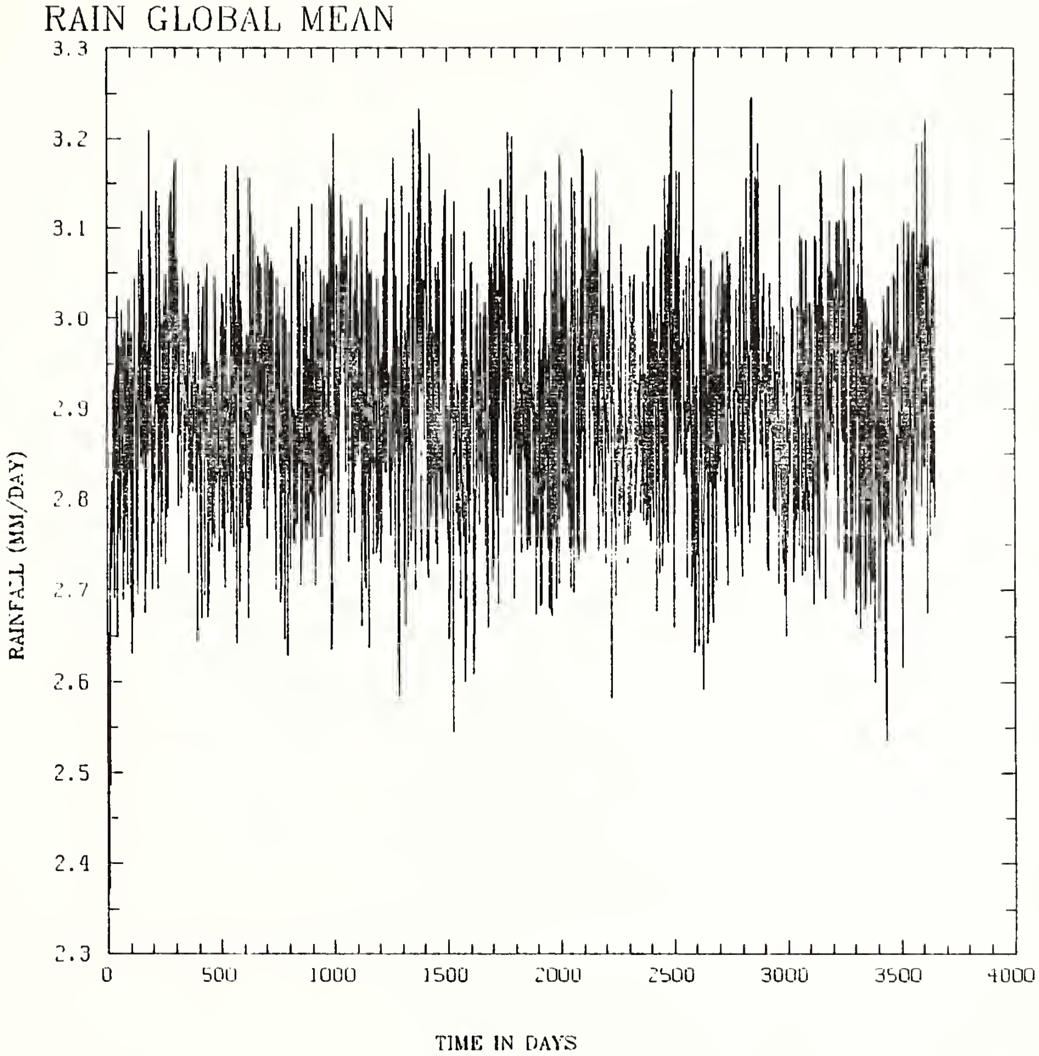

Fig.2 The global mean precipitation accumulated over 24 hours for each day in the ten year integration.

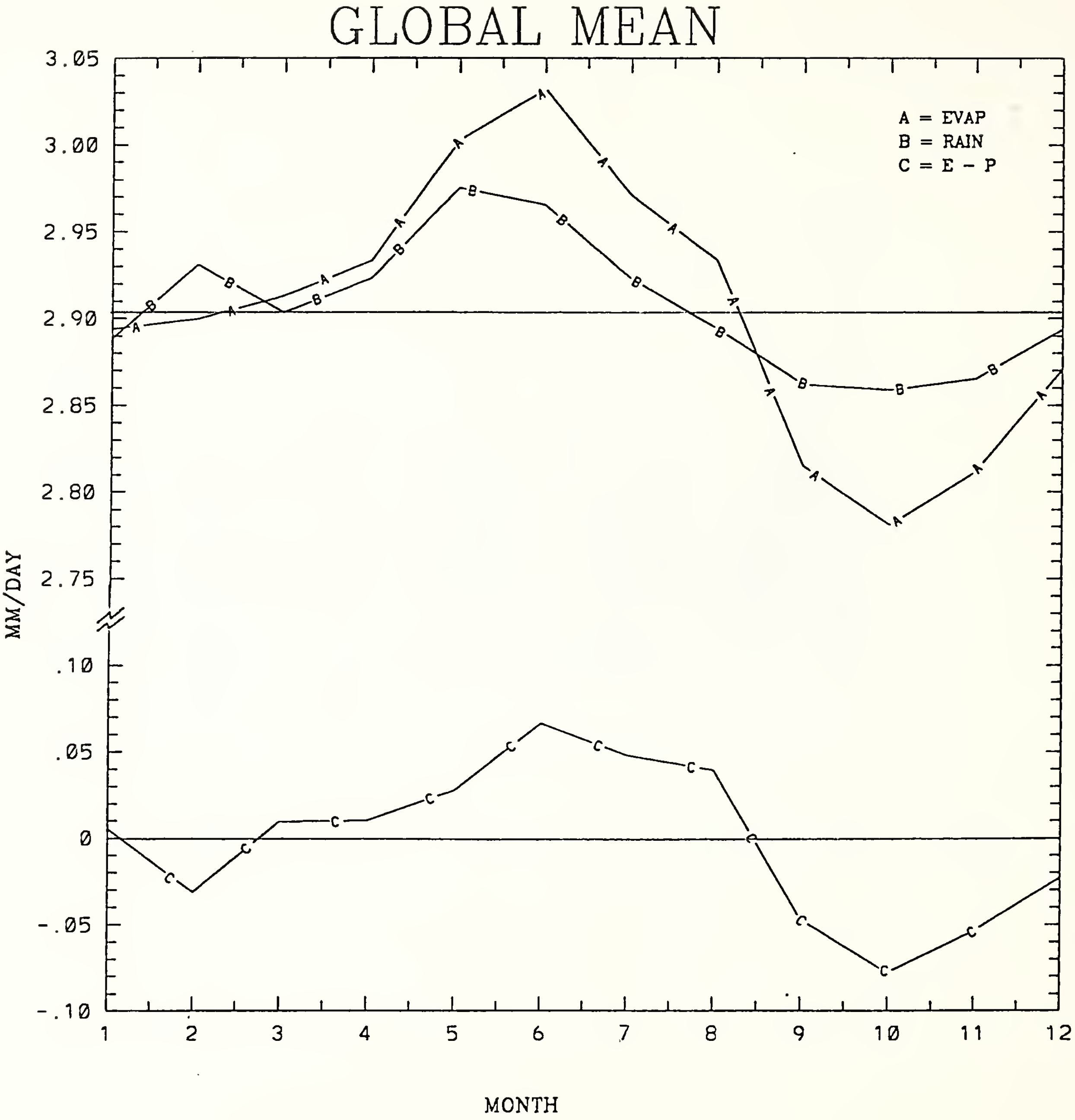

Fig.3 Global mean monthly mean precipitation as a function of calendar month, averaged over 10 years. Unit mm/day.

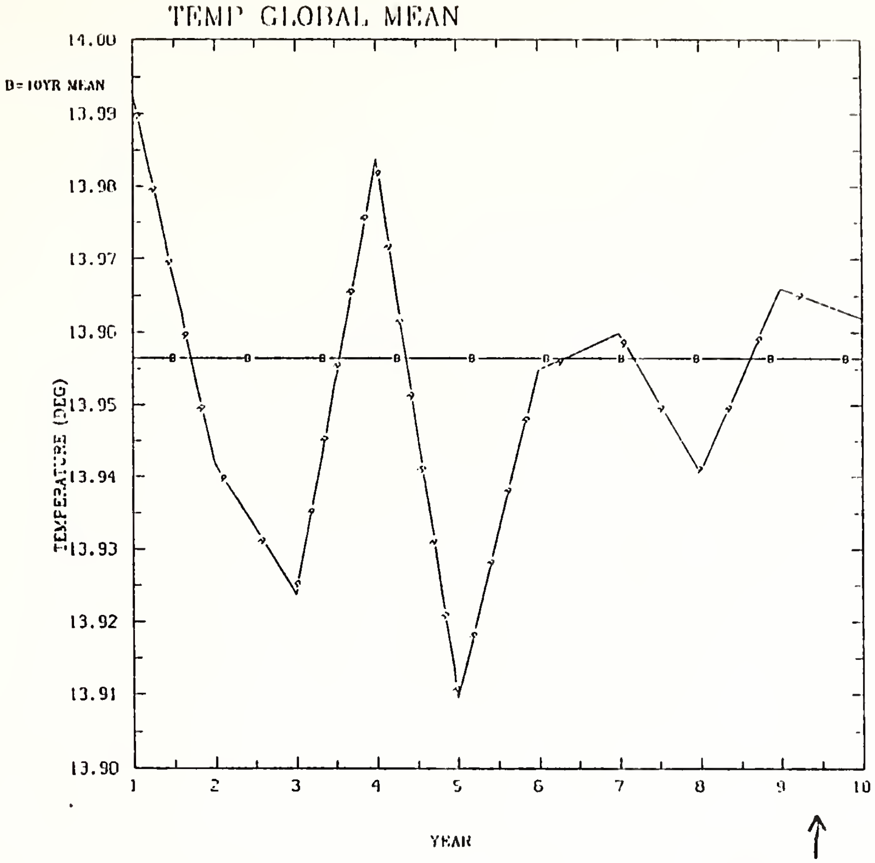

**Fig.4** Time series of annual mean global mean temperature (top) and precipitation (bottom).

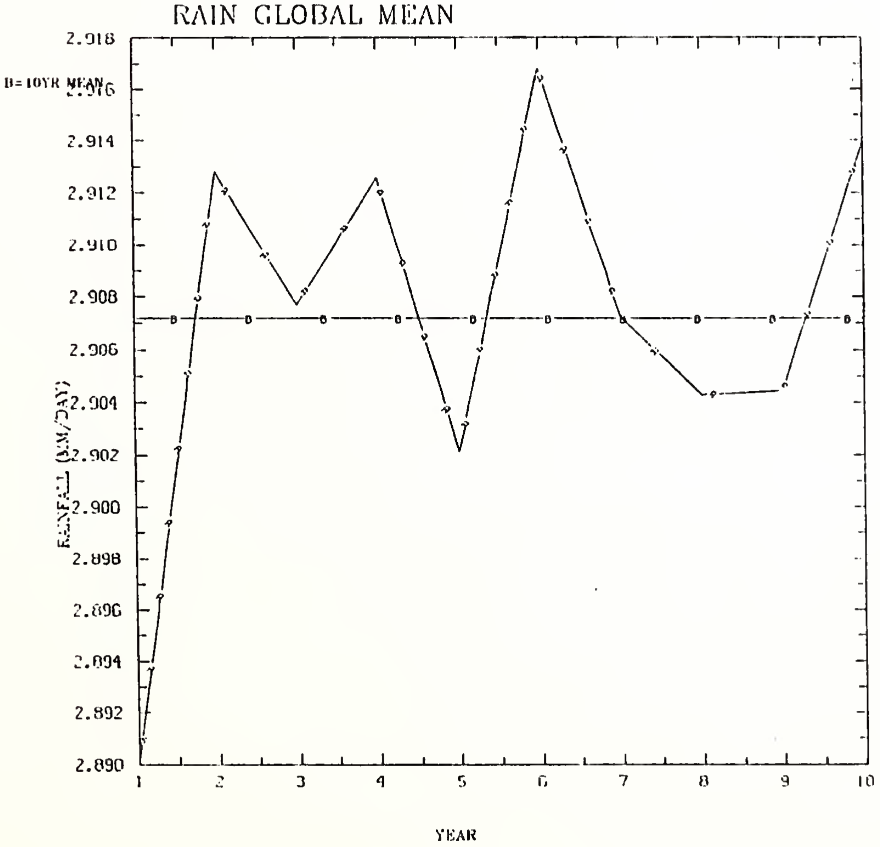

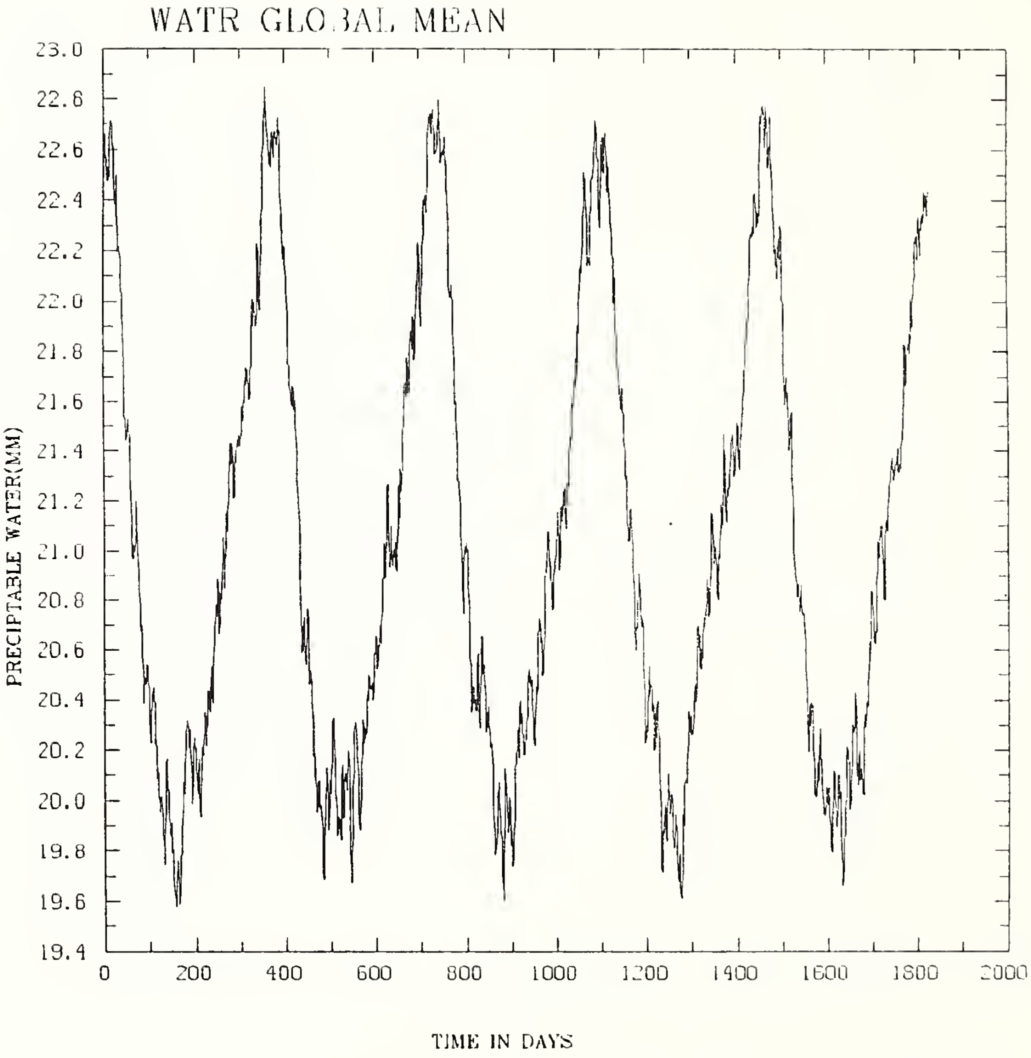

Fig.5 The global mean precipitable water at each day of the last five years in the 10-yr run.

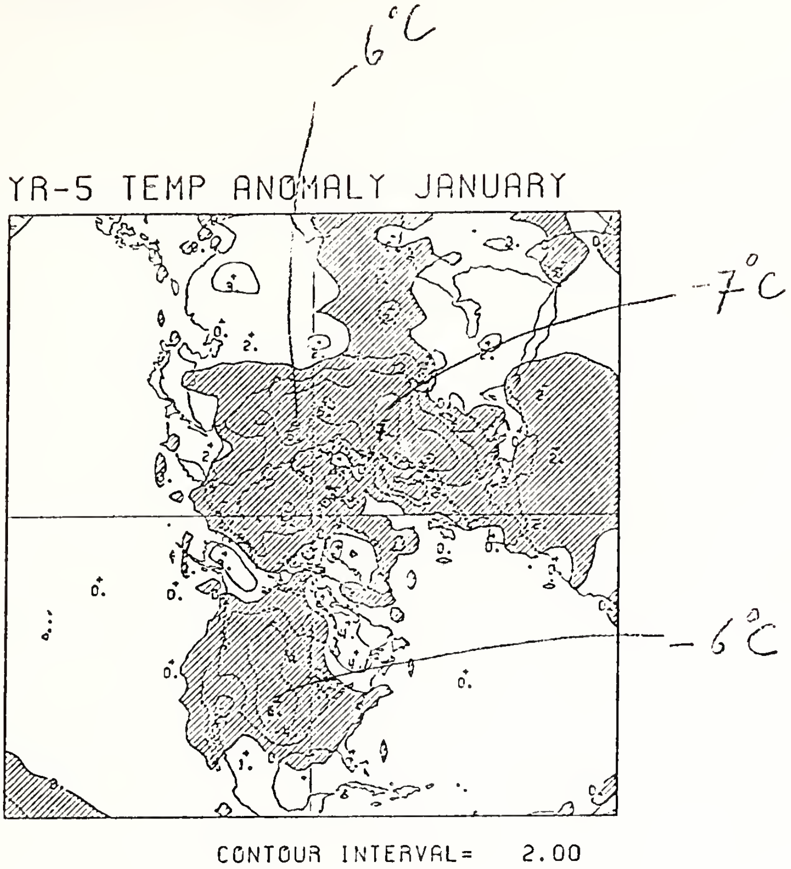

Fig.6 Anomaly in monthly mean surface temperature in January of year 5. Shading is negative. Contour interval 2 C.

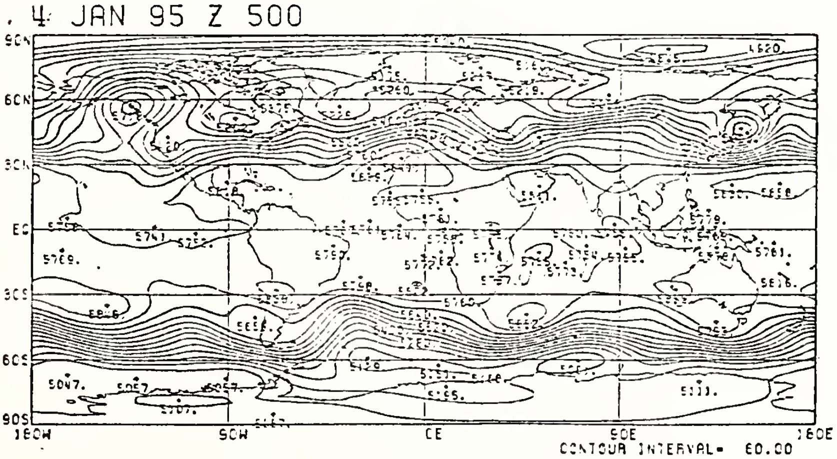

Fig.7 The 500 mb height at January,4 of year 5. Units gpm.

# Inter-decadal Variability of U.S. Westcoast Precipitation in a GCM

Shyh-Chin Chen
Scripps Institution of Oceanography
University of California, San Diego 0224
La Jolla, CA 92093

The wintertime precipitation in the mountains of the western United States during a warm or cool period has a pronounced influence on the streamflow (see Cayan (1990)). During a warm year, streamflow at intermediate elevations responds more immediately to precipitation events; during a cold year much of the discharge is delayed until the snow melts in spring and summer. Previous efforts at studying these extremes have been hampered by a limited number and length of observational analyses. In this study, we augment this limited observational record by analyzing a simplified general circulation model (GCM) (Chen and Roads, 1988, 1989; Chen et al., 1992). We first analyze the ability of the model to reproduce major characteristics of warm and cool storms. Then, a longer model run is investigated in order to understand inter-annual and inter-decadal variability of winter-mean precipitation and temperature along the west coast of U.S. In addition to having a self consistent hydrologic budget, this model is able to generate substantial numbers of low frequency events which are quite realistic. The model also has stationary statistics (e.g. no problems due to station moves or missing data).

Compared to other general circulation models in the community, this model can be integrated very efficiently (due to the many simplifications in the physical parameterizations and the resolution in the model, see Chen et al. (1991)). However, on our workstations, it still takes us several months to integrate the model for 544 consecutive perpetual winters. Here we define 90 model simulation days as a winter in the model. From this fairly long record of model data, time series of precipitation and temperature of three adjoining model grid points at (123.75W, 40.99N), (123.75W, 37.42N) and (118.125W, 37.42N), which represent the far West, are examined. These three points are all in upslope regions of the model smooth orography. The model climatological temperature and precipitation averaged over these three points are 2.5 $^{o}$C and 0.212 cm day$^{-1}$. In a typical model time series, shown in Fig. 1b, slowly varying daily temperature anomalies are embedded in highly fluctuating short-term temperature variations; precipitation occurs in even shorter bursts. These characteristics are similar to those observed wintertime time series, shown in Fig. 1a, which are obtained from compiling station data near central Sierra in the American river basin for the 1981-82, 82-83 and 87-88 winters (see also Cayan, 1990).

To discriminate warm from cool wet events, a warm/wet event is defined if the temperature and precipitation anomalies of a storm are higher than one standard deviation. Similarly, a cool/wet event is defined when the temperature and precipitation anomalies are lower than one standard deviation. Using this criterion, the warm/wet and cool/wet daily episodes can be easily identified in a scatter diagram of the daily temperature and precipitation anomalies as shown in fig. 2a. As may be seen, the daily events have temperatures clustered mostly around climatology with fewer numbers reaching large positive and negative anomalies, i.e. roughly a Gaussian-type distribution. Precipitation events are quite different however, there are large anomalies during the storm days; on most other days there is either very little rainfall or none at all. Nevertheless, several warm/wet and coo/wet storm extremes can be found. The composite 500 mb anomaly circulation patterns during the warm/wet and cool/wet daily episodes are similar to those from the observations based on northern California temperature and precipitation (see Chen et al., 1990). Generally, cool storms have intense positive anomalies over the northern-central Pacific and transport cold Arctic air to the West coast. In contrast, warm storm circulations are characterized by anomalous south-westerlies and presumably more rainfall than snowfall occurs in the warm/wet event. In essence, circulation differences between cool and warm storms in the model are quite similar to observed differences, although the model warm/wet negative anomaly to the west of California is not as zonally extensive as it is in nature.

Let us now examine the low frequency behavior of the model. Figure 1b shows the winter-mean anomalies time series for the first 160 simulated winters. Pronounced low frequency ("inter-annual" and "inter-decadal") variations over the west coast are evident, even though the model is integrated under a controlled environment in which the sea surface temperature, a frequently discussed external forcing parameter that is postulated to be responsible to the short term climate variation over U.S. (e.g. Trenberth et al., 1990; Namias 1991), is unchanging. Many other external forcing parameters, such as feedback in cloud radiation, soil moisture, albedo, greenhouse gases, etc. are also unchanged. The precipitation variability is quite large; in many cases deviations from the climatology are as large as the climatology itself. Extended wet and dry periods occur. For example a dry spell starts near the 15th winter and persists for about 10 winters; a wet period also occur near the end of the series. Many similar extended dry and wet periods over the west coast (not shown) are also found throughout the entire time series.

The scatter diagram of this seasonal time series is given in Fig. 2b. Unlike the daily distributions shown in Fig. 1b, the drought can be clearly identified by those periods with precipitation anomalies less than one standard deviation. Except for extremes at the four corners of the parameter space, the majority of the cases are clustered around the climatologies. However, it appears that the model has a slight tendency to become dry during warm or wet during cool spells (the correlation of the anomalies is -0.23). This relationship may be due to the time-invariant sea surface temperature; the cooler atmosphere temperature will extract more moisture from ocean surface through the evaporation process than the warmer atmosphere does. However, there are several warm-wet and cool-dry extremes which have a very robust circulation that offsets the evaporation effect.

From the winter extremes we compile composite circulations. Fig. 3 shows composite 500 mb heights over the northern hemisphere of these wintertime extremes. Since these composite patterns are constructed from a local index, the circulation over the western U.S. region is consistent with the index. For example, in the cool-wet case, the anomalous circulation indicates a weakening of the wintertime Alaskan ridge over west coast of U.S. and a southward displacement of the jet stream. These anomalous climatic conditions would favor more frequent intrusions of cool storms from northern Pacific. In contrast, the warm-dry circulations displace the wintertime storm track further northward into Canada as a result of the enhanced Alaskan ridge over Western U.S.

Interestingly, as shown in Fig. 3, anomalous circulation patterns associated with the local extremes have clearly identifiable global features. Moreover, the pattern associated with the warm/dry (warm/wet) extreme appears to be a mirror image of the cool/wet (coo/dry) extreme. This indicates that there may be two oscillating circulation patterns associated with the atmospheric hydrological and temperature extremes over the west coast of U.S. In other words, the short term climatic extremes over Western U.S. are governed by the variation of large-scale circulation patterns in this model. As stated earlier, since this simulation is performed under a fixed external forcing conditions, it is fair to say that the variations we found here are due to the intrinsic non-linear dynamical nature of the atmosphere. We find that we need more thorough analyses to understand the spatial and temporal behavior of these dominant patterns. In particular, we intend to determine how these spatial patterns are associated with the evolving low frequency patterns in the model.

In reality there are many external forcings, e.g. sea surface temperature variations, that will interfere with the evolution of these anomalous circulations. However, studies of a simplified atmosphere should prove helpful in better understanding and ultimately predicting hydrological extremes in California and elsewhere.

**References**:

Cayan, D. R., 1990, Cool vs. Warm winter precipitation and its effect on streamflow in California, Betancourt, J. ed., Proceedings of the 7th Annual PACLIM Workshop.

Chen, S.-C, and J. O. Roads, 1988, Development of a simplified NMC spectral model with empirically-determined forcings, Proceedings of the 13th Annual Climate Diagnostics Workshop, Boston, Mass. Nov. 1-4, 1988.

Chen, S.-C, and J. O. Roads, 1989, Winter simulation in a simplified NMC spectral model with empirically-determined forcings, Proceedings of the 14th Annual Climate Diagnostics Workshop, La Jolla, CA, Oct. 16-20, 1989.

Chen, S.-C, J. O. Roads, and J. Alpert, 1990,Warm/wet and cool/wet western U.S. simulations in a general circulation model, Proceeding of the 15th Annual Climate Diagnostics Workshop, Ashville, N.C. Oct. 29-Nov. 2.

Chen, S.-C, J. O. Roads, and J. Alpert, 1992, Variability and predictability in an empirically-forced global model, submitted to J. of Atmos. Sci.

Namias, J. 1991, Spring and summer 1988 drought over the Contiguous United States- Causes and prediction, J. Climate, v.4, p54-65.

Trenberth, K.E., G.W. Branstator and P.A. Arkin 1990, Origins of the 1988 North American drought, Science, v.242, p1640-1645.

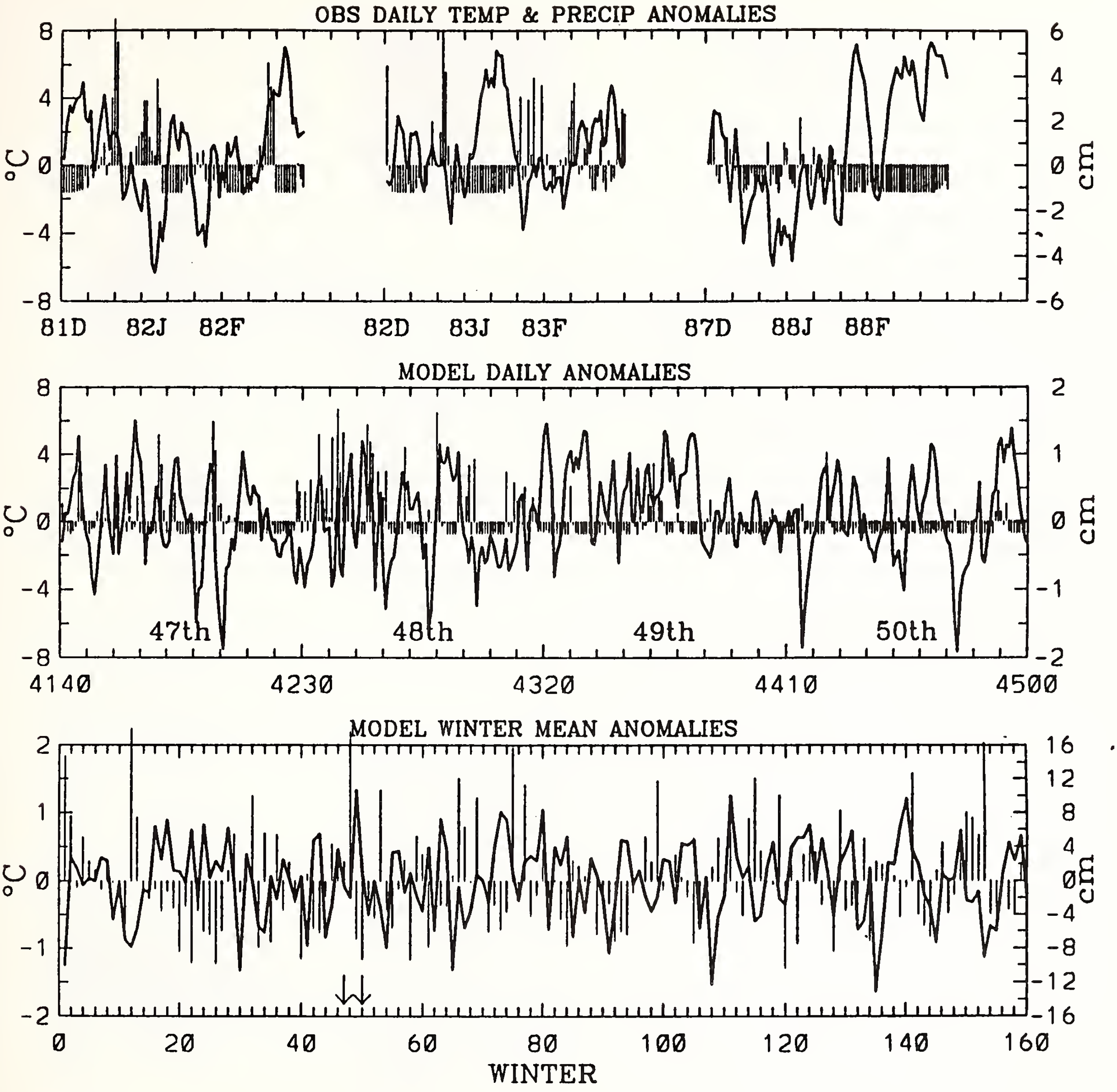

Figure 1. (a) Wintertime (DJF) daily temperature (solid curves) and precipitation anomalies near the central Sierra and the American river basin. The temperature anomalies are in degrees Celsius and daily accumulated precipitation anomaly are in centimeters. (b) Same as (a) except for model day 4140 through 4500. (c) Same as (b) except model winter-mean anomalies for the first 160 winters are shown. Precipitation anomalies in centimeters refer to the 90 days accumulated rainfall anomalies. Two downward arrows mark the model's 47th through 50th winters; the daily sequences for these winters are shown in (b).

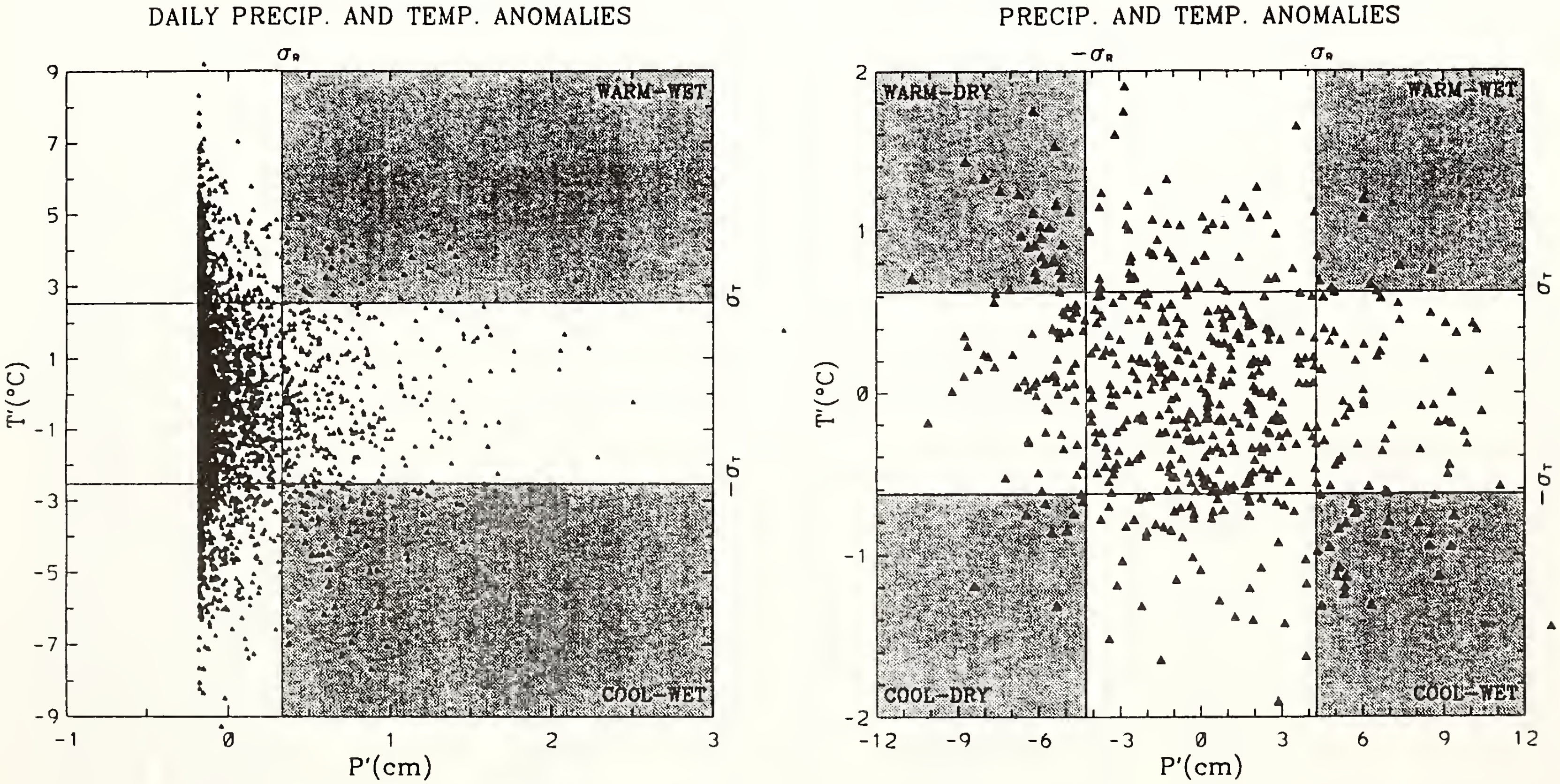

Figure 2. (a) Scatter diagram of daily temperature and precipitation anomalies from 4829 simulation days. The standard deviations of temperature, $\sigma_T$, and precipitation, $\sigma_R$, divide the parameter space into two extremes, warm-wet and cool-wet, which are shaded. (b) Same as (a) except winter-mean anomalies for 544 simulated winters are shown. The parameter space is divided into four extremes (warm-wet, warm-dry, cool-wet and cool-dry winters) by $\pm\sigma_T$ and $\pm\sigma_R$.

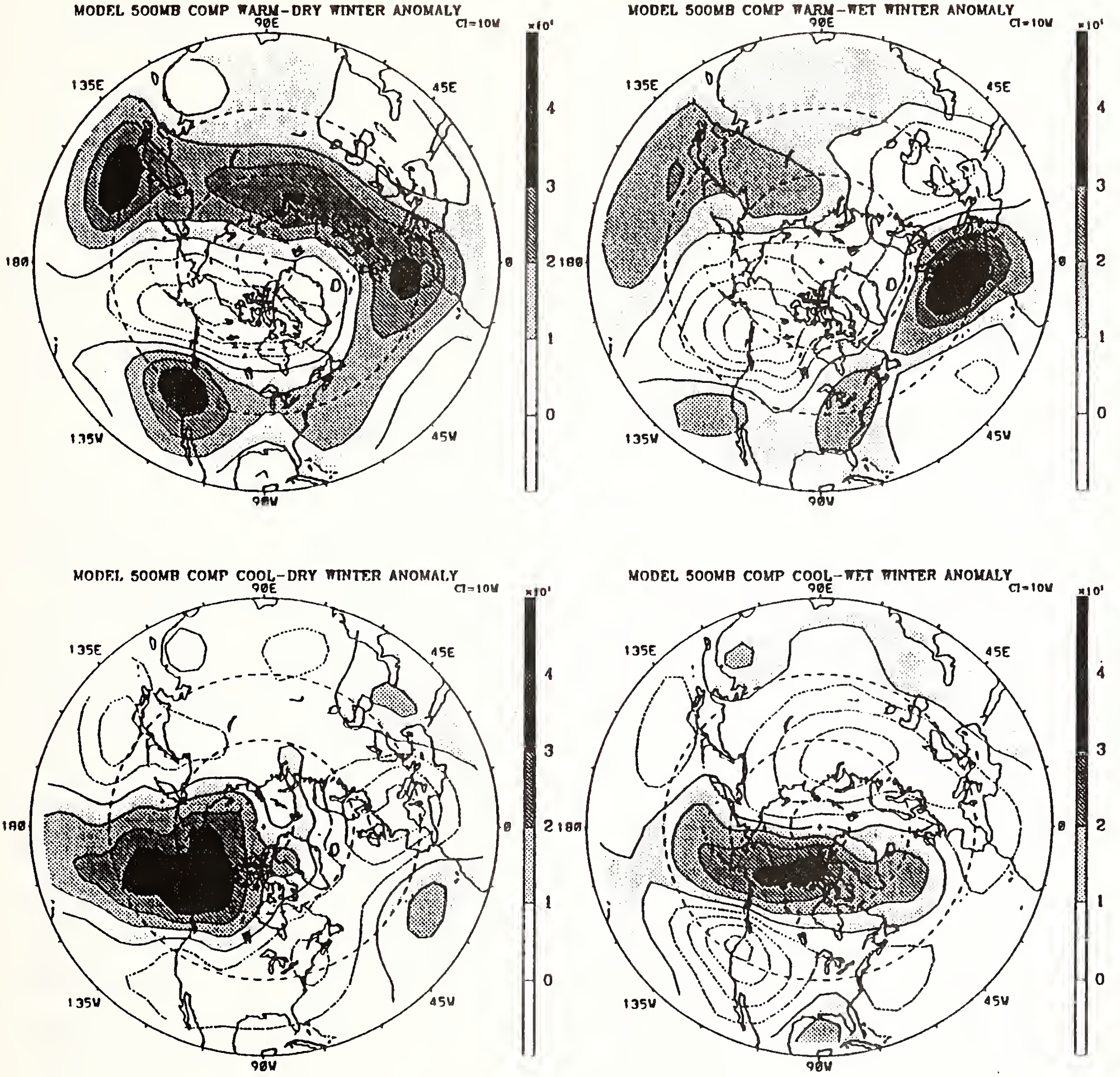
MODEL 500MB COMP WARM-DRY WINTER ANOMALY
MODEL 500MB COMP WARM-WET WINTER ANOMALY
MODEL 500MB COMP COOL-DRY WINTER ANOMALY
MODEL 500MB COMP COOL-WET WINTER ANOMALY
CI=10M
x10¹
90E
135E
45E
180
0
135W
45W
90W
4
3
2
1
0

Figure 3. Composite 500 mb height anomalies for winter-mean extremes, warm-dry (upper left), warm-wet (upper right), cool-dry (lower left) and cool-wet (lower right). The contour interval is 10 meter and positive values are shaded.

# A MODEL OF THE GLOBAL HYDROLOGIC CYCLE

*J. O. Roads*[1], *S.-C. Chen*[1]
*J. Kao*[2], *D. Langley*[2], *G. Glatzmaier*[2]

1. Scripps Institution of Oceanography
University of California, San Diego, 0224
La Jolla, CA 92093

2. Los Alamos National Laboratory
Los Alamos, NM

## 1. INTRODUCTION

We describe briefly how well general circulation models (GCMs) can simulate relevant aspects of the global hydrologic cycle. In particular, we determine how well we can model the annual and seasonal mean global precipitation, evaporation and atmospheric water vapor transport. Seasonal variations are about the largest short term climate variation that we can easily observe. If we can globally model these large amplitude variations correctly, then we will have greater confidence in our ability to globally model and predict the more subtle variations associated with forced and natural interannual variability.

A prototypical model of the global hydrologic cycle is the Los Alamos GCM (see Kao *et al.*, 1990) which is a derivative of the original National Center for Atmospheric Research (NCAR) GCM. We compare aspects of the hydrologic cycle in a 10 year simulation with this GCM to global observations. Global observations of the water vapor, water-vapor flux and water-vapor flux divergence are derived from the National Meteorological Center's final analysis for the period 1986-1990. The new precipitation data set of Legates and Willmott (1990) is used for the global precipitation observations. Global evaporation is derived as a residual of the precipitation and water-vapor flux divergence.

All of the available observations can potentially have non-negligible errors. We therefore find that the GCM output reciprocally aids in our understanding of the observed hydrologic cycle.

## 2. RESULTS

The most noticeable discrepancy between the GCM and observations is in the moisture field itself, which is too small because of a cold bias (see Fig. 1). This cold bias is smallest in the lower troposphere. However, the dry bias is spread more evenly throughout the troposphere, because of the exponential variation of moisture with temperature. Moreover, the dry bias is really only noticeable in the rotational fluxes (see Fig. 2). The divergent moisture fluxes (see Fig. 3) are only slightly larger for the slightly more intense GCM hydrologic cycle. Thus, we are almost certain that the GCM dry bias does not have a large impact on the perceived global atmospheric hydrology. Still, we are concerned about a misplaced South Pacific convergence zone (SPCZ) over Australia; also nearby is the Indonesian archipelago that has some of the largest values for precipitable water and precipitation in the world. If values in this region are incorrect, then these errors may have had wide ramifications elsewhere and may be related to the misplaced SPCZ in the GCM. Therefore, it is possible that correction of this GCM dry bias will result in substantial improvements in the GCM's hydrologic cycle here and elsewhere. We are also concerned about the misplaced summertime (see Fig. 4) precipitation over the U.S. In essence, both large and small scale errors probably need to be corrected so that we can have the utmost confidence in the ability of this GCM to globally simulate interannual variability.

Overall, though, the comparisons between the LANL GCM and available observations are quite good. Most of the large-scale features, as described by the moisture flux streamfunction, moisture flux potential, precipitation potential, and evaporation potential are really quite close. Seasonal cycle variations are quite reasonable. Even smaller scale features, such as the moisture flux convergence, precipitation, and evaporation, are well simulated. We are, in fact, quite pleased with most of the simulation. Certain aspects of the simulation may therefore be studied further to determine characteristics of the global interannual variability; interannual variations are much more difficult to examine with the presently incomplete observations.

Further details of this study can be found in Roads *et al.* (1991).

## REFERENCES

Kao, C.-Y., G.A. Glatzmaier, and R.C. Malone, 1990: Global three-dimensional simulations of ozone depletion under postwar conditions. *J. Geophys. Res.*, **91**, 1039-1053.

Legates, D.R. and C.J. Willmott, 1990: Mean seasonal and spatial variability in gauge-corrected global precipitation. *Inter J. Climatology*, **10**, 111-127.

Roads, J.O., S.-.Chen, J. Kao, D. Langley, and G. Glatzmaier, 1991: Global aspects of the Los Alamos general circulation model hydrologic cycle. *J. Geophys. Res.*, submitted.

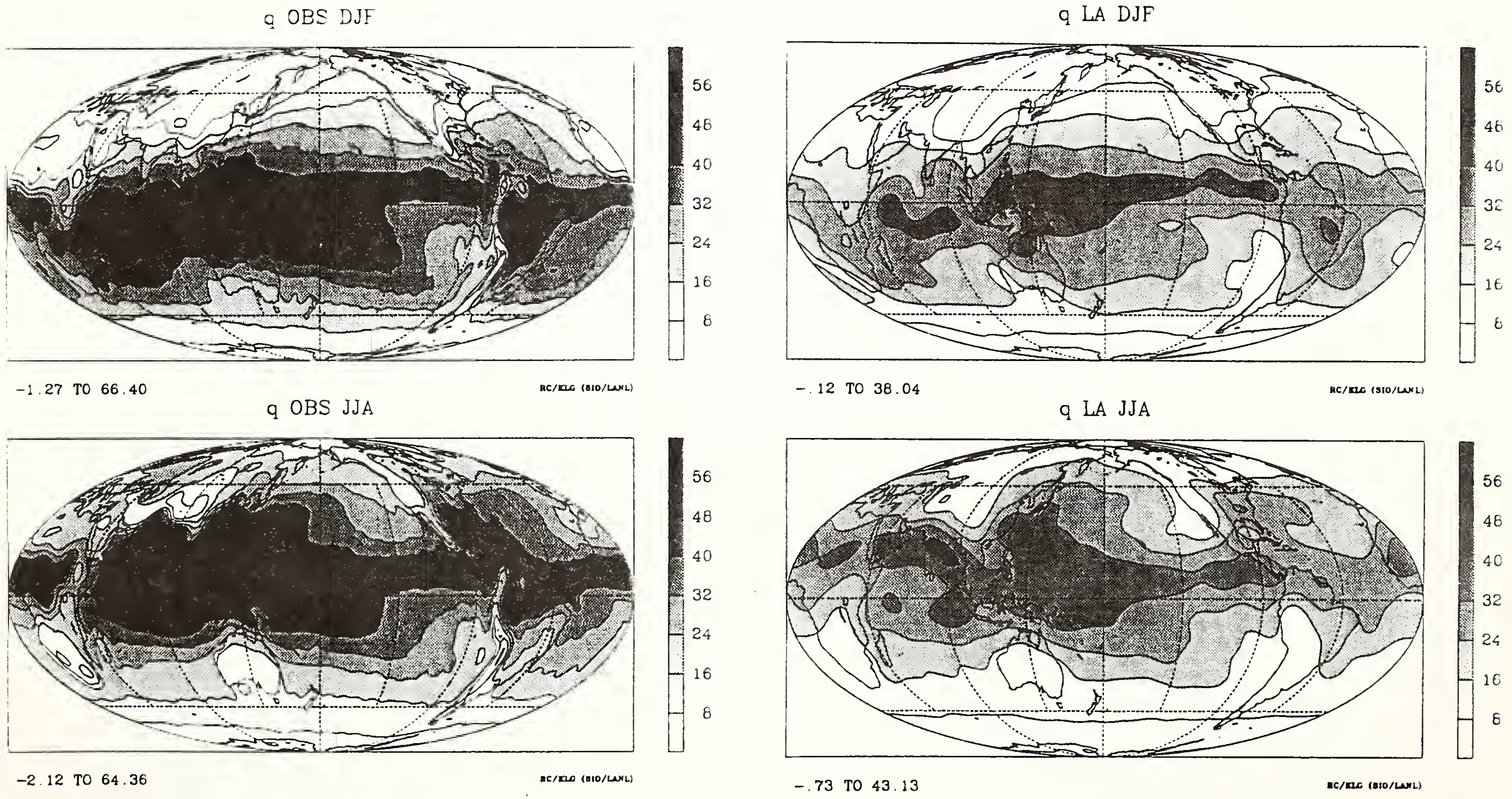

Figure 1

**Fig. 1 left panel.** The observed global precipitable water ($kg\ m^{-2}$) on a 2.5x2.5° grid during winter (upper panel) and summer (lower panel) for the period 01/01/87-12/31/89. Contour intervals are 8 $kg\ m^{-2}$. Winter is the December to February 3-month average and summer is the June to August 3-month average.

**Fig. 1 right panel.** Same as Fig. 1 left panel except the winter and summer averages for the 10 year LANL GCM simulation are shown.

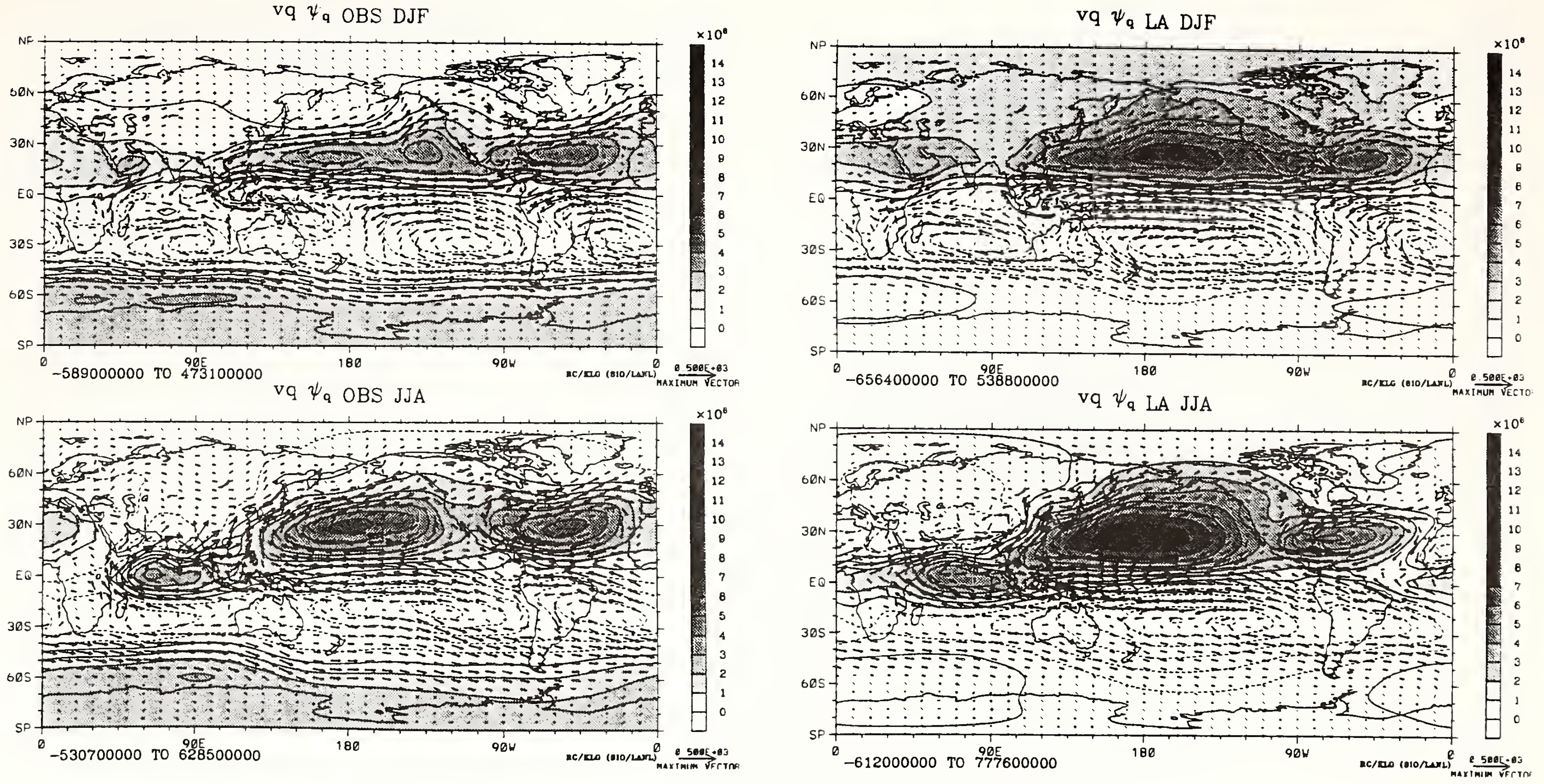

vq $\psi_q$ OBS DJF

vq $\psi_q$ OBS JJA

vq $\psi_q$ LA DJF

vq $\psi_q$ LA JJA

Figure 2

**Fig. 2 left panel.** The observed total moisture flux ($kg\ m^{-1}s^{-1}$) and streamfunction ($kg\ s^{-1}$) for winter (upper panel) and summer (lower panel). The arrow length corresponding to 500 $kg\ m^{-1}s^{-1}$ is shown in the lower right hand corner of each panel. The contour interval for the streamfunction is $10^8\ kg\ s^{-1}$.

**Fig. 2 right panel.** Same as Fig. 2 left panel except the winter and summer averages for the 10 year LANL GCM simulation are shown.

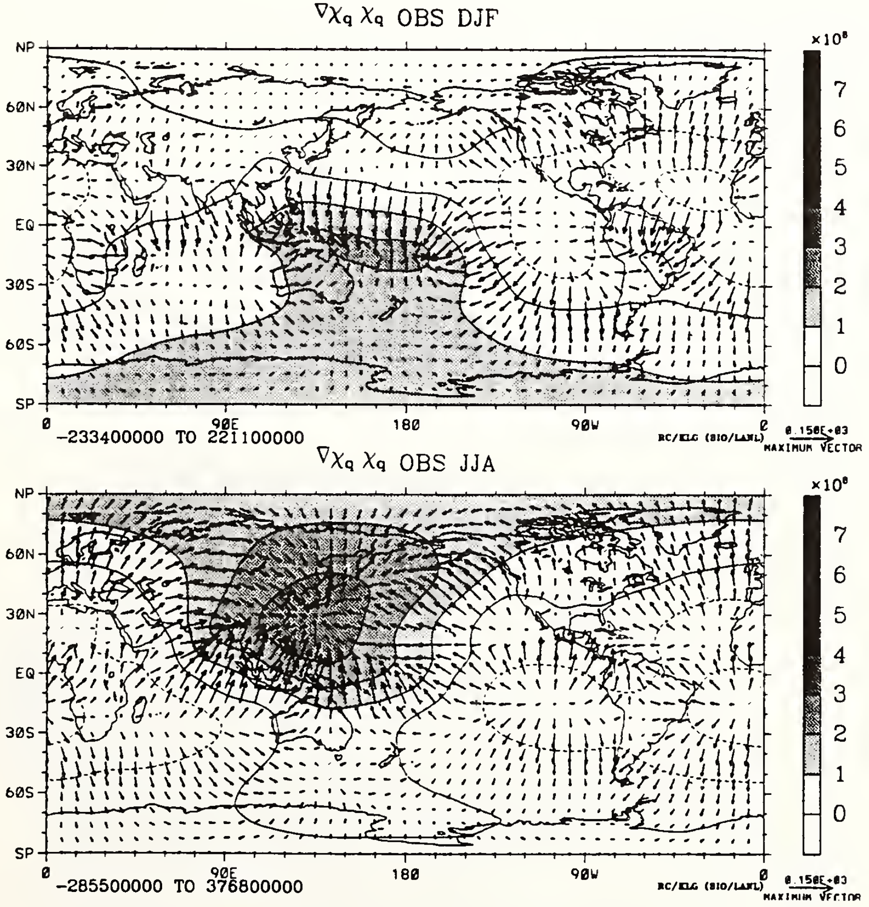

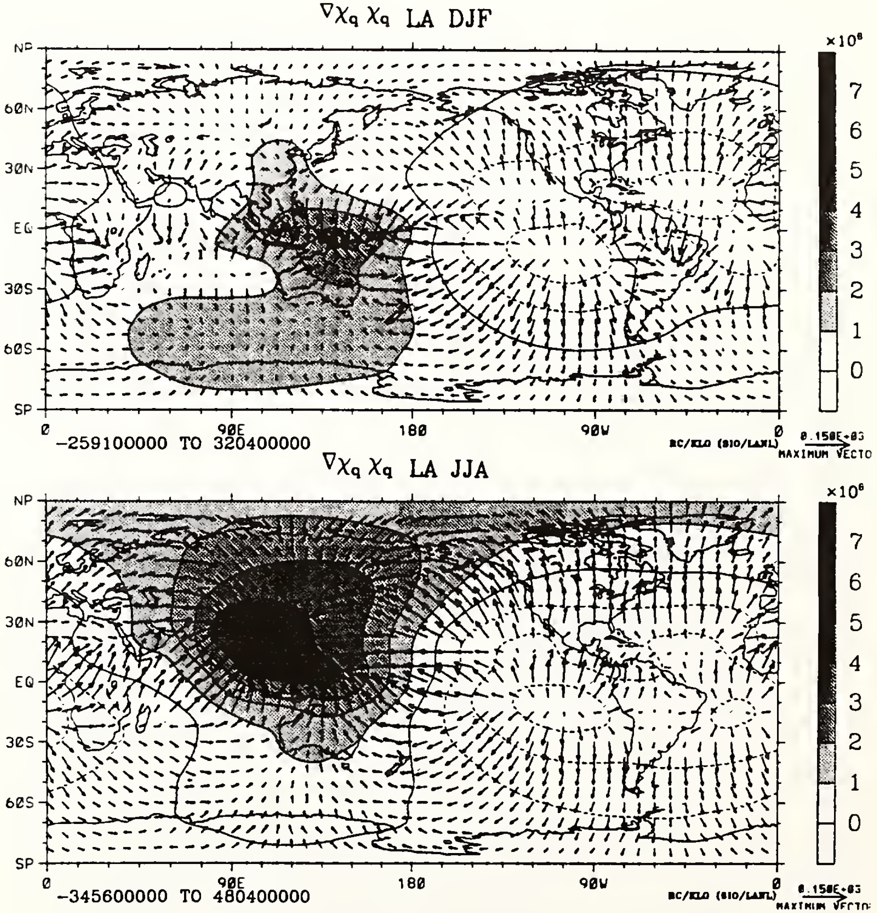

Figure 3

**Fig. 3 left panel.** The observed divergent component of the moisture flux ($kg\ m^{-1}s^{-1}$) and moisture flux potential ($kg\ s^{-1}$) for winter (upper panel) and summer (lower panel). The arrow length corresponding to 150 $kg\ m^{-1}s^{-1}$ is shown in the lower right hand corner of each panel. The contour interval for the potential is $1x10^8\ kg\ s^{-1}$.

**Fig. 3 right panel.** Same as Fig. 3 left panel except the winter and summer averages for the 10 year LANL GCM simulation are shown.

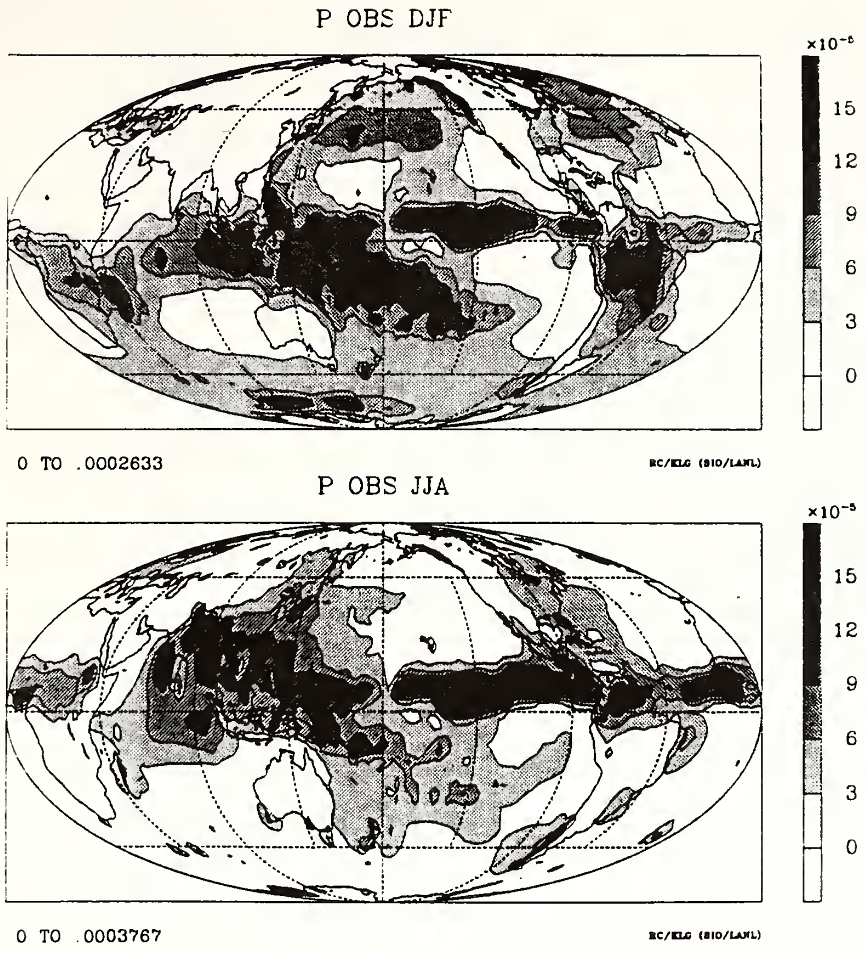

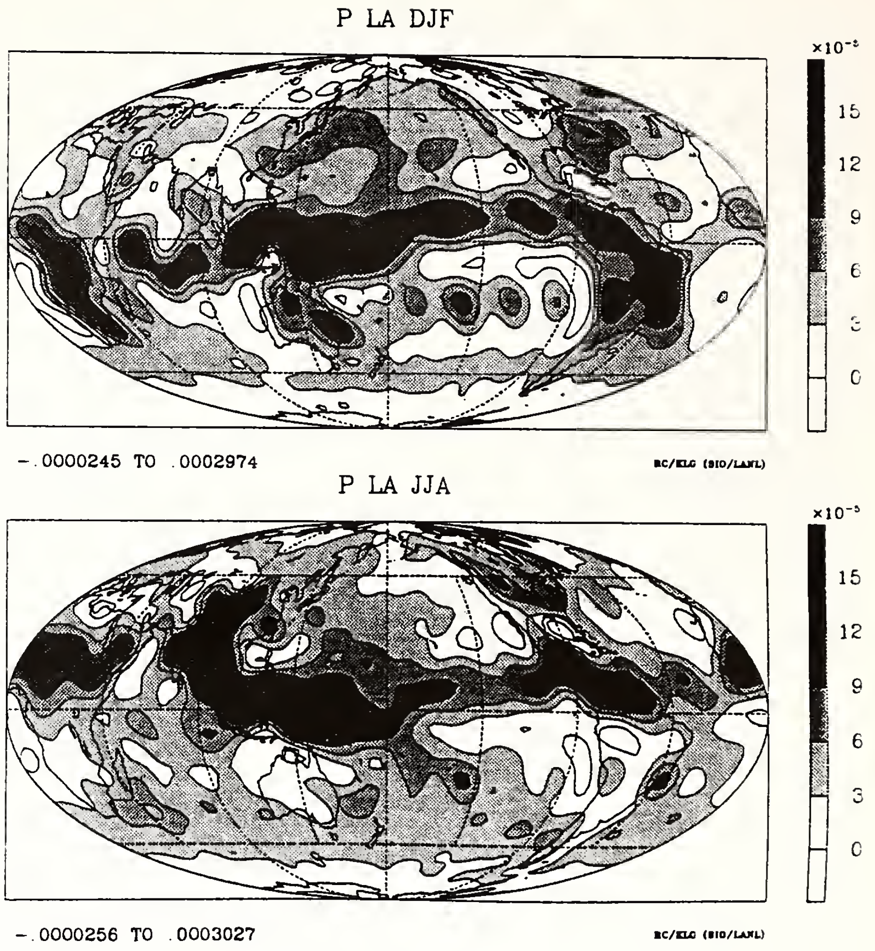

Figure 4

**Fig. 4 left panel** The observed corrected LW precipitation ($kg\ m^{-2}s^{-1}$) for winter (upper panel) and summer (lower panel). The contour interval for the precipitation is $3x10^{-5}$ $kg\ m^{-2}s^{-1}$.

**Fig. 4 right panel.** Same as Fig. 4 left panel except the winter and summer averages for the 10 year LANL GCM simulation are shown.

# Diurnal Variations in Tropical Rainfall During 1986-90

John E. Janowiak
Climate Analysis Center, NMC, NWS, NOAA
Washington, D. C. 20233

The diurnal variation in tropical rainfall has been studied by numerous authors. Gray and Jacobson (1977) found strong early morning maxima in deep convection in the tropics using island station data. Augustine (1984) found evidence of a dual peak in tropical convection in much of the central and eastern tropical Pacific using IR data from satellite. Meisner and Arkin (1987) documented the diurnal cycle in precipitation in the Americas during 1982-84 while Gruber and Chen (1988) determined the diurnal variation in outgoing longwave radiation from the NOAA polar orbiting satellites for the entire globe (50°N-50°S). In each of these studies, either the spatial or temporal characteristics of the data were limiting factors in each analysis. This paper describes an attempt to document the diurnal character of rainfall in the global tropics during the period 1986-90 using 3-hourly geostationary IR data that was collected for the Global Precipitation Climatology Project (Janowiak and Arkin, 1988).

Infrared data from the GOES, GMS, and Meteosat geostationary satellites were used in this study. The combined data from these satellites yields near global coverage - no data were available for the region between about 50°-90°E (Indian Ocean). The data are in the form of 5-day accumulations of 16-class histograms of infrared "brightness temperatures" for 2.5° latitude/longitude grids. Although the data were accumulated over pentads, the data for the individual observation times (00 UTC, 03 UTC, etc.) were saved separately, so that the diurnal character of these data were preserved.

In this study, the occurance of rainfall was defined on the basis of a brightness temperature threshold. Initially, a threshold of 235K was used which means that the analysis to determine the diurnal variation of rainfall was based on the fractional coverage of "pixels" colder that 235K in a 2.5° lat/lon grid. However, some studies indicate that the daily maxima in intense convection is in the early morning (local time) in the tropical Pacific (Gray and Jacobson (1977) and Fu et al. (1990), so the analysis was repeated using a 220K threshold.

Figure 1 shows the mean spatial pattern of grids with various fractional coverages of precipitating pixels for December-February (1986-90) as defined by the 235K and 220K brightness temperature thresholds described above. In essence, the isolines in the figures demark the frequency of deep convection. The ITCZ in both the Atlantic and Pacific, the SPCZ and the convection in the continents in the Southern Hemisphere are readily seen from these figures. A noteworthy observation is that the diurnal variance of rainfall (Fig. 2) is much greater over land than over water for the same amount of convection, as pointed out by Meisner and Arkin (1987). This is apparent when comparing the amount of convection (Fig. 1) with the diurnal variation in the convection (Fig. 2) between the South American continent and the SPCZ, for instance.

An harmonic analysis on the fractional coverage of cloud below the 235K and 220K thresholds was performed on the seasonal mean data. The results for the December-February (DJF) season are shown in Figures 3 and 4. Figure 3, which shows the results for the 235K threshold, indicates a predominance of the first harmonic over most regions, with a preferred time of between 1800 and 2100 local time for rainfall maxima. The amplitudes of the first harmonic are also noticably stronger over land areas. Over the oceans, the preferred time of maxima appears to be near local noon, in general. Although only results for the DJF season are shown, it appears that the times of maxima are more spatially uniform in the summer hemisphere.

Another interesting result, which is consistent with the work of Gray and Jacobson (1977) and Fu et al. (1990), is that the preferred time for more intense convection is earlier in the day, as witnessed by the results of an harmonic analysis that was performed on the 220K threshold data (Fig. 4). In particular, note that the maxima in the near equatorial oceanic regions is anout local noon for the 235K threshold and about 0600 local time for the 220K threshold.

The result that intense convection, as defined by a 220K brightness temperature threshold, appears to peak about 6 hours earlier than convection defined by a 235K threshold has prompted thought of further analysis. It is now planned to do similar investigations using thresholds below 220K to determine if the diurnal peak in intense convection is even earlier in the day.

## REFERENCES

Augustine, J. A., 1984: The diurnal variation of large-scale inferred rainfall over the tropical Pacific Ocean during 1979. Mon. Wea. Rev., 112, 1745-1751.

Fu, R., A. D. Del Genio, and W. B. Rossow, 1990: Behavior of deep convective clouds in the tropical Pacific from ISCCP radiances. J. Climate, 3, 1129-1152.

Gray, W. M, and R. W. Jacobson, 1977: Diurnal variation of deep cumulus convection. Mon. Wea. Rev., 105, 1171-1188.

Gruber, A. and T. S. Chen, 1988: Diurnal variation of outgoing longwave radiation. J. Climatology, 8, 1-16.

Janowiak, J. E. and. P. A. Arkin, 1988: The Global Precipitation Climatology Project: description, goals, and progress. Proceedings of the 13th Annual Climate Diagnostics Workshop, Cambridge, MA, October 31 - November 4, 1988. NTIS PB89-178115AS, Natl. Tech. Inf. Serv.

Meisner, B.N. and P. A. Arkin, 1987: Spatial and annual variations in the diurnal cycle of large-scale tropical convective cloudiness and precipitation. Mon. Wea. Rev., 115, 2009-2032.

## Figure Captions

Figure 1. Seasonal mean fractional coverage of cloud < 235K (top) and < 220K (bottom) for DJF (1986-90).

Figure 2. 1st Harmonic (top) and 2nd harmonic (bottom) of fractional coverage of cloud colder than 235K for DJF (1986-90). Vectors are plotted if the harmonic explains > 50% of the variance. For 1st harmonic, vectors pointing "north" imply time of maximum at local noon; pointing "east" at 1800 local time, etc.. For 2nd harmonic, dual maxima are implied, 12 hours apart.

Figure 3. Same as Fig. 2, except for 220K threshold.

DJF (1986-90) Mean % Coverage of Cloud < 235K

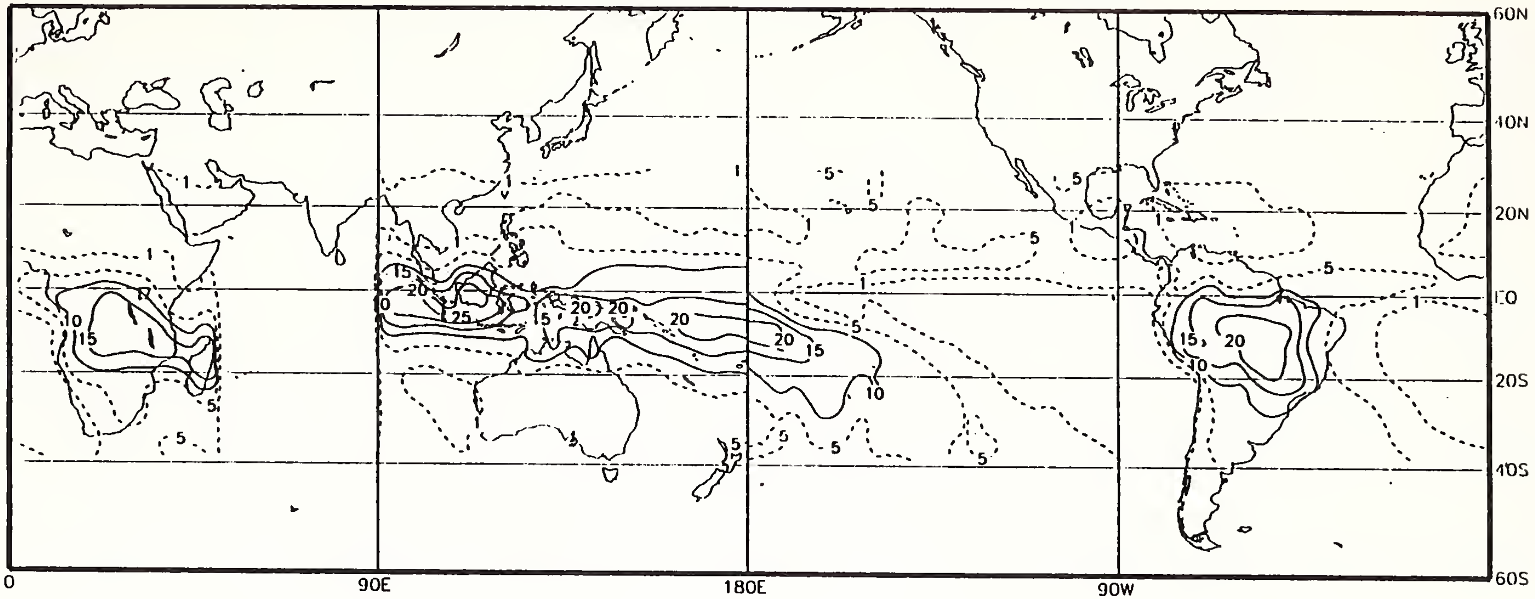

DJF (1986-90) Mean % Coverage of Cloud < 220K

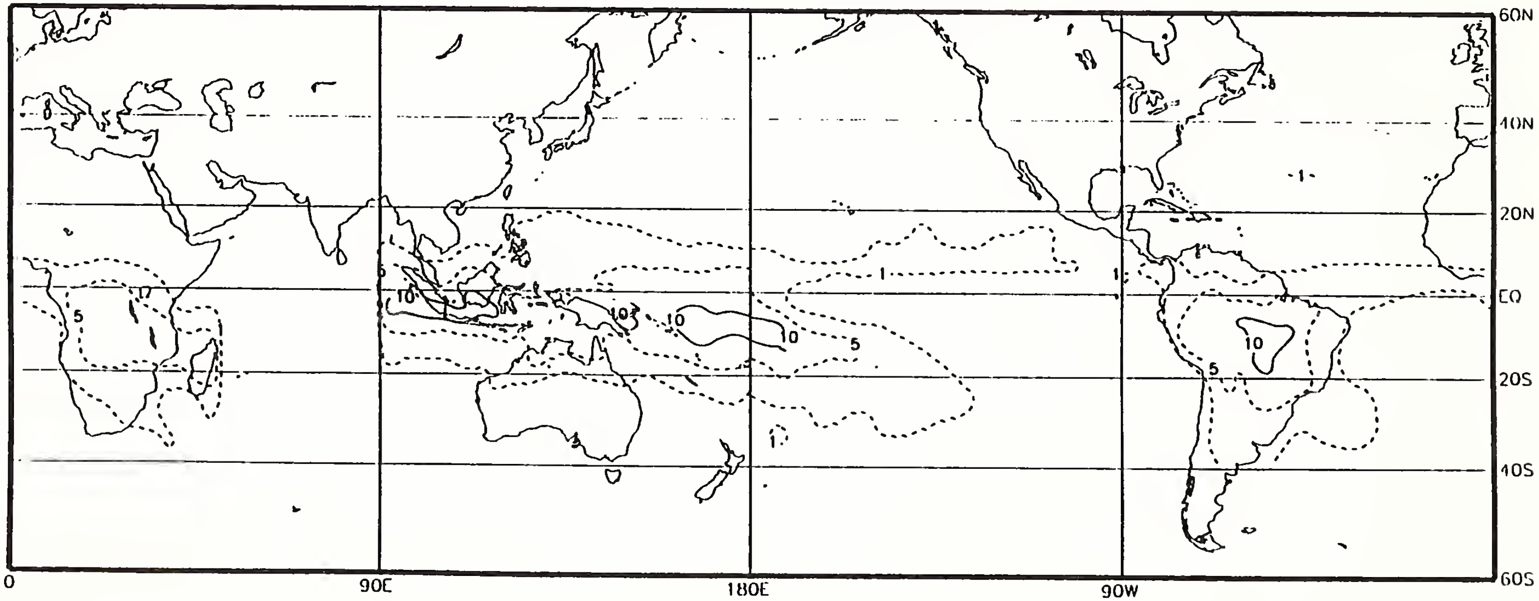

1st (top) & 2nd (bot) Harmonics of DJF (1986–90) Mean 3–hr Coverage of Cloud < 235 K
(up Arrow is local noon maximum: right is 1800 LST max)

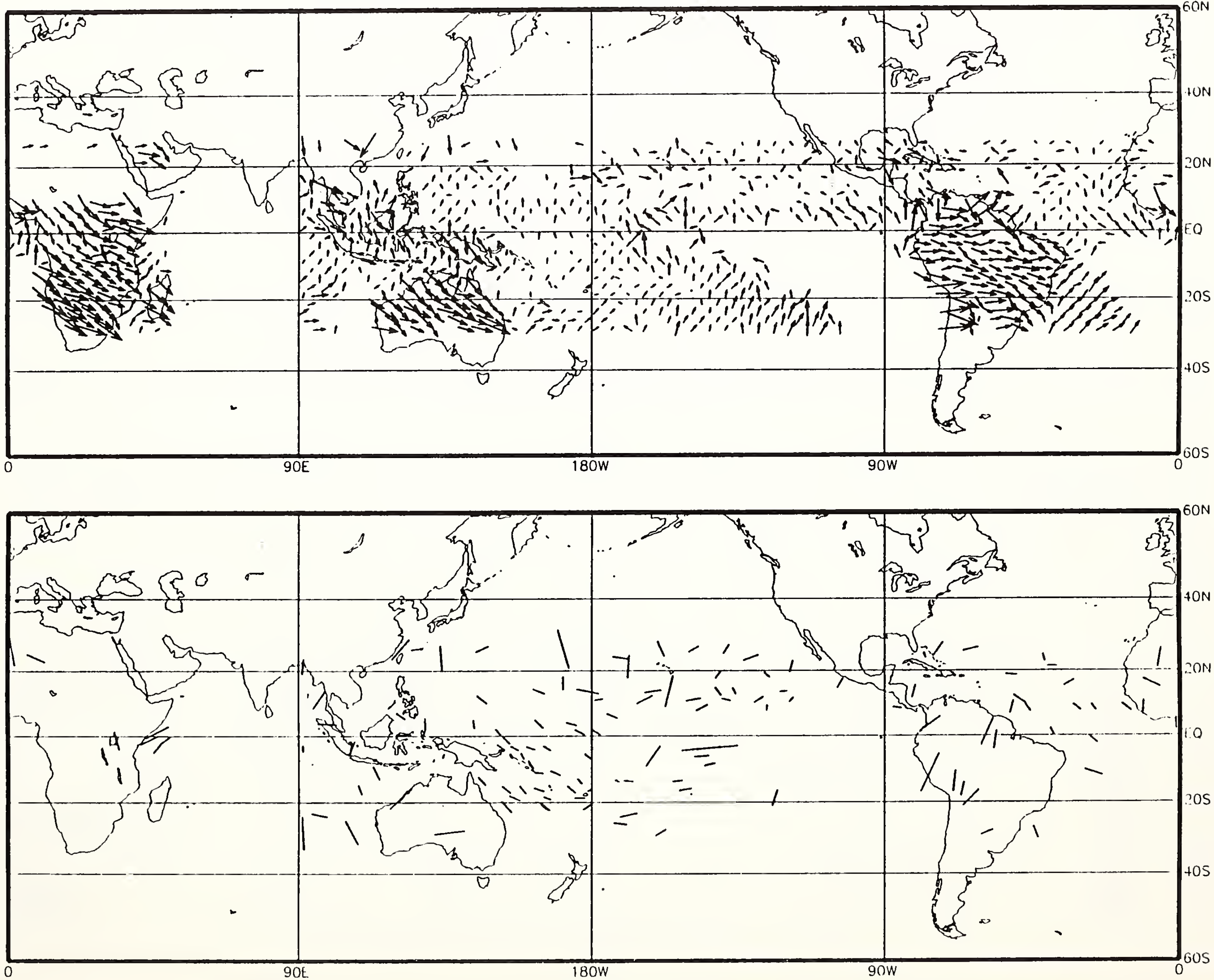

1st (top) & 2nd (bot) Harmonics of DJF (1986–90) Mean 3–hr Coverage of Cloud < 220 K
(up Arrow is local noon maximum: right is 1800 LST max)

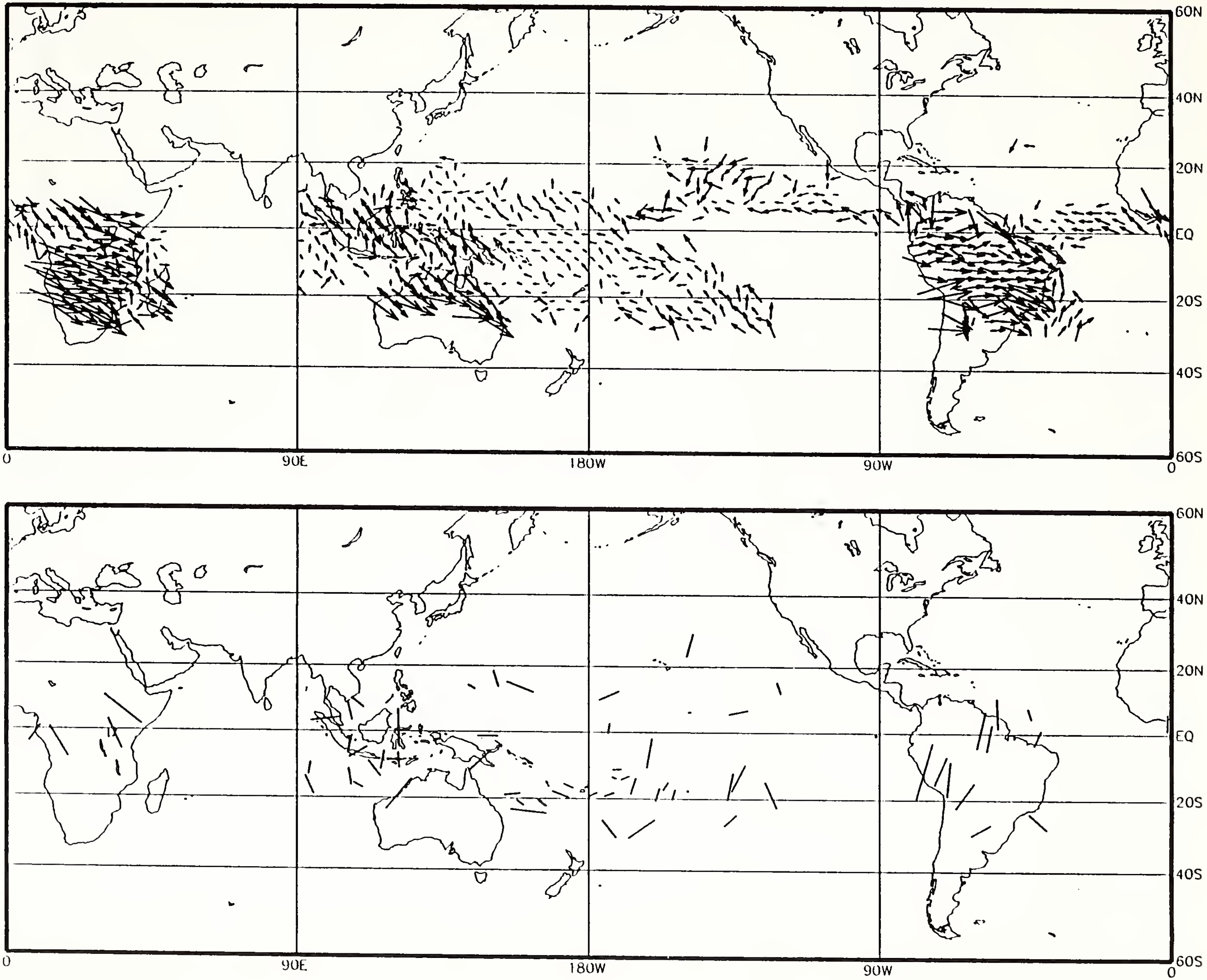

# ANALYSIS OF SAHEL RAINFALL IN THE CONTEXT OF THE GLOBAL TROPICS

S. E. Nicholson and I. Palao
Florida State University
Department of Meteorology
Tallahassee, Florida 32306

Relatively dry conditions have prevailed in the Sahelian region of West Africa for nearly two decades (Fig. 1). A number of researchers have analyzed the casual mechanisms of droughts in the region and have arrived at vastly different conclusions concerning its relationship to such large-scale parameters as sea-surface temperatures, ENSO or the position or the ITCZ. An analysis of the various studies shows that they differ markedly with respect to the geographical region used to represent the Sahel, the station network, and the months or the years utilized in the analysis. In particular, many studies are biased towards the western part of the region. This may account for some to the discrepancies between the results of various investigators.

We have systematically examined the effect of some of these differences by separately analyzing various parts of the broad region termed the Sahel and both the June-July and August-September periods. The rationale for the latter distinction is prior work that suggested that while both contribute significantly to mean annual rainfall, it is changes in the latter two-month period which generally account for the drought deficits. We have also distinguished between high and low frequency variations on the premise that one set of factors might produce the long downward trend observed since about 1950 while another set is responsible for the relatively large fluctuations within the long wet and dry episodes (Fig. 1). However, the results of this portion of the study are not discussed here.

The approach we have taken is to identify some of the major characteristics of rainfall variability in the region as a whole and to determine to what extent they are applicable to rainfall time series for the individual regions shown in Fig. 2 and to the June-June and August-September periods. Then, the relationships to ENSO and SSTs are similarly compared for the various regions and two-month periods. The relevant characteristics are illustrated in Figs. 1 and 3. The first three (Fig. 1) are related: the long-term trend since the 1950s, the high proportion of low frequency variance in the time series and the interannual persistence, i.e. the tendency for long sequences of years with rainfall continually above - or below - the mean. These are quantified using linear regression, spectral analysis and lag 1 autocorrelation coefficients, respectively. A fourth characteristic is the large spatial coherence, i.e., the large spatial scale of the major rainfall anomaly patterns in the region. This characteristic, which is illustrated by the anomaly patterns for 1983 and for the

*Editor's Note: Refer back to article on pp. 185 for figures 1-4 which are mentioned in the text above.*

decade 1980 to 1989 (Fig. 3), is the rationale for investigators to evaluate the region as a whole. The spatial coherence is quantified for the June-July and August-September periods using the interregional correlations within the analysis sector (Fig. 2).

Fig. 4 shows the percent variance, for annual rainfall, which is on time scales greater than 7 years.. In most of the regions that are broadly classed as Sahel (9 to 11, 13 to 16, 18 to 21) this is about or in excess of 50%. Exceptions are the western region 13 and the northeastern region 11. The contribution falls to around 25% south of the Sahel. The downward (Fig. 5) trends are also most pronounced in those regions with large variance at greater than 7 years. Moreover, the trends are apparent only in August-September, not in the rainfall series for June-July. Likewise, interannual persistence (Fig. 6) is generally highest in the areas with much low frequency variance in annual rainfall and it is almost exclusively limited to the August-September period.

Fig. 7 shows the correlation between each region of the analysis sector (Fig. 2) and several base regions (two in the extreme west, a four-region composite in the central Sahel, and the Guinea Coast). Two features are evident. First, the correlations with region 13 and with the Guinea Coast are relatively small and spatially limited. Secondly, the interrgional correlations are much higher in August-September than in June-July. Thus, the August-September period is not only the principal contributor to the rainfall decline, but it also accounts for the relatively high spatial coherence of the major rainfall anomalies.

Figs. 8 and 9 show the various relationships to ENSO and SSTs in individual sectors of the Atlantic and Indian Oceans. In the ENSO year (Fig. 8), the only areas which show a preference for higher or lower rainfall are the northwestern Sahel (region 13) and the Guinea Coast. Surprisingly, the effect in June-July (preferentially wet) is opposite that for August-September (preferentially dry). The corresponds to a net effect of zero on annual rainfall in the NW Sahel. In the June-July period (Fig. 9) strong correlations between SSTs and rainfall are apparent only for the Guinea Coast. For August-September, they are strongest for the NW Sahel, strong for the western region 18, but relatively weak for the central Sahel. In general, correlations with Sahel rainfall are as high or higher for the Indian Ocean as for the Atlantic, and they are universally negative.

These results suggest two major conclusions. First, the region's drought and general characteristics of rainfall variability are accounted for primarly by the August-September season. Secondly, the characteristics of rainfall variability and the relationship to tropical phenomena like ENSO or SST fluctuations are markedly different for the far western Sahel than for the central core of the region. .

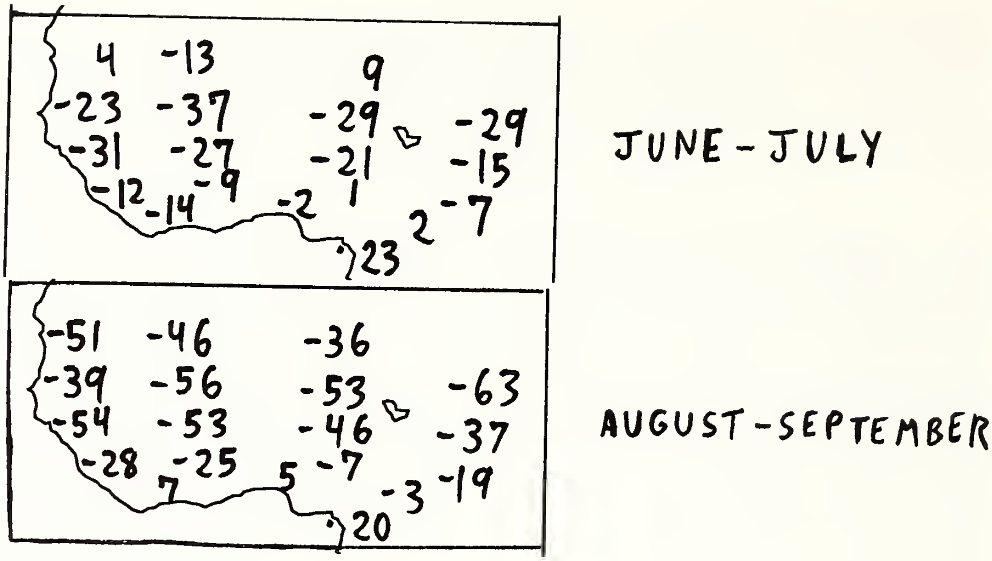

5. Slope of the rainfall regression line for the period 1950 to 1985, using standardized units for direct comparison of June-July and August-September (slopes exceeding .20 are significant at the 5% level).

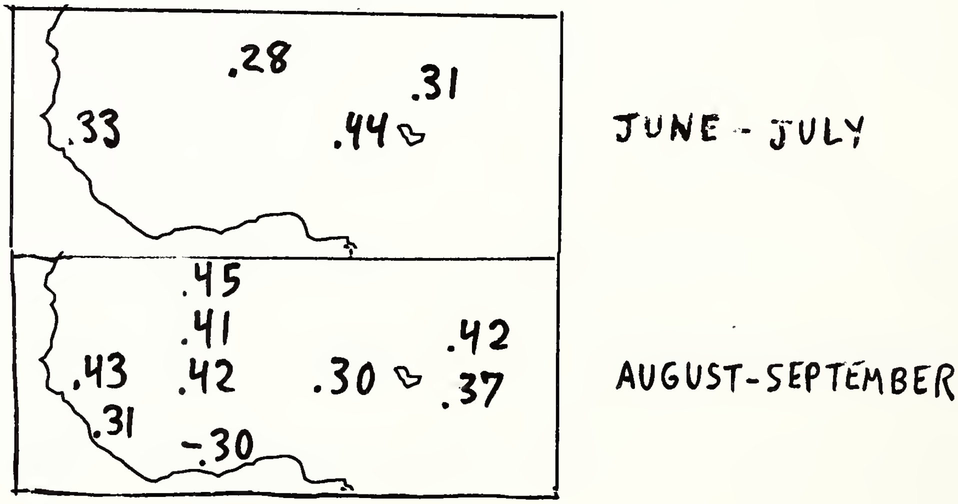

6. Lag 1 correlation between seasonal rainfall in consecutive years, for the "seasons" June-July and August-September (only those significant at the 5% level are plotted).

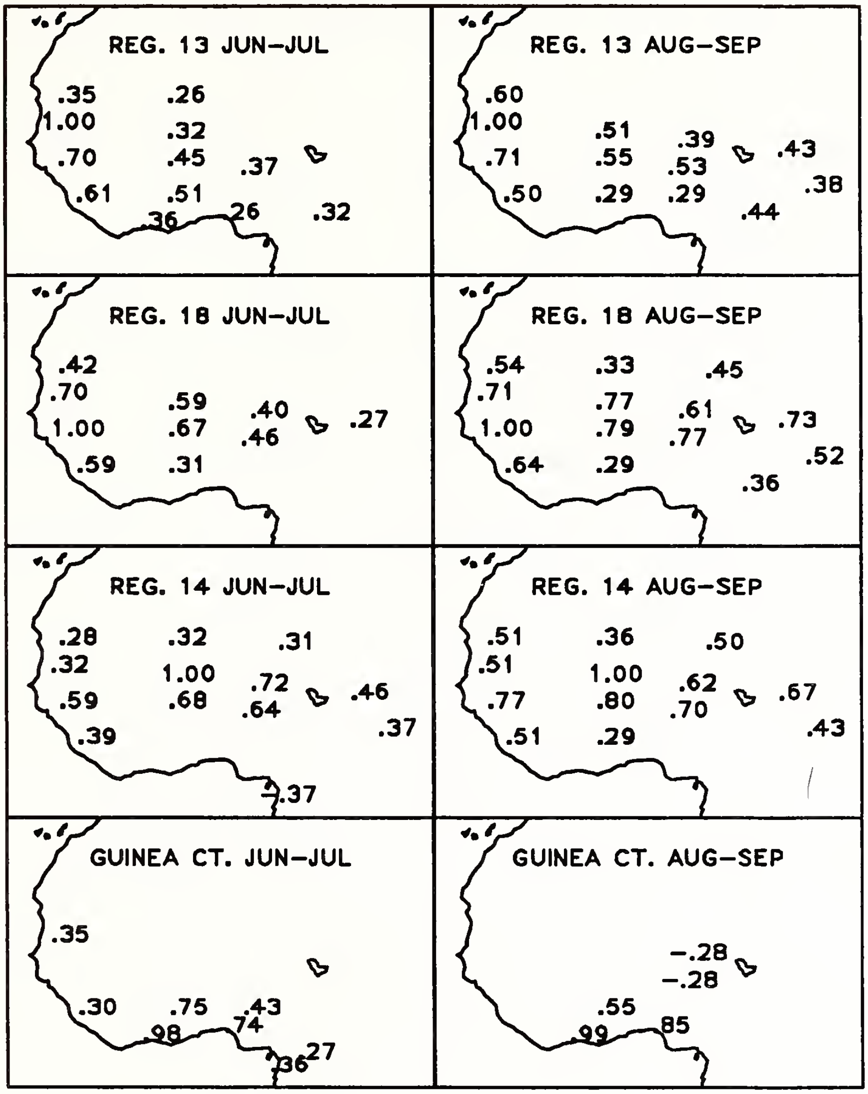

7. Interregional rainfall correlation using the indicated base regions (see Fig. 2) and time periods.

JUNE - JULY AUGUST- SEPTEMBER

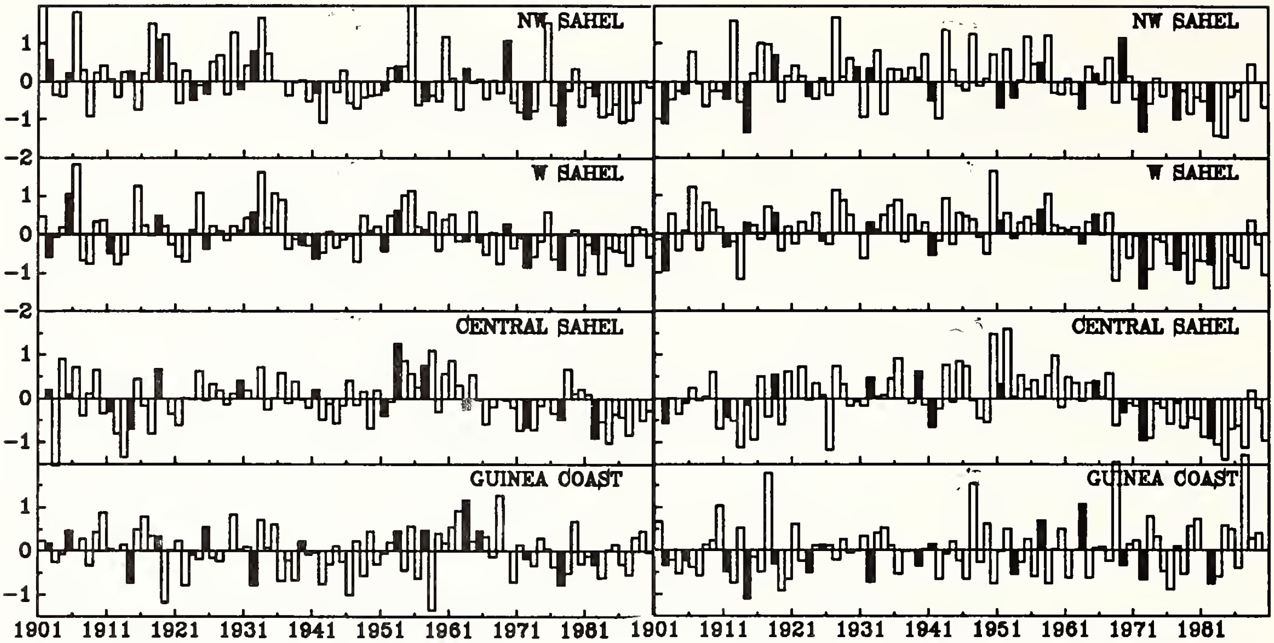

ANNUAL

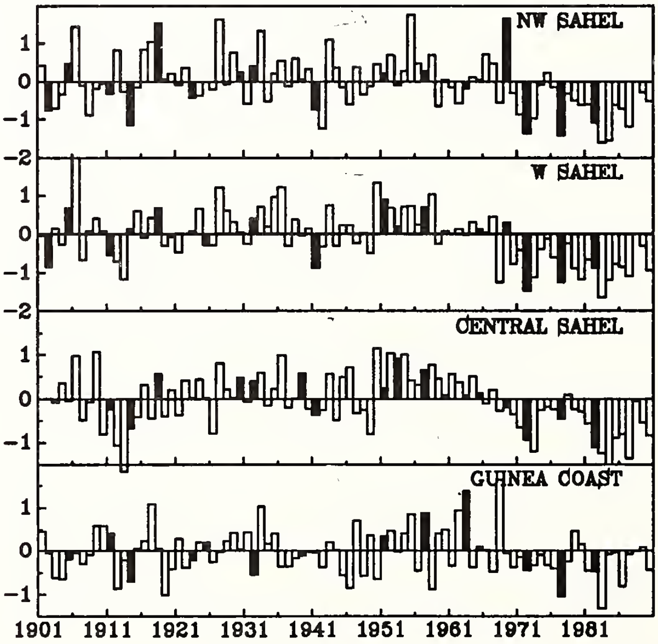

8. Rainfall time series for key regions, expressed as in Fig. 1, with ENSO years shaded (top: June-July, August-September; bottom; annual).

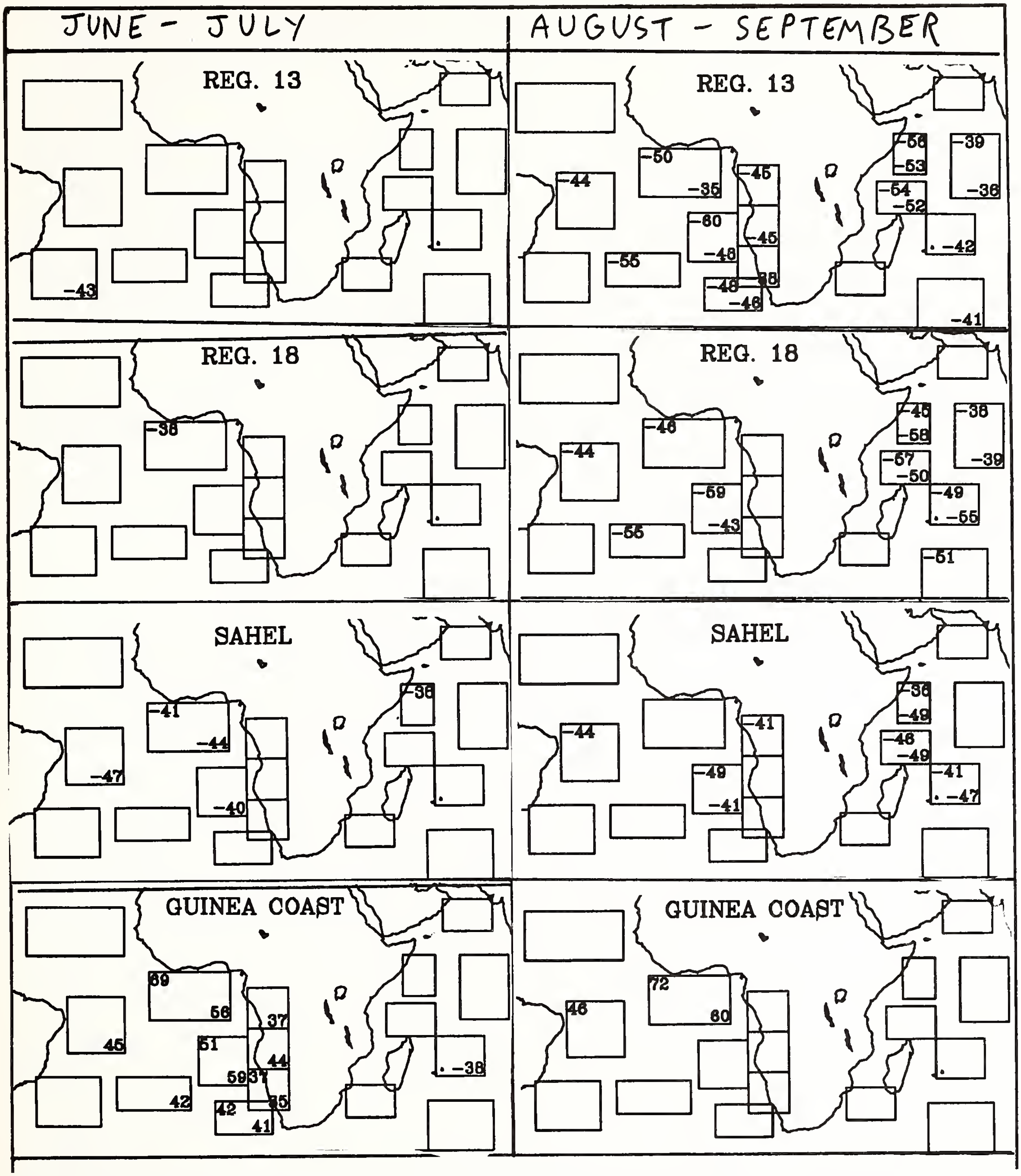

9. Correlation between SSTs in the indicated sectors and rainfall for several West African regions (see Fig. 2 for location). Upper number indicates correlation with concurrent SSTs; lower number, with SSTs in the previous two-month period. Only correlations significant at the 5% level are plotted. "Sahel" consists of regions 14, 15, 19 and 20; "Guinea Coast", regions 28 and 29.

# SURFACE TEMPERATURE and PRECIPITATION PATTERNS DURING THE 1980'S

C. F. Ropelewski and M. S. Halpert
Climate Analysis Center/NMC, NWS/NOAA, Washington, D.C. 20233

## 1. INTRODUCTION

Estimates of global surface temperature based on meteorological data indicate that the decade of the 1980's has been the warmest such period in the instrumental record. Much less attention has been focused on the patterns of the temperature anomalies during this period even though the most simple analyses readily show that the temperature anomalies are not uniform in magnitude or sign over the globe, Ropelewski et al, 1992. In this paper we provide a more complete description of the patterns of global temperature anomalies during 1980's and present some preliminary analyses to relate these anomaly patterns to decadal mean precipitation anomalies.

## 2. DATA

Monthly surface temperature and precipitation data for the period 1950 to 1990 were obtained from the Climate Anomaly Monitoring System (CAMS) data base, Ropelewski et al., 1985. Sea surface temperatures are taken from the NMC/CAC operational analyses and compared to the COADS/ICE climatology, Reynolds, 1988. Monthly snow cover data for the period 1973 to 1990 were derived from weekly operational analyses of satellite snow cover maps, Ropelewski, 1991.

## 3. DECADAL ANOMALY PATTERNS

### 3.1 Temperature

Analyses of global and hemispheric temperature anomaly time series indicate that the largest anomalies tend to occur in the Northern winter and spring and that the global signal is dominated by the Northern Hemisphere, Jones, (1988), Halpert and Ropelewski, (1991). Large differences are evident in the temperature anomaly patterns between the first and second half of the year, Fig. 1. The December - May period shows temperature anomalies greater than 1°C covering Alaska and western Canada and another large area with positive anomalies over Russia. Large negative anomalies were found over Greenland. In contrast, during the June - November season, small negative anomalies were found over Alaska and western Canada. suggesting a reduction in the amplitude of the annual cycle over this region during the past decade. Negative SST anomalies in the North Pacific and positive temperature anomalies in North America, for the December to May season, have been statistically associated with ENSO, Ropelewski and Halpert, (1986). However, preliminary examination of the December to May temperature anomalies for individual years during the 1980's indicates that the large positive temperture anomalies over northwestern North America were also present during the non-ENSO years of the 1980's.

In the Northern Hemisphere warm season (June to November) the decadal temperature anomaly patterns were less pronounced with the largest area of warm anomaly over Northern Africa and Southern Europe. At least a part of the African temperature anomaly pattern is likely a reflection of the decadal scale drought in the Sahel.

In the Southern Hemisphere, the largest positive temperature anomalies occurred during the warm (December-May) season expect for the Antarctic Peninsula. The largest areas of positive temperature anomalies occurred over in the sub-tropics in the Pacific and mid-latitudes in the Atlantic and Indian Oceans. The Pacific SST anomaly may be related to the Southern Oscillation.

In the Southern Hemisphere cold season (June to November) decadal temperature anomalies over Australia and southern Africa, as well as hemispheric SST anomaly patterns, were similar to the warm season patterns. The largest seasonal changes (December - May season versus June - November) over land areas occurred in South America, where negative anomalies larger the -1.0°C during the June - November were replaced by much smaller negative anomalies during December - May.

The magnitudes of decadal SST anomalies were generally small and positive, except in an area of the North Pacific and in the North Atlantic around Greenland. SST anomalies in all three Southern Ocean basins averaged above normal, with a substantial area of positive anomaly, greater than 0.5°C, in the eastern Pacific. This latter feature is most likely a reflection of the very large SST anomalies associated with the El Niño/Southern Oscillation (ENSO) event of 1982/83 and to some extent the 1986/87 ENSO.

### 3.2 Precipitation

Global precipitation anomalies are more difficult to characterize than temperature, to a large extent, because precipitation tends to have much more spatial structure. In addition, large regions of the globe experience a pronounced annual cycle in precipitation, with the majority, if not all, of the precipitation falling over part of the year. Analysis is presented for the Northern Hemisphere only since no precipitation data are readily available over water and the land areas represent such a small percentage of the Southern Hemisphere.

Precipitation anomalies are represented by percentiles of gamma distributions fit to the 1951 to 1980 data. The December through February season decadal analysis, Fig. 2, shows relatively dry areas for northern North America and northeastern Asia. The North American dry area is roughly coincident to the areas showing positive temperature anomalies during December to May season and suggests an inverse relationship between winter precipitation (snowfall) and temperature in these regions. A similar relationship is suggested in the precipitation and temperature anomalies in central Eurasia. Further analysis suggests that snow cover-temperature relationships are strongest in the spring season over Eurasia (Fig. 3). The Eurasian precipitation percentile patterns are not particularly well related to the surface temperature patterns during winter.

The spring (March through May) precipitation analysis, Fig. 2, continues the winter pattern of above median precipitation over Northern Europe and below median to the south. The low amounts of winter and spring precipitation in southern Europe and northern Africa suggests that the median annual precipitation reflects a failure of the normal seasonal rains in the Mediterranean region. In North America, above median spring precipitation is evident in an area stretching from the Great Basin southward into Mexico. Dry spring conditions for the decade appear in the southeastern United States. Dry winter and spring areas in eastern Asia suggest even less than median precipitation in the 1980's during normally dry seasons.

The summer (June through August) precipitation analysis, Fig. 2, shows the drought conditions in the Sahel regions of western Africa. Decadal summer rainfall in the Sahel was below the 30th percentile over a wide area. Generally speaking, precipitation of less than the 30th percentile for one rainy season represents drought conditions. The low percentiles in the Sahel over a ten year period signify catastrophic shifts in the decadal precipitation pattern. The analysis also suggests that the area of precipitation deficiency extended well southward of the Sahel and into coastal regions of western Africa.

Below median summer precipitation for the decade is also evident in the area from northeastern China through Southeast Asia. Thus, of the major summer monsoon precipitation regions in the Northern Hemisphere, only India shows no significant decadal anomaly.

The dry conditions in Southeast Asia and the Sahel extended into the September through November season during the

1980's. This suggests that normal monsoon conditions were not, in general, alleviated by late season rains in these regions during the 1980's. Large portions of North America, including much of the United States, experienced above median fall precipitation during the decade. An exception was over the eastern United States, with "normal" conditions in an area from New England extending through the Middle Atlantic area and dry conditions in extreme southern Florida.

## 4. DISCUSSION

The preliminary analysis outlined here suggests that the Northern Hemisphere dominates the temperature record during the decade during the 1980's and that temperature anomalies in the first half of the year, December - May, in both hemispheres dominated the annual anomaly patterns. The Southern Oscillation has a clear effect on the global temperature patterns, but it does not explain all of the observed patterns or variations. Finally the prelimary analysis suggests that Northern Hemispheric surface temperature anomalies may be related to snow cover anomalies.

ACKNOWLEDGEMENTS: Thanks to M. Chelliah, D. Garrett, John Kopman, at the CAC. We also wish to thank P. L. Heinselman, Saint Louis University for her help with analysis of the snow cover data. This work was partially supported by the NOAA Climate and Global Change Program under the Global Climate Perspectives System Project.

## REFERENCES

Halpert, M. S., and C. F. Ropelewski [Eds.], 1991, Climate Assessment: A Decadal Review, 1981-1990. [U. S. Govt. Printing Office: 1991 - 281-557/40426, 109 pp.

Jones, P.D., 1988: Hemispheric surface air temperature variations: recent trends and an update to 1987. J. of Climate, **1**, 654-660.

Reynolds, R. W., 1988: A real-time global sea surface temperature analysis. J. of Clim., **1**, 75-86.

Ropelewski, C.F., M.S. Halpert, M. Chelliah, D. R. Garrett and P.L. Heinselman, 1992: Surface temperatue and precipitation patterns during the 1980's: Climate variability or climate change? Proc. of the 3rd AMS Climate Change Symposium, Jan 5-10, 1992, Atlanta, GA.

-------------------, 1991: Real-time climate monitoring of global snow cover. Palaeogeography, Palaeoclimatology, Palaeoecology (Global and Planetary Change Section), Elsevier Science Publishers , 222-229

-------------- and M.S. Halpert, 1986: North American precipitation and temperature patterns associated with the El Niño/Southern Oscillation (ENSO). Mon. Wea. Rev., **114**, 2352-2362.

-----------------, J. E. Janowiak and M.S. Halpert, 1985: The analysis and display of real time surface climate data. Mon. Wea. Rev., **113**, 1101-1106.

Vinnikov, K. Ya., Groisman, P. Ya and K. M.Lugina, 1990: Empirical data on contemporary global climate changes (temperature and precipitation), J. of Climate, **3**, 662-677.

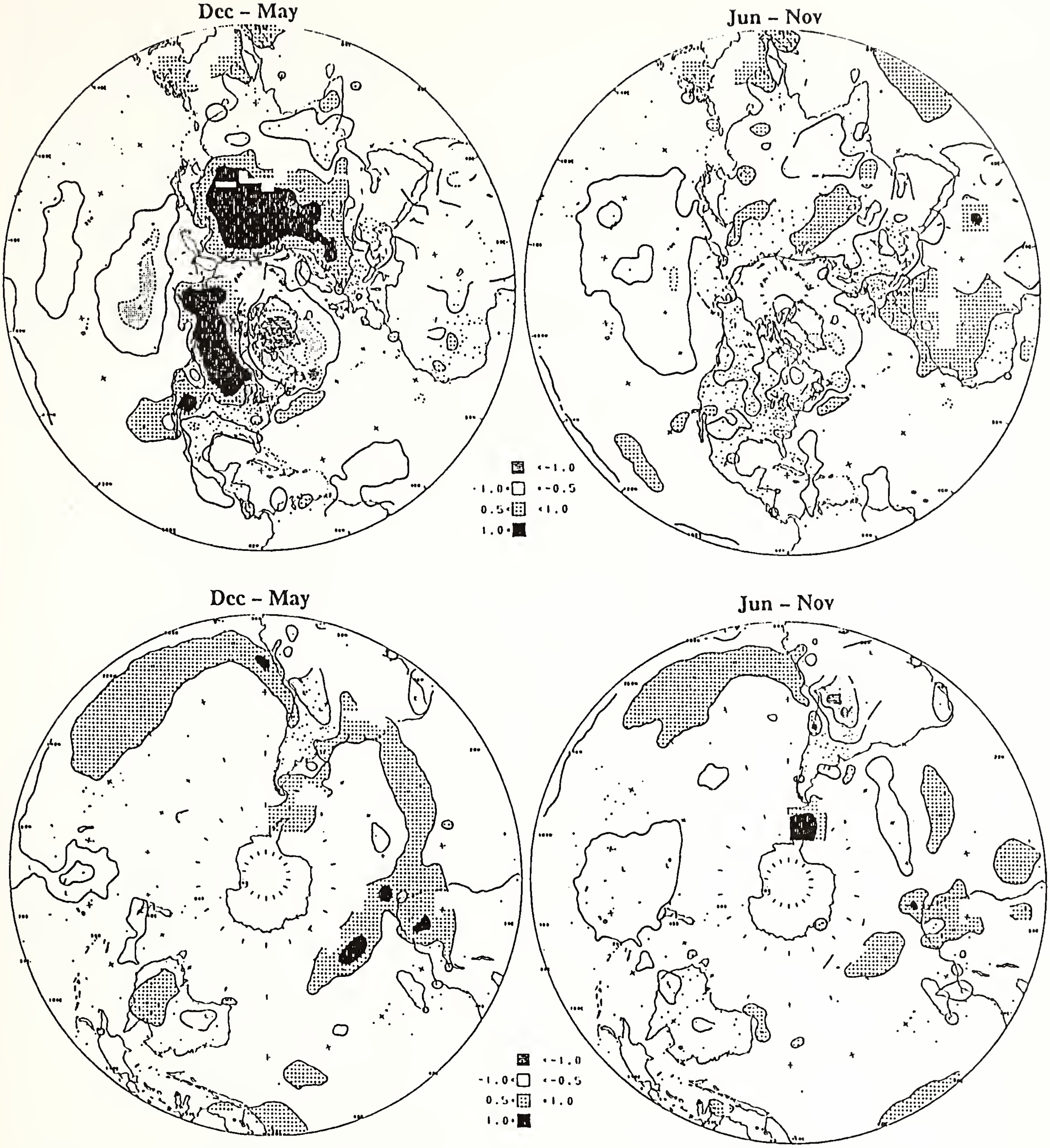

Fig. 1. Decadal (1981- 1990) mean surface temperature anomaly patterns for the December through May season (left) and June through November season (right). The analysis based on station data over land and sea surface temperature over water. Anomalies for station data are from the 1951-1980 base period, and from the COADS/ICE climatology (Reynolds, 1988) over water. Small plus signs indicate data locations over land. The contour interval is $0.5^{\circ}C$ with negative anomalies dashed.

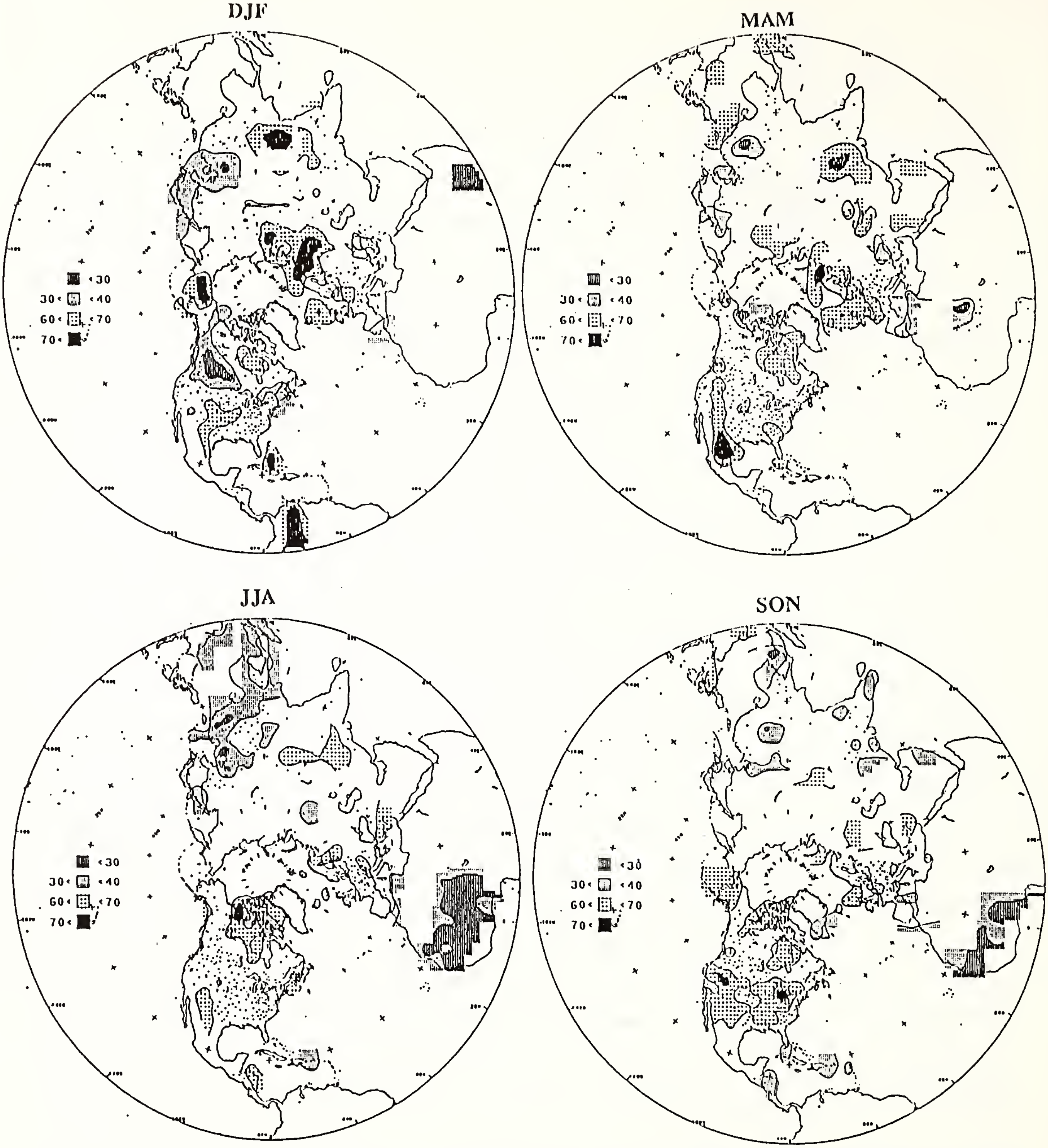

DJF

MAM

JJA

SON

Fig. 2. Seasonal Northern Hemisphere precipitation percentiles for the decade 1981-1990. The percentiles are based on a gamma distribution fit to data in the 1951 to 1980 base period. Station locations are denoted by a dot. The analysis is truncated in regions with insufficient data.

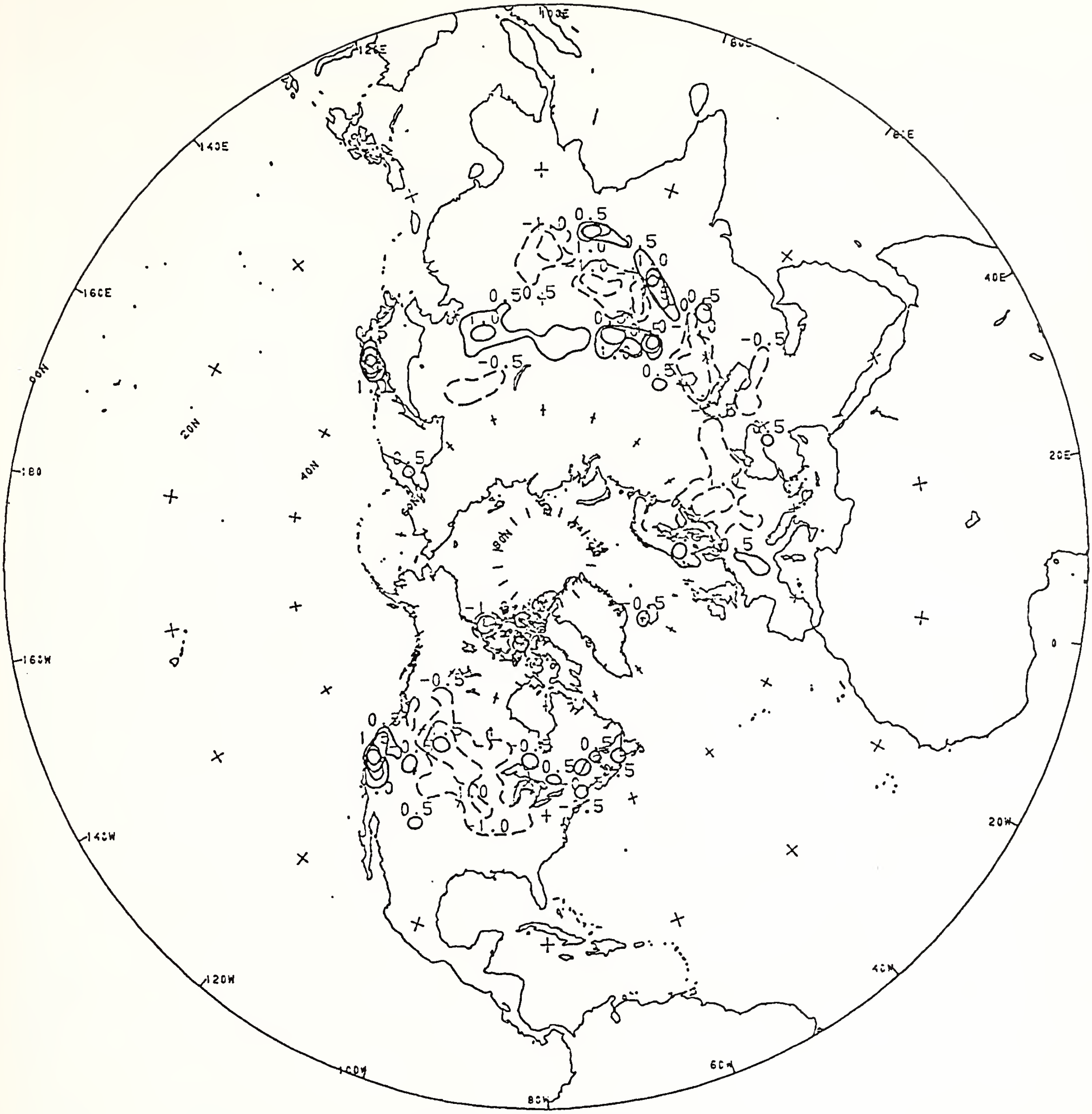

Fig. 3. Schematic of Northern Hemisphere December-to-May season mean snow cover anomaly for 1981-90 with respect to the 1973 to 1990 base period. Dashed (solid) outlined areas experienced below (above) normal snow cover.

# CLUSTER ANALYSIS OF GROWING SEASON PRECIPITATION IN CENTRAL AND EASTERN NORTH AMERICA

Michael B. Richman
Cooperative Institute for Mesoscale Meteorological Studies
The University of Oklahoma
Norman, OK 73019

and

Xiaofeng Gong
Weather Bureau of Liaoning Province
Shenyang, People's Republic of China

## 1. INTRODUCTION

In geophysical studies, investigators often need to classify the variables under investigation into relatively homogeneous groups, for indentification of the underlying physics and to assess the potential for predictability. Cluster analysis (CA) is one of a number of multivariate techniques that can be used to accomplish such classification. A key to a successful clustering algorithm is the ability to define clusters (groups of similar variables or observations) which exhibit two properties: external isolation and internal cohesion (Cormack, 1971). External isolation requires that variables (or observations) within one cluster be separated from those in another cluster by a fairly empty space. Internal cohesion requires the variables (or observations) within one cluster be similar to one another. CA imposes a characteristic structure on the data for exploratory purposes. It does so in several analysis steps -- by calculating dissimilarity amongst the variables and by using various formulae for admission of a variable into a cluster.

Interestingly, there have been only limited comparisons of the various methodological considerations for CA research. The majority of them have appeared in the psychological and biological literature (i.e., Gower, 1967; Johnson, 1967; Kuiper and Fisher, 1975; Blashfield, 1976; Milligan, 1980). While these papers do provide some critical guidance for geophysical work, CA results are dependent upon the data structure and none of the cited studies incorporated an exhaustive list of the available algorithms (or even a large subset). Several published meteorological studies have applied CA to precipitation data. Kikuchihara (1984) used complete linkage CA to establish homogeneous precipitation regions in Japan. A number of researchers used Ward's method successfully (Goosens, 1985; Winkler, 1985; Reich, 1986; Easterling, 1989) for their precipitation studies. These are all hierarchical methods. Non-hierarchical methods have been applied less often to geophysical studies. Gadgil and Joshi (1983) used K-means CA to establish a precipitation subdivision of India, as did Winker (1985) for heavy precipitation in the central and eastern U.S. Ronberg and Wang (1987) employed an algorithm known as the nucleated agglomerative method to regionalize Chinese precipitation.

The purpose of this work is to review a large range of available clustering techniques which have already been used on an individual basis in the geophysical science research. The analyses were designed to shed light on the sensitivities of CA methods to various aspects of the analysis to provide a general guide in selecting appropriate algorithms. This paper is drawn from an extensive review and Monte Carlo comparison of CA methodology (Gong and Richman, 1992).

## 2. CLUSTER ANALYSIS METHODOLOGY

Consider $\underline{X}$ a p x n matrix of raw data, where p references observations and n references entities or variables. The first required step is to transform $\underline{X}$ into a new n x n (or p x p) matrix of either similarities or dissimilarities. This is the fundamental stage before invoking a clustering algorithm. Hierarchical clustering methods (i.e., CA which creates a nested sequence of partitions from the dissimilarity matrix by successive mergers) require specific measurements of dissimilarity in order to merge the most similar variables. Since there is no general agreement on a best similarity/dissimilarity measure, we therefore chose to adopt three dissimilarity coefficients to maximize the utility of our work. These are discussed below.

### 2.1 *Distance measures*

#### a. Euclidean Distance

If one considers a data matrix $\underline{X}$, the Euclidean distance between variables $x_i$ and $x_j$ is given by

$$d_{ij} = \left[(x_i - x_j)^T (x_i - x_j)\right]^{1/2}$$

assuming the p-observations are independent. Since observations are rarely independent in most data sets, a Principal Component (PC) transformation is applied to $\underline{X}$ and the PC scores are used to calculate the distances.

#### b. Theta Angle between Variables (T)

The angle between variables has also been used as a dissimilarity coefficient. The value ranges from 0° for identical vectors to 90° for vectors with no common elements. The angle between $x_i$ and $x_j$ is given by

$$\Theta = \text{Arc cos} \left[\frac{x_i^T x_j}{|x_i| |x_j|}\right]$$

#### c. Inverse Correlation Coefficient (IC)

Since the correlation coefficient has historically been applied to CA, we computed the inverse correlation to form a dissimilarity coefficient

$$r_{ij}^{-1} = \left| \frac{x_i^T x_j}{(x_i^T x_i)^{1/2} (x_j^T x_j)^{1/2}} \right|^{-1}$$

The values range from 1 for identical entities to $+\infty$ for those with no similarity.

### 2.2 *Seed Points*

Since we are also examining non-heirarchical routines (CA which does not form a nested sequence of partitions), the *a priori* choice of partition is a prerequisite. These seed points are the estimates of cluster centroids, around which the clusters may be formed. There is no widely-accepted best method and the effects of choosing a different method are not well documented. We chose three different methods in the hope of determining if one was more accurate and documenting possible sensitivities of each cluster algorithm to individual partition methods.

a. Sequential (S)
The first k data entities in matrix X are chosen as the seed points for k clusters.

b. Randomly (R)
The k seed points are chosen via a pseudo-random number generator.

c. Gridded (G)
An equal area grid is overlaid on a map of the spatial domain and the k variables closest to each grid box centroid is used.

### 2.3 *Clustering Algorithms*

The first group tested were hierarchical methods. These are all agglomorative algorithms which start with each variable in its own cluster and then combine the two least dissimilar variables. The combination process continues in discrete steps until only one cluster remains (with all n variables). The analyst decides at which level the CA should be interpreted. All methods yield "hard clusters" where every variable is assigned to only one of k clusters. Distance formulae for the 5 hierarchical methods employed will now be presented.

a. Single Linkage (SL) - under this method, a cluster is defined as a group of variables such that every member of the cluster is more similar to at least one member of the same cluster than it is to any member of another cluster. If $d_{ij}$ is the distance between clusters i and j, and the clusters are to be merged, the distance between the new cluster k and any other cluster m will be

$$d_{km} = \min(d_{im}, d_{jm})$$

Hence, SL CA joins clusters by the shortest link between them. This can sometimes lead to "chaining", where single variables are more likely to join an existing cluster than to act as the nucleus of a new cluster.

b. Complete Linkage (CL) - under this method, the distance between clusters is determined by the distance between two entities, one from each cluster, that are most distant. The distance between cluster k, merged by i and j, and other cluster m will be

$$d_{km} = \max(d_{im}, d_{jm})$$

In this case $d_{im}$ and $d_{jm}$ are distances between the most distant members of clusters i and m, and clusters j and m, respectively. The bias in CL CA tends to run counter to SL, as the chance of a cluster obtaining a new member becomes smaller as the size of the cluster increases.

c. Average Linkage between Merged Groups (AL1) - this technique treats the distance between two clusters as the average distance between all pairs of variables where one member of a pair belongs to each cluster. This distance between cluster k, merged by clusters i and j, and another cluster m is determined by

$$d_{km} = \frac{N_i}{N_i+N_j} d_{im} + \frac{N_j}{N_i+N_j} d_{jm}$$

where $N_i$ and $N_j$ are the number of entities in those clusters.

d. Average Linkage within the New Group (AL2) - this technique evaluates not only the similarity between all pairs of variables that belong to two different clusters (as AL1 does), but also the similarity of all pairs of variables which belong to the same cluster. The key concept is to use this in order to characterize a cluster by the average of all links within it. The sum of pairwise distances between cluster k, merged by cluster i and j, and another cluster m is:

$$d_{km} = d_{im} + d_{jm}$$

e. Ward's Method (W) - this hierarchical method was designed to generate clusters in such a way that mergers at each stage are chosen so as to minimize the within-group sum of squares (hence optimizing an objective statistic). At each stage it combines two clusters, k and m, that result in the least increase in the function

$$W_{km} = \frac{N_k N_m}{N_k + N_m} (\bar{x}_k - \bar{x}_m)^T (\bar{x}_k - \bar{x}_m)$$

where $\bar{x}_k$ and $\bar{x}_m$ denote the centroids k and m.

We have also applied two types of non-hierarchical hard clustering methods previously used in atmospheric sciences. Non-hierarchical methods must have their cluster centroids chosen, *a priori*, with "seed points". The two methods used alter cluster membership so as to obtain a new partition according to the nearest centroid sorting algorithm.

f. K-Means clustering (KM) - this method begins with the prespecification of k seed points as the centroids for k clusters. The Euclidean distance is then computed between the variables and the centroids and each variable is assigned to the initial partition. The centroids are then recomputed according to the nearest centroid sorting formula. The nearest centroid ($Y_{mj}$) is given by:

$$Y_{mj} = \frac{1}{N_m} \sum_{i=1}^{N_m} x_{ij} \qquad (j = 1,2,\dots,p;\ m = 1,2,\dots,k)$$

where $N_m$ represents the number of variables assigned to cluster m. Variables are reassigned to the new clusters until convergence is achieved.

g. Nucleated Agglomorative clustering (NA) - this method is based on the same sorting algorithm as shown above for KM. The key difference is that the procedure performs as agglomorative clustering at a range from $k_{max}$ (a number of initial clusters) to a predetermined number $k_{min}$. This makes NA useful for examining a range of values for the number of clusters. Moreover, the seed points only need to be calculated once.

## 3. DATA

The data set used for this study was the enlarged Richman-Lamb precipitation network for North America (Richman *et al.*, 1991). The data used for this study were the daily precipitation totals for 766 locations in the eastern two-thirds of the U.S. and Canada for the May-August periods of 1949-1987. The grid-like station location of the network is displayed in Fig. 1. It is bounded on the west and east by the Rocky Mountains and Atlantic Ocean, to the south by the Gulf of Mexico, and to the north by the limit of agriculture or the availability of precipitation stations with at least moderate density. The daily values were totaled to 7-day values (i.e., 1-7 May, 8-14 May, ..., 20-27 August) prior to the clustering. Hence the clusters should be indicitive of weekly precipitation over the period of observation (39 years). There were a total of 663 observations.

## 4. RESULTS

In order to objectively evaluate the aforementioned methods, we needed to keep as many parameters as possible fixed. One decision made in CA is the determination of the number of clusters to be retained. Rather than selecting a single value, we chose to keep a range of 8 to 25 to reflect all of the significant precipitation variability without losing signal. This allowed both direct comparisons between methods for a fixed cluster number and evaluation of the effects of changing the number of clusters on each method. Hence we calculated separate solutions for 8,9,...,25 clusters for a total of 18 analyses. For the hierarchical techniques outlined under sections 2a-2e, each of the 766 variables starts as its own cluster and is then merged until we reach 25 clusters. The analysis is then repeated at 24 clusters, etc. Under the KM method (2f), 8 to 25 seed points are chosen for separate clustering, whereas for the NA method (2g) $k_{max} = 25$ and $k_{min} = 8$ in one step. Since each of the hierarchical techniques is repeated for the three dissimilarity coefficients (and the non-hierarchical ones for three initial partition methods), we end up with 21 clustering methods (7x3), each one of which contain 18 different solutions (8-25 clusters) for a total of 378 analyses. These will be summarized by the use of boxplots and by spatially mapping the clusters on the precipitation network for a representative solution.

The evaluation of the relative accuracy of each clustering method was based on matching the CA spatial pattern against its corresponding interstation correlation field. In order to accomplish this, each cluster's geometric centroid was selected and this served as the base point (1.0) for the correlation analysis. Variables (stations) inside a cluster were assigned values of 1.0, whereas those outside the cluster were assigned values of 0.0, in accordance with the usual practice for hard clustering methods. This means we are correlating a binary value (stations in the cluster versus those outside the cluster) with a continuous variable (precipitation correlation field), and this is known as a biserial correlation. Milligan (1980) successfully used the biserial correlation to match synthetic data. For an 8 cluster solution, 8 correlation matching coefficients are obtained and averaged to represent a single value for the 8 cluster match. This is repeated for 9 clusters, etc., until all 18 average matches are obtained. These are then summarized in the boxplots (Fig. 2).

Figure 2 also contains orthogonally and obliquely rotated principal component (PC) solutions as a basepoint comparison for the previous work of Richman and Lamb (1985; 1987). The PCs had their loadings "binarized" or made into hard clusters at the +0.2 loading isopleth. This hardening of the PC loadings reduced their accuracy considerably, from biserial match of close to +0.90 to approximately +0.75. However, we considered this essential to try to make comparisons between the methods. It does point to a penalty incurred when one uses hard clusters to portray precipitation.

The key results of this work (Fig. 2) indicate single linkage (SL) methods all performed poorly with biserial correlations of less than 0.4. In order to determine why the matches were low, we present a representative solution mapped to the domain for 16 clusters (mid-way between 8 and 25). These CA results are shown in Fig. 3 and illustrate the nature of the regionalization for each method. Under all three SL methods, the chaining solutions are evident, with one large cluster and 15 much smaller ones (Figs. 3a-3c). This is obviously a pathological result of the SL algorithm as it bears no resemblance to the known patterns of interstation covariation. The complete linkage (CL) methods are summarized in Fig. 2 and Fig. 3d-f. All three CL methods are more accurate than SL. The inverse correlation (IC) and Euclidean distance (ED) solutions have considerably higher correlations than the theta angle (T), with medians being in the 0.65 range for the former. The spatial maps (Fig. 3d-f) show less chaining than SL, although CLT had 8 very large small clusters. The first average linkage (AL1) method could only be mapped for the IC and ED measures, as T led to severe fragmenting (stations from different areas of the domain would be included in a single cluster). The median values shown in the boxplots are close to +0.7. The spatial patterns now show fairly equally sized clusters (Fig. 3g,h), yet there is not much agreement between the two AL1 regionalization's boundaries. The second average linkage (AL2) technique had similar accuracy levels to AL1 for the IC and ED coefficients (Fig. 2). The AL2T solution was now stable enough to be mapped, yet the biserial correlation was much lower having boxplots with no overlap between AL2T and AL2IC (or AL2ED). Inspection of AL2T (Fig. 3k) shows some chaining in south Texas, whereas AL2IC and AL2ED (Fig. 3i,j) have more equal sized precipitation regions. The final hierarchical CA method tested, Wards (W), showed the least range in WIC and WED (Fig. 2) and slightly more for WT, as well as a fairly high correlation. The spatial regionalizations provided by W (Fig. 3l-n) show similar sized clusters to those of AL1 and AL2, where the western regions are slightly larger than those to the east. However, the regional boundaries of all of the methods vary considerably.

Analysis of the non-hierarchical techniques revealed slightly higher median values than the hierarchical ones overall (Fig. 2). Interestingly, a bias in the initial partition method for KMS was uncovered. Since the first partition was based on variables 1-8 to 1-25 (all in the southern edge of the domain), the regionalization (Fig. 3o) has a distinctly smaller set of clusters in the south. This is an important finding as KM CA applications are growing in popularity in the atmospheric sciences. KMR and KMG do not appear to show this bias (Fig. 3p,q), although the random selection of seed points would be suseptible to this initial partition influence and the analyst would not necessarily be able to uncover it. There is still considerable variability in the regional boundaries of the various methods, both within CA method and within any given dissimilarity coefficient. The second non-hierarchical method, nucleated agglomorative (NA), was notable as it showed no sensitivity to partitioning method (Fig. 2). It also seemed to have more stable regions (Fig. 3r,s,t) despite several areas in the midwest and east being variable. However, due to the high biserial correlations, fairly low range, no apparent sensitivity to the seed method, and increased stability, we feel that the NA method is the one of choice for hard clustering of precipitation data.

The rotated PCs had very high biserial correlations, in excess of 0.75 (recall they were in excess of 0.85 prior to binarization) and lower ranges than any of the CA methods. The agreement among the two rotational method's (Varimax versus Harris-Kaiser B'B) regions is striking. This may help shed some light on the degree of inter-rotational variability in the context of another regionalization method. However, a direct comparison between PCA and CA is difficult as PCA does not yield hard clusters with no overlap. Contrarily, the orthogonally rotated PCs have a high degree of overlap at the loading level (+0.2) chosen to maximize the biserial correlation.

## 5. CONCLUSIONS

The intercomparison of various clustering techniques is of interest to geophysical researchers. This work used a well-studied North American growing season precipitation data set, to investigate the capability of various clustering methods to recover that input data structure and test the applicability of a large range of clustering algorithms for regionalization. Overall, the findings largely confirmed what was known about SL techniques -- they lead to chaining solutions. The CL methods also yielded inferior regionalizations. In general, the theta angle (T) was found to negatively impact SL, CL, AL1, and AL2 methods, yet it was equally accurate with the IC and ED coefficients tested for W. Both the IC and ED dissimilarity measures were about as accurate for all hierarchical techniques. However, the nonhierarchical techniques tested (KM and NA) generally outperformed the top hierarchical ones (AL1, AL2, W). Overall, the NA was thought to be the best methods as they showed no sensitivity to initial partition, as did KM.

The PC results are included, yet we hesitate to draw too many comparisons between them and the CA methods. Isoplethed loadings of PCs have overlapping classifications where some stations may be assigned to multiple regions and others may not be classified to any regions. The CA methods tested herein all classify each station to only one of the regions and there are no unclassified stations. As a result, the regions tend to be irregularly shaped under CA. These do not always match the interstation correlations well and, hence, lead to lower biserial correlations. This points to the potential for fuzzy clustering methods which yield clusters with gradients (similar to PCA). The regionalizations provided by the various CA methods tend to be different, both for any one algorithm and for any one dissimilarity coefficient. This instability leads to a problematic physical interpretation as one needs to consider which one is most meaningful? Based on the relatively larger stability of NA methods, we recommend them for precipitation regionalization where hard clusters are desired. In cases where an overlapping regionalization is acceptable, PCA is recommended.

## ACKNOWLEDGEMENTS

This research was supported by NSF grant ATM 89-08545 and EPA Cooperative Agreement CR-816318-02-0. Some of the computational support was provided by the National Center for Supercomputing Applications. We wish to thank Ginger Rollins for typing the manuscript.

## REFERENCES

Blashfield, R.K., 1976: Mixture model tests of cluster analysis: accuracy of four agglomerative hierarchical methods. *Psychological Bulletin, 83*, 377-388.

Cormack, R.M., 1971: A review of classification. *J. Royal Statistical Soc. (Series A), 134*, 321-367.

Easterling, D.R., 1989: Regionalization of thunderstorm rainfall in the contiguous United States. *Int. J. Climatol., 9*, 567-579.

Gadgil, S and N.V. Joshi, 1983: Climatic clusters of the Indian region. *J. Climatol., 3*, 47-63.

Gong, X.-F. and M.B. Richman, 1992: An examination of cluster analysis methodology in geophysical reserach. Part I: precipitation data. Submitted to *J. Climate.*

Goosens, C., 1985: Principal component analysis of Mediterranean rainfall. *J. Climatol., 5*, 379-388.

Gower, J.A., 1967: A comparison of some methods of cluster analysis. *Biometrics, 23*, 623-627.

Johnson, S.C., 1967: Hierarchical clustering schemes. *Psychometrika, 32*, 261-274.

Kikuchihara, H., 1984: The regional division of Japan by precipitation. *The Geophysical Magazine, 41,* 61-157.

Kuiper, F.K. and L.A. Fisher, 1975: A Monte Carlo comparison of six clustering procedures. *Biometrics, 31,* 777-783.

Milligan, G.W., 1980: An examination of the effect of six types of error perturbation of 15 clustering algorithms. *Psychometrika, 45,* 325-342.

Reich, V.T., 1986: Die raumliche struktur des niederschlagsfeldezs hierachische gruppierungs verfahren und dendrogramme. *Zeitschrift fur Meteorologie, 36,* 293-333.

Richman, M.B. and P.J. Lamb, 1987: Pattern analysis of growing season precipitation in southern Canada. *Atmosphere-Ocean, 25,* 137-158.

Richman, M.B. and P.J. Lamb, 1985: Climate pattern analysis of three- and seven-day summer rainfall in the central United States: some methodological considerations and a regionalization. *J. Climate Applied Meteor., 24,* 1325-1343.

Richman, M.B., P.J. Lamb, and J.R. Angel, 1991: Relationships between monthly precipitation over central and eastern North America and Southern Oscillation. *Proceedings of the Fifteenth Annual Climate Diagnostics Workshop,* U.S. Dept. of Commerce, Washington, D.C., 373-383.

Ronberg, B. and W.-C. Wang, 1987: Climate patterns derived from Chinese proxy precipitation records: An evaluation of the station networks and statistical techniques. *J. Climatol., 7,* 391-416.

Winkler, J.A., 1985: Regionalization of the diurnal distribution of summertime heavy precipitation. *Preprints, Sixth Conf. on Hydrometeorology,* American Meteorological Society, Boston, MA, 9-16.

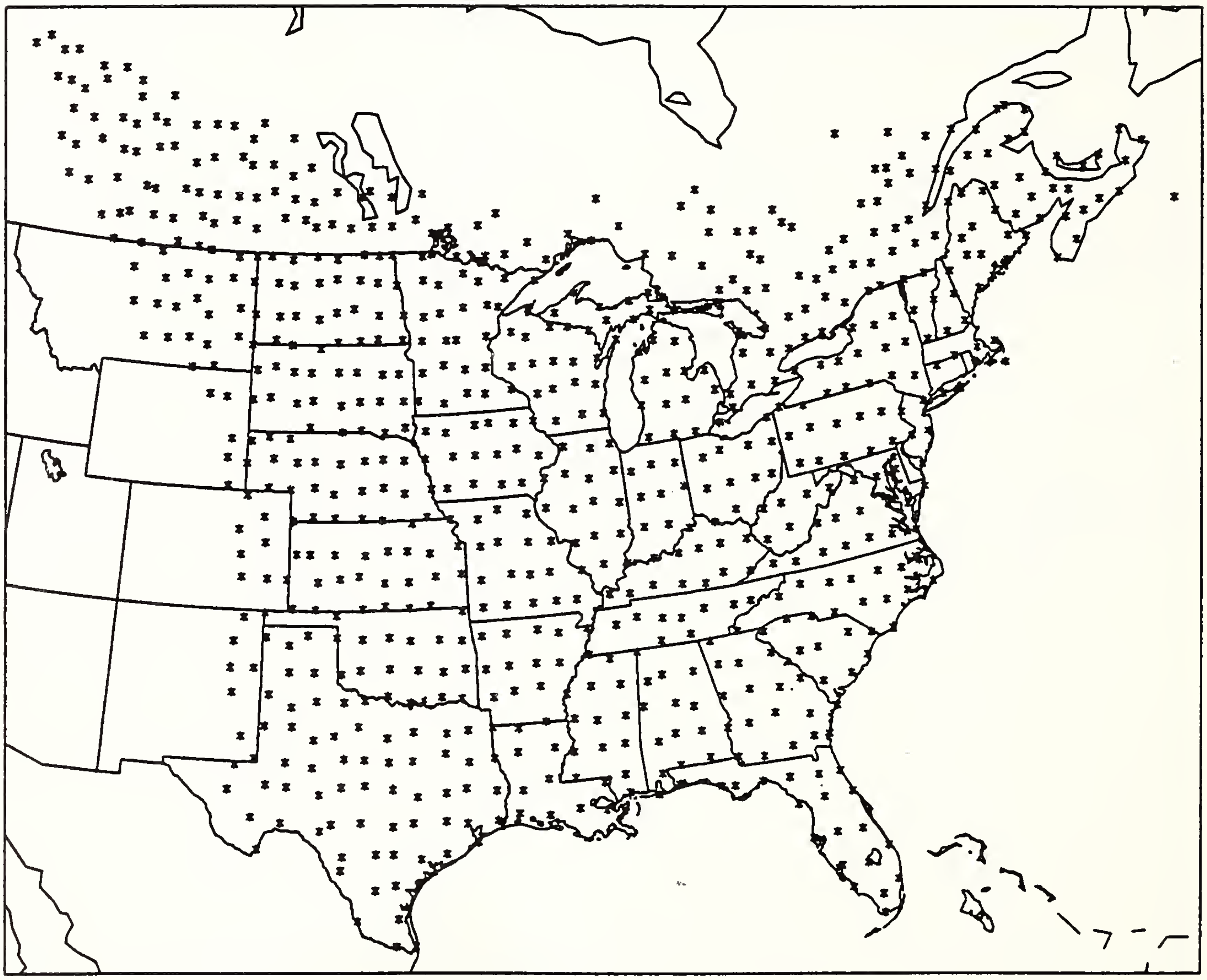

*Figure 1.* Precipitation station network (766 locations).

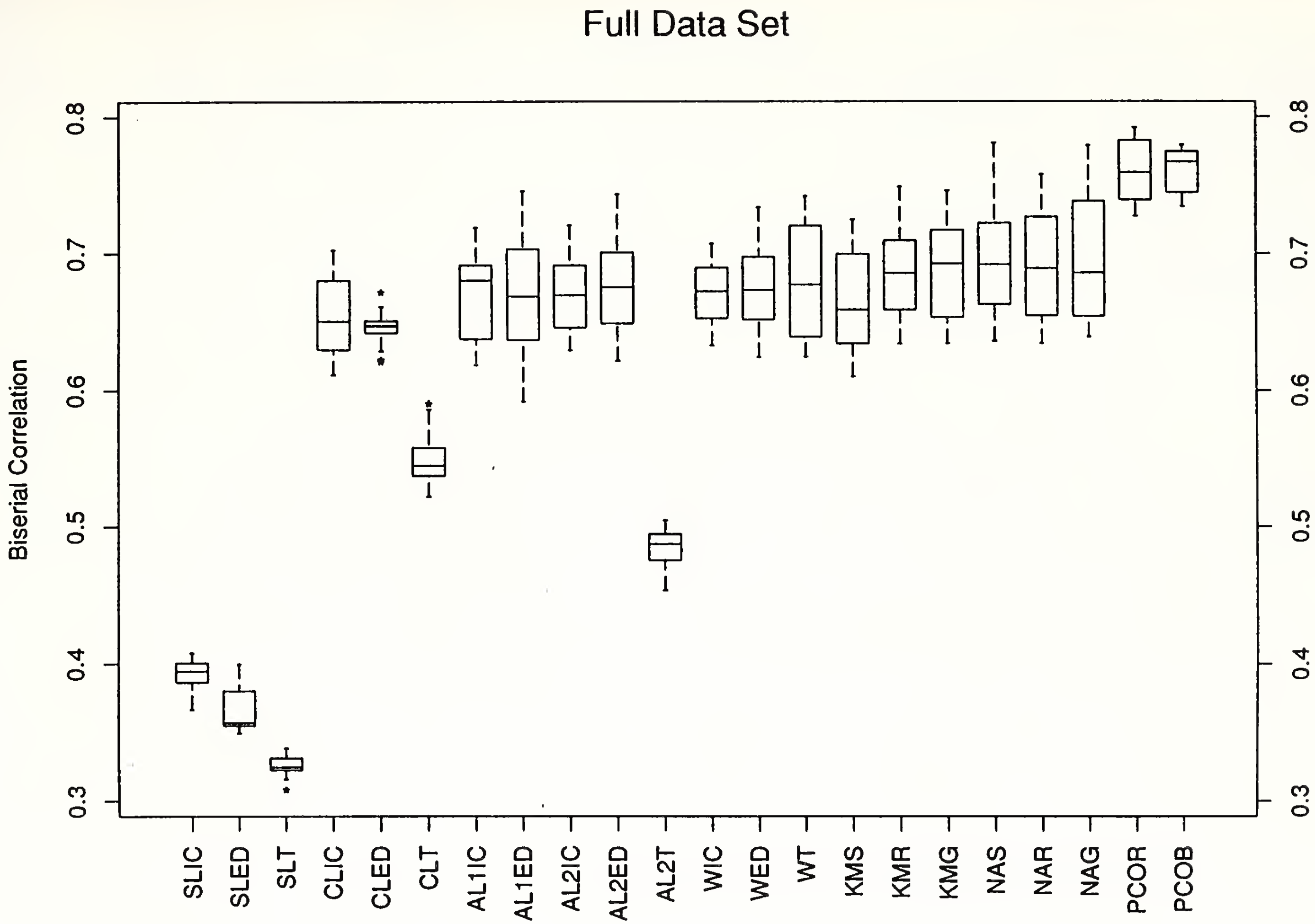

*Figure 2.* Box and whisker plots for the matches for each of the cluster/PC analysis methods to the corresponding interstation correlations (see text for details). Box indicates median value and interquartile ranges, while whiskers show 1.5 interquartile range and any outliers (asterisks).

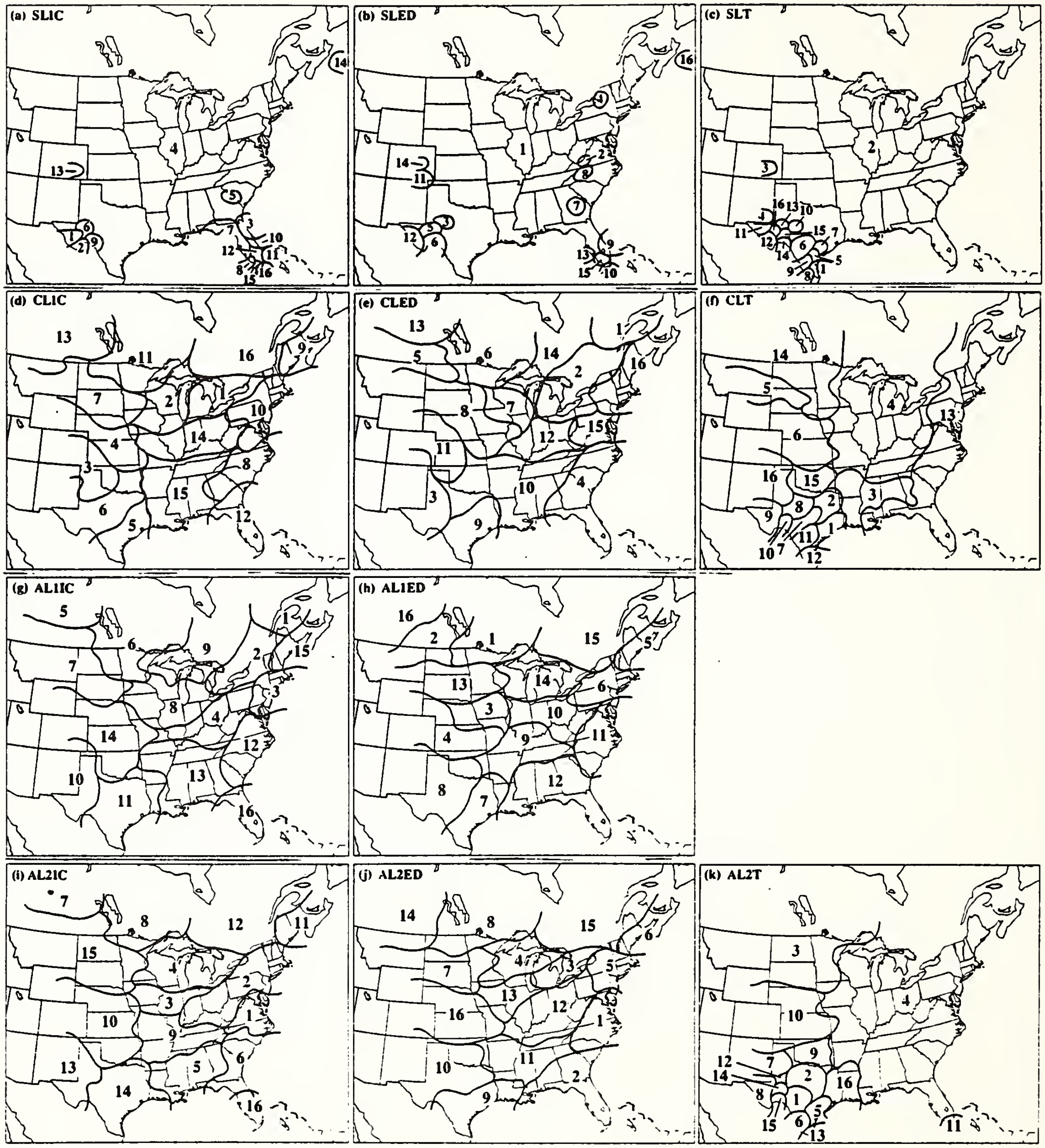

*Figure 3.* Regionalization of the eastern two-thirds of central North American growing season precipitation by various clustering methods and rotated PCA. Number of clusters/PCs is 16 in all analyses.

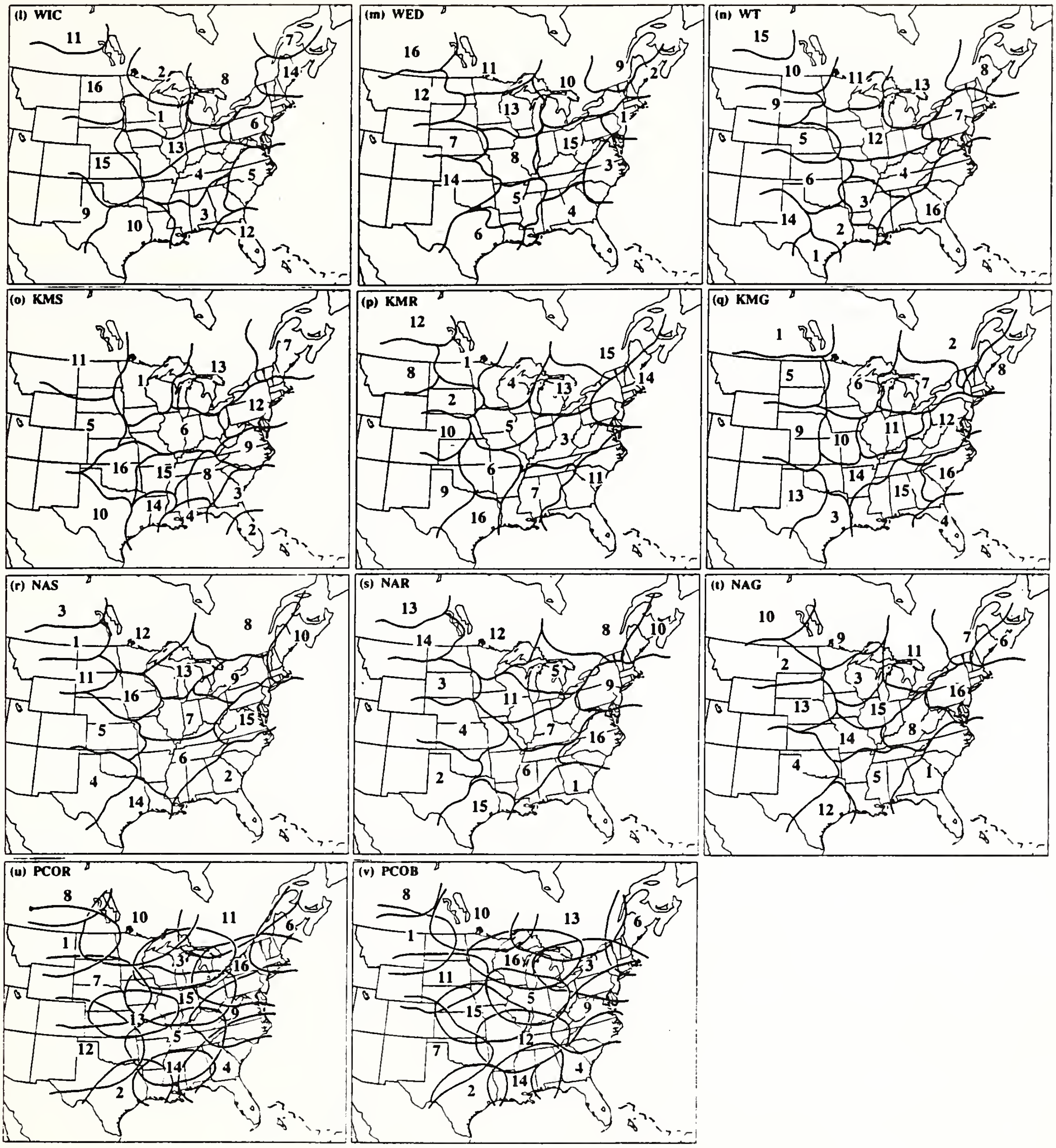
(l) WIC
(m) WED
(n) WT
(o) KMS
(p) KMR
(q) KMG
(r) NAS
(s) NAR
(t) NAG
(u) PCOR
(v) PCOB

*Figure 3.* Continued.

# RELATIONSHIPS BETWEEN WATER VAPOR BUDGET COMPONENTS OVER CENTRAL NORTH AMERICA IN SUMMER 1979

Abraham Zangvil[1], Diane H. Portis and Peter J. Lamb[2]

Cooperative Institute for Mesoscale Meteorological Studies
The University of Oklahoma
Norman, Oklahoma 73019

## Introduction

The atmospheric moisture budget of a given continental region is a complex function of the meteorological-hydrological processes in the region and surrounding areas, and of the soil characteristics and type of land use. Since precipitation over the region is derived from both moisture advected into the region by the winds, and by moisture evaporating at the surface within the region, this recycling may provide an important feedback mechanism between land surface processes and precipitation, which may be reflected in the moisture budget of the region. The study of the relationships between the water vapor budget components on different time and space scales may therefore provide information concerning the hydrological cycle of the region and the atmospheric processes leading to the formation and variation of precipitation.

## Data and Procedure

The area over which the study is made is a rectangle, 1300 x 750 km in size centered over east central Illinois (Fig. 1). The basic data set is comprised of NWS rawinsonde observations at 00 and 12 UT from May to August 1979 interpolated onto a 190 km grid with a 50 mb vertical resolution. The computations performed for this area were based on both the flux form and the advection form of the moisture budget equation. They are:

1. The vertically integrated water vapor flux divergence and the total precipitable water at the original observation times, 00 UT and 12 UT. A subdivision of the vertical integration into surface-700 mb and 700-300 mb was sometimes used.
2. 12 hr precipitation totals for 00 and 12 UT and totals for 12 to 00 UT based on hourly precipitation measurements from 590 stations. 24 hr totals were also used.
3. 12 hr averages of the water vapor flux divergence terms over the same 12 hr periods based on rawinsonde data at 00 and 12 UT. 24 hr averages were also used.
4. 12 and 24 hr differences of total precipitable water, based on the 00 and 12 UT observed precipitable water.
5. The 12 and 24 hr totals of the evaporation were calculated as a residual in the water vapor budget equation.
6. The top level used in most of the vertical integrations was 300 mb.

---

[1] On leave from the Jacob Blaustein Institute for Desert Research, Ben Gurion University of the Negev, Sede Boker, Israel.

[2] Also in School of Meteorology, the University of Oklahoma.

## Results

Some insight into the relationship between the different moisture budget components can be obtained from the vertical-time sections in Fig. 2. A very good correspondence can be seen between the vertical moisture advection and rainfall (in phase) and between the horizontal moisture advection and the local time-change of specific humidity. It is also observed that moist low level advection preceeds the rainfall maximum by about 24 hours.

The correlation coefficients between the various moisture budget terms are given in Table 1. Only values above the 95% significance level of 0.20 are shown in this Table. A notably high negative value appears between the horizontal moisture advection and the time change of precipitable water. A high positive correlation is also found between rainfall and vertical moist advection, and between rainfall and total precipitable water (which is not a bonafide component of the moisture budget). Of interest is the fact that an insignificant correlation exists between evaporation and the time change of precipitable water when the 24 hr budget is used, but when the 12 hr budget is used a much higher correlation appears, probably due to the fact that day time high evaporation is associated with storage of water vapor in the atmosphere. A significant correlation is noted between the evaporation and dry vertical advection, and between dry vertical advection and precipitable water. No significant correlation is observed between horizontal moist advection and precipitation.

More insight into the relationships between different moisture budget terms can be gained by performing a cross spectrum analysis. Some highlights of this analysis are presented next. Attention is focused on the frequency band corresponding to a period of 10-11 days. A considerable percentage of the total variance of rainfall, precipitable water, and the horizontal divergence of the moisture flux is contained in the vicinity of this frequency band (not shown). Some examples of the cross spectrum analysis are shown in Figs. 3, 4, and 5. A coherence square of 0.82 near 11 days is observed between the rainfall and the horizontal divergence term below 700 mb (Fig. 3). A phase difference of 170° is noted between these two terms showing that maximum low level convergence occurs about 8 hours prior to the maximum rain intensity. Note that no significant correlation existed between the rainfall and the horizontal advection of moisture. However, in Fig. 4 a coherence square of nearly 0.70 is observed near 11 days period between the rainfall and the moist advection in the layer between 700 to 300 mb with a phase difference of 60°. This means that rainfall maximum follows 1.7 days after a moist advection maximum. Very outstanding is the coherence square of 0.93 and phase difference of 180° between moisture advection below 700 mb and the time change of precipitable water seen in Fig. 5. Finally, coherence square of 0.90 is found between the evaporation and time change of precipitable water in the period range of 1 to 2 days with no phase difference (not shown). This means that, for the short time scales, local evaporation is connected with an increase in precipitable water. This is not the case for the longer time scales.

## Acknowledgements

This research was supported by NSF Grants ATM 85-20877 and ATM 89-08545.

Table 1. Correlation coefficient between the 24 hr moisture budget components including PW. (P is precipitation; E - evaporation; VA and HA vertical and horizontal moisture advection, respectively. PW is precipitable water and dPW is the time change of precipitable water.

| Budget terms | | | Correlation |
|---|---|---|---|
| P | and | VA | -0.68 |
| P | and | PW | +0.58 |
| E | and | VA | +0.40 |
| E | and | dPW | +0.16 (0.40 for 12 hr) |
| HA | and | dPW | -0.89 |
| VA | and | PW | 0.31 |

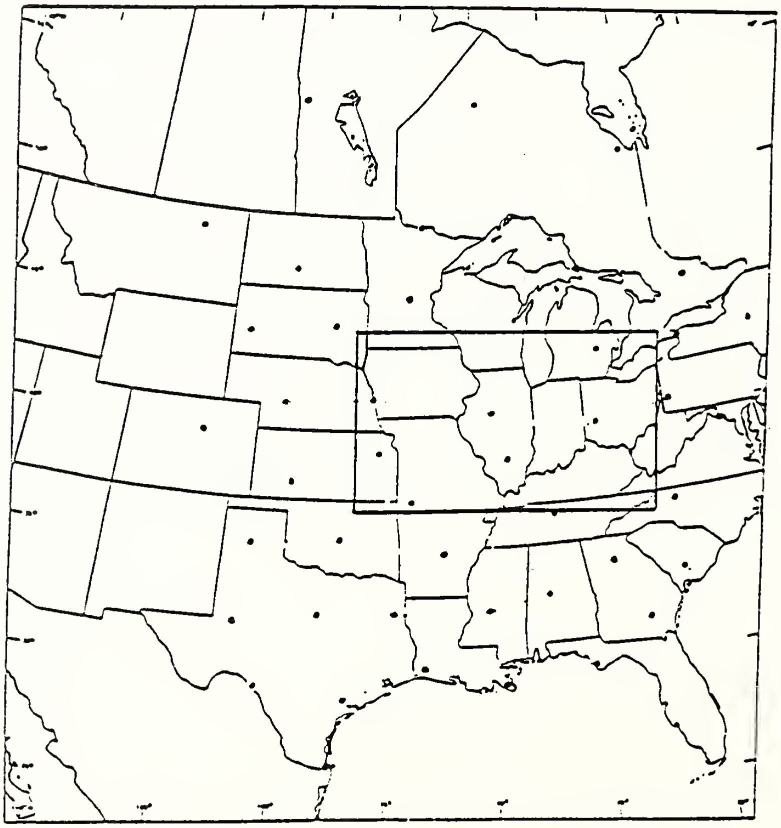

*Fig. 1.* Orientation map showing the rectangular region over which the calculations were performed. Dots mark the original rawinsonde stations used.

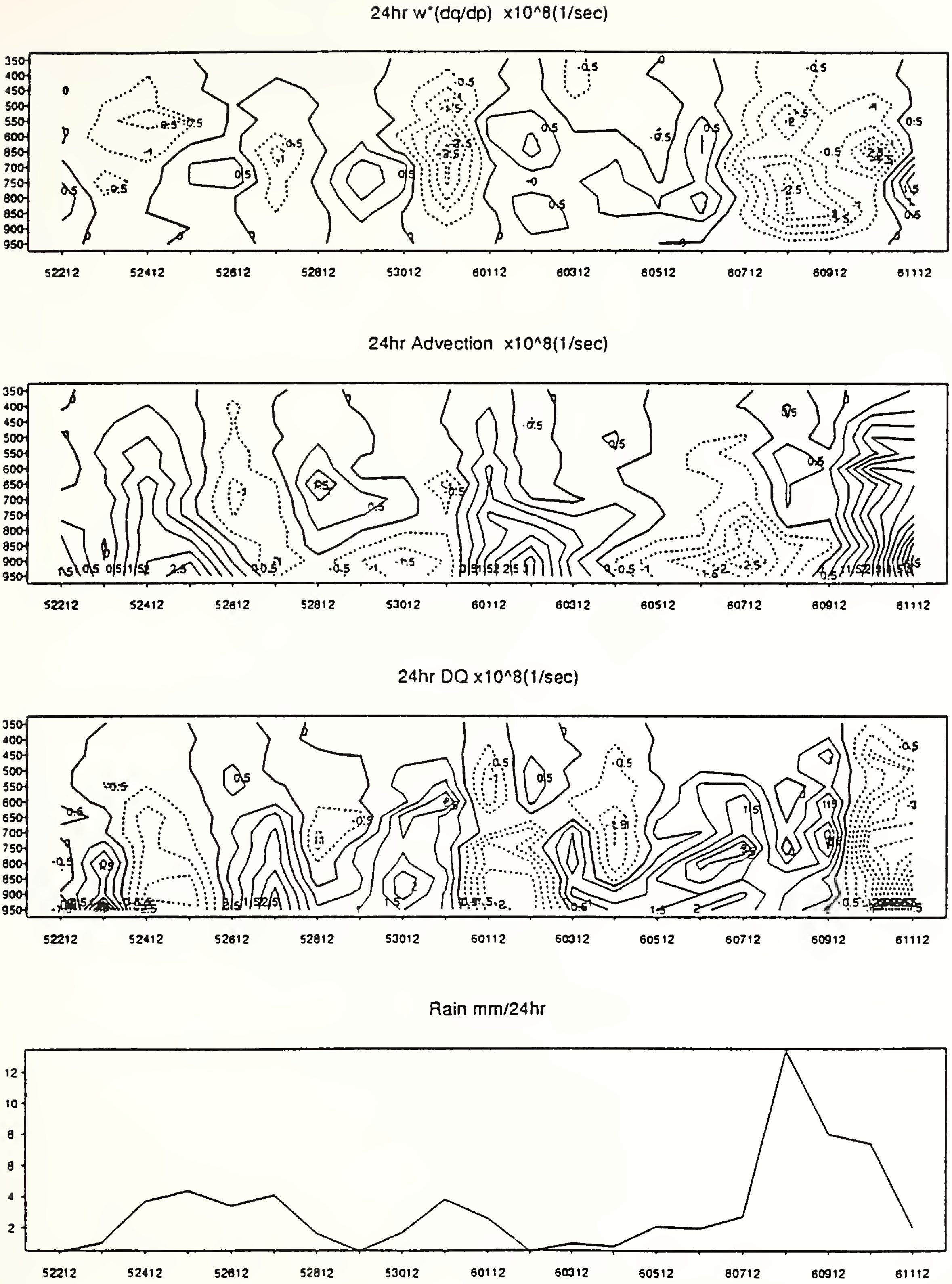

*Fig. 2.* Vertical-time sections of the 24 hr budget terms: vertical moisture advection, horizontal moisture advection and time change of specific humidity (first, second and third panels from the top, respectively). The vertical coordinate is in mb and the horizontal is time at the end of the 24 hr periods (month, day, and time, UT). The lower panel shows the corresponding 24 hr total rainfall.

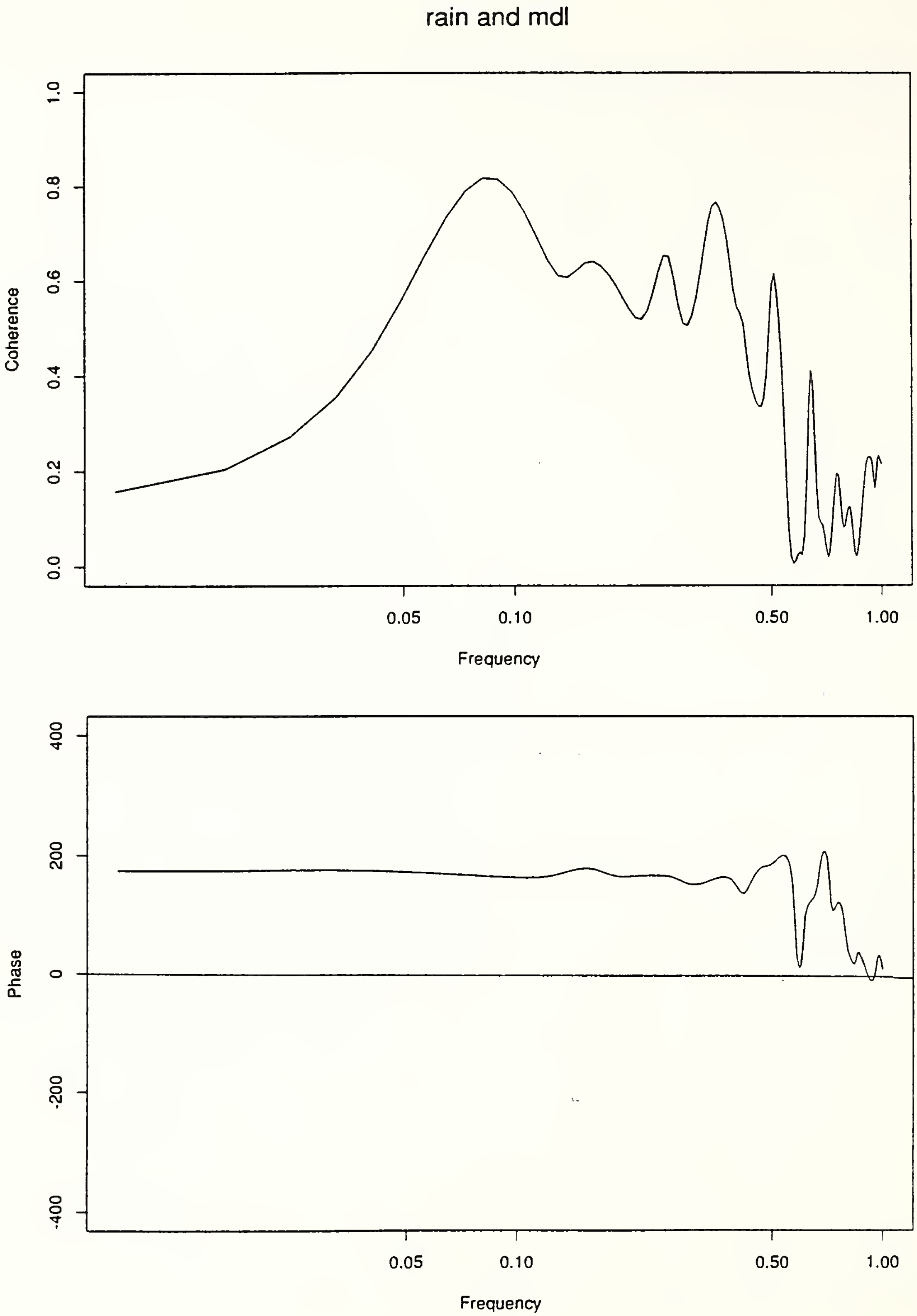

*Fig. 3.* Coherence (upper panel) and phase difference (lower panel, in degrees) as a function of frequency (day$^{-1}$) between the rainfall and the divergence term below 700 mb. The values of the ordinate in the upper panel are actually coherence squared and the 95% confidence limit is 0.4.

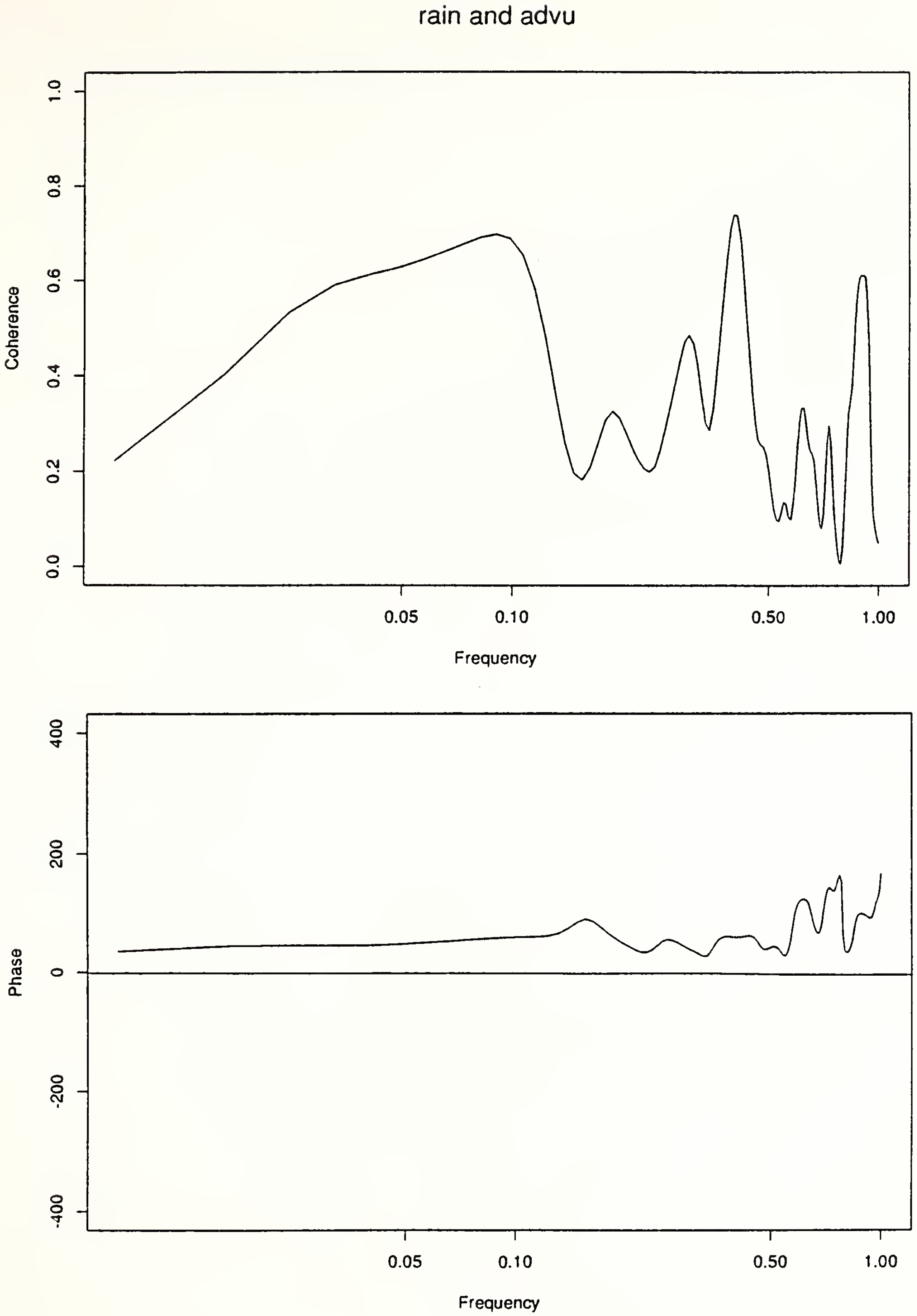

*Fig. 4.* Same as Fig. 3 but for the rainfall and moisture advection between 700 and 300 mb.

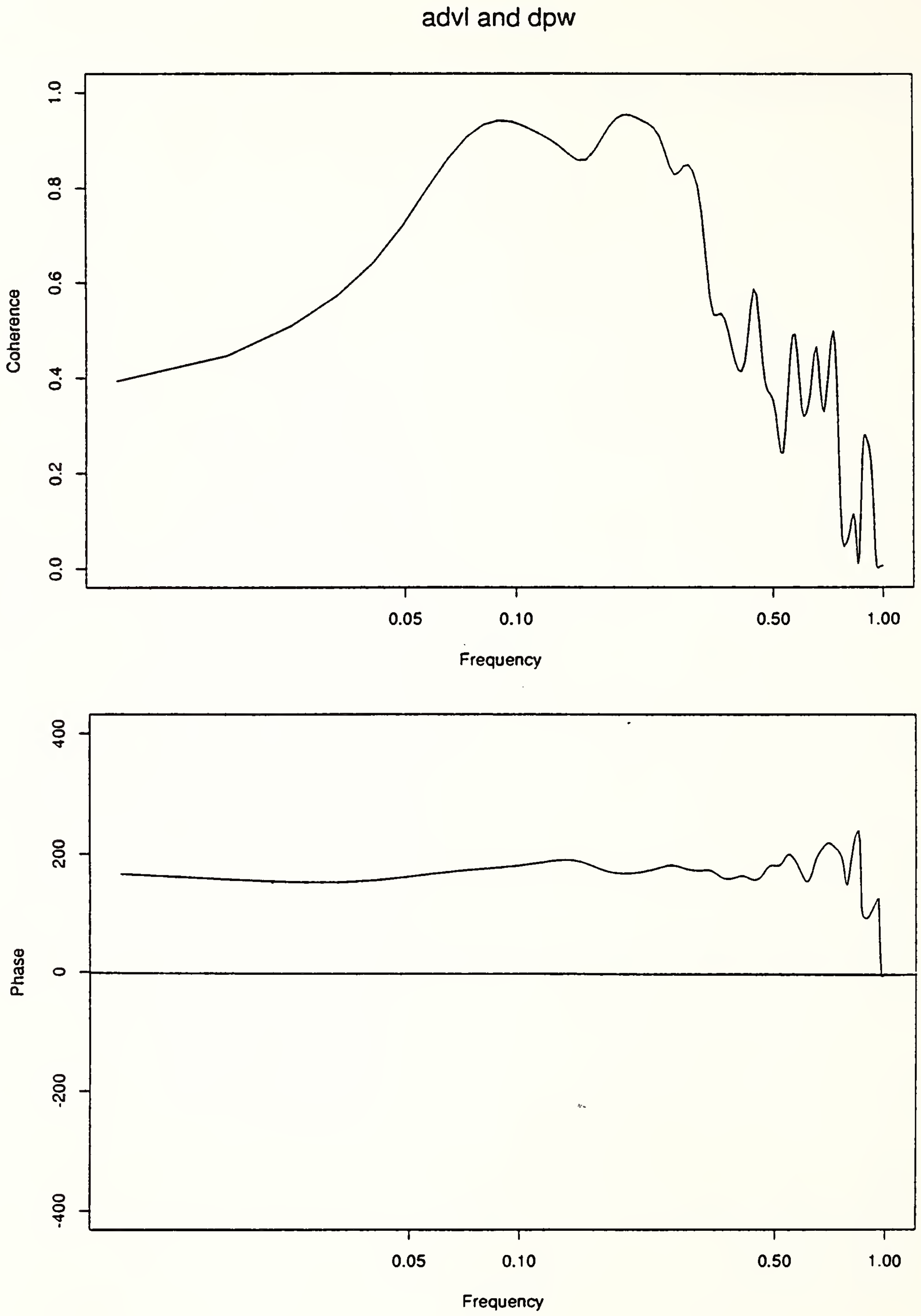

*Fig. 5.* Same as Fig. 3 but for moisture advection below 700 mb and time change of total precipitable water.

# Comparison of Climate Datasets using Spatial Histograms

Stanley L. Grotch

Program for Climate Model Diagnosis and Intercomparison
Atmospheric and Geophysical Sciences Division
Lawrence Livermore National Laboratory
Livermore, California 94550

## Introduction

One of the most commonly used procedures in statistical analysis is the display of a distribution using a histogram. Although frequently used in many aspects of meteorology, surprisingly the technique has received relatively little recent attention as a climate diagnostic, particularly for intercomparisons. As will be seen, histograms can provide valuable information for both data verification and for statistical intercomparison.

Because histograms are often used, their construction is very well known. In the spatial context considered here, all of the data values in a specified region (say, global, land-based gridpoints) are binned into discrete ranges of the desired variable. Rather than producing the more commonly-encountered frequency or number-based histograms, here the relative area represented by each gridpoint is used. If each precipitation range bin is incremented using the cosine(latitude) for the relevant gridpoint, an area-weighted spatial histogram is obtained. The average of this distribution is the familiar area-weighted average of the variable for the region considered and the integrated area between any two values $x_1$ and $x_2$ (divided by the total histogram area) represents the fraction of the specified area with variable values between $x_1$ and $x_2$.

## Data Verification Example

A recent global climatology of precipitation has been published by Legates and Willmott (1990). These data of monthly average total precipitation are presented on a 0.5° latitude by 0.5° longitude grid and cover the approximate time period: 1920-1980. When these precipitation data (uncorrected) for the entire globe are binned using fractional area, the spatial histograms shown in Fig. 1 are obtained for the seasonal averages DJF and JJA. Both of these distributions show a striking feature, a sharp "resonance" centered at about 3.5 and 1.8 mm/day for the two seasons, respectively.

What is the nature or cause of this feature? Other histograms for different regions can be developed to spatially locate the gridpoints with this range of precipitation. Spatial histograms for the two hemispheres considered separately show that the resonance is primarily a Southern Hemisphere phenomenon. In Fig. 2, histograms for the two seasons for land and water gridpoints are contrasted indicating that the feature is largely SH, water-based.

Alternatively, the locations of the desired gridpoints can be found much more simply and directly using statistical/graphical software now available on personal computers. By merely highlighting with a cursor the appropriate precipitation range on the histogram (see Fig. 3), the locations of the gridpoints in the selected range are simultaneously highlighted on a map, immediately showing their locations. The procedure also works in reverse: if any desired region is highlighted on a map by simply drawing a line around it, the appropriate subset of the histogram darkens to show the contribution of the selected gridpoints. With a color monitor the points can be even more clearly differentiated using color coding. This feature is of *immense utility* in climate-related statistical work for it permits *truly interactive* intercomparisons among different types of data.

Using this interactive feature it is readily determined that these two resonances are due to an unusually small spread in precipitation assigned to groups of Southern Ocean gridpoints, largely in the range 35°-50°S (Fig. 3). Whether this phenomenon is real or an artifact resulting from very limited data coverage for this region remains to be determined. However, the simple technique of spatial histograms has very clearly flagged either an interesting Southern Ocean phenomenon or a possible problem with the data for this region. As will be seen, although other datasets do show this feature to varying degrees, possibly because of commonalities in data sources, none of the GCM simulations of the control climate which were examined yield such characteristics.

### Global Histograms of Precipitation as Predicted by Six GCM Simulations

As a second illustration of the utility of spatial histograms, the global histograms for seasonally averaged DJF precipitation for three observational datasets are compared with those derived from six GCM simulations. Area-weighted global histograms for the three observational sets: Schutz-Gates (Jan), Jaeger (DJF), and Legates-Willmott (uncorrected, DJF) are presented in Fig. 4. All show similar shapes as well as the "resonance" feature described previously (less-so in the Schutz-Gates set). Because Legates-Willmott have incorporated some of Jaeger's data in the Southern Oceans, this may not be surprising.

In Fig. 5 the same precipitation distributions are displayed (with the same scaling) for six different GCM simulations of "current climate". There is clearly a striking difference between the GCM simulations and the observational datasets, particularly in the lowest precipitation ranges (< 0.5

mm/day) of these histograms. For all of these simulations, the GCMs have little area with very low precipitation amounts relative to observation.

More quantitatively, for DJF precipitation, the observational datasets cover 16-21 % of the global area with precipitation rates below 0.5 mm/day. These six GCMs, on the other hand, only yield from 1-9 % of the Earth's area below this low precipitation threshold. The substantial disagreements for this low tail of the precipitation distribution are an important cause for concern.

### Use of Histograms to Suggest Underlying Physical Mechanisms

Because the use of histograms is widespread in scientific studies, the statistical literature regarding their properties is extensive. Many of the spatial precipitation histograms developed for different regions or seasons show very interesting regularities that could be suggestive of underlying causal mechanisms. For example, when binned using the log(precipitation), the global JJA distribution shows a nearly linear drop-off for most of the upper tail of the distribution. For October, nearly the central 50% of the globe's area has a near-uniform distribution. It could be informative to determine what physical mechanism(s) give rise to this behavior in these distributions.

### Conclusions

The DJF and JJA precipitation distributions for the Legates-Willmott dataset show an interesting "resonance" feature due to gridpoints in the Southern Oceans. Six GCM simulations of current climate do not show this feature. However, the spatial distributions derived from these simulations all are at variance with observational data for low values of precipitation.

Although widely used in scientific work, the spatial histogram, representing the *entire distribution* rather than focusing merely on its average or variance has been under-utilized in climate work. The examples presented here show that, as another diagnostic, the technique can be useful in alerting the user to potential problems.

### Acknowledgement

This work was performed under the auspices of the U.S. Department of Energy , Environmental Sciences Division, under contract W-7405-ENG-48 to the Lawrence Livermore National Laboratory.

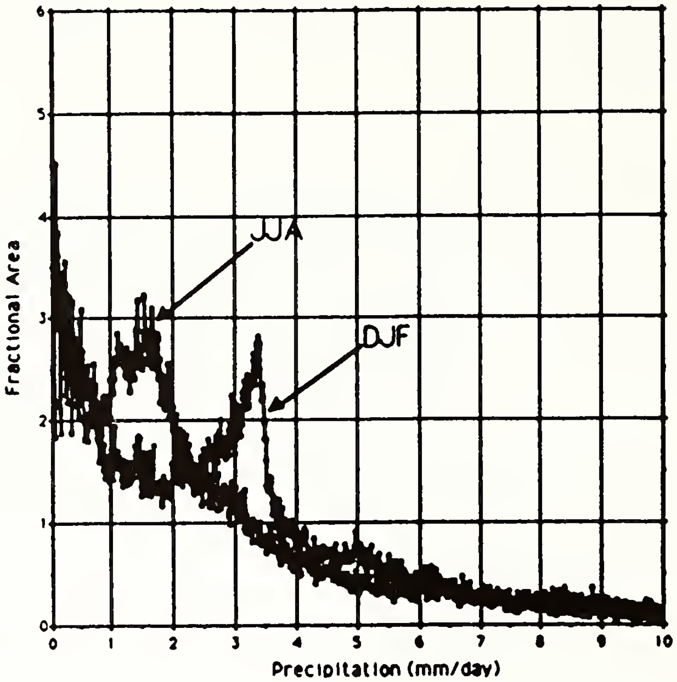

Figure 1 Area-weighted distributions of seasonally averaged DJF and JJA global precipitation. A "resonance" feature is clearly visible in both seasonal distributions.

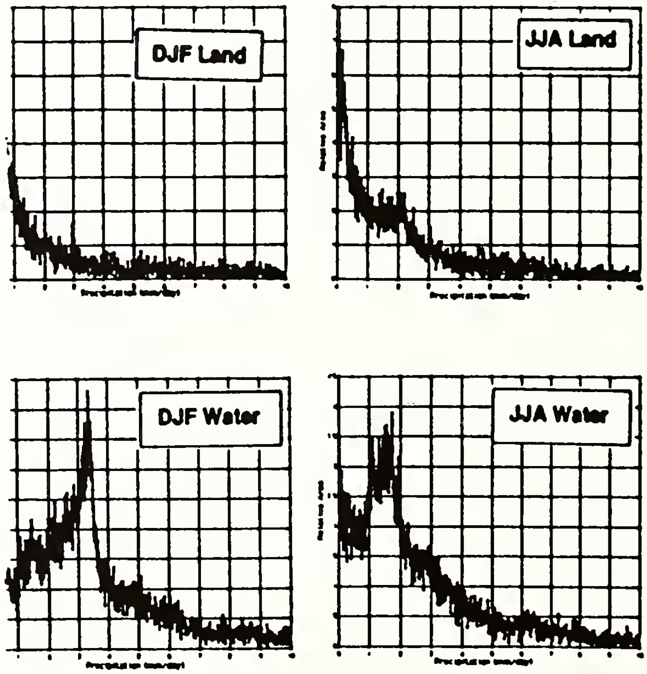

Figure 2 Area-weighted histograms of seasonally averaged DJF and JJA precipitation for land and water based gridpoints, separately. The resonance features are much more apparent in the water-based distributions in both seasons.

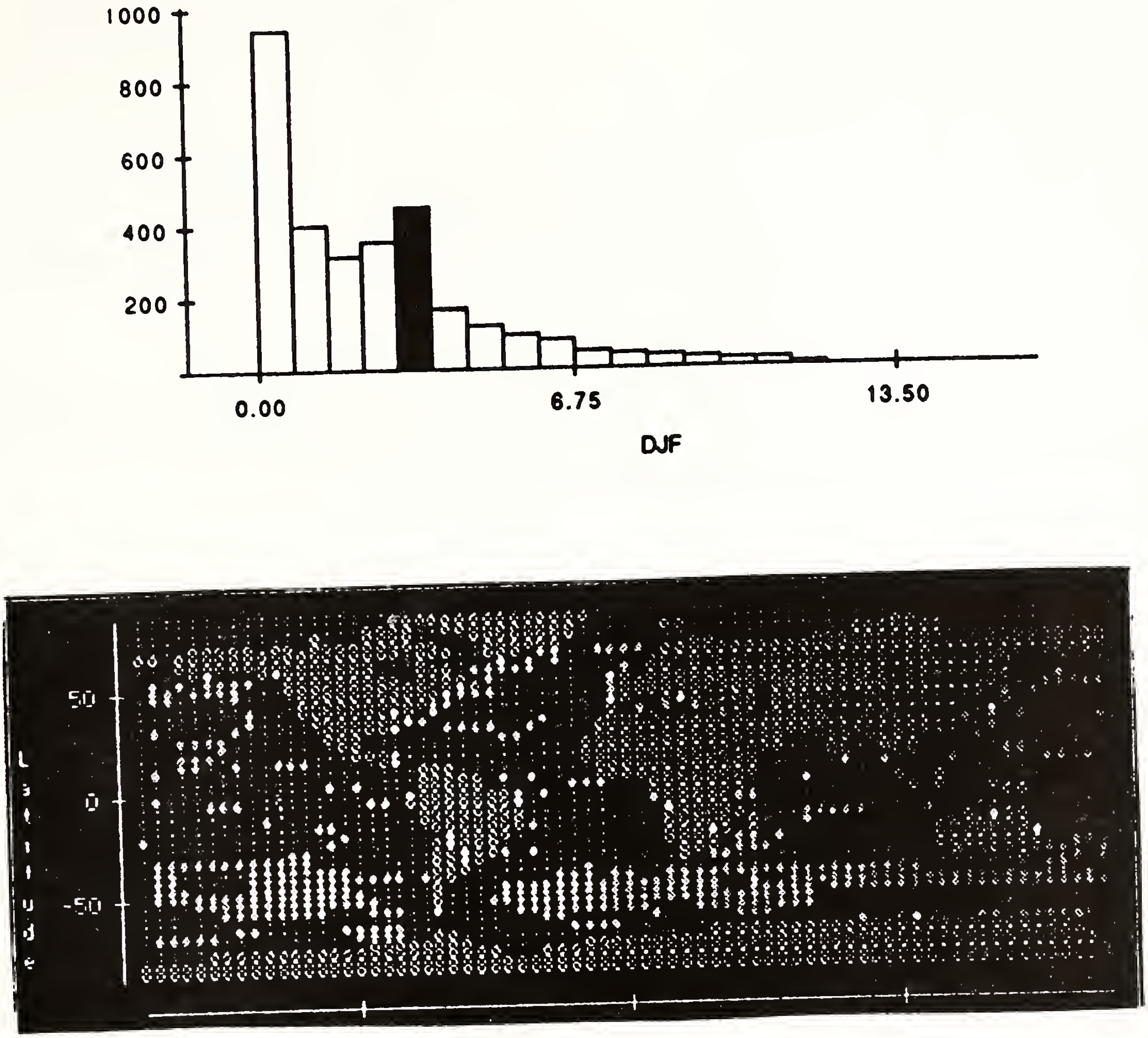

Figure 3 When a desired precipitation range of data is highlighted on the histogram the corresponding gridpoints in that range are also indicated on any other displays including maps. This capability permits the rapid location of the gridpoints in the range selected. Here, the points in the resonance region lie predominantly in the Southern Oceans.

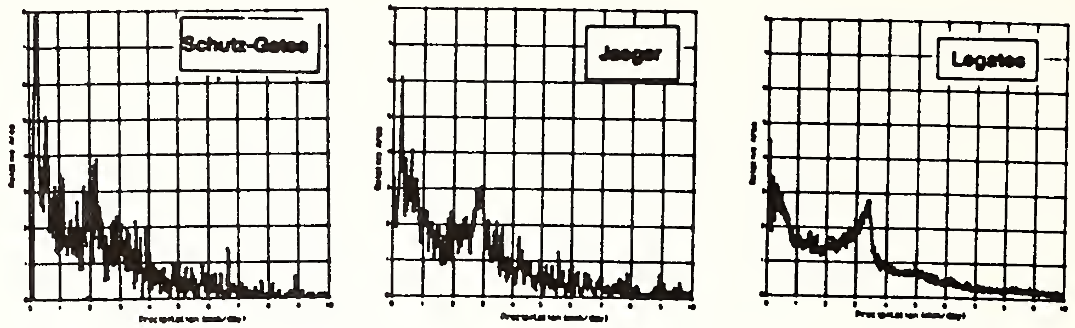

Figure 4 Area-weighted global histograms of seasonally averaged DJF precipitation for three observational datasets are displayed side by side.

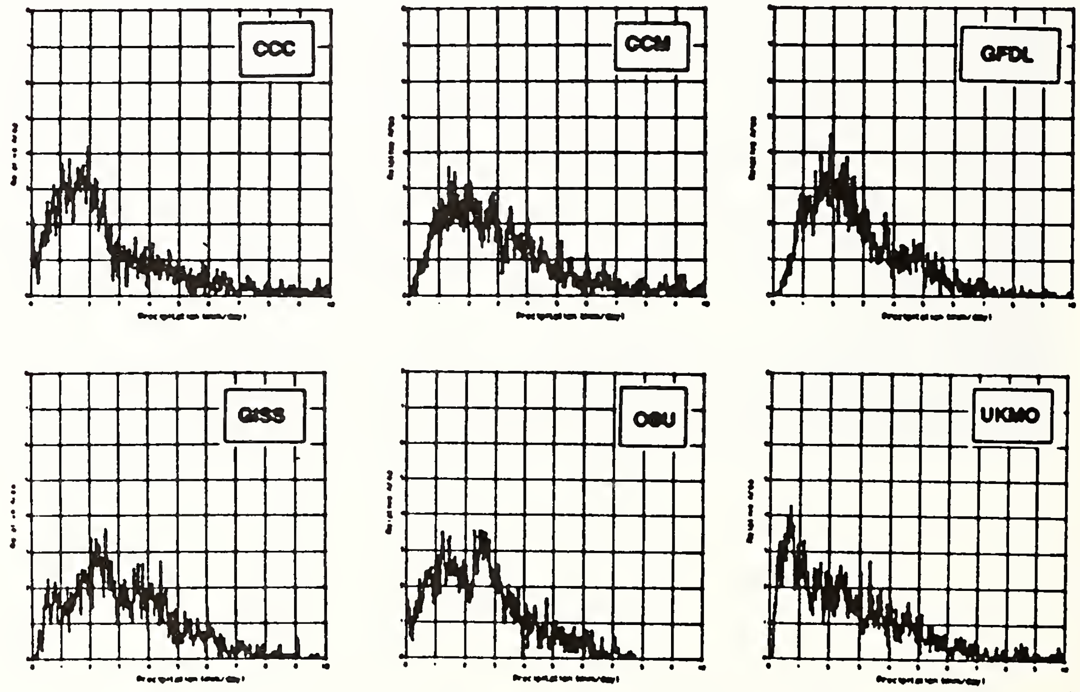

Figure 5 Area-weighted global histograms of seasonally averaged DJF precipitation for six GCM simulations of "current climate" are displayed side by side. When compared to observation (Fig. 4) there are distinct differences apparent, particularly in the lowest precipitation range (< 0.5 mm/day).

# MOISTURE FLUX ESTIMATES IN THE VICINITY OF SOUTH AMERICA

Muyin Wang, Jan Paegle, Julia Nogues-Paegle
Dept. of Meteorology, University of Utah
Salt Lake City, Utah 84112

The mid-latitude areas located poleward of the Amazon Basin and the Gulf of Mexico are two important agricultural regions of the world. Because of this, it is important to understand the principal sources of the atmospheric water vapor which control the local rainfall. It is commonly accepted that the Amazon Basin is a major source of water vapor for central portions of South America. However, the relative contributions of water vapor flux from the equatorially facing boundaries compared to the potential contributions from the eastward facing Atlantic coastlines has not been specifically addressed in previous studies. Moreover, the relative roles of different atmospheric layers to the water vapor flux has not been studied in detail for this region, the sensitivity of flux estimates to analysis method has not been quantified.

The present goal is to begin to fill these gaps in our understanding of the atmospheric component of the water vapor flux cycle. We will demonstrate that the Amazon Basin is indeed the principal moisture source for Central South America and show that most of the variability is associated with low-level wind systems just east of the Andes. Also we will describe the sensitivity of these results to analysis method.

The water vapor flux is computed from numerical approximation to:

$$
\begin{aligned}
Flux &= \int_0^Z \left[ \oint (qV_n)\, dS \right] dZ \\
&= -\int_{1000}^{300} \left[ \oint (qV_n)\, dS \right] \frac{dp}{g}
\end{aligned}
$$

Where $dS$,$dZ$ are path lengths, $V_n$ is the wind component normal to the corresponding path, and q is specific humidity. The box we chose is shown in Fig.1, and has east, west, north and south boundaries at $45°W$, $65°W$, $20°S$ and $40°S$, respectively. This region is located just south of the Amazon Basin, and includes almost all the agriculturally productive area. Figures 2a and 2b give summer time (January and February) monthly averaged moisture flux calculated for the above area. The results based on ECMWF data are indicated by shaded arrows in the figure. It is clear that the major moisture source in summer time is the Amazon Basin, and the Atlantic Ocean is a water vapor sink instead of a source.

To confirm our conclusion, we also do the same analysis using NMC (National meteorology Center) data. The results are given by open arrows in Fig.2. The two analysis systems give the same conclusion, regarding the relative importance of the Amazon Basin. The differences between NMC and ECMWF analyses will be discussed below.

We know that the low level jet sometimes plays an important role for controlling convection. But how important is it in the moisture flux transport?

Fig.2c and 2d shows results similar to those of Figs.2a and 2b, but only the boundary layer contributions, which means only the water vapor flux below 775mb included. Figs 2c and 2d show the averages over January and February, 1989, respectively. Comparing the north wall of Fig.2c and 2d with Fig.2a and 2b we find that most of the fluxes are contributed by the boundary layer. This is reasonable, because generally the water vapor content decreases rapidly with height. Comparing the east wall in the two figures, we see that only a very small amount of water vapor fluxes goes out from the boundary layer. In January the boundary layer outflow on the east wall is less than 8% of the total east wall outflow for both ECMWF and NMC data. In February, it is still about 8% in ECMWF data, but reaches 20% in NMC data.

Fig.3 shows day to day variations of moisture fluxes for the South American case. The solid curves are the total flux from all the four walls for the entire column(1000-300mb). The dashed curves show the contribution from the boundary layer(1000 and 850mb levels) of the north wall alone. Weak diurnal oscillations are evident on both curves. By examining the two curves shown in fig.3 we find that the day to day variations in the total moisture flux can be explained mainly by the boundary layer variations of moisture flux through the north wall. Similar comparisons were also done for the other walls(not shown), and we found that the strongest diurnal oscillations occur on the west boundary of the domain, where the low level jet is most active. Based on the studies about low level jet behavior we know that the low level jet would be expected to display strong diurnal oscillations and a nocturnal maximum during summer time east of the Andes. So we may consider that the day to day variations in the total water vapor flux is due to synoptic evolution of the low level jet.

Now we need determine how much the results depend upon data analysis system. This will give a crude estimate of the uncertainties in the two data sets.

Now let us first go back to Fig.1. The differences between the two analysis systems are especially big on the west boundary, where they have opposite signs to each other. The smallest differences are in north and east boundaries, where the differences are less than 10%. But overall the differences for the total fluxes are around 50% in January, and 100% in February. In February, ECMWF analyses show inflow , while NMC analyses suggest outflow.

The uncertainties in the western border may be partly due to the terrain effects. If we examine the box shown in Fig.1 more carefully, we see that the northern part of the west boundary intersects the Andes. We repeated the calculations for a box displaced eastward with the new west and east boundaries located at 60°$W$ and

40°$W$, respectively. This time we do get a better agreement on the west boundary, but a new problem arises in the south boundary. As shown in figure 4 in February, ECMWF gives inflow in the south boundary, while NMC gives outflow. One possible reason for this is because as we move the box eastward, most of its south boundary is located above the sea which is a data void. This time in the west boundary the two analyses give inflow for both January and February. Besides, the amount of the flux computed from the two analyses are much closer than before. Now the difference of the total net fluxes in January is only $0.03*10^8$kg/s, about 2%, and in February, is $0.49*10^8$kg/s, about 30%, which are much smaller than 52% for the original box. This result shows that around mountain areas the disagreement between the two analysis systems are very big.

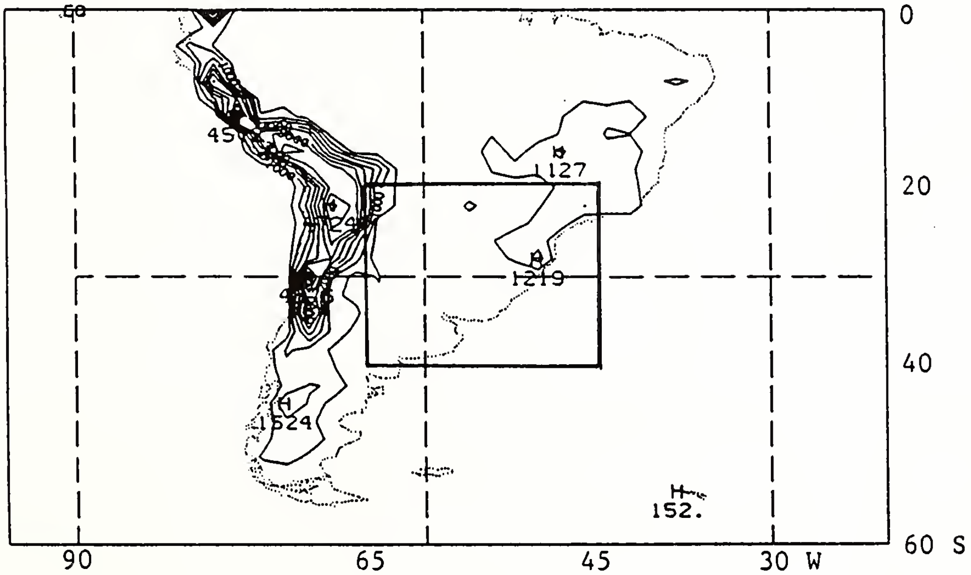

Fig. 1 South American topography (solid contours analyzed at 500m contour interval) and domains of moisture flux calculation (bold line square).

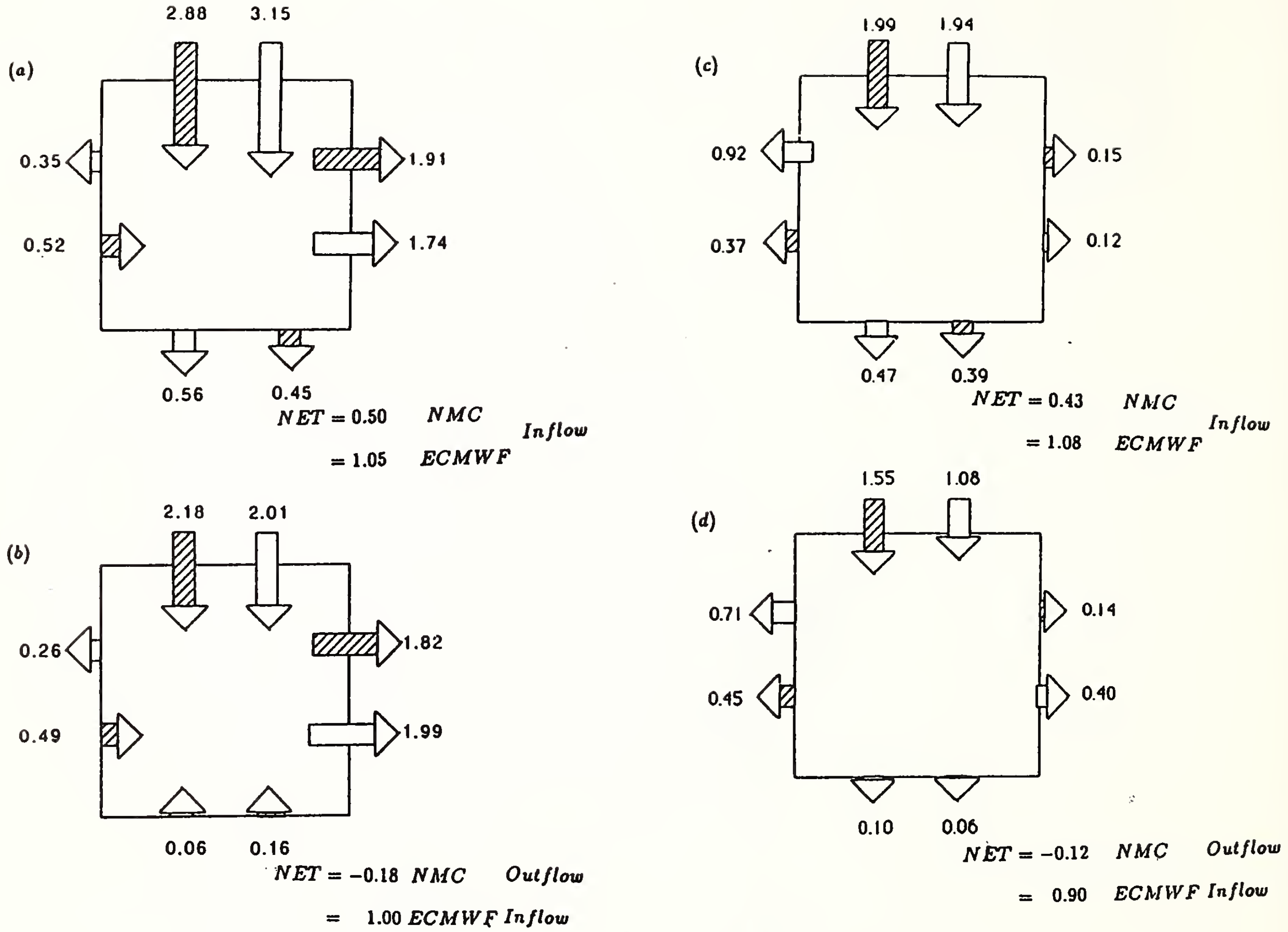

Fig. 2 Monthly average of water vapor flux over South America. The shaded arrows are the computation results based on ECMWF data and open arrows are based on NMC data. The unit of the arrows is $10^8$ kg/s. (a) January, 1989, for the whole coulumn(1000-300mb). (b) February, 1989, for the whole coulumn(1000-300mb). (c) January, 1989, boundary contributions(1000-775mb). (d) February, 1989, boundary contributions (1000-775mb).

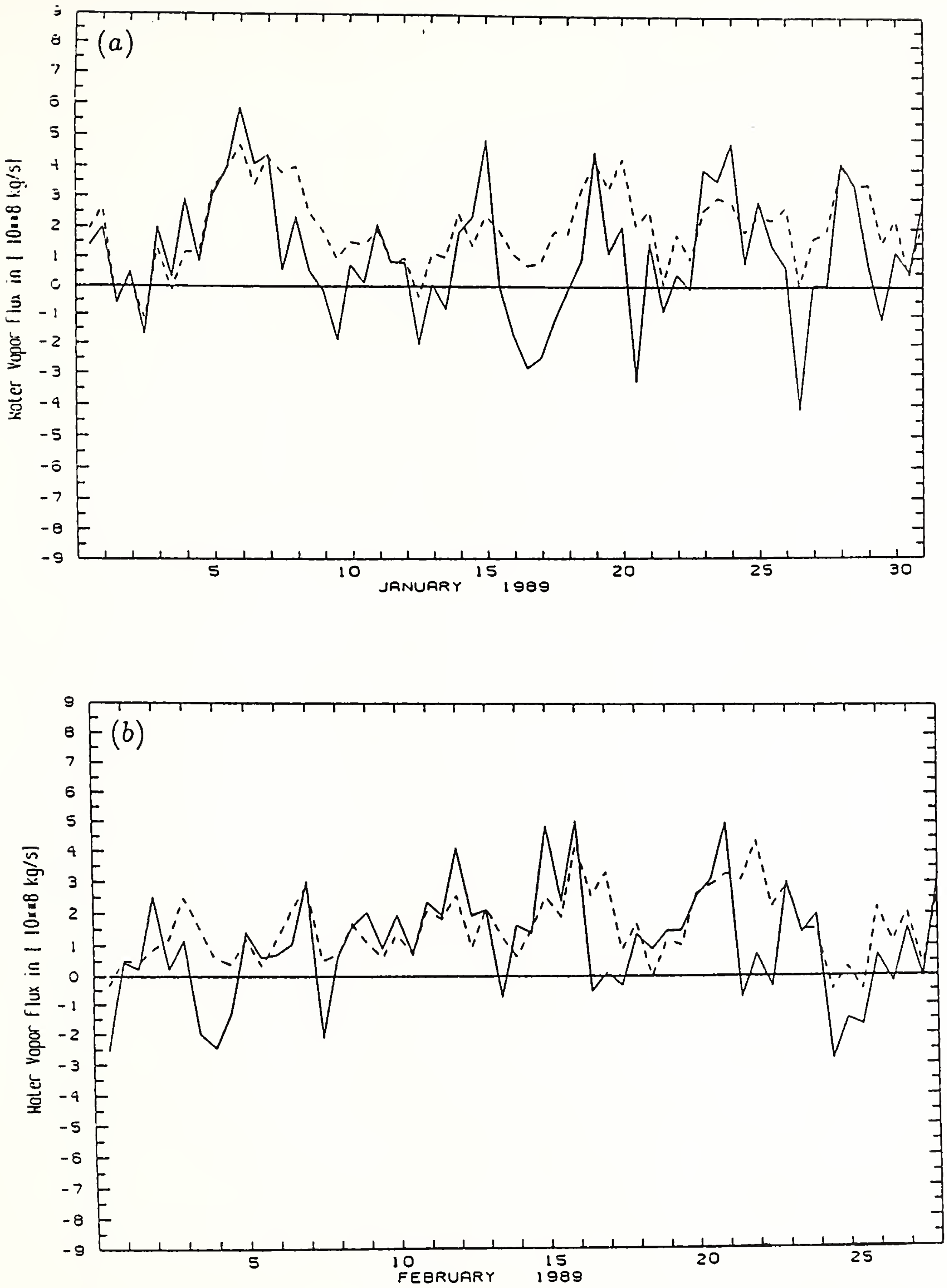

Fig. 3 Day to day variations of water vapor flux on boundary (1000-775mb) north wall (dashed line) and the total sum along the four walls for the whole column (1000-300mb) (solid line). (a) January, 1989. (b) February, 1989

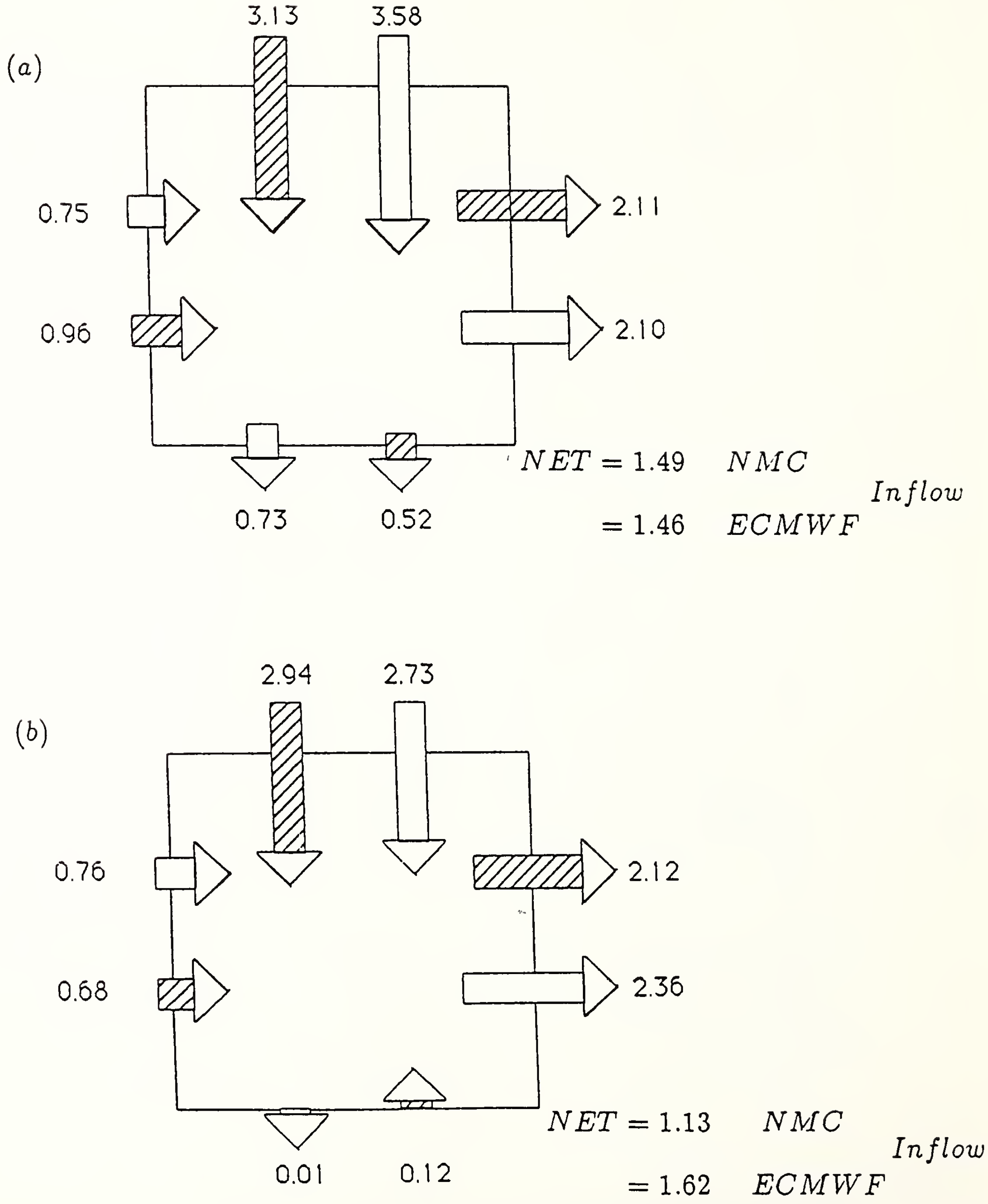

Fig. 4 As in Fig. 2.4, but for North American monthly averaged moisture flux for the whole column. (a) June, 1989, (b) July, 1989.

# A COMPARISON OF TROPICAL OCEAN MODELS: HINDCAST SKILL SCORES AND PHYSICAL PROCESSES DURING EL NIÑO EVENTS

Arthur J. Miller@, Tim P. Barnett@, Nicholas E. Graham@,
Josef M. Oberhuber# and Mojob Latif *

@Scripps Institution of Oceanography, La Jolla, CA 92093
#Meteorological Institute, University of Hamburg, 2000 Hamburg 13, Germany
*Max-Planck-Institute for Meteorology, 2000 Hamburg 13, Germany

Several different numerical models have been used routinely for hindcasting (and recently forecasting) tropical ocean variability. Many factors contribute to differences between model simulations, from differences in resolution, coordinate systems and wind stress forcing to more subtle differences like the influence of vertical mixing and the damping/forcing effects of surface heat flux parameterizations. It is therefore interesting to attempt to understand the major differences in model El Niño evolution among some of the most widely implemented models. Do the models hindcast SST anomalies with similar fidelity? Are the regions of highest hindcast skill the same from model to model? Are the structures of simulated El Niño events consistent among the models? Do the flux processes which control SST have comparable balances of terms in the heat budgets for the different simluations?

To begin to attempt to answer these questions, we examine here the similarities and differences in model El Niño development and decay in a subset of the ocean models which today form a primary basis for our understanding of tropical ocean response to wind stress variability. We force all the models considered here with the same winds (FSU) over the same time interval (1970-85). All the model SST anomalies are damped by Newtonian relaxation, although the details of the damping parameterization differs from model to model. The ocean models which we study are the Lamont model (Zebiak and Cane, 1987), the MPIZ model (Latif, 1987) and the OPYC model (Oberhuber, 1986, 1991; Miller et al., 1991). Hindcast skill of SST output (courtesy of Ben Giese) for the GFDL model (Philander and Siegel, 1985) is also discussed. The Lamont ocean model consists of a shallow-water layer (which predicts currents and thermocline depth) which influences a constant-depth model of SST. The MPIZ ocean model is similar to the GFDL model being set in $z$-coordinates with Richardson number-dependent vertical mixing. The OPYC model is formed from 8 isopycnal-coordinate interior layers which are fully coupled to a surface turbulent bulk mixed layer model.

Our primary variable for model/model and model/observations comparison is SST, since that is the most important variable in affecting the atmosphere. We use canonical correlation analysis to identify large-scale patterns of variability among model variables and the wind forcing. We examine in detail the terms in the surface layer temperature eqution which influence the variations of SST, namely, vertical advection/mixing processes, meridional and zonal advection, surface heat fluxes and model parameterized horizontal eddy diffusion (which is negligbly small).

Part of the differences in model responses can be attributed to the differences in background mean conditions upon which the anomalous response forms. The Lamont model has its climatology prescribed from observations, while the MPIZ and OPYC models must develop their own climatologies which will differ from each other and that observed.

As one measure of overall performance, Figure 1 shows the models versus observations in the so-called Niño-4, 3 and 2 regions of the tropical Pacific. In the western Pacific (Nino-4), the GCMs do a much better job of reproducing the observations than the simple model. In this region, the oceanic response is mostly locally forced by the wind. This results in is a very strong comparability of SST response among the GCMs in this region. For example, the correlation in SST between OPYC and GFDL is 0.87 in the Nino-4 region.

Also, the delay in the observed onset of the '82-'83 El Niño occurs in each of the three GCMs. In the eastern Pacific (Nino-3), where equatorial wave propagation has much more influence on the SST, similar results hold. OPYC and GFDL SST exhibit a 0.90 correlation there. The three GCMS each produce a similar 82-83 event, with a initial peak which is too weak and a follow up peak which is too strong with respect to the observations. The Lamont model has a better correlation here than in Nino-4, but it is still short of the level of the GCMs. For the cold events of the '70s, the MPIZ model appears to do the best job.

In the Nino-2 region, in constrast, the Lamont model outperforms the GCMS. The stronger correlation with observations is evident, and the 3 El Niñoevents of this time interval are fairly well reproduced by the Lamont model. Inspection of the three GCM time series reveals little "stand-out" evidence for El Niños except for the '82-'83 events. The three GCMs exhibits phase and amplitude discrepancies in their representations of the peak of the '82-'83 event, evidently a consequence of slightly different wave propagation and vertical mixing characteristics among the models.

Although the model variability when averaged over large regions compares rather well with observations (and among the models), the smaller scale structure of the model responses differs considerably from observations (and model to model) as can be seen in pointwise comparisons of model and observations. For example, rms error, $\epsilon \equiv T_m - T_o$, tends to accentuate regions of the basin where the models produce excessive SST variability. The Lamont model response is too large in the central eastern Pacific where the rms error is approximately 1°C, while in the remainder of the basin the error tends to vary between 0.4 and 0.7 C. The rms error plots of the MPIZ, GFDL and OPYC models each reveal twin peaks, one in the east and one in the west Pacific. The rms error in the western Pacific in the GCMs is due to the thermocline being too diffuse there.

In order to quantify the pointwise variability in rms error, we compute a skill score, $S = 1 - (\epsilon^2/T_o^2)$, which is a measure of the variance explained by the model hindcasts. Evidently $S = 1$ corresponds to perfect skill, while $S \leq 0$ implies excessively poor skill. Figure 2 shows the skill scores for SST fields which have been smoothed in time by a 5-month running mean. All three GCMs have a peak in skill in the central Pacific. The Lamont model skill maximum, in contrast, hugs the eastern boundary and is the strongest with values in the 0.60's south of the equator there. The MPIZ model produces a wide horseshoe-shaped skill maximum (values in the 0.40's and 0.50's) with significant skill north and south of the equator in the central Paciifc and along the equator in the eastern central Pacific, but dropping off near the eastern boundary. OPYC exhibits similar skill scores as the MPIZ model, but the peak is located more in the central Pacific with off-equatorial tongues of skill extending eastward from the central Pacific maximum. The GFDL skill tends to be smaller than the other two GCMs both in areal extent and amplitude. Of the GCMs, only the MPIZ model appears to have significant skill near the eastern boundary. In the western Pacific, all three GCMs have strongly negative skill.

A second quantitative measure of model verisimilitude, the anomaly correlation, $r \equiv < T_m T_o > /(\sigma_m^2 \sigma_o^2)^{1/2}$, accounts for SST time variations rather than the absolute variance levels of $S$. Plotted in Figure 4 is the pointwise anomaly correlation with the COADS observations for the four models. The results are fairly similar to the skill scores, although the areal extent of what might be considered to be useful results appears to be larger in the correlation maps than the skill maps. The three GCMs have maxima in the central Pacific while the Lamont model maximum occurs in the eastern basin and the along the South American coast. The largest correlations, more than 0.8, are found in the GFDL model in the central Pacific and in the MPIZ model in the central equatorial Pacific between 130W and 120W. All four models have correlations greater than 0.5 over a similar area of the domain, though OPYC also exhibits some 0.5 regions furthur poleward than do the other two models. The correlation results suggest that the three models are all producing significant results, but the four models yield their best results in different parts of the basin. This suggests that improvements in any one model may be made by identifying the reasons for the strengths of the other models.

It is of interest to consider the relationship of the models' anomalous SST error and the model SST anomalies themselves. This is because if there is a systematic relationship between model SST and SST error, the possibility exists (if the model response is nearly linear) that a large part of the error can be removed from the model runs by invoking a statistical error correction scheme to improve model performance. For example, if the model SST anomalies in a certain region are consistently too large by a factor of two, one can increase the strength of SST damping by including a Newtonian damping coefficient related to the error. If, however, the error is unrelated to the observed SST this formalism fails. Consider therefore, the correlation between error and SST, $\beta \equiv < \epsilon T_m > / \sigma_m^2$, for the three simulations (not shown). The three GCMS exhibit high values of $\beta$ along the equator with strongest values in the regions where the skill is lower. One can immediately see that in the Western Pacific, where the skill scores, $S$, are the worst for all four models, $\beta$ is very large for all four models, greater than 0.8 for the three GMCs and greater than 0.6 for the Lamont model. This suggests that the error there can be considerably reduced in the west Pacific in all four models and that significant improvements in modeling SST variability along the equator can be anticipated for the GCMs.

We examined canonical correlation analysis (CCA) modes and reconstructions of the '82-'83 El Niño event for the three models for which we had upper-ocean heat budgets, the terms of which are anomalies of SST, zonal advection, meridional advection, vertical advection/entrainment and heat flux. By this means we can determine which terms are predominant for the development of the model El Niños.

In the Lamont model, the dominant CCA mode is associated with 52% of the SST variability in the basin (Figure 4a). In line with what we have seen from the skill maps, the strongest signal in SST is near the Coast of South America and the amplitude drops off in the western basin. The pattern has one sign across the entire equatorial Pacific. In the eastern basin, where the mode is strongest, the dominant process which establishes this SST mode is upwelling. To a much lesser degree, zonal advection (in the west-central Pacific) and meridional advection (north and south of the equator in the eastern basin) also contribute to the exitation of this mode.

For the MPIZ model, we find that the first CCA mode explains 26% of the basinwide SST variance. This mode (Figure 4b) has one sign across the equatorial Pacific, with maximum amplitude near 160W. The CCA mode reveals that all three advection components contribute significantly to this mode. However, near-equatorial meridional advection appears to control the strong basin-wide signature of this mode. Zonal advection (in the west Pacific) and vertical advection (in the eastern Pacific) contribute somewhat lesser affects along the equator.

The second CCA mode of the MPIZ model (10% of the total variance of SST) has a nodal line near 160W with SST anomalies of opposing sign over each side of the basin. With roughly the same balance of forcing terms as the first mode, it tends to be 90 degrees out of phase with the first, indicating cool SST in the Eastern basin preceding El Niño and warm SST in the Eastern basin following the development of the basin-wide warm anomaly of CCA mode 1. The net effect of the first and second CCA modes thus suggests an eastward propagation of the warm events. The third CCA mode (11% of the variance of basinwide SST) tends to be associated with the cold events of the mid-70's and '84-'85. With broad basin scale and the maximum near 180W, the balance of terms is again roughly the same as the previous modes.

The top CCA modes of OPYC each contribute to the development of El Niño events. The first two modes (9% and 20% of total SST variance) have broad equatorial scale with largest amplitudes in the western basin, the first mode being distinguished by an opposite-signed region off the coast of South America. The third mode (11% of total SST variance) is more confiend to the eastern basin with peak amplitude in SST near 100W. The balance of terms which affect SST tends to be different for the eastern basin and the central/western basin. In the eastern basin, warming due to anomalous downwelling and meridional advection is counterbalanced by cooling by zonal advection. In the central/western basin, the balance is similar to the MPIZ model with zonal advection and near-equatorial meridional advection warming SST. Inspection of the time series for these three modes indicates that during course of the 82-83 event, the sequence of CCA mode excitation was -3, -2 , 1, 2, 3. The indicates a cool east Pacific before the event followed by a warming in the central Pacific progressively expanding towards the South American coast. In contrast, during the '72-'73 event, the third mode was excited first (warming in the Niño-2 and 3 regions) followed by the first and second modes (warming in the interior ocean).

The reconstructions of the '82-'83 events (using the top three CCA modes) in the three models tend to reveal the same features seen in the analysis of the CCA modes alone. All three models exhibit characteristic patterns of SST forcing by zonal advection along the western flank of the developing SST anomaly, meridional advection north and south of the equator and upwelling/entrainment effects along the equator and along the eastern flank of the SST anomaly (Barnett et al., 1991). But the three models show different dominant balances of the three terms. For the Lamont model, upwelling tends to control the large-scale structure of the El Niño response. For the MPIZ model, meridional and zonal advection dominate the large-scale pattern of SST which evolves. In the OPYC model, the three forcing terms are of comparable amplitude.

In summary, the models each appear to have their maximum skill in different regions of the basin. By attempting to ascertain how the models produce their El Niños, we can determine why the models perform better in different regions. leading us to develop better ocean models.

*Acknowledgments.* Support was provided by NOAA Grant NA90-AA-D-CP526, NASA Grant NAG5-236, the Vettleson Foundation and the University of California INCOR program for Global Climate Change. Supercomputing resources were provided by the Department of Energy through Lawrence Livermore National Laboratories and by the National Science Foundation through the San Diego Supercomputer Center and the National Center for Atmospheric Research. Tony Tubbs and Jack Ritchie of SIO did much of the computational analysis of the data from the models.

## References

Barnett, T. P., M. Latif, E. Kirk, and E. Roeckner, On ENSO Physics, *J. Climate, 4*, 487-515, 1991.

Latif, M., Tropical ocean circulation experiments, *J. Phys. Oceanogr.*, *17*, 246-263, 1987.

Miller, A. J., J. M. Oberhuber, N. E. Graham and T. P. Barnett: Tropical Pacific Ocean response to observed winds in a layered general circulation model. Submitted to *J. Geophys. Res.*, 1991.

Oberhuber, J. M., About some numerical methods used in an ocean general circulation model with isopycnic coordinates, in *Advanced Physical Oceanographic Numerical Modeling*, J. J. O'Brien, ed., Reidel, pp. 511-522, 1986.

Oberhuber, J. M., Simulation of the Atlantic circulation with a coupled sea ice - mixed layer - isopycnal general circulation model, submitted to *J. Phys. Oceanogr.*, 1991.

Philander, S. G. H. and A. D. Siegel, Simulation of El Niño of 1982-1983, in *Coupled Ocean-Atmosphere Models*, J. Nihoul, ed., Elsevier, pp. 517-541, 1985.

Zebiak, S. E. and M. A. Cane, 1987: A model ENSO, *Mon. Wea. Rev.*, **115**, 2262-2278.

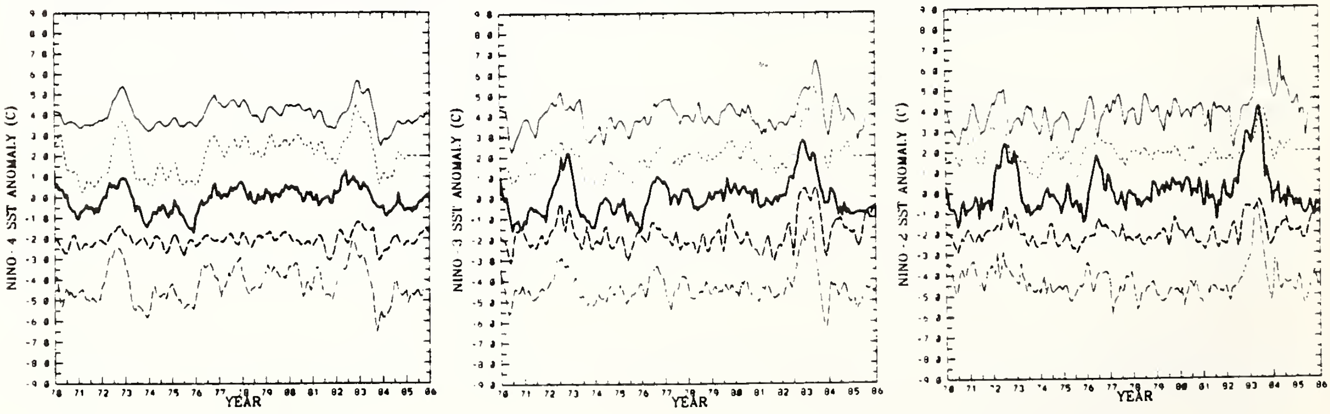

**Figure 1.** Time series of SST anomalies in Niño-4, 3 and 2 regions for COADS (thick), OPYC (thin), GFDL (short dash), Lamont (thick dash), MPIZ (long dash).

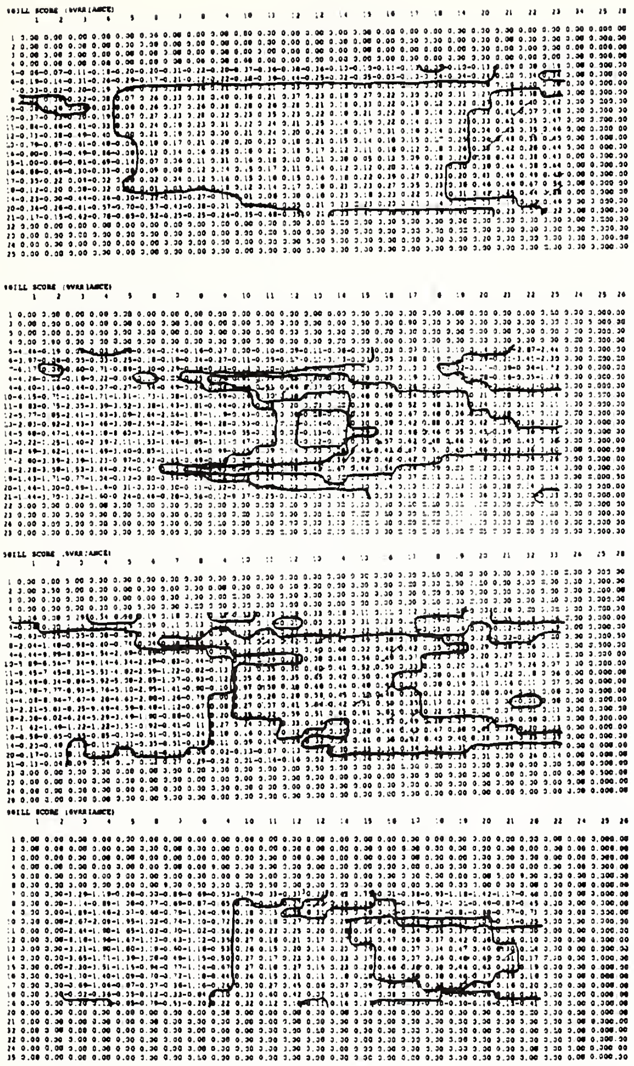

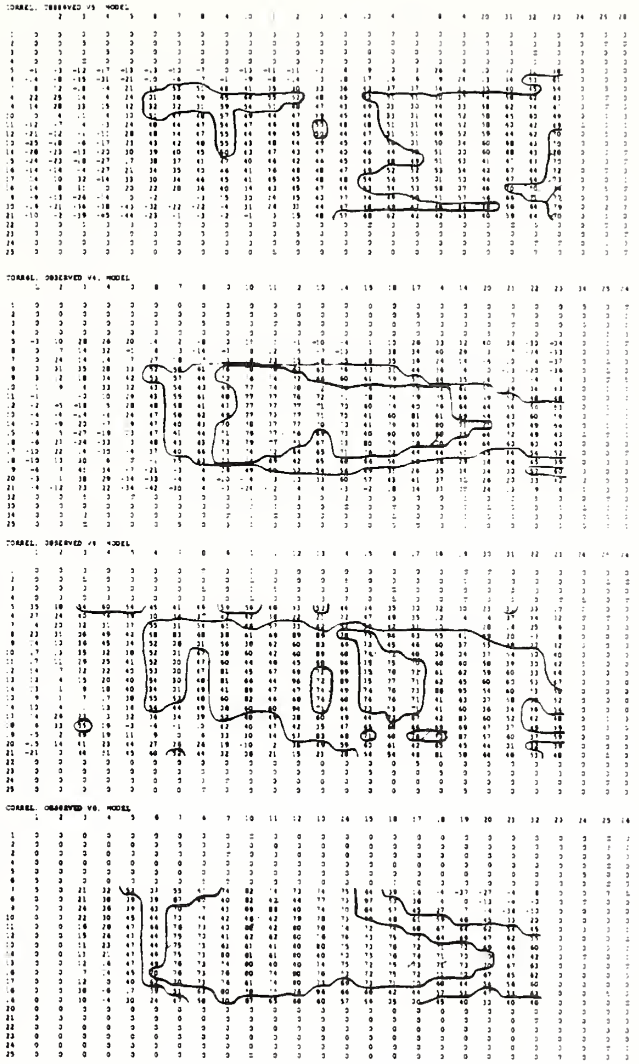

**Figure 2**. Left: Skill scores for (top to bottom) Lamont, MPIZ, OPYC and GFDL models, each smoothed by a 5-month running mean. The zero line and the 0.3 levels are contoured. The stretched latitudinal coordinates are indicated in Figure 4, e.g. 13 corresponds to the equator, 10 to 2N, 7 to 8N and 5 to 16N. The longitudinal coordinates are als shown in Figure 4, e.g., 1 corresponds to 139E, 8 to 179W and 23 to 89W.

**Figure 3**. Right: As in Figure 2, but for anomaly correlation. The 0.5 and 0.7 levels are contoured.

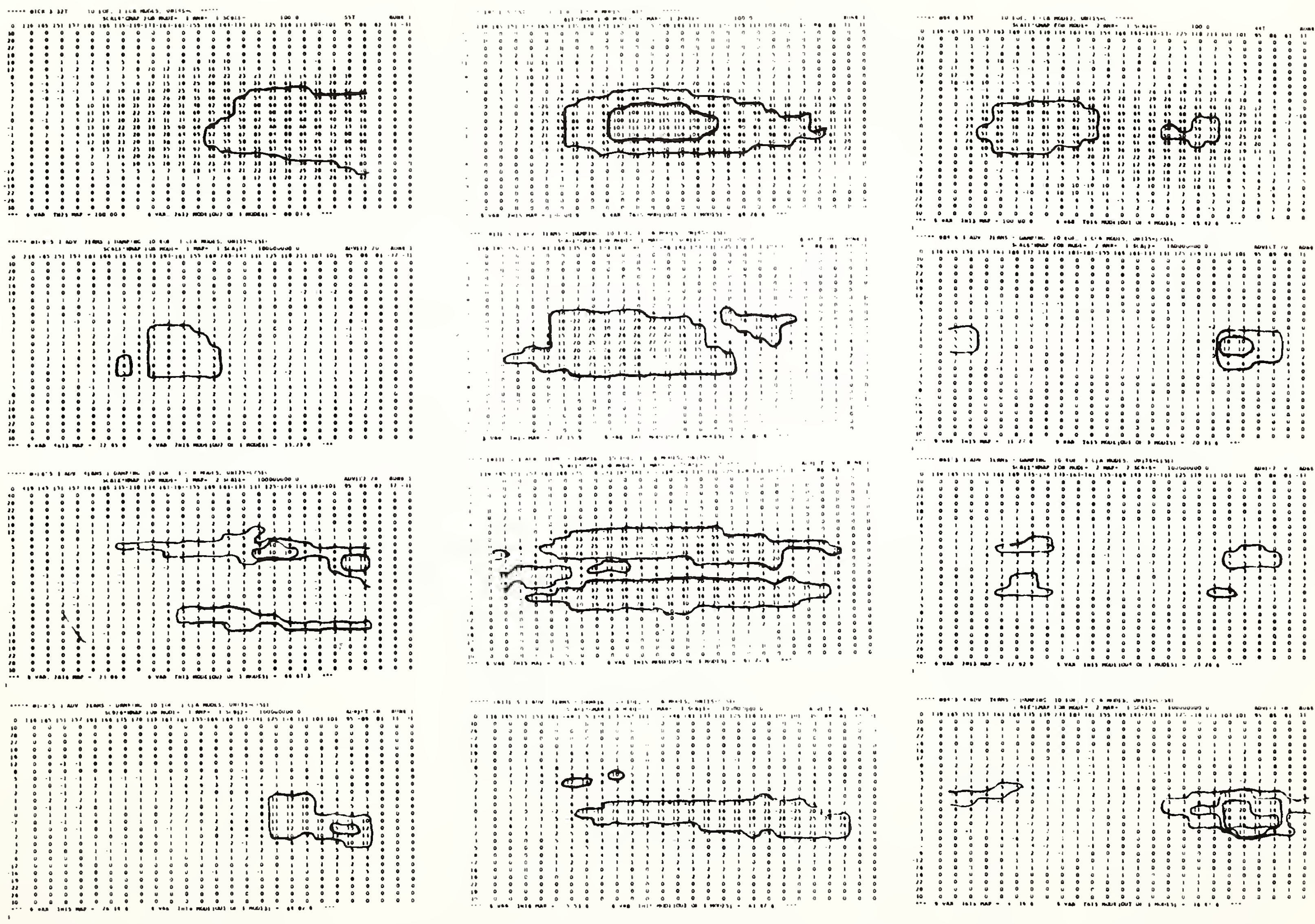

**Figure 4.** Canonical correlation analysis modes for (a) Lamont model: mode 1, 52% of basin-wide SST variance, (b) MPIZ model: mode 1, 26%, and (c) OPYC model: mode 2, 20%. (top to bottom) Maps of SST (CI=0.5C), zonal advection (CI=$5\times10^{-8}$C/s; except 10 is the only contour for the MPIZ model), meridional advection (CI as in zonal) and vertical advection/entrainment (CI as in zonal) are shown; time series of the modes are not shown.

# Considerations of the Predictability of ENSO with a Low Order Coupled Model

Nicholas E. Graham and Tim P. Barnett
*Scripps Institution of Oceanography, La Jolla, CA 92093*

Mojib Latif
*Max-Planck-Institut für Meteorologie, Hamburg, Federal Republic of Germany*

## 1. *Introduction*

The El Niño-Southern Oscillation (ENSO) is the most energetic manifestation of recurring interannual variability in the present global climate system. Although apparently expressed and determined to an important degree by processes internal to the tropical Pacific, ENSO has major effects on the climate over much of the Pacific Hemisphere and beyond. Clearly then, the goal of forecasting the evolution of the ENSO cycle is important from both practical and theoretical perspectives. Even imprecise forecasts would benefit large numbers of people. Further, its recurrent character provides an good testing arena for models and hypotheses concerning larger issues of climate variability and change.

Although many coupled models, covering a wide taxonomic range of complexity and purpose [see McCreary and Anderson, (1991) and Neelin et al. (1992) for reviews], reproduce some aspects of ENSO-like behavior, only that described by Zebiak and Cane (1987; henceforth ZC) has been extensively tested as a forecast tool. The apparent predictive ability of this relatively simple model (henceforth the STANDARD model) has been discussed by Cane et al. (1987; cf. Barnett et al. 1988).

More recently, Goswami and Shukla (1991; henceforth GS) have explored some of the predictive characteristics of the STANDARD model in detail. As the primary validating index for the model forecasts, GS use simulated NIÑO3 (90° W - 150° W, 5° N to 5 ° S) SST anomalies from an integration (henceforth the CONTROL simulation) of the ocean component of the model forced with observed [Florida State University (FSU)] surface wind stress data. Goswami and Shukla indicate that, although observed NIÑO3 SST data are reliable, the use CONTROL values as a validating index allows consistent comparisons between other CONTROL and forecast variables (for which the observations are not as good). It is also possible that such an approach might reduce the effects of systematic errors in the ocean model on the model forecasts. Whatever the justification, it is important to note that there is an implicit assumption underlying conclusions drawn on the basis of such comparisons. This assumption is that the observed wind data used to force the model, and the model's response (in terms of SST) to that forcing, are sufficiently accurate (in comparison to observations) to provide a relevant validating standard.

One of the main findings of GS is that the growth of model forecast errors appears to be governed by two separate processes with distinct time scales. One of these (GS termed this the "fast" process), has a doubling time of 4 to 5 months and describes the rapid divergence of forecast and CONTROL NIÑO3 SST at short lead times. Goswami and Shukla suggested that the fast process is in large part due to the inability of the atmospheric component of the model to accurately simulate the large-scale patterns of surface wind variability, and to the fact that the model wind field is (to a high degree) determined only by the contemporaneous SST field.

The other process of error growth (the "slow" process) identified by GS has a much longer doubling time of about 15 months. They suggest (as have others) that the slow, somewhat systematic evolution of this process is the manifestation of a robust quasi-oscillatory mode present in both the real and simulated coupled ocean-atmosphere systems, the existence of which underlies any ability the model may have in providing useful forecasts at long lead times. The distinction between "fast" and "slow" processes was also noted by Blumenthal and Cane (1989) whose innovative statistical analysis of the model's behavior clearly indicated the presence of two modes of forecast evolution, one that decays rapidly, and a similar one that decays much more slowly.

In this note we describe the results of experiments motivated by a desire better understand the findings of GS (and those of Blumenthal and Cane), and perhaps improve the forecast performance of the STANDARD model. These experiments fall into three categories. First we repeated the forecast experiments of

GS, emphasizing comparisons with both OBSERVED (here indicating a combination of COADS and CAC data) and CONTROL NIÑO3 SST. Second, in recognition of the systematic problems with the atmospheric component of the model noted by GS, we replaced the atmospheric component of the model with statistical formulations based on the historical field-to-field relationship between tropical Pacific SSTs and surface wind stress. Third, the character of the STANDARD model's predictability is examined using the "perfect model" approach. We explore the model's performance in an idealized setting where the model physics are exactly correct, but where the the observations of surface wind stress (used to initialize the model) are flawed.

The results of this suite of experiments lead to some unexpected and intriguing hypotheses concerning the behavior of the STANDARD model and the predictability of ENSO. Among these is the suggestion that the "fast" error growth process reflects the presence of spurious high frequency variability in the CONTROL SSTs rather than serious shortcomings in the coupled model. These errors in the CONTROL SSTs are probably due to a convolution of both real and spurious signals in the observed wind data with the highly parameterized ocean model physics.

Further, the results clearly suggest that the coupled model has considerable useful skill at time scales of up to about 1 year, and that the character of this predictive ability is consistent with what would be seen in a model with approximately correct physics.

## 2. *Construction of statistical atmospheric models*

The statistical atmospheric model was calculated as follows. Given SST ($T$; in this note these came from the CONTROL simulation) and FSU-Lamont surface wind stress ($\tau$) data sets (for 1967-90) express each in terms of "fixed-phase" EOFs (i.e., a separate set of EOFs for each calendar month; cf. Hasselmann and Barnett, 1981) so that (for a specified month)

$$T = \alpha e$$

$$\tau = \beta f$$

Here $\alpha$ and $\beta$ are the EOF temporal coefficients and $e$ and $f$ are the spatial coefficients. The use of a fixed-phase rather than "time invariant" formulation (one model for all months) allows some account to be taken of the modulation of the atmospheric response to a given SST anomaly pattern by the total SST.

Next, with subscripts denoting mode indices, obtain the matrix of regression coefficients ($C$) relating the EOFs of the two fields;

$$C_{m,n} = \frac{< \alpha_m \beta_n >}{< {\alpha_m}^2 >}$$

where $< \ldots >$ denotes the expectation of the enclosed expression. Coupled simulations with the statistical-dynamical coupled model (SDCM) proceed using the SST field produced by the oceanic component ($T^\star$) of the model to generate a statistical estimate of the associated surface wind stress field ($\hat{\tau}$), *vis*,

$$\alpha^\star = e\, T^\star$$

then, taking advantage of the orthogonality of the EOFs,

$$\hat{\beta} = C \alpha^\star$$

and finally

$$\hat{\tau} = \hat{\beta} f$$

There remains the question of choosing the number of EOF modes to be used to represent each field. For the results described here, models were constructed using 3, 6, and 9 EOF modes from each field. It is important to place these values in perspective; Latif et al. (1990) and GS present results showing that wind stress fields reconstructed with just a few "time invariant" EOFs will produce much of the ENSO time scale variability in the two wind-driven ocean models. Their results thus suggest that there are not, in fact, 9 EOFs worth of information in the system modeled here.

This question of the number of variables required to describe the system raises the issue of artificial skill. The coefficients obtained from empirically fitted models respond to chance correlations as well as systematic "real" relationships, and this behavior becomes more exaggerated as the number of useless or redundant predictor variables is increased. Thus, empirical models tend to perform better when tested against the data used in their derivation (i.e., to hindcast) than in a true forecast setting (hence the term "artificial skill").

One method of estimating the true forecast skill of a statistical model is cross-validation. In cross-validation, subsets of paired predictor and predictand data are deleted from the sample and the statistical model constructed using the remaining cases. The model so derived is then applied to the deleted cases. Under the assumption that the information in the deleted sample is independent from that in the retained sample, the model "predictions" so obtained give an unbiased estimate of how the model would perform in an actual forecast setting (Stone 1974; Michaelsen 1985). As applied to the wind stress and SST data used here, the decorrelation time of approximately one year allowed the sequential deletion of single samples in deriving the cross-validation estimates of model performance [each fixed-phase regression model was based on 24 cases (years)].

A second method for obtaining an estimate of true forecast skill is to develop the model using one part of the data set, then use that model to make predictions for the remaining data. In the work described here, we applied this "subset" technique by deriving the statistical models for the 1965-75 period, and then used these models in prediction experiments with initial conditions for 1976-90.

Hindcast tests with the statistical atmospheric model shows that it performs well at reproducing the zonal wind anomalies in the central equatorial Pacific with correlations of 0.7 to 0.8 using 9 EOFs from each field. Using cross-validation the correlations are slightly lower, typically 0.65 to 0.75, showing that the effects of artificial skill appear to be modest (for this variable).

## *3. Results*

Figure 1 shows correlations of forecast NINO3 SST from the STANDARD model as a function of lead time using both CONTROL and OBSERVED NINO3 as a reference (for 288 forecast simulations initialized January, 1967 through December, 1990; each 24 months in length) Note the rapid drop in correlation with lead time during the first several months in the CONTROL curve; this is a manifestation of the "fast" error growth process noted by GS. Also shown is the corresponding correlation curve for the average of six consecutive forecasts validating at the same time ("lag averaged" forecasts). Lag averaging makes little systematic improvement when the validating measure in CONTROL NINO3. [A curve showing correlations *vs.* lead time for a fixed-phase, first-order Markov (autocorrelation) model (similar to persistence) is shown if Fig. 4].

Compare the CONTROL curves with those in which the observed NINO3 SST is used as a reference (henceforth OBSERVED will denote comparisons with observations) Note three features: the OBSERVED curves are much flatter and show no evidence of a "fast" error growth process; the OBSERVED correlations are considerably higher than the CONTROL values at lead times more than 4 months; lag averaging systematically raises the OBSERVED correlations.

The character of these differences is intriguing; on the average, the forecast trajectories evolve away from the CONTROL system considerably faster than from the real system. Why is there no "fast" error growth in the OBSERVED curves? Under what circumstances would a coupled model predict "reality" better than the evolution of one of its components driven with an observed forcing field? The SDCM results described below may provide some insight.

Figure 2 shows the correlation curves for the hindcast SDCM models using 3, 6 and 9 EOFs, here referenced to CONTROL NINO3 SST (same 288 initial conditions used for the STANDARD model). In comparison with the corresponding STANDARD model curve, each shows clear improvement with much less suggestion of a distinct "fast" error growth process. Note too that increasing the number of EOFs increases the hindcast skill of the model.

These results show that when operated in a hindcast setting the statistical atmospheric models avoid the behavior responsible for the "fast" process in the STANDARD model. At the same time they raise further questions. How are these problems avoided ? Should we infer that there are really 9 EOFs (or more) worth of useful information in the system ? Such a finding that would plainly disagree with the results of Latif et al. (1989) and GS? Is artificial skill in the SDCM influencing the results even though one of its components is dynamic? If so, what does this suggest about the nature of the "fast" process ?

For some guidance, consider the results from the cross-validation and subset models shown in Fig. 3. Both correlation curves (for 9 EOF models; others are similar) show a rapid decay of forecast performance nearly identical to that seen in the STANDARD model-CONTROL comparison. It seems reasonable to conclude that the hindcast SDCM results are contaminated by artificial skill, an idea consistent with the hindcast model's improvement in forecast performance with increasing number of independent variables (i.e., more EOF modes). In the SDCM integrations, artificial skill can come into play by improving the surface wind stress field produced at model initialization. To the degree that the statistically produced wind stress field is correct at the initial step of a forecast simulation, the SST field at the end of that step will also be correct (i.e., identical to CONTROL). Given this correct (or nearly so) SST field, the statistical model would then produce the correct wind field for the second step, and so on.

The decline in performance of the SDCM under independent validation emphasizes a critical point; much of the increase in SDCM hindcast skill (over the standard model) results from asystematic relationships between the surface wind and CONTROL SST fields, i.e., artificial skill. Does the nearly identical performance of the independently validated SDCMs and the STANDARD model suggest something about the nature of the "fast" error growth process? Consider the two experimental results presented so far. First, the standard model predicts OBSERVED NIÑO3 SST much better than CONTROL (at lead times longer than 4 months) and, in the former case, shows no suggestion of a "fast" error growth process. Second, although the SDCMs did an excellent job of hindcasting CONTROL SSTs, their estimated true forecast skill is nearly identical to that of the STANDARD model.

A hypothesis that is consistent with these findings is the following: the "fast" process does not result from the introduction of errors by the atmospheric component of the coupled model, rather it reflects the presence of spurious variability in the CONTROL SSTs. This spurious variability probably arises from interactions between both correct and incorrect elements of the ocean model's physics (particularly the thermodynamic parameterizations) with both real and spurious signals in the observed surface wind stress data. The fact that these interactions apparently have little effect on the evolution of the model coupled system (*vis.* the slow decline of the OBSERVED correlation curve in Fig. 1) can be understood when consideration is given to the distinct difference between the rapid response time scale of the ocean model SST field and the much longer time scale of the model dynamics (see the model equations in ZC). As a consequence, high frequency variability in the surface winds is readily expressed by the model SST field, but tends to be filtered out in the dynamic response. In fact, experiments show that even if the SST anomaly field is set to zero everywhere at the initial step of each forecast simultion, after a few months the SST forecasts are quite similar to those obtained using the usual forecast method. Thus, to an important degree the evolution of the coupled system is determined by the dynamical signals contained in the model ocean at initialization.

To test this hypothesis the following "perfect model" experiment was performed. First, the STANDARD model was allowed to run for an extended period on its own. The fields from this simulation represent the "reality" of an idealized world where the model physics are exactly correct. Next, the surface wind stress fields from this integration were perturbed by adding normally distributed noise with a fixed variance to the temporal amplitudes of the EOFs of the model wind field. The amplitudes were then smoothed with a 1-2-1 filter and scaled so that each EOF accounted for its original fraction of the total variance. The resulting wind fields retain realistic spatial coherence with the smallest scale features (the high EOF modes) having the lowest signal-to-noise ($\frac{S}{N}$) ratio. The operation of perturbing the wind field represents the process of imperfectly observing and analyzing the real wind field; thus the perturbed winds taken to be (in a broad sense) analogous to the available surface wind stress products. Here the amplitude of the noise had a variance equal to the total signal variance so that the resulting field has an overall $\frac{S}{N}$ ratio of 1.0.

The perturbed winds are then used to drive the ocean model and produce the restart files required to make forecast simulations. The SSTs produced by this simulation are analogous to the CONTROL SSTs. Finally, a suite of (288) forecast integrations were conducted using the restart files; the resulting SSTs are analogous to the usual STANDARD model forecasts.

This experiment allows examination of the sensitivity of the coupled model forecast system (albeit in an idealized setting) to observational errors in surface wind stress used to initialize the ocean component of the model. To the degree that the contrast between the correlation *vs.* lead time curves referenced to

"CONTROL" and "OBSERVED" NIÑO3 from the experiment resembles that seen in Fig. 1, the results will be consistent with the idea that the "fast" process is one of error decay rather than error growth. These curves are shown in Fig. 4. It is clear that there is considerable similarity between the behavior of the forecast system in this idealized setting and that seen in the real world trials.

The results outlined above are consistent with the hypothesis that the "fast" process is (in part at least) the result of wind-induced errors in the CONTROL SST field. There are also clear indications that the physical basis of the STANDARD model and the paradigm behind the forecast methodology are sound.

*Acknowledgements.* Many thanks to M. Cane and S. Zebiak for many useful discussions concerning the design of these experiments and interpretation of the results (not to mention the use of their model). This work was supported in part by NSF under Grant ATM89-11592, by NOAA under Grant NA86AA-D-CP104 for the Experimental Climate Forecast Center at Scripps Institution of Oceanography, and by a grant from the G. Unger Vetlesen Foundation to the Scripps Institution of Oceanography.

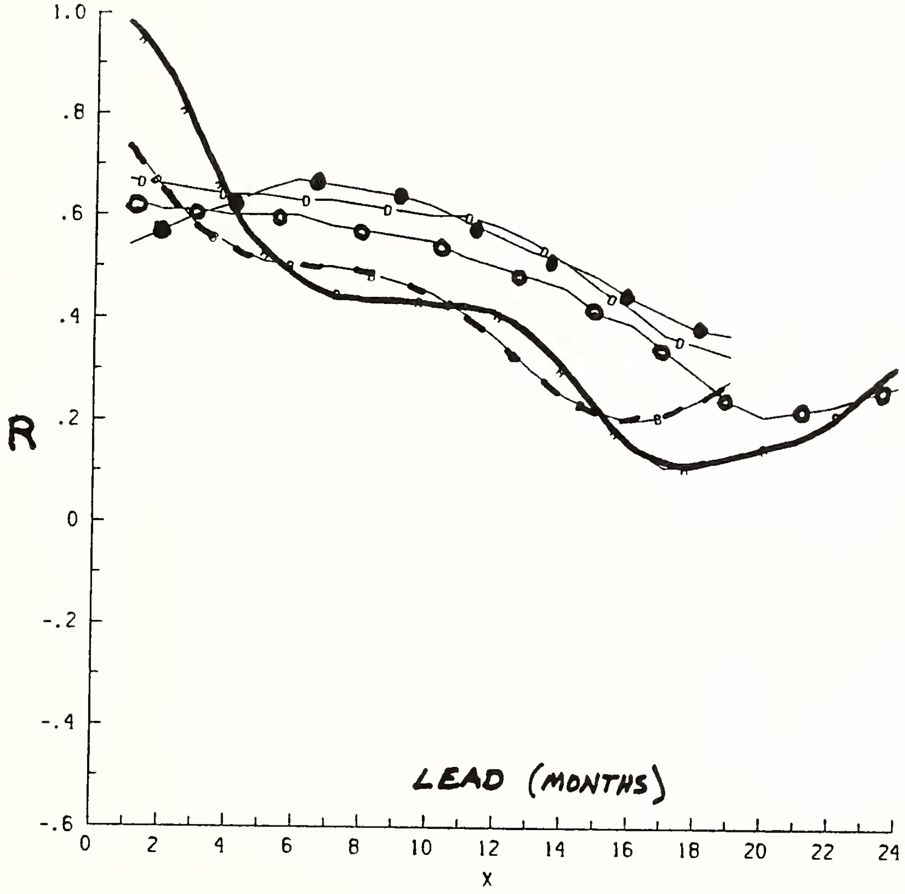

Figure 1. Correlations *vs.* forecast lead time for STANDARD model, for 288 24-month forecast simulations, initial conditions 1/1967 - 12/1990. Curves are listed by validating NIÑO3 data source: CONTROL (solid); CONTROL, lag averaged (dashed); OBSERVED (open circle); OBSERVED, lag averaged (thin solid); OBSERVED, initial SST field set to zero, lag averaged (closed circle).

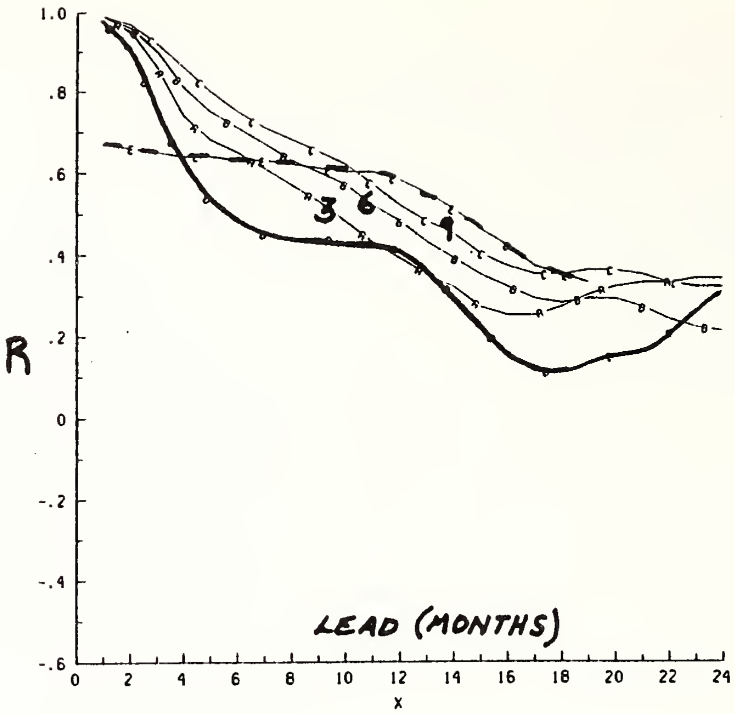

Figure 2. Correlations *vs.* forecast lead time for STANDARD and SDCM models, for 288 24-month forecast simulations, initial conditions 1/1967 - 12/1990. Curves listed by validating NIÑO3 data source: CONTROL, STANDARD MODEL, (solid); OBSERVED, STANDARD MODEL, lag averaged (dashed). Other curves are for SDCM hindcasts using 3, 6, and 9 EOF modes from SST and $\tau$ fields.

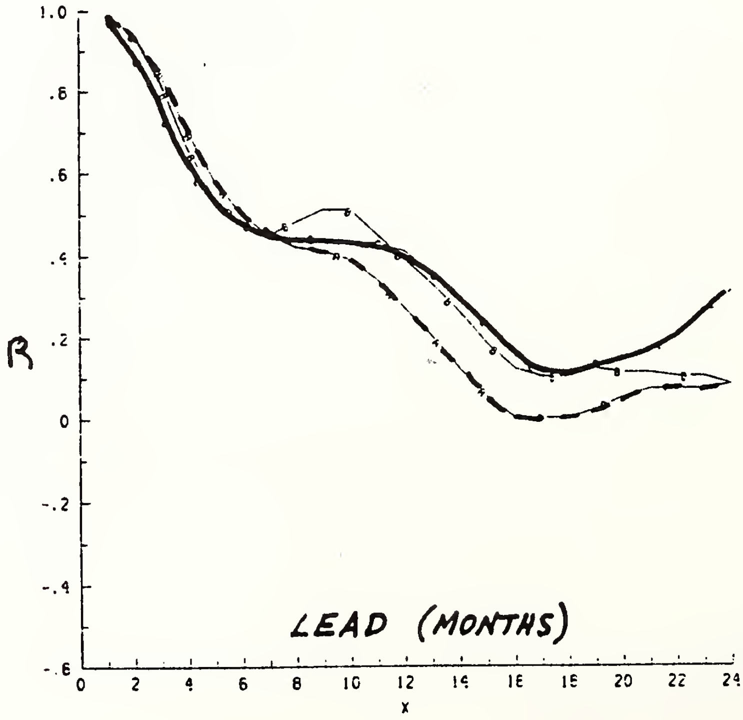

Figure 3. Correlations *vs.* forecast lead time for STANDARD and SDCM models; all referenced to CONTROL NIÑO3 SST. STANDARD MODEL (as in Fig. 1, solid); (cross-validated) SDCM using 9 EOF modes (1967-90, dashed); subset SDCM (thin solid, 1976-90, see text).

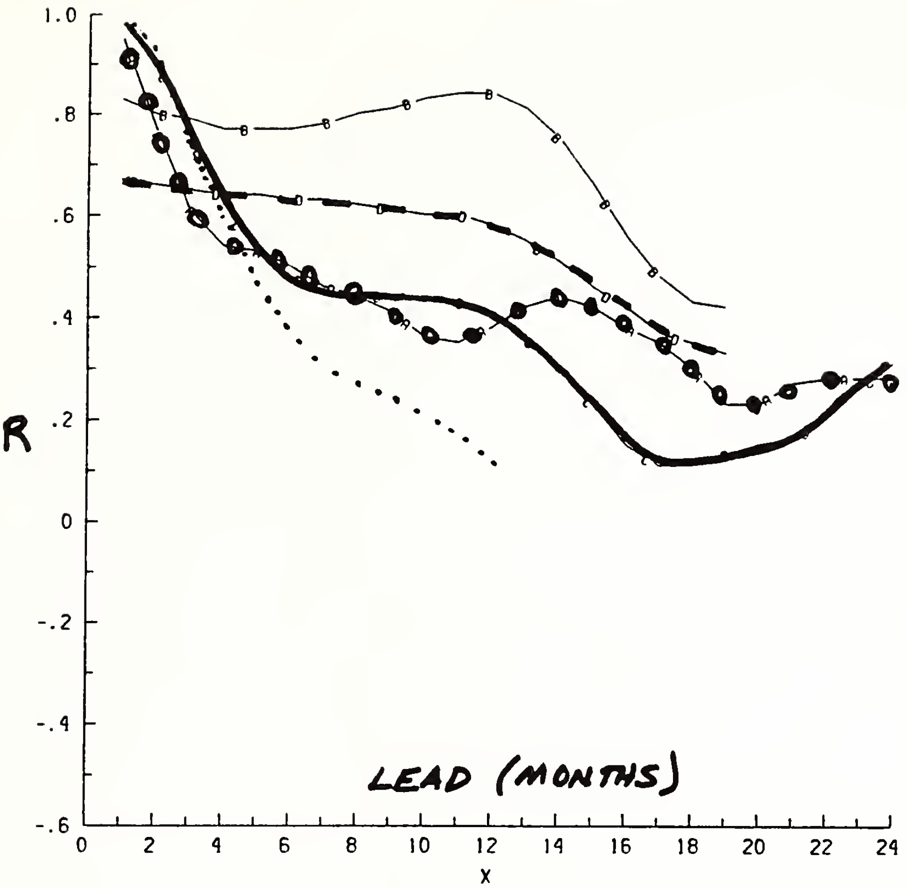

Figure 4. Correlations *vs.* forecast lead time. Solid and dashed curves are from actual forecasts referenced to CONTROL and OBSERVED NIÑO3 (as in Fig. 2). Open circle and thin solid curves are analogous curves from "perfect model" experiments; open circles, referenced to simulated SSTs from ocean model with degraded wind stress data; thin solid, referenced to "real" SSTs from free running STANDARD model. Dotted line is for "fixed-phase" first-order Markov process.

## Seasonal Forecasts Can Be Used in Fire Management Planning

Morris H. McCutchan, Bernard N. Meisner,
Francis M. Fujioka, and Richard A. Chase

Pacific Southwest Research Station
USDA Forest Service
4955 Canyon Crest Drive
Riverside, CA 92507-6099

The effectiveness and efficiency of the wildland fire management program is dependent upon matching the planned protection organization and budget for each local area as closely as possible to the wildfire severity potential for the area during the fire season. However, the severity of individual local fire seasons–and the related fire protection requirements–can vary significantly from year to year with weather conditions. Since the basic protection organization must be planned and implemented before the fire season, the organization typically is based on meeting some arbitrary "average worst" level of historically experienced wildfire severity. This planning strategy has been required because of the inability to estimate the wildfire severity potential (and its consequences in terms of expected fire suppression costs and resource losses) for a given local area. As a result, the budgeted local protection force often does not match the actual weather conditions. A methodology for planning the annual fire protection program and efficiently allocating resources based on a forecast of local seasonal wildfire severity over broad areas has been suggested (Chase 1991).

The authors know of no routine forecasts of seasonal wildfire severity for the United States, particularly as severity is evaluated vis-a-vis expected weather, as in this study. The Climate Analysis Center (CAC) of the National Weather Service has been routinely issuing seasonal forecasts of average temperature and total precipitation for nearly a decade (Wagner, 1989). The CAC forecasts were not specifically designed to predict wildfire severity. Nevertheless, we decided to determine whether the forecasts could be used in fire management planning.

This paper reports a preliminary study of the accuracy of using the CAC forecasts as the basis for fire management planning in the western United States.

### Data

The temperature and precipitation data used in this research are from 10 fire weather stations representative of the weather at seven National Forests (Figure 1 and Table 1). These forests are primarily decadent mixed conifer stands with a heavy accumulation of litter and downed woody material. A major portion of the downed material is greater than 3 inches in diameter and responds slowly to variations in temperature and precipitation. Such fuels are classified as type G in the National Fire Danger Rating System (Deeming, et al., 1977).

We first needed to determine whether a relationship exists between observed seasonal mean temperature, total precipitation, and wildfire severity potential. The National Fire Danger Rating System's burning index (Deeming, et al. 1977), when accumulated over the fire season, is a measure of seasonal wildfire severity potential for a particular National Forest. For each fire weather station we computed the accumulated burning index (ABI), the seasonal mean temperature, and the total precipitation for June-August (the primary fire season on these forests) using all available data (Table 1). The values of ABI, temperature, and precipitation were each sorted and categorized as Below Normal (lower 30 percent), Near Normal (middle 40 percent), or Above Normal (upper 30 percent).

Categorical seasonal forecasts of temperature and precipitation from the Climate Analysis Center for June-August 1983-1990 were tabulated for each site. A forecast was considered to be either Above or Below Normal whenever the indicated likelihood for that category exceeded 35 percent. Seasonal forecasts issued before 1983 were not presented in terms of categorical percentages and thus could not be used.

## Analysis and Results

We constructed 3x3x3 contingency tables relating the observed mean temperature and total precipitation categories to observed ABI (Table 2). We found a good relationship between seasonal temperature and precipitation and the ABI, with precipitation as the primary discriminant. For example, when the precipitation was Below Normal, the ABI was most often Above Normal, regardless of the temperature. Near Normal precipitation would most often result in Near Normal ABI. When the precipitation was Above Normal, the ABI was most likely Below Normal, unless the temperature was concurrently Above Normal; then the ABI was most often Near Normal. We found less correlation between seasonal temperature, precipitation and wildfire severity potential at locations where the fuel types are primarily grasses and shrubs, because these fuels primarily respond to daily variations in temperature and precipitation. Therefore, seasonal weather forecasts may be more useful in forests with woody fuel types.

Having found a good relationship between the observed temperature and precipitation and ABI, we looked at the relationship between the forecast seasonal temperature, precipitation and observed ABI (Table 3). The relationship was weak, which may be the result of several factors: the total number of cases (10 sites x 8 years) was relatively small; a large number of the forecasts were for Near Normal temperature and precipitation; and the number of Near Normal ABI's was greater than expected, while the number of Above Normal ABI's was smaller than expected. With little variation in both the forecast weather and the observed ABI's, it was difficult to determine a relationship between them.

We also compared the forecasts with the reported weather at the sites. The precipitation forecasts had a Heidke skill score of 0.11, while the temperature forecasts had a Heidke skill score of -0.10. The precipitation skill is comparable to previously published results (Wagner, 1989), but the temperature skill is substantially less than expected. This low skill may be due to the fact that many of our sites were in areas where the potential predictability and, most likely, the actual predictability are low (Barnett, 1981).

## Application to Fire Management Planning

To demonstrate how the seasonal forecasts might be used in fire management planning, we trained an artificial intelligence (AI) computer program (Naylor, 1985) to differentiate among Above Normal, Near Normal and Below Normal ABI's for each site using the observed temperature and precipitation data. We then provided the forecast temperature and precipitation, and compared the program's predicted ABI categories with those observed.

The ABI was correctly predicted 62 percent of the time for Mt. Elizabeth, CA and 75 percent of the time for McKenzie River, OR. One might expect similar results for the other West Coast sites–Boulder and Cinnamon, OR–where the potential predictability is also high (Barnett, 1981). However, the available training data sets for those sites were smaller than those for Mt. Elizabeth and McKenzie River. With fewer training data, the AI program is less likely to determine the true relationship among the variables. The potential predictability for the Idaho and Montana sites is much lower (Barnett, 1981) and the CAC forecasts reflected that fact, as most of the forecasts were for Near Normal temperature and precipitation. With little variance in the forecast temperature and precipitation, the AI program was unable to predict the larger variance in the observed ABI's. For the eight sites where the AI program was able to determine a relationship between temperature, precipitation and ABI, in only a few instances did the predicted ABI differ from that observed by more than one category.

## Concluding Remarks

We found a good relationship between seasonal wildfire severity potential and *observed* seasonal mean temperature and total precipitation for forests where woody fuels are dominant. Thus, accurate predictions of seasonal weather could be used in fire management planning to accurately predict wildfire severity potential.

The relationship between wildfire severity potential and *forecast* temperature and precipitation was weak. Because wildfire severity potential was more closely related to precipitation than to temperature, and because precipitation is more difficult to predict accurately, one would expect a weaker relationship with forecast values. In addition, at many of the sites in this study both the actual and potential predictability of seasonal temperature and precipitation are low. We also noted an unusually small number of seasons with Above Normal wildfire severity potential since the CAC forecasts have been issued as categorical probabilities. As more data become available, the relationship between forecast weather and wildfire severity potential might be better defined. Even with the overall poor relationship, we have shown that it is feasible to use predictions of seasonal wildfire severity potential in fire management planning for some sites. Forecasts for regions where the predictability is higher should have even greater utility.

Many forests have fuel types that are dominated by grasses and brush. At those locations wildfire severity potential may be more closely related to temperature, rather than precipitation, and the accumulated burning index (ABI) might not be the best measure of wildfire severity potential for the fire season. Once appropriate weather and wildfire severity parameters are identified, it might be possible to forecast seasonal wildfire severity potential for a variety of locations and fuel types.

## References

Barnett, Timothy P. 1981: Statistical prediction of North American air temperatures from Pacific predictors. *Mon. Wea. Rev.*, 109, 1021-1041.

Chase, Richard A. 1991: Incorporating seasonal severity into annual fire program planning. p. 34-41 *In* Proc. 11th Conf. Fire and Forest Meteor., Missoula, MT, April 16-19, 1991. Soc. Amer. Foresters, Bethesda, MD.

Deeming, John E., Robert E. Burgan and Jack D. Cohen. 1977: The National Fire Danger Rating System–1978. USDA Forest Service Gen. Tech. Rep. INT-39, 63 p. Intermountain Forest and Range Experiment Station, Ogden, UT 84401.

Naylor, Chris. 1985: Build Your Own Expert System. Halstead Press, New York, NY, 249pp.

Wagner, A. James. 1989: Medium- and long-range forecasting. *Weather and Forecasting* 4, 413-426.

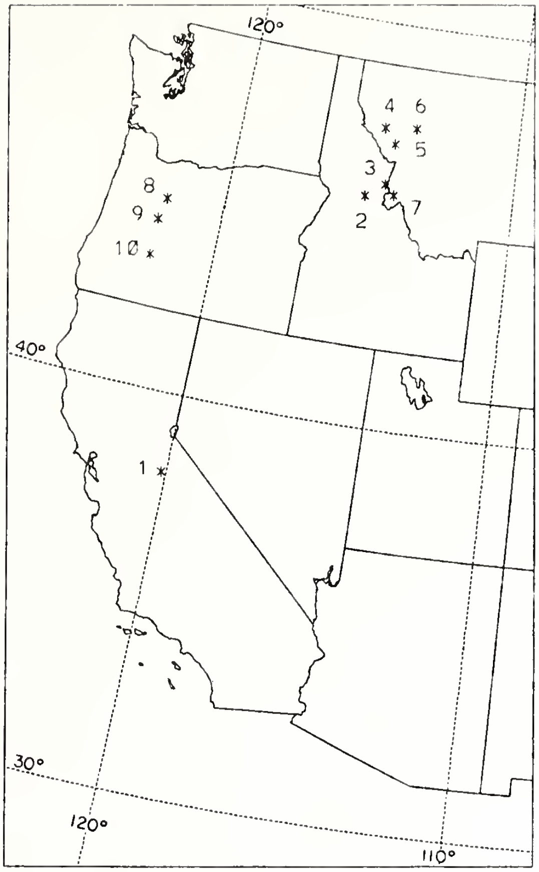

Figure 1. Location of fire weather stations used in this study. (See table 1 for a description of each station.)

Table 1. Description of the fire weather stations used in this study.

| No. | Name | State | National Forest | Elev (ft) | Lat (deg) | Long (deg) | Site | Aspect (deg) | Period of Record |
|---|---|---|---|---|---|---|---|---|---|
| 1. | Mt. Elizabeth | CA | Stanislaus | 4938 | 38.04 | 120.15 | Valley | 315 | 1961-1990 |
| 2. | Red River | ID | Nez Perce | 4600 | 45.72 | 115.21 | Slope | 180 | 1954-1990 |
| 3. | Moose Creek | ID | Nez Perce | 2460 | 46.07 | 114.55 | Valley | None | 1954-1990 |
| 4. | Plains | MT | Lolo | 2510 | 47.43 | 114.85 | Valley | 195 | 1954-1990 |
| 5. | Nine Mile | MT | Lolo | 3300 | 47.08 | 114.42 | Valley | 230 | 1954-1990 |
| 6 | Condon | MT | Flathead | 3684 | 47.53 | 113.72 | Valley | 180 | 1961-1990 |
| 7. | West Fork | MT | Bitterroot | 4390 | 45.83 | 114.20 | Ridge | 225 | 1961-1990 |
| 8. | Boulder | OR | Willamette | 3570 | 44.70 | 122.00 | Valley | 360 | 1978-1990 |
| 9. | McKenzie | OR | Willamette | 1500 | 44.16 | 122.16 | Valley | 360 | 1961-1990 |
| 10. | Cinnamon | OR | Umpqua | 4636 | 43.26 | 122.14 | Valley | None | 1970-1990 |

Table 2. Contingency tables of observed accumulated burning index (ABI) when observed mean temperature (T) and total precipitation (P) are above, near, or below normal for June-August for varying periods of record at 10 representative fire weather stations on 7 National Forests in the Western United States.

a. When P is above normal

| | | | T | | |
|---|---|---|---|---|---|
| | Frequency | Above | Normal | Below | Total |
| | Above | 3 | 6 | 1 | 10<br>12% |
| ABI | Normal | 11 | 9 | 7 | 27<br>31% |
| | Below | 28 | 16 | 5 | 49<br>57% |
| | Total | 42<br>49% | 31<br>36% | 13<br>15% | 86<br>100% |

b. When P is near normal

| | | | T | | |
|---|---|---|---|---|---|
| | Frequency | Above | Normal | Below | Total |
| | Above | 6 | 14 | 11 | 31<br>28% |
| ABI | Normal | 10 | 27 | 21 | 58<br>52% |
| | Below | 7 | 12 | 4 | 23<br>20% |
| | Total | 23<br>21% | 53<br>47% | 36<br>32% | 112<br>100% |

c. When P is below normal

| | | | T | | |
|---|---|---|---|---|---|
| | Frequency | Above | Normal | Below | Total |
| | Above | 8 | 13 | 26 | 47<br>62% |
| ABI | Normal | 3 | 12 | 8 | 23<br>30% |
| | Below | 0 | 2 | 4 | 6<br>8% |
| | Total | 11<br>14% | 27<br>36% | 38<br>50% | 76<br>100% |

Table 3. Contingency tables of observed accumulated burning index (ABI) when forecast mean temperature ($T_f$) and total precipitation ($P_f$) are above, near, or below normal for June-August, 1983-1990, at 10 fire weather stations on 7 National Forests in the Western United States.

a. When $P_f$ is above normal

| | | $T_f$ | | | |
|---|---|---|---|---|---|
| | Frequency | Above | Normal | Below | Total |
| ABI | Above | 1 | 2 | 0 | 3<br>30% |
| | Normal | 1 | 1 | 0 | 2<br>20% |
| | Below | 1 | 4 | 0 | 5<br>50% |
| | Total | 3<br>30% | 7<br>70% | 0<br>0% | 10<br>100% |

b. When $P_f$ is near normal

| | | $T_f$ | | | |
|---|---|---|---|---|---|
| | Frequency | Above | Normal | Below | Total |
| ABI | Above | 1 | 7 | 2 | 10<br>15% |
| | Normal | 5 | 23 | 8 | 36<br>55% |
| | Below | 4 | 13 | 3 | 20<br>30% |
| | Total | 10<br>15% | 43<br>65% | 13<br>20% | 66<br>100% |

c. When $P_f$ is below normal

| | | $T_f$ | | | |
|---|---|---|---|---|---|
| | Frequency | Below | Normal | Above | Total |
| ABI | Above | 0 | 0 | 2 | 2<br>50% |
| | Normal | 0 | 0 | 1 | 1<br>25% |
| | Below | 0 | 1 | 0 | 1<br>25% |
| | Total | 0<br>0% | 1<br>25% | 3<br>75% | 4<br>100% |

# Forecast Skill and Low Frequency Variability in 90-day integrations of a GCM

Wilbur Chen and Huug van den Dool

Climate Analysis Center
NOAA/NWS/NMC

A series of 90-day numerical integrations using the Medium Range Forecasting (MRF) model were conducted at the National Meteorological Center (NMC) by Drs. Saha, Kalnay, Kanamitsu, and van den Dool during a window of opportunity when the Cray super computer was newly installed. The first forecast was initiated on May 3, 1990 and 90-day integrations were run daily ending on September 6, 1990. Shorter integrations were also obtained thereafter. These short term forecasts all ended on December 6, 1990. The conventional forecast performance and the intra-seasonal variability related issues have been investigated by NMC staffs. This article focuses on the low frequency behavior of the model outputs. Particular attention was paid to the capability, or the lack of it, for the model to generate and maintain a blocking mean flow pattern. Only the 500mb geopotential height (Z) field is investigated in this study.

Figure 1 presents the standard deviations (SD) of the 500mb Z for the analyses and the forecasts. The contour interval is 10 m. The area with an SD greater than 80m is shaded. As the forecast lead time increases, the average SD is seen to decrease. The variance ratio of the forecast to the observed (analyses) is indicated at the lower-left-hand corner of each panel. Since we are more interested in forecasts at medium/extended ranges, 5-day mean forecasts are used in this article, where D+3, D+8, D+13,... denote day 1-5, day 6-10, day 11-13,...mean forecast. For D+13 forecast in Fig.1d, the variance ratio drops to 46%. No further decrease in variance is observed for longer range forecasts (not shown). Another interesting feature to observe is that the locations of the SD maxima of the forecast field are different from those of the observed. Taking the D+8 forecasts (Fig.1c), for example, the North Pacific maximum shifts westwards to near the dateline. Due to these dislocations, the average predicted weather patterns are likely to be different from the real atmosphere.

From early October on, the atmosphere began to experience large disturbances. Some of the weather anomalies were persistent blocking anticyclones. It is our interest to examine how capable the NMC MRF model is to simulate and predict blocking flows. Figure 2a presents the distribution of the number of days that the atmosphere showed a positive anomaly (PAN) greater than 120m from Oct 7 to Dec 2 1990. The PAN contour interval is 5, the first contour is 10, and the shaded area is greater than 15. In North Pacific near the dateline, the PAN is about 40 days out of a total of 57. Over the Iceland, the PAN is about 25. The areas with higher PAN are obviously the most likely locations for blocking flows to occur during this period of time. An area with

ACs and most of the D+13 ACs are way above 0.5 in the PAC area. A short while later, beginning from Oct 22 (case #16), the D+8 forecasts start to encounter great difficulty, and continue to have problems for at least seven days. Figure 5 contrasts the AC scores obtained from these two regimes: forecasts initiated on Oct 8-12 shown in the upper panel and those initiated on Oct 24-28 in the lower panel. While most of the upper panel ACs stay above 0.5 beyond day 15, all of the lower panel ACs drop below 0.5 at about day 7. The regime dependency of these consecutive forecasts are clearly illustrated.

It is important to find out what their respective initial conditions looked like and what evolutions took place from the favorable regime to the unfavorable one. Figure 6 provides these pictures, where the analyses from October 9 to November 4 and a few d+8 forecasts are shown and compared. The initial conditions for the period Oct 9 to 12 are pretty much similar in terms of large-scale patterns (first 4 panels of column 1), with positive anomalous heights over eastern Asia and eastern North Pacific and a negative anomalous height over the eastern Siberia. The circulation pattern gradually evolved to those shown on Oct 24-27 (first 4 panels of column 3), with anomalous ridge firmly established over the western North Pacific and anomalous trough over the eastern North Pacific. The D+8 forecasts valid on Oct 17-22 are shown in the second column. The skillful prediction of the evolution is clearly observed from this series of charts. As already shown in Fig. 3a, the D+13 ACs of these cases are mostly above 0.5.

The D+8 forecasts initiated on Oct 24-27 on the other hand yielded very little skill, as shown in column 4 of Fig.6. This time the evolution of the large-scale pattern begins with a regime described earlier and leads to a regime with an anomalous ridge at the dateline over the North Pacific and an anomalous trough moving from its northwest to its northern flank. It is interesting to note that the favorable and unfavorable initial conditions we just described are very different from those presented by Palmer(1988). He reported that the skill of medium/extended range forecasts over the Pacific/North America region is strongly correlated with the fluctuations of the Pacific/North American (PNA) mode. Our favorable regime does not look like the positive PNA mode, nor does our unfavorable regime look like the negative PNA mode. Further investigations appear to be needed in order to clarify the picture of what flow regimes are favorable for extended-range forecasts and what regimes are not favorable.

Witnessing the capability of the MRF model to generate and maintain a blocking flow more than 20 days over the North Pacific, as shown in Fig. 4 and 5a, we would like to inquire further as to whether the model also has similar capability for the North Atlantic/Europe region, and if not, why not. A long-lasting blocking flow prediction over the North Atlantic is found in the forecasts initiated on Nov 6, 1990. The left panels of Figure 7 show the forecasts with increasing forecast lead time up height anomalies exceeding 240m is found to be a good indication of the location of a blocking anticyclone (not shown). Comparisons of similar distributions of forecasts are shown in Figs. 2b to 2e, for various forecast lead times. Over the North Pacific, the D+3 forecasts show very good simulation; for longer range forecasts, however, the area with large anomalies shrinks rapidly. Over the United States, not even the D+3 forecasts show a PAN exceeding 10 except over the New England area. The North Atlantic positive anomalies were missing in the forecasts except for those of D+3. The blocking heights over the region between Greenland and Sweden were simulated by D+3 forecasts, with a reduced number of days (Fig. 2b). The predicted blocking then erroneously shifted westwards toward Greenland (Fig.2c) and then toward Baffin Bay (Fig.2d and 2e). The extented forecasts also show increasing biased blocking heights over the Arctic Ocean (Fig.2d and 2e).

Figure 2 suggests that, as far as counting of large positive anomaly is concerned, the potential for high forecast skill is much more favorable over the North Pacific than over the North Atlantic. Indeed, Fig. 3 strongly supports this observation. In this figure, the conventional anomaly correlations (ACs) are shown for the Pacific (PAC) sector (120E-120W,20N-80N) on the upper panel and the Atlantic (ATL) sector (80W-40E,20N-80N) on the lower panel. Curves A, B, and C represent the skill fluctuations from case to case for the D+3, D+8, and D+13 forecasts, respectively. The first case in this figure corresponds to the forecasts initiated on October 6 1990 and the last case November 21 1990. For the PAC sector, the D+8 ACs are above 0.5 more than half of the time, and the D+13 ACs are also above 0.5 on many occasions. However, the forecast skill over the ATL sector is seen to be much lower.

A few interesting features can be observed from Fig. 3. Taking case #34 (forecasts initiated on Nov 8 1990) for instance, both D+8 and D+13 show ACs near 0.85 for the PAC sector. How about D+18 or even longer forecasts? Figure 4 shows the predictions (left panels) and their verifications (right panels) from D+3 up to D+23 for this case. The PAC blocking high is predicted amazingly well up to D+18, including the progression (D+8) and the retrogression (D+18).

However, it is also interesting to observe that the neighboring integrations (case #33, #35 for examples) do not consistently yield good D+13 forecasts. Other cases (#28 and 46, for examples) also show similar large fluctuations in D+13 forecast skill. Therefore, the highly skillful forecast in these cases is likely not regime dependent and not something one can count on. A slight initial perturbation (butterfly effect of Lorenz) can lead to a grossly different solution within a couple of weeks.

On the other hand, Fig. 3a does show how forecast skill depends sometimes upon the weather regime. Note that from case #3 up to case #10 (Oct 8-15 initial conditions) all of the D+8 to D+28. The verifications are shown on the right panels. The D+3 forecast correctly shows a strong block between Iceland and Norway. The block is maintained in the forecasts while it disintegrated in the real atmosphere during the following week. Further down the road, the block in the forecasts gets stronger and retrogresses and then spreads over to the Arctic Sea. On D+28, the block in the forecast has split into two parts with its main portion over the area north of the Hudson Bay. During this period of time, the real atmosphere had another strong blocking anticyclone established that moved slowly eastwards over the North Atlantic. The model however did not catch this newly developed block. So, what we see in this case is that the model is able to maintain the blocking flow more than 30 days, but, it evolved incorrectly and moved to the wrong location. The predicted weather events would have been grossly different from the real atmosphere.

Does this forecast bias occur fairly often and show up consecutively? Figure 8 presents five adjacent integrations: three immediately prior to and one immediately after the Nov 6 initial conditions. The first column are the analyses, serving as the initial conditions as well as the verifications. The D+3 and D+8 forecasts are shown in column 2 and 3, respectively. While D+3 forecasts show very good predictions, the D+8 forecasts all show consistent bias in the sense that the block gets stronger and retrogresses to Greenland or even further west. The implication is that the ensemble forecasts generated within this period of time (be it consisting of 9 integrations with initial conditions 6-hour apart) will contain the same bias described above.

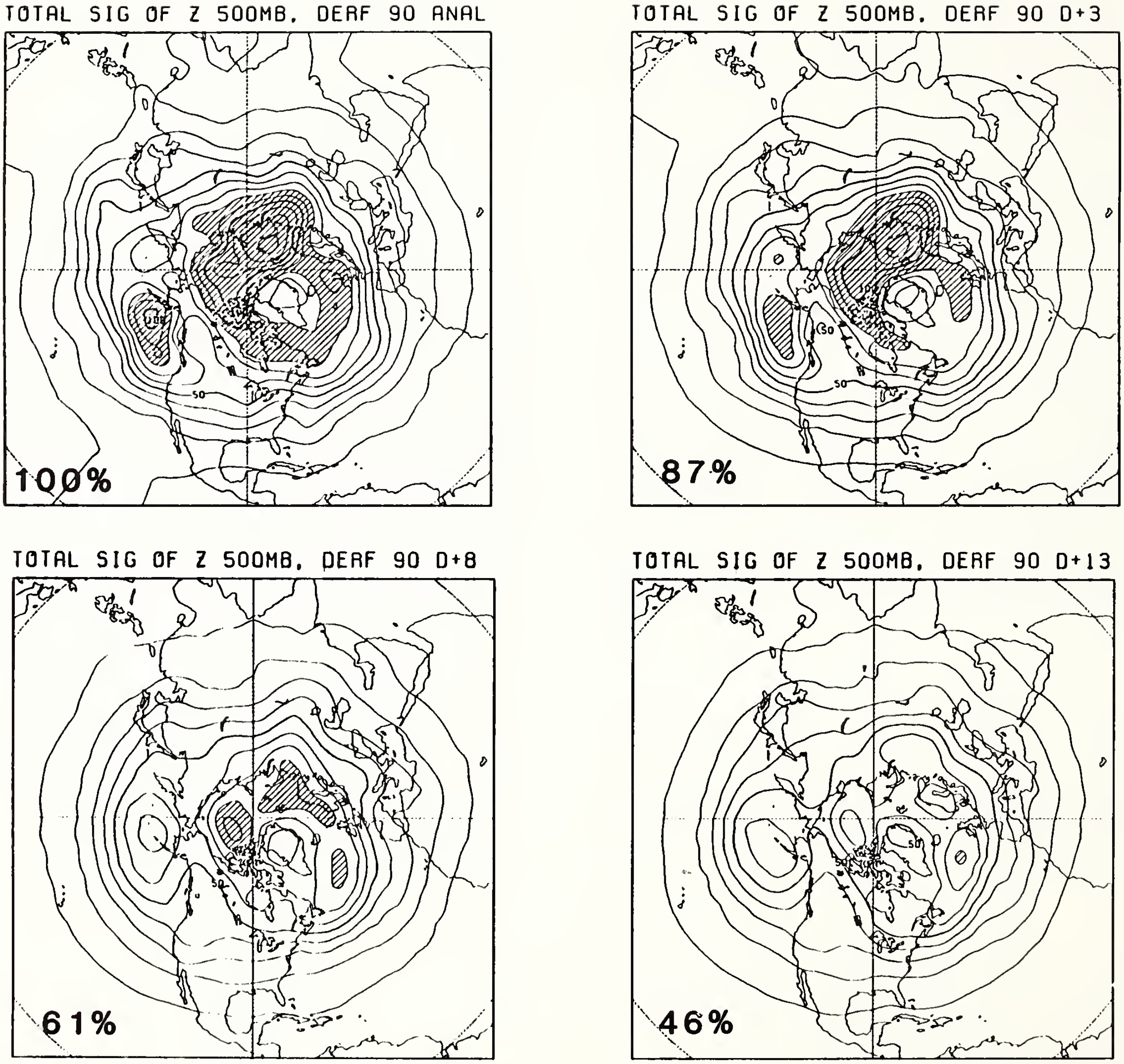
TOTAL SIG OF Z 500MB, DERF 90 ANAL
100%
TOTAL SIG OF Z 500MB, DERF 90 D+3
87%
TOTAL SIG OF Z 500MB, DERF 90 D+8
61%
TOTAL SIG OF Z 500MB, DERF 90 D+13
46%
50

Figure 1. Standard deviations of 500mb Z for the analyses and the forecasts, contour interval 10 m, area greater than 80 m is shaded.

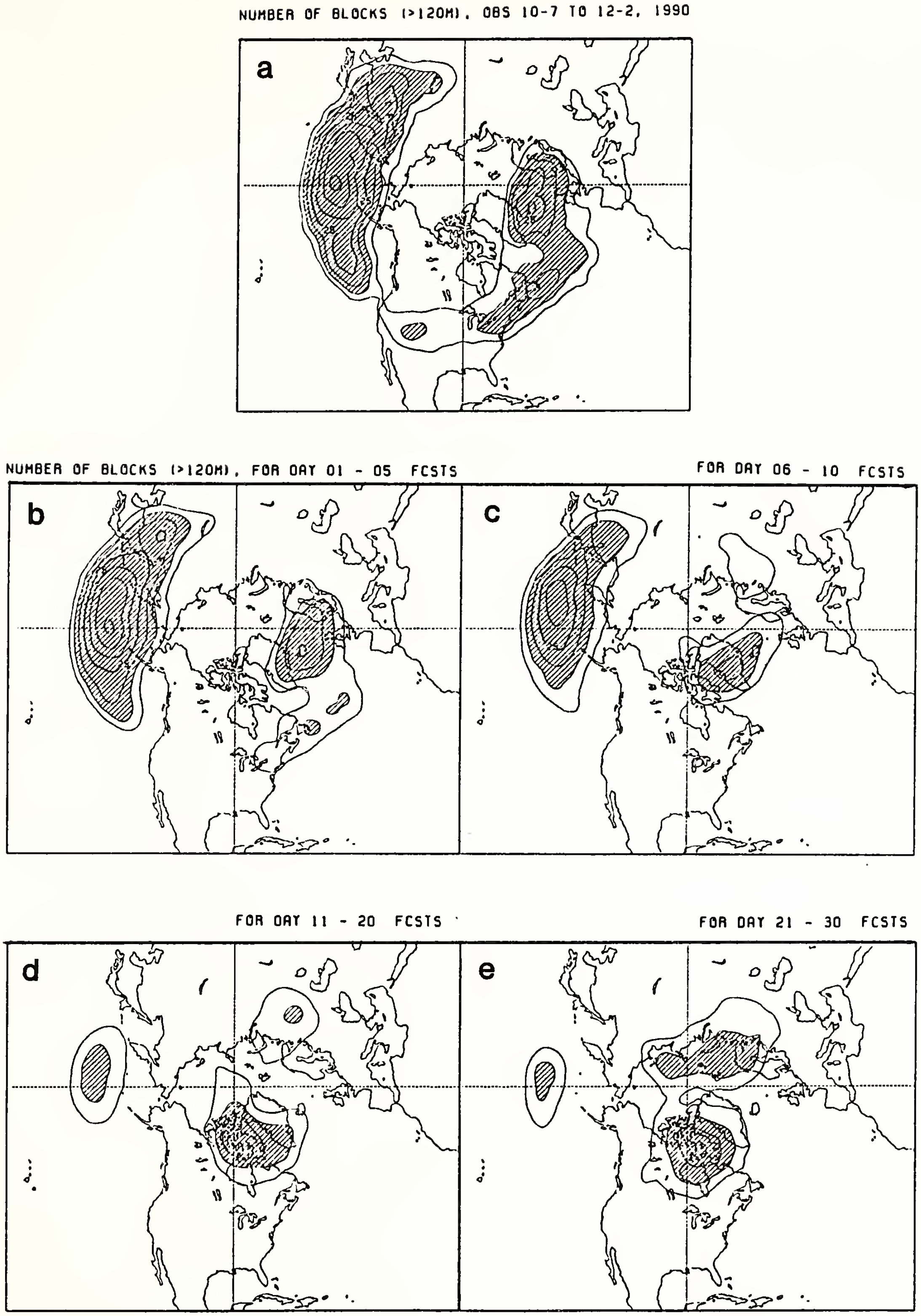
NUMBER OF BLOCKS (>120M), OBS 10-7 TO 12-2, 1990
a
NUMBER OF BLOCKS (>120M), FOR DAY 01 - 05 FCSTS
b
FOR DAY 06 - 10 FCSTS
c
FOR DAY 11 - 20 FCSTS
d
FOR DAY 21 - 30 FCSTS
e

Figure 2. (a) Distribution of number of days the atmosphere showed positive anomaly greater than 120 m, from Oct 7 to Dec 2 1990, contour interval 5, first contour 10, area greater than 15 shaded. Comparisons of similar distributions for forecasts are shown in (b) to (e), for various forecast lead time.

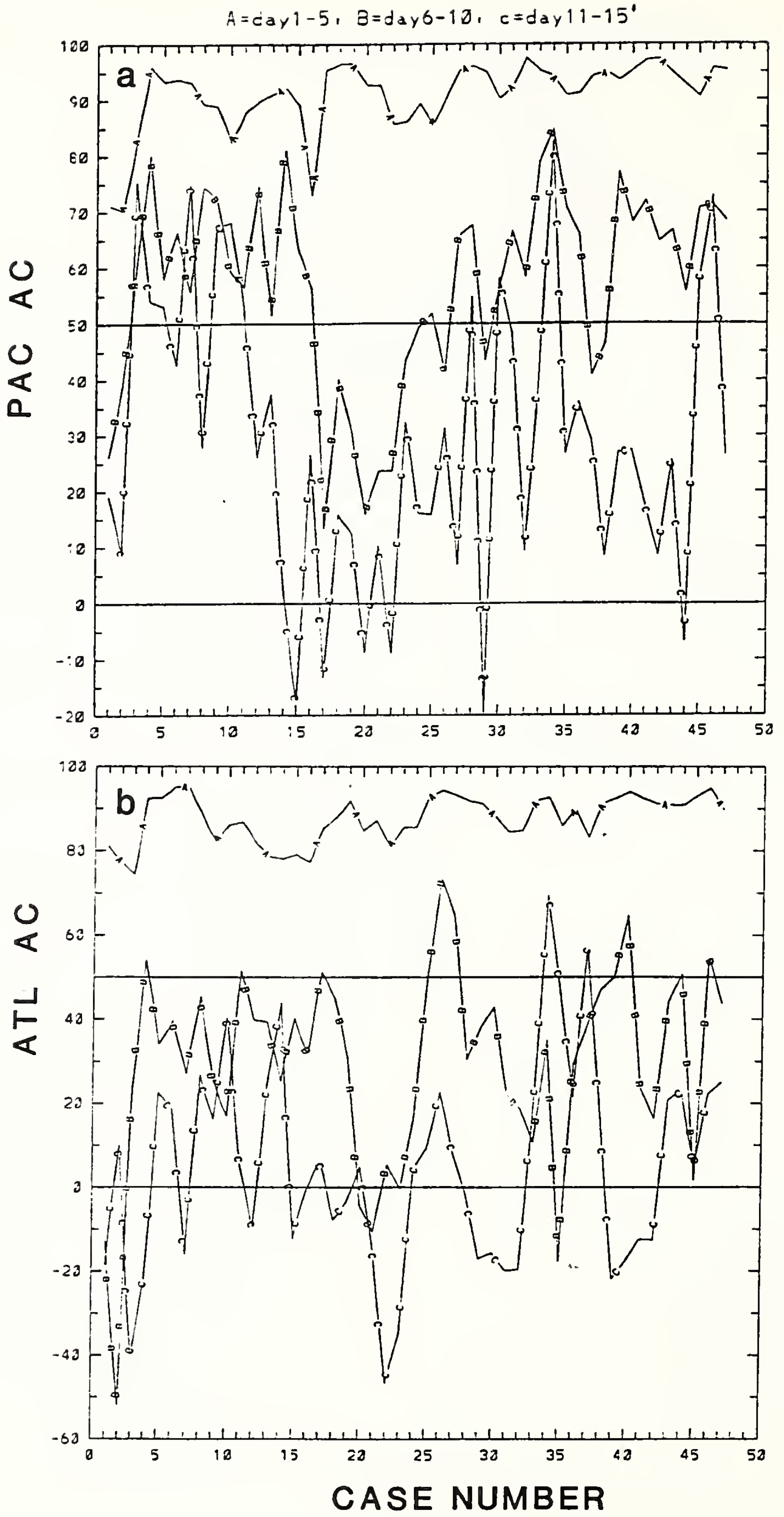

Figure 3. Anomaly correlations (ACs) for (a) Pacific (PAC) sector (120E-120W,20N-80N) and (b) Atlantic (ATL) sector (80W-40E,20N-80N). Curve A, B, and C represents the skill fluctuations from case to case for the D+3, D+8, and D+13 forecasts, respectively. The first case corresponds to the forecasts initiated on October 6 1990 and the last case November 21 1990.

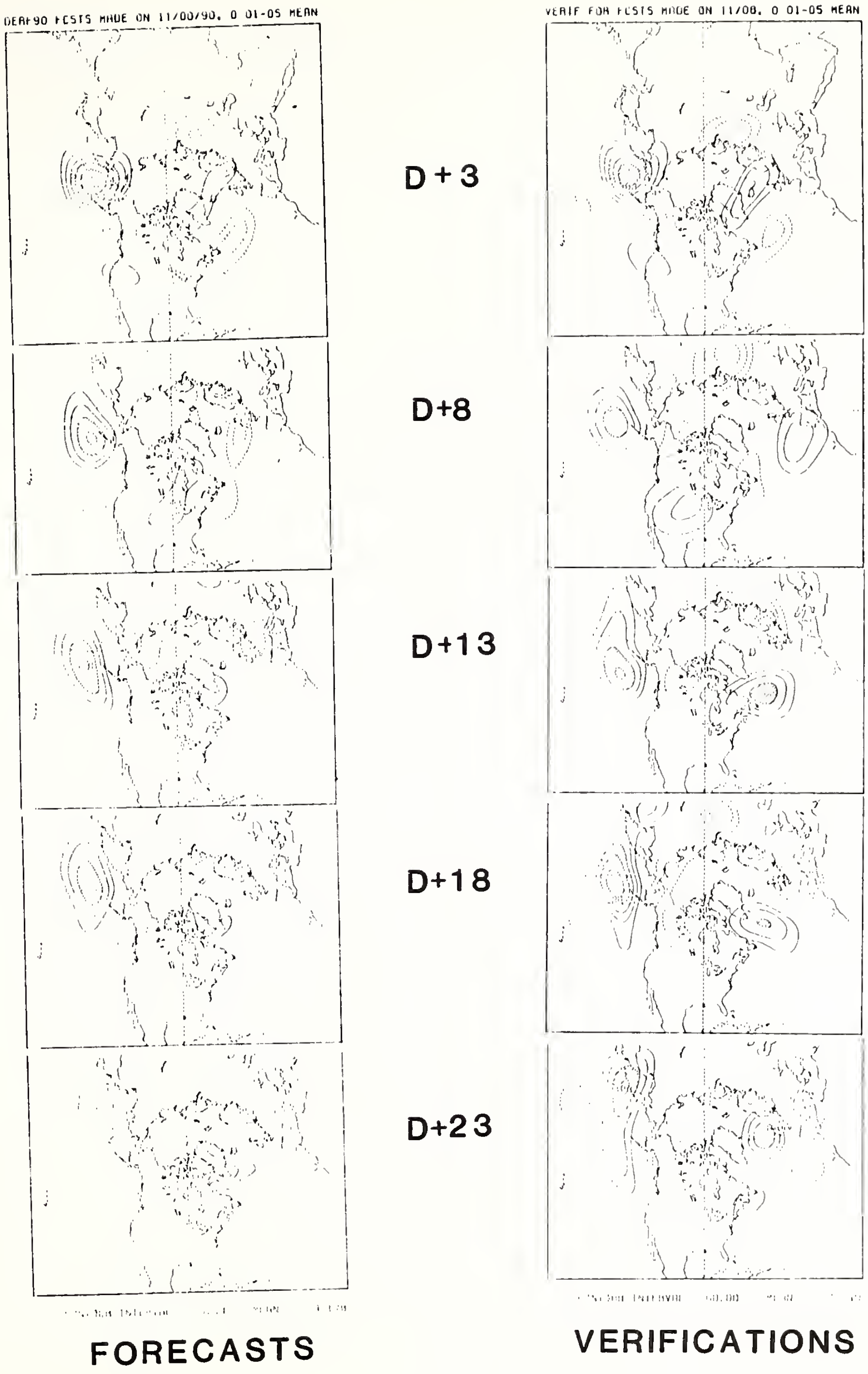
DERF90 FCSTS MADE ON 11/08/90. 0 01-05 MEAN
VERIF FOR FCSTS MADE ON 11/08. 0 01-05 MEAN
D+3
D+8
D+13
D+18
D+23
FORECASTS
VERIFICATIONS

Figure 4. Left hand panels, D+3 to D+23 forecasts for case #34 (forecasts initiated on Nov 8 1990); right hand panels, the verifications.

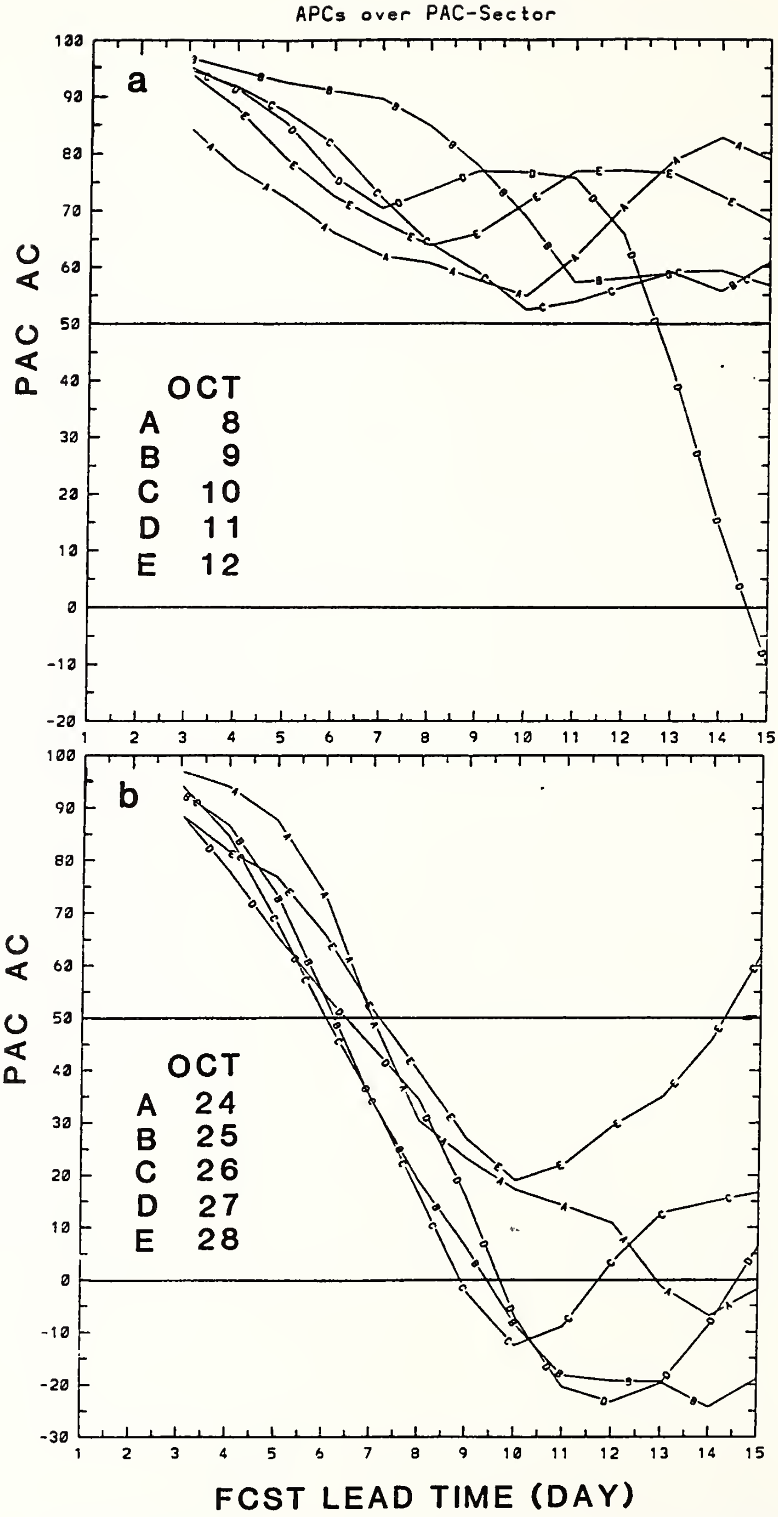

Figure 5. Comparison of AC scores obtained from two different regimes: (a) forecasts initiated on Oct 8-12 1990; (b) forecasts initiated on Oct 24-28 1990.

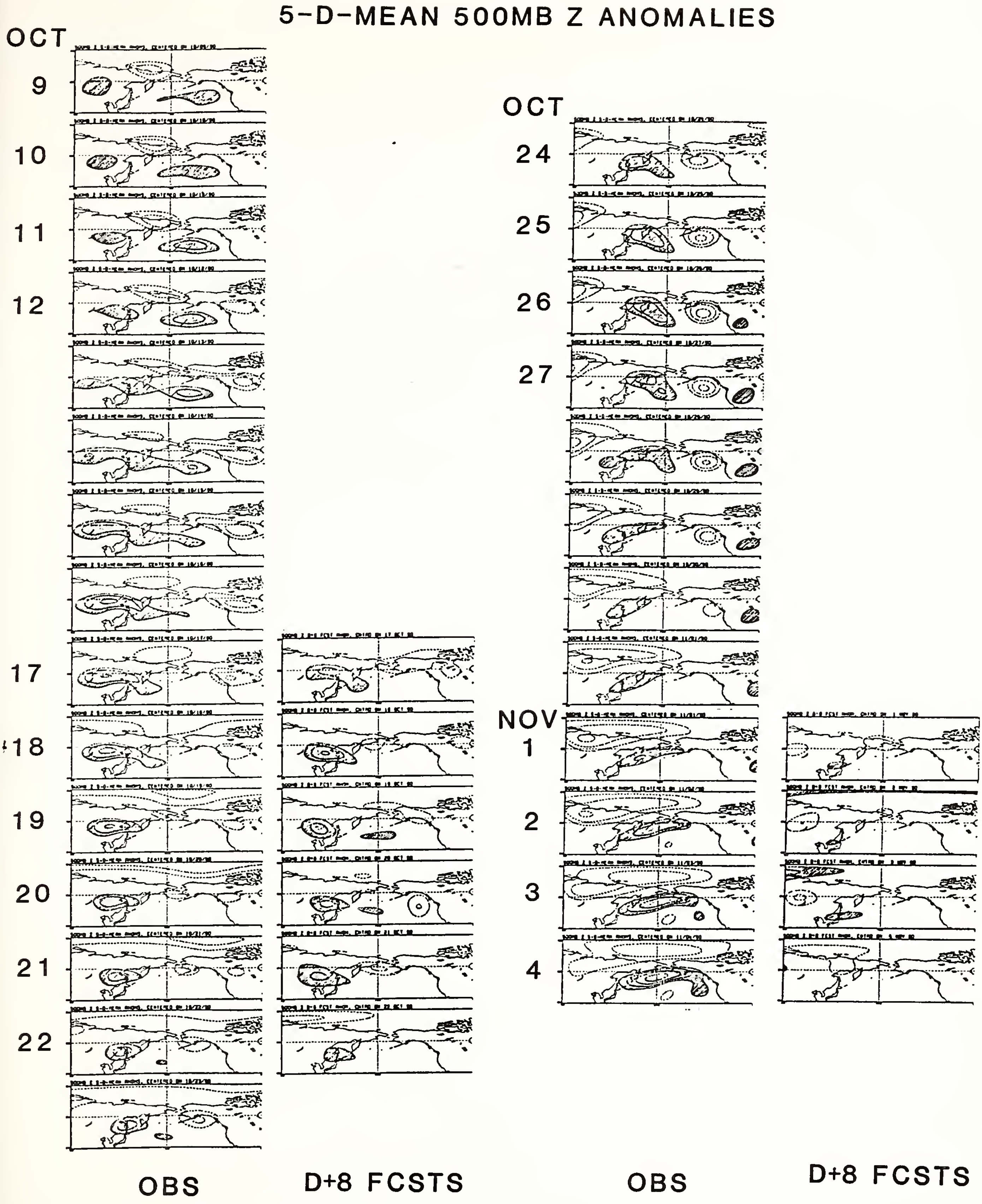

Figure 6. The daily sequence of analyses (5-day mean) for the period Oct 9 to Nov 4 1990 (column 1 and 3). A few D+8 forecasts are shown in column 2 and 4, lining up with the verifications on their left.

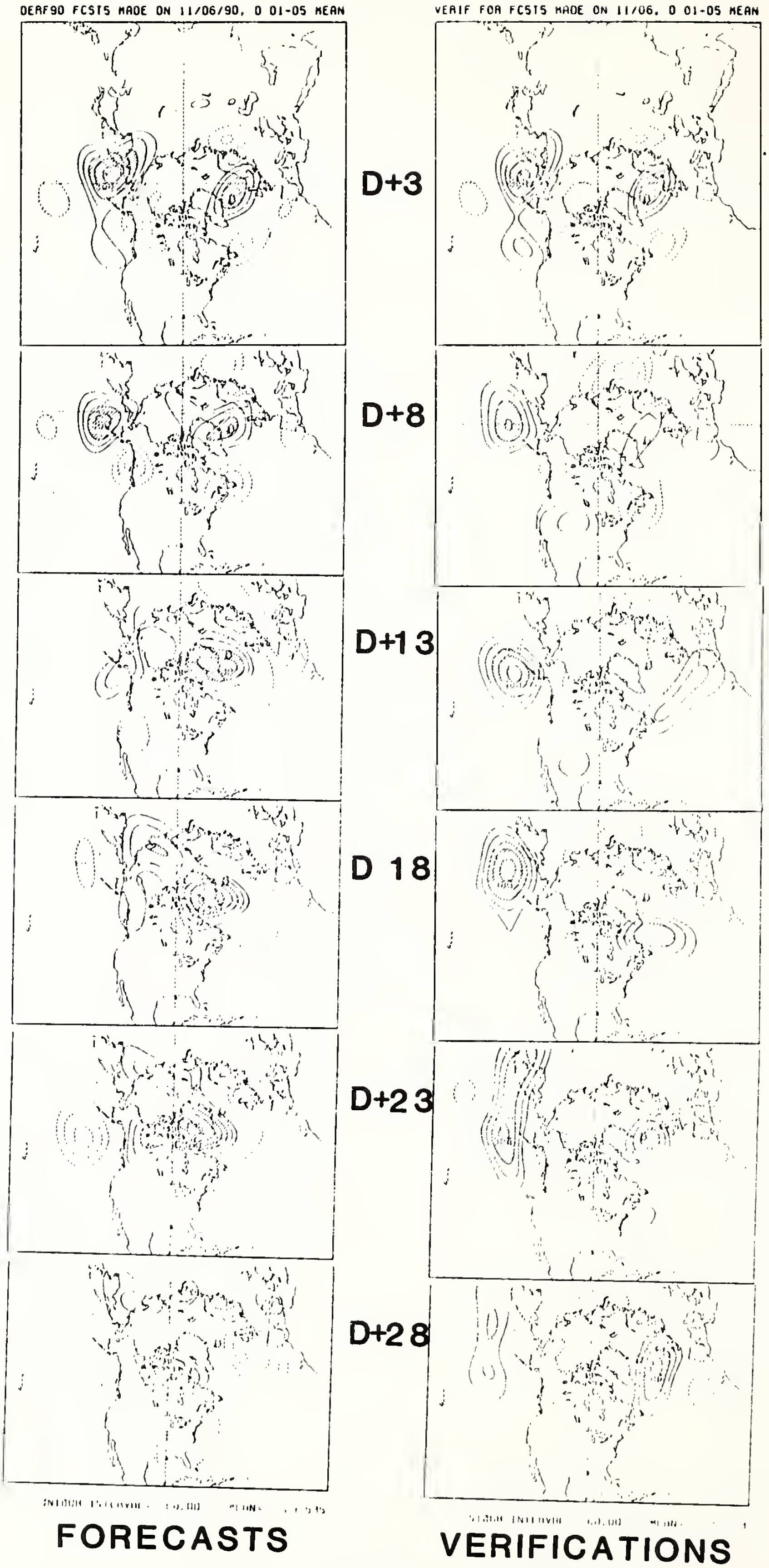
DERF90 FCSTS MADE ON 11/06/90, D 01-05 MEAN
VERIF FOR FCSTS MADE ON 11/06, D 01-05 MEAN
D+3
D+8
D+13
D 18
D+23
D+28
FORECASTS
VERIFICATIONS

Figure 7. D+3 to D+28 forecasts initiated on ovember 6 1990 (left hand panels). The verifications are on the right hand panels.

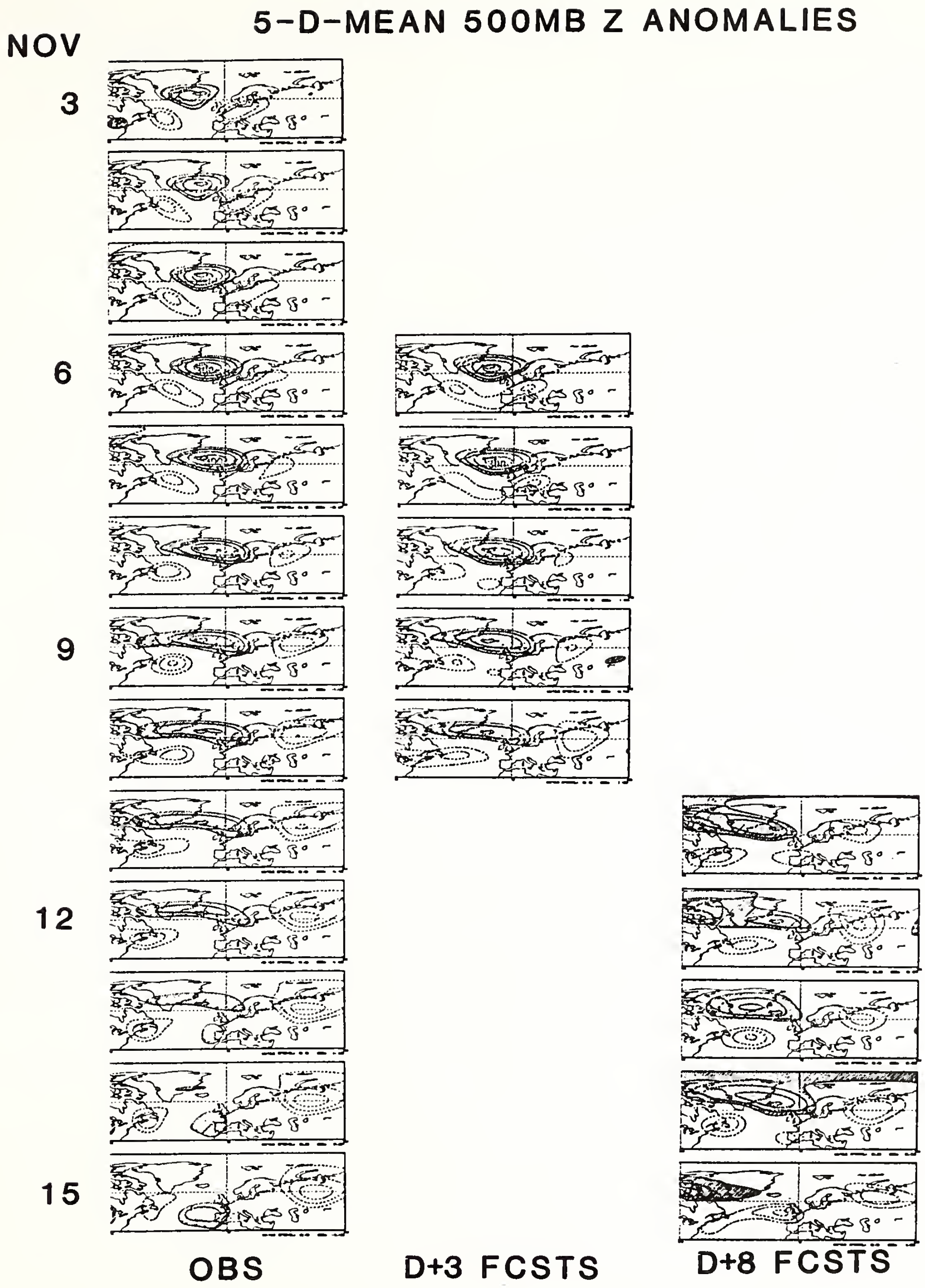

Figure 8. D+3 and D+8 forecasts for five consecutive integrations, initiated on Nov 3 to 6 1990 (column 2 and 3). The initial conditions and verifications are shown in column 1.

# A Study of Seasonal Climate Prediction with a Simple Coupled Ocean-Atmosphere Model

Thomas J. Phillips

Program for Climate Model Diagnosis and Intercomparison
Atmospheric and Geophysical Sciences Division
Lawrence Livermore National Laboratory
PO Box 808, L-264, Livermore, CA 94550

Comprehensive data from future satellite initiatives such as EOS will make it feasible to attempt prediction of the global atmospheric seasonal climate from knowledge of the ocean state. However, many questions--e.g., what ocean variables make superior climate predictors and what atmospheric variables can be predicted most readily--remain to be answered before global seasonal climate prediction becomes a practical endeavor. Because records of existing global data from both observations and from coupled ocean-atmosphere GCMs are too short to provide definitive answers to such questions, it is appropriate to use time series generated by simpler coupled models for preliminary studies. Then, as more global data become available, these climate prediction issues can be revisited from a more advanced starting point.

A simple model consisting of a mixed-layer ocean coupled synchronously to a two-layer atmosphere was used for the present study. The depth and temperature of the mixed layer were model prognostics--depth being a function of absorbed solar radiation, wind stirring and convective overturning, and temperature a function of the net heat flux at the top of the mixed layer and of turbulent heat exchange with a deeper ocean layer below. The atmospheric model was governed by the nonlinear moist primitive equations represented in vertical layers centered on 750 and 250 hPa and in the horizontal on grid points at 3-degree latitude intervals between 80 S and 80 N, but in the zonal direction as a Fourier series truncated at wave number 3 in a 120-degree longitudinal sector. The model was forced by a seasonal solar cycle, and the radiative fluxes were simply parameterized, with cloud effects prescribed. Surface sensible and latent heat fluxes were estimated by bulk aerodynamic formulae, and a moist convective adjustment scheme kept the atmospheric lapse rate conditionally stable. Land surface processes were treated very crudely: the continents were represented as constant-albedo rectangular blocks, without orography, that covered 50 % of the model's Northern Hemisphere and 20 % of its Southern Hemisphere (Figure 1), and there was no storage of heat or moisture in the soil. The mixed-layer ocean, therefore, was the only source of climate memory in the coupled system.

Starting with the model atmosphere at rest and with its surface temperature everywhere set to 300 K, it took more than 30 simulated years to attain a quasi-equilibrium climatic state. An additional 50-year integration then was performed, from which the mean and interannual variability of the seasonal ocean/atmosphere climate were computed. The model was able to qualitatively simulate the observed large-scale seasonal changes in the temperature and depth of the ocean mixed layer and in the atmospheric fields. However, the ocean was simulated unrealistically at high latitudes, and the meridional and vertical atmospheric temperature gradients and jet streams were too weak. The interannual variability of most oceanic and atmospheric fields also was several times too low, and the El Niño-Southern Oscillation (ENSO) was not simulated.

The 50-year time series of 4 ocean variables--the temperature, depth, and heat content of the mixed layer, and the net surface heat flux--and of 6 atmospheric variables--750-250 hPa thickness and static stability, and 750 hPa and 250 hPa zonal and meridional winds--were considered in this climate prediction study. Spatial averages of the ocean variables computed over tropical, subtropical, and midlatitude sectors in both model hemispheres were used as climate preditors (Figure 1), while the entire fields of the atmospheric variables were treated as predictands. As a way of removing the annual cycle from the data, the 50-year seasonal mean was subtracted from the individual seasonal averages. Then the ocean/atmosphere time series were stratified by season, and correlations of the predictands lagging each predictor by up to 8 seasons were computed. The resulting lagged correlation maps were tested for statistical field significance at the 5 % level. A total of 194 maps were found to be significant, but at most only about 40 % of the local variance of an atmospheric field was explained by an ocean predictor (Figure 2). From comparing the number of significant correlations at each lag with that expected to occur by chance, it was found that the model atmosphere displayed modest predictability out to a lag of 3 seasons.

From aggregate measures of predictive power and consistency of the predictors and predictands, it was observed that the mixed-layer temperature (or, equivalently, the sea surface temperature) was the most powerful single predictor of atmospheric seasonal climate. Ocean variables in the tropics were the strongest predictors, but those in the Northern Hemisphere extratropics performed much better than their Southern Hemisphere counterparts; predictive consistency was relatively insensitive to predictor location, however (Figure 3). The 750-250 hPa thickness was the most predictable atmospheric field, but static stability and 250 hPa zonal winds also were marginally predictable (Figure 4). Spring and autumn ocean variables were most effective in predicting subsequent seasonal atmospheric states, but the model atmosphere was more predictable in summer and winter than in the transitional seasons. Many of these results are consistent with previous investigations of seasonal climate prediction based on observational data of more limited scope (in geographical coverage, types of predictors/predictands considered, etc.).

A more detailed discussion of this study appears in Phillips (1991).

## Acknowledgments

This work was completed under the auspices of the U.S. Department of Energy Environmental Sciences Division at the Lawrence Livermore National Laboratory under Contract W-7405-ENG-48.

## References

Phillips, T.J., 1991: An application of a simple coupled ocean-atmosphere model to the study of seasonal climate prediction. *J. Climate* (submitted).

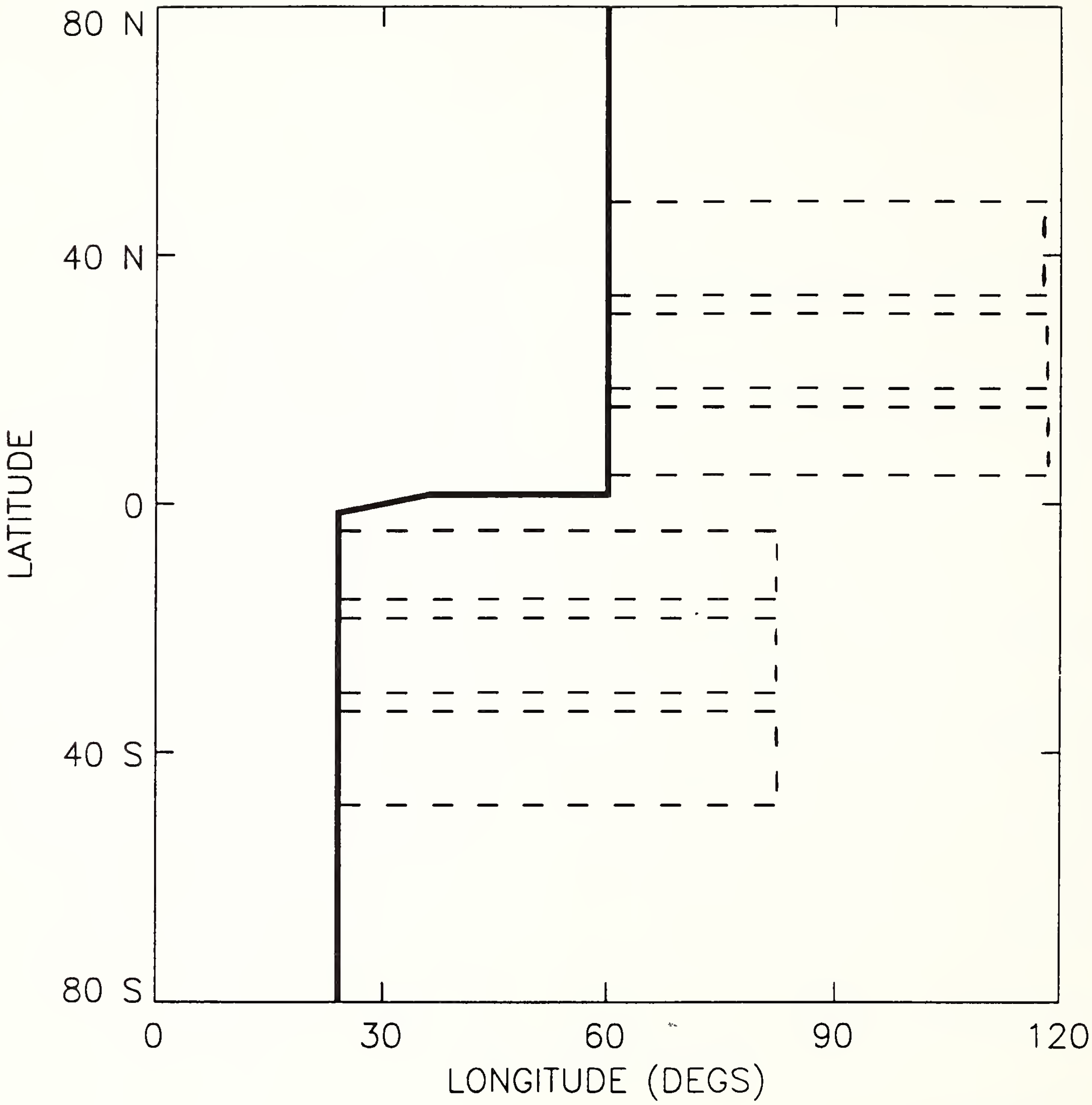

**Figure 1:** Northern and Southern Hemisphere tropical, subtropical, and mid-latitude regions (dashed-line rectangles) for spatial averaging of the model's ocean predictor variables. The outlines of the schematic continents in the 120-degree longitudinal sector also are shown by heavy lines.

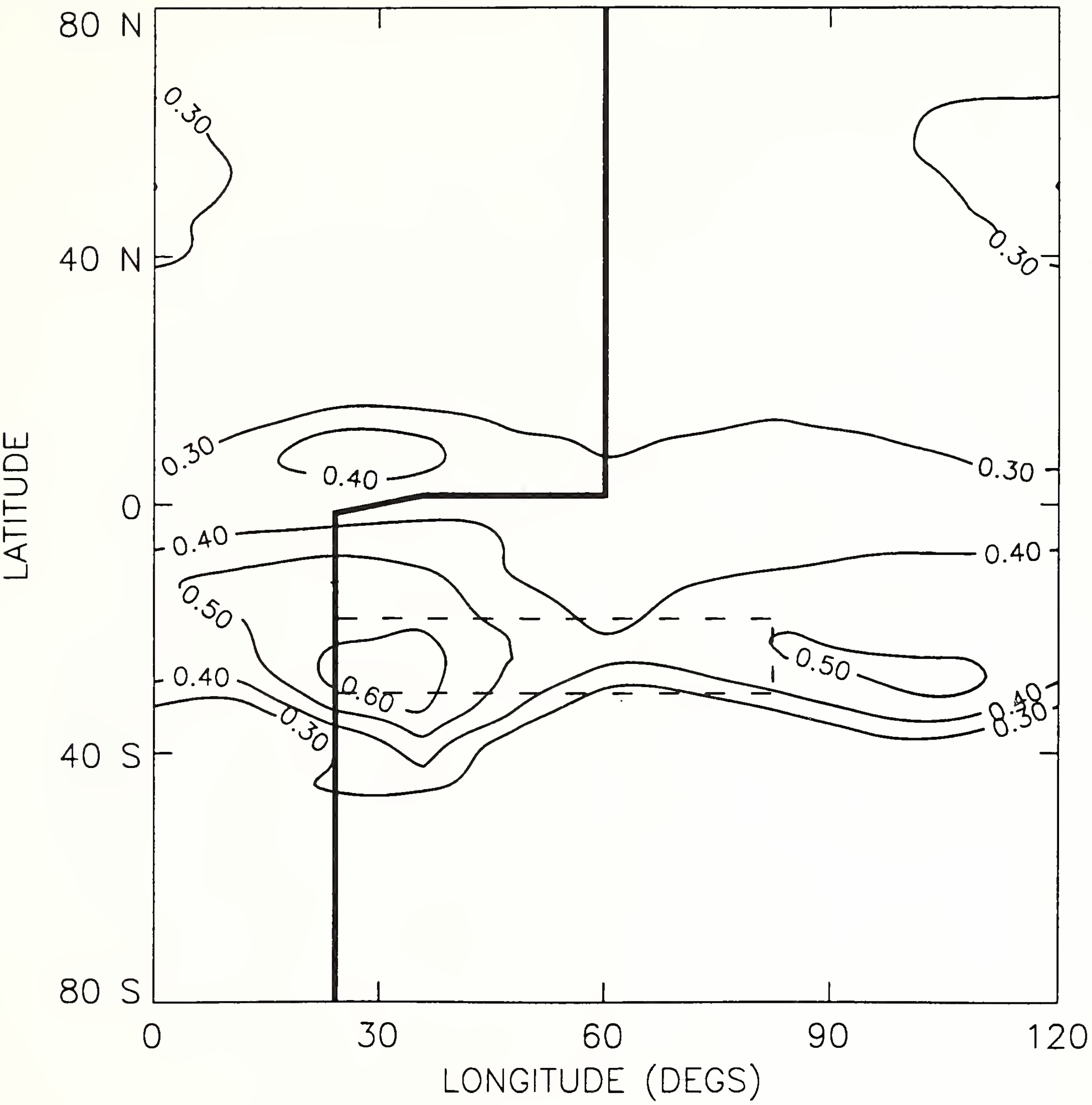

Figure 2: Map of locally significant correlations of autumn mixed-layer temperature in the Southern Hemisphere subtropics (dashed-line rectangle) correlated with 750-250 hPa atmospheric thickness in the following winter.

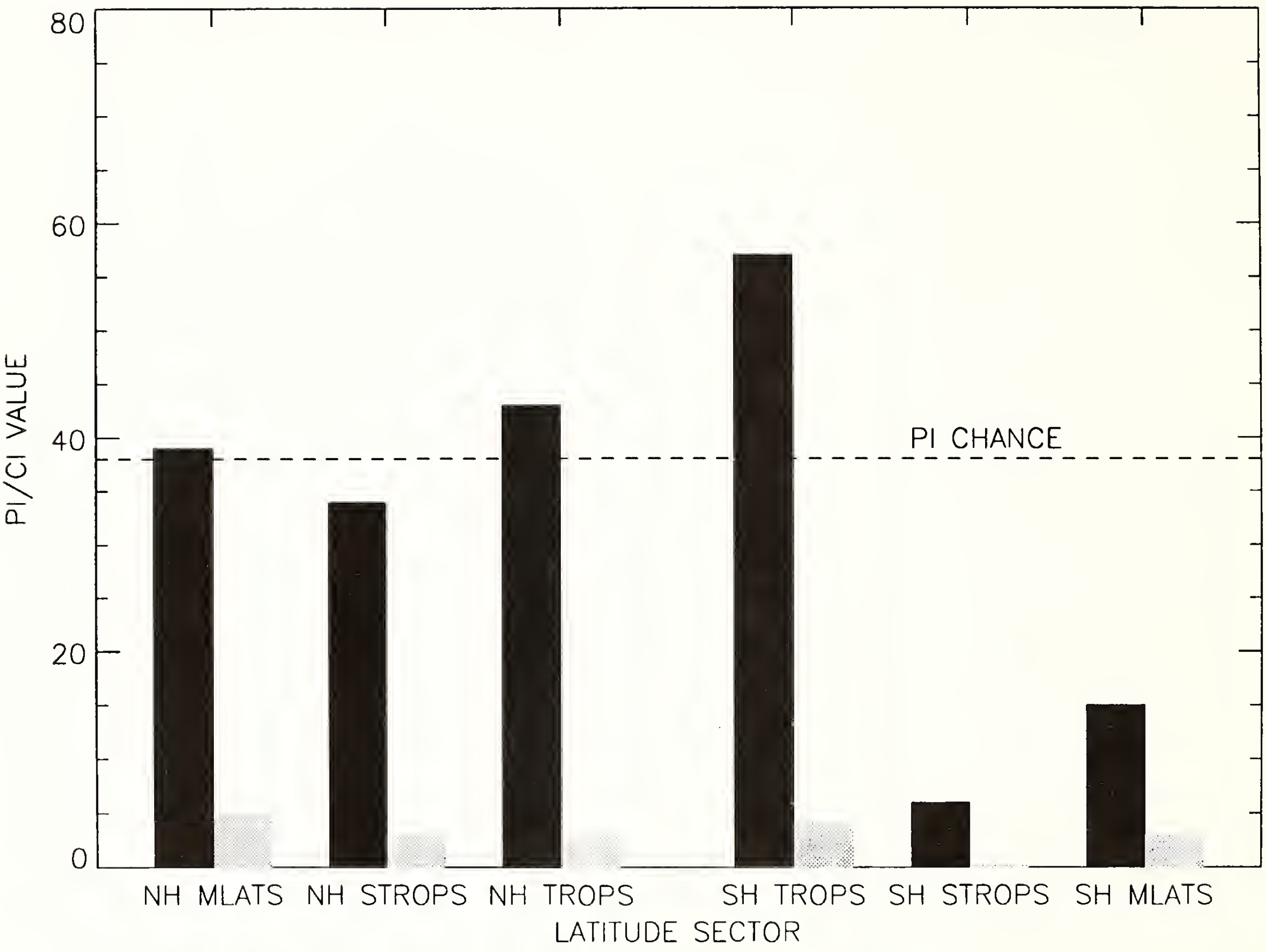

Figure 3: Power index PI (in black) and consistency index CI (in gray) as a function of the latitude sector of the ocean predictors. PI is the total number of significant lagged correlations, while CI is the total number of significant correlations at consecutive lags. Indices are aggregated over 4 ocean predictors in four seasons, and over 6 atmospheric predictands lagging the predictors by up to 8 seasons. The PI value expected from chance occurrences of significant correlations is indicated by the dashed line.

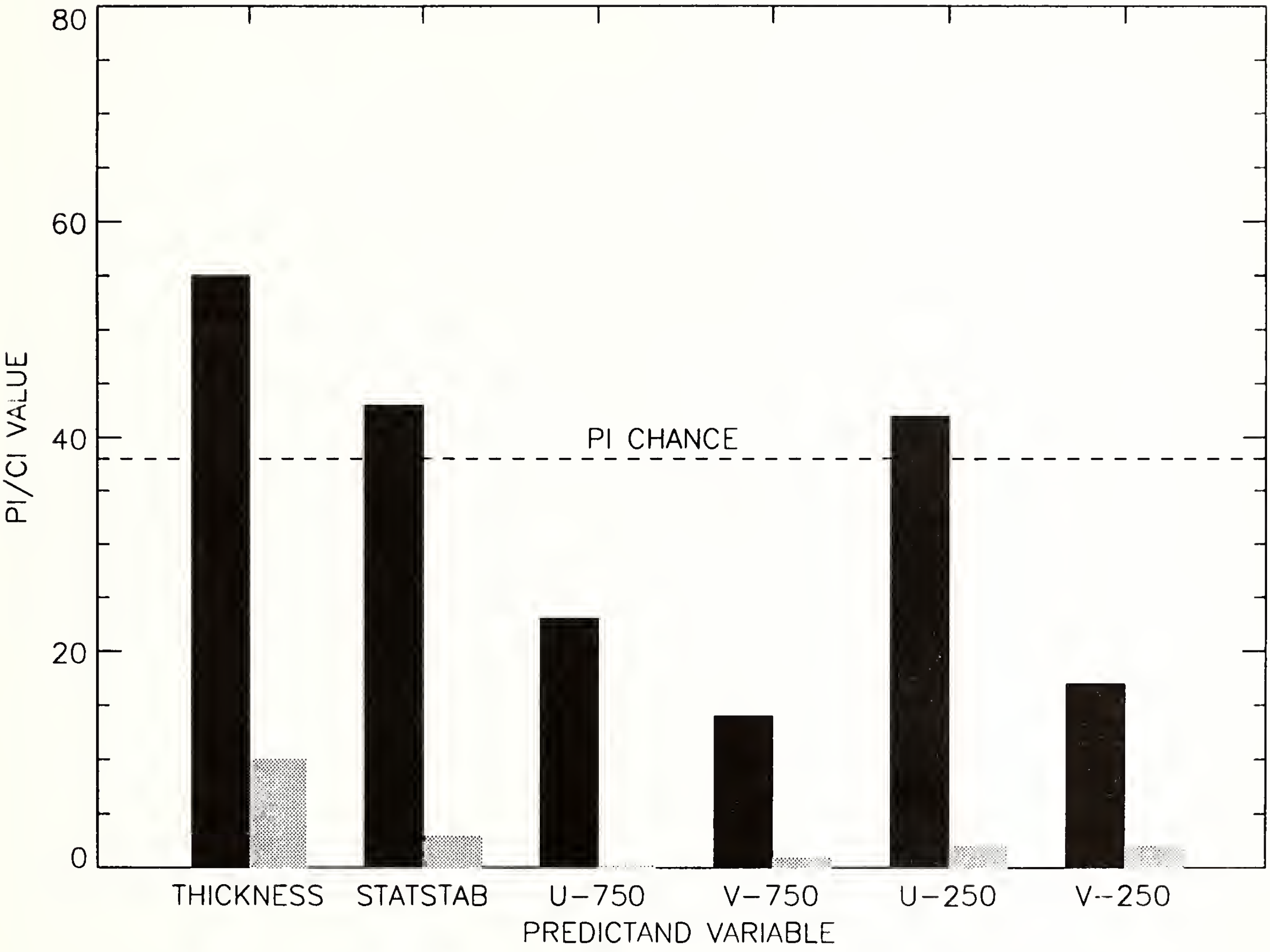

**Figure 4:** As in Figure 3 except for PI and CI as a function of atmospheric predictand.

# PREDICTION OF NINO 3 SEA-SURFACE TEMPERATURES USING LINEAR INVERSE MODELING

Cécile Penland and Theresa Magorian

Cooperative Institute for Research in Environmental Sciences, University of Colorado,
Boulder, CO 80309-0449

## 1. Introduction

A statistical prediction method based on Principal Oscillation Pattern (POP) analysis is used to forecast sea-surface temperatures (SSTs) in the region of the equatorial Pacific Ocean known as Niño 3. Xu and von Storch (1990) have recently used POP analysis to find a pair of damped oscillatory patterns closely associated with the Southern Oscillation and characterized by a single oscillation period of about three years. Their analysis was concerned with predicting the phase of a particular *pattern*, or POP, pair. Earlier, Penland (1989) had shown how groups of POPs could be combined to predict a measured field in a chosen geographical location. Representing several frequencies in the prediction, rather than just one, can be expected to yield better forecasts of what is actually measured, although the simplicity of interpreting a single cyclic phenomenon is sacrificed.

Like canonical correlation analysis (CCA: Barnett et al. 1988; Graham et al.1987a,b), our technique involves a linear transformation of a predictor field to produce a forecast of a predictand field. Here, the predictand field is the predictor field at some later time. CCA derives a transformation which *maximizes the correlation* between the predictand and the transformed predictor field. In contrast, POP analysis is based on an eigenvalue problem resulting from *minimizing the error* between the predictand and the transformed predictor field. Estimations of the transformation matrices, or Green functions, are obtained directly from the multivariate time series data. Also, the dynamics of the system is assumed to be continuous and linearly Markovian. The analysis, therefore, is equivalent to linear inverse modeling.

## 2. The data set

The analysis was applied to monthly-averaged SSTs obtained from the Comprehensive Ocean-Atmosphere Data Set (Slutz et al., 1985). The data are available on a 2°×2° grid, which we consolidated into a 4°×10° grid. The grand mean and the phase-averaged annual cycle were removed from the monthly-averaged data, which were otherwise unfiltered. Our predictands are the average SST in a region containing Niño 3 (8°N-8°S; 150°W-90°W), hereafter designated as such. We considered the time period January 1950 to December 1984 for the training period, and verified on the time after that. In choosing predictors for SSTs in Niño 3, SSTs in three tropical (32°N-32°S) ocean domains were considered: the Pacific (Pac: 100E-70°W), the Indian-Pacific (PacIn: 30°E-70°W) and the global tropical oceans (Glob).

Empirical Orthogonal Functions (EOFs) were calculated for each domain; the EOF eigenvalues are shown in Fig. 1. The leading EOF in any of the domains is indistinguishable from the leading EOF in the others and is dominated by an equatorial Pacific pattern (not shown). The leading 10 principal components (PCs) explain 63%, 61% and 56% of the variance in the Pac, PacIn and Glob domains, respectively; however, this explained variance is not uniform geographically. Each set of 10 EOFs explains 80-95% of the variance in Niño 3, and little error is made by considering only their contribution to the SSTs in the region (Fig. 2). The time series constructed by combining the 10 leading PCs from the PacIn domain and averaging over Niño 3 correlates very highly (98%) with the SST anomaly time series there, insignificantly better than do time series constructed with leading PCs from either Pac or Glob.

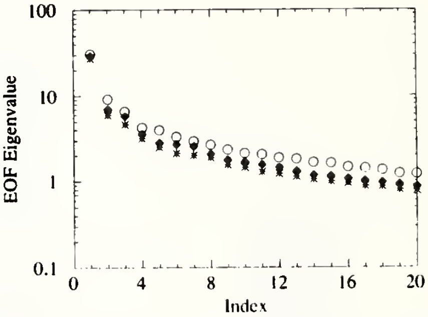

Fig. 1: EOF eigenvalues for the different ocean basins: Circles: Glob. Diamonds: PacIn. Stars: Pacific.

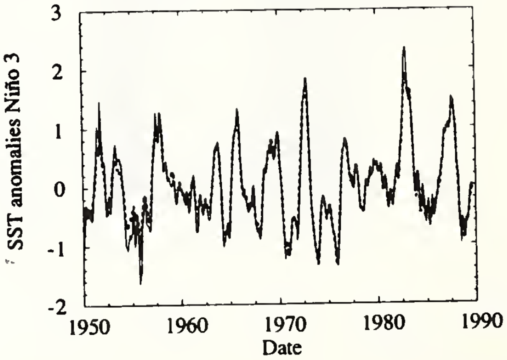

Fig. 2: SST time series in region 8°N-8°S, 150°W-90°W (Niño 3). Solid line: Monthly-averaged SSTs from COADs. Dashed line: Contribution to Niño 3 SSTs from 10 leading PCs calculated in PacIn.

## 3. Prediction technique

Crucial to our predictions is the assumption that the SST anomaly field propagates linearly. This allows us to perform the analysis entirely in EOF space and then transform to geographical space for interpretation. If the SST anomaly field propagates linearly, then so do its PCs. For M retained EOFs, the $\alpha$th principal component $c_\alpha(t)$ is assumed to evolve as

$$\frac{dc_\alpha}{dt} - \sum_{\kappa=1}^{M} B_{\alpha\kappa}c_\kappa = \varepsilon_\alpha + \xi_\alpha, \qquad (1)$$

where **B** is a deterministic, constant M×M matrix, and $\varepsilon_\alpha$ is the error in the $\alpha$th PC tendency due to linear interactions between retained and neglected PCs. We ignore $\varepsilon_\alpha$ completely. The quantity $\xi_\alpha$ represents not only subgrid and subscale processes but also nonlinear effects; it is assumed that this can be treated as a Gaussian white noise forcing of the $\alpha$th PC.

A prediction of the PC field at time $t+\tau$ is made from the PC field at time $t$, c(t), via a *Green function* $\mathbf{G}(\tau)$. Given c(t) and Eq.(1), the most probable prediction of c(t+τ) at later time $t+\tau$ is $\mathbf{G}(\tau)$c(t). We calculate the Green function by choosing some lag $\tau_o$ and forming the matrix $\mathbf{G}(\tau_o)$ whose elements are

$$G_{\alpha\beta}(\tau_o) \equiv \langle c_\alpha(t+\tau_o)c_\beta(t)\rangle/\lambda_\beta . \qquad (2)$$

The $\beta$th EOF eigenvalue $\lambda_\beta$ is $\langle c_\beta^2(t)\rangle$. The eigenvalues $\{g_n(\tau_o)\}$ of $\mathbf{G}(\tau_o)$, along with the corresponding eigenvectors $\{\mathbf{u}_n\}$ and adjoint eigenvectors $\{\mathbf{v}_n\}$ are then combined to obtain the Green function at *any* lag $\tau$ (Penland 1989):

$$\mathbf{G}(\tau) = \sum_{n=1}^{M} \mathbf{u}_n[g_n(\tau_o)]^{\tau/\tau_o}\mathbf{v}_n^T . \qquad (3)$$

The eigenvalues $\{g_n(\tau_o)\}$ of $\mathbf{G}(\tau)$ are complex, giving both a decay time and a period of oscillation to each mode $\mathbf{u}_n$. For a truly linear Markov process, $\mathbf{G}(\tau)$ is independent of $\tau_o$. For a real system where nonlinearities affect dynamics, the Green function must be calculated at a variety of lags $\tau_o$ to estimate the error inherent in the assumption of linear propagation. In the following, the Green function at lag $\tau$ calculated with parameters obtained with specified lag $\tau_o$ (Eq. 3) is denoted $\mathbf{G}(\tau;\tau_o)$.

Given the PC field c(t) at time $t$ and Green functions obtained with lag $\tau_o$, the most probable prediction $\hat{x}_i(t+\tau)$ of the SST anomaly field $x_i(t+\tau)$ at later time $t+\tau$ and geographical location $i$ is

$$\hat{x}_i(t+\tau) = \sum_{\alpha,\beta=1}^{M} \varphi_{i\alpha}G_{\alpha\beta}(\tau;\tau_o)c_\beta(t), \qquad (4)$$

where $\varphi_{i\alpha}$ is the value of the $\alpha$th EOF at location $i$. The prediction of the average SST anomaly field in Niño 3 is obtained by taking the average of $\hat{x}_i(t+\tau)$ for all locations $i$ within the region.

## 4. Results

As shown above, the average SST in the Niño 3 region is negligibly affected by first projecting the SSTs in the PacIn region onto the leading 10 PCs, and it is the projected average which is our predictand. Using the first 10 PCs of SSTs in the PacIn region as predictors, the eigenvalues and eigenfunctions of $\mathbf{G}(\tau_o;\tau_o)$ were calculated for $\tau_o$ = 5, 7, 9 and 11 months and combined as in Eqs. (3-4) to predict the SST anomalies. The root mean square error in prediction is shown as a function of lead time $\tau$ for the various $\tau_o$'s, as is the mean square error for prediction by persistence (Fig. 3). For lead times less than seven months, prediction errors using $\tau_o$ = 5, 7 and 9 months are strikingly similar. This similarity is due to the approximate independence on $\tau_o$ by the eigenvectors and their adjoints, giving credence to the assumption of linear Markovianity within that time frame.

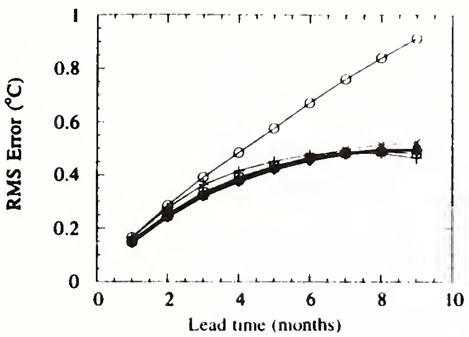

Fig. 3: RMS prediction error as a function of lead time in Niño 3. Circles: Persistence. × signs: $\tau_o$=5 months. Diamonds: $\tau_o$=7 months. Squares: $\tau_o$=9 months. + signs: $\tau_o$=11 months.

Of particular interest is an eigenvector with a decay time of 8-10 months and period of 27-32 months. Fig. 4 shows the pattern obtained with $\tau_o$ = 7 months. The pattern correlation between this and the corresponding mode obtained with $\tau_o$ = 5, 9 and 11 months are 99.0%, 98.7% and 97.6%, respectively, while the pattern correlation between

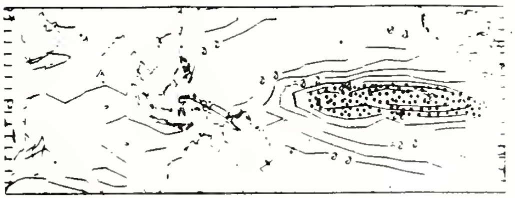

a) Real part.

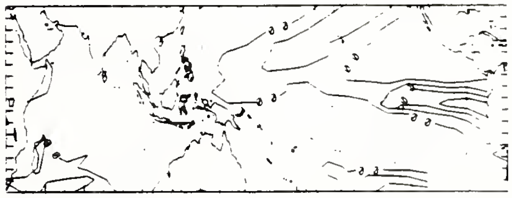

b) Imaginary part.

Fig. 4: Eigenvector of $\mathbf{G}(\tau, \tau_o$=7 months) having decay time of 8.6 months and an oscillation period of 29.1 months. Contour interval = 0.025 (multiplied by 1000 on plot). Regions with loadings ≥ 0.100 are shaded.

its adjoint eigenvector (Fig. 5) obtained with $\tau_o = 7$ months and the adjoint obtained with $\tau_o = 5$, 9 and 11 months are 99.1%, 95.0% and 83.5%, respectively. Looking at the real part of this adjoint, we find that a sensitive region is located in the southern Indian Ocean and is as important in exciting the 30-month mode as the equatorial Pacific. The imaginary part of the adjoint reveals that another phase of the 30-month mode is sensitive to the Indonesia region as well as to the equatorial eastern Pacific.

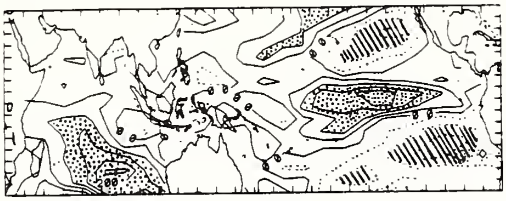

a) Real part.

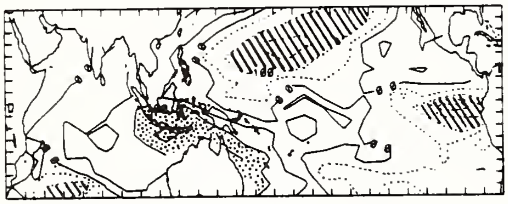

b) Imaginary part.

Fig. 5: Adjoint of eigenvector shown in Fig. 4. Contour interval = 0.050. Regions with loadings ≥ 0.100 are shaded; regions with loadings ≤ -0.100 are striped.

Similar modes with periods of about 30 months were found using PCs calculated in the Pac and Glob regions, although other modes showed more dependence on the oceanic domain. Nevertheless, prediction of SST anomalies in Niño 3 seemed not to depend crucially on which of these domains was used to calculate the predictor PCs (Fig. 6). The question, then, is whether this apparent domain-independence is due to a dominant mode common to all the domains, or does each complete set of modes act in concert to describe the same field as the others?

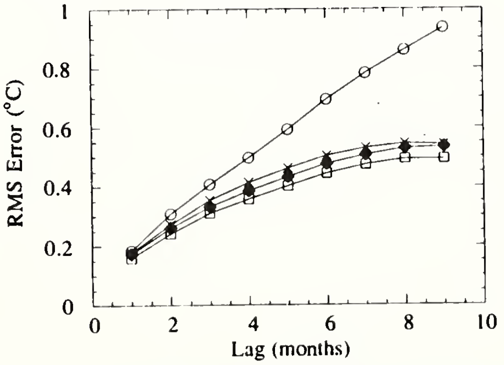

Fig. 6: RMS prediction error as a function of lead time in Niño 3 using PCs calulated in Pac (squares), Pacin (Diamonds), and Global (× signs) tropical oceans. For comparison is the RMS error incurred by prediction by persistence (circles).

To answer this question, we considered Pac and PacIn predictors. The Green function $\mathbf{G}(\tau;\tau_o)$ was decomposed into K matrices $\mathbf{G}_k(\tau;\tau_o)$, where $\mathbf{G}_k(\tau;\tau_o)$ is the contribution to the summation (3) either from one real mode or from one complex conjugate pair, and where K is the number of complex conjugate pairs plus the number of exponentially decaying structures. That is, K=6 for the Pac region, which has two real modes, and K=5 for PacIn, whose modes are all complex. Then, we calculated the RMS error between the SST anomalies in Niño 3 and prediction using each of the matrices $\mathbf{G}_k(\tau;\tau_o)$ by itself in Eq. (4). Of course, predictions made this way are worse than those made using the combined Green function $\mathbf{G}(\tau;\tau_o)$ (Fig. 7a,b). However, it is interesting to remark that none of the error curves using just one mode or mode pair has the same monotonic curvature as that obtained with $\mathbf{G}(\tau;\tau_o)$, and that none stands out as making significantly better predictions than the others. These individual error curves do not go smoothly to zero at zero lag. Mathematically, this is due to the fact that the outer product between any individual mode and its adjoint is not the identity matrix; physically, the modes interfere, and this mode interference is important in describing the SST anomaly field. Finally, we note that the individual error curves in the Pac and PacIn regions do not

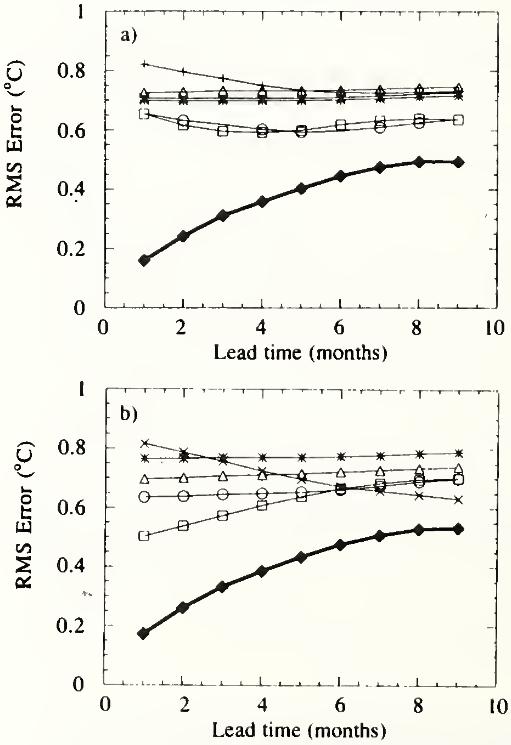

Fig. 7: RMS prediction error as a function of lead time in using all 10 leading PCs (solid diamonds) in a) Pac and b)PacIn regions, compared with prediction using individual real modes or complex mode pairs. a) Pac region. Circles: modes 1/2. Asterisks: mode 3. × signs: modes 4/5. Squares: modes 6/7. Triangles: mode 8. + signs: modes 9/10. b) PacIn region. Circles: modes1/2. Asterisks: modes 3/4. × signs: modes 5/6. Squares: modes 7/8. Triangles: modes 9/10.

look alike, although the error curves using $\mathbf{G}(\tau;\tau_0)$ calculated in the respective regions do. We conclude that the independence of domain is not due to a single dominant, domain-independent mode, although the modes calculated in different regions are highly correlated and some are very similar. Rather, the modes calculated in any of the three domains have large loadings in the Pacific and act together to describe the SST anomaly field.

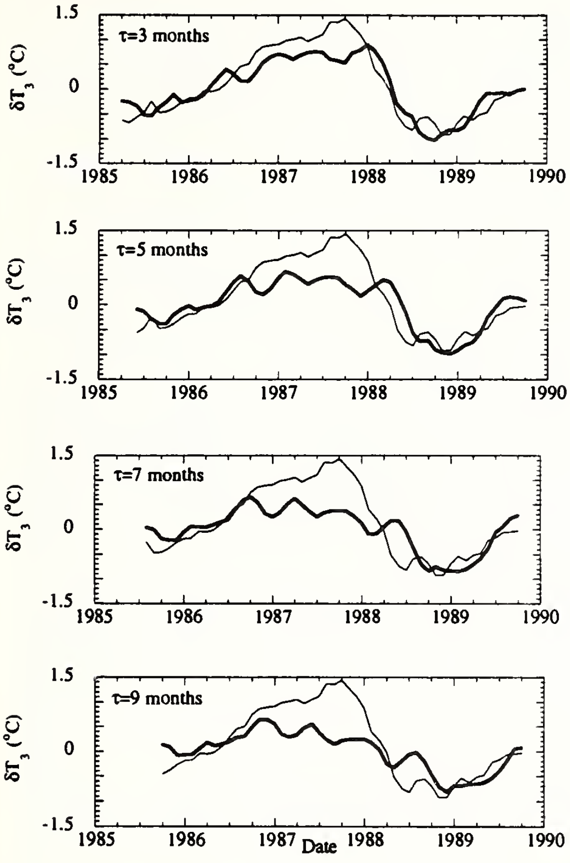

Fig. 8: Comparison of prediction (heavy line: $\tau_0$=7 months) and verification (light line) for $\tau$ = 3, 5, 7 and 9 months.

Returning our attention to PacIn preditors, we compare predictions at lead times of 3, 5, 7 and 9 months with verifications of Niño 3 SST anomalies in Fig. 8. Predictions were made with Green functions calculated with $\tau_0$ = 7 months and a training period between January 1950 and December 1984. We find that the prediction method performed quite well for periods of rising SST anomalies. The analysis does not like to persist large anomalies and once the anomalies are large enough, it will try to drag them down. Correlations between predictions and verifications are too good (Fig. 9), showing a rosier picture than RMS errors. As lead time increases, the size of the prediction must decrease systematically since the eigenvalues $\{g_n(\tau_0)\}$ require each mode to decay, and correlations cannot detect a consistent over- or underestimation of the *size* of the SST anomaly if the trend is well-reproduced.

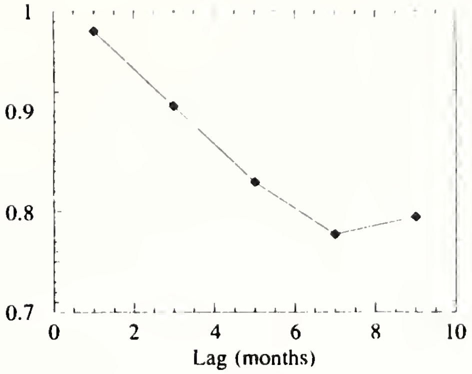

Fig. 9: Correlation between prediction ($\tau_0$=7 months) and verification as a function of lead time.

Linear dynamics implies a Gaussian distribution of SST anomalies, and we can use the functional form of the distribution (Penland 1989; Wilks 1962) to calculate confidence intervals for the prediction of the anomaly at any location, or any linear combination of anomaly values at various locations, such as the average SST in Niño 3. Fig. 10 shows the prediction (light solid line) of the Niño 3 anomaly based on the PC field of January 1989 and the subsequent verification (heavy solid line). The dashed lines delimit the 95% confidence interval. Although the confidence interval is large, it is heartening to see that the verification time series is well within its limits during this time period.

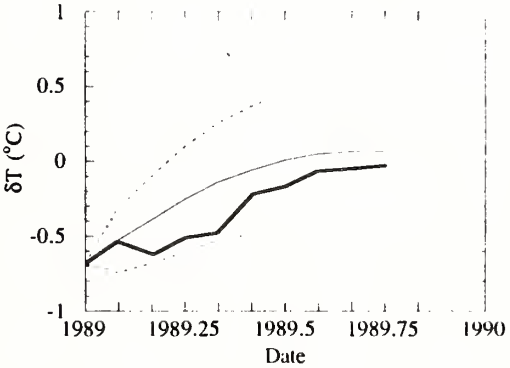

Fig. 10: Prediction of Niño 3 SST, based on PC field of January 1989, and subsequent verification. Dashed lines show 95% confidence interval.

## 5. Discussion

Prediction of SST anomalies in Niño 3 using 10 PCs as predictors is useful up to a lead time of about nine months. There is a trade-off in the number of PCs chosen: 10 PCs try to predict the field with a maximum of five periodicities, but more PCs (for example, 20 PCs) introduce much more noise than signal into the Niño 3 region and make the predictions less reliable.

The time-averaged RMS error made by this prediction scheme is consistently better than prediction by persistence; however, the linearity of the dynamical model constrains large anomalies to decay. It is expected, therefore, that the method would describe well the transitions between warm and cold events while inaccurately predicting their duration (cf. Fig. 8).

Prediction of SST anomalies in Niño 3 did not depend significantly on whether the predictors were calculated in the Pacific, Pacific-Indian or Global tropical oceans. This apparent independence on domain did not depend upon a single dominant, domain-independent mode but rather to the combined effects of all the modes in a set.

The dependence of the calculated Green functions on $\tau_0$ was remarkably weak for $\tau_0$ between 5 and 9 months. This implies that the first 10 PCs of Pacific-Indian SSTs can accurately be assumed to behave as a multivariate linear Markov process on these time scales. That is, Gaussian statistics give good estimates for confidence intervals and forecasts of prediction error on these time scales.

*Acknowledgements:* The authors are pleased to acknowledge useful conversations with Tim Barnett, Maurice Blackmon and Prashant Sardeshmukh. We also gratefully acknowledge support by NOAA Grant # NA16RC0115-01.

## REFERENCES

Barnett, T., N. Graham, M. Cane, S. Zebiak, S. Dolan, J. O'Brien, and D. Legler, 1988: On the prediction of the El Niño of 1986-1987. *Nature*, **241**, 192-196.

Graham, N.E., J. Michaelsen, and T.P. Barnett: 1987a: An investigation of the El Niño-Southern Oscillation cycle with statistical models. 1. Predictor field characteristics. *J. Geophys. Res.*, **92**, 14 251 - 14 270.

Graham, N.E., J. Michaelsen, and T.P. Barnett: 1987b: An investigation of the El Niño-Southern Oscillation cycle with statistical models. 2. Model results. *J. Geophys. Res.*, **92**, 14 271 - 14 289.

Penland, C., 1989: Random forcing and forecasting using Principal Oscillation Pattern analysis. *Mon. Wea. Rev.*, **117**, 2165-2185.

Slutz, R.J., S.J. Lubker, J.D.Hiscox, S.D. Woodruff, R.L. Jenne, D.H. Joseph, P.M. Steurer, and J.D. Elms, 1985: *Comprehensive Ocean-Atmosphere Data Set. Release 1.* NOAA Environmental Research Laboratory, Boulder, Colorado, 268pp.

Wilks, S., 1962: *Mathematical Statistics.* Wiley & Sons, New York, 644pp.

Xu, J.-S., and H. von Storch, 1990: Predicting the state of the Southern Oscillation using Principal Oscillation Pattern analysis. *J. Climate*, **3**, 1316-1329.

# The Potential for Long-Range Streamflow Forecasting Based on ENSO

John A. Dracup and Ercan Kahya

4532 Boelter Hall
Civil Engineering Department, UCLA
Los Angeles, CA 90024

## ABSTRACT

The extreme phases of the Southern Oscillation (SO) have been linked to fairly persistent classes of atmospheric anomalies (e.g., precipitation and temperature) over the low and midlatitudes at regional and global scale. This study examines the relationships between the extreme low index phases of the Southern Oscillation and unimpaired stream discharges over the contiguous U.S. using 1009 stations. Of particular interest in this investigation is the identification of areas of land that appear to have consistent and strong El Niño-Southern Oscillation (ENSO) related streamflow signals. The analysis of several hundred stations over the western and southern states by an empirical approach indicates apparently ENSO-related streamflow responses exist within the Pacific Northwest and the Florida-Georgia core areas. Once an El Niño event sets in, a long-term forecasting utility may be available for these regions. The results of this analysis, confirming the previous precipitation studies, also demonstrates the midlatitude hydrologic response to tropical ENSO phenomena.

## 1. INTRODUCTION

Precipitation anomalies during the evolution of ENSO events have been sufficiently analyzed over the tropics and mid-latitudes (e.g., Rasmusson and Carpenter 1982, 1983; Bradley et al. 1987; Ropelewski and Halpert 1986, 1987). The importance of ENSO-streamflow relationships (mostly for predictive purposes) has been emphasized by recent studies. Cayan and Peterson [1989] investigated the influence of North Pacific atmospheric circulation on streamflow in the western United States. They pointed out that streamflow anomalies might be predicted two seasons in advance by using the Southern Oscillation Index (SOI). Koch et al. [1991] indicated that knowledge of the SOI in the late summer and fall seasons preceding the water supply forecast period (which is often April to September) may provide guidance as to the nature of streamflow in the coming water year. Kuhnel et al. [1990] showed that the Southern Oscillation (SO) signal is readily detectable for rainfall and runoff in the southeast Australia, but not in the southeast United States. The present study applied a different approach to the relatively broad domain in order to specify streamflow patterns associated with ENSO events in the contiguous United States.

Ropelewski and Halpert [1986, 1987] have determined that linkages definitely exist between the low index phases of the Southern Oscillation and precipitation in both hemispheres at global scale. They identified some core areas with dry/wet periods corresponding to an apparent ENSO signal. Streamflow, which filters noisier precipitation fields, is the integral form of land and atmospheric processes and is a more interesting phase of water than precipitation. Some areas that were not identified for precipitation appear to be core regions for streamflow. In this study, we shall address the fluctuation of streamflow anomalies during the evolution of warm episodes, thereby identifying core areas over the U.S. that are assumed to have strong, consistent ENSO-related streamflow responses.

## 2. DATA SET AND METHODOLOGY

Monthly unimpaired streamflow amounts used in this study were compiled by Wallis et al. [1991]. The data set contains 1009 high-quality stream gauge records in the United States, each with 41 years of observation (1948-1988). Stations are more densely distributed over the eastern United States. Each record contains a total of nine moderate/strong low-index phase of the SO years (El Niño), namely 1951, 1953, 1957, 1965, 1969, 1972, 1976, 1982, and 1986. The definition and classification of the ENSO years are based on the studies of Quinn et al. [1978] and Rasmusson and Carpenter [1982].

We adapted an empirical methodology described by Ropelewski and Halpert [1986, 1987] with some minor changes and extensions to search ENSO-streamflow relationships over the contemporaneous United States. Briefly, the method of analysis initially involves transformation of monthly streamflows to percentile ranks and construction of the 24-month warm event composite that is based on the nine latest ENSO episodes. The first harmonic extracted from a such composite is assumed to be the ENSO signal appearing in streamflow anomaly. The amplitude and phase of the harmonic indicate the strength of relationship and time of maximum anomaly within the ENSO cycle, respectively. The statistical significance of the amplitude is assessed by Schuster's test for autocorrelated series (Conrad and Pollak, 1950). The vectorial display of these harmonics over a map enables us to subjectively identify some candidate regions that are the areal extents of ENSO influence on streamflow. We select all stations in a candidate region with a first harmonic of the highest percentage for the variance reduction and with a relatively low level of chance (mostly less than 15%). Time series of monthly original streamflow volumes for each station within a candidate region are transformed to percentiles based on log-normal frequency distribution. Then ENSO composites are constructed again for each station and averaged within the region. As a result, an *aggregate* ENSO composite is obtained to detect subjectively a single *season* within the ENSO cycle. Finally, the index time series for the region are plotted against the season detected and examined for the consistency of the ENSO-related streamflow signal.

## 3. RESULTS AND DISCUSSIONS

This study is still in progress. So far, we have performed the analysis for stations in the western and southern states. Figure 1 shows two candidate regions, namely the Florida-Georgia (FG) and Pacific Northwest (PNW).

The FG region contains 24 stream gauges and exhibits a vectorial coherency of 0.89. In the FG region, 13 stations had less than 5% and the remaining 11 stations had less than 15% of significance level based on Schuster's significance test. Figure 2a illustrates the aggregate composite for the region, indicating pronounced dry and wet periods within the ENSO cycle. These apparent two seasons, which are opposite in sign and apart from each other about 12 months, are the natural consequences of the assumption that a simple sine curve represents the fluctuation of streamflow anomalies over the idealized two-year ENSO composite. Further analyses applied to this region to check the consistency of the possible ENSO-related signal. We plotted index time series (spatially averaged percentiles) for both seasons. Figure 2b reveals the consistent ENSO-streamflow relationships: seasonal October-April (concurrent with the onset of the ENSO) negative departures from median occurred during 7 out of 9 ENSO years. The four of eight driest October-April seasons happened during the evolution of ENSO events. There are two failure cases for the dry period during 1953 and 1965, but both positive anomalies are fairly small (i.e., less than 5%). In Figure 2c, six substantially above-normal departures (i.e., greater than 70%), two slightly below-normal departures (i.e., less than 2.4%), and one 13.7 percent negative departure are observed for the January-April wet season following the year of ENSO occurrences. Six out of 9 cases confirmed the wet season. If we consider two episodes (1952 and 1977) neutral, the FG region is said to be a core area that has strong positive streamflow anomalies associated with the mature phase of ENSO phenomena. This is consistent with the precipitation result of Douglas and Englehart [1981] and Ropelewski and Halpert [1986]. The consistent results of two opposite seasons are a double check for the relationships implied by the aggregate composite of the FG region.

The PNW region is defined by 35 stations and a coherency of 0.92. The calculated significance level for the amplitude of the 22 harmonics was less than or equal to 6 percent. The remaining 13 amplitudes had a level of significance between 6 and 16 percent, except for one with a higher significance level. An aggregate composite for this region is depicted in Figure 3a. A long wet season coinciding exactly with twelve months of ENSO years is detected and examined by the relevant index time series (Figure 3b). Seven out of 9 episodes confirmed this wet season. Moreover, 1953 and especially 1957 ENSO years having minor negative departure (less than 6%) provide extra corroboration for the findings. Six out of the ten wettest years (above 64%) occurred during the years of event and none of the four driest cases (below 30%) coincided with ENSO occurrences. These prolonged positive streamflow anomalies for the PNW need to be further explained. Redmond and Koch [1991] suggest that combined effects of precipitation and temperature have an important impact on snow accumulation in the PNW. Therefore we will analyze precipitation and temperature aggregate composites for the region. In addition, Cayan and Peterson [1989] indicate negative streamflow anomalies in the PNW during the mature phase of ENSO. The dry period from January(+) to July(+) obviously is consistent with their indication. The distinction between streamflow and precipitation in terms of the response to ENSO forcing in the PNW is roughly explained through the respective aggregate composites. Ropelewski and Halpert [1986] suggest unstable but lighter-than-average precipitation anomalies. The climatic reason for this is the fluctuation in timing of the light precipitation between fall and spring (Cayan and Peterson, 1989). In contrast, high land streamflows are not strongly affected by these timing changes, so they demonstrate coherent and consistent ENSO-related signals.

## 4. CONCLUSION

The first step in seeking predictive utilities for long-range streamflow forecasting has been determined to be an identification of possible candidate regions in the United States. The core areas which potentially have streamflow anomalies associated with the low SO phase have been identified among the candidate regions. Applying the further analyses in the candidate regions, the season that reveals the sign and magnitude of the ENSO-related streamflow signal has been detected for each core area.

We have demonstrated the existence of significant midlatitude streamflow responses to the ENSO with specific regional boundaries in South Atlantic and Pacific Northwest states, and due to characteristic differences in precipitation and streamflow fields, the latter have also been shown to be a reasonable alternative as a climatic surface parameter in order to find large-scale circulation signals in the U.S. After completing the current analysis for the El Niño phase, we will proceed to study the relationships between La Niña occurrence and streamflow over the same domain. Since, the extremes of the SO have occurred 18 of the 41 years (44%) of the study period, the relationships specified by this study offer some utility for the long-range seasonal prediction of streamflow for several regions in the U.S.

# REFERENCES

Bradley, R.S., H.F. Diaz, G.N. Kiladis, and J.K. Eischeid. 1987. ENSO Signal in Continental Temperature and Precipitation Records, *Nature*, Vol. 327, pp. 497-501.

Cayan, D.R., and D.H. Peterson. 1989. The Influence of North Pacific Atmospheric Circulation on Streamflow in the West, PACLIM, *AGU Monograph*, Washington D.C.

Conrad V., and L.W. Pollak. 1950. *Methods in Climatology*, Harvard University Press, Cambridge, MA.

Douglas, A.E., and P.J. Englehart. 1981. On a Statistical Relationship between Autumn Rainfall in the Central Equatorial Pacific and Subsequent Winter Precipitation in Florida, *Mon. Wea. Rev.*, Vol. 109, pp. 2377-2382.

Koch, R.W., C.F. Buzzard, and D.M. Johnson. 1991. *Variation of Snow Water Equivalent and Streamflow in relation to the El Niño/Southern Oscillation,* presented at the Western Snow Conference, Juneau, AK, April.

Kuhnel, I., T.A. McMahon, B.L. Finlayson, A. Haines, P.H. Whetton, and T.T. Gibson. 1990. Climatic Influences on Streamflow Variability: A Comparison Between Southeastern Australia and United States of America, *Water Resources Research*, Vol. 26. No. 10, pp. 117-122.

Quinn, W.H., D.O. Zopf, K.S. Short, and R.T.W. Kuo Yang. 1978. Historical Trends and Statistics of the Southern Oscillation, El Niño, and Indonesian Drought, *Fish. Bull.*, Vol. 76, pp. 663-678.

Rasmusson, E.M., and T.H. Carpenter. 1982. Variations in Tropical Sea Surface Temperature and Surface Wind Fields associated with the Southern Oscillation/El Niño, *Mon. Wea. Rev.*, Vol. 110, pp. 354-384.

Rasmusson, E.M., and T.H. Carpenter. 1983. The Relationship Between Eastern Equatorial Pacific Sea Surface Temperatures and Rainfall Over India and Sri Lanka, *Mon. Wea. Rev.*, Vol. 111, pp. 517-528.

Redmond, K.T., and R.W. Koch. 1991. Surface Climate and Streamflow Variability in the Western United States and Their Relationship to Large Circulation Indices, *Water Resources Research,* Vol. 27, No. 9, pp. 2381-2399.

Ropelewski, C.F., and M.S. Halpert. 1986. North American Precipitation and Temperature Patterns Associated with the El Niño Southern-Oscillation (ENSO), *Mon. Wea. Rev.*, Vol. 114, pp. 2352-2362.

Ropelewski, C.F., and M.S. Halpert. 1987. Global and Regional Scale Precipitation Patterns Associated with the El Niño/Southern Oscillation, *Mon. Wea. Rev.*, Vol. 115, pp. 1606-1626.

Wallis, J.R., D.P. Lettenmaier, and E.F. Wood. 1991. A Daily Hydroclimatological Data Set for the Continental United States, *Water Resources Research,* Vol. 27, No. 7, pp. 1657-1663.

## FIGURE CAPTIONS

Figure 1: The plot of first harmonic dials for (a) the Pacific Northwest, and (b) the Florida-Georgia regions.

Figure 2: a) Aggregate composite of Florida-Georgia region, b) the relevant index time series for dry season, c) same as (b) except for wet season.

Figure 3: a) Aggregate composite of Florida-Georgia region, b) the relevant index time series for wet season.

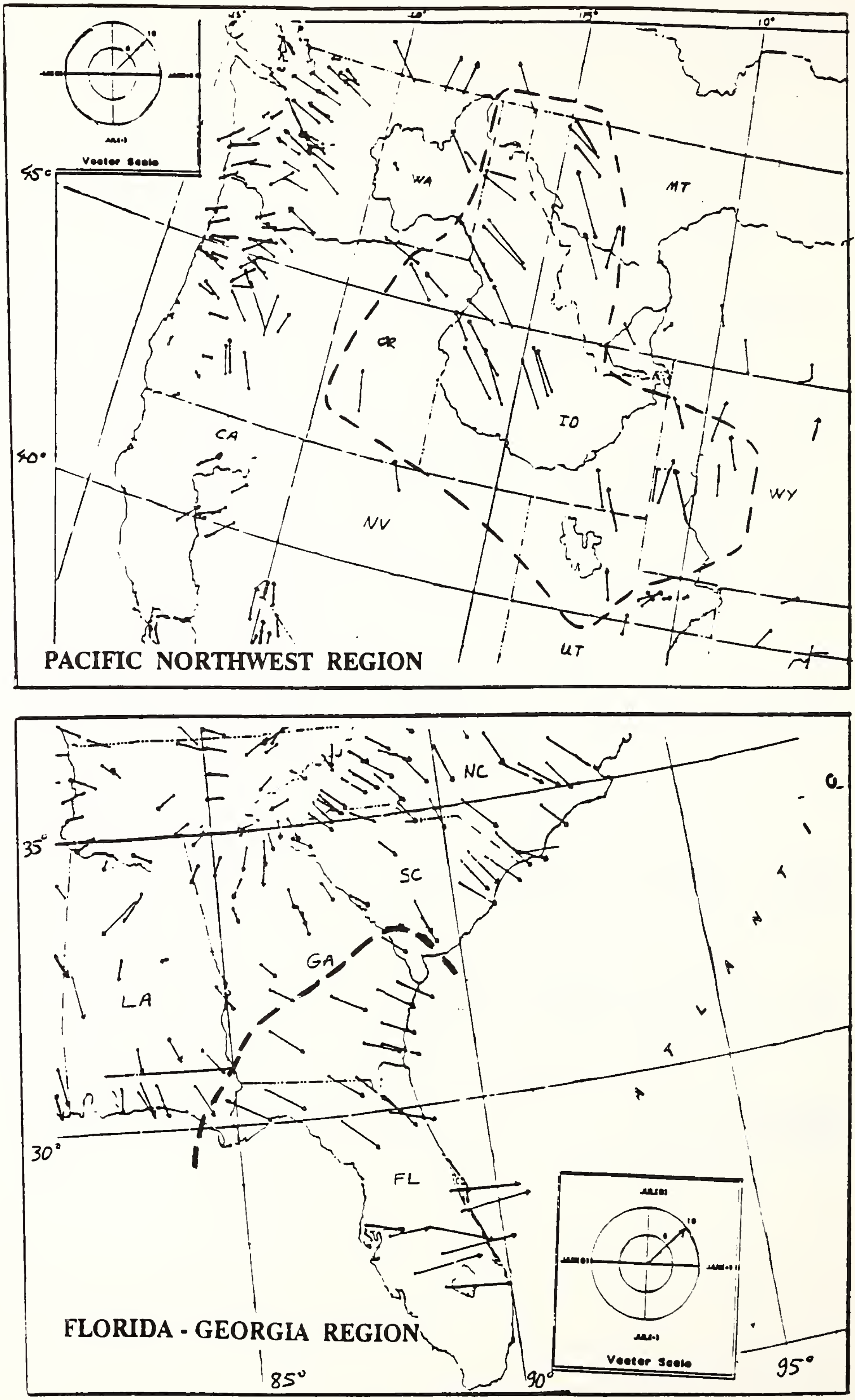
a)
Vector Scale
45°
40°
WA
MT
OR
ID
CA
NV
WY
UT
PACIFIC NORTHWEST REGION
b)
NC
35°
SC
GA
LA
30°
FL
FLORIDA - GEORGIA REGION
Vector Scale
85°
90°
95°

Figure 1

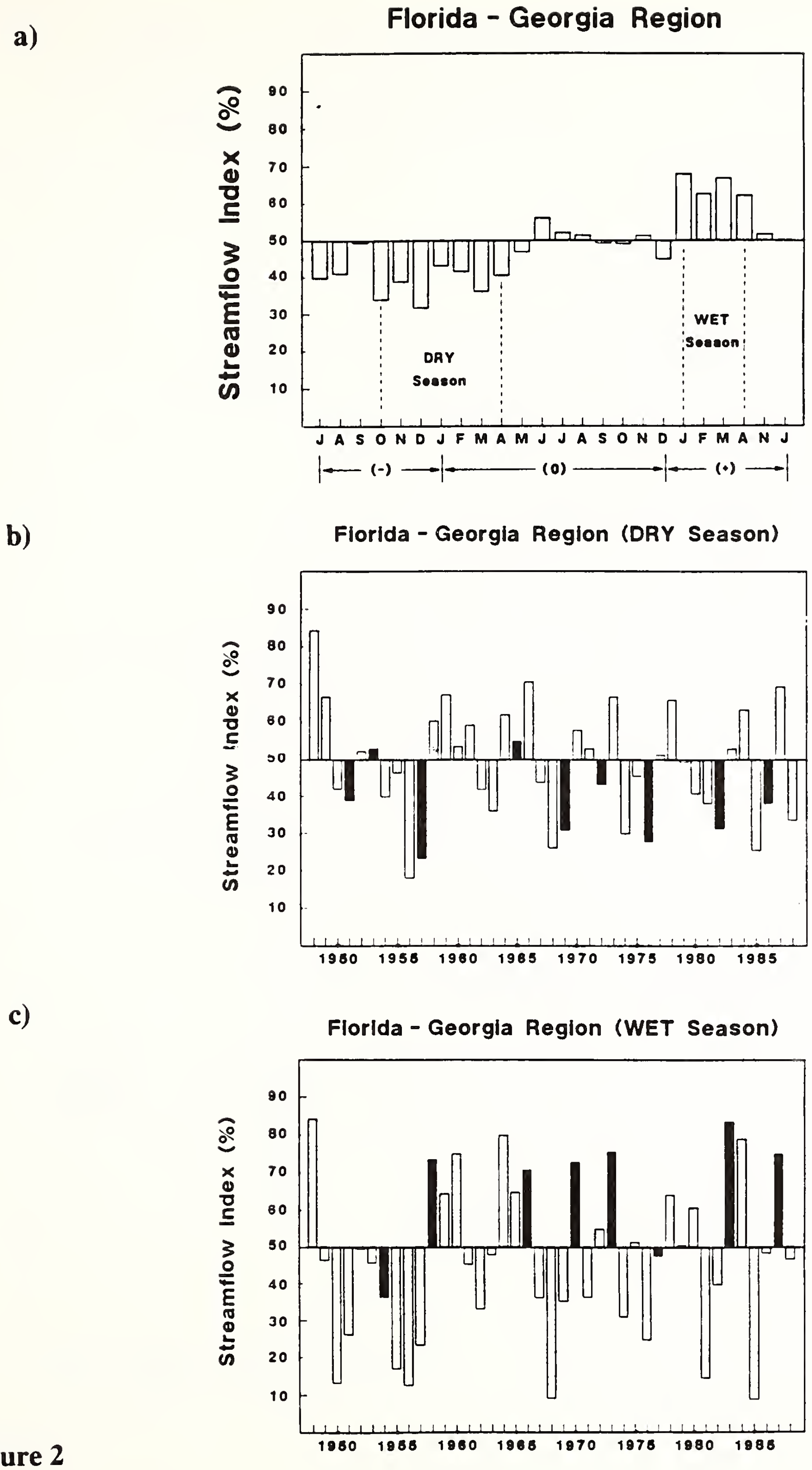
a)
Florida - Georgia Region
Streamflow Index (%)
90
80
70
60
50
40
30
20
10
J A S O N D J F M A M J J A S O N D J F M A N J
DRY Season
WET Season
(-)
(0)
(+)
b)
Florida - Georgia Region (DRY Season)
Streamflow Index (%)
90
80
70
60
50
40
30
20
10
1950 1955 1960 1965 1970 1975 1980 1985
c)
Florida - Georgia Region (WET Season)
Streamflow Index (%)
90
80
70
60
50
40
30
20
10
1950 1955 1960 1965 1970 1975 1980 1985

Figure 2

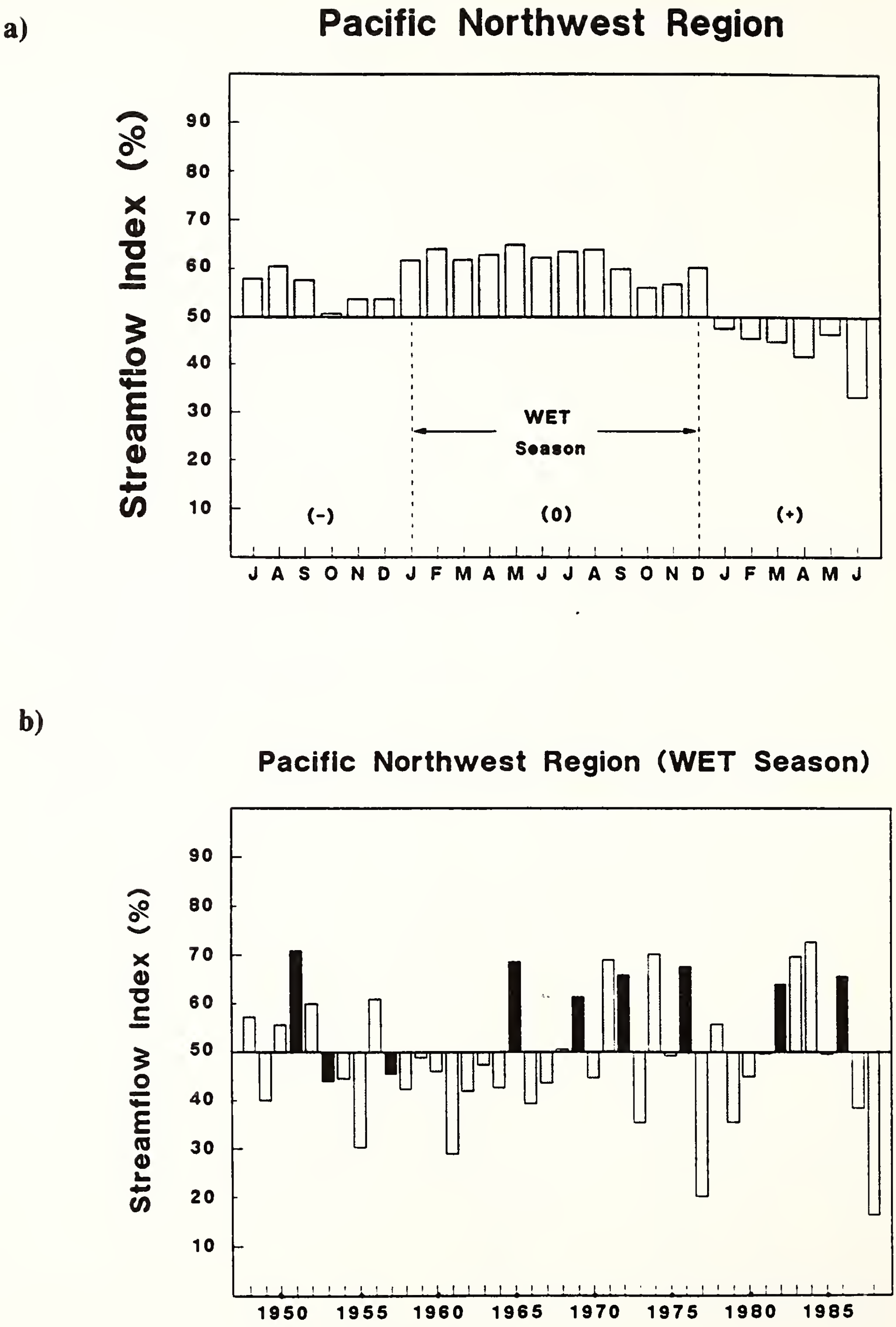
a)
Pacific Northwest Region
Streamflow Index (%)
90
80
70
60
50
40
30
20
10
WET
Season
(-)
(0)
(+)
J A S O N D J F M A M J J A S O N D J F M A M J
b)
Pacific Northwest Region (WET Season)
Streamflow Index (%)
90
80
70
60
50
40
30
20
10
1950
1955
1960
1965
1970
1975
1980
1985

Figure 3

# Regime Transitions During the Winter of 90-91: Their Influence on Numerical Extended-Range Prediction[1]

David P. Baumhefner

*National Center for Atmosperic Research[2] P.O. Box 3000, Boulder, CO 80307*

## 1. Introduction

Recent experience in numerical prediction of time-mean flow beyond the limit of daily deterministic predictability has revealed moderate success in the mid-latitudes (Tracton *et al.*, 1989; Baumhefner, 1991) as well as in the tropics (von Storch and Baumhefner, 1991). A major difficulty associated with these predictions is that only a minority of the forecasts sampled are skillful. This fact requires a careful selection of cases when skill is actually present. Possible selection techniques may include analysis of multiple forecast dispersion characteristics (Baumhefner, 1989), identification of potential scale interaction scenarios (Colucci and Baumhefner, 1991) and classification of planetary-wave regimes. This report addresses the last of these topics by analyzing the behavior of large-scale anomalies and their transitions during the winter of 90-91, and comparing them to the variations in time-mean forecast skill. The basic hypothesis in this study is that transitions between regimes may be particularly difficult to forecast and may account for a relatively large number of poor forecasts; on the other hand, stable or quasi-stationary regimes may contribute primarily to skillful forecasts.

## 2. Regimes

The large-scale low-frequency flow was examined for the winter of 90-91 by plotting the climatologically anomalous heights at 500 mb in a longitude-time domain. An unfiltered example of these plots is shown in Figure 1 (top) for 12 JAN to 7 FEB. There is some hint of low-frequency regimes (*e.g.*, day 76-90 in the Pacific) in this plot; however, the higher frequency baroclinic features obscure much of the pattern. These patterns were then subjected to various space and time filters in order to highlight longer time-scales. Figure 1 (bottom) illustrates a method that most clearly delineates the patterns of interest—it filters out 2-D spectral waves greater than 7 *without* time-filtering. For the 12 JAN-17 FEB period, there are three distinct regimes: days 72-80 are weak amplitude quasi-stationary patterns, days 81-91 are strong amplitude, somewhat retrograding patterns, and days 92-98 show a dramatic reversal of amplitude that is nearly stationary. The transitions between regimes occur in day 79 (19 JAN) and day 91 (31 JAN), as shown on Fig. 1 by the horizontal solid line. Other well-identified transitions occur on 5 DEC, 17 DEC, 31 DEC, 12 JAN, —, —, 10 FEB, and 21 FEB 90-91.

---

[1] Proc. of the 16th Climate Diagnostics Workshop, Lake Arrowhead, CA, October 91, CAC-NMC/NWS/NOAA, WWB Room 606, 5200 Auth Road, Washington, D.C. 20233

[2] The National Center for Atmospheric Research is sponsored by the National Science Foundation.

## 3. Six-to-Ten Day Forecast Skill

To document the hypothesis described in the introduction, the NMC and ECMWF 6-10 day time-mean forecast skill for the winter of 90-91 were compared to the identified transitions between regimes. Figure 2 (top) plots the daily skill centered on the varifying day 8 of the 5 day mean (*e.g.*, for day 20 the initial state for the forecast was day 12, or 12 DEC). The temporal continuity is quite poor, therefore a 5 point running filter is applied to the scores in order to show the long-term trends (Fig. 2, bottom). The transitions identified from the spectral filtering are drawn as vertical lines, but advanced 5 days to coincide with the vertification scores that were integrated through the transition. In six of the eight cases for the NMC model, the skill is clearly deteriorating during the transition. Surprisingly, ECMWF's model skill is much less affected by transitions in regimes. The reverse relationship of high skill during stable periods is also borne out, at least for the NMC model. If the daily unfiltered scores for the European Centre forecasts are examined, there is a tendency for one or two forecasts to react poorly during a transition, but the model seems to recover more rapidly than the NMC forecasts.

## 4. Forecast Example

The least skillful period during the winter occurred in the middle of January with both models showing zero correlation with observed anomalies (Fig. 2). An example of one of these forecasts which began on 14 JAN (day 74, Fig. 1) and passed through the transition period of 19 JAN (day 79) is shown in Fig. 4. This forecast is derived subjectively by NMC staff using a composite of 3-4 different models and weighting each according to recent skill and synoptic behavior. The observed transition is toward increasing amplitude and retrograding patterns, whereas the forecast is nearly the opposite with progressing features of decreasing amplitude. Another case not shown was moderately successful for the transition that occurred on 31 JAN (day 91), as the scores indicate in Fig. 2.

## 5. Summary

This report presents some preliminary results on the relationship between regime transitions and forecast skill. Although the stated hypothesis in general seems to be fulfilled, there is considerable variability between different models and situations. A more rigorous experiment is being designed to test the hypothesis using a Monte-Carlo (multiple forecast) approach and longer forecasts.

*Acknowledgments.* I would like to thank S. Tracton at CAC-NMC for providing the skill scores of the NMC and ECMWF model forecasts. Some of these ideas are based on the daily discussions that are disseminated to the public by the NMC staff concerning the operational 3-5 and 6-10 day products.

## 6. References

Baumhefner, D.P., 1989: Prediction of forecast skill using Monte Carlo ensembles of 30 day forecasts. *Proceedings of 14th Climate Diagnostic Workshop*, Climate Analysis Center, National Weather Service, National Oceanic and Atmospheric Administration, Washington, D.C., 339-343.

Baumhefner, D.P., 1991: Evaluation of long-range forecast skill from Monte Carlo ensemble integrationsof a low resolution NCAR Community Climate Model. *Proc. ICTP/WMO Conference on Long-range Weather Forecasting Research*, Trieste, Italy. WMO/TD#395, 15-19.

Colucci, S.J., and D.P. Baumhefner, 1991: Initial weather regimes as predictors of numerical long-range forecast skill. *Proc. 9th Conference on Numerical Weather Prediction*, AMS, Denver, 654-658.

Tracton, M.S., K. Mo, W. Chen, E. Kalnay, R. Kistler, and G. White, 1989: Dynamical Extended Range Forecasting (DERF) at the National Meteorological Center. *Mon. Wea. Rev.*, **117**, 1605–1635.

von Storch, H. and D.P. Baumhefner, 1991: Principal Oscillation Pattern Analysis of the Tropical 30- to 60- Day Oscillation. Part II: The Prediction of Equatorial Velocity Potential and its Skill. *Climate Dynamics*, **6**, 1–12.

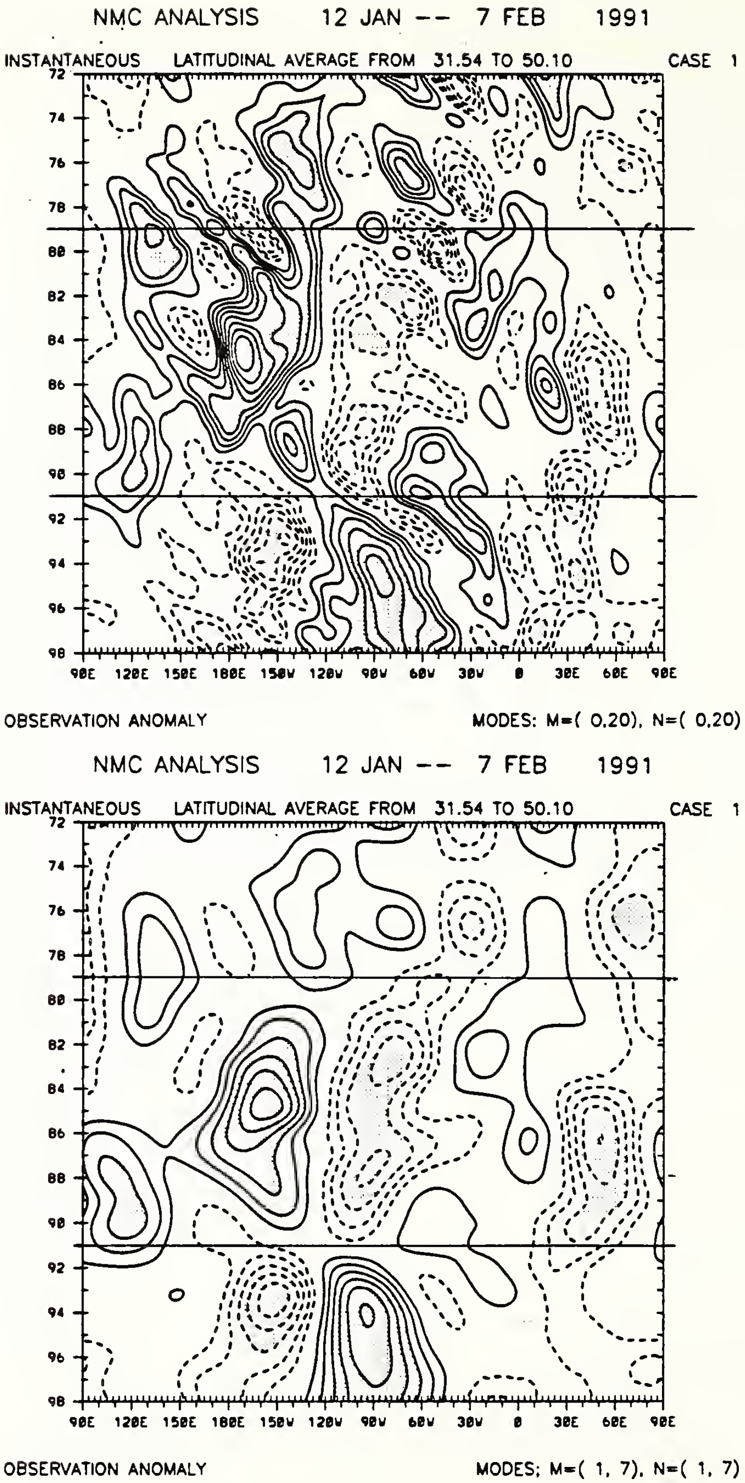

Figure 1: (TOP) Anomaly of 500 mb NMC analyzed geopotential derived from 1979-1985 CAC climatology. Data plotted for period 12 JAN-7 FEB 1991 over all longitudes averaged over 30-50°N latitude. Day# begins at 1 NOV (72=12 JAN). Contour interval = 60 m with negative values dashed. Zero contour omitted. Shading begins at ±180 m. Data filtered to first 20 2-D wavenumbers. Solid horizontal linear lines are transitions of large-scale flow. (BOTTOM) Same as top, except for 2-D waves 1-7. Contour interval = 40 m. Shading begins at ±120 m.

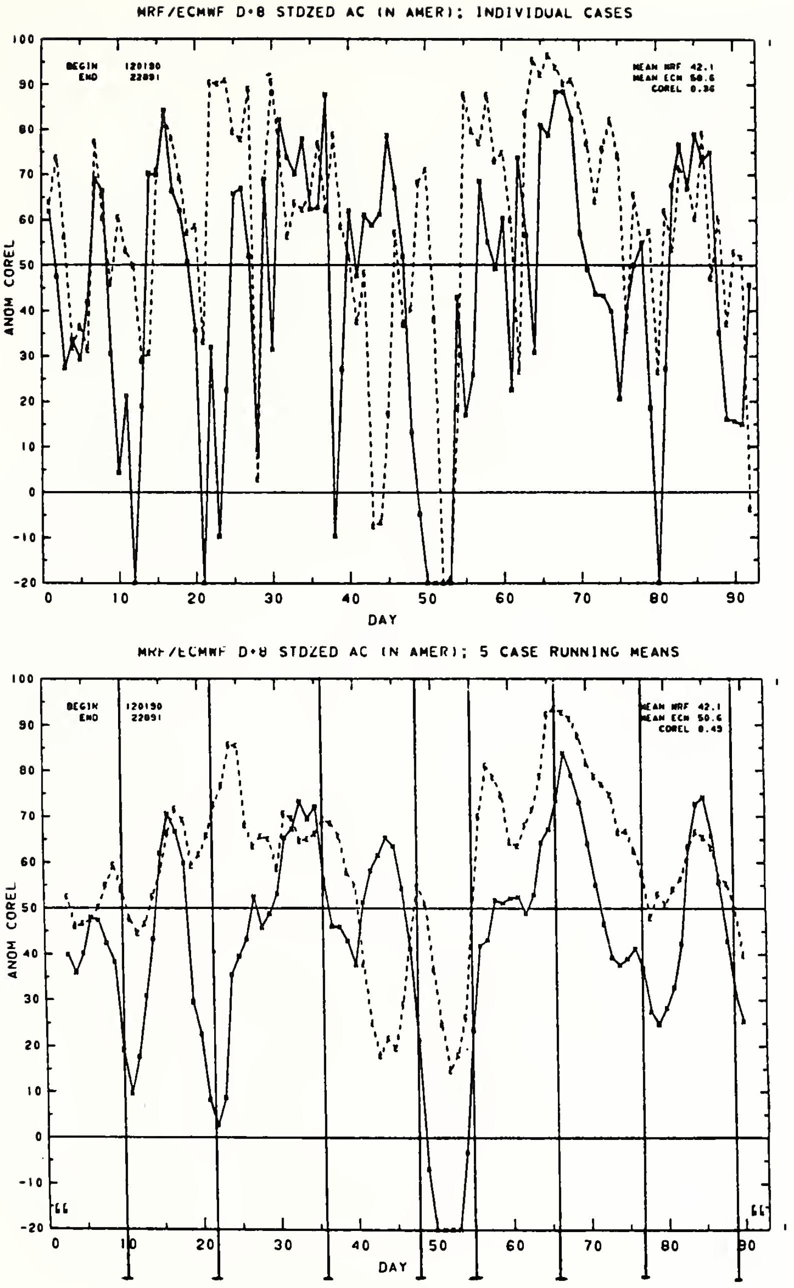

Figure 2: Standardized Anomaly Correlation (AC) over North America of 5-day time-mean forecasts centered at day 8 (6-10 days) for DEC, JAN, FEB of 1990-91. (TOP) Daily forecast skill for NMC (solid) and ECMWF (dashed). Skill plotted at day 8 of forecast. Day# begins at 1 DEC (1 = 1 DEC). Values on ordinate are AC×100 and values below –20 are plotted as –20. (BOTTOM) Same as top, but 5 point running filter applied to data. Transitions identified for winter of 90-91 plotted as vertical lines, but displaced 5 days into the forecast.

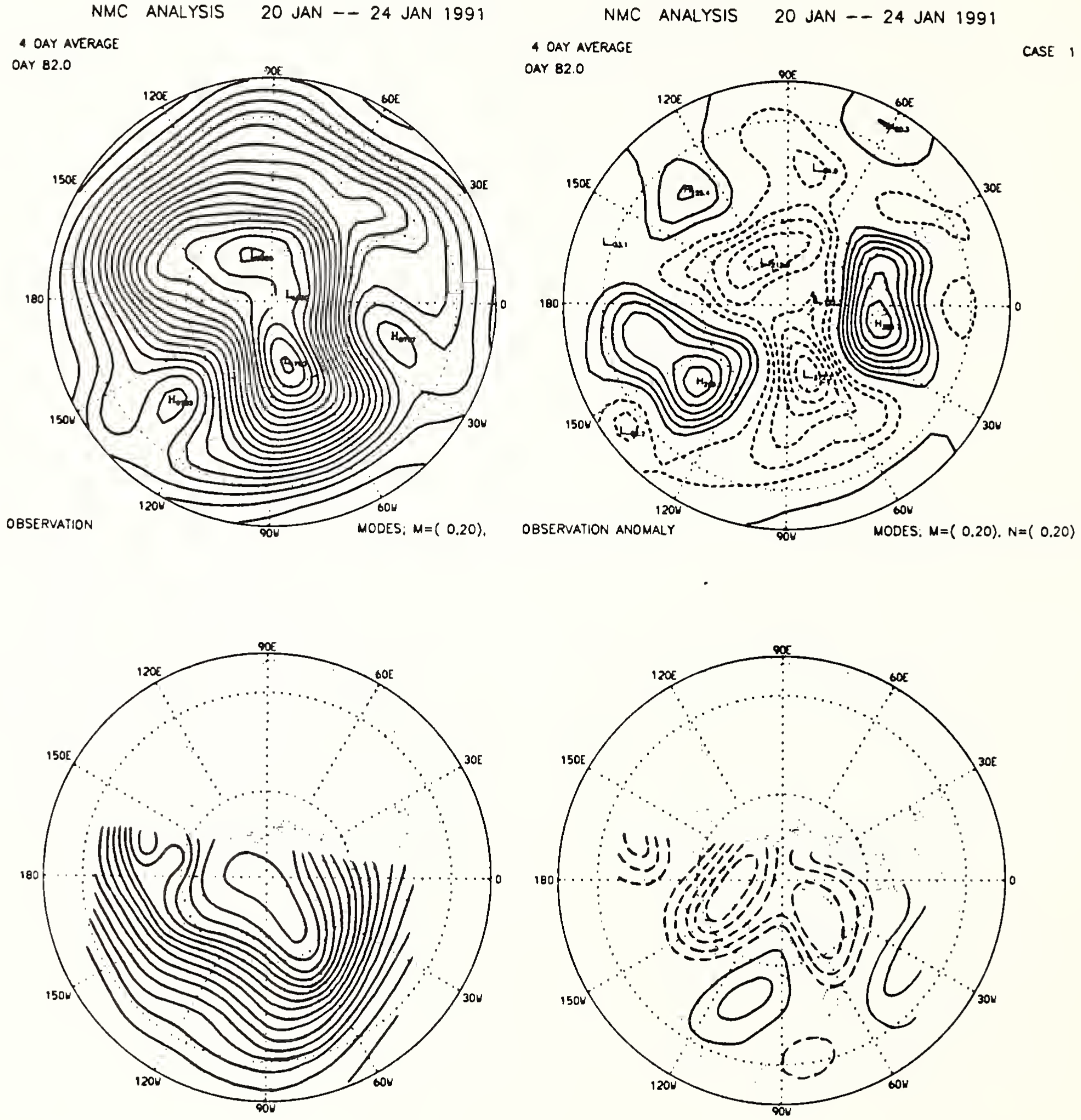

Figure 3: 5 day time-mean of 500 geopotential (left) and its anomaly (right) derived from 1979-1985 climatology for period 20-24 JAN 91. (TOP) NMC observed analyses filtered to first 20 modes. Contour interval = 60 m with zero contour omitted. (BOTTOM) NMC operational forecast transcribed from fax map. Same contour interval.

# Examination of Actual Analysis Differences for Use in Monte Carlo Forecasting

Stephen J. Augustine
University of Michigan, Dept. of Atmospheric, Oceanic and Space Sciences
Ann Arbor, MI 48109-2143

Steven L. Mullen
University of Arizona, Dept. of Atmospheric Sciences
Tucson, AZ 85721

David P. Baumhefner
National Center for Atmospheric Research
P. O. Box 3000, Boulder, CO 80307

## I. Introduction

Skill scores of extended-range operational model forecasts are substantially decreased during blocking events (Tracton 1990 MWR), leading to the hypothesis that blocks may be inherently less predictable than other "typical" flow patterns. One method of examining this hypothesis is Monte Carlo forecasting, in which an ensemble of forecasts is produced from perturbed forms of a single initial state and the spread of forecasts about the ensemble average is examined. The perturbation technique is used to produce a series of equally-likely possible representations of the initial state, and hence must be developed realistically. One source of insight for perturbation technique development is actual analysis difference. Analysis differences can be used to estimate random atmospheric observational errors, so that the effects of measurement uncertainty on forecast error growth can be studied through Monte Carlo techniques. The focus of this work is to determine the differences between the different analysis techniques used to analyze the GWE FGGE data. Especially important will be to examine the vertical variation of analysis differences, to examine analysis differences in areas of frequent baroclinic activity, and to compare land/sea and latitudinal (i.e. tropics/extratropics) variations in analysis differences.

## II. Data/Methodology

A total of 116 synoptic-time analyses, from 1 Jan-5 Mar '79, were sampled from the FGGE data at T31 resolution. The 7 analysis techniques examined include the analyses and re-analyses from ECMWF, NMC, and GFDL, and the GLAS analysis. The fields chosen were temperature and the u- and v-wind components, since these are the basic state variables required to investigate differences in the mass and momentum fields. Data were analyzed at 6 mandatory pressure levels (850mb, 700mb, 500mb, 300mb, 250mb, 100mb).

For each field at each pressure level, the analyses were compared two at a time. For each comparison, the RMS difference was computed at each gridpoint and the systematic difference was subtracted out, so that a temporally-averaged value of random analysis difference could be determined. The temporally-averaged random differences were then spatially averaged, providing an estimate of random observational error from each comparison. The estimates of random observational error were then averaged over all comparisons so a general estimate of observational error could be computed at each pressure level for each field. The random differences were then normalized at all gridpoints by their respective climatological variances, computed from the ECMWF re-analysis, and then averaged over spatial domain and over all comparisons, so that an estimate of the signal/noise ratio (S/N) could be obtained. All computations were done over the Northern Hemisphere, as well as over the tropics (20S-20N) and the extratropics (20N-90N) so latitudinal differences could be examined. Land/sea differences were examined both over the entire Northern Hemisphere and within the domain 30N-60N, an area dominated by frequent synoptic activity. Vertical variations were also examined.

## IV. Results

### A. Latitudinal Variation

Temperature differences in the tropics are 0.3-0.6 K less than those in the extratropics, except in the upper troposphere/lower stratosphere (Fig. 1a). In both regions, there is a general decrease in temperature difference from 850mb to 300mb. Temperature differences generally increase with height from 300mb, although there is a decrease from 250mb to 100mb in the extratropics.

The normalized temperature variances (Fig. 1b) show a substantial difference in S/N between the two regions. In the extratropics, S/N is less than 0.5 at all levels. However, the S/N in the tropics is much greater than 1.0, indicative of the fact that the climatological variability of temperature is very small in the tropics. The values shown in the plot are skewed higher due to the extremely high S/N produced by comparisons involving the NMC operational analysis. Removing those comparisons reduces the S/N, but only to within the 1.0-1.5 range.

The differences in the u- and v-wind components are almost identical, so only the u-component is discussed here. The differences in the tropics and extratropics increase with height in similar fashion up to 250mb, but then diverge above 250mb (Fig. 2a). Unlike the temperature differences, the values of the u-wind differences are similar between the tropics and extratropics at the lowest 5 levels examined. Differences at the examined levels in the tropics range from 2.7m/s at 850mb to 6m/s at 100mb, while differences in the extratropics range from 3m/s at 850mb to 5m/s at 250mb.

The normalized u-component variances show that again a substantial difference in S/N exists between the tropics and extratropics, indicative of the fact that the climatological variance is lower in the tropics than in the extratropics. The vertical variation of S/N is similar between the two regions, but the comparable S/N in the lower troposphere and upper troposphere, combined with the increase with height in u-wind difference (Fig. 2a), indicates the climatological variability of the lower troposphere is much smaller.

### B. Land/Sea Variation

The results over the entire Northern Hemisphere are similar to those in the region 30N-60N, so only the latter are presented here. Temperature differences are 0.2-0.7K smaller over land than over oceans (Fig. 3a), while u-wind differences are 1-2m/s smaller over land than over oceans (Fig. 4a). Temperature errors over oceans decrease from 850mb to 300mb, while those over land decrease from 850mb to 500mb and increase above 500mb. Errors in the wind fields increase with height up to the tropopause level, then decrease with height.

The S/N over land is also smaller than the S/N over oceans for temperature (Fig. 4a) and for u-wind at all levels except 850mb (Fig. 4b). The S/N is less than 0.2 at all levels examined for both fields, indicating analysis variance is much smaller than climatological variability. The S/N is greatest in the upper troposphere/lower stratosphere and lower troposphere.

## V. Summary

Latitudinal variations are important for modeling analysis difference, especially when considering the mass field. There is much more analysis uncertainty over the tropics than over the extratropics, due to the lower climatological variability of both temperature and wind in the tropics. Land/sea variations are also relevant for modeling analysis difference in the mass and momentum fields, although large differences in S/N were not found for this particular breakdown. Vertical variations are important as well, since differences in both the T and u fields were shown to vary with height and be maximized in the upper troposphere/lower stratosphere. Finally, scatterplots of the individual analysis-analysis comparisons showed large spread of the individual values. The ECMWF analysis and re-analysis and NMC re-analysis were found to be the most similar analyses, and the NMC operational analysis and GFDL analysis were the most distinct analyses.

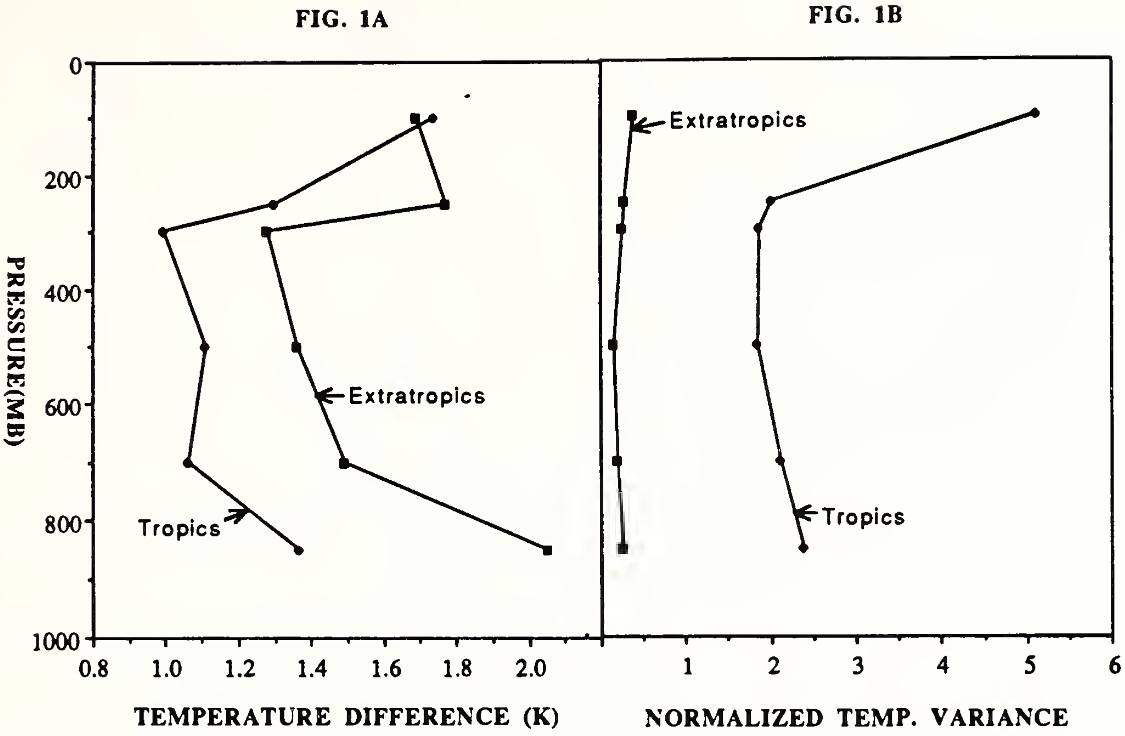

Fig. 1: (A) Vertical profile of temperature random difference (averaged over all analysis comparisons) for latitudinal breakdown; (B) Vertical profile of normalized temperature variance for latitudinal breakdown.

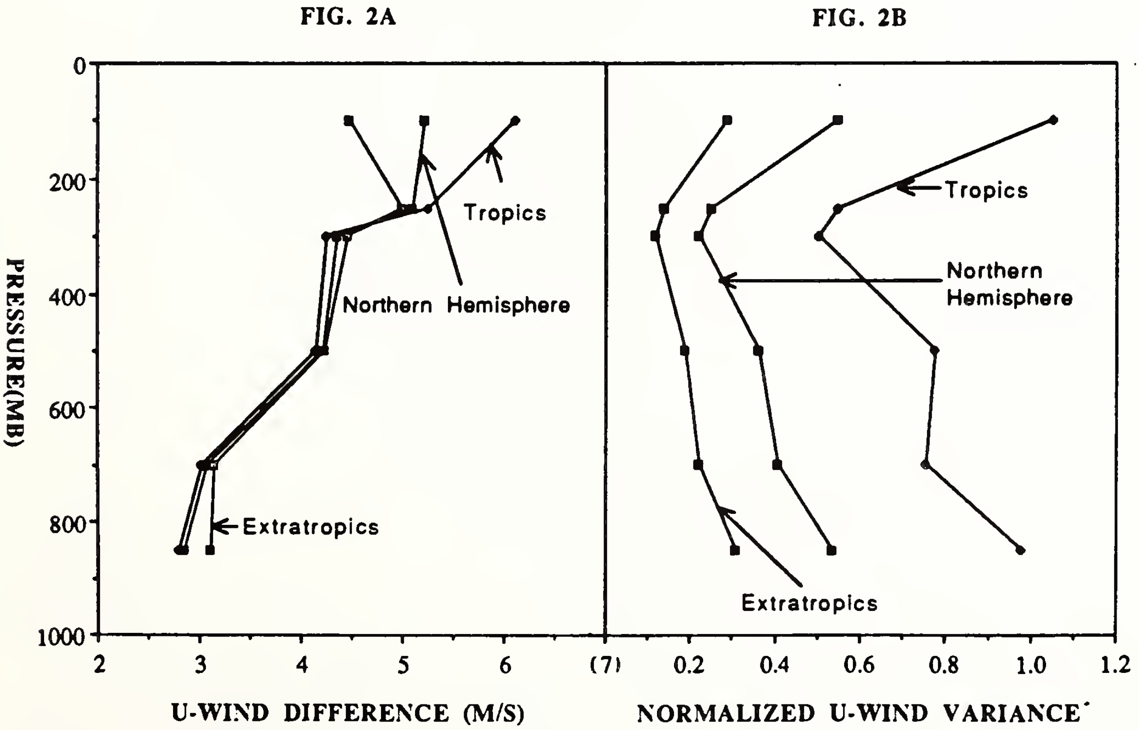

Fig. 2: (A) Vertical profile of u-wind random difference (averaged over all analysis comparisons) for latitudinal breakdown; (B) Vertical profile of normalized u-wind variance for latitudinal breakdown.

FIG. 3A FIG. 3B

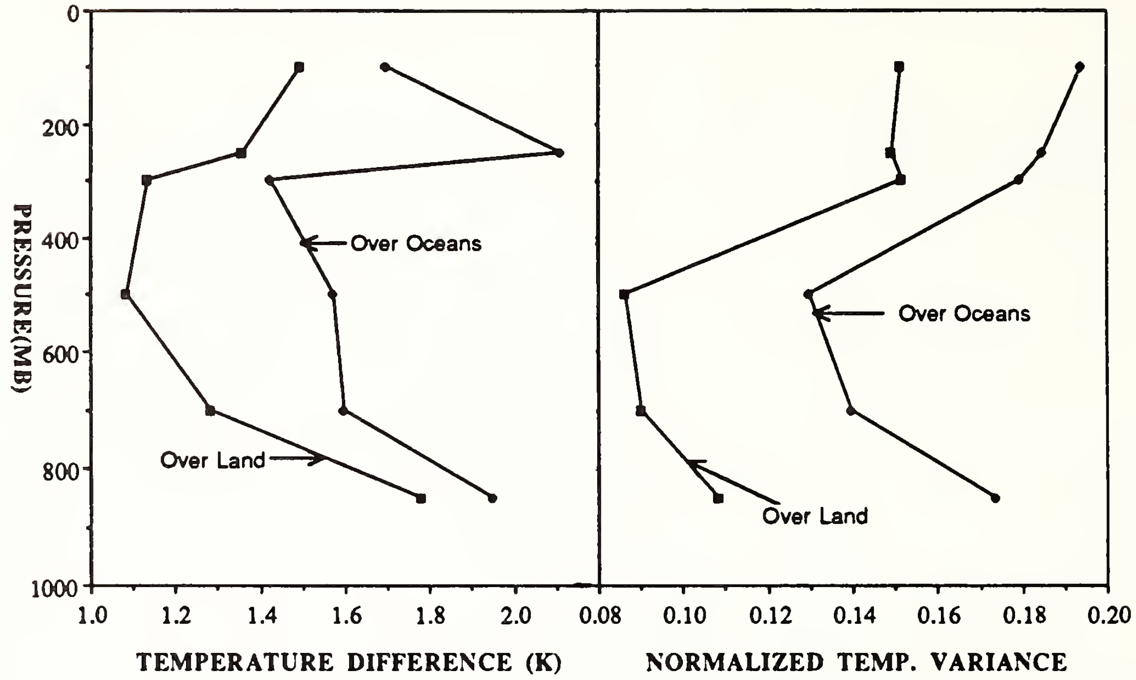

Fig. 3: (A) Vertical profile of temperature random difference (averaged over all analysis comparisons) for land/sea breakdown, within the region 30N-60N; (B) Vertical profile of normalized temperature variance for land/sea breakdown, within the region 30N-60N.

FIG. 4A FIG. 4B

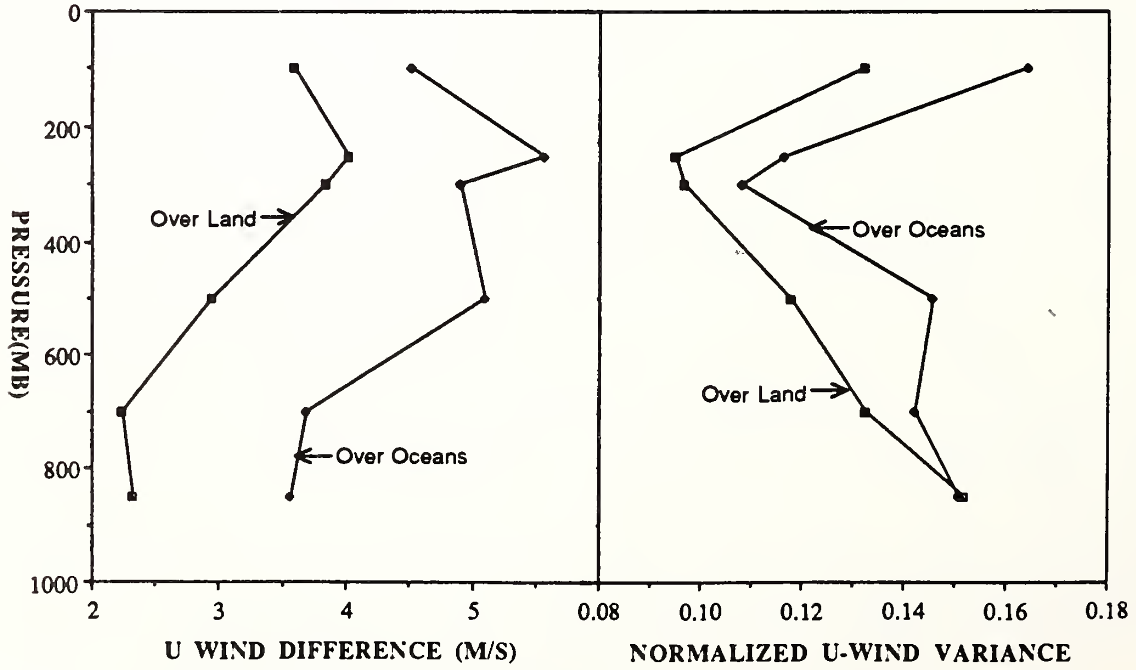

Fig. 4: (A) Vertical profile of u-wind random difference (averaged over all analysis comparisons) for land/sea breakdown, within the region 30N-60N; (B) Vertical profile of normalized u-wind variance for land/sea breakdown, within the region 30N-60N.

# Potential for long-range prediction of monthly mean surface temperatures over Eurasia

Wilhelm May
and
Roland A. Madden
National Center for Atmospheric Research[1]
P. O. Box 3000, Boulder, Colorado 80307

Because the monthly average of temperature at a given location is a finite time average of daily values that result from a continous process of passing weather systems, it will differ from year to year. We presume that this variability that is due to the statistical sampling of daily weather alone cannot be predicted at long range, that means beyond deterministic predictibility limits about two weeks.

This variability which is refered as climate noise will be compared to the actual interannual variability of monthly mean temperatures. As we assume that the actual variability may consist of a climate signal in addition to the climate noise, we conclude that there is potential for long range prediction of the temperature, where the actual variability exceeds the climate noise.

To estimate the climate noise we use available daily mean temperatures for the period from January 1979 through June 1989. Spectra are computed within seasons. The seasons are slightly overlapping segments of 96 days starting at March 1, June 1, September 1 and December 1 respectively. Using these spectra and the power transfer function for a N-day average we determine the expected variance of monthly means like

$$\sigma_N^2 = \int_0^\infty s(f) H_N^2(f) df$$

or like

$$\sigma_N^2 = \sum_{f=0}^{.5} s(f) H_N^2(f) \Delta f = \sum_{f=0}^{.5} S(f) \Delta f$$

in the discrete form. $s(f)$ is the spectrum of daily data within seasons, $f$ the frequency and $H_N^2(f)$ the power transfer function for an average of N days. $S(f)$ is the spectrum after weighting with the power transfer function.

As we assume that weather variations are uncorrelated on time scales longer than 96 days, and the spectrum due to weather is white on periods as long as that, we use a low-frequency white noise extension near zero frequency. That means we assume that

---

[1] The National Center for Atmospheric Research is sponsored by the National Science Foundation.

$$s(0) = s(1/96)$$

This assumption is similar to modeling the spectrum near zero frequency by a first order autoregressive process. This model, however, might not be valid for the whole spectrum.

We get the actual variance of the monthly mean temperature in the standard way, that is

$$\sigma_A^2 = \frac{1}{n-1}\sum_{i=1}^{n}(T_i - \overline{T})^2$$

where n is the number of years, $T_i$ the monthly mean temperature for the i'th year and $\overline{T}$ the grand mean from a data set containing monthly means of daily mean temperatures from 1950 until 1979.

Figure 1 shows the contribution of the spectral estimates to the climate noise after they were weighted with the power transfer function for 31-day averages. It can be seen, how important the contributions at low frequencies or long periods are for the climate noise.

The standard deviation of the climate noise $\sigma_N$ for a 31-day average over Eurasia is given in figure 2 for the local winter. For this season we find high values of the climate noise in the northern part, reaching from Finland in the west to Yakutsk in the east. Further south towards the tropics the climate noise decreases. It decreases also near the European and Asian coast due to the influence of the ocean, which lead to smaller day-to-day variations of the temperature.

This general pattern is the same for spring and fall with somewhat smaller values. But for the summer the standard deviation of the climate noise decreases by a factor of 3 everywhere but the tropics and near the coast (fig. 3).

The ratio $\sigma_A^2/\sigma_N^2$ of the actual variability and the climate noise gives the potential for long-range prediction. It is given in figure 4 for January. For this month the actual variability exceeds the climate noise everywhere except western and northern Europe and also in the northern part of Asia. Indicated by shading are those areas, where the ratio exceeds a value of 1.5. This value is somewhat arbitrary, but is useful to emphasize those areas, where there is a major potential for long-range prediction. In particular 1/3 of the actual variance has some potential for long-range prediction in these areas. In the central part of the continent, the Himalaya and India and all along the Asian coast line the ratio is higher than 2.

The general pattern of the ratio is the same for April. But for October and especially July we find some potential for long-range prediction for western Europe and some northern parts of Asia,too (fig. 5). On the other hand there is no potential predictibility evident in India for July.

Acknowledgements: W. May is supported by NOAA under Award No. NA90AA-D-AC826.

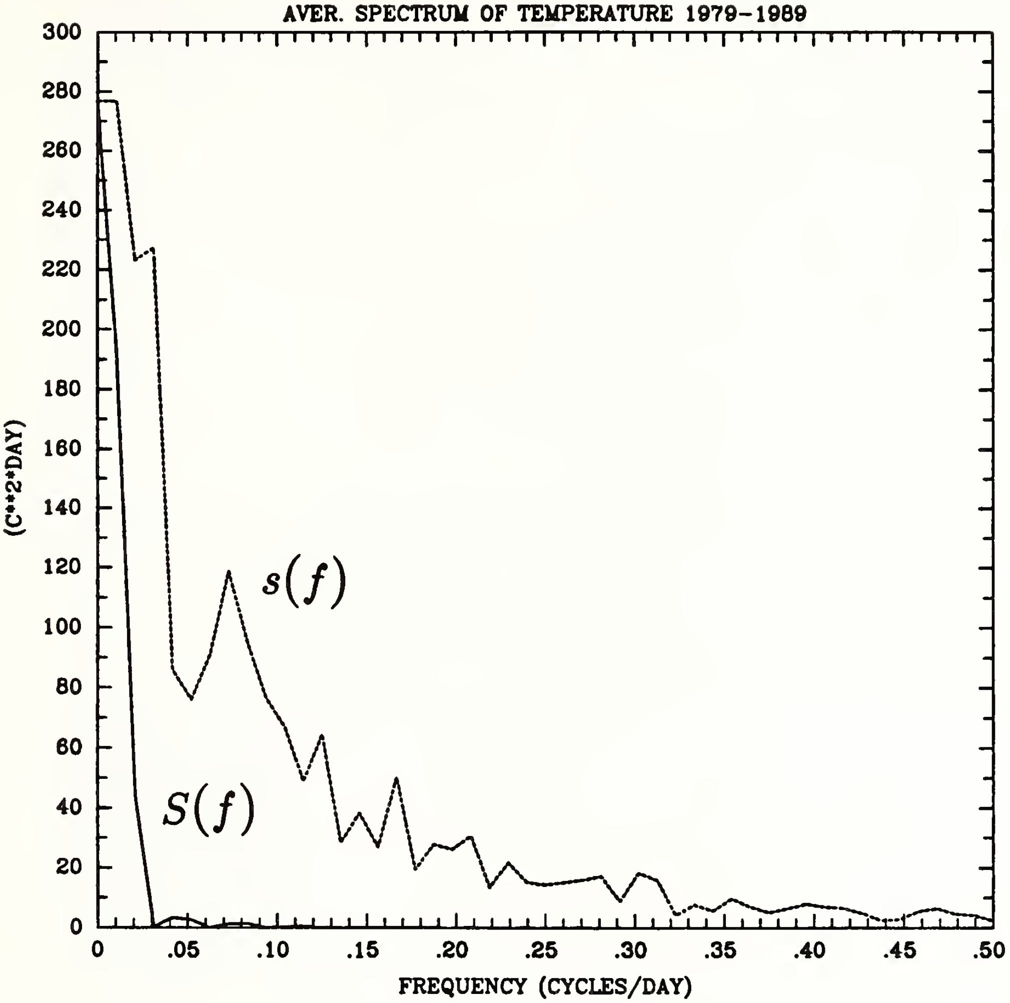

Fig. 1. December-January-February spectrum for daily temperature data at Bulgan, Mongolia (103.55°E, 48.80°N) before (dashed line) and after (solid line) weighting with the power transfer function for a 31-day average.

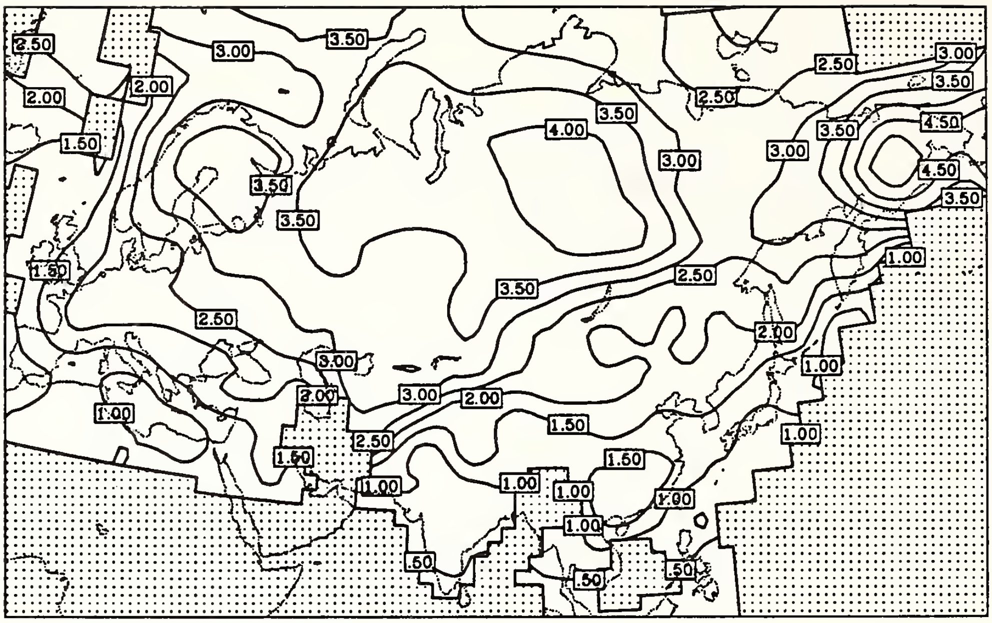

Fig. 2. Standard deviation in °C of the climate noise for December-January-February. Contour interval is .5 °C.

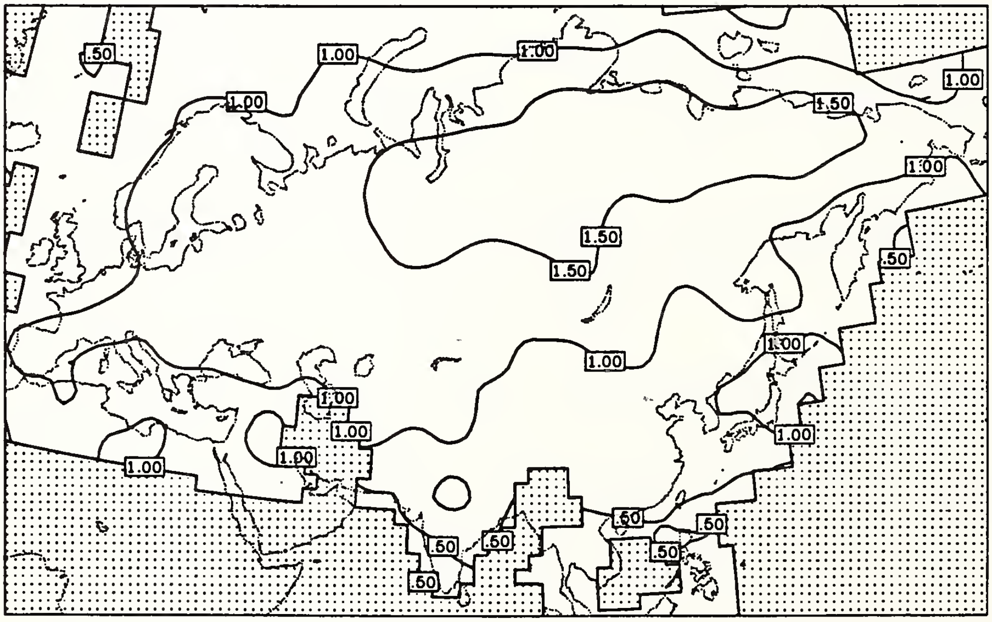

Fig. 3. Standard deviation in °C of the climate noise for June-July-August. Contour interval is .5 °C.

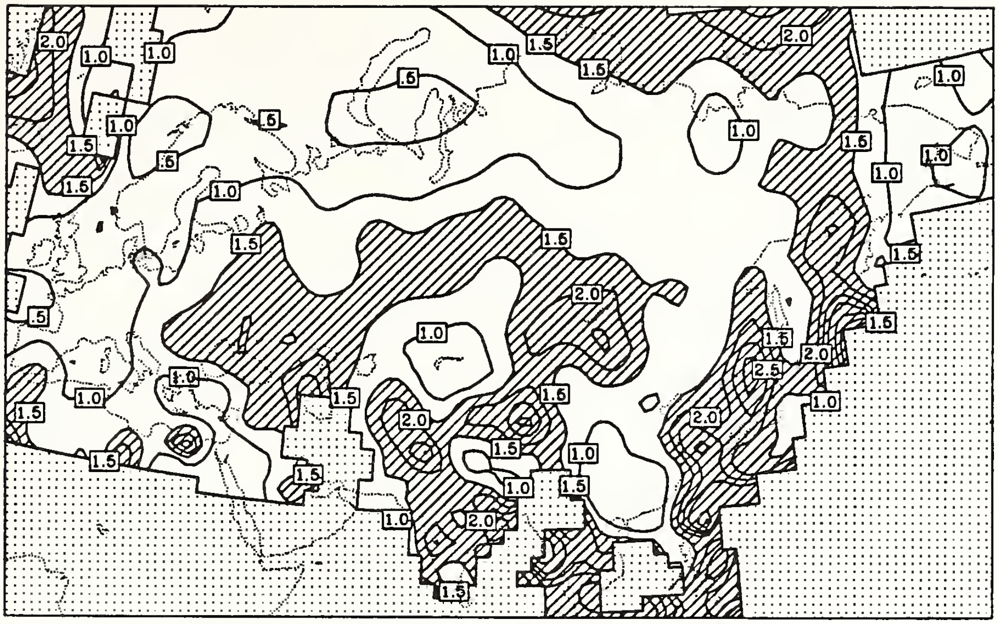

Fig. 4. Ratio of actual interannual variance of January monthly mean temperatures to the variance of the climate noise for December-January-February. Contour interval is .5. Ratios greater then 1.5 are indicated by shading.

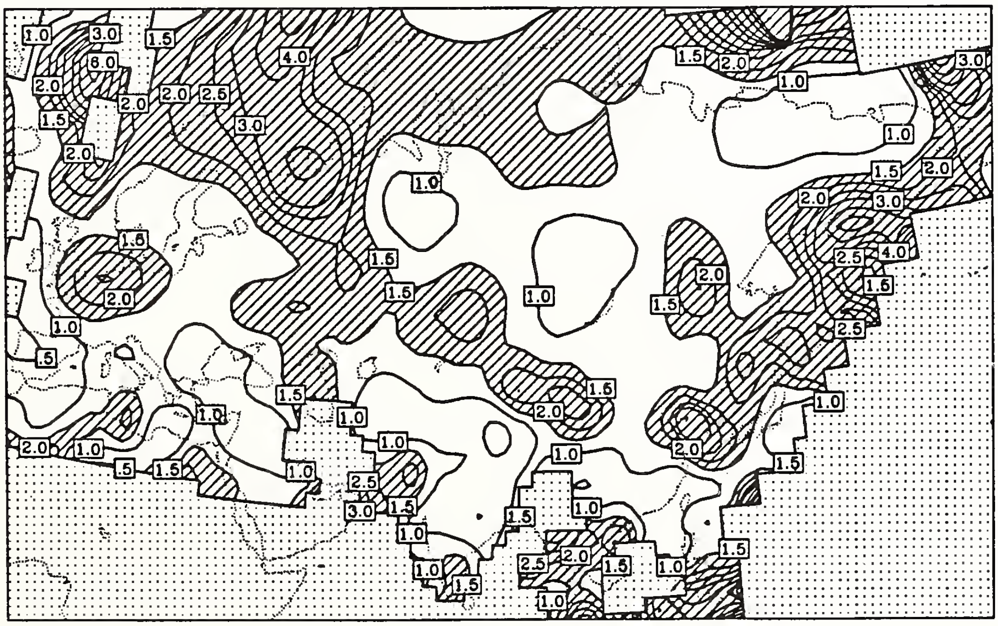

Fig. 5. Ratio of actual interannual variance of July monthly mean temperatures to the variance of the climate noise for June-July-August. Contour interval is .5. Ratios greater then 1.5 are indicated by shading.

# CAN PRECIPITATION BE USED AS A PREDICTOR IN LONG-RANGE TEMPERATURE FORECASTS ?

Jin Huang and Huug M. van den Dool

Climate Analysis Center
National Meteorological Center
Washington D.C. 20233

## 1. Introduction

In this contribution, we will examine the relation between monthly mean precipitation (MMP or P) and monthly mean temperature (MMAT or T) over the United States with the emphasis on the possibility of using MMP as a predictor in MMAT forecasts.

The physical rationale behind using precipitation to forecast temperature is that precipitation affects soil moisture which in turn affects current and future surface temperature by controlling the partitioning between the sensible and latent heat fluxes. Ideally we would like to have the most recent (not time-averaged!) measured soil moisture data averaged over a suitable spatial domain. Since such measurements are rare we will use here the MMP anomaly as a first order proxy for the soil moisture anomaly. This will be the benchmark for later studies in which we calculate soil moisture using a physical model.

Our purpose is as follows. (1) To describe the relationship between MMP and MMAT with different leads and lags over the U.S.; (2) To examine whether use of MMP as another predictor increases the forecast skill in MMAT forecasts when previous MMAT is also used as a predictor; (3) To investigate the possible asymmetry of the lagged P-T relation in dry versus wet months; (4) To confirm/reject some of our speculation about soil moisture.

## 2. Data and methods

Three sets of surface air temperature and precipitation data are examined. The first two are observed monthly mean data during the period of 1931-87 at 327 climate divisions and at 130 stations, respectively. Use of the two data sets serves as a mutual check on the credibility of the results which may be sensitive to sampling and data problems. An auxiliary grid point data set is derived from a 10 year run with the National Meteorological Center (NMC) Medium-Range Forecast (MRF) model. In this model, there were no interactive changes in the boundary conditions. Therefore, soil moisture anomalies did not exist and could not be the cause of any P-T relations.

Regular and "one-sided" regression models are used in this study. The "one-sided" regression is our newly proposed nonlinear regression model, consisting of two linear regressions -- one for wet cases and one for dry cases. The purpose of doing one-sided regression is to distinguish the possibly different P-T relation occurring in wet antecedent months from those in dry antecedent months.

Two verification methods are used to verify the results of regression forecast models. The verification skill measure is the correlation between the predicted temperature and the actual value. The first method is dependent verification, which uses the whole time series of the data to do both prediction and verification. This method tends to overestimate the skill. However, the overestimation is smallest if the predictors are chosen in advance and if the number of predictors is small, i.e. our situation is one in which the overestimation is limited. The second method is called independent verification, in which the time series of data set is divided into two parts. The first part is used for prediction and the second part is for verification. In this way, we faithfully mimic the operational setting. We have to deal, however, with more sampling fluctuation and the effects of "climate change".

## 3. Results

We mainly show the results calculated at climate divisions and mention the results at stations when necessary. For more details and definitions we refer to Huang and Van den Dool.

Fig. 1a shows the auto- and cross- pattern correlations between MMP and MMAT with one-month lag — i.e. the T-T, P-P, P-T and T-P correlations. It is found that the P-T correlation is always negative (except in December) with maximum in summer. The temperature persistence is large in summer and winter. Both one-month lagged T-P and P-P correlations are generally very small. The fact that the P-T correlation is so much higher than the T-P correlation is an important feature of the physics explaining the P-T relationship through soil moisture anomalies.

The geographical distribution of P-T correlation is represented by the temporal correlation shown in Fig. 1b. We focus on the P-T correlation in summer, specifically, the July/August correlation. It is found that any positive correlation is absent in the map, thus in general, a wet (dry) July is followed by a cool (warm) August. The maximum center is in the Oklahoma, Texas and Kansas regions. The P-T correlation at stations are similar to those at climate divisions but with slightly smaller magnitude (about 0.1). The negative P-T correlation in the interior of the continent is totally missing in the results based on the output of the 10 year run of the MRF model which, by design, does not have soil moisture anomalies. This result is consistent with the role of the soil moisture in the observed P-T correlation.

However, the correlation between current precipitation and future temperature does not, in itself, mean that we can improve the temperature forecast by adding precipitation as a predictor. MMP's predictive variance may already have been accounted for by using temperature persistence, because simultaneous MMAT-MMP correlation is very highly negative (up to −0.7).

In order to determine the possible contribution of MMP in MMAT forecasts, we compare the skill of the one-predictor model (July MMAT) with that of the two-predictor model (Both July MMAT and MMP). In both models, the predictand is August MMAT. We use both dependent and independent verification methods. Tables 1 and 2 (first row) lists the year-to-year mean of the pattern correlation between the prediction and actual values by dependent and independent verifications, respectively. It is found that generally the inclusion of MMP as a second predictor increases little the skill of MMAT forecasts.

Tables 1 and 2 also show that the contribution of MMP to the skill of the MMAT forecasts is higher in wet months than in dry months. The results suggest that MMP can be profitably used as a second predictor for MMAT forecasts, but in wet months only. This may be due to the general dry summer in the interior continent and thus soil moisture and temperature are not sensitive to the negative anomalies. The difference between the wet and dry cases is also found in temperature persistence itself. Therefore, we also conclude that we can use the single predictor P-T and T-T schemes more confidently to make the empirical MMAT forecasts in wet months.

Figs. 2(a) and (b) show the comparison between this new empirical tool (both MMAT and MMP in wet months) and the traditional empirical tool (MMAT only, regular regression and all months). Including MMP in wet months has increased the correlation between the predicted and actual MMAT about 0.2 in the entire U.S. continent. For example, the maximum TC in the central U.S has increased from 0.5 to 0.7. When applying to independent data (not shown), we found a similar very substantial improvement in MMAT forecasts due to the inclusion of MMP as a predictor in wet months.

## 4. Summary and discussions

The monthly mean precipitation (MMP) - air temperature (MMAT) relation over the U.S. has been examined by analyzing the observed MMP and MMAT during the period of 1931-87. The main purpose is to examine the possibility of using MMP as a second predictor for the MMAT forecasts and to shed light on the physical relationship between MMP and MMAT. We use both station and climate division data.

It was found that the lagged MMP-MMAT correlation is generally negative with the maxima in summer and in the interior U.S. continent. On the whole, including MMP as a second predictor improved very little the MMAT forecasts because the first predictor (temperature persistence) has accounted for the MMP's predictive variance. However, upon introduction of the "one-sided" regression, the inclusion of MMP as a second predictor can make for a better MMAT forecasts in wet months. The higher skill in wet months than that in dry months suggests that for the monthly or longer range MMAT forecasts, we can use the lagged MMP-MMAT correlation and temperature persistence more confidently in wet months.

In the introduction, we alluded to the role of soil moisture in the lagged P-T and T-T relationships. We here summarize the evidence consistent with this idea.

1) The observed P-T correlation, MMP leading MMAT by a month, is much larger than the T-P correlation. This rules out that MMP and MMAT are correlated only because each of them is correlated to some common slowly varying cause.

2) When using data generated by a model that has no soil moisture feedback, the lagged P-T correlation over the center of the U.S is entirely absent.

3) The P-T relation is present only in the warmer months, when the potentially large latent

heat flux is subject to large change as a results of soil moisture variation.

The overall gain of using MMP as a second predictor in MMAT forecasts has been small so far. This may be because we really ought to use some measure of soil moisture rather than a proxy. This will be pursued in the future. What we gained here so far is perhaps due to a priori skill discrimination between wet an dry cases which is of value in operational forecasts as well. We have found that in (antecedent) wet cases, we make for better forecasts, even if we do not use MMP as an explicit predictor.

Table 1 Year-to-year mean of the pattern correlation (x100) between the predictions and observations for July/August, using dependent verification method. Each column is for different predictor(s). Each row is for different types of regression model.

| | MMP | MMAT | MMP&MMAT |
|---|---|---|---|
| Regular | 22.8 | 34.0 | 36.8 |
| One-sided | 24.5 | 36.2 | 40.0 |
| Dry | 25.3 | 34.2 | 37.8 |
| Wet | 24.0 | 38.9 | 43.0 |

Table 2 Year-to-year mean of the pattern correlation (x100) between the predictions and observations for July/August, using independent verification method. Each column is for different predictor(s). Each row is for different types of regression model.

| | MMP | MMAT | MMP&MMAT |
|---|---|---|---|
| Regular | 12.2 | 27.1 | 25.8 |
| One-sided | 7.9 | 25.9 | 22.2 |
| Dry | –5.3 | 19.5 | 13.0 |
| Wet | 23.8 | 34.2 | 33.3 |

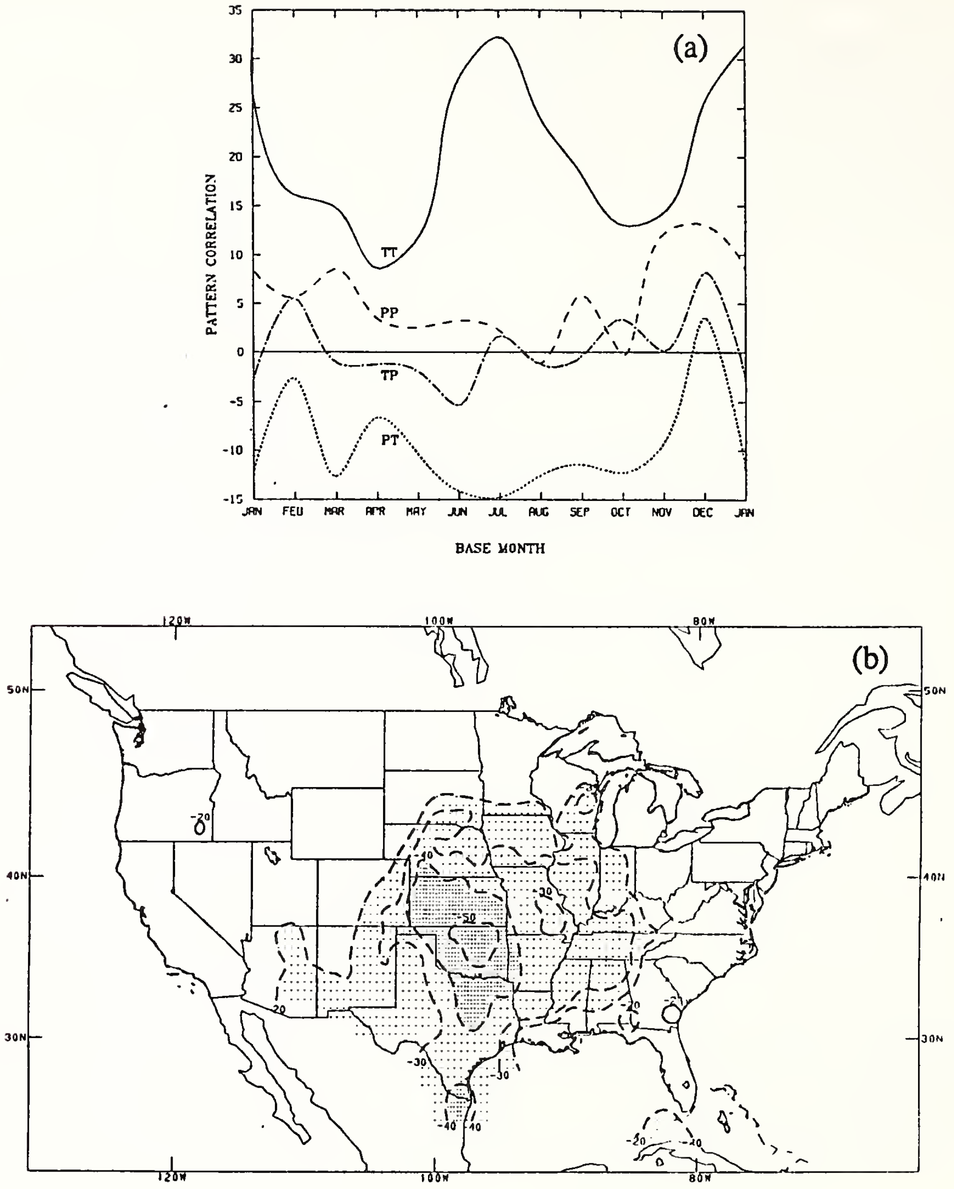

Fig. 1 (a) Pattern correlation (%) as a function of the leading month at 327 climate divisions over the U.S. with one month lag. The four curves are for T-T (solid line), T-P (dashed line), P-P (dotted and dashed line) and P-T (dotted line). (b) Temporal correlation (%) between July MMP and August MMAT. Correlations of –0.2 to –0.4 are lightly shaded and correlations smaller than –0.4 are heavily shaded.

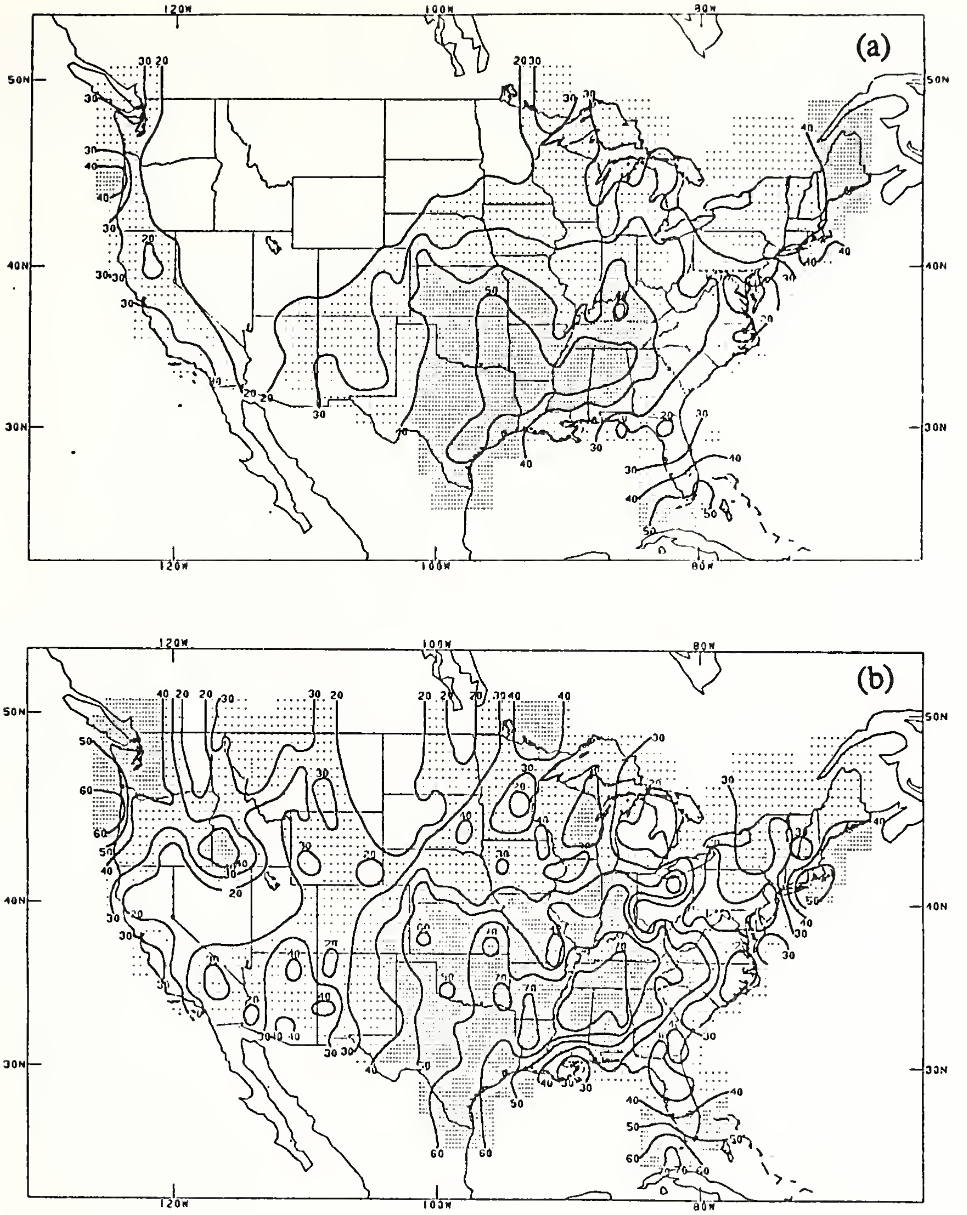

Fig. 2 Temporal correlations between actual August MMAT and the MMAT predicted by regression models, using dependent verification method in (a) regular regression model with July MMAT as the predictor; (b) one-sided regression model in wet Julys with July MMP and MMAT as predictors. Correlations of 0.2 to 0.4 are lightly shaded and correlations larger than 0.4 are heavily shaded.

# ON THE QUALITY OF CAC'S PROBABILISTIC 30-DAY AND 90-DAY FORECASTS

Allan H. Murphy
UCAR Visiting Scientist
CAC/NMC/NWS/NOAA
Washington, D.C. 20233

Jin Huang
Research Scientist
CAC/NMC/NWS/NOAA
Washington, D.C. 20233

## 1. Introduction

The 30-day (monthly) and 90-day (seasonal) forecasts formulated by the Climate Analysis Center (CAC) have been expressed in both probabilistic and nonprobabilistic formats since 1982. In general, however, these temperature and precipitation forecasts have been evaluated as nonprobabilistic forecasts using categorical measures of overall performance such as the Heidke skill score (e.g., Livezey, 1990). Two notable exceptions are the papers by Gilman (1986) and Epstein (1988), which contain brief descriptions of the reliability and accuracy/skill, respectively, of the probabilistic forecasts.

This paper contains some results of a diagnostic verification of CAC's probabilistic 30-day and 90-day forecasts. The diagnostic approach taken here follows a methodological framework described by Murphy and Winkler (1987) and recently applied in two studies of the quality of short-range weather forecasts (Murphy *et al.*, 1989; Murphy and Winkler, 1992). Space limitations necessarily preclude an in-depth evaluation of the quality of CAC's probabilistic forecasts in this postprint.

## 2. CAC's Probabilistic 30-Day and 90-Day Forecasts

CAC's probabilistic monthly and seasonal forecasts consist of probabilities assigned to three mutually exclusive and collectively exhaustive categories of average temperature and precipitation amount. These categories are below normal, near normal, and above normal (where "normal" refers to the mean in the case of temperature and to the median in the case of precipitation), and they are defined for each location in such a way that the events occur with historical climatological probabilities equal to 0.30, 0.40, and 0.30, respectively. Since previous studies have shown that CAC forecasters exhibit little if any skill in assigning probabilities to the near-normal category, this category is always assigned a probability of 0.40.

Recently, a readily accessible verification data base containing CAC's 30-day and 90-day forecasts and the matching observations has been made available through the efforts of R.E. Livezey and J.D. Hoopingarner. In the case of the probabilistic forecasts, this data base currently contains forecasts/observations for 100 locations for a 101-month period extending from 1 August 1982 through 31 December 1990. Since monthly and seasonal forecasts are formulated twice each month and once each month, respectively, the overall verification sample consists of 20,200 monthly and 10,100 seasonal forecasts. For convenience, we will sometimes refer to the monthly (seasonal) temperature and precipitation forecasts as MT and MP (ST and SP) forecasts, respectively.

## 3. Some Results

It is useful here to introduce notation to describe the forecasts and observations. Let $\underline{f}$ = (f1,f2,f3) denote a generic forecast, where f1 (f2, f3) is the probability of below (near, above) normal temperature or precipitation. These three probabilities are nonnegative and sum to one. Analogously, let $\underline{x}$ = (x1,x2,x3) denote a generic observation, where x1 (x2, x3) equals one if below (near, above) normal temperature or precipitation occurs and zero otherwise. Since $f3 = 0.60 - f1$ ($f2 = 0.40$) for all forecasts and $x3 = 1 - x1 - x2$ for all observations, it follows that a forecast possesses one degree of freedom and an observation possesses two degrees of freedom.

As noted by Murphy and Winkler (1987), all of the nontime-dependent information relevant to the quality of forecasts is contained in the joint distribution of forecasts and observations, $p(\underline{f},\underline{x})$. Moreover, this information can be made more accessible by factoring $p(\underline{f},\underline{x})$ into conditional and marginal distributions. Two such factorizations can be identified: (a) $p(\underline{f},\underline{x}) = p(\underline{x}|\underline{f})p(\underline{f})$ and (b) $p(\underline{f},\underline{x}) = p(\underline{f}|\underline{x})p(\underline{x})$. These basic joint, conditional, and marginal distributions, which relate to several different characteristics of forecasting performance, necessarily play a fundamental role in the diagnostic approach to forecast verification. In fact, three classes of verification methods can be identified (e.g., Murphy *et al.*, 1989): (a) the basic distributions; (b) summary measures of these distributions (means, variances, etc.); and (c) performance (or verification) measures and their decompositions. Some of these methods will be used here to describe the quality of CAC's probabilistic temperature and precipitation forecasts.

Figures 1 and 2 contain diagrams characterizing the reliability and sharpness of the 30-day temperature and precipitation forecasts (the forecast probabilities have been assigned to classes of width 0.05 - namely, 0.08-0.12, 0.13-0.17, etc. - and each class is associated with the midpoint of the respective interval). Figures 1a and 1b, usually referred to as reliability diagrams, show the relationship between the forecast probability, f1 (or f3), and the relative frequency of the relevant event given that probability, $p(x1=1|f1)$ [or $p(x3=1|f3)$]. [The latter are components of the conditional distribution $p(\underline{x}|\underline{f})$.] For perfectly reliable forecasts, the empirical curves would correspond exactly to the 45° line representing equality between $f1$ and $p(x1=1|f1)$ [or $f3$ and $p(x3=1|f3)$]. It is evident that the 30-day forecasts are quite reliable, although some underforecasting [$f1 < p(x1=1|f1)$ or $f3 < p(x3=1|f3)$] can be seen for relatively low and high probability values. This underforecasting is particularly noticeable when the probability forecasts (i.e., $f1$ or $f3$) fall in the interval from 0.48-0.52; in these cases, the relative frequency of occurrence of the corresponding event is about 0.70 (except in the case of $f3$ for the precipitation forecasts).

The distribution $p(f1)$ [or $p(f3)$] in the Figures 1b and 2b characterizes the sharpness of the forecasts. Sharp forecasts would consist mostly of forecast probabilities near zero or one. As expected, the sharpness of CAC's 30-day forecasts is quite modest; the forecasts tend to cluster around the climatological value of 0.30 (note that the probabilities $f1$ and $f3$ cannot approach one because $f2 = 0.40$). Moreover, the temperature forecasts clearly exhibit greater sharpness than the precipitation forecasts.

The reliability and sharpness diagrams depict the information contained in the distributions $p(\underline{x}|\underline{f})$ and $p(\underline{f})$, respectively. Since the joint distribution $p(\underline{f},\underline{x})$ can be reconstructed from these conditional and marginal distributions, it follows that the latter provide a "complete" description of the quality of CAC's probabilistic forecasts.

Another complete description of forecast quality can be obtained from the distributions $p(\underline{f}|\underline{x})$ and $p(\underline{x})$. These distributions are depicted in Figures 3 and 4 for the 30-day temperature and precipitation forecasts, respectively. The conditional distributions $p(f1|x1)$ and $p(f3|x3)$ characterize the degree of discrimination provided by the forecasts. For example, $f1$ would provide perfect discrimination if the distributions $p(f1|x1=1)$ and $p(f1|x1=0)$ did not overlap. The greater the amount of overlap between these conditional distributions, the smaller the degree of discrimination.

Examination of Figures 3 and 4 reveals that the MT forecasts exhibit a modest degree of discrimination, with larger probabilities being used more frequently - and smaller probabilities being used less frequently - when the relevant event occurs than when it doesn't occur, and vice versa. On the other hand, the MP forecasts exhibit very little discrimination; the distributions $p(f1|x1=1)$ and $p(f1|x1=0)$ [and $p(f3|x3=1)$ and $p(f3|x3=0)$] overlap almost completely.

The distribution $p(\underline{x})$, components of which are shown in the discrimination diagrams [recall that $p(x2) = 1 - p(x1) - p(x3)$], simply indicates the relative frequency with which the three categories of average temperature and precipitation amount were observed in the verification data sample. Thus, this characteristic relates to the forecasting situations, rather than to the forecasts or the relationship between the forecasts and observations.

Quantitative measures of various characteristics of the relationship between the forecasts and observations are presented in Tables 1 and 2. Table 1 contains measures of bias, accuracy, and skill, whereas Table 2 contains measures of reliability, resolution, and discrimination. The results in Table 1 indicate that some overall (or systematic) bias exists in the forecasts. The monthly and seasonal temperature forecasts overforecast the below-normal and near-normal categories and exhibit a fairly strong tendency to underforecast the above-normal category. This result is not surprising in view of general tendency for observed monthly and seasonal temperatures to be above normal during this eight-year period. The monthly and seasonal precipitation forecasts exhibit a similar - albeit considerably weaker - tendency. Specifically, the near-normal precipitation category is overforecast and the above-normal precipitation category is underforecast.

Accuracy is measured here using the ranked probability score (RPS) (Epstein, 1969; Murphy, 1971), which is a mean square error measure that takes the underlying ordinal nature of the temperature and precipitation variables into account. The accuracy of both CAC's forecasts ($RPS_f$) and climatological forecasts ($RPS_c$) is shown in Table 1. Moreover, a skill score (SS) representing the improvement in the RPS for CAC's forecasts over the RPS for climatological forecasts is also included ($SS = 1 - RPS_f/RPS_c$). This latter score indicates that, as far as the overall results are concerned, only the monthly temperature forecasts show positive skill.

Reliability and resolution are measured by REL and RES, respectively, both of which are necessarily nonnegative, which are obtained as terms in a decomposition of the RPS (e.g., see Murphy and Daan, 1985). (In this decomposition, sample climatology is used as a standard of reference.) The REL term measures the correspondence between the empirical reliability curve and the 45° line in the reliability diagram, and this term equals zero only for perfectly reliable forecasts. On the other hand, the RES term measures the "distance" between the reliability curve and a horizontal line in the reliability diagram corresponding to the sample relative frequency of the event ($x1$ or $x3$), and larger values of RES are indicative of greater resolution. (For perfectly reliable forecasts, RES is a measure of sharpness.) The overall results presented in Table 2 indicate that, according to REL, the reliability of CAC's probabilistic forecasts is quite high. However, resolution - and, in effect, sharpness - is low, with RES exceeding REL (which implies positive skill) only in the case of the MT forecasts.

The measures of discrimination in Table 2 relate to the differences between the conditional means of the forecast probabilities given occurrence and nonoccurrence of the relevant events. Specifically, $d1 = \langle f1|x1=1\rangle - \langle f1|x1=0\rangle$ and $d3 = \langle f3|x3=1\rangle - \langle f3|x3=0\rangle$. These measures indicate appreciable positive discrimination only in the case of the monthly temperature forecasts.

## 4. Conclusion

Over the limited range of probability values used in CAC's probabilistic temperature and precipitation forecasts, the forecast probabilities are generally quite reliable. Some tendency exists (at least in the temperature forecasts) for underforecasting to occur when relatively high probabilities are assigned to the below-normal or above-normal categories. The temperature forecasts are clearly sharper than the precipitation forecasts, although forecast probabilities for both types of forecasts tend to cluster around the climatological value (0.30).

Both the temperature and precipitation forecasts exhibit some overall bias, with the bias in the former due to the unusually warm temperatures during the 1980s. Quantitative measures of various characteristics of performance support the belief that the 30-day and 90-day forecasts are quite reliable, but that only the 30-day temperature forecasts exhibit appreciable resolution (or sharpness) and discrimination, as well as positive skill. In this regard, it is important to recognize that the modest levels of skill associated with CAC's probabilistic forecasts (in an overall sense) are due primarily to the absence of substantial resolution or sharpness, not to their lack of perfect reliability.

Space limitations have precluded the presentation here of results stratified by location or season. However, preliminary analysis of such results suggests that most if not all four types of forecasts (i.e., the MT, MP, ST, and SP forecasts) exhibit positive characteristics for some locations and/or seasons. For example, the monthly temperature forecasts exhibit skill levels exceeding 0.16 (16%) for areas in the northcentral and midwestern U.S. during the winter season (December-February). We plan to prepare one or two papers on this topic for formal publication, and these papers will contain information regarding various characteristics of the forecasts, the observations, and their relationship, as well as similar information for several stratifications of the verification data sample.

In conclusion, we want to emphasize the difference between the traditional approach to forecast verification and the diagnostic approach to forecast verification briefly illustrated here. The traditional approach, which generally involves the computation of one or two overall measures (e.g., a skill score), overlooks fundamental characteristics of forecasting performance. [In essence, it arbitrarily reduces the dimensionality of the verification problem (see Murphy, 1991).] Moreover, it does not provide an adequate framework for comparing the performance - or the usefulness - of forecasts across different forecasting systems, models, or forecasters. Diagnostic verification, on the other hand, provides a sound basis for absolute and comparative evaluation of forecasting systems and, in addition, produces the kinds of information that modelers and forecasters can use to guide their efforts to improve forecasting performance.

## References

Epstein, E.S., 1969: A scoring system for probabilities of ranked categories. *Journal of Applied Meteorology,* **8**, 985-987.

Epstein, E.S., 1988: Long range weather prediction: limits of predictability and beyond. *Weather and Forecasting,* **3**, 69-75.

Gilman, D.L., 1986: Expressing uncertainty in long-range forecasts. *Namais Symposium* (J.O. Roads, Editor). La Jolla, California, Scripps Institution of Oceanography, Reference Series 86-17, pp. 174-187.

Livezey, R.E., 1990: Variability of skill of long-range forecasts and implications for their use and value. *Bulletin of the American Meteorological Society,* **71**, 300-309.

Murphy, A.H., 1971: A note on the ranked probability score. *Journal of Applied Meteorology,* **10**, 155-156.

Murphy, A.H., 1991: Forecast verification: its complexity and dimensionality. *Monthly Weather Review,* **119**, 1590-1601.

Murphy, A.H., B.G. Brown, and Y.-S. Chen, 1989: Diagnostic verification of temperature forecasts. *Weather and Forecasting,* **4**, 485-501.

Murphy, A.H., 1985: Forecast evaluation. *Probability, Statistics, and Decision Making in the Atmospheric Sciences* (A.H. Murphy and R.W. Katz, Editors). Boulder, Colorado, Westview Press, pp. 379-437.

Murphy, A.H., and R.L. Winkler, 1987: A general framework for forecast verification. *Monthly Weather Review,* **115**, 1330-1338.

Murphy, A.H., and R.L. Winkler, 1992: Diagnostic verification of probability forecasts. *International Journal of Forecasting,* **8**, in press.

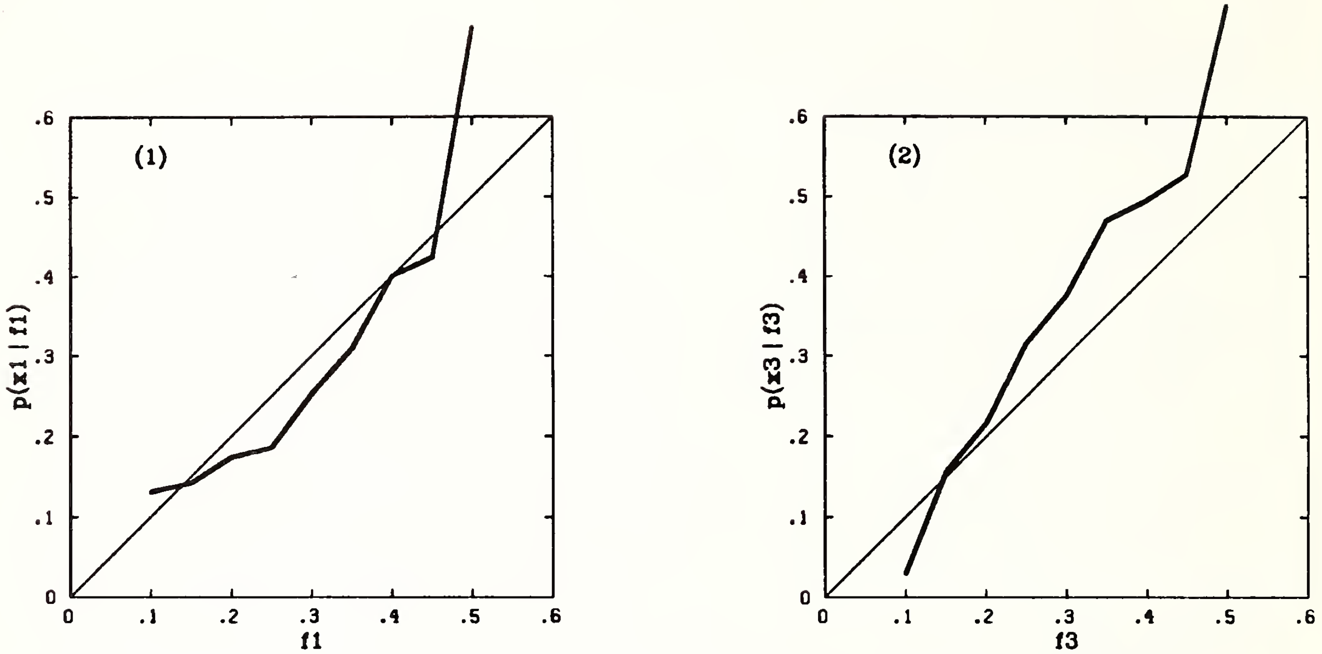

Figure 1a. Reliability diagrams for MT : (1) f1 and (2) f3.

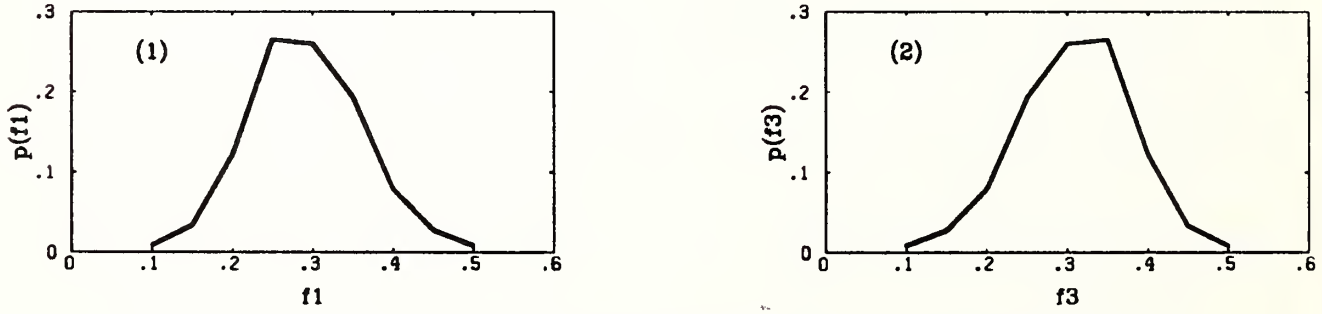

Figure 1b. Sharpness diagrams for MT : (1) f1 and (2) f3.

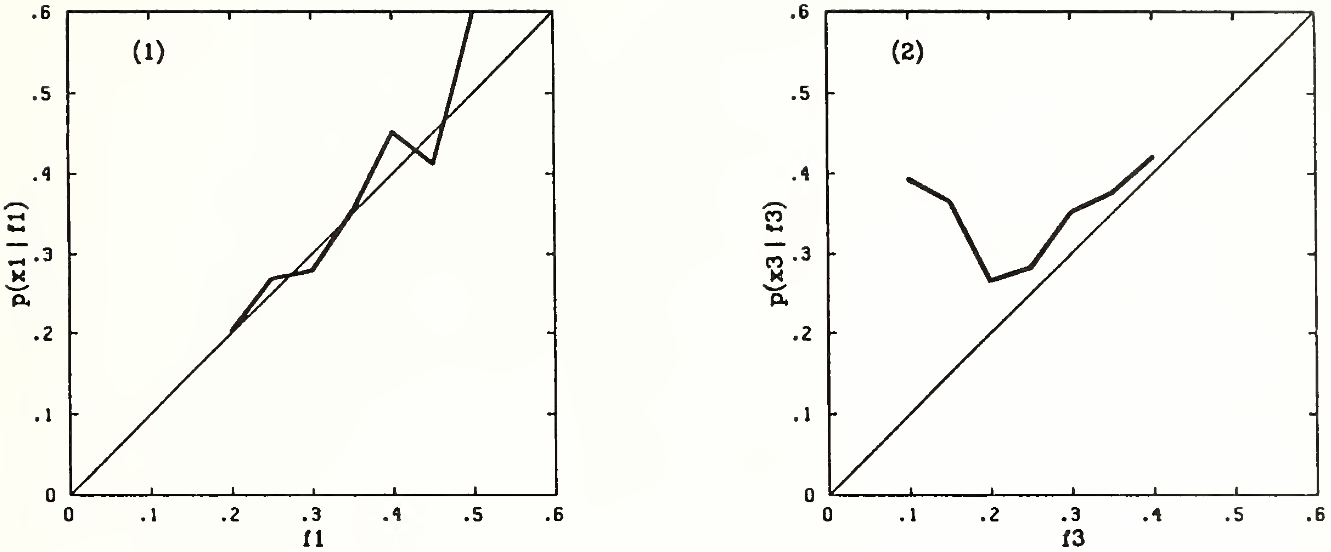

Figure 2a. Reliability diagrams for MP : (1) f1 and (2) f3.

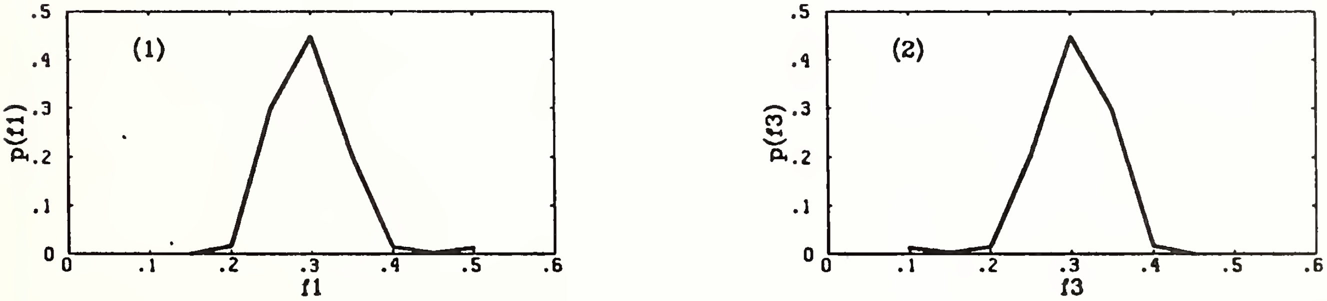

Figure 2b. Sharpness diagrams for MP : (1) f1 and (2) f3.

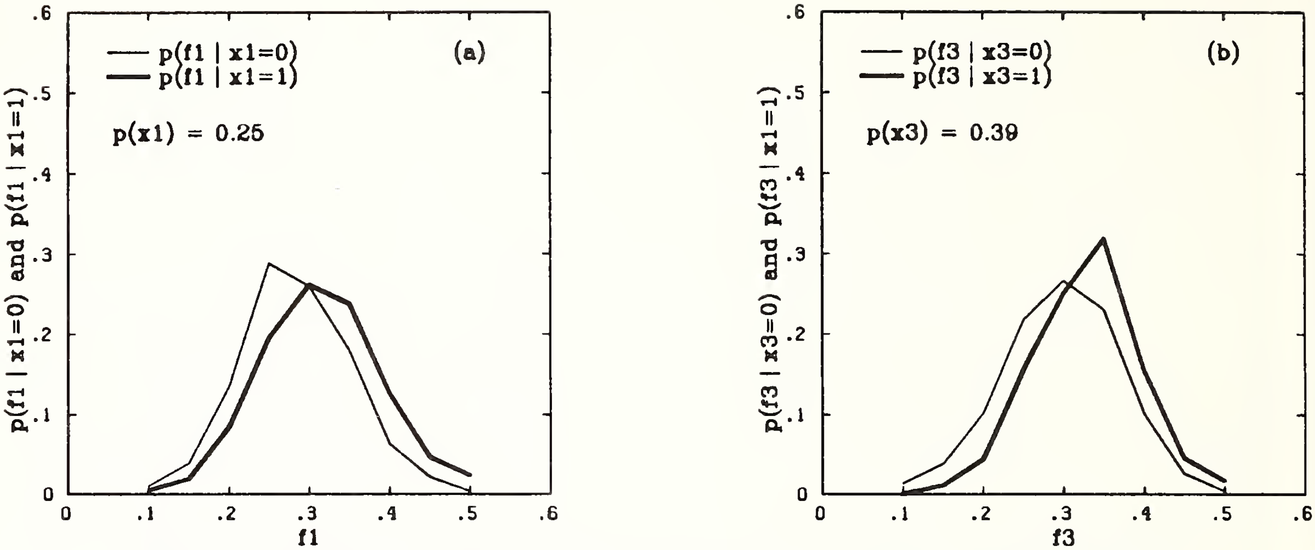

Figure 3. Discrimination diagrams for MT : (a) f1 and (b) f3.

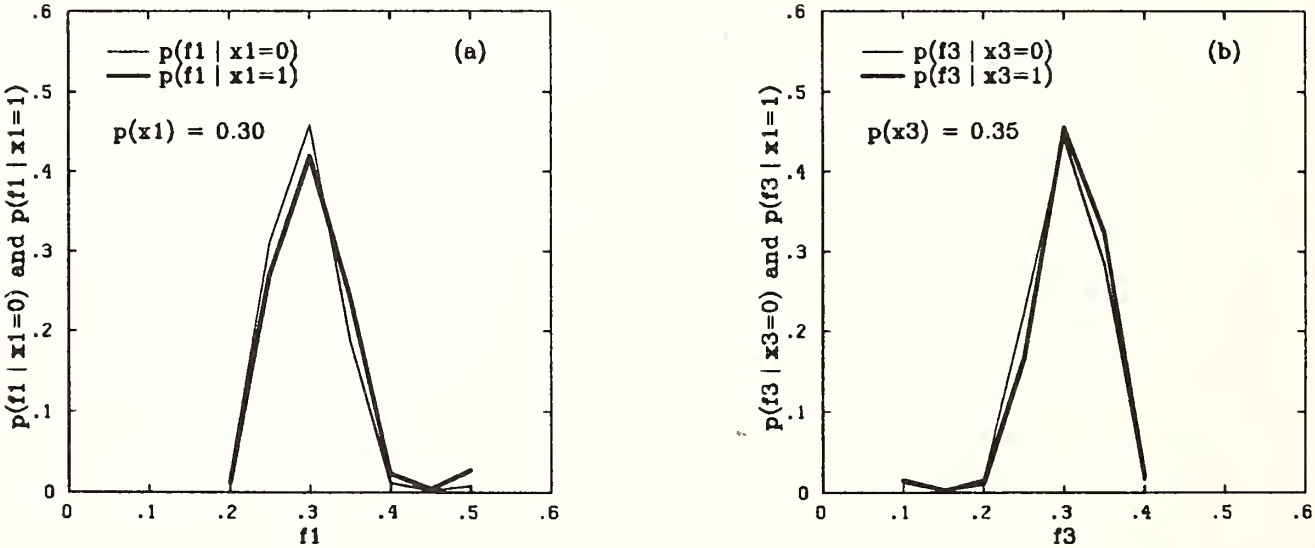

Figure 4. Discrimination diagrams for MP : (a) f1 and (b) f3.

Table 1. Overall bias, accuracy, and skill of CAC's probabilistic 30-day and 90-day forecasts (angled brackets denote a mean value).

| Forecast | Bias | Accuracy | | Skill | Sample |
|---|---|---|---|---|---|
| type | $\langle \underline{f} \rangle - \langle \underline{x} \rangle$ | $RPS_f$ | $RPS_c$ | SS | size |
| MT | (0.04,0.04,-0.08) | 0.42 | 0.44 | 0.04 | 20,200 |
| MP | (0.00,0.04,-0.05) | 0.44 | 0.44 | 0.00 | 20,200 |
| ST | (0.07,0.04,-0.11) | 0.43 | 0.43 | 0.00 | 10,100 |
| SP | (0.00,0.04,-0.05) | 0.44 | 0.44 | 0.00 | 10,100 |

Table 2. Overall reliability, resolution, and discrimination of CAC's probabilistic 30-day and 90-day forecasts.

| Forecast | Reliability | Resolution | Discrimination | |
|---|---|---|---|---|
| type | REL | RES | d1 | d3 |
| MT | 0.01 | 0.02 | 0.03 | 0.03 |
| MP | 0.00 | 0.00 | 0.01 | 0.00 |
| ST | 0.02 | 0.00 | 0.01 | 0.00 |
| SP | 0.00 | 0.00 | 0.00 | 0.00 |

# A NUMERICAL SIMULATION OF THE CATALINA EDDY

Kyozo Ueyoshi and John O. Roads
Scripps Institution of Oceanography
University of California, San Diego
La Jolla, CA 92093-0224

and

Jordan Alpert
National Meteorological Center
Washington, D.C. 20233

A shallow cyclonic eddy termed the *Catalina Eddy* has occasionally been observed during summer in the bight of southern California (Mass and Albright, 1989). The Catalina Eddy occurs within ~ 100 km from the coastal mountains with a depth typically extending up to the marine inversion level of several hundred meters above sea level and a diameter on the order of 100–200 km (Clark and Dembek, 1991). The Catalina Eddy is produced by the interaction between the synoptic-scale northerly flow and the formidable topography along the southern California coast. A favorable synoptic situation that enhances the increased low-level climatological northerly flow along the central California coastline is the presence of the prominent east-west pressure gradient between the subtropical East Pacific high and the inland thermal low over California. Increased northerlies impinging on the San Rafael mountains north of Santa Barbara result in enhanced mesoscale lee troughing in the bight and establishment of a narrow ridge alongshore, leading to establishment of cyclonic vorticity in the bight.

This paper describes numerical simulations and predictions of a Catalina Eddy event with a high-resolution multi-level limited area model. The model is initialized and forced at the lateral boundaries by the National Meteorological Center's (NMC) 2.5° × 2.5° global objective analysis and also by NMC's medium range forecast model (MRF) 1-10 day forecasts. In our previous effort to simulate mesoscale disturbances such as the Catalina Eddy (Ueyoshi and Roads, 1991) the integrations were performed up to 1 model-day utilizing the NMC analysis as fixed lateral boundary conditions. In this paper we describe the results of continuous 5- to 7-day simulations of the Catalina Eddy event of 26-30 June 1988 (Mass and Albright, 1989) by utilizing time-dependent lateral boundary conditions obtained from NMC's global objective analysis as well as NMC's MRF forecasts.

The three-dimensional fine mesh model is a moist hydrostatic primitive equation model with nonuniformly spaced 12 $\sigma$-levels in the vertical. The horizontal resolution is about 10 times (0.25° $\simeq$ 25 km) that of NMC's 2.5° × 2.5° objective analysis. The model utilizes a fourth-order accurate version of Arakawa's potential enstrophy and total energy conserving horizontal finite-difference scheme (Arakawa and Lamb, 1981). More details of the model are given in Ueyoshi and Han (1991) and Ueyoshi and Roads (1991).

Figure 1 shows a time series of the surface mean flow fields that evolved after the model was initialized and forced by the NMC analysis for 00 UTC 25 June 1988. The model was integrated continually for 7 model-days. The lateral boundary conditions in the buffer zone surrounding the model domain were continually updated by linearly interpolating in time the twice-daily NMC analyses. Inside the model domain, however, the model physics alone determines the processes and the NMC analysis was not used. An eddy is seen to evolve within the southern California bight. Unlike a Santa Ana event described in Ueyoshi and Roads (1991), a Catalina Eddy event seems to require a relatively longer time (~ 12 h) to develop to full intensity. We note that the intensity of the eddy at a mid-morning hour of 18 UTC (10 PST) is relatively weak compared with the eddy intensity at an evening hour of 06 UTC (22 PST), indicating that the formation and evolution of the eddy is also influenced by the diurnal characteristics of the ambient flow such as the stability of the near-surface air.

We also performed a series of the experiments utilizing NMC's MRF forecasts for the time period of this particular Catalina Eddy event. The MRF forecast data consists of 1-10 day forecasts (once-daily at 00 UTC) of temperature, relative humidity and wind components at the 12 mandatory pressure levels made by

NMC's global spectral model (MRF model). The skill of the MRF forecasts of those surface variables was assessed by Roads *et al.* (1991) for the period of 1 June 1988 to 31 May 1990.

Shown in Fig. 2 are a series of the surface mean flow fields that developed after the model was initialized and forced by the MRF forecasts made at 00 UTC 24 June 1988 for 00 UTC 25 June – 00 UTC 30 June 1988. Therefore, at the time of the model initialization the 24-h forecast made at 00 UTC 24 June for 00 UTC 25 June was utilized. The lateral boundary conditions were subsequently specified by interpolating linearly in time the MRF forecasts available at 24-h intervals. Thus, at the end of this 5-model-day integration the model was utilizing the 6-day forecasts as the lateral boundary conditions. An eddy is observed to develop in the bight, although the vortex is not as intense as when the NMC analysis is used and seems to be confined near the sea shore. This suggests that present-day operational forecast models are capable of predicting the large-scale flow responsible for mesoscale disturbances, the Catalina Eddy in this particular case, for at least 3 days in advance.

Another experiment with MRF forecasts was performed utilizing the 3- to 8-day forecasts made at 00 UTC 22 June for 00 UTC 25 June – 00 UTC 30 June. The surface flow patterns do not show a discernable eddy as in the previous experiments, although we detect an indication of eddy formation (Fig. 3).

Figure 4 illustrates the 24-h isallobaric charts ending at 06 UTC 27 June and 06 UTC 28 June for the three simulations described above. The model results from the 7-day simulation with the NMC analyses compare favorably with observations (Mass and Albright, 1989). In the 24-h isallobaric patterns for the 5-day experiment initialized with the 24-h MRF forecasts the onset of the event is also clearly seen, although it is not as distinctive as in the NMC case. However, the isallobaric charts for the second MRF simulation initialized with the 72-h MRF forecasts do not indicate the characteristic pressure changes found in the observations and also in the two experiments described above. It suggests that beyond ∼ 3 days ahead the MRF forecasts seems to fail to predict synoptic-scale conditions that are essential to the development of this particular eddy event.

Clark and Dembek (1991) suggested that the formation of the Catalina Eddy probably cannot be characterized by a single value of the Froude Number. An example consistent with their assertion is the flow pattern evolved at 06 UTC 01 July for the NMC case (not shown) which exhibits a well-developed eddy. The flow over Temblor Range north of San Rafael mountains at this hour is southwesterly, rather than climatological northwesterly, indicating the complexity of the mechanism for eddy formation.

In summary, we found that the NMC objective analysis can a useful tool for obtaining fine-scale regional climatology when used as initial and boundary conditions for a high-resolution mesoscale model. We also found that the MRF outputs can be used for reasonably accurate predictions of mesoscale disturbances up to ∼ 3 days when utilized as lateral boundary forcing of a fine-scale model. We intend to further investigate the mechanisms for the eddy formation and dissipation by utilizing the high-resolution mesoscale model.

## REFERENCES

Arakawa, A., and V.R. Lamb, 1981: A potential enstrophy and energy conserving scheme for the shallow water equations. *Mon. Wea. Rev.*, **109**, 18-36.

Clark, J., and S. Dembek, 1991: The Catalina Eddy event of July 1987: A coastally trapped mesoscale response to synoptic forcing., *Mon. Wea. Rev.*, **119**, 1714-1735.

Mass, C., and M.D. Albright, 1989: Origin of the Catalina Eddy. *Mon. Wea. Rev.*, **117**, 2406-2436.

Roads, J.O., K. Ueyoshi, S.C. Chen, J. Alpert and F. Fujioka, 1991: Medium-range fire weather forecasts. To appear in *International J. of Wildland Fire.*

Ueyoshi, K, and Y.-J. Han, 1991: A three-dimensional simulation of airflow and orographic rain over the island of Hawaii. *J. Meteor. Soc. Japan.*, **69**, 127-152.

Ueyoshi, K. and J.O. Roads, 1991: A preliminary simulation of western U.S. weather and climate. *Proc. of the 15th Annual Climate Diagnostics Workshop, 29 Oct.-2 Nov. 1990*, Asheville, Climate Analysis Center/NMC, NOAA, 439-444.

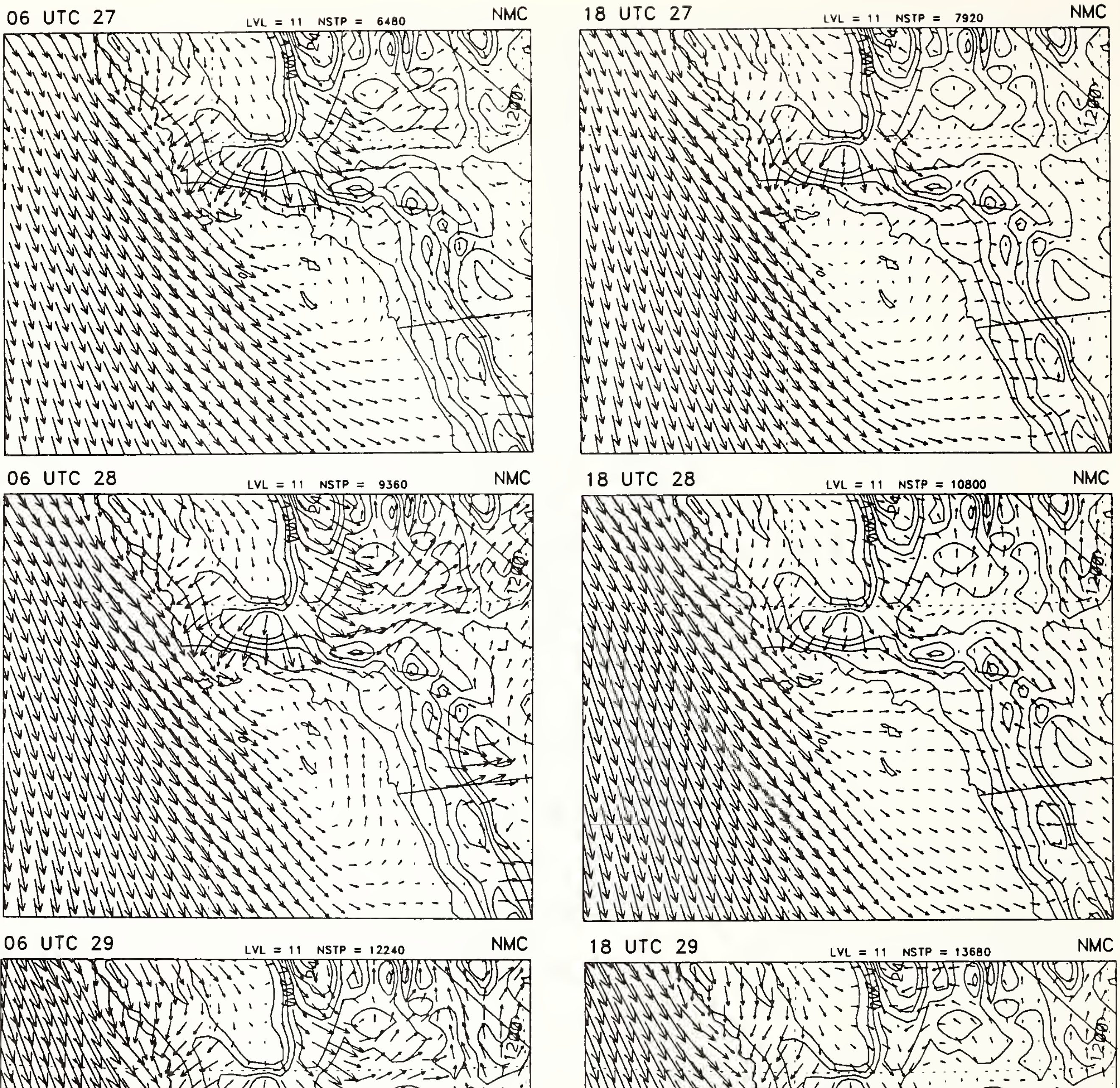

Fig. 1. Evolution of simulated wind fields at ~ 100 m above the earth's surface for southern California at 06 UTC and 18 UTC 26–30 June 1988. NMC's large-scale objective analyses were utilized as initial and lateral boundary conditions. A wind vector with a length of one east-west grid length corresponds to ~ 6.2 m s$^{-1}$.

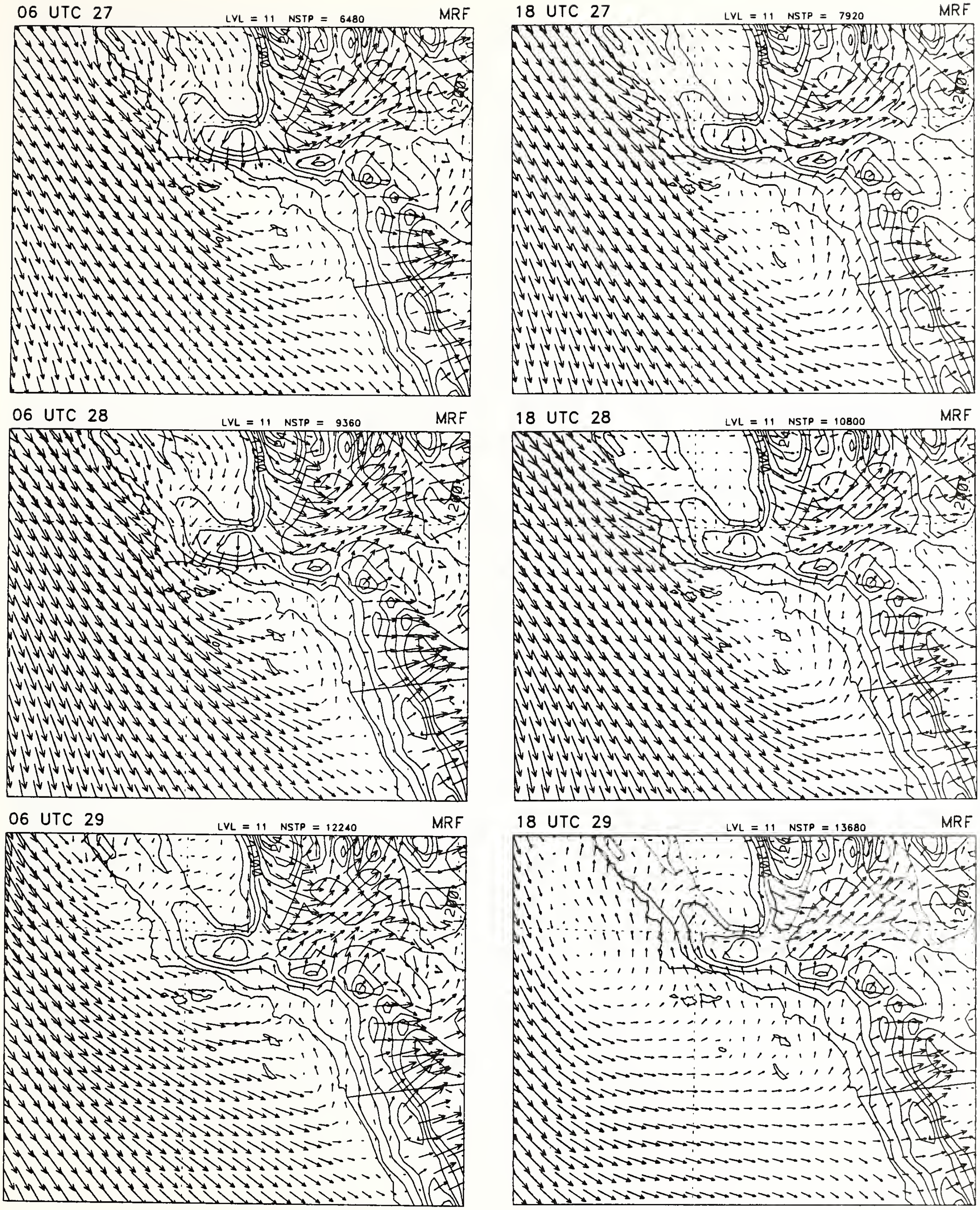

Fig. 2. As in Fig. 1 except that the 1- to 6-day MRF forecasts made at 00 UTC 24 June 1988 for 00 UTC 25–30 June 1988 were used.

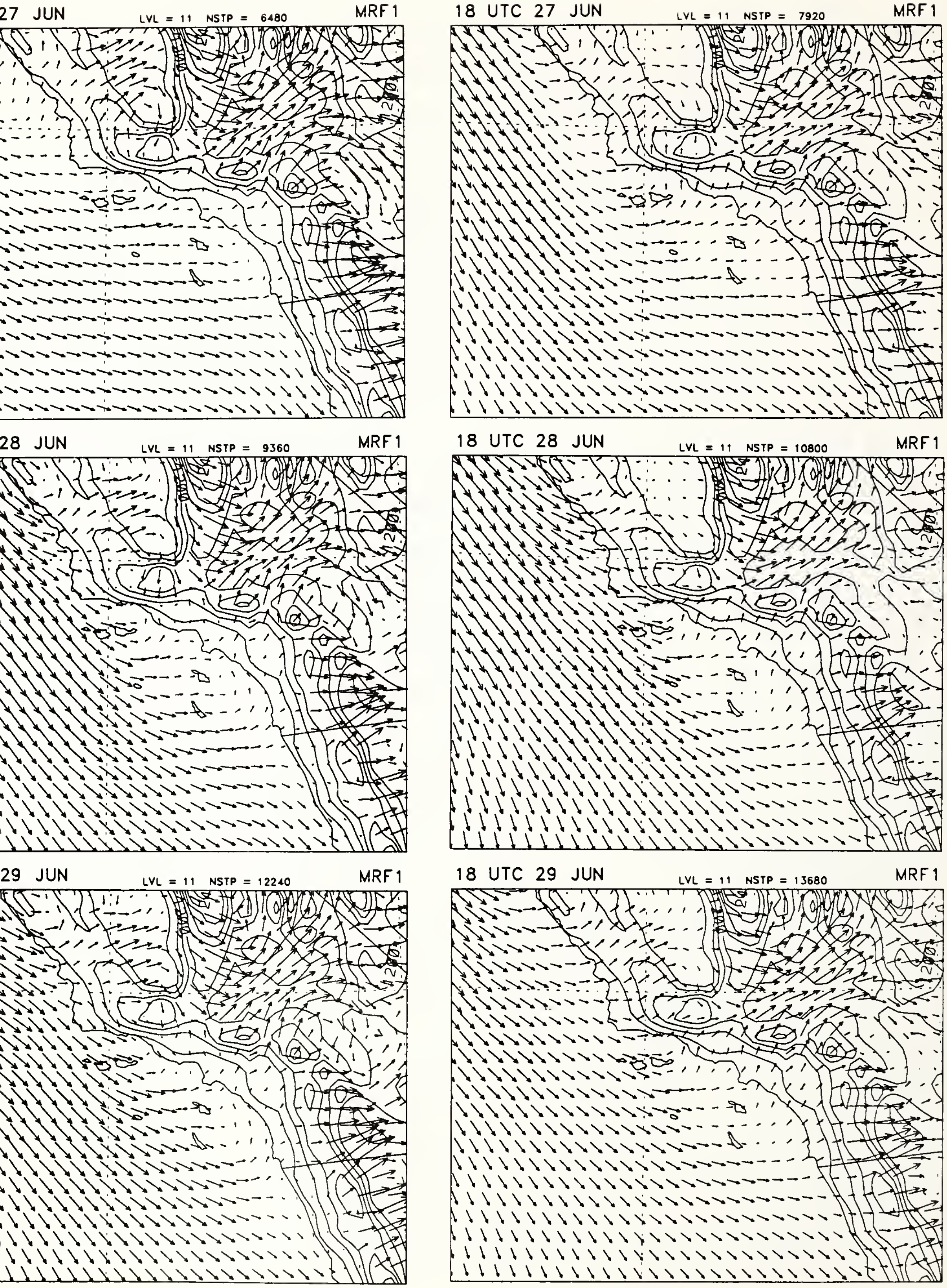

Fig. 3. As in Fig. 1 except that the 3- to 8-day MRF forecasts made at 00 UTC 22 June 1988 for 00 UTC 25–30 June 1988 were used.

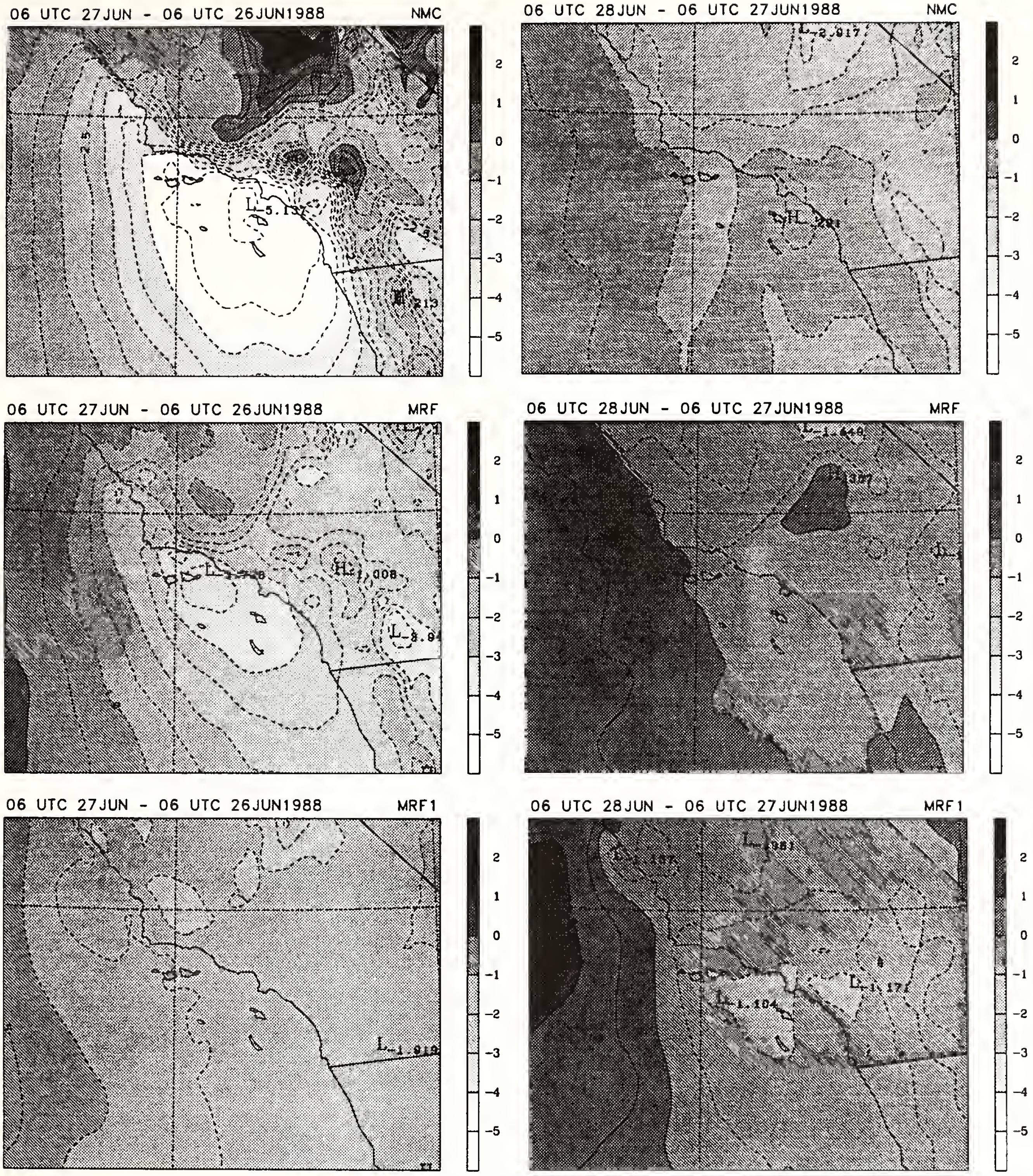
06 UTC 27JUN - 06 UTC 26JUN1988 NMC
06 UTC 28JUN - 06 UTC 27JUN1988 NMC
06 UTC 27JUN - 06 UTC 26JUN1988 MRF
06 UTC 28JUN - 06 UTC 27JUN1988 MRF
06 UTC 27JUN - 06 UTC 26JUN1988 MRF1
06 UTC 28JUN - 06 UTC 27JUN1988 MRF1
2
1
0
-1
-2
-3
-4
-5

Fig. 4. The 24-h isallobaric patterns for periods ending at 06 UTC 27 June 1988 and 06 UTC 28 June 1988. The top panels are for the NMC case; the middle panels for the MRF case with 1–6 day forecasts and the bottom panels for the MRF case with 3–8 day forecasts. The units are in millibars.

# PREFERRED MODES OF SEASON-TO-SEASON CHANGES IN 700MB HEIGHT ANOMALIES

ARTHUR V. DOUGLAS
Atmospheric Sciences Department, Creighton University, Omaha, NE 68178

PHILLIP J. ENGLEHART
Board of Public Utilities, Kansas City, KS 66101

In the development of seasonal forecasts, lag relationships of seasonal 700mb height anomalies have become a key tool. (Figure 1). High levels of persistence are noted throughout the tropics and subtropics between all seasons. This persistence results from low frequency signals associated with the SOI and tropical SST anomalies. In mid latitudes, very few areas of significant persistence are noted. However, a few areas of reversal occur, especially in the summer-to-fall, and fall-to-winter periods (Figure 1). The ability to forecast a major reversal in the circulation between seasons is key to improving extended range forecasts. This paper explores the preferred modes of change in fields of 700mb height anomalies. These modes are then related to a tropical index (SOI related) and North Pacific SST anomalies. By relating the modes of 700mb height reversal to these low frequency phenomena, we hope to illustrate which types of reversal appear to be forced by air-sea interactions.

Preferred modes of change in seasonal 700mb height anomalies are shown in Figures 2-5. Differences in height anomalies for each pair of seasons (e.g., fall-to-winter) were computed by subtracting the gridded height anomalies of one season from the previous season (e.g., winter minus fall). The grid used was near equidistant and composed of 76 grid points ($10^0$ X $10^0$ at low latitudes, but approximately $10^0$ latitude X $40^0$ longitude in subpolar regions). These difference fields were then subjected to a principal component analysis, using the procedures discussed by both North and Preisendorfer. Only significant components were saved for varimax rotation (Figures 2-5).

The preferred patterns of height change often resemble the development or breakdown of PNA or west Atlantic patterns (e.g., patterns #2 and #4 for fall-to-winter, Figure 5). An examination of those years with large time coefficients (for the components) found that 60% to 80% of the time, the centers of change represented an actual reversal in height anomalies (i.e., positive anomaly being replaced by negative anomaly, rather than a simple intensification of an anomaly already in place). For each set of paired seasons (e.g., fall-to-winter) 50% to 60% of the preferred change in height anomalies can be explained by four or five rotated components. This helps a forecaster narrow down the type of reversal or drastic change in height anomalies that could occur between seasons.

The time coefficients for the rotated components were then correlated with two data sets: North Pacific SST and a tropical Pacific index. The tropical index was created by averaging Wright's normalized rainfall index for the equatorial Pacific with the normalized SST anomaly for Puerto Chicama, Peru. Both time series are positive during an el Nino (strong central Pacific equatorial convection and high SSTs at Puerto Chicama with el Nino).

A number of the rotated components show significant relationships with North Pacific SST. Highly significant relationships are found in winter-to-spring (#2, #3, #4) and spring-to-summer (#1, #2,). Less often, major changes in height anomalies are related to the state of the tropical Pacific (e.g. #4 of winter-to-spring, and #2 of spring-to-summer). It may seem surprising that the tropical index is not better related to height changes. Actually this should be expected, since the SOI (as expressed by the tropical index) is associated with long-term persistence of height anomalies in the tropics (Figure 1). Specifically, el Nino is most frequently associated with the PNA pattern which develops in the fall and frequently persists into early spring. This helps explain why the fall-to-winter fields of reversal show no relationship with tropical forcing since the latter phenomena encourages persistence rather than reversal.

**Figure 1.** Lag relationships between seasonal 700mb height anomalies. Period of analysis 1948-88.

**Figures 2-5.** Relationships between the preferred modes of seasonal 700mb height changes and North Pacific SST and the tropical index. Time coefficients of the rotated components of height change (right hand maps) were correlated with SST of the first paired season (left hand maps). Relationships with the tropical index (correlation coefficients in bottom right of each component map) are for three seasons, leading up to and during the period of reversal. Period of analysis 1948-88.

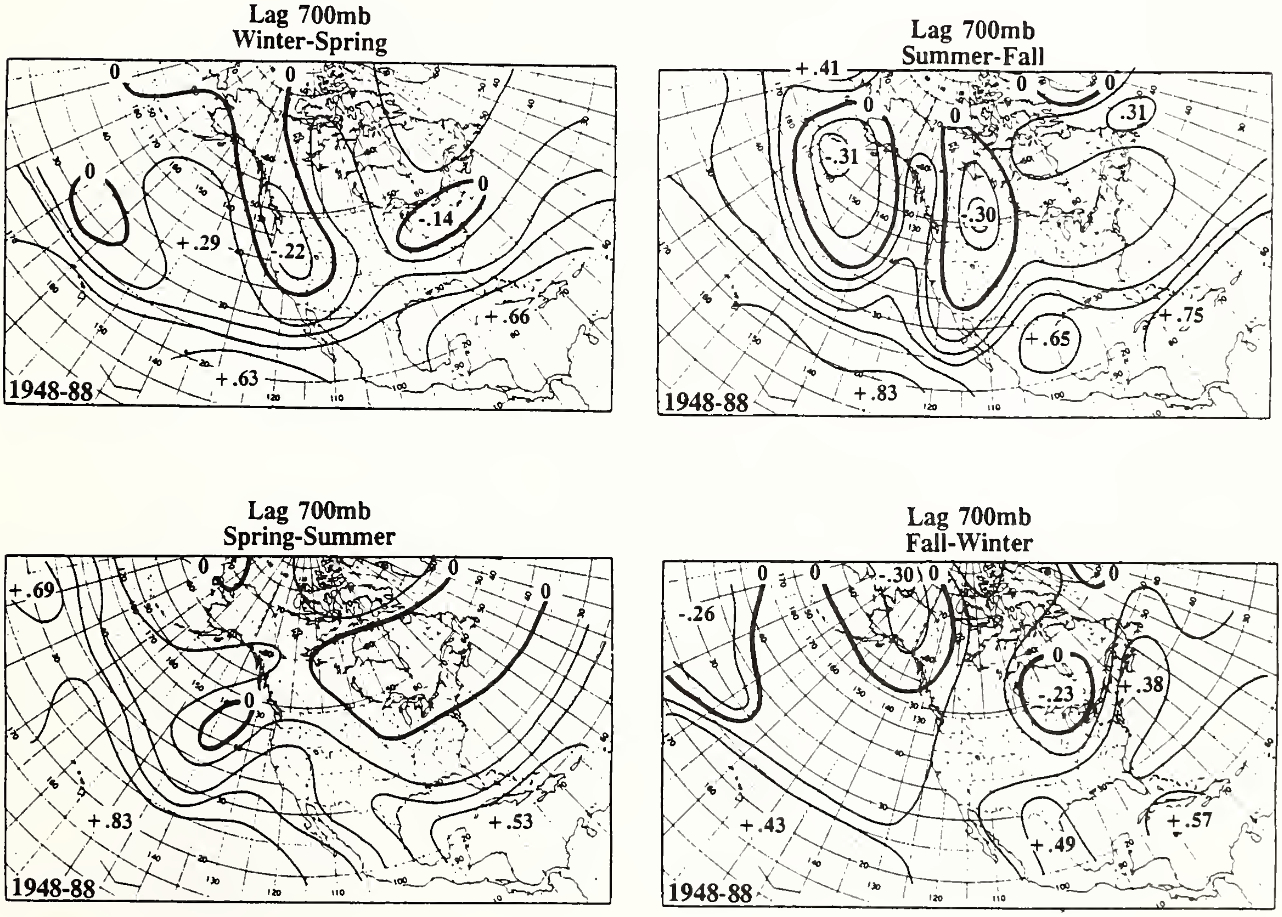

Lag 700mb Winter-Spring

Lag 700mb Summer-Fall

Lag 700mb Spring-Summer

Lag 700mb Fall-Winter

FIGURE 1.

# RELATIONSHIPS BETWEEN FACTORS OF SEASONAL HEIGHT DIFFERENCES AND SEASONAL SSTS

## Winter to Spring

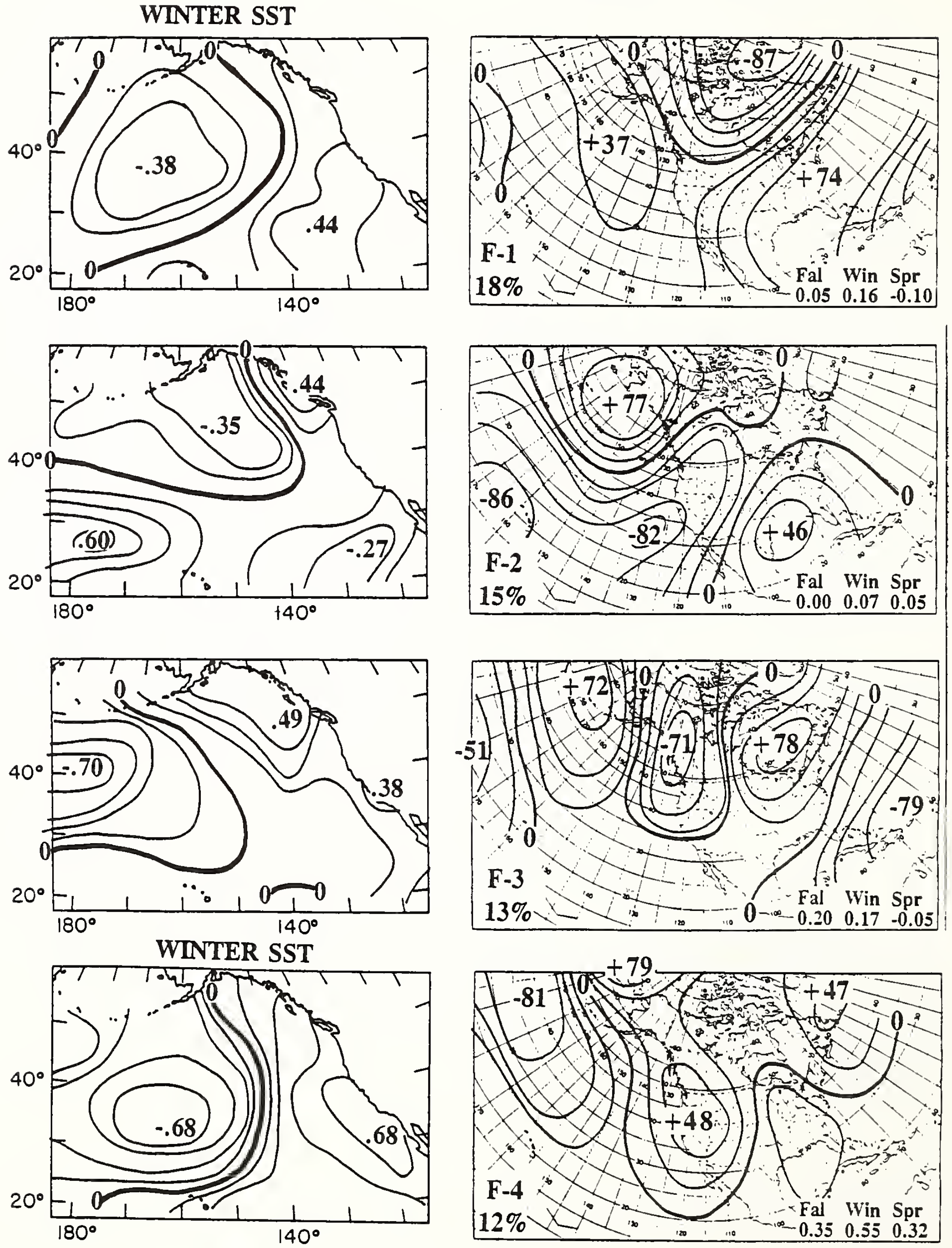

FIGURE 2.

# RELATIONSHIPS BETWEEN FACTORS OF SEASONAL HEIGHT DIFFERENCES AND SEASONAL SSTS

## Spring to Summer

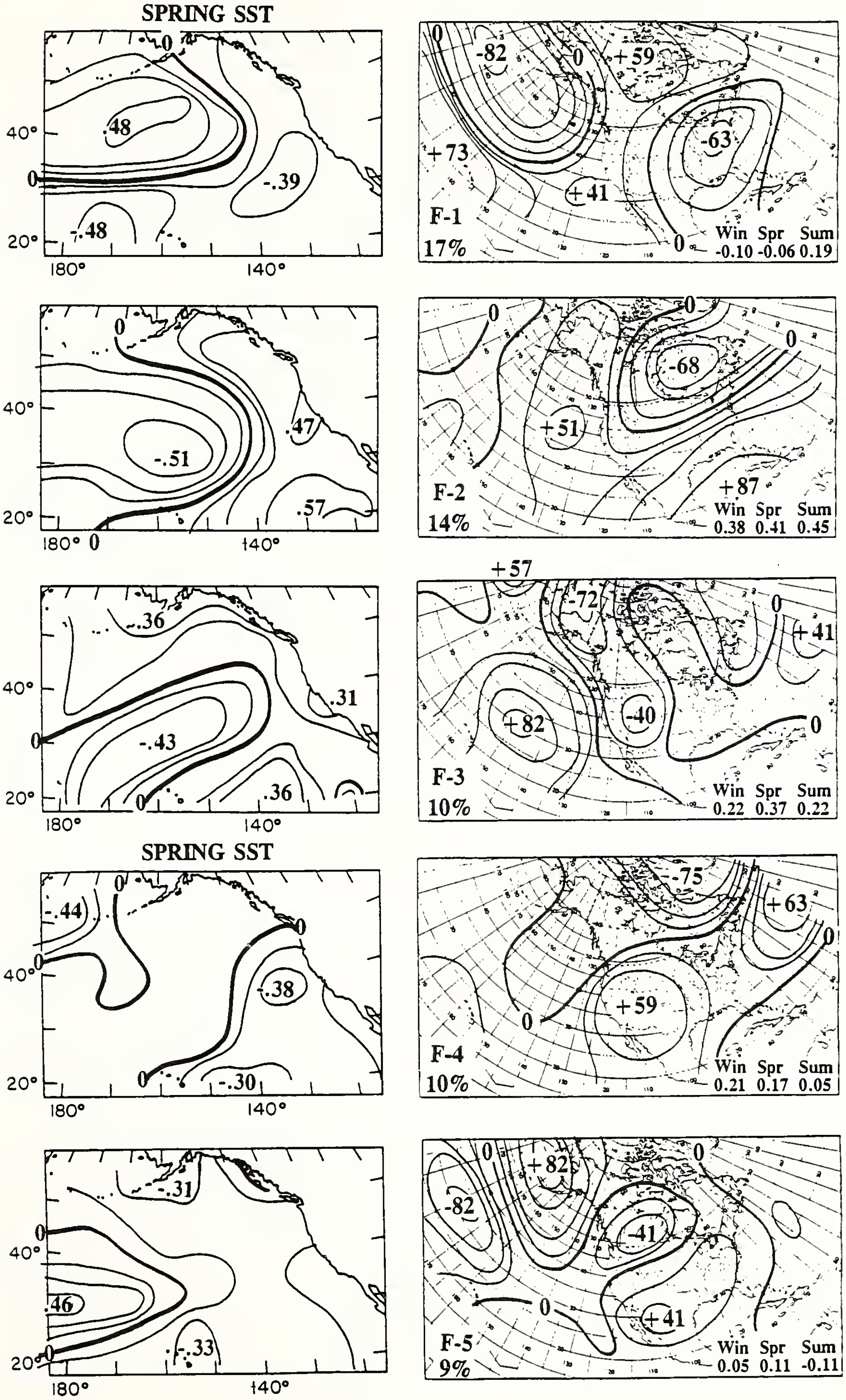

FIGURE 3.

# RELATIONSHIPS BETWEEN FACTORS OF SEASONAL HEIGHT DIFFERENCES AND SEASONAL SSTS

## Summer to Fall

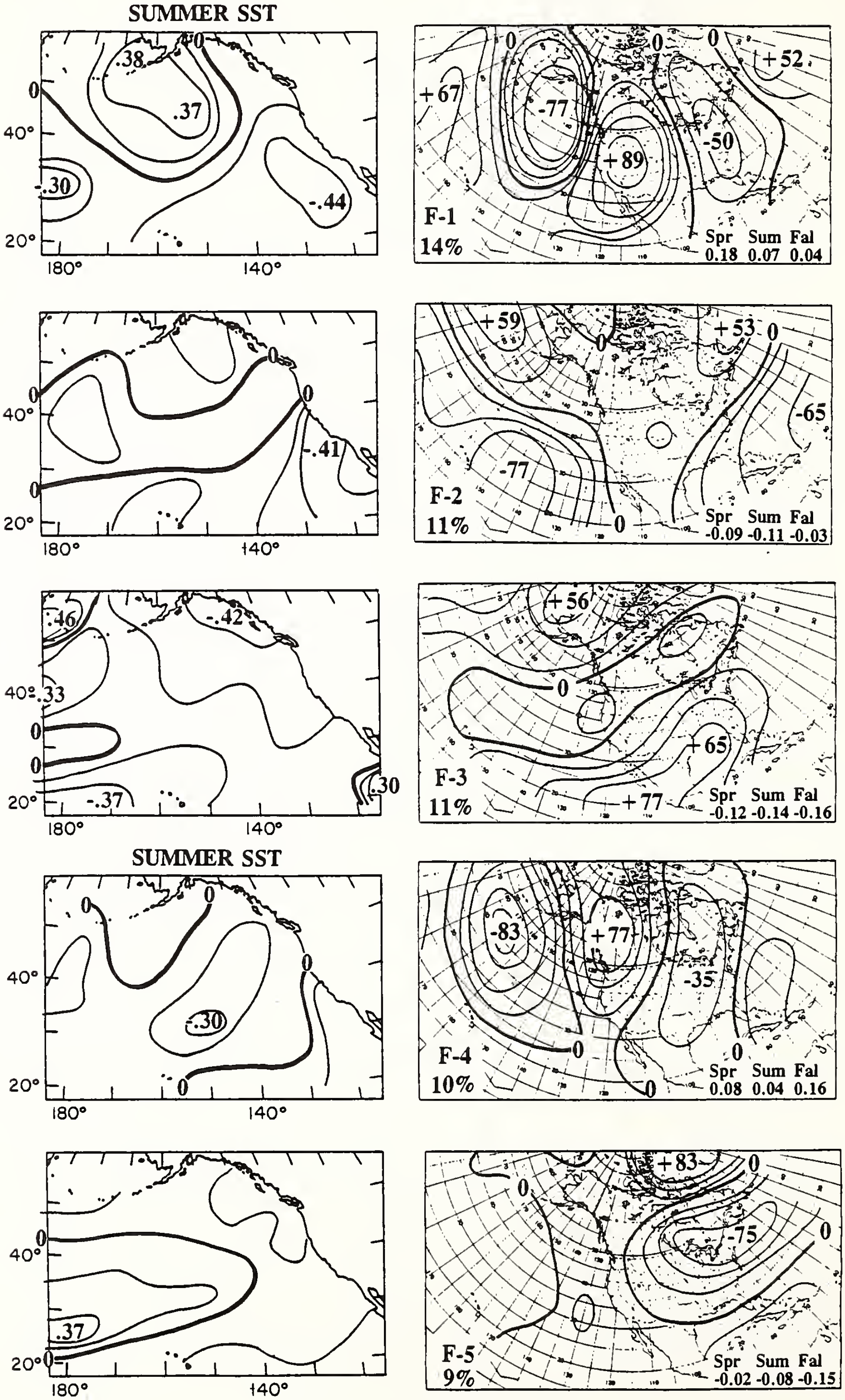

FIGURE 4.

# RELATIONSHIPS BETWEEN FACTORS OF SEASONAL HEIGHT DIFFERENCES AND SEASONAL SSTS

## Fall to Winter

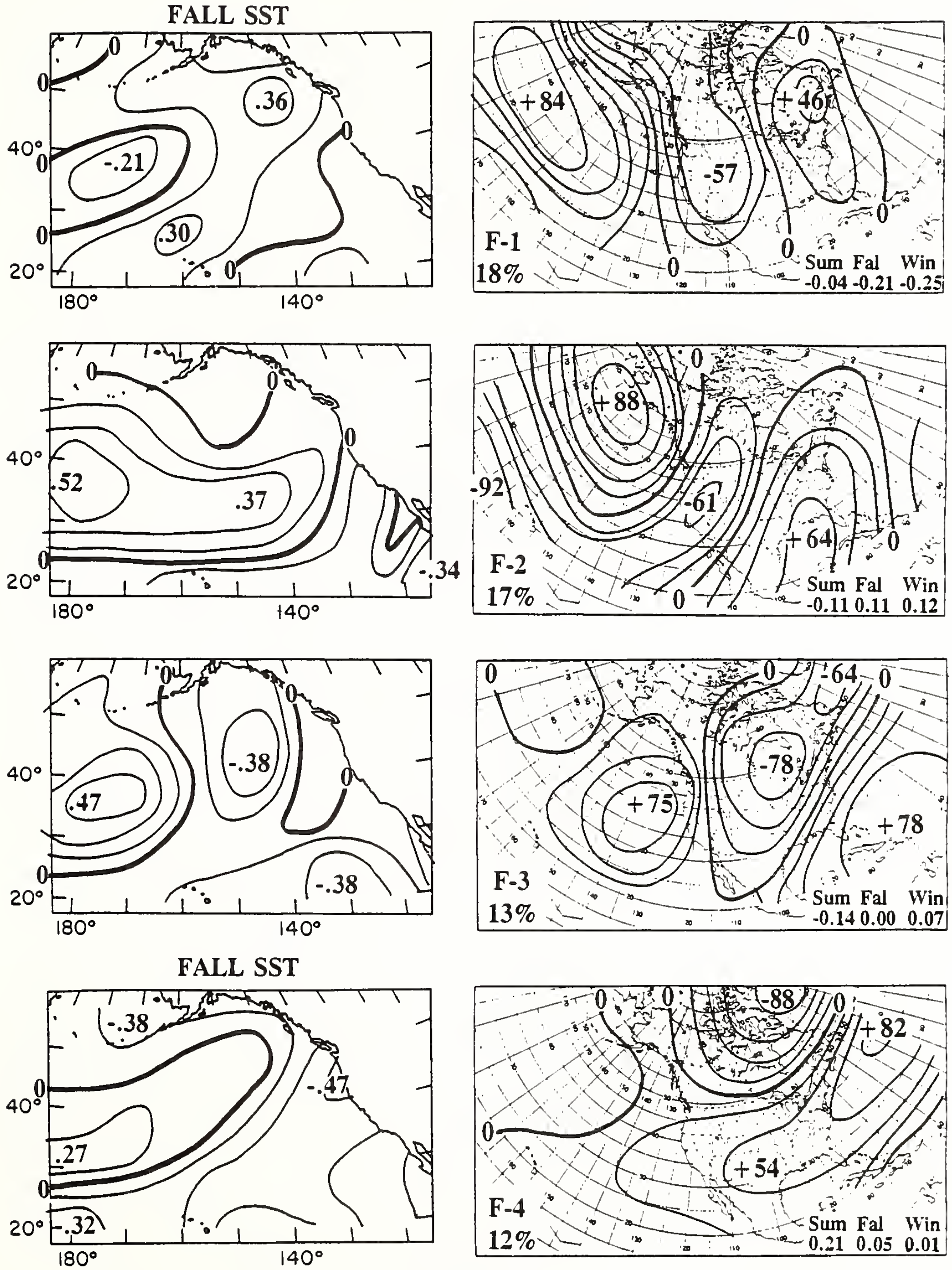

FIGURE 5.

# STRONG EXTENDED RANGE SEASONAL PREDICTIVE POTENTIAL FOR ATLANTIC HURRICANE ACTIVITY

William M. Gray and Christopher W. Landsea
Dept. of Atmospheric Science, Colorado State University
Fort Collins, Colorado 80523

and

Paul W. Mielke, Jr. and Kenneth J. Berry
Dept. of Statistics, Colorado State University
Fort Collins, Colorado 80523

## 1 Introduction

Surprisingly strong long range predictive signals exist for Atlantic basin seasonal tropical cyclone activity. This paper describes two seasonal statistical forecast schemes for the prediction of Atlantic basin tropical cyclone (TC) activity. The first scheme is of greatest interest because it describes a surprisingly strong 6–11 month extended range prediction for Atlantic basin seasonal TC activity which can be made on 1 December of the prior year. The second scheme describes a similar seasonal statistical prediction which can be made on 1 August, or just before the beginning of the active part of the TC season. A third seasonal forecast is made on 1 June or at the time of the official start of the hurricane season. This third statistical scheme is still in the developmental stage and will be reported on later.

By seasonal tropical cyclone (TC) activity we mean the seasonal number of

- Named Storms (N)
- Named Storm Days (ND)
- Hurricanes (H)
- Hurricane Days (HD)
- Intense or Cat. 3-4-5 Hurricanes (IH)
- Intense Hurricane Days (IHD)
- Hurricane Destruction Potential (HDP)[1]

This study involves the independent (jackknife) hindcast of each of these 7 seasonal TC parameters for the 41 years of 1950–1990. We find that considerable skill above what would be expected from climatology is available for both the 1 December previous year forecast and the 1 August forecast. If the atmosphere continues to behave in the future as it has over the last 41 years, then a high degree of extended range future seasonal forecast skill becomes available. We have no reason for thinking that the atmosphere will not behave during the next few decades as it has during the last four decades.

---

[1] Hurricane Destruction Potential (HDP) = $\sum(V_{max})^2$ for each $V_{max}$ equal or greater 65 knots for each 6-hour period which the hurricane is in existence. HDP is expressed in units of $10^4$ knots$^2$. For instance, a hurricane of 100 knots existing for 1 full day (or four 6-hr time periods) would accrue 4 HDP units.

## 2 Extended Range 6–11 Month Seasonal Prediction by 1 December of the Previous Year

This prediction is based on two measures of West African rainfall during the prior year plus the phase of the stratospheric Quasi-Biennial Oscillation of zonal winds at 30 mb and 50 mb which can be extrapolated 10 months into the future with reasonable accuracy. These predictors, both of which are available by late November, can be utilized to make surprisingly skillful forecasts of Atlantic tropical cyclone activity in the following year.

The extended range forecast scheme is based on an optimization of the combination of these two lag rainfall relationships plus a 10-month extrapolation (November to September) of the absolute value of the QBO zonal winds at 30 mb ($U_{30}$) and at 50 mb ($U_{50}$) and the resulting wind shear between these levels at 10° N latitude. Hence, there are five forecast predictors: extrapolated QBO $U_{30}$, $U_{50}$, $|U_{30} - U_{50}|$ and August–September Western Sahel ($R_s$) and August–November Gulf of Guinea ($R_G$) rainfall (see Fig. 1). These five forecast parameters specify next year's expected number of named storms (N), named storm days (ND), etc.

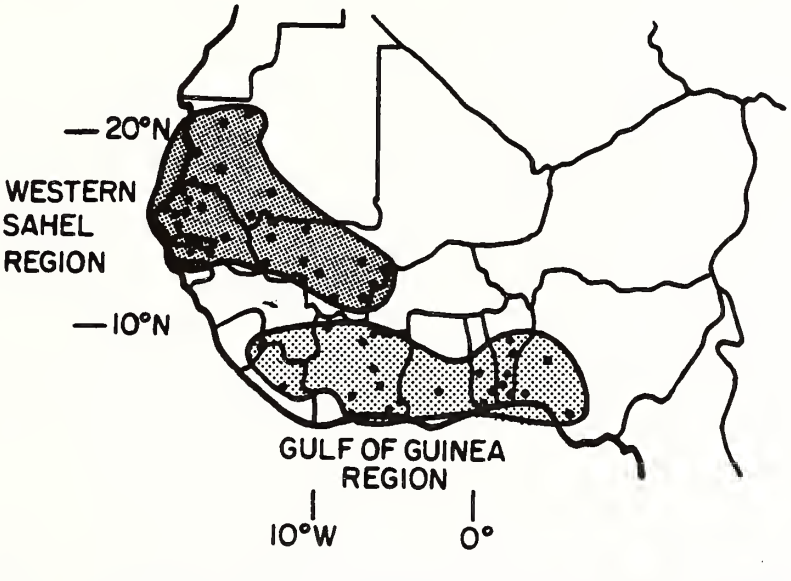

Figure 1: Location of rainfall stations which make up the Western Sahel ($R_s$) and the Gulf of Guinea ($R_G$) precipitation indices.

Extensive statistical analyses have been made of these five late November predictors and seven following season predictants for the 41-year period of 1950–1990. We have developed optimized regression equations for the most skillful extended range hindcasts. The statistical methodology for these analyses consists of four distinct, but interrelated steps: (1) Least-absolute deviation regression provides prediction values for each of the n years. (2) A cross-validation (jackknife) procedure ensures that the prediction for any year is independent of the observations for that year. (3) The predicted values and observed values for all n years are compared by calculating a measure of agreement. (4) The probability of the measure of agreement is obtained under the null hypothesis.

The forecast equations take the following form:

$$(\textit{Seasonal Forecast}) = \beta_o + \beta_1[a_1 U_{50} + a_2 U_{30} + a_3|U_{50} - U_{30}|] + \beta_2[a_4 R_s + a_5 R_G] \tag{1}$$

where the $\beta$'s and a's are arbitrarily determined constants given in Table 1.

Table 1: Term constants and coefficients of prediction equation (1).

| Predictants | Term Coefficient | | | QBO Wind | | | Rainfall | |
|---|---|---|---|---|---|---|---|---|
| | $\beta_0$ | $\beta_1$ | $\beta_2$ | $a_1$ | $a_2$ | $a_3$ | $a_4$ | $a_5$ |
| (N) | 11.732 | 0.135 | 0.701 | 1.000 | 0.252 | −0.640 | 1.000 | 2.498 |
| (NS) | 64.072 | 1.031 | 7.149 | 1.000 | −0.320 | −3.384 | 1.000 | 2.302 |
| (H) | 7.560 | 0.049 | 0.759 | 1.000 | −0.320 | −3.384 | 1.000 | 2.302 |
| (HD) | 33.303 | 0.215 | 6.645 | 1.000 | 1.781 | −1.370 | 1.000 | 2.144 |
| (IH) | 3.571 | 0.042 | 0.717 | 1.000 | 0.103 | −1.415 | 1.000 | 2.455 |
| (IHD) | 7.605 | 0.124 | 2.006 | 1.000 | −0.080 | −1.410 | 1.000 | 2.292 |
| (HDP) | 95.326 | 0.686 | 24.747 | 1.000 | 1.066 | −1.346 | 1.000 | 1.700 |

Table 2 shows the 41-year hindcast measure of variance explained by the Least Absolute Deviation (Or LAD analysis) and by an Ordinary Least Squares (or OLS) analysis using the independent jackknife method. This table shows that skillful extended range prediction, at least of Atlantic seasonal hurricane activity, is indeed possible. Considering the difficulties inherent in any seasonal weather prediction scheme plus the extraordinary 6–11 month extended range of this relationship, we consider this to be an important finding. Until recently, few serious researchers would have imagined that there might be seasonal predictive signals this strong extending this far into the future. In addition, full exploitation of all potential Atlantic predictive signals has not yet been made. Further study of additional unexploited regional or global variables including West African land temperatures, land and ocean surface pressure, Atlantic SSTs plus other potential seasonal predictors have not yet been accomplished. Consequently, it is likely that with additional research, some further improvements will be possible.

Table 2: December 1 prediction equation amount of TC activity variance explained by an independent (jackknife) hindcast forecasts for the 41-year period of 1950–1990 by Least Absolute Deviation (LAD) and by Ordinary Least Squares (OLS) analysis. The probability of no predictive relationship is shown in the right column.

| Forecast Parameter | LAD Measure of Agreement | Variance Explained by OLS ($r^2$) Method | Probability of No Relationship |
|---|---|---|---|
| (N) | 0.440 | 0.395 | $0.22 \times 10^{-5}$ |
| (NS) | 0.514 | 0.488 | $0.89 \times 10^{-7}$ |
| (H) | 0.447 | 0.466 | $0.15 \times 10^{-5}$ |
| (HD) | 0.491 | 0.511 | $0.46 \times 10^{-6}$ |
| (IH) | 0.498 | 0.581 | $0.95 \times 10^{-7}$ |
| (IHD) | 0.451 | 0.517 | $0.27 \times 10^{-6}$ |
| (HDP) | 0.447 | 0.527 | $0.11 \times 10^{-5}$ |

## 3 Seasonal Prediction by 1 August

The majority of seasonal Atlantic basin Hurricane activity occurs after 1 August. Ninety-eight percent of all of the intense (or Saffir/Simpson Cat. 3-4-5) hurricane activity takes place after this date and 75 percent of US coastal hurricane spawned destruction is caused by these less frequent but much more destructive intense hurricanes. The 1 August forecast provides an improvement on the previously issued 1 December and 1 June forecasts by including additional forecast parameters and June–July meteorological information.

This early August forecast takes the following form:

$$\tilde{y} = b_o + b_1 \left[a_1 U_{50} + a_2 U_{30} + a_3 |U_{50} - U_{30}|\right]$$

$$+ b_2 \left[a_4 R_S + a_5 R_G\right]$$

$$+ b_3 \left[a_6(SLPA) + a_7(SOI) + a_8(SSTA) + a_9(ZWA)\right]$$

where

$\tilde{y}$ is the predictant (NS, NSD, H, etc.)

a's and b's are empirically derived coefficients

$U_{50}, U_{30}$ are extrapolated September QBO zonal winds at 30 and 50 mb at 10°N

$|U_{50} - U_{30}|$ absolute value of the extrapolated vertical wind shear between 50 and 30 mb.

$R_s$ is the Western Sahel June–July precipitation.

$R_G$ is the previous year August through November precipitation in the Gulf of Guinea region.

SLPA is the Sea Level Pressure Anomaly in the lower Caribbean basin in June–July.

SOI is the Tahiti minus Darwin Sea Level Pressure differences for June–July.

SSTA is the Sea Surface Temperature Anomaly in Nino 3 in June and July.

ZWA is the Zonal Wind Anomaly in the Caribbean basin in June–July.

Through extensive statistical analysis we have determined that the most skillful 41–year independent (jackknife) hindcasts could be made of the seven predictants (N, NS, H, HD, IH, IHD, and HDP) with this equation through use of the following constants and coefficients of Table 3.

Table 3: Constants and coefficients for 1 August statistical forecasts.

| | $b_0$ | $b_1$ | $b_2$ | $b_3$ | $a_1$ | $a_2$ | $a_3$ | $a_4$ | $a_5$ | $a_6$ | $a_7$ | $a_8$ | $a_9$ |
|---|---|---|---|---|---|---|---|---|---|---|---|---|---|
| NS | 11.073 | 0.097 | –.655 | –0.855 | 1.0 | 0.792 | 0.081 | 1.0 | –1.462 | 1.0 | –0.387 | 0.024 | 0.110 |
| NSD | 68.919 | 1.023 | 5.233 | –5.355 | 1.0 | 0.559 | –0.376 | 1.0 | 1.062 | 1.0 | –0.873 | –1.506 | 0.089 |
| H | 7.377 | 0.042 | –.119 | 0.485 | 1.0 | 1.978 | –0.101 | 1.0 | –8.079 | 1.0 | –0.886 | 0.174 | –0.660 |
| HD | 33.513 | 0.493 | 4.496 | –4.324 | 1.0 | 0.894 | 0.266 | 1.0 | 0.614 | 1.0 | –0.050 | –0.076 | 0.182 |
| IH | 3.453 | .0415 | 1.142 | –0.670 | 1.0 | 0.591 | –0.479 | 1.0 | 0.598 | 1.0 | 0.497 | 0.641 | 0.057 |
| IHD | 5.499 | .0542 | 6.260 | –1.219 | 1.0 | 0.840 | 2.141 | 1.0 | 0.243 | 1.0 | 1.139 | 0.497 | 0.034 |
| HDP | 94.121 | 0.843 | 48.360 | –1.155 | 1.0 | 1.768 | 1.028 | 1.0 | 0.305 | 1.0 | 4.954 | –1.101 | 1.006 |

Table 4 shows the amount of last 41–year (1950–1990) hindcast variance that can be independently (jackknife) explained by a Least Absolute Deviation (LAD) and by an Ordinary Least Squares (OLS) method of analysis. Note that this 1 August predictive equation can explain slightly over 60 percent of year to year variation in intense hurricane activity. This is a very skillful forecast.

Table 4: August 1 prediction equation amount of TC activity variance explained by an independent (jackknife) statistical analysis for the 41-year period of 1950–1990 by Least Absolute Deviation (LAD) and by Ordinary Least Squares (OLS) analysis. The probability of no predictive relationship is shown in the right column).

| Forecast Parameter | LAD Measure of Agreement | Variance Explained by OLS ($r^2$) | Probability of No Relationship |
|---|---|---|---|
| (N) | 0.451 | 0.434 | $0.25 \times 10^{-6}$ |
| (NS) | 0.611 | 0.591 | $0.12 \times 12^{-8}$ |
| (H) | 0.468 | 0.436 | $0.55 \times 10^{-6}$ |
| (HD) | 0.505 | 0.559 | $0.22 \times 10^{-6}$ |
| (IH) | 0.622 | 0.680 | $0.33 \times 10^{-8}$ |
| (IHD) | 0.611 | 0.615 | $0.85 \times 10^{-9}$ |
| (HDP) | 0.577 | 0.591 | $0.72 \times 10^{-8}$ |

## 4 Discussion

We did not expect that such strong relationships would exist between various climate parameters and seasonal hurricane activity with such long lag responses. These predictions should now be made every year.

It is remarkable that Atlantic seasonal hurricane activity, manifesting itself as multiple sporadic mesoscale events, would show such a strong and a long period lag response to forcing functions far removed in space and time. We know of no other climate signals showing this degree of extended range skill. This is further evidence for the primary role of global and regional circulation patterns on variable seasonal hurricane frequency and intensity. Previously, we had viewed hurricanes and the weaker weather systems which spawn them, more as the product of rapidly varying local circulation characteristics which had a large random component and which were impossible to predict more than a few days in advance, let alone 10 months in advance. Although this view is still true for individual hurricane systems, it is not for the seasonal aggregate of systems. The climate signal has a strong influence in determining the seasonal number of short lived and transitory events (i.e., hurricanes) likely to be activated.

*Acknowledgement*

This research has been supported by a climate grant from the National Science Foundation.

Bibliography

Gray, W. M., C. W. Landsea, P. W. Mielke and K. J. Berry, 1991: Predicting Atlantic seasonal hurricane activity 6–11 months in advance. Submitted to *Wea. and Forecast.*

Gray, W. M., C. W. Landsea, P. W. Mielke and K. J. Berry, 1991: Predicting Atlantic seasonal hurricane activity by 1 August. Submitted to *Wea. and Forecast.*

Landsea, C. W., 1991: West African monsoonal rainfall and intense hurricane associations. Dept. of Atmos. Sci. Paper No. 484, Colo. State Univ., Ft. Collins, CO, 272 pp.

# PREDICTABILITY OF INTENSE ATLANTIC HURRICANES AND WESTERN SAHEL RAINFALL FROM WEST AFRICAN RAINFALL

Christopher W. Landsea and William M. Gray
Department of Atmospheric Sciences, Colorado State University
Fort Collins, CO 80523

## 1 Introduction

This paper discusses the surprisingly strong Atlantic basin hurricane and Western Sahel rainfall prediction signals that are available from earlier West African rainfall. Previous reports have detailed the concurrent association of Western Sahel rainfall and tropical cyclone variations (Gray 1990, Landsea 1991, Landsea and Gray 1991, and Landsea *et al.* 1991).

## 2 Predictive Relationships

June to July West Sahel Rainfall: Although the Atlantic basin hurricane season officially begins on 1 June, intense hurricane activity does not occur climatologically before August (Landsea, 1991). It was hoped that predictive signals might be available within the African rainfall data which falls before 1 August. Rainfall data throughout Africa were examined on monthly and multimonthly periods. It was found that the Western Sahel monsoon rains of June and July show a substantial positive correlation with intense hurricane activity in the following months.

The previously studied 38 station (locations denoted in Fig. 1) June to September Western Sahel rainfall index (Gray, 1990; Landsea, 1991; and Landsea and Gray, 1991) has been used to create a June to July rainfall index. Stations were included within the index if they had at least 30 of 42 years of data. Values of this rainfall index from 1949 to 1990 are shown in Fig. 2 (top diagram). The time series has a strong multidecadal decrease, though not as severe as that noted for the entire June to September rainy season. This June to July rainfall shows predictive correlations with Atlantic basin tropical cyclone activity for the years 1949 to 1990: named storms (r = 0.38) and hurricanes (r = 0.39), but especially for intense hurricanes (r = 0.64) and intense hurricane days (r = 0.71). Fig. 3 illustrates the extreme differences in the number and duration of intense hurricanes for the ten wettest versus the ten driest June to July Western Sahel periods.

As previously documented by Bunting *et al.* (1975), the early season rainfall in the Sahel is useful as a predictor for the remaining months of the rainy season. Our research reconfirms this assessment. We find that almost 40% of the variance in the August to September Western Sahel rainfall can be foretold from the June to July Western Sahel rainfall amounts.

Previous Year August to November Gulf of Guinea Rainfall Using the same analysis technique where individual station linear correlation coefficients are generated, it was found that the rainfall along the Gulf of Guinea coast shows a surprisingly strong and extended period lag relationship to the following year's tropical cyclone activity and Western Sahel rainfall.

A 24 station index was created for the Gulf of Guinea region for the August to November time period. All stations within the boldface line in Fig. 1 with at least 17 of 42 years of data (the less stringent data requirement is due to poorer data reliability and availability) were utilized. The time series of this Gulf of Guinea index is portrayed in Fig. 2b and shows the following correlations to the *following* year Atlantic tropical cyclone activity: named storms (r = 0.48), hurricanes (r = 0.56), intense hurricanes (r = 0.66), and intense hurricane days (r = 0.63). Fig. 4 presents

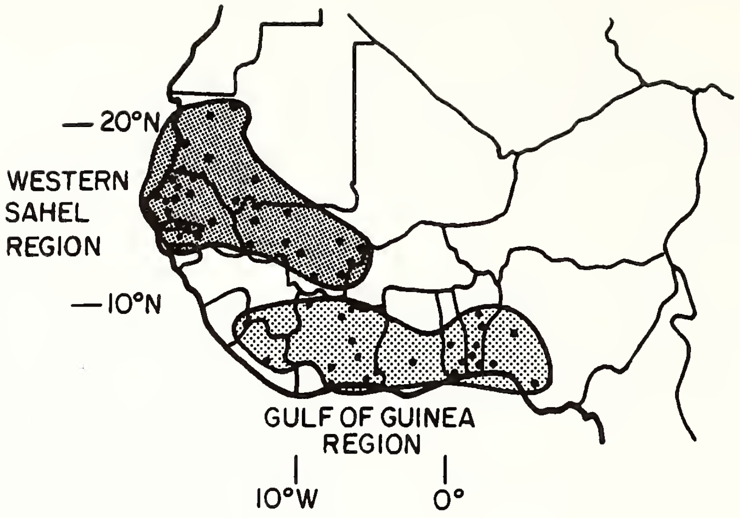

Figure 1: Location of rainfall stations which comprise the June to July Western Sahel and August to November Gulf of Guinea rainfall indices.

differences in the intense hurricane tracks in the years following the ten wettest and the ten driest Gulf of Guinea August to November periods between 1949 and 1989.

The Gulf of Guinea August to November rains also provide a measure of extended range predictability for the Western Sahel rainfall 6 to 10 months in the future. While our analysis of the spatial linear correlation coefficients showed that there is a fairly strong association in the Western Sahel itself (likely due to the tendency for rainfall anomalies to "persist" from season to season), the strongest correlations are found along the Gulf of Guinea coast. Correlating the Gulf of Guinea rainfall index directly to the June to September rainfall index gives a value of r = 0.60, or over one third of the variance.

Thus the late rains along the Gulf of Guinea provide a 6 to 10 month lead time for Western Sahel rainfall and Atlantic basin tropical cyclones and also an 8 to 10 month lead for the forecast of the intense hurricane activity, since over 98% of these storms occur after 1 August.

## 3 Physical Mechanisms

The June to July Western Sahel rainfall relationship to the following months' rain has already been explained by Bunting et al (1975) as a "persistence" of the strength and location of the monsoonal trough. This persistence is likely due to slowly varying conditions associated with Atlantic/global SST anomaly patterns as well as land surface processes (short term moisture recycling, for example) which tend to favor a continuation of existing conditions.

The rainfall along the Gulf of Guinea in August to November corresponds to the second rainfall maximum for the region. It is hypothesized that rainfall anomalies along the Gulf of Guinea provide an anomalous water vapor source (either positive or negative) through soil moisture evaporation and/or plant life evapotranspiration for next year's rainfall.

It is remarkable that seasonal amounts of Atlantic seasonal hurricane activity, manifesting itself in many sporadic mesoscale events, would show such a strong, long period lag response to West African rainfall amounts far removed in space and time.

*Bibliography*

Bunting, A.H., M.D. Dennett, J. Elston, and J.R. Milford, 1975: Seasonal rainfall forecasting in West Africa, *Nature*, **253**, 622-623.

Gray, W.M., 1990: Strong association between West African rainfall and U.S. landfall of intense hurricanes, *Science*, **249**, 1251-1256.

Landsea, C.W., 1991: West African monsoonal rainfall and intense hurricane associations. Dept. of Atmos. Sci. Paper No. 484, Colo. State Univ., Ft. Collins, CO 80523, 272 pp.

Landsea, C.W. and W.M. Gray, 1991: The strong association between western Sahel monsoon rainfall and intense Atlantic hurricanes. Accepted to *J. Climate*, 34 pp.

Landsea, C.W., W.M. Gray, P.W. Mielke, Jr., and K.J. Berry, 1991: Multidecadal variations of Sahel monsoon rainfall and intense U.S. landfalling hurricanes. Submitted to *J. Climate*, 13 pp.

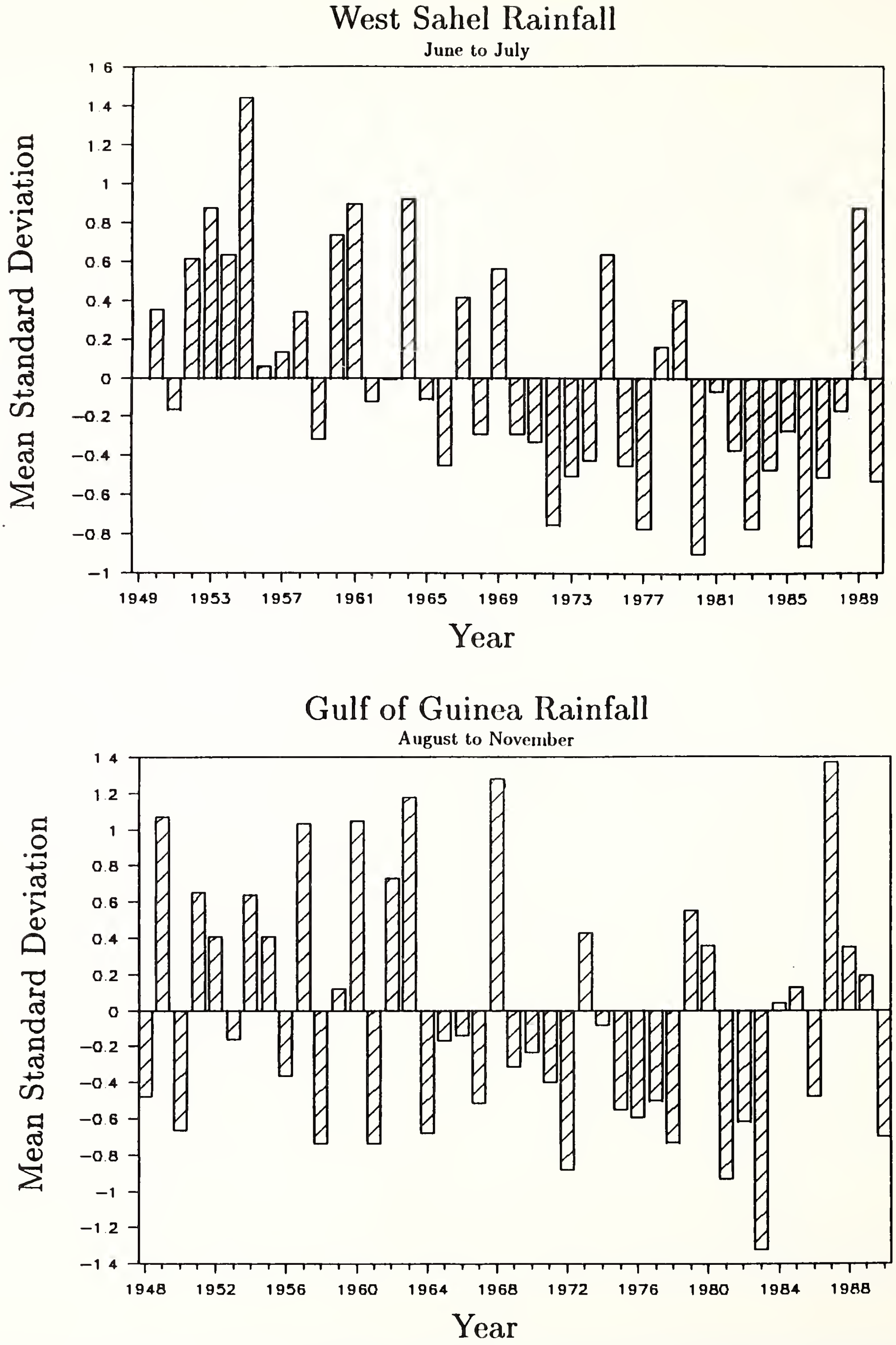

Figure 2: (top panel) June to July rainfall anomalies in yearly mean standard deviations for 1949 to 1990 from 28 Western Sahel region stations; (bottom panel) August to November rainfall anomalies in yearly mean standard deviations for 1948 to 1990 from 24 Gulf of Guinea region stations.

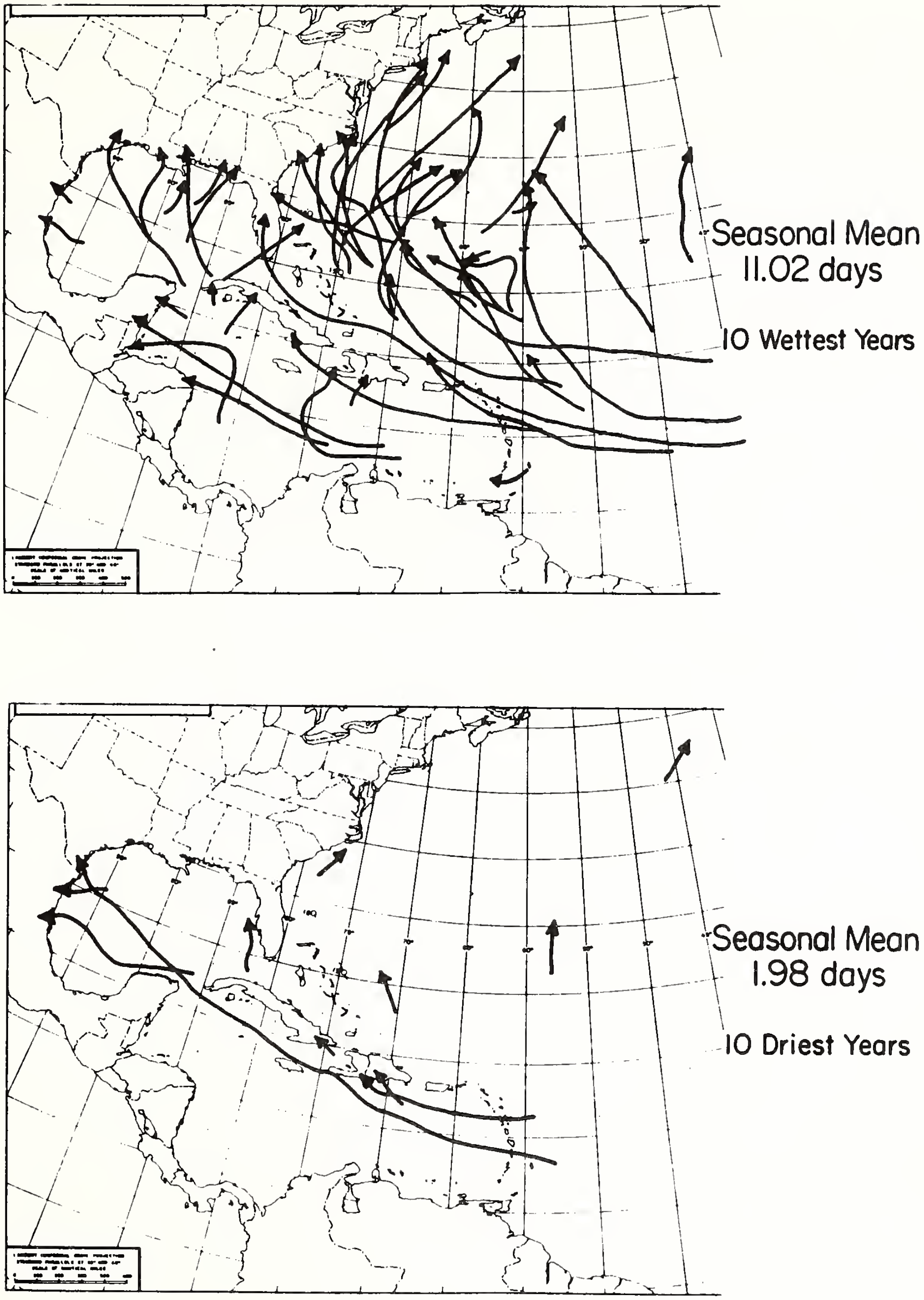

Figure 3: Tracks of intense hurricanes in the Atlantic basin for the seasons after the ten wettest (top panel) and the ten driest (bottom panel) June to July periods in the Western Sahel.

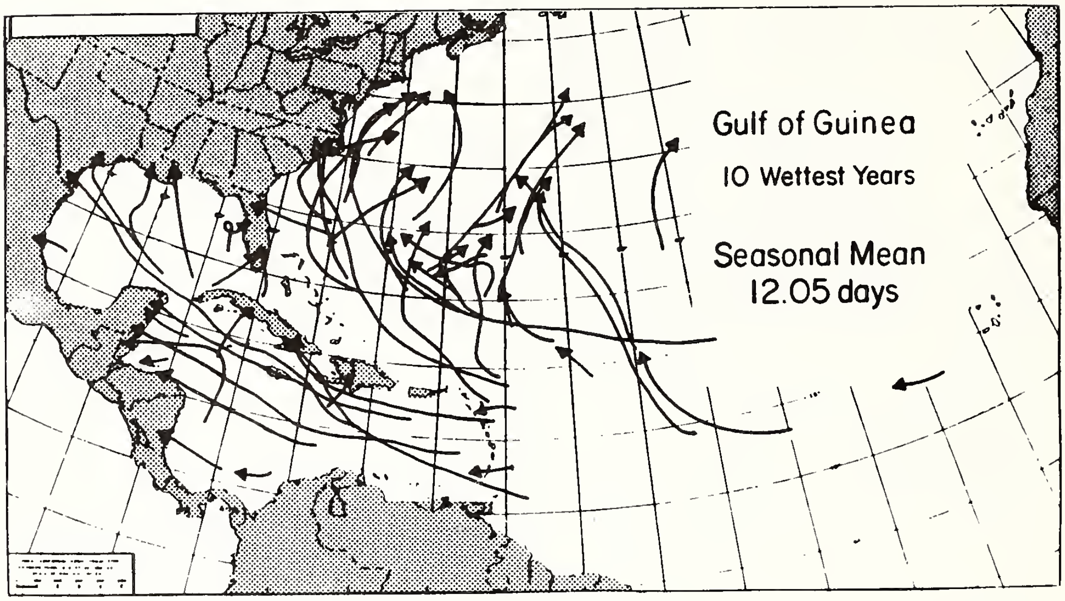

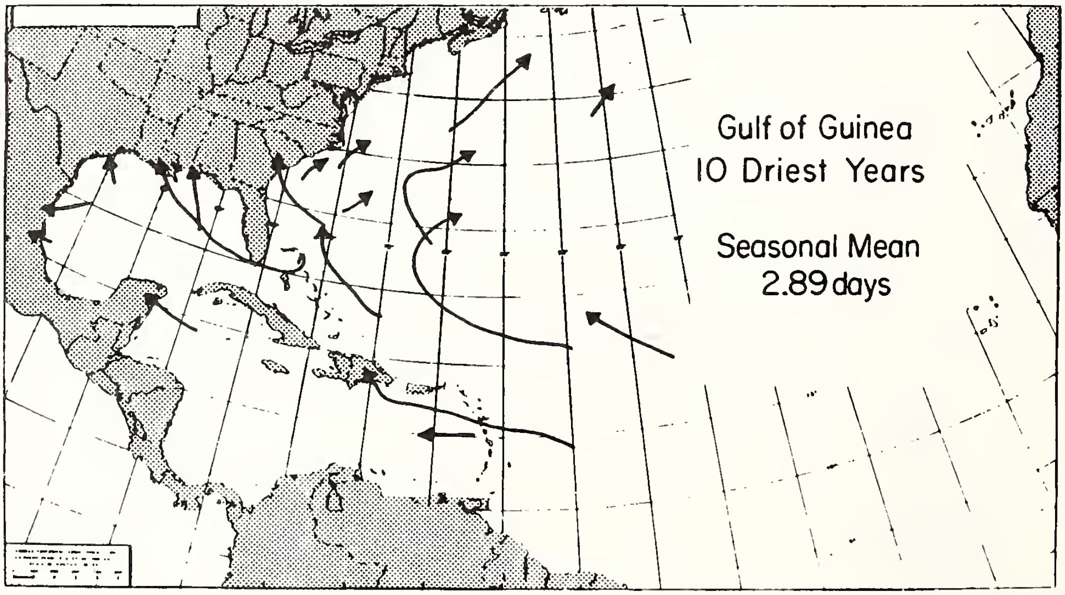

Figure 4: Tracks of intense hurricanes in the Atlantic basin for the year following the ten wettest (top panel) and the ten driest (bottom panel) August to November periods in the Gulf of Guinea region.

# Long-lead forecasts of time-mean U.S. surface temperature using canonical correlation analysis

Anthony G. Barnston
Climate Analysis Center, NMC/NWS/NOAA

1. Introduction. In this study the skill potential of canonical correlation analysis (CCA) in predicting time-average surface temperature at long lead across the continental U.S. is examined. In particular, one-month mean temperature predicted at least one-half month in advance and three-month mean temperature predicted at least one month in advance are investigated. These specific objects of study reflect the needs of the general public and specialized interests, and are already being routinely and officially forecast with essentially zero lead time at the Climate Analysis Center division of the National Meteorological Center (NMC). Being primarily beyond the time range within which numerical weather forecasts are useful, the long-lead version of the 1- and 3-month forecasts would rely nearly exclusively on empirical rather than dynamical methods. Such methods currently used for the zero-lead 3-month forecasts are persistence (either directly by station or in the form of gridpoint-wise autocorrelations using varying time lag), analog/antianalog, bivariate regression on both of these, and univariate regression on specific variables such as a Southern Oscillation Index or a zonally averaged subtropical 700 mb height index (Erickson 1983). While CCA has recently begun being employed operationally to forecast fluctuations of the El Nino/ Southern Oscillation (ENSO) (Barnston and Ropelewski 1992), it has never been applied directly to forecasts of the U.S. surface climate in real time. This study is designed to determine CCA's skill potential as a function of lead time, season, and location within the U.S. as well as to determine the features of the optimized linear relationships (i.e. the predictors that appear to provide the bulk of predictive skill).

CCA is a multivariate statistical technique that calculates linear combinations of a set of predictors that maximizes relationships, in a least-squares error sense, to similarly calulated linear combinations of a set of predictands. Because the predictor and predictand are each a set of variables, the method can depict relationships between corresponding favored spatial patterns of either (e.g., if the sets of variables are gridded fields). Furthermore, if either set is a temporal sequence of such fields (referred to as "stacked" fields), CCA can highlight the evolution of the predictor or predictand spatial patterns. For example, the first 100 out of 200 predictor variables might be a 10 by 10 two-dimensional gridded field of 1-month mean sea surface temperatures (SSTs) centered 1.5 months before forecast time, while variables 101-200 are the same field centered a half month before forecast time. The analysis could find predictor patterns at both prior times (implying a temporal evolution) that are associated with a specified predictand pattern which itslef might be "stacked" in time.

CCA is used in a similar manner in this study to that used in ENSO diagnosis/prediction (Graham et al. 1987a, 1987b), real-time ENSO prediction (Barnston and Ropelewski 1992) and, more originally, to that used in the short-term U.S. climate fluctuation study of Barnett and Preisendorfer (1987). CCA has previously been described in the non-meteorological literature (Hotelling 1936, Anderson 1984) as well as in empirical meteorological or geophysical contexts (Glahn 1963, Davis 1977, Barnett 1981, Nicholls 1987).

2. Data. In this study the predictor data are half-monthly mean values of (1) gridded (5 deg latitude by 10 deg longitude boxes) near-global SST totalling 235 grid points, (2) extratropical Northern Hemispheric approximately equal-area gridded 700 mb height using 358 grid points poleward of 20N, and (3) U.S. surface

temperature at 59 roughly equally separated stations. The predictand data are the same as the third predictor data set--U.S. surface temperature at the same 59 stations. The 700 mb data are obtained from NMC; the SST data from the COADS (Slutz et al. 1985) through 1979 and either ship data or blended ship/satellite data thereafter (Reynolds 1988); the U.S. surface temperature data from the National Climatic Data Center (NCDC) through 1983 and from NMC thereafter. The period of study is 1955-1990, constrained by the onset of relatively good tropical Pacific SST data in the middle 1950's.

The predictor fields are introduced in a temporal sequence consisting of four consecutive periods prior to forecast time. The periods are of equal duration, and usually (but not necessarily) equal to that of the predictand period. In these experiments the final predictor period is not adjacent to the predictand period--i.e. a lead time is inserted. There are 2608 predictor elements within the four temporally "stacked" sets of predictor fields (4 X [ 235(SST) + 358(700mb) + 59(sfc T) ] ).

Before beginning the CCA analysis, the predictor and predictand data are detrended (using a single linear regression line) to filter out artifactual intrusions such as dataset biases that vary slowly over time. The linear detrending results in temporal stationarity, allowing the analysis to focus on short-term climate variability rather than on much slower variations that could be either real or artificial. The data are then standardized, resulting in equal weighting of all the variables for the correlation-based CCA.

3. CCA overview and procedure. As a linear modeling technique, CCA is maximally advanced in that it fits two or more predictors with two or more predictands. CCA uses eigenvalues and eigenvectors in a specialied way, such that the structure of the covariance between predictor and predictand variables is defined under the constraint of maximization of the cross-datset correlation explained with each successive mode. It is more complex than standard empirical orthogonal function (EOF) analysis which calculates an orthogonal coordinate system that maximizes variance explained in a single dataset with each successive mode. The CCA procedure is now very briefly described; for more detail the above-cited references, including the appendix in Barnett and Preisendorfer (1987), may be consulted.

Following any preprocessing of the predictor and predictand datasets (such as filtering, detrending, standardization, or final interfield predictor weighting), it is advisable to pre-orthogonalize these datasets individually using EOF analysis, and then analyze the resulting amplitude time series with CCA. Final interfield predictor weighting may be done after all other preprocessing to adjust the relative weights of different predictor fields as wholes, as these may initially differ markedly due to, for example, differing numbers of grid points. The orthogonalization then eliminates redundancies in the large datasets, which safeguards against degeneracies in estimated inverse matrices in the CCA. It also reduces noise, which helps to reduce the degree of overfitting in the CCA.

Next, a covariance matrix between each predictor (predictand) and all predictands (predictors) is formed; note that only cross-dataset pairings are used. This is generally not a square matrix, but becomes square when it is post- or premultiplied by its transpose, each of which operation is carried out for the predictor and predictand CCA solutions, respectively. The predictor and predictand product matrices are then used to obtain CCA eigenvectors and eigenvalues for predictors and predictands, with equal eigenvalues for corresponding mode numbers. (A short-cut for this procedure is to apply it only to the predictor product matrix. The predictand eigenvectors may then be computed more easily using the predictor eigenvectors.) The square roots of the eigenvalues are the correlations between the predictor and predictand canonical component time series associated with the canonical loading patterns for the mode in question. The predictor and predictand canonical loading patterns are linear combinations of the respective input variables that maximize the cross-dataset covariance accounted for by the mode.

To perform CCA for varying predictand lead times, the process is repeated for each case--that is, the predictand is never "stacked" but rather consists of only a single period. In this study the number of periods between the final predictor period and the predictand period is varied from 0 to 4, with an additional fractional period inserted, increasing all of these by the amount of the intended basic (minimal) lead time. For example, for 1-month mean forecasts made at a half-month lead, the number of periods separating the final predictor and the predictand periods would be set at 0.5 periods (months in this case), 1.5, 2.5, 3.5 and 4.5 periods. For 3-month forecasts made at 1-month lead the number of separating periods would be 0.33 (i.e. 1 month), 1.33 (4 months), ... , 4.33 (13 months).

4. Cross-validation tests to estimate skill. To estimate the forecast skill of CCA for any of the 59 predictand U.S. surface temperature stations for any lead time for any target period, a cross-validation technique was used as follows: Each of the 36 years from 1955 to 1990 was held out in turn and CCA was used to develop a prediction model from the remaining 35 years. The predictor data for the withheld year was then projected onto the predictor CCA loading patterns and predictand values were generated and verified against observed data. Both predictor and predictand data for the withheld (target) year were expressed as standardized anomalies with respect to the statistics of only the non-withheld years. The process was repeated for each of the 36 years held out as the forecast target. A temporal correlation was then computed between the 36 forecasts and the corresponding observed temperatures.

As a competitor for the CCA cross-validation correlation skill, the autocorrelation of the predictand temperatures over the lead time in question (i.e. persistence) was computed. Rather than using a single, full sample autocorrelation, the persistence skill was calculated in the framework of cross-validation to make it comparable to the CCA skill. To do this, the persistence autocorrelation coefficient was developed separately for each year held out as target year, producing differentially damped persistence forecasts among target years. (Note that uniform damping would not affect the correlation skill score, but differential damping would degrade it slightly.)

5. Results. The temporal correlation between the CCA cross-validation forecasts and the observed surface temperatures averaged over the 59 U.S. stations is shown in Fig. 1 for 24 half-month-apart phasings ("seasons") of the annual cycle for five lead times ranging from 1/2 month (solid line) to 9/2 months (line with largest dashes) for 1-month mean predictor and target periods. While the skill clearly is not high for much of the year a tendency for some skill is noted in late winter and, more clearly, in late summer. Lengthening the lead time does not appear to diminish the tendency for these modest skill peaks. A similar plot of cross-validated persistence skill (not shown) shows mostly lower skills than those of Fig. 1, with the exception of 1/2-month lead forecasts for target period 18 (forecasts for September made at mid-August) for which a persistence skill of 0.20 is obtained.

The skill of mid-July forecasts for August (target period 16 at 1/2-month lead) has the highest skill score (0.27) among 1/2-month lead forecasts and is explored in greater detail. Figure 2 displays the geographic distribution of the skill for these forecasts, revealing relatively high skill in the eastern half of the U.S.--particularly in the Midwest, Tennessee Valley and south-central Texas. Inspection of the predictor and predictand CCA loading patterns (not shown) reveals that the first canonical mode, explaining 8 (13) percent of the variance of the original predictor (predictand) data set, is the source of much of the organized skill structure. The patterns leading to warm surface temperatures in the high skill areas in Fig. 2 include the final stages of a warm ENSO episode in early spring (positive SST anomalies in the east tropical Pacific, negative SST anomalies south of the Aleutian Islands, and positive 700 mb height anomalies in the Northern Hemisphere (NH) west subtropical Pacific). Additionally, throughout the spring there is non-Pacific tropical and NH-subtropical warmth (positive SST anomalies in the subtropical NH Atlantic and east equatorial Indian oceans, and positive 700 mb height anomalies in the subtropical NH east Atlantic and NH east Indian oceans). The polarity of these predictor anomaly patterns would be reversed for subsequent cold U.S. temperatures in the high skill areas.

The scenario dipicted above implies an importance of ENSO episodes for North American climate even for summer, and suggests that ENSO may have residual effects in the low-latitude Atlantic and Indian oceans. Spring warmth in the subtropical Atlantic 700 mb height followed by a generally warm summer in the U.S. is reminiscent of a similar relationship shown by Erickson (1983). Inspection of the loading patterns for target period 15 for longer lead times (note the skill peaks in Fig. 1) indicates markedly similar scenarios and high skill regions as those described above for the half-month lead time. This implies that the best predictors may occur well prior to the onset of the target period.

The correlation skill for 3-month mean predictor and target periods (i.e. seasonal forecasts) made at leads of 1, 4, ..., 13 months is shown in Fig. 3 in similar format to that of Fig. 1. For 3-month means the skill appears slightly higher than for 1-month means (particularly for the late winter modest skill peak), suggesting that the forecast system is finding its strongest signals on the lower frequency (seasonal) time scale as opposed to a quicker (monthly) time scale. As was the case with the monthly forecasts, increasing the lead time by as much as 3 months does not seem to lower the skill. However, the skills of forecasts at 7, 10 and 13 months lead do show a progressive decay. The skill of seasonal persistence forecasts (not shown) is lower than or equal to those seen in Fig. 3.

The skill of January-February-March forecasts made at the end of November (target period 6 at 1-month lead) is in the middle of a generally skillful period as shown in Fig. 3 (although its skill of 0.22 is not the highest among its immediate "neighbors") and is explored in greater detail. Figure 4 shows the geographic distribution of the skill for these forecasts, revealing relatively high skill in the Gulf region and secondary peaks in the Great Lakes and along much of the immediate West Coast. Inspection of the predictor and predictand CCA loading patterns (not shown) reveals that the first three canonical modes, explaining 7 (17), 6 (7) and 8 (2) percent respectively of the original predictor (predictand) variance, contribute most systematically to the skill structure as shown in Fig. 3.

Mode 1 captures the onset of the mature phase of an ENSO episode, in that the southeastern and south-central states tend to have negative temperature anomalies when (1) the SST in the central and east tropical Pacific becomes increasingly above normal beginning in the previous spring, (2) the SST just north of Australia becomes increasingly below normal beginning the previous summer, and (3) the SST south of Alaska becomes below normal but not notably until fall. Mode 2 includes some signs of ENSO but without tropical Pacific SST participation, in that much of the eastern two-thirds of the U.S. has below normal temperatures when (1) the SST in the central Indian Ocean is above normal the previous summer (associated with a poor monsoon), and (2) there is a positive Pacific/North American (PNA) 700 mb height anomaly pattern in the fall. Mode 3 describes a mature ENSO event the previous winter which dissipates over the spring and summer, where the west coast region has above normal temperatures when (1) the central and eastern tropical Pacific SST is above normal and the SST near 40N, 170W is below normal the previous winter, slowly dissipating during spring and summer, (2) the SST in the equatorial/ NH tropical Atlantic and in the east tropical Indian Ocean is above normal the previous spring and summer, and (3) the 700 mb height anomaly pattern is that associated with a low Southern Oscillation Index the previous winter and to a lesser degree the spring (i.e. forming a Tropical/Northern Hemisphere, or TNH, pattern with some PNA features also).

The three modes are all linked to tropical phenomena (particulary the ENSO), although mode 2 incorporates extratropical events as well. The NH extratropical winter climate connection to the tropics has been documented in innumerable studies in the last decade and earlier. As was the case with monthly long-lead forecasts, seasonal forecasts made at considerably longer lead than 1 month, or for slightly different target periods, retain similar CCA loading patterns to those described above. This suggests that late winter seasonal temperature forecasts for the U.S. are determinable (with modest skill) several months prior to the beginning of the winter in many instances.

6. Skill sensitivity tests. Various tests were performed to determine whether forecast skills could be increased further. Adjustments of the relative weights among the predictor fields and among the four predictor periods showed that, in general, the SST predictors are the most valuable, followed by the 700 mb height predictors. Increasing the weight of the SST somewhat increases the skill, particularly for the late winter 3-month mean forecasts. Changes in the weighting of the four predictor periods does not generally improve skill, and omitting the earliest one or two periods tends to degrade skill.

Spatially truncating seemingly irrelevant portions of the predictor domains (such as low to mid-latitude 700 mb height from 0 to 100 deg east longitude, or portions of the higher latitude Southern Hemisphere SST) does not generally increase skill. Eliminating all predictand points except those in a given sector of the U.S. usually degrades skill, suggesting that the overall predictand pattern enhances recognition of the large scale predictor-predictand relationships.

Increasing the averaging period of the four predictor periods for 1-month mean forecast target periods tends to increase skill somewhat, but other averaging period changes do not help; no such changes improve skill of the 3-month target period forecasts.

Allowing more canonical modes into the forecast system sometimes improves forecast skill, but not consistently. Allowing fewer modes often degrades the skill.

7. Outlook for January-February-March 1992. Using the above-described CCA model for forecasting the first three months of 1992 from data ending in August 1991 (i.e. a 4-month lead) and weighting the SST predictors double for some additional skill (0.31 rather than 0.22), a forecast for below normal temperatures in the southern tier of states (most strongly in west Texas) and above normal in the northern tier (most strongly in upper Michigan) appears. This is somewhat consistent with the mild to moderate warm ENSO currently in progress despite the clockwise rotation of the expected ENSO-related U.S. temperature anomaly pattern.

8. Conclusions and desired future accomplishments. There appears to be some skill in statistical forecasts of 1- and 3-month mean U.S. temperature at nonzero lead beyond that of the persistence control. This is the case especially in late winter in the Gulf region and late summer in parts of the central and eastern U.S. In these cases the skill is largely insensitive to the amount of lead time--from zero to at least several months. Much of the skill is linked to the tropics and

ENSO, even for the late summer forecasts to some extent. The SST appears to be the most valuable predictor field, perhaps partly because it is the only one that is quasi-global.

The CCA appears to capture the large scale, low frequency part of the predictability reasonably well. What is missing is usage of local effects such as SST in the immediate vicinity of the station (e.g. San Diego, New Orleans) or soil moisture. While these effects may act largely through persistence, the U.S surface temperature predictor is an insufficient provider of such detailed local information because of the pre-orthogonalization. A way of locally engineering this information into the forecast system is desired. One possibility is to introduce the surface temperature of the final predictor period after the pre-orthogonalization step for one station, thus preserving the local information. With this sort of information added on an individual station basis, forecast skill should increase for some stations.

## References

Anderson, C. W., 1984: An Introduction to Multivariate Statistical Analysis, 2nd ed., Wiley and Sons, 675 pp.

Barnett, T. P., 1981: Statistical prediction of North American air temperature from Pacific predictors. Mon. Wea. Rev., 109, 1021-1041.

Barnett, T. P. and Preisendorfer, R., 1987: Origins and levels of monthly and seasonal forecast skill for United States surface air temperatures determined by canonical correlation analysis. Mon. Wea. Rev., 115, 1825-1850.

Barnston, A. G. and C. F. Ropelewski, 1992: Prediction of ENSO episodes using canonical correlation analysis. J. Climate, 5, in press.

Cane, M. A., S. E. Zebiak and S. C. Dolan, 1986: Experimental forecasts of El Nino. Nature, 321, 827-832.

Davis, R., 1977: Techniques for statistical analysis and prediction of geophysical fluid systems. Geophys. Astrophys. Fluid Dyn., 8, 245-277.

Erickson, C. O., 1983: Hemispheric anomalies of 700 mb height and sea level pressure related to mean summer temperatures over the United States. Mon. Wea. Rev., 111, 545-561.

Glahn, H., 1963: Canonical correlation and its relationship to discriminant analysis and multiple regression. J. Atmos. Sci., 25, 23-31.

Craham, N. E., J. Michaelsen and T. P. Barnett, 1987a: An investigation of the El Nino-Southern Oscillation cycle with statistical models. 1. Predictor field characteris tics. J. Geophys. Res., 92, 14251-14270.

Craham, N. E., J. Michaelsen and T. P. Barnett, 1987b: An investigation of the El Nino Southern Oscillation cycle with statistical models. 2. Model results. J. Geophys. Res., 92, 14271-14289.

Hotelling, H., 1936: Relations between two sets of variates. Biometrika, 28, 321- 377.

Inoue, M. and J. J. O'Brien, 1984: A forecasting model for the onset of a major El Nino. Mon. Wea. Rev., 112, 2326-2337.

Nicholls, N., 1987: The use of canonical correlation to study teleconnections. Mon. Wea. Rev., 115, 393-399.

Reynolds, R. W., 1988: A real-time global sea surface temperature analysis. J. Climate, 1, 75-86.

Slutz, R., S. J. Lubler, J. D. Hiscox, S. D. Woodruff, R. J. Jenne, D. H. Joseph, P. M. Steurer, and J. D. Elius, 1985: Comprehensive Ocean Atmosphere Data Set, National Oceanic and Atmospheric Administration, Boulder, CO. (Available from Climate Research Program, ERL, R/E/AR6, 325 Broadway, Boulder, CO 80303.)

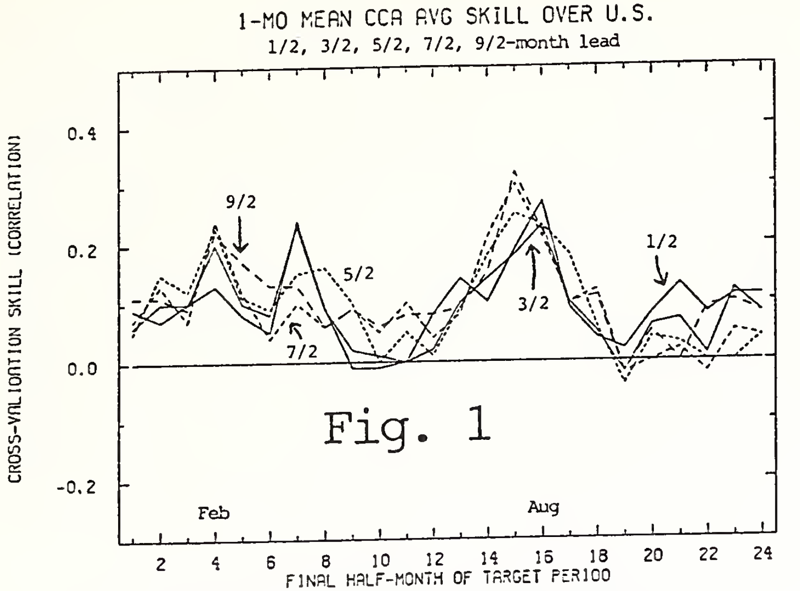

Fig. 1

Cross-validation correlation skill averaged over the U.S. for 1-month predictor and target periods, at five lead times (0 lead defined as when target period begins exactly at the time of the forecast).

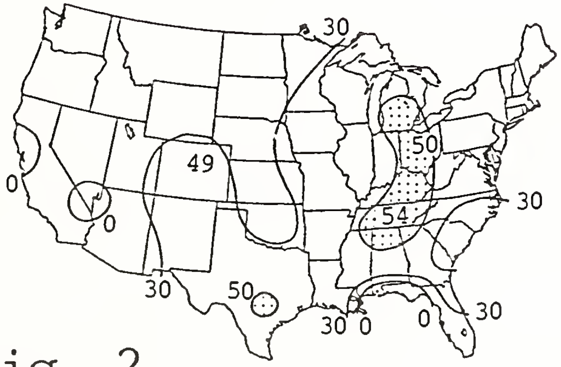

Fig. 2

mean skill = 27
(X100)

Geographic distribution of skill for forecasts for August made in mid-July (1/2-month lead).

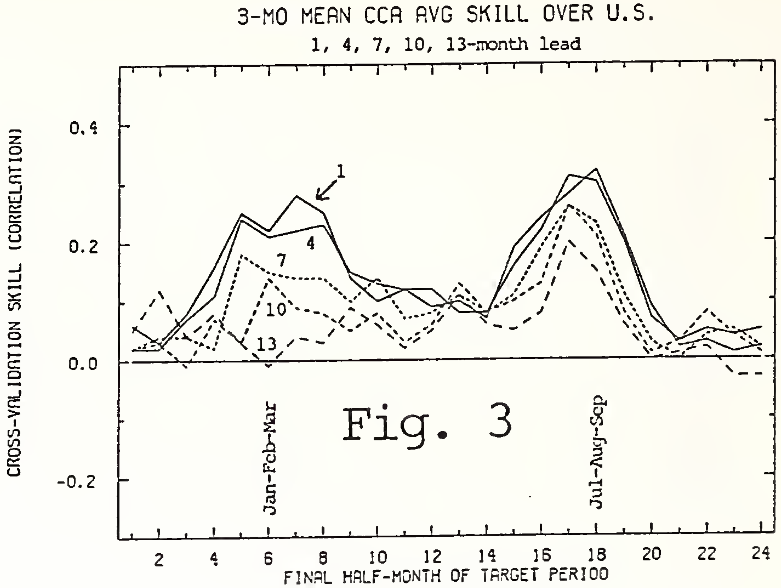

Fig. 3

As in Fig. 1 but for 3-month predictor and target periods.

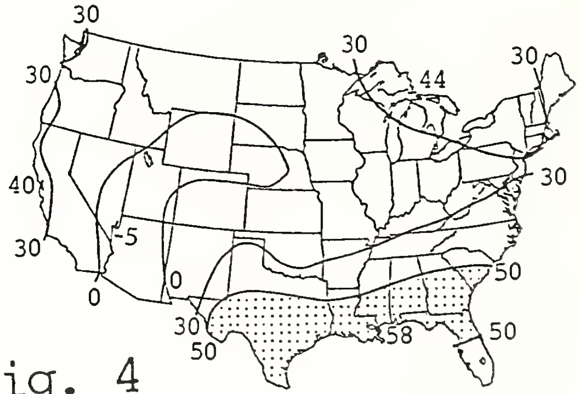

Fig. 4

mean skill = 22

As in Fig. 2 but for forecasts for Jan-Feb-Mar made at the end of November (1-month lead).

# FURTHER STUDIES OF SKILL CHARACTERISTICS OF U.S. LONG-RANGE FORECASTS. PART I: SURFACE TEMPERATURE AND PRECIPITATION FORECASTS

by

Robert E. Livezey and Jonathan D. Hoopingarner

Climate Analysis Center/NMC/NWS/NOAA

A program of modernization and automation of the U.S. Climate Analysis Center's Prediction Branch has led to the creation of accessible digital files of monthly and seasonal forecasts. These include forecasts of monthly U.S. temperature and precipitation categories (in three classes) and hemispheric 700 mb height anomalies produced 24 times a year since 1974, and of seasonal U.S. temperature and precipitation categories produced four times a year from 1958 through 1981 and 12 times a year thereafter. Probability forecasts are also available for all surface forecasts since 1982 and surface forecasts for Alaska/Canada and mid- and high-latitude Eurasia are available since 1987.

These data form the basis for a program of detailed documentation of the variability over time, and by season, location, parameter, class, regime, etc., of the skill of U.S. monthly and seasonal prediction practices. Ideally the information generated will not only prove useful for management of forecast operations and for the forecasters themselves, but also to potential users in deciding whether to include the forecasts as part of their particular decision-making process (Livezey, 1990). In this first part attention will be focused on temperature and precipitation forecasts and highlights of their analysis. In part II a number of aspects of the skill characteristics and history for monthly mean N.H. 700 mb height anomaly forecasts will be presented.

For the categorical forecasts examined here a skill score that measures the percent of hits above that expected from random forecasts is most heavily employed. Time series and annual cycles of map skills, maps of local skills, and summary contingency tables are produced for all surface forecasts and examined carefully for meaningful variability.

One example of this variability is embodied in Table 1 and Figure 1, namely a large increase in the difference in skill between official U.S. monthly mean temperatures forecasts and forecasts of persistence between the 1970's and 1980's. This increase in the advantage of the official forecasts over persistence is statistically significant and can be partially attributed to improvements in global numerical weather prediction (GNWP, Kalnay and Livezey, 1985). In fact the two periods were selected to coincide with the pre- and post-installation of GNWP at NMC. Note also from Table 1 that forecasts produced from objective specifications from monthly mean N.H. 700 mb height anomaly forecasts (NOP) perform almost as well as the official forecasts which use the objective specification and other tools (like persistence) in a subjective blend.

Table 1: Skill of Monthly Surface Temperature Forecasts for the United States and All Months

| | Official | Persistence | Objective Specification |
|---|---|---|---|
| Pre-GNWP (1970's) | 9.2 | 11.5 | |
| Post-GNWP (1980's) | 13.8 | 8.1 | 12.7 |

Examination of skill climatologies (Fig. 2) reveals that the recent advantage of official over persistence forecasts is entirely realized during the cold half of the year when persistence skill is particularly low and official skill particularly high. Similarly, it can be seen in Fig. 3 that the small advantage in skill of official over objectively specified forecasts comes completely from summertime forecasts when persistence skill is relatively high.

Other characteristics of the skill of monthly temperature forecasts can be illustrated through contingency tables and skill maps that have been tested for field significance. An example of the former comprises Table 2. Although it is for a period with perhaps the lowest skill of the year it illustrates two general characteristics of the forecasts. First, note that the forecasts and observations are similarly distributed. Second, there are relatively few two-class forecast errors (forecast above when below was observed and vice-versa). Every other monthly forecast set has fewer two-class errors than the worst case shown here.

Table 2: Distribution of Monthly Surface Temperature Forecasts and Observations for Fall (1981-1990) for the United States in Percent

| | | | FOR | | |
|---|---|---|---|---|---|
| | | B | N | A | |
| O | B | 9 | 11 | 6 | 26 |
| B | N | 10 | 18 | 13 | 41 |
| S | A | 6 | 15 | 12 | 33 |
| | | 24 | 44 | 32 | 100 |

| | |
|---|---|
| Correct: | 39 |
| One class error: | 49 |
| Two class error: | 12 |

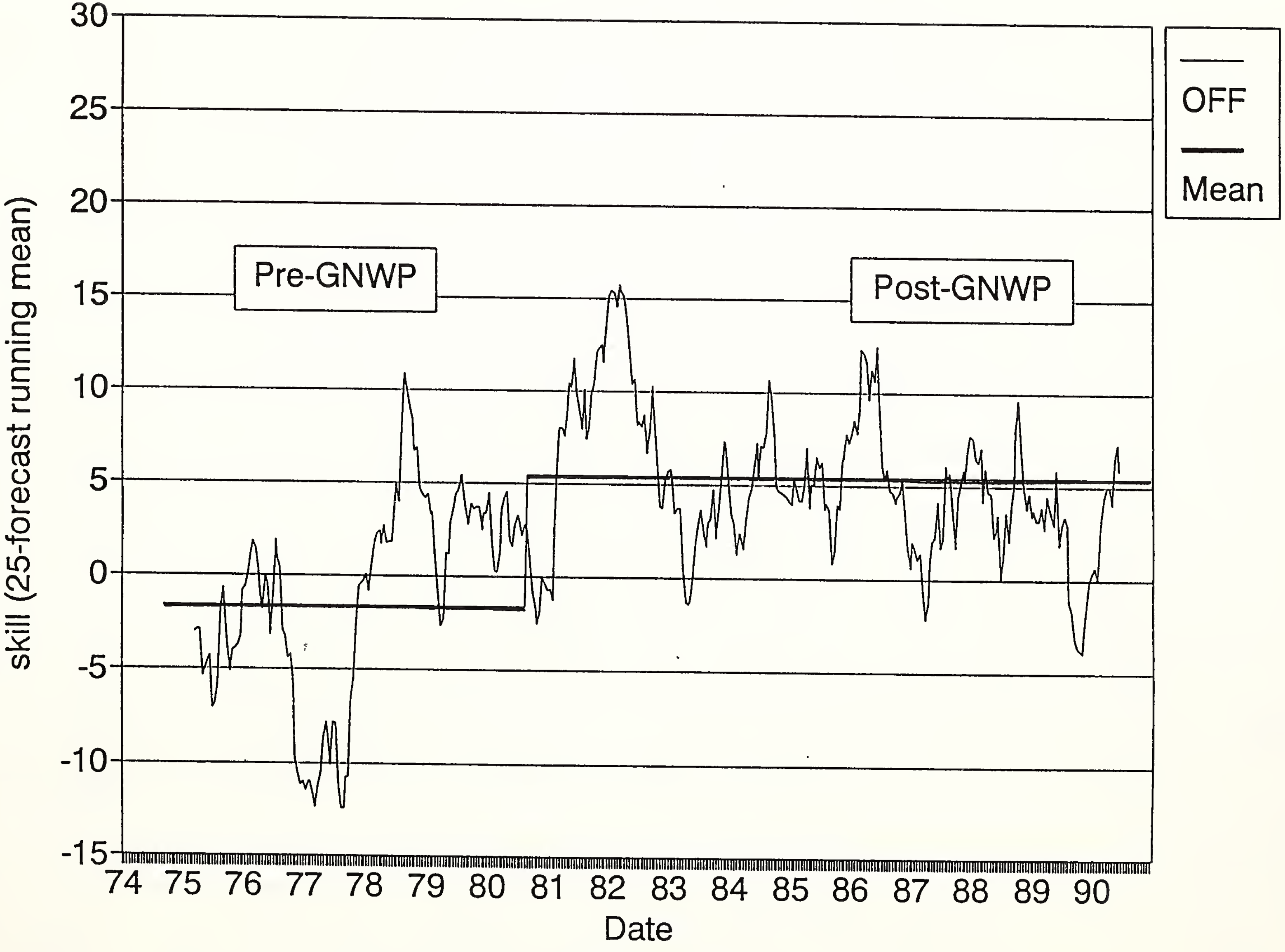

Figure 1. Differences in skill (25-forecast running mean) of official (OFF) and presistence (OPR) forecasts of monthly mean U.S. temperature.

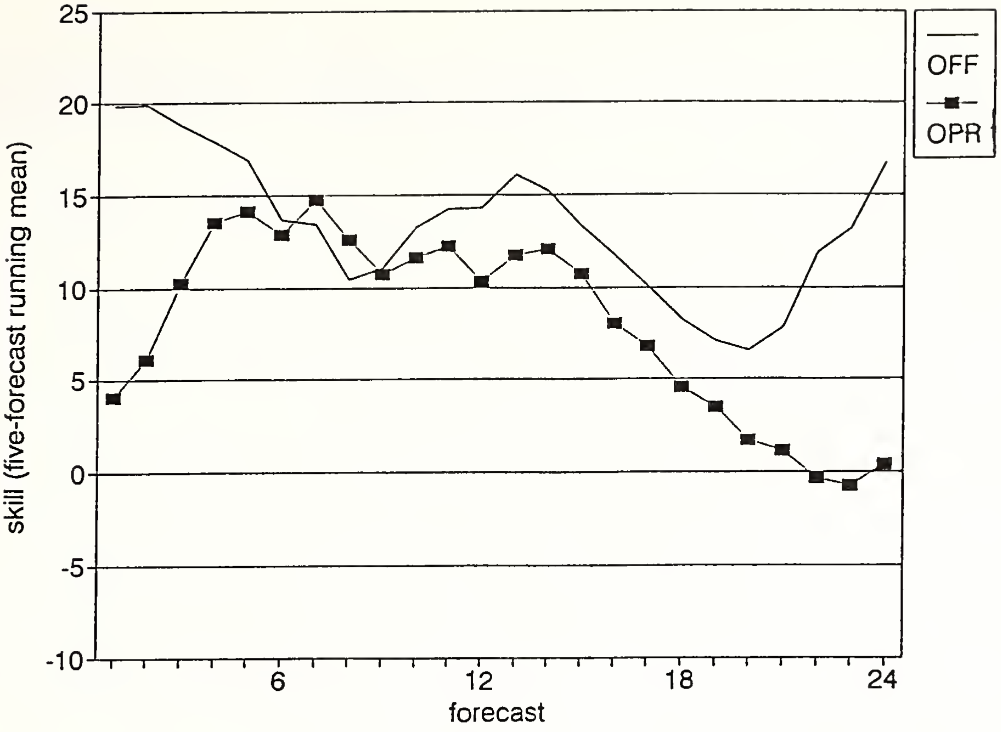

Figure 2. Annual cycle of difference in skill of official (OFF) and persistence (OPR) forecasts of monthly mean U.S. temperature (5-forecast running mean; 1 denotes January, 2 mid-January to mid-February, etc).

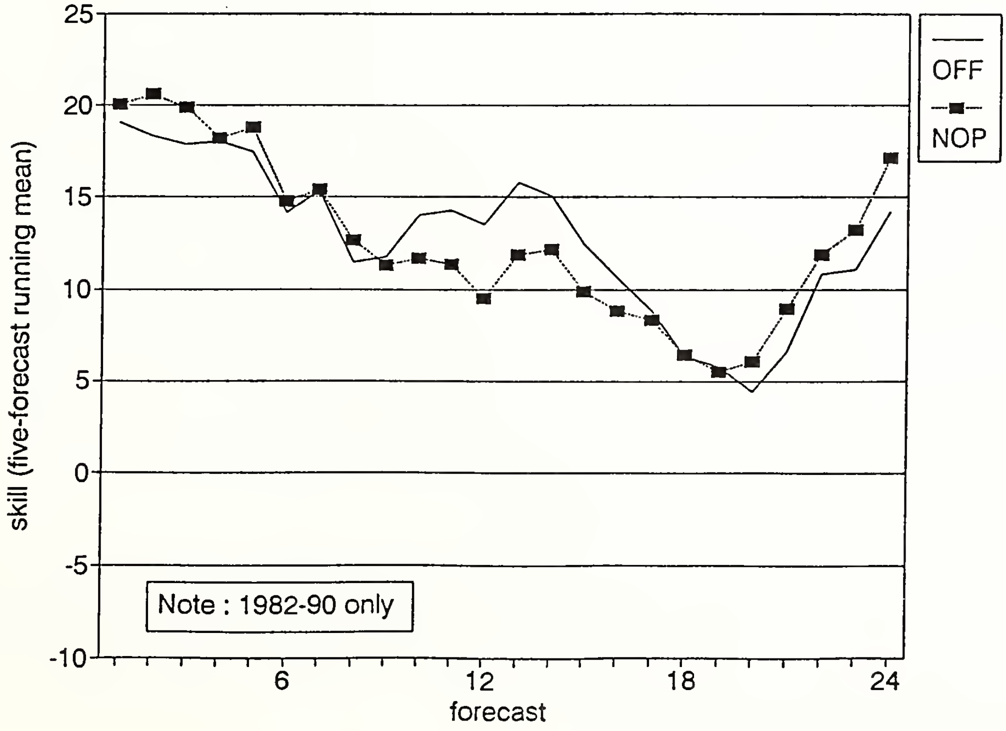

Figure 3. Same as Fig. 2 except for official (OFF) and objectively specified forecasts (NOP).

# FURTHER STUDIES OF SKILL CHARACTERISTICS OF U.S. LONG-RANGE FORECASTS. PART II : N.H MONTHLY MEAN 700 MB HEIGHT ANOMALY FORECASTS

by

Jonathan D. Hoopingarner and Robert E. Livezey

Climate Analysis Center / NMC / NWS / NOAA

Forecasts of monthly mean Northern Hemisphere sub- and extratropical 700mb height anomalies have been routinely made and archived in the Prediction Branch of the Climate Analysis Center (CAC) since the early 1970's. The addition of new equipment and personnel allowed CAC to institute operational digitization and archival of these height forecasts in August of 1989. A grant from the U.S. Forest Service made the wholesale digitization of the historical backlog feasible and work was completed in May 1990.

Both operational and historical digitization is accomplished in an interactive process which allows for extensive quality control. Verifications are performed on a 545-point diamond grid for compatibility with existing observational data sets.

Forecast skill is measured by the percent reduction in squared error from that of a climatology (zero-anomaly) forecast. This score is -1 for random forecasts, zero for climatology forecasts and +1 for perfect forecasts. Murphy and Epstein (1989) have shown that it can be decomposed into four terms that describe the error in phase of the forecast, the error due to difference of amplitude, the overall or unconditional bias of the forecast anomalies, and the error due to mismatched climatology. For large samples the latter two mostly compensate each other. The square root of the first term is a correlation, either anomaly or temporal, depending on whether the skill is for a forecast map at a particular time or a forecast history at a particular gridpoint respectively. The other terms, of course, also have spatial and temporal analogs.

Both types of skills, map and local history, and their decompositions have been computed for forecasts from 1973 through 1990. Thus, two types of non-summary presentations are possible: time histories of map skills and their constituent terms and maps of local history skills and their constituent parts.

Figures 1 through 4 show time series for an area bounded by 30° and 180°W, from 15° to 90°N, roughly corresponding to the

North American continent. The time series show clear trends in skill (an increase), the phase error (figure 1, a decrease) and in the bias term (figure 2, from too high forecast heights in the 1970's to too low in the 1980's). The former result is obviously related to the trend in advantage of the operational U.S. monthly mean surface temperature forecasts over persistence forecasts described in the companion talk. Mean annual cycles of both terms over the last decade show that the skill in forecasting phase resides in cold-season forecasts (figure 3, forecast 1 is for January, 2 mid-January to mid-February, etc.) and that the cold bias is a result of spring and fall forecasts (figure 4) when signal-to-noise ratios are large and observed warm biases cannot be confidently anticipated by forecasters.

Maps of winter local history (last decade) skills reveal that overall skill at this time of the year (figure 5) is a result of skill in both the timing (figure 6) and amplitude (figure 7) of events and is concentrated over the high-latitude oceans (including the Arctic) and to a lesser extent over the eastern half of North America. Forecasts almost mimic random forecasts over eastern Asia (figure 5).

Note the huge amplitude errors at 15°N in the Caribbean reflected in figures 5 and 7. These are spurious and once these are removed the overall skill score will be enhanced, especially in the Pacific / North American sector.

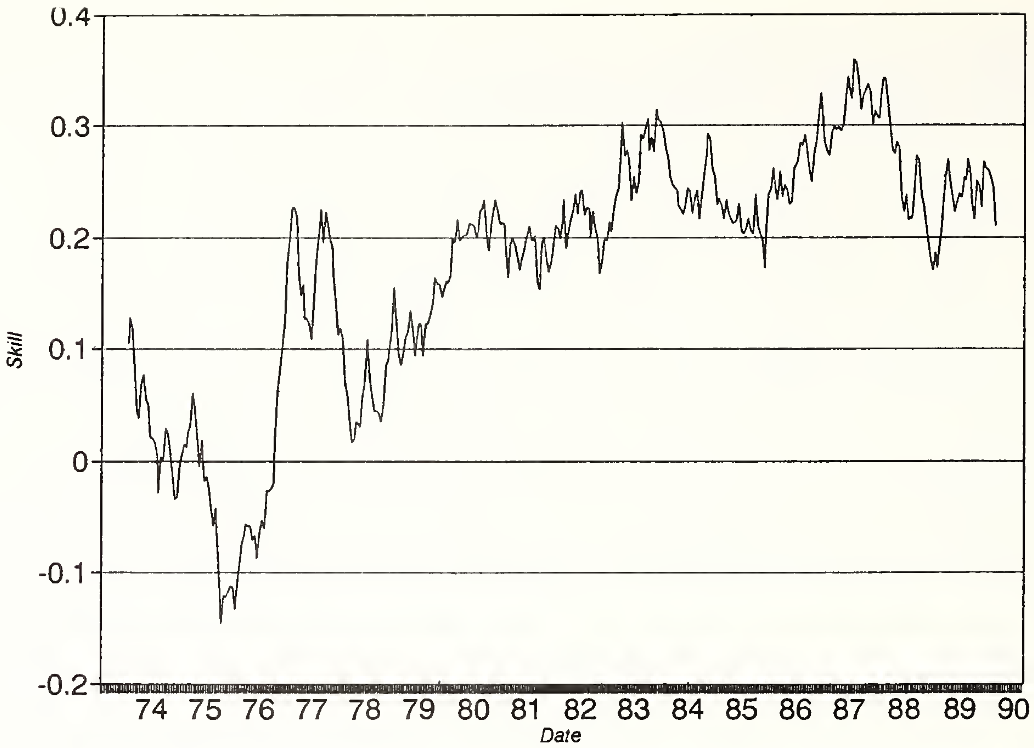

Figure 1. Time series of (25-forecast running mean) anomaly correlation between semi-monthly 30-day mean 700mb height forecasts and observations.

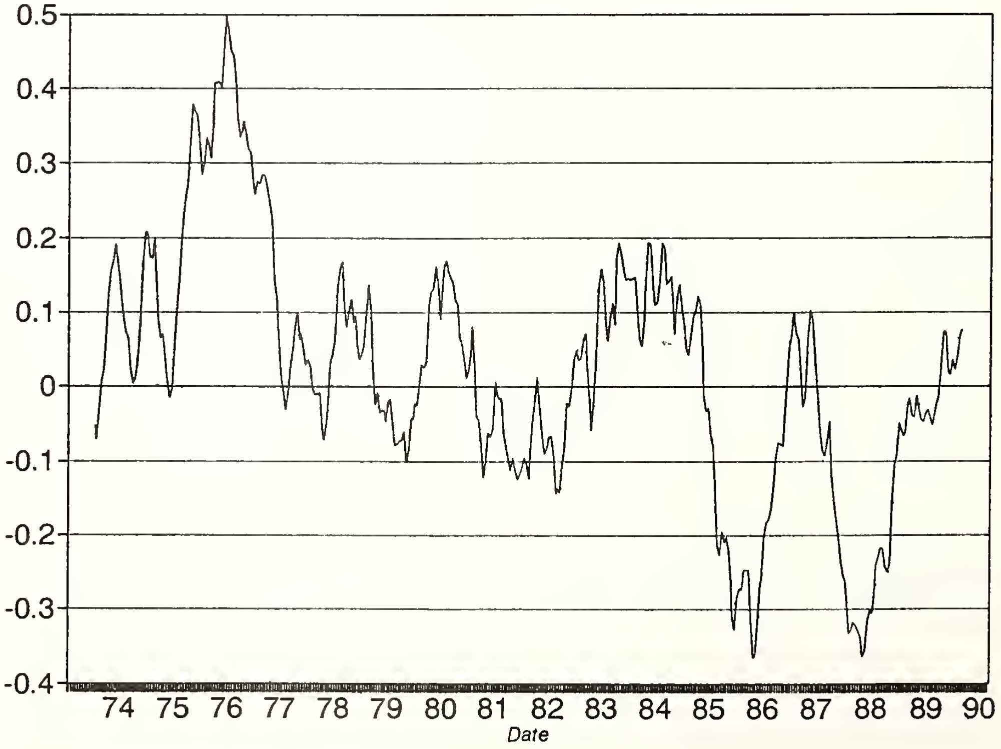

Figure 2. Same as Fig. 1 except for unconditional bias.

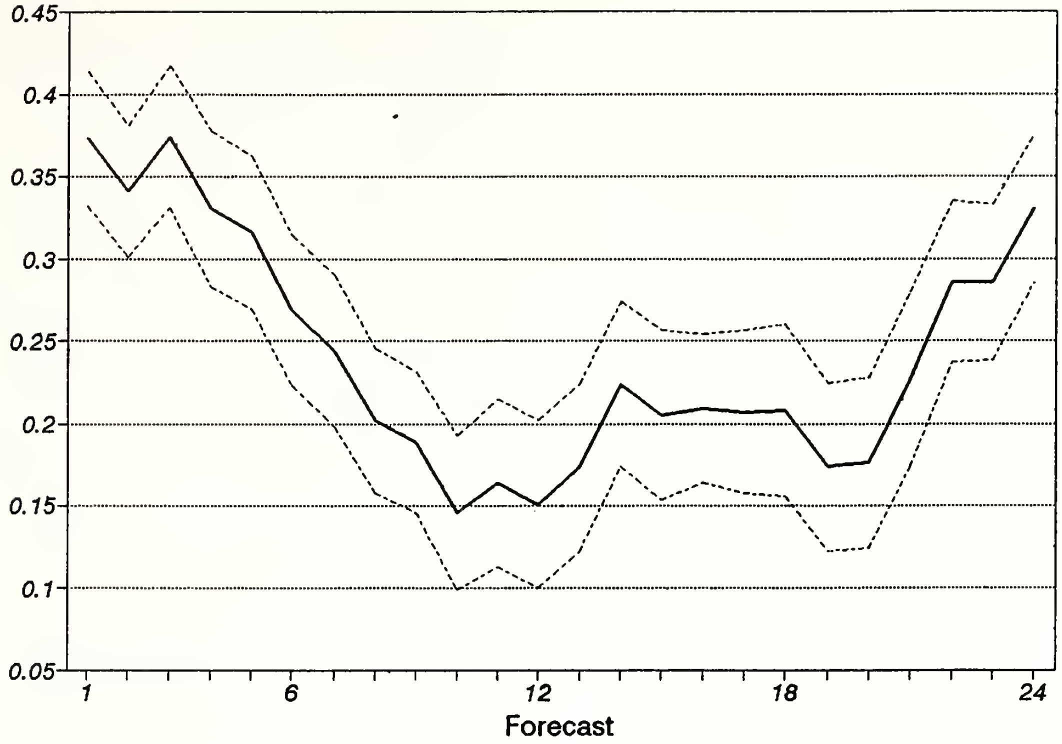

Figure 3. Annual cycle of anomaly correlation between semi-monthly 30-day mean 700mb heights and observations.

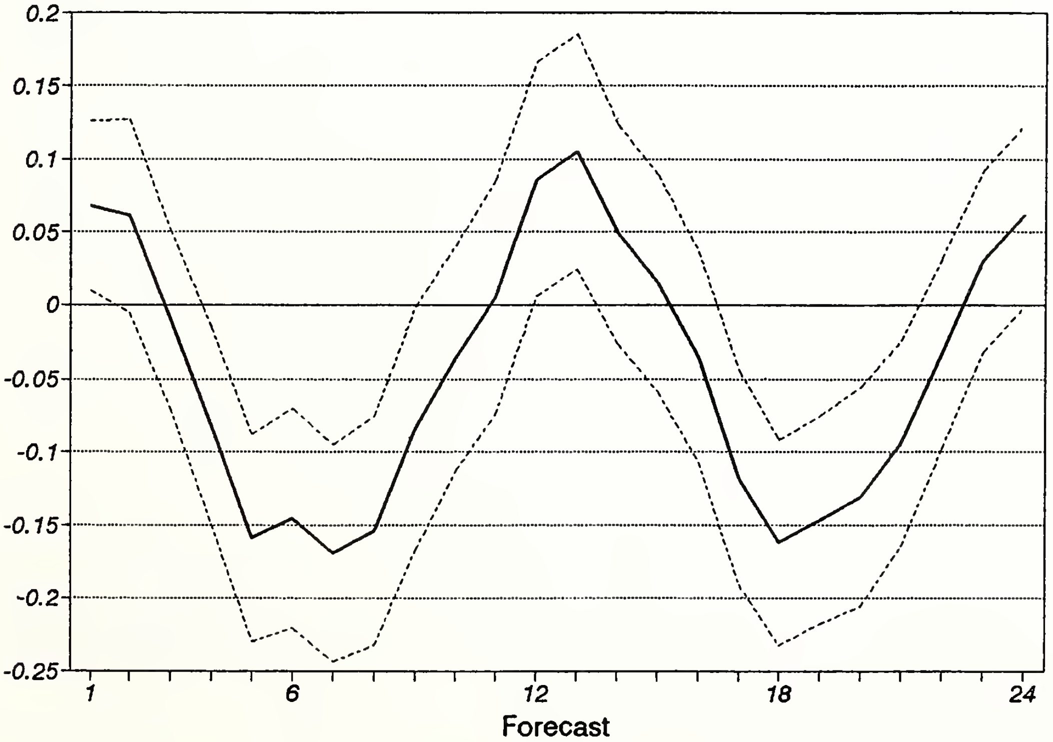

Figure 4. Same as Fig. 3 except for unconditional bias.

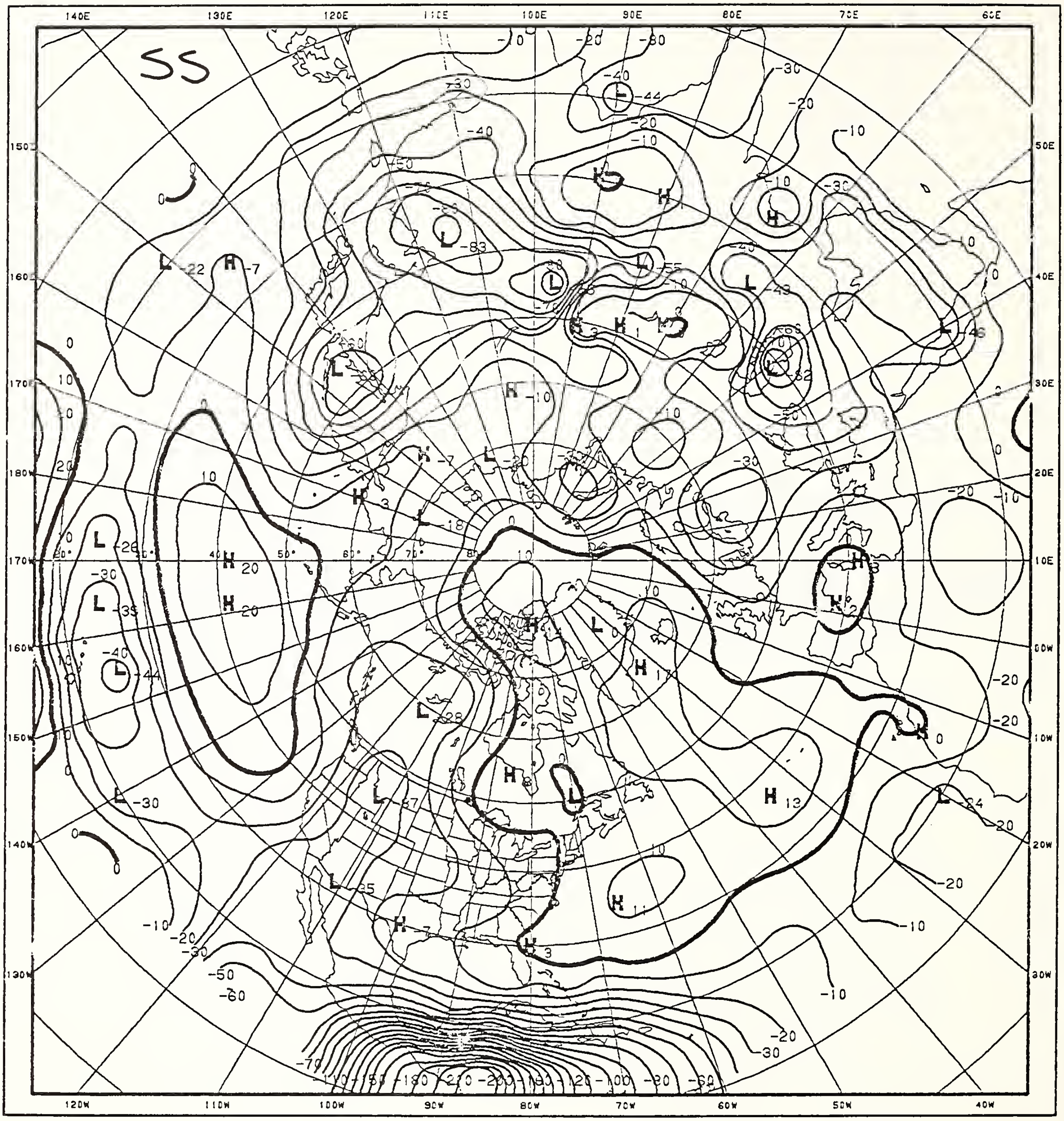

Figure 5. Skill for winter forecasts (5 overlapping semi-monthly 30-day mean forecasts centered on January) of 700mb height for the period 1981 to 1990. Values are times 100.

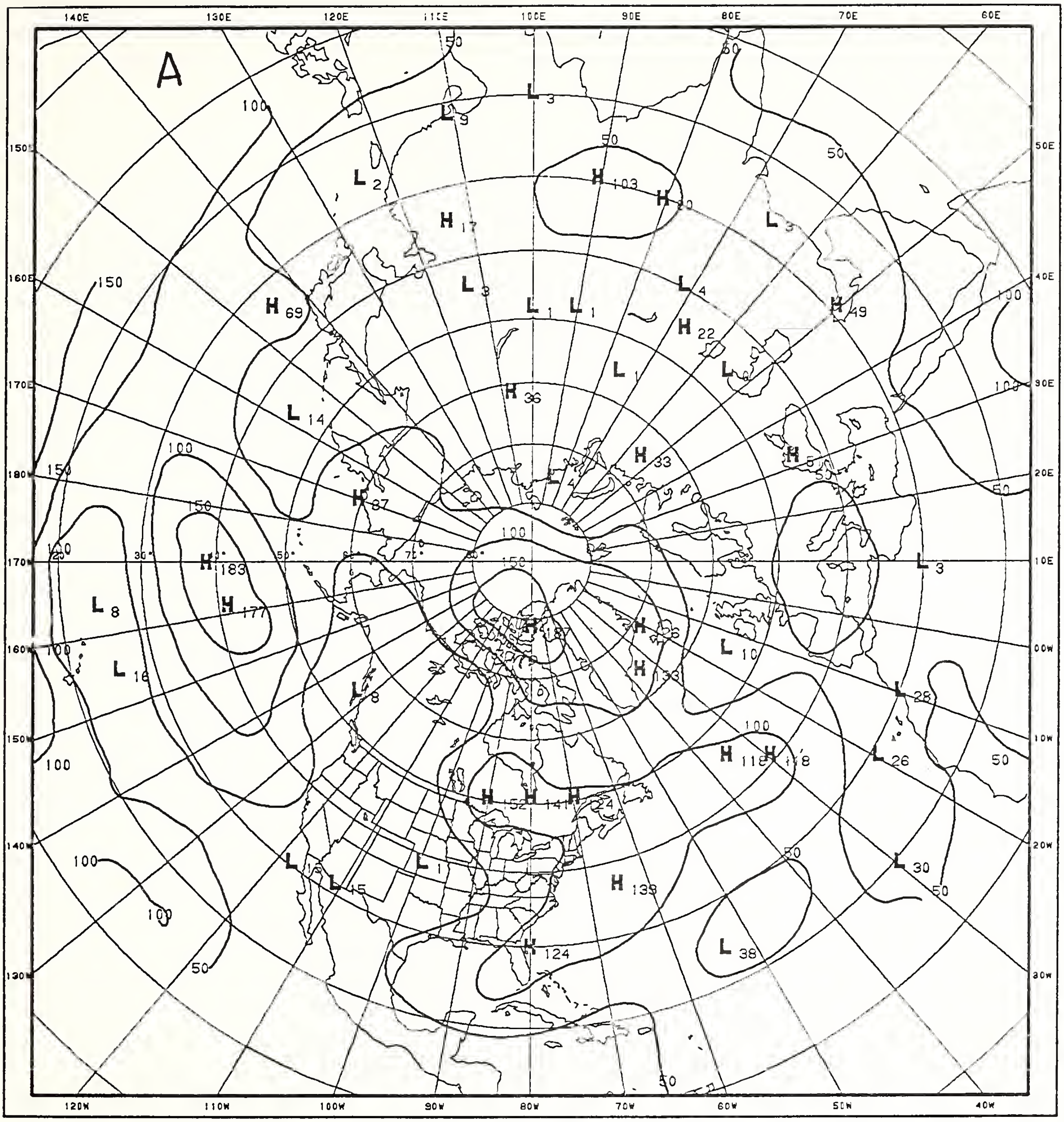

Figure 6. Same as Fig. 5 except for temporal correlation squared (explained variance). Values are times 1000.

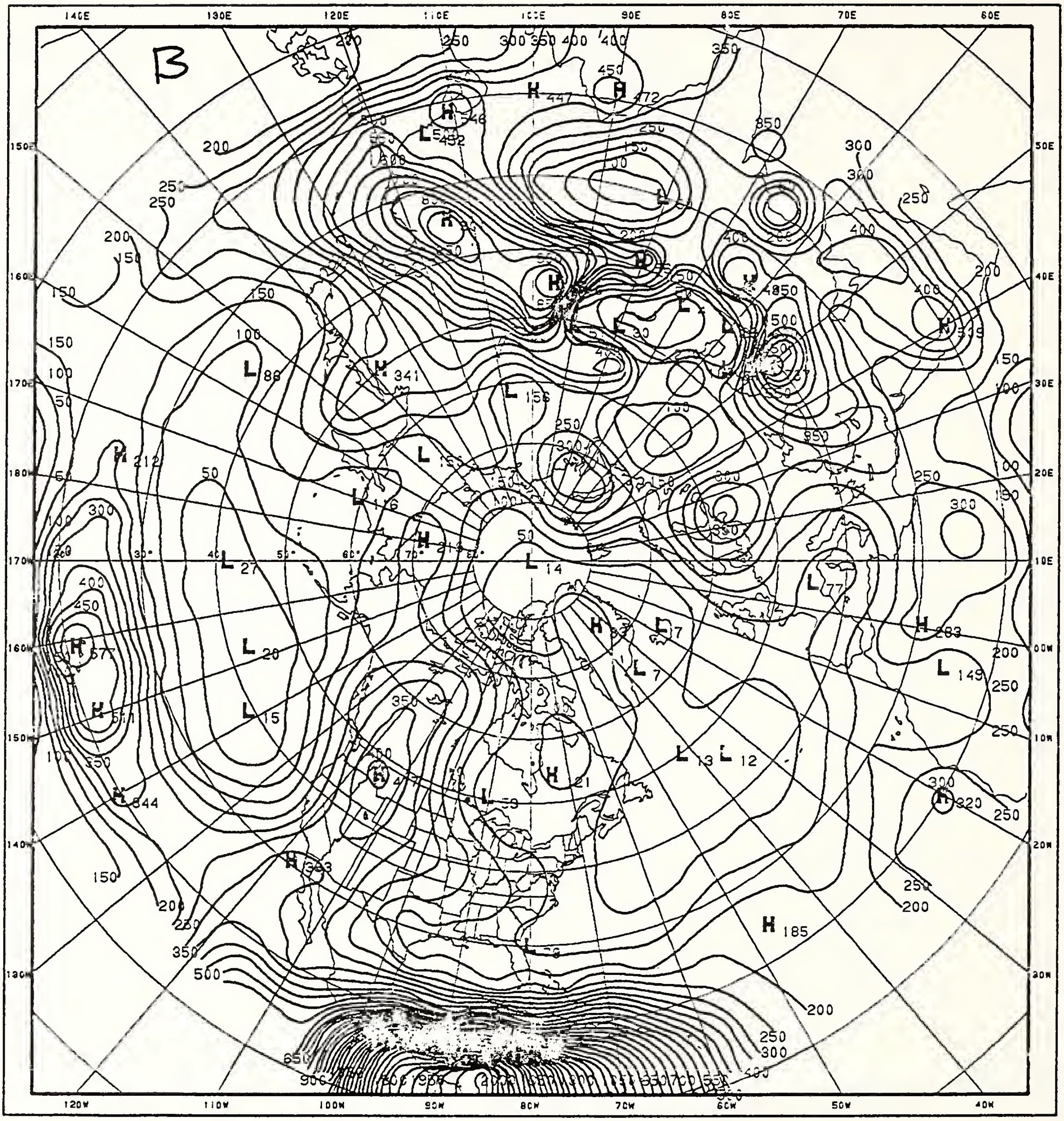

Figure 7. Same as Fig. 5 except for amplitude error. Values are times 1000.

# VERIFICATION OF MONTHLY OUTLOOKS FOR TEMPERATURE, DEWPOINT AND WIND SPEED IN THE CONTIGUOUS UNITED STATES

William H. Klein and Joseph J. Charney
Department of Meteorology
University of Maryland
College Park, MD 20742

At the last three Climate Workshops and in the July 1991 issue of *Agricul. Forest Meteor.*, Klein and Whistler described a system for specifying monthly mean anomalies of midday temperature (T), dewpoint (D) and wind speed (W) at 127 surface stations in the contiguous United States for use by the United States Forest Service. Linear regression equations containing 1 to 6 terms were derived for each element and month from concurrent fields of 700 mb height anomaly (H) observed over North America and adjacent areas, plus the previous month's observed local anomaly of T, D or W, during the 20-year period: 1964-1983. In this paper we present the results of testing the forecast system on *prognostic* values of H prepared twice a month at CAC during the 18 years: 1973-1990. Further details are given in Table 1. Note that we verified at 114 (instead of 127) stations due to missing data and converted our anomaly forecasts into percentiles (P). Also, we included mid-month to mid-month forecasts in our test in order to increase the sample size, and we pooled the data for any one period with its four adjacent periods to reduce the noise.

Our primary statistic was the Heidke skill score (HSS), computed for 2 classes (above or below the 50th P), 3 classes (based on the 30th and 70th Ps used by CAC), 4 classes used operationally by the Forest Service (P below 50, 50-74.9, 75-89.9, and 90 or above) and 5 classes (like the 4-class system except that cases with P of 90 or above were classified as either 90-97.5 or above 97.5). Fig. 1 shows the four different values of HSS obtained for each weather element by pooling the data for all months and all stations. The results were remarkably consistent in that all scores dropped rapidly from 2 to 3 classes and then slowly but steadily from 3 to 5 classes. In all cases the skill was positive, but it was highest for T and lowest for W. A similar result was obtained by correlating forecast with observed values of each element, with simple correlation coefficients of .244, .217 and .172 for T, D and W, respectively. The relative rank of the elements given above is the same as that obtained originally in deriving the specification equations.

It has previously been found by CAC that their monthly forecasts have more skill for "above" and "below" normal classes than for near normal. We found a similar result when we computed the values of HSS separately for each class. For example, Fig. 2 shows the scores for forecasts of T in a 4-class system for the months of January, April, July and October, as well as for the entire year (mean of 24 overlapping monthly periods marked "Total"). In every case, the 1st and 4th classes outperformed the middle two classes. It is especially encouraging that forecasts of $P > 90$, the most critical category for fire outbreaks, consistently had greater skill than those for any other class. It is also noteworthy that the scores were generally highest in January and lowest in October, in agreement with CAC experience. Similar results were obtained for D and W (not shown).

The positive values of HSS discussed thus far indicate that the forecasts were more skillful than climatology or a random guess. However, Table 2 suggests that their improvement over local month-to-month persistence was only marginal on an overall basis. The first two lines show that the forecasts had greater bias than persistence (undesirable) but smaller absolute errors (desirable). In terms of simple correlation (line 3) the forecasts of T and D were equal to persistence, but the forecasts of W were inferior. The last two lines show that, for both 2 and 5 classes, the forecasts had more skill than persistence for T and D but less skill for W. Similar results were obtained for 3- and 4-class HSS, but with intermediate values, and therefore they are not shown here.

Because the specification equations were derived from a sample of data ending in 1983 (Table 1), and since data after 1983 were not obtained until long after the project began, we divided the test period into two unequal sub-periods: 1973-1983 and 1984-1990. Fig. 3 shows the 4-class HSS for all stations and months, separately for each element, each sub-period, and the total period. The skill scores for both T and D were higher in the second than the first sub-period, but they were slightly lower for W.

Fig. 4 is similar to Fig. 3 but for persistence instead of specification forecasts. It shows that the HSS of persistence decreased sharply from the first to the second period for both T and D and remained about the same for W. Since the increased skill of the T and D specification forecasts since 1984 occurred in a period of *lower*, rather than higher, persistence, the prognostic heights on which the specifications are based must have been more skillful during the second period. This impressive improvement can probably be attributed to increased accuracy of numerical model predictions during the first 10 days of the month in the 1980's and the consequent greater skill of monthly mean heights predicted by CAC, as discussed by Livezey and Hoopingarner in the previous two papers.

We are planning to expand this project in several ways as follows: 1) determine geographical variations of skill, 2) verify forecasts of precipitation, 3) express forecasts in probability form, 4) extend the study to Alaska and 5) verify forecasts made on independent *observed*, rather than prognostic, heights.

## Acknowledgments

This research was supported by the U.S. Department of Agriculture, Forest Service, Riverside, California under Cooperative Agreement No. PSW900081CA. We are grateful to Morris McCutchan, John Benoit and Francis Fujioka of the Forest Service for help in various aspects of this project. We also thank Paul Dallavalle of the Techniques Development Laboratory and Ed O'Lenic of the Climate Analysis Center (both in the National Weather Service) for providing surface and 700 mb data, respectively.

Table 1.

Differences in data and methodology between derivation and testing of monthly multiple regression equations for specifying midday anomalies of surface temperature, dewpoint and wind speed in the contiguous United States from the concurrent field of 700 mb heights and previous month's local anomaly of that weather element.

| Characteristic | Dependent data | Independent data |
|---|---|---|
| Period of record | 20 yr: 1/64-12/83<br>(calendar months only) | 18 yr: 1/73-12/90<br>(calendar & mid months) |
| 700 mb heights | Observed | Prognostic |
| Surface data | 127 stations | 114 stations |
| Units | Anomalies | Percentiles |
| Time smoothing | Key period + 2 adjacent | Key period + 4 adjacent |
| Primary statistic | Reduction of variance | Heidke skill score |

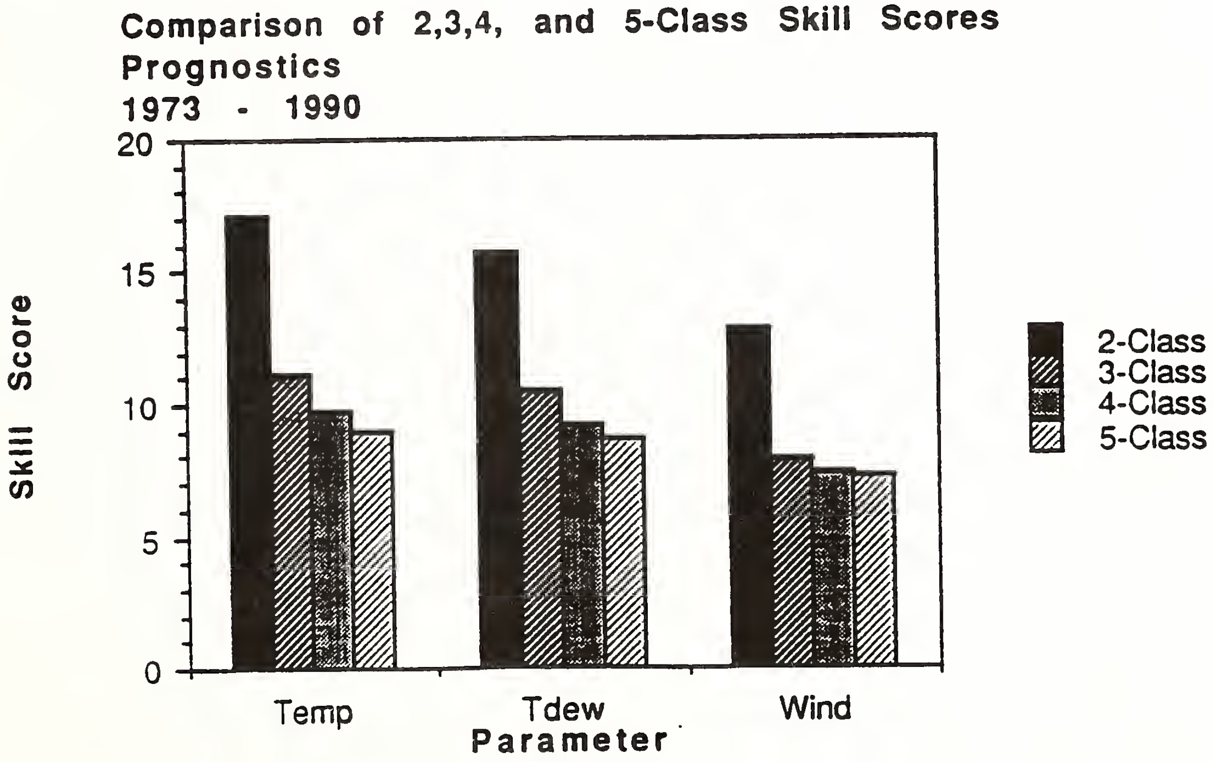

Fig. 1 Heidke skill scores for 2, 3, 4, and 5 classes for specifications of midday monthly mean temperature, dewpoint and wind speed from prognostic 700 mb heights. Data were averaged for 114 stations, two forecasts per month and 18-year period.

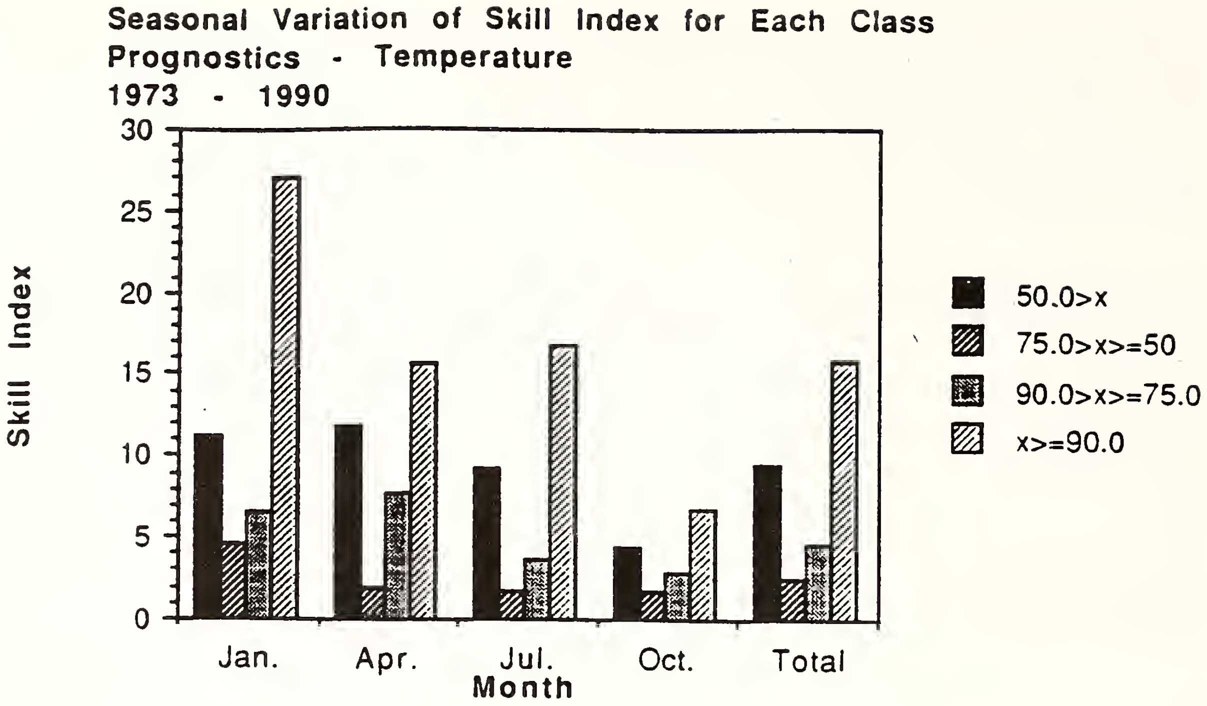

Fig. 2 Same as Fig. 1 but for Heidke skill scores computed separately for each of four classes defined in percentiles on the right. Scores are given for temperature forecasts during four individual months and the year as a whole (Total).

Table 2.

Verification statistics for specification and persistence forecasts of 30-day mean percentiles for midday surface temperature (T), dewpoint (D) and wind speed (W) in the contiguous United States from January 1973 to December 1990, averaged for 114 stations and two forecasts per month.

| Statistic | Specification (Prognostic Heights) | | | Local Persistence | | |
|---|---|---|---|---|---|---|
| | T | D | W | T | D | W |
| Bias (forecast minus observed) | -2.0 | 1.2 | -0.1 | -0.1 | -0.1 | 0.1 |
| Mean Absolute Error | 26.6 | 26.4 | 26.9 | 29.0 | 29.5 | 28.7 |
| Correlation (forecast vs observed) | 0.24 | 0.22 | 0.17 | 0.24 | 0.22 | 0.27 |
| Skill Score (2 classes) | 17.1 | 15.7 | 12.9 | 16.1 | 15.0 | 18.8 |
| Skill Score (5 classes) | 9.0 | 8.7 | 7.3 | 7.3 | 7.9 | 9.7 |

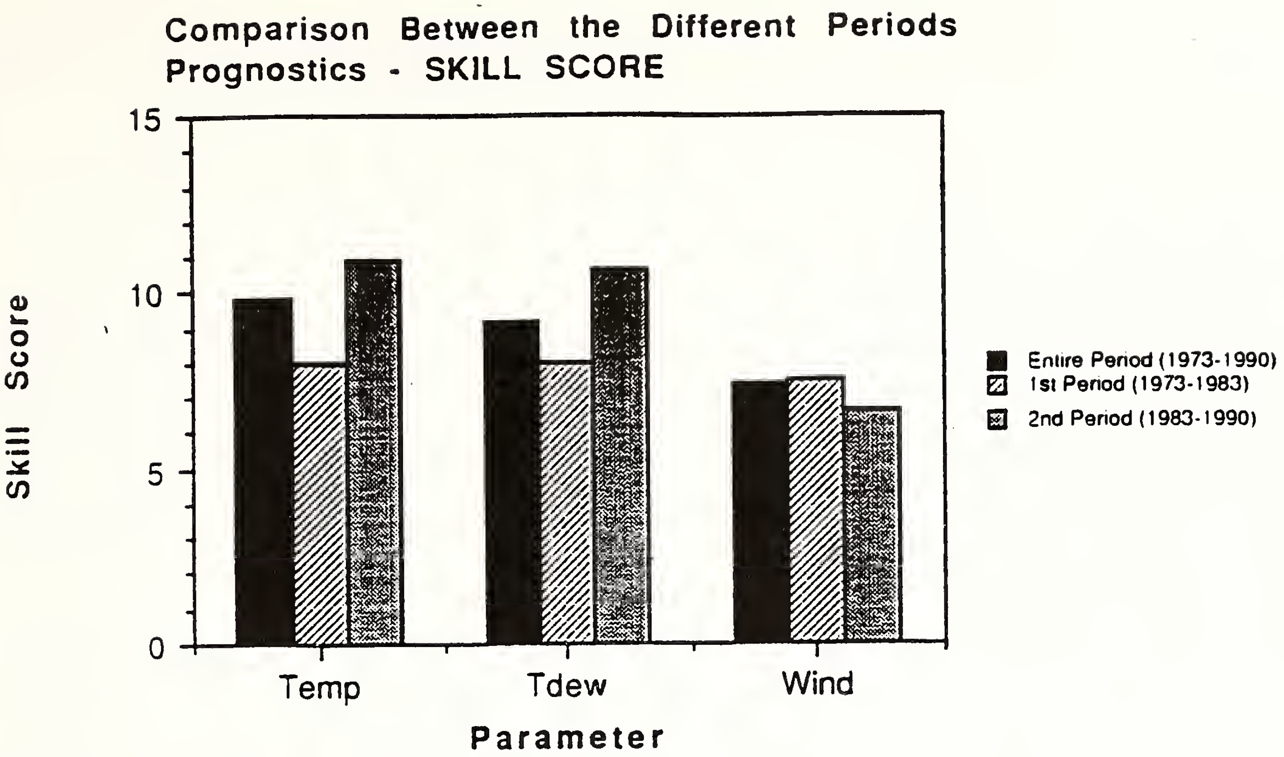

Fig. 3 Same as Fig. 1 but for Heidke skill scores computed for the 4-class system, the entire period and two sub-periods defined on the right.

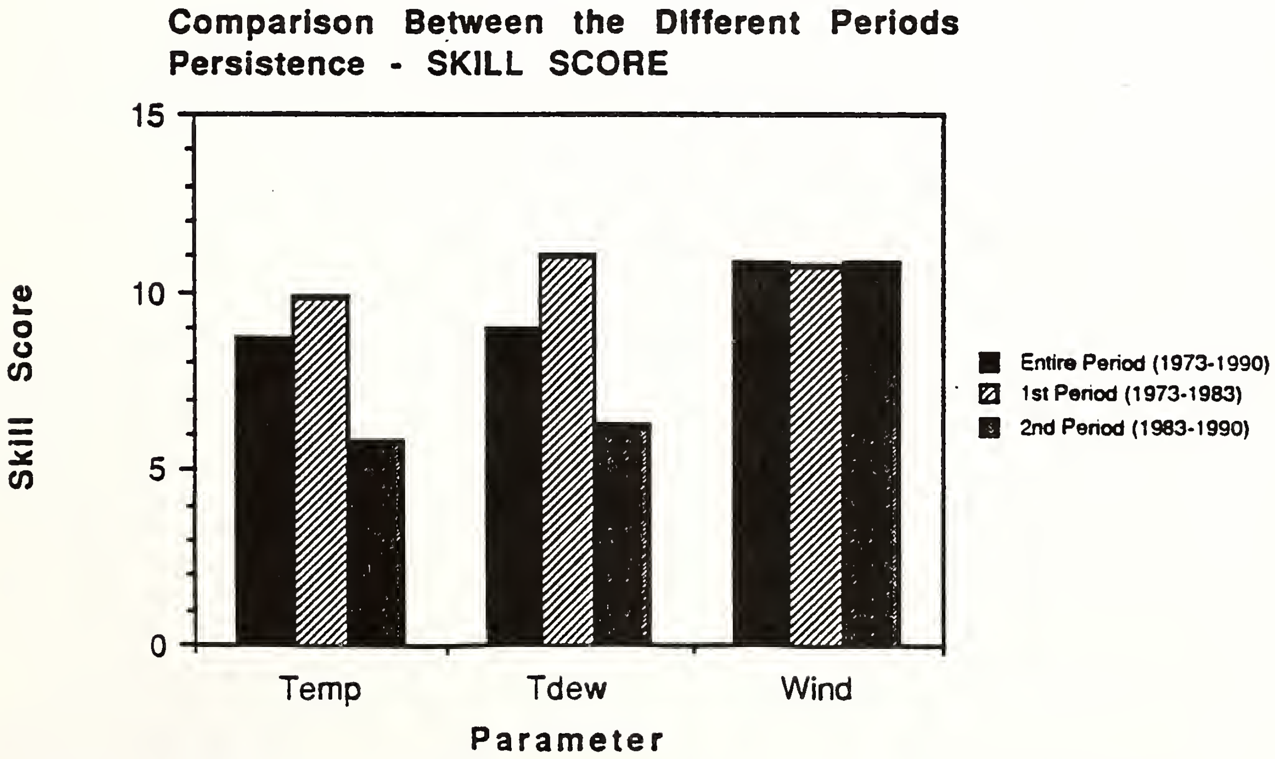

Fig. 4 Same as Fig. 3 but for forecasts made by local month-to-month persistence.

# Verifying Monthly Fire Weather Forecasts: Presenting Expected Accuracy to Users

Bernard N. Meisner
Pacific Southwest Research Station, USDA Forest Service
4955 Canyon Crest Drive, Riverside, CA 92507-6099

Expected weather has been forecast for over a century (Kutzbach, 1979), and statistics designed to measure the accuracy of a set of forecasts have been available for decades (Brier, 1990). Only in recent years, however, has it been possible to assess the accuracy of an individual forecast (Kerr, 1989). Information concerning the expected accuracy of a forecast can be as valuable to decision makers as the forecast itself (Epstein, 1988). While the literature is replete with ideas on how to predict forecast skill (e.g., Leslie and Holland, 1991; Kalnay and Dalcher, 1987), and how to incorporate forecasts into decision processes (e.g., Murphy, 1991), little information is available on how to convey, in map form, the degree of uncertainty in a particular forecast.

Probabilities of observing some forecast weather events are routinely computed for specific locations (Glahn and Lowry, 1972). At present, the only products that attempt to show, in map form, the degree of uncertainty in the forecast are those for hurricane strikes (Sheets, 1985), precipitation occurrence (Glahn and Lowry, 1972), and long range (monthly and seasonal) temperature and precipitation (Wagner, 1989). The hurricane and precipitation maps each depict the chance of a single event. Experience has shown that there is much confusion regarding the correct interpretation of both the precipitation forecasts and the long-range outlooks.

This paper discusses how predictability information can best be incorporated into a weather forecast. The example chosen is the monthly fire weather forecast prepared by the USDA Forest Service at the Pacific Southwest Research Station's Forest Fire Laboratory in Riverside, CA. For this particular example, I will use an accuracy estimate based on the previous performance of the fire weather forecast system in predicting categories of afternoon (1300 LST) temperature for various regions of the United States. However, any forecast could be considered. Similarly, any valid technique for estimating the accuracy of the forecasts could be selected.

## Monthly Fire Weather Forecasts

Monthly fire weather forecasts are based on the National Weather Service Climate Analysis Center's prediction of the mean 700 mb height field for the coming 30-day period, as well as persistence. Regression equations, based on the "perfect prog" approach, produce estimates of the 30-day mean afternoon air and dew point temperatures for approximately 100 locations across the country (Klein and Whistler, 1991). These temperatures, in turn, are used to compute a version of the Chandler Burning Index (Chandler, et al., 1983) as modified by McCutchan, et al. (1991) that estimates both the burning intensity (a measure of the energy released within a fire) and rate of fire spread.

The forecasts are presented in terms of percentiles of the empirical climatological distribution for each site (Figure 1). Percentiles can be directly related to expected levels of fire severity which, in turn, can be used to determine anticipated fire suppression needs. It is also assumed that the spatial variations of the percentiles are smaller than those of the parameter itself, so that forecasts for intermediate locations can be accurately estimated using interpolation (McCutchan, et al., 1991).

## Presenting the Expected Accuracy to Users

The percentiles of the afternoon temperature were grouped into four categories: less than 50 percent, 50-75 percent, 75-90 percent, and greater than or equal to 90 percent. Data from June, mid-June to mid-July, July, mid-July to mid-August, and August were combined to yield accuracy estimates for summer forecasts. The stations were grouped into 11 regions that were both climatologically and statistically consistent.

A contingency table relating the frequency of forecast categories to those observed was computed for each region (e.g., Table 1). The contingency data can also be presented graphically (Figure 2), where the length of the bar represents the percent of time that the observed category was equal to that forecast. The length of the line above the bar represents the percentage of time that the observed category was greater than that forecast, and the length of the line below the bar represents the percentage of time that the observed category was less than that forecast. As expected, the extreme categories, in general, are predicted more accurately than those in the middle (van den Dool and Toth, 1991). Predictions of extreme temperature for the Piedmont Plateau, Appalachians/Southern Plains and Ohio Valley are much more accurate than similar predictions for the Great Basin/Southwest Desert, Rocky Mountains, or Sierra Cascades.

By combining the forecast categories (Figure 1) with the verification information (Figure 2) it is possible to produce an estimate of forecast accuracy. Figures 3 through 5 show possible ways of presenting, in map form, both the forecast and an estimate of its accuracy.

Isopleths of confidence can be superimposed on the forecast map (Figure 3); this presentation is similar to the standard practice of the National Meteorological Center, where two sets of isopleths are plotted on the same base map, with the first set as solid lines and the second set as dashed lines. Problems can arise here if the two sets of lines are somewhat parallel, as in the example shown where the degree of accuracy expected is directly related to the forecast temperature percentile. As color graphics become more available the contours could be plotted in different colors to aid in discriminating between them.

Shading can be used to indicate those regions where the confidence in the forecast is particularly high or low (Figure 4). The computer programming to draw the shading can be somewhat complex, but the result is probably much more readily understood than the isopleths in Figure 3.

The width of the isopleths of the forecast parameter can be made proportional to the degree of confidence (Figure 5), and the isopleths can even be made to disappear where the confidence is very small. This method of presentation has the advantage of producing a map with less "clutter." One can argue whether the practice of not making the forecast in a region of low confidence is valid. Most users would no doubt prefer any forecast to none, but–in some situations–persistence or climatology might be given in lieu of a forecast.

Meteorology, through the proper presentation of predictability information, can lead the other sciences by demonstrating "how professionals deal with incomplete, contradictory, and uncertain information" (Tennekes, 1988).

## References

Brier, Glenn W., 1990: A historical and personal perspective of model evaluations in meteorology. *Bull. Amer. Meteor. Soc.*, 71, 349-351.

Chandler, Craig, Phillip Cheney, Phillip Thomas, Louis Trabaud and Dave Williams, 1983: Fire in Forestry. Vol. I: Forest fire behavior and effects. New York, Wiley and Sons, 450 p.

Epstein, Edward S., 1988: Long-range weather prediction: limits of predictability and beyond. *Wea. Forecasting*, 3, 69-75.

Glahn, Harry R. and Dale A. Lowry, 1972: The use of model output statistics (MOS) in objective weather forecasting. *J. Appl. Meteor.*, 11, 1203-1211.

Kalnay, Eugenia and Amnon Dalcher, 1987: Forecasting forecast skill. *Mon. Wea. Rev.*, 115, 349-356.

Kerr, Richard A., 1989: Telling weathermen when to worry. *Science*, 244: 1137-1139.

Klein, William and Bruce T. Whistler, 1991: Specification of monthly mean anomalies of fire weather elements in the United States. *Ag. Forest Meteor.*, 56, 145-172.

Kutzbach, Gisela, 1979: A Thermal Theory of Cyclones. Amer. Meteor. Soc., Boston, MA. 255 p.

Leslie, Lance M. and Greg J. Holland, 1991: Predicting regional forecast skill using single and ensemble forecast techniques. *Mon. Wea. Rev.*, 119, 425-435.

McCutchan, Morris H., Bernard N. Meisner, Francis M. Fujioka, John W. Benoit and Benjamin Ly, 1991: Monthly fire weather forecasts. *Fire Management Notes* (in press).

Murphy, Allan H., 1991. Probabilities, odds and forecasts of rare events. *Wea. Forecasting*, 6, 302-307.

Sheets, Robert C., 1985: The National Weather Service hurricane probability program. *Bull. Amer. Meteor. Soc.*, 66, 4-13.

Tennekes, Hendrik, 1988: The outlook: scattered showers. *Bull. Amer. Meteor. Soc.*, 69, 368-372.

van den Dool, Huug M. and Zoltan Toth, 1991: Why do forecasts for "Near Normal" often fail? *Wea. Forecasting*, 6, 76-85.

Wagner, A. James., 1989: Medium- and long-range forecasting. *Wea. Forecasting*, 4, 413-426.

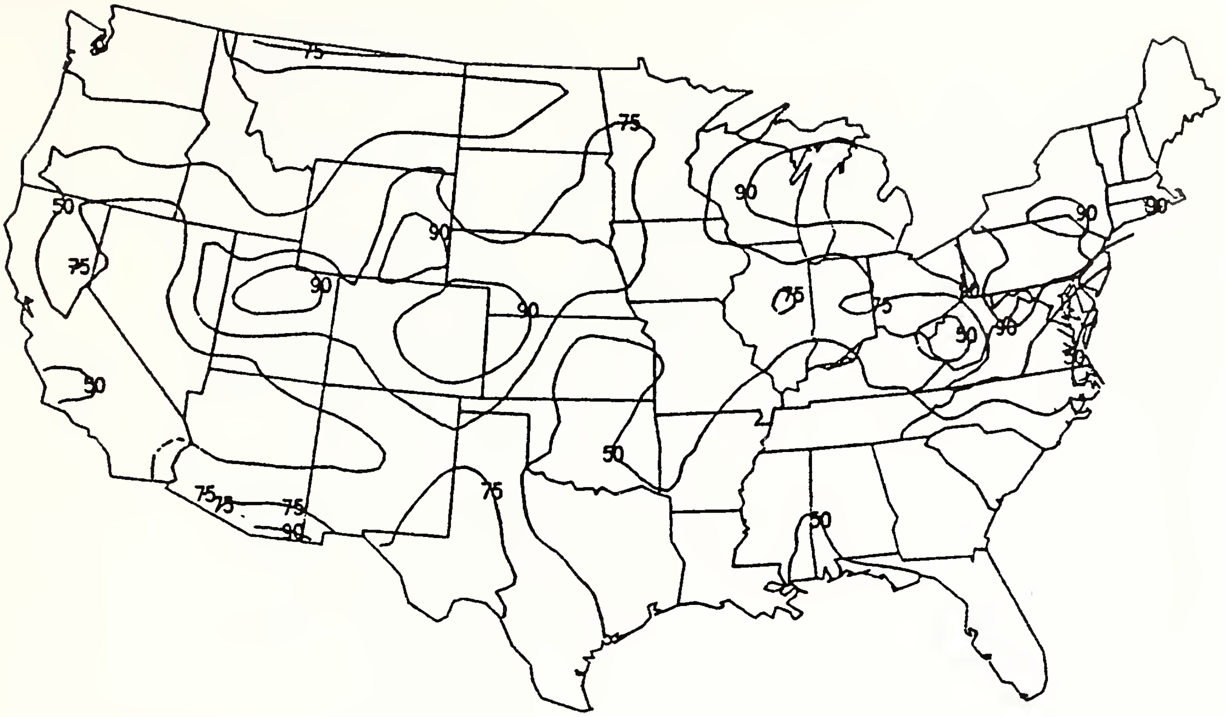

Figure 1. Predicted mean afternoon (1300 LST) temperature percentiles for July 1-31, 1991. Contours of temperature percentiles are based on a 20-year climatology at each of 127 National Weather Service sites.

Table 1. Frequencies and Row Percentages of Forecasts and Observations
Pacific Southwest Region (see Figure 2 for location)
Summer (June - August)

| Forecast Category | Observed Category <br> <50% | 50-75% | 75-90% | >90% |
|---|---|---|---|---|
| <50% | 25<br>(44%) | 14<br>(25%) | 12<br>(21%) | 6<br>(10%) |
| 50-75% | 31<br>(37%) | 28<br>(34%) | 12<br>(15%) | 12<br>(14%) |
| 75-90% | 19<br>(38%) | 7<br>(14%) | 9<br>(18%) | 15<br>(30%) |
| >90% | 0<br>(0%) | 1<br>(25%) | 0<br>(0%) | 3<br>(75%) |

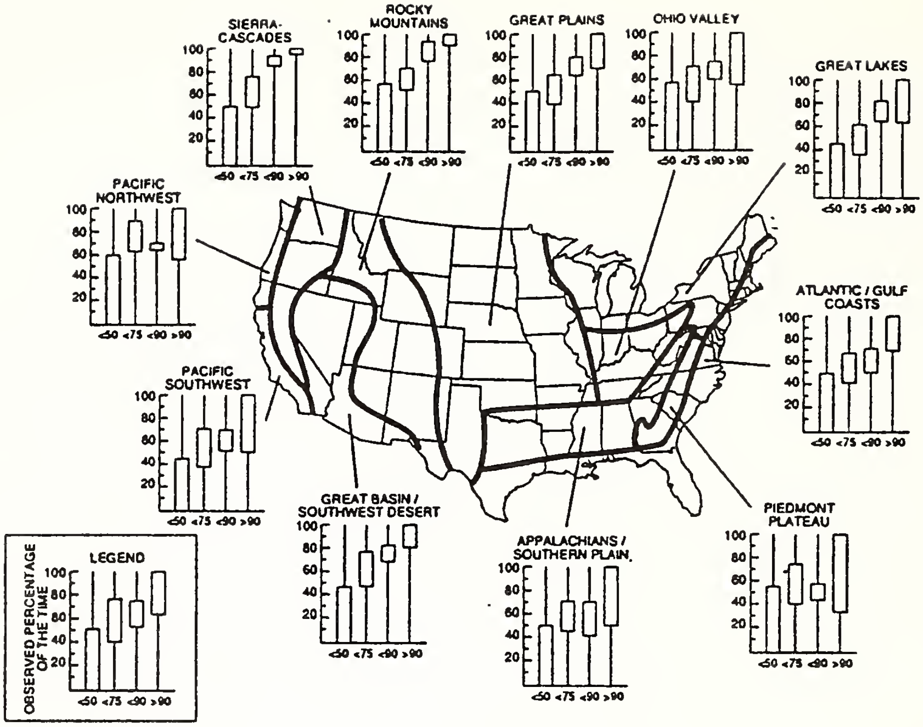

Figure 2. Relative accuracy of the fire weather temperature forecasts for various regions of the United States for June-August, 1973-1983. For each of the four percentile categories, the bar represents the percentage of time that the observed weather matched the forecast. The line below (above) the bar represents the percentage of the time that the observed temperature category was less (greater) than that forecast.

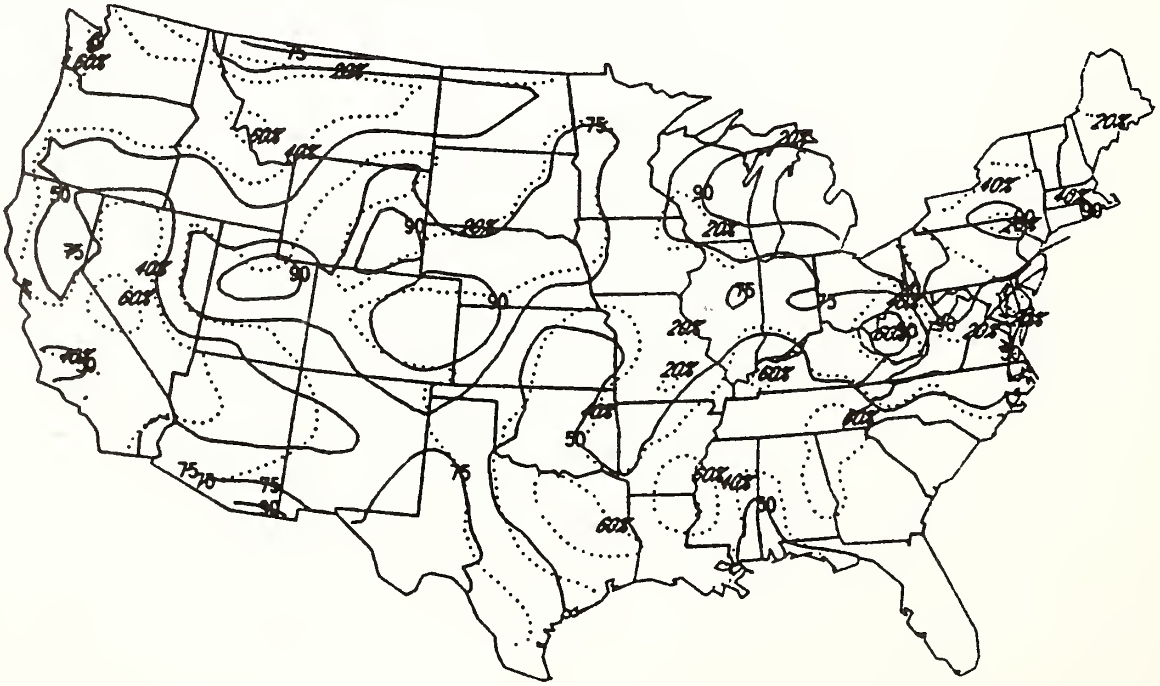

Figure 3. Same as Figure 1, but with dashed contours added to indicate the percentage of time that the forecast temperature percentile category was observed.

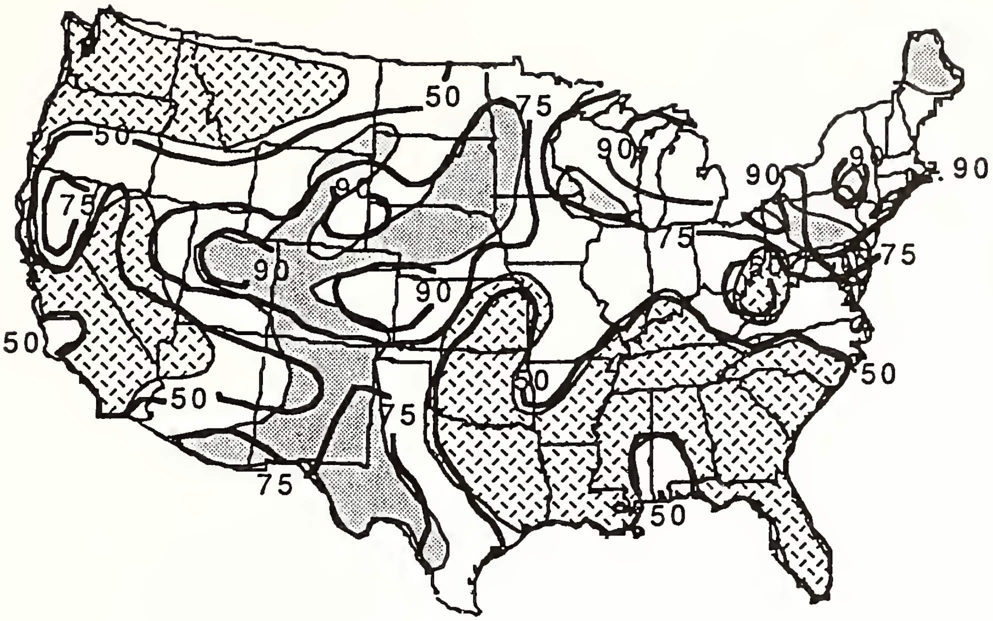

Figure 4. Same as Figure 3, but with shading used to depict the degree of confidence in the forecast. Areas where the temperature category has been correctly forecast at least 40 percent of the time are hatched; areas where the temperature category has been correctly forecast less than 20 percent of the time are shaded.

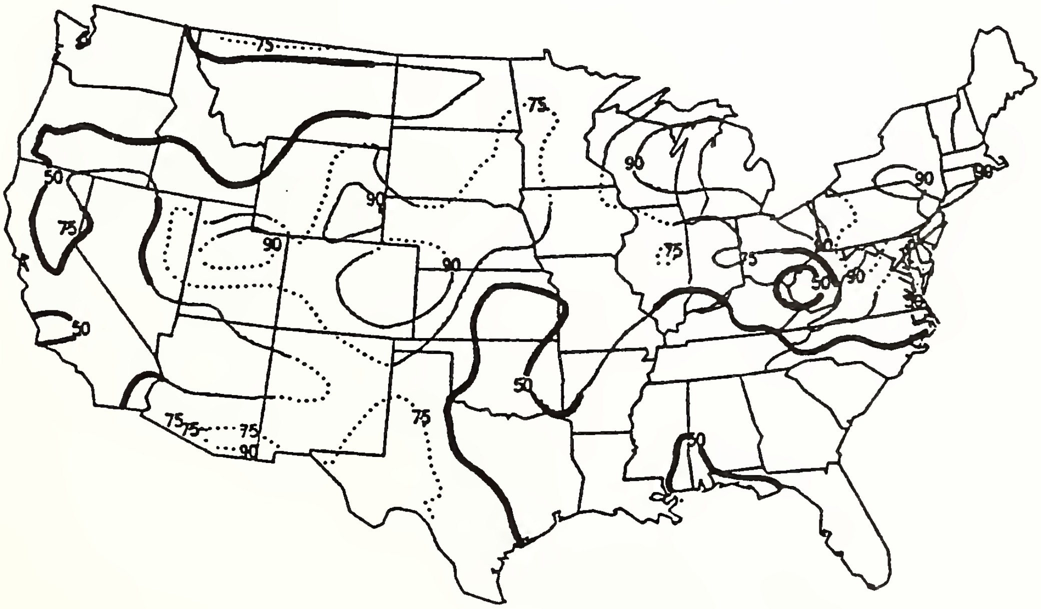

Figure 5. Same as Figure 3, but with contour width used to depict the degree of confidence in the forecast. Thick contours show where the confidence is high; thin contours, where the confidence is moderate; and dashed contours, where the confidence is low.

# APPENDIX

# Large–Scale Atmosphere–Ocean Heat Exchange and the Maintenance of Extratropical Kinetic Energy

Steven R. Silberberg
CIRES/University of Colorado, Campus Box 449, Boulder, CO 80309-0449

## 1. Introduction

In an effort to increase our understanding of the energy cycle (Lorenz 1955) and the global circulation, recent literature has emphasized the role of atmospheric heat sources and sinks in the maintenance of kinetic energy. The primary emphasis of such studies is to understand how diabatic heating maintains the subtropical westerly jetstreams of both Northern and Southern Hemispheres (e.g. Blackburn 1985, Nogues-Paegle and Zhen 1987, Chen et al. 1988, and Hurrell and Vincent 1990, 1991). In addition, the generation of kinetic energy by heating during the onset of the Indian summer monsoon was diagnosed by Krishnamurti and Ramanathan (1982).

These studies employed irrotational and rotational kinetic energy equations in isobaric coordinates to take advantage of the relationship between isobaric irrotational motion, vertical motion, and diabatic heating in the deep tropics. However, in extratropical latitudes where temperature advection is large, vertical motion associated with adiabatic cooling does not balance diabatic heating in the thermodynamic equation, resulting in an uncertain relationship between irrotational motion and heating on isobaric surfaces. In contrast, a direct relationship between diabatic heating, irrotational mass circulations, and the generation of irrotational kinetic energy is achieved through analysis in isentropic coordinates that includes the isentropic mass balance (Johnson et al. 1985, Silberberg 1991). In this study, the role of large-scale atmosphere-ocean heat exchange and continental cooling in the maintenance of Northern Hemisphere wintertime extratropical kinetic energy is examined through analysis of irrotational and rotational kinetic energy transport equations in isentropic coordinates.

## 2. The relationship between diabatic heating, isentropic irrotational mass circulations, and irrotational kinetic energy generation.

In isentropic coordinates, the relationship between irrotational mass circulations and diabatic heating stems from the isentropic continuity equation given by

$$\frac{\partial}{\partial t}\rho J_\theta + \nabla_\theta \bullet \rho J_\theta \vec{U} + \frac{\partial}{\partial \theta}\rho J_\theta \dot{\theta} = 0 \quad , \tag{1}$$

where $\rho J_\theta = -(1/g)(\partial p/\partial \theta)$ is the hydrostatic mass in an isentropic layer, $\vec{U}$ is the horizontal velocity, and $\dot{\theta} = d\theta/dt$ is diabatic heating. When (1) is time-averaged so the mass tendency may be neglected, the vertical divergence of diabatic mass flux is equal and opposite to the horizontal mass divergence.

Partitioning the isentropic mass transport $(\rho J_\theta \vec{U})$ into irrotational and rotational components yields

$$\rho J_\theta \vec{U} = (\rho J_\theta \vec{U})_\chi + (\rho J_\theta \vec{U})_\psi = \nabla_\theta \chi + \vec{k} \times \nabla_\theta \psi \quad , \tag{2}$$

where the mass transport potential $(\chi)$ and streamfunction $(\psi)$ respectively, are defined by

$$\nabla_\theta \bullet \rho J_\theta \vec{U} = \nabla^2_\theta \chi \quad , \tag{3a}$$

and

$$\vec{k} \bullet \nabla_\theta \times \rho J_\theta \vec{U} = \nabla^2_\theta \psi \quad . \tag{3b}$$

The mass balance in isentropic coordinates along with the relationships in (2) and (3a) reveal that the time-averaged irrotational mass transport balances the time-averaged heating (Johnson et al. 1985).

With these relations, the isentropic irrotational and rotational kinetic energy transport equations may be expressed in schematic form as

$$\frac{\partial}{\partial t}(\rho J_\theta k_\chi) = FD(k_\chi) + C(k_\chi , k_\psi) + G(k_\chi) + D(k_\chi) \quad , \tag{4}$$

$$\frac{\partial}{\partial t}(\rho J_\theta k_\psi) = FD(k_\psi) - C(k_\chi , k_\psi) + G(k_\psi) + D(k_\psi) \quad , \tag{5}$$

where the tendencies of mass-weighted irrotational ($k_\chi$) and rotational ($k_\psi$) kinetic energy result from the three-dimensional divergence of the transport (FD), conversion (C), generation by cross-contour flow (G), and frictional dissipation (D). In particular, the generation of irrotational kinetic energy

$$G(k_\chi) = -(\rho J_\theta \vec{U})_\chi \bullet \nabla_\theta \Psi_M \quad , \tag{6}$$

where $\Psi_M$ is the Montgomery streamfunction, illustrates the relationship between thermally forced irrotational mass circulations and irrotational kinetic energy generation. Owing to the simple time-mean mass balance in isentropic coordinates, the irrotational kinetic energy transport equation provides insight into the relationship between diabatic heating, isentropic irrotational mass circulations, and the generation of irrotational kinetic energy.

## 3. Results

In the analyses that follow, the irrotational and rotational kinetic energy balance is shown for the 260-270K and 280-290K isentropic layers of the Northern Hemisphere during the Global Weather Experiment boreal winter. Time-averaged budgets were computed twice daily from ECMWF Main IIIb analyses on a 3.75° latitude-longitude grid from 12Z 1 December 1978 to 12Z 28 February 1979. Frictional dissipation was determined as a residual in the respective kinetic energy equations.

The 260-270K and 280-290K isentropic layers were chosen because of their interaction with the midlatitude marine boundary layer through which sensible and latent heat is exchanged with the atmosphere. Representative of the polar cold dome (Fig. 1a), the 260-270K layer consists of polar air masses located poleward and to the rear of migratory extratropical cyclones. The pressure topography of this layer (Fig. 1a) reveals minimum pressures and furthest equatorward extent over Asia and North America. Large horizontal gradients of pressure located along the east coasts of Asia and North America depict strong baroclinic zones where continental air masses interact with the warmer underlying ocean. The distribution of diabatic mass flux determined from (1) (Fig. 1b) exhibits cooling over polar regions and the Asiatic and North American continents, while strong heating is evident over the eastern seaboards of Asia and North America and the adjacent western Pacific and Atlantic Oceans. This strong heating is evidence of large-scale sensible and latent heating within the marine boundary layer. Similar in pattern to the diabatic mass flux, regions of mass divergence (Fig. 1c) are located over polar latitudes, Asia and North America, while regions of mass convergence are confined to the eastern seaboards of both continents and adjacent oceans. Pronounced equatorward flow from heat sink to source and converging into the storm track regions of the Pacific and Atlantic Oceans is evident in the irrotational mass circulation vectors (Fig. 1d).

The 280-290K layer ranges from the earth's surface in the subtropics (Fig. 1e) to the midtroposphere in polar regions. Large horizontal gradients of pressure depict the primary extratropical baroclinic zones along the eastern seaboards of Asia and North America. Cooling is located over polar and continental regions (Fig. 1f) and relative to the 260-270K layer, the region of strong ocean-atmosphere heat exchange in the 280-290K layer is shifted equatorward (cf. 1b and 1f). Mass divergence is evident over the oceanic storm tracks in the 280-290K layer (Fig. 1g) which is opposite to mass convergence diagnosed along the storm tracks in the 260-270K layer (cf. 1c and 1g). In a similar manner over the continents and polar regions, 280-290K mass convergence lies above 260-270K mass divergence. The 280-290K irrotational mass transport vectors are directed poleward from the oceanic storm tracks to higher latitudes, flowing from oceanic storm track heat source to continental/polar heat sink. The reversal of mass divergence and irrotational mass circulations between the 260-270K and 280-290K layers describes an extratropical Hadley-type mass circulation with a lower branch of continental polar air flowing equatorward, and a return branch of modified midlatitude air flowing poleward (Johnson et al. 1985). Equatorward of the oceanic storm tracks, the 280-290K irrotational mass circulation is directed toward the equator and describes the advance of modified polar air.

The importance of these thermally forced irrotational mass circulations to the maintenance of extratropical kinetic energy is presented in Fig. 2 which shows the primary terms in (4) and (5). With the tendencies of mass-weighted irrotational and rotational kinetic energies diagnosed to be negligible over the winter period, the primary balance of kinetic energy in the 260-270K layer is between generation and dissipation (Fig. 2a-d). Irrotational kinetic energy generation and dissipation maxima (Figs. 2a and b) are collocated poleward of the time-averaged Aleutian and Icelandic Lows indicating near simultaneous generation and dissipation of irrotational kinetic energy in the boundary layer of cyclones. Over northern Eurasia and North America where irrotational generation and dissipation do not balance, irrotational kinetic energy is converted to rotational kinetic energy (fig. not shown) to help maintain the rotational flow. Rotational generation (Fig. 2c) is positive along the baroclinic zones of Asia and North America and negative downstream and northeast of the positive maxima. Within the confines of the rotational kinetic energy budget, rotational dissipation (Fig. 2d) nearly balances positive and negative rotational generation centers, describing the near simultaneous generation and dissipation of rotational kinetic energy in the boundary layer. Over northern Eurasia and North America, the lack of balance between rotational dissipation and generation provides further evidence of maintenance of the rotational flow by conversion from irrotational to rotational kinetic energy.

Conversion from irrotational to rotational kinetic energy plays a leading role in the maintenance of kinetic energy in the 280-290K layer. Regions of irrotational generation in the midlatitudes and poleward of the oceanic storm tracks (Fig. 2e) are balanced by conversion from irrotational to rotational kinetic energy (Fig. 2f), illustrating the nearly total conversion of irrotational kinetic energy to support the rotational flow. Positive/negative couplets of rotational kinetic energy generation (Fig. 2g) are located over eastern Asia and North America with secondary centers evident over northwestern North America, northern Eurasia, Greenland, and the Atlantic Ocean. Note that the *total source* of rotational kinetic energy for the 280-290K layer is the sum of the *negative* of the conversion term in Fig. 2f and the rotational generation term. The residually determined rotational dissipation (Fig. 2h) resembles the conversion term as modified by rotational generation maxima and minima. This indicates that the primary source of rotational kinetic energy in the 280-290K layer results from diabatically forced irrotational kinetic energy generation.

## 4. Summary

The role of diabatic heating in the maintenance of extratropical kinetic energy for the Northern Hemisphere 1978-79 winter has been investigated through analysis of irrotational and rotational kinetic energy transport equations in isentropic coordinates. Inclusion of the isentropic mass balance allows for a direct link between heating, mass divergence, and irrotational kinetic energy generation. The analysis reveals continental cooling and strong sensible and latent heating in the marine boundary layer of both isentropic layers. A reversal of mass divergence and thermally forced irrotational mass circulations describes a Hadley-type extratropical mass circulation that is linked with irrotational kinetic energy generation in both layers. In the 260-270K layer, irrotational and rotational kinetic energy is mainly generated and dissipated *in situ* in the boundary layer. Over northern Eurasia and North America, irrotational kinetic energy is converted to help maintain the rotational flow against frictional dissipation. In the 280-290K layer, irrotational generation and conversion exhibit nearly similar patterns, while the residually determined rotational dissipation resembles the sum of the conversion and rotational generation terms. This indicates that irrotational kinetic energy generated by thermally forced irrotational mass circulations is directly converted to rotational kinetic energy. Based on the results for these two isentropic layers, it is suggested that diabatic heating forces an irrotational mass circulation that acts to maintain the extratropical Northern Hemisphere wintertime kinetic energy against the effects of frictional dissipation in the lower troposphere.

## References

Blackburn, M., 1985: Interpretation of ageostrophic winds and implications for jet stream maintenance. *J. Atmos. Sci.*, **42,** 2604-2620.

Chen, T.-C., R.-Y. Tzeng and H. van Loon, 1988: A study on the maintenance of the winter subtropical jet streams in the Northern Hemisphere. *Tellus,* **40A,** 392-397.

Hurrell, J.W. and D.G. Vincent, 1990: Relationship between tropical heating and subtropical westerly maxima in the Southern Hemisphere during SOP-1, FGGE. *J. Climate,* **3,** 751-768.

-----, 1991: On the maintenance of short-term subtropical wind maxima in the Southern Hemisphere during SOP-1, FGGE. *J. Climate,* **4,** 1009-1022.

Johnson, D.R., R.D. Townsend, and M.-Y. Wei, 1985: The thermally coupled response of planetary scale circulation to the global distribution of heat sources and sinks. *Tellus,* **37A,** 106-125.

Krishnamurti, T.N. and Y. Ramanathan, 1982: Sensitivity of monsoon onset to differential heating. *J. Atmos. Sci.,* **39,** 1290-1306.

Lorenz, E.N., 1955: Available potential energy and the maintenance of the general circulation. *Tellus,* **7,** 157-167.

Nogues-Paegle, J.E. and Z. Zhen, 1987: The Australian subtropical jet during the second observing period of the Global Weather Experiment. *J. Atmos. Sci.,* **44,** 2277-2289.

Silberberg, S.R., 1991: The irrotational and rotational kinetic energy balance in isentropic coordinates during the Global Weather Experiment boreal winter. Ph.D. dissertation, University of Wisconsin–Madison, 211 pp.

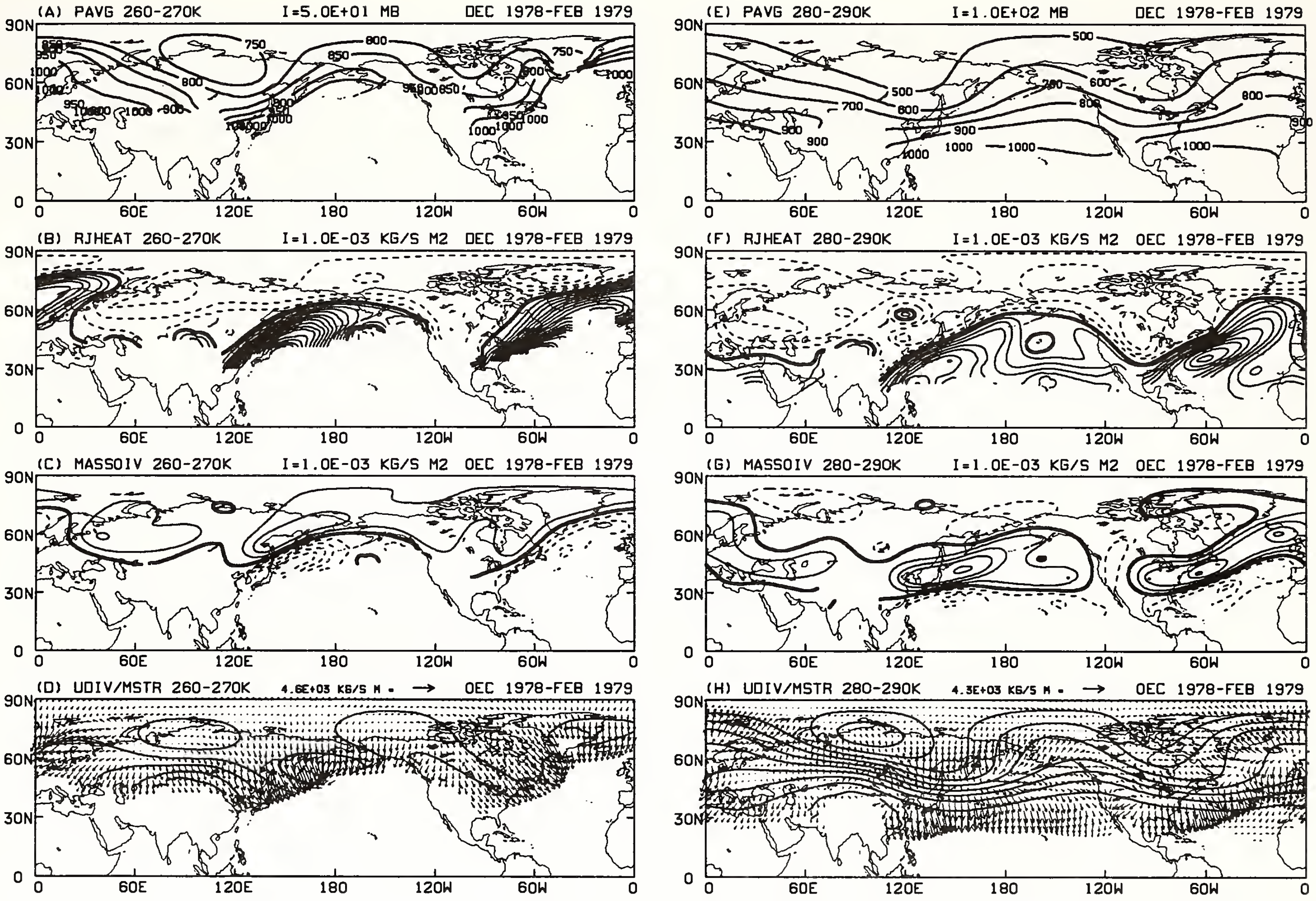
(A) PAVG 260-270K I=5.0E+01 MB DEC 1978-FEB 1979
(B) RJHEAT 260-270K I=1.0E-03 KG/S M2 DEC 1978-FEB 1979
(C) MASSDIV 260-270K I=1.0E-03 KG/S M2 DEC 1978-FEB 1979
(D) UDIV/MSTR 260-270K 4.6E+03 KG/S M → DEC 1978-FEB 1979
(E) PAVG 280-290K I=1.0E+02 MB DEC 1978-FEB 1979
(F) RJHEAT 280-290K I=1.0E-03 KG/S M2 DEC 1978-FEB 1979
(G) MASSDIV 280-290K I=1.0E-03 KG/S M2 DEC 1978-FEB 1979
(H) UDIV/MSTR 280-290K 4.3E+03 KG/S M → DEC 1978-FEB 1979
90N
60N
30N
0
0
60E
120E
180
120W
60W
0

Fig. 1. Time-averaged values for December 1978–February 1979 of (A) 260-270K layer average pressure (50 mb), (B) 260-270K diabatic mass transport ($1\times10^{-3}$ kg $s^{-1}$ $m^{-2}$), (C) 260-270K layer integrated mass divergence ($1\times10^{-3}$ kg $s^{-1}$ $m^{-2}$), (D) 260-270K layer integrated irrotational mass transport vectors (kg $s^{-1}$ $m^{-1}$), and Montgomery streamfunction (500 $m^2$ $s^{-2}$), (E) 280-290K layer average pressure (100 mb), (F) 280-290K diabatic mass transport ($1\times10^{-3}$ kg $s^{-1}$ $m^{-2}$), (G) 280-290K layer integrated mass divergence ($1\times10^{-3}$ kg $s^{-1}$ $m^{-2}$), and (H) 280-290K layer integrated irrotational mass transport vectors (kg $s^{-1}$ $m^{-1}$), and Montgomery streamfunction (500 $m^2$ $s^{-2}$). In (B), (C), (F), and (G), positive values are solid, negative values are dashed, and the zero line is bold. Contours not drawn where each layer is underground.

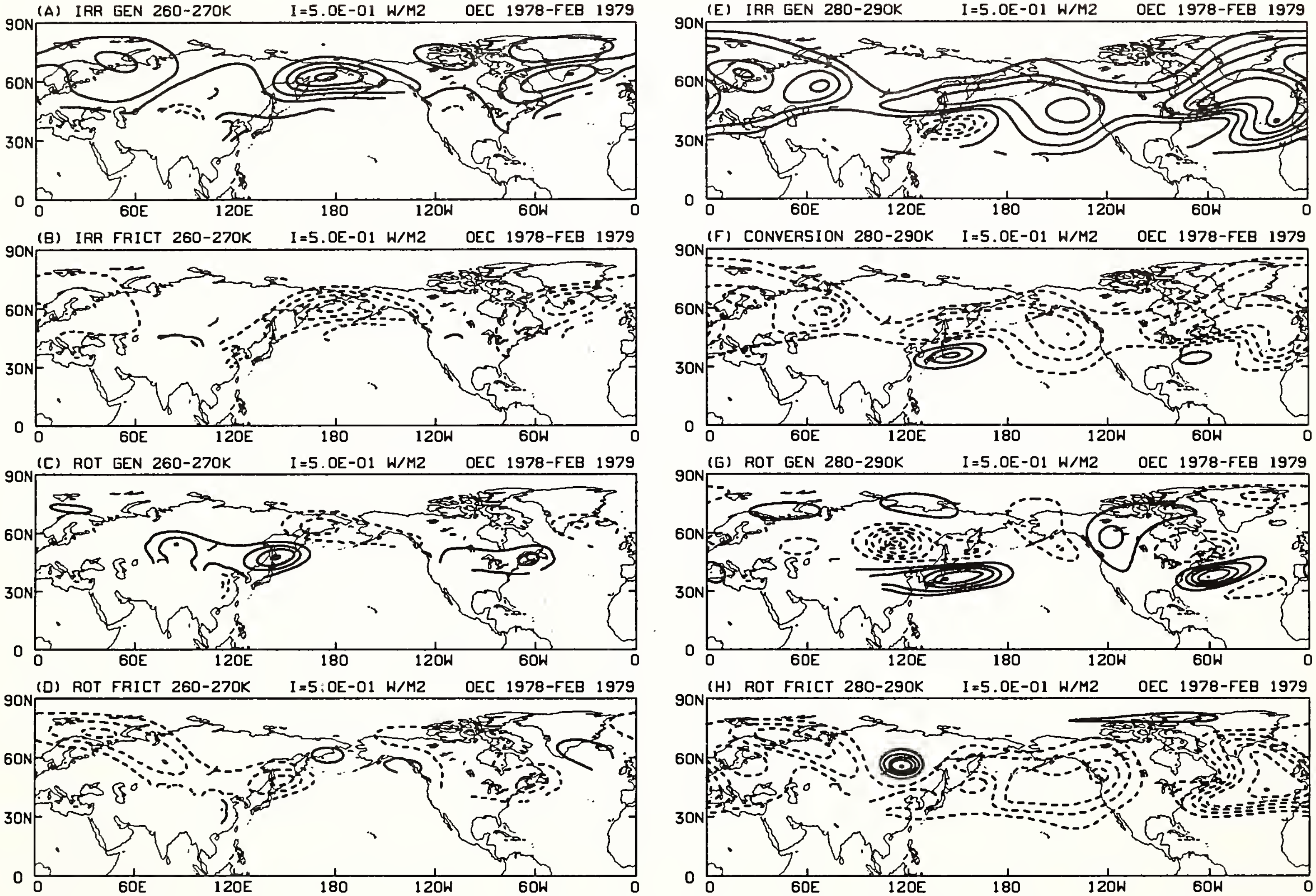
(A) IRR GEN 260-270K I=5.0E-01 W/M2 OEC 1978-FEB 1979
(B) IRR FRICT 260-270K I=5.0E-01 W/M2 OEC 1978-FEB 1979
(C) ROT GEN 260-270K I=5.0E-01 W/M2 OEC 1978-FEB 1979
(D) ROT FRICT 260-270K I=5.0E-01 W/M2 OEC 1978-FEB 1979
(E) IRR GEN 280-290K I=5.0E-01 W/M2 OEC 1978-FEB 1979
(F) CONVERSION 280-290K I=5.0E-01 W/M2 OEC 1978-FEB 1979
(G) ROT GEN 280-290K I=5.0E-01 W/M2 OEC 1978-FEB 1979
(H) ROT FRICT 280-290K I=5.0E-01 W/M2 OEC 1978-FEB 1979
90N
60N
30N
0
60E
120E
180
120W
60W

Fig. 2. Time-averaged energy conversions for December 1978–February 1979. (A) 260-270K irrotational kinetic energy generation (0.5 W $m^{-2}$), (B) 260-270K irrotational frictional dissipation (0.5 W $m^{-2}$), (C) 260-270K rotational kinetic energy generation (0.5 W $m^{-2}$), (D) 260-270K rotational frictional dissipation (0.5 W $m^{-2}$), (E) 280-290K irrotational kinetic energy generation (0.5 W $m^{-2}$), (F) 280-290K conversion from rotational to irrotational kinetic energy (0.5 W $m^{-2}$), (negative values denote conversion from irrotational to rotational kinetic energy), (G) 280-290K rotational kinetic energy generation (0.5 W $m^{-2}$), (H) 280-290K rotational frictional dissipation (0.5 W $m^{-2}$). Positive values are solid, negative values are dashed, and the zero line is suppressed. Contours not drawn where each layer is underground.

* U.S. G.P.O.:1992-313-153:60422

**DATE DUE** SUBJECT TO RECALL

| | | | |
|---|---|---|---|
| | | | |
| SEMESTER | | | |
| ~~APR 2 9 [illegible]~~ | | | |
| | | | |
| | | | |
| | | | |
| | | | |
| | | | |
| | | | |
| | | | |
| | | | |
| | | | |
| | | | |
| | | | |
| | | | |
| | | | |
| | | | |

Demco, Inc. 38-293

A000019272283

A000019272283